frontiers | Research Topics

Organoids, organs-on-chip, nanoparticles and in silico approaches to dissect the tumor-immune dynamics and to unveil the drug resistance mechanisms to therapy in the tumor microenvironment

Edited by
Fabrizio Mattei, Jason T. George and Mohit Kumar Jolly

Published in
Frontiers in Immunology

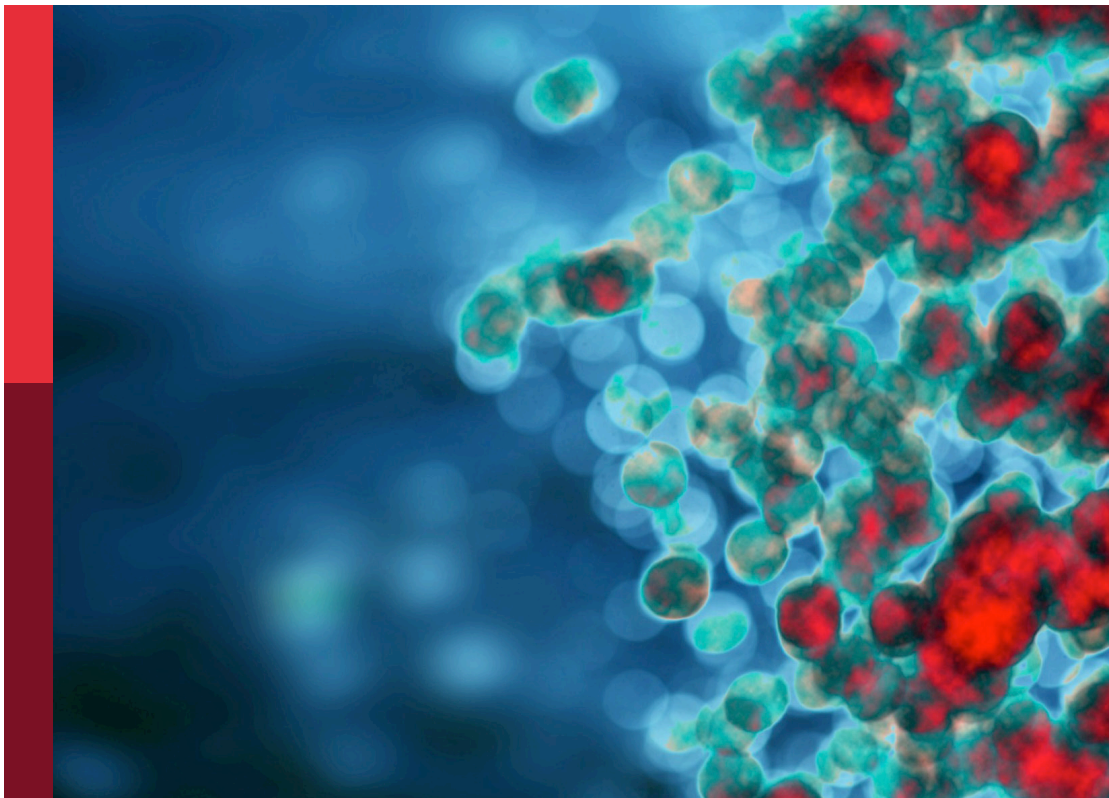

ISSN 1664-8714
ISBN 978-2-8325-3137-2
DOI 10.3389/978-2-8325-3137-2

About Frontiers

Frontiers is more than just an open access publisher of scholarly articles: it is a pioneering approach to the world of academia, radically improving the way scholarly research is managed. The grand vision of Frontiers is a world where all people have an equal opportunity to seek, share and generate knowledge. Frontiers provides immediate and permanent online open access to all its publications, but this alone is not enough to realize our grand goals.

Frontiers journal series

The Frontiers journal series is a multi-tier and interdisciplinary set of open-access, online journals, promising a paradigm shift from the current review, selection and dissemination processes in academic publishing. All Frontiers journals are driven by researchers for researchers; therefore, they constitute a service to the scholarly community. At the same time, the *Frontiers journal series* operates on a revolutionary invention, the tiered publishing system, initially addressing specific communities of scholars, and gradually climbing up to broader public understanding, thus serving the interests of the lay society, too.

Dedication to quality

Each Frontiers article is a landmark of the highest quality, thanks to genuinely collaborative interactions between authors and review editors, who include some of the world's best academicians. Research must be certified by peers before entering a stream of knowledge that may eventually reach the public - and shape society; therefore, Frontiers only applies the most rigorous and unbiased reviews. Frontiers revolutionizes research publishing by freely delivering the most outstanding research, evaluated with no bias from both the academic and social point of view. By applying the most advanced information technologies, Frontiers is catapulting scholarly publishing into a new generation.

What are Frontiers Research Topics?

Frontiers Research Topics are very popular trademarks of the *Frontiers journals series*: they are collections of at least ten articles, all centered on a particular subject. With their unique mix of varied contributions from Original Research to Review Articles, Frontiers Research Topics unify the most influential researchers, the latest key findings and historical advances in a hot research area.

Find out more on how to host your own Frontiers Research Topic or contribute to one as an author by contacting the Frontiers editorial office: frontiersin.org/about/contact

Organoids, organs-on-chip, nanoparticles and in silico approaches to dissect the tumor-immune dynamics and to unveil the drug resistance mechanisms to therapy in the tumor microenvironment

Topic editors

Fabrizio Mattei — National Institute of Health (ISS), Italy

Jason T. George — Texas A and M University, United States

Mohit Kumar Jolly — Indian Institute of Science (IISc), India

Citation

Mattei, F., George, J. T., Jolly, M. K., eds. (2023). *Organoids, organs-on-chip, nanoparticles and in silico approaches to dissect the tumor-immune dynamics and to unveil the drug resistance mechanisms to therapy in the tumor microenvironment*. Lausanne: Frontiers Media SA.

doi: 10.3389/978-2-8325-3137-2

Table of contents

05 Editorial: Organoids, organs-on-chip, nanoparticles and *in silico* approaches to dissect the tumor-immune dynamics and to unveil the drug resistance mechanisms to therapy in the tumor microenvironment
Fabrizio Mattei, Jason T. George and Mohit Kumar Jolly

09 Developing a 3D B Cell Lymphoma Culture System to Model Antibody Therapy
Russell Foxall, Priyanka Narang, Bridget Glaysher, Elin Hub, Emma Teal, Mark C. Coles, Margaret Ashton-Key, Stephen A. Beers and Mark S. Cragg

29 Advances in Modeling the Immune Microenvironment of Colorectal Cancer
Paul Sukwoo Yoon, Nuala Del Piccolo, Venktesh S. Shirure, Yushuan Peng, Amanda Kirane, Robert J. Canter, Ryan C. Fields, Steven C. George and Sepideh Gholami

39 Co-Stimulatory Bispecific Antibodies Induce Enhanced T Cell Activation and Tumor Cell Killing in Breast Cancer Models
Karsten M. Warwas, Marten Meyer, Márcia Gonçalves, Gerhard Moldenhauer, Nadja Bulbuc, Susanne Knabe, Claudia Luckner-Minden, Claudia Ziegelmeier, Claus Peter Heussel, Inka Zörnig, Dirk Jäger and Frank Momburg

61 Multi-Omics Analysis for Transcriptional Regulation of Immune-Related Targets Using Epigenetic Data: A New Research Direction
Chenshen Huang, Na Zhang, Hao Xiong, Ning Wang, Zhizhong Chen, Zhizhan Ni, Xiaohong Liu, Boxu Lin, Bujun Ge, Bing Du and Qi Huang

74 Organoid Models for Precision Cancer Immunotherapy
Cai-Ping Sun, Huan-Rong Lan, Xing-Liang Fang, Xiao-Yun Yang and Ke-Tao Jin

84 Identification of epigenetic dysregulation gene markers and immune landscape in kidney renal clear cell carcinoma by comprehensive genomic analysis
Linli Xie, Shuang Wu, Rong He, Sisi Li, Xiaodan Lai and Zhe Wang

104 3D cancer models: One step closer to *in vitro* human studies
Nicoletta Manduca, Ester Maccafeo, Ruggero De Maria, Antonella Sistigu and Martina Musella

122 Intersection of nanomaterials and organoids technology in biomedicine
Chen Shen, Zi-jian Zhang, Xiao-xue Li, Yun-peng Huang, Yong-xiang Wang, Hui Zhou, Li Xiong, Yu Wen, Heng Zou and Zhong-tao Liu

136 The tumor stroma influences immune cell distribution and recruitment in a PDAC-on-a-chip model
Marlene Geyer, Lisa-Marie Gaul, Sabrina Luigia D`Agosto, Vincenzo Corbo and Karla Queiroz

148 Data driven model discovery and interpretation for CAR T-cell killing using sparse identification and latent variables
Alexander B. Brummer, Agata Xella, Ryan Woodall, Vikram Adhikarla, Heyrim Cho, Margarita Gutova, Christine E. Brown and Russell C. Rockne

166 Incorporating lesion-to-lesion heterogeneity into early oncology decision making
Rukmini Kumar, Timothy Qi, Yanguang Cao and Brian Topp

175 *In vitro* models to study natural killer cell dynamics in the tumor microenvironment
Valentina Carannante, Martin Wiklund and Björn Önfelt

frontiers | Frontiers in Immunology

TYPE Editorial
PUBLISHED 18 July 2023
DOI 10.3389/fimmu.2023.1253551

OPEN ACCESS

EDITED AND REVIEWED BY
Fabio Malavasi,
University of Turin, Italy

*CORRESPONDENCE
Fabrizio Mattei
fabrizio.mattei@iss.it

RECEIVED 05 July 2023
ACCEPTED 10 July 2023
PUBLISHED 18 July 2023

CITATION
Mattei F, George JT and Jolly MK (2023) Editorial: Organoids, organs-on-chip, nanoparticles and *in silico* approaches to dissect the tumor-immune dynamics and to unveil the drug resistance mechanisms to therapy in the tumor microenvironment. *Front. Immunol.* 14:1253551.
doi: 10.3389/fimmu.2023.1253551

Editorial: Organoids, organs-on-chip, nanoparticles and *in silico* approaches to dissect the tumor-immune dynamics and to unveil the drug resistance mechanisms to therapy in the tumor microenvironment

Fabrizio Mattei[1]*, Jason T. George[2] and Mohit Kumar Jolly[3]

[1]Department of Oncology and Molecular Medicine, Istituto Superiore di Sanità, Rome, Italy, [2]Department of Biomedical Engineering, Texas A&M University, College Station, TX, United States, [3]Center for BioSystems Science and Engineering, Indian Institute of Science, Bangalore, India

KEYWORDS

preclinical models, advanced *in vitro* models, 3D models, advanced algorithms for immuno-oncology, personalized medicine for cancer patients, organs-on-chip platforms, nanotechnologies, drug delivery

Editorial on the Research Topic:

Organoids, organs-on-chip, nanoparticles and *in silico* approaches to dissect the tumor-immune dynamics and to unveil the drug resistance mechanisms to therapy in the tumor microenvironment

The relationships between cancer and immune system are under intense investigation and have currently made giant steps thanks to the great development of advanced *in vitro* models as useful preclinical systems (1–4). Advanced models of study represent a large set of tools that are important for enabling scientists to study in detail specific biological events, including those related to the multifaceted dynamics of the tumor microenvironment (TME) and the associated phenomena such as drug resistance and crosstalk between cancer and immune cells.

In this Research Topic we collected a set of key articles (6 Research papers and 6 Review articles) exploring diverse aspects of the TME. Advanced models of study, such as *in vitro* 3D models, Organs-on-Chip (OOC), and mathematical algorithms for onco-immunology applications, including multi-omics models, have been discussed in these articles.

In their Research article, Brummer et al. proposed a quantitative advanced mathematical model based on Sparse Identification of Non-linear Dynamics (SINDy) algorithm (5), applied to a real biological system in order to discover cell-cell interaction dynamics in *in vitro* experimental data. They employed such a model to specifically investigate the interaction dynamics of CAR T-cell populations and glioblastoma. In the future, this model may be applied to optimize the efficacy of CAR-T-based therapies in aggressive and inoperable tumors such as glioblastoma.

Carannante et al. contributed a Review on how *in vitro* 3D systems can be further implemented to reach high-fidelity recapitulation of the tumor microenvironment to study the activity of Natural Killer (NK) cells. NK cells are key actors participating in cancer immunosurveillance and maintaining tissue homeostasis (6). The Authors proposed multiple ways to implement the existing 3D platforms to develop spheroids and organoids, useful to generate specific systems allowing researchers to monitor in real time the NK behavior (i.e., Caspase activity within spheroids, quantitative evaluation of NK infiltration into spheroids) and NK-based therapeutic efficacy.

Foxall et al. developed a 3D spheroid model for real time monitoring of antibody-specific therapy in diffuse large cell B cell lymphoma (DLBCL). This neoplastic disease is one of the most common types of non-Hodgkin lymphoma (7). This advanced 3D model was shown to be a reliable tool to investigate how cancer-associated fibroblasts (CAFs) and tumor-associated macrophages (TAMs), important constituents of the TME, interact with DLBCL. This model accurately recapitulates key features of the DLBCL TME necessary for elucidating TAM-CAF direct and indirect crosstalk.

Pancreatic ductal adenocarcinoma (PDAC) is an aggressive type of cancer (8) for which Geyer et al. evaluated the impact of the tumor stromal components on immune cell distribution and recruitment in a PDAC advanced preclinical model. The dense stromal microenvironment of PDAC creates a barrier for immune cell infiltration and poses a challenge for immunotherapeutic strategies. The study establishes a 3D PDAC model cultured under flow, consisting of an endothelial channel, pancreatic stellate cells (PSCs), and PDAC organoids, to investigate the role of the TME on immune cell recruitment. The findings suggest that stromal cells form a physical barrier and a biochemical microenvironment that influences immune cell distribution. Additionally, targeting the stroma led to an increase in immune cell infiltration. This study highlights the potential of this model for contributing to understanding the cellular interactions and identifying key players in the immunosuppressive moiety of PDAC.

In their Research article, Huang et al. exploited a multi-omics approach to evaluate transcriptional and epigenetic regulation of GPRC5B, a G protein-coupled receptor (GPCR) (9) associated to macrophages activity. In their proposed pipeline, the Authors used a model employing RNA sequencing (RNA-seq) assay for transposase-accessible chromatin using sequencing (ATAC-seq) and chromatin immunoprecipitation with high-throughput sequencing (ChIP-seq). They were able to show that GPRC5B represent a central GPCR for colon adenocarcinoma prognosis by direct modulation of the transcription factor (TF) GATA4. This study is a representative example on the usefulness of multi-omics approaches for TF investigations to optimize cancer therapy.

Xie et al. showed a Research article on kidney renal clear cell carcinoma (KIRC), one of the most lethal tumors of the urinary tract, with limited treatment solutions and poor prognosis (10). By using the R Limma package, the Authors exploited a multi-omics approach to find associations between prognosis and epigenetic modifications in KIRC patients. Of note, they identified a set (8 genes) of dysregulated epigenetic protein coding genes (epi-PCGs) (11) that can be successfully employed to evaluate KIRC prognosis. Specifically, such a signature predicted a strong association with KIRC prognosis. Indeed, patients with a high signature score experienced significantly worse clinical trajectories than those with a low score, thus suggesting that the use of a restricted epi-PCG gene set could provide a useful prognostic signature to investigate on pathological mechanisms of KIRC. This is an important prerequisite for developing novel and efficacious KIRC-specific drug targets.

In their Perspective article, Kumar et al. debated the value of commonly used response grading criteria in early oncology trials, namely the Response Evaluation Criteria In Solid Tumors (RECIST), version 1.1 (v1.1) (12). The Authors argue that RECISTv1.1 is ambiguous regarding lesion-to-lesion variation and can introduce bias in decision-making problems. They provided theoretical examples of how lesion-to-lesion variability can lead to misclassification of patient response. The Authors review immune checkpoint inhibitor (ICI) clinical trial data and find that lesion-to-lesion heterogeneity is widespread in ICI-treated patients. They then conclude that the incorporation of lesion-to-lesion heterogeneity through Quantitative Systems Pharmacology (QSP) models can constitute a complementary implementation to the RECISTv1.1 model. Therefore, ameliorating decision-making processes in early-stage oncology drug development can lead to key benefits in cancer patient care.

Manduca et al. contributed a Review article overviewing the current advanced *in vitro* models utilized to investigate on the interactions between immune and cancer cells to better recapitulate the complexity of the TME dynamics (3, 13–15). The Authors also discussed advantages and disadvantages of employing complex *in vitro* systems such as spheroids, organoids and organs-on-chip platforms (OOC). Accessibility versus fidelity represent two central parameters to appropriately chose the ideal platform to study a specific TME event. Simultaneous control of many relevant biological factors facilitates the use of accessible systems, such as spheroids or organoids, whereas if one intends to reproduce an event occurring in the TME, the use of OOC platforms is highly beneficial due to its high-fidelity recapitulation of the TME events. This article highlights that advanced *in vitro* systems are invaluable tools for studying the TME, considering that it is both very difficult and expensive to analogously do so *in vivo*.

Shen et al. proposed a review article overviewing the impact of the nanomaterials and the associated bioprinting methods in the use of organoids and spheroids. Nanomaterials can represent a very useful architectural implementation when generating organoids or spheroids in 3D culture systems, which can assist to better maintain the unit stability, affordability, and recapitulation fidelity (16). For example, a new methodology based on the use of neodymium magnets (17) is debated, which allows spheroids to be developed under the action of magnetic fields. Nanomaterials are also used to improve the efficiency of drug delivery and screening in spheroids and organoid units. Therefore, using specific types of nanomaterials can be very useful for the development of high-fidelity and highly accessible spheroid/organoid units, which can be properly optimized to recapitulate specific events of the TME.

In a Review article, Sun et al. provided an exhaustive overview of the various culture methods for tumor organoids (18) to study

the complexity of the TME and to emulate their associated dynamics. Specifically, they debated the pros and cons of three main culture techniques, namely submerged Matrigel culture, air-liquid interface culture, and microfluidic 3D culture. They also discussed on how these different organoid culture methods can be applied to evaluate immunotherapeutic strategies, such as adoptive cell transfer, ICI and other antibody-based therapies. Collectively, these approaches represent promising tools for personalized medicine in cancer.

Warwas et al. proposed a Research article in which the use of co-stimulatory bispecific antibodies (BiMAb) (19) in breast cancer models has been addressed to enhance T cell activation and tumor cell killing. The study analyzed various BiMAb targeting breast cancer antigens and bi-functional fusion proteins targeting tumor necrosis factor ligand (TNFL) superfamily members. The functional activity of the BiMAb was assessed using tumor cell lines and purified T cells in monolayer and tumor spheroid models. The results showed that the combination treatment of BiMAb with co-stimulatory antibodies significantly enhanced T cell activation, proliferation, cytokine secretion, and tumor cytotoxicity. Co-stimulation also overcame the immunosuppressive effects of TGF-β and IL-10. The study suggests that co-stimulatory BiMAb, assayed in advanced tumor models of study (spheroids), could provide a more localized and effective activation of the immune system in breast cancer treatment.

In their Review article, Yoon et al. discussed the advancements made in the culture methods for colorectal cancer (CRC). CRC currently represents one of the most widespread type of solid malignancy (20). Here, the pros and cons associated to 2D, 3D, and complex preclinical models (including OOCs), have been reported in detail for CRC in order to reflect on the optimal way to recapitulate and investigate the CRC TME. Their rational and optimized use (i.e., exact type of cells and hydrogel to be loaded in the OOC; defined microstructure of the OOC) constitutes a crucial step in studying the immune microenvironment of CRC and evaluating the effectiveness of immunotherapies.

In conclusion, this Editorial represents a relevant reference to those researchers specifically interested in developing novel ideas based on the use of new preclinical advanced models (such as organoids and OOCs), algorithms based on multi-omics approaches and drug delivery nanotechnologies to be applied in immuno-oncology. These systems represent promising biotools for TME mimicking studies and for the optimization of cancer therapy strategies in the context of cancer patient's personalized medicine.

Author contributions

All authors listed have made a substantial, direct, and intellectual contribution to the work and approved it for publication.

Funding

FM is supported by two grants from NextGenerationEU/MUR/PNRR: Project "HEAL ITALIA" (PE00000019, Miss.4, Comp.2, Invest.1.3, years 2022-2025) and Project "Rome Technopole Foundation" (ECS00000024, Miss.4, Comp.2, Invest.1.5, years 2022-2025). JG is supported by the Cancer Prevention and Research Institute of Texas (CPRIT RR210080). JTG is a CPRIT Scholar in Cancer Research. MJ is supported by Ramanujan Fellowship (SB/S2/RJN-049/2018) awarded by Science and Research Board, Government of India.

Conflict of interest

The authors declare that the research was conducted in the absence of any commercial or financial relationships that could be construed as a potential conflict of interest.

Publisher's note

References

1. Maulana TI, Kromidas E, Wallstabe L, Cipriano M, Alb M, Zaupa C, et al. Immunocompetent cancer-on-chip models to assess immuno-oncology therapy. *Adv Drug Delivery Rev* (2021) 173:281–305. doi: 10.1016/j.addr.2021.03.015

2. Candarlioglu PL, Dal Negro G, Hughes D, Balkwill F, Harris K, Screen H, et al. Organ-on-a-chip: current gaps and future directions. *Biochem Soc Trans* (2022) 50 (2):665–73. doi: 10.1042/BST20200661

3. Mattei F, Andreone S, Mencattini A, De Ninno A, Businaro L, Martinelli E, et al. Oncoimmunology meets organs-on-chip. *Front Mol Biosci* (2021) 8:627454. doi: 10.3389/fmolb.2021.627454

4. Ravi VM, Will P, Kueckelhaus J, Sun N, Joseph K, Salié H, et al. Spatially resolved multi-omics deciphers bidirectional tumor-host interdependence in glioblastoma. *Cancer Cell* (2022) 40(6):639–655.e13. doi: 10.1016/j.ccell.2022.05.009

5. Kaheman K, Kutz JN, Brunton SL. SINDy-PI: a robust algorithm for parallel implicit sparse identification of nonlinear dynamics. *Proc Math Phys Eng Sci* (2020) 476 (2242):20200279. doi: 10.1098/rspa.2020.0279

6. Vivier E, Artis D, Colonna M, Diefenbach A, Di Santo JP, Eberl G, et al. Innate lymphoid cells: 10 years on. *Cell* (2018) 174(5):1054–66. doi: 10.1016/j.cell.2018.07.017

7. Chaganti S, Illidge T, Barrington S, Mckay P, Linton K, Cwynarski K, et al. Guidelines for the management of diffuse large B-cell lymphoma. *Br J Haematol* (2016) 174(1):43–56. doi: 10.1111/bjh.14136

8. Kuznetsova A, Popova O, Panchenkov D, Dyuzheva T, Ivanov A. Pancreatic ductal adenocarcinoma: tumor microenvironment and problems in the development of novel therapeutic strategies. *Clin Exp Med* (2023) 23(3):619–43. doi: 10.1007/s10238-022-00886-1

9. Wu V, Yeerna H, Nohata N, Chiou J, Harismendy O, Raimondi F, et al. Illuminating the Onco-GPCRome: Novel G protein-coupled receptor-driven oncocrine networks and targets for cancer immunotherapy. *J Biol Chem* (2019) 294 (29):11062–86. doi: 10.1074/jbc.REV119.005601

10. Su J, Zhou L, Zhang Z, Xiao X, Qin Y, Zhou X, et al. The components of tumor microenvironment as biomarker for immunotherapy in metastatic renal cell carcinoma. *Front Immunol* (2023) 14:1146738. doi: 10.3389/fimmu.2023.1146738

11. Nicetto D, Donahue G, Jain T, Peng T, Sidoli S, Sheng L, et al. H3K9me3-heterochromatin loss at protein-coding genes enables developmental lineage specification. *Science* (2019) 363(6424):294–7. doi: 10.1126/science.aau0583

12. Mottin L, Goldman JP, Jäggli C, Achermann R, Gobeill J, Knafou J, et al. Multilingual RECIST classification of radiology reports using supervised learning. *Front Digit Health* (2023) 5:1195017. doi: 10.3389/fdgth.2023.1195017

13. Lucarini V, Buccione C, Ziccheddu G, Peschiaroli F, Sestili P, Puglisi R, et al. Combining type I interferons and 5-aza-2'-deoxycitidine to improve anti-tumor response against melanoma. *J Invest Dermatol* (2017) 137(1):159–69. doi: 10.1016/j.jid.2016.08.024

14. Vacchelli E, Ma Y, Baracco EE, Sistigu A, Enot DP, Pietrocola F, et al. Chemotherapy-induced antitumor immunity requires formyl peptide receptor 1. *Science* (2015) 350(6263):972–8. doi: 10.1126/science.aad0779

15. Musella M, Guarracino A, Manduca N, Galassi C, Ruggiero E, Potenza A, et al. Type I IFNs promote cancer cell stemness by triggering the epigenetic regulator KDM1B. *Nat Immunol* (2022) 23(9):1379–92. doi: 10.1038/s41590-022-01290-3

16. Moghaddam AS, Khonakdar HA, Arjmand M, Jafari SH, Bagher Z, Moghaddam ZS, et al. Review of bioprinting in regenerative medicine: naturally derived bioinks and stem cells. *ACS Appl Bio Mater* (2021) 4(5):4049–70. doi: 10.1021/acsabm.1c00219

17. Yuksel C, Ankarali S, Yuksel NA. The use of neodymium magnets in healthcare and their effects on health. *North Clin Istanb* (2018) 5(3):268–73. doi: 10.14744/nci.2017.00483

18. Devarasetty M, Forsythe SD, Shelkey E, Soker S. *In vitro* modeling of the tumor microenvironment in tumor organoids. *Tissue Eng Regener Med* (2020) 17(6):759–71. doi: 10.1007/s13770-020-00258-4

19. Hoseini SS, Cheung NV. Immunotherapy of hepatocellular carcinoma using chimeric antigen receptors and bispecific antibodies. *Cancer Lett* (2017) 399:44–52. doi: 10.1016/j.canlet.2017.04.013

20. Siegel RL, Wagle NS, Cercek A, Smith RA, Jemal A. Colorectal cancer statistics, 2023. *CA Cancer J Clin* (2023) 73(3):233–54. doi: 10.3322/caac.21772

frontiers in Immunology

ORIGINAL RESEARCH
published: 08 February 2021
doi: 10.3389/fimmu.2020.605231

Developing a 3D B Cell Lymphoma Culture System to Model Antibody Therapy

Russell Foxall[1], Priyanka Narang[1], Bridget Glaysher[2], Elin Hub[2], Emma Teal[1], Mark C. Coles[2,3], Margaret Ashton-Key[1,4], Stephen A. Beers[1†] and Mark S. Cragg[1*†]*

[1] Antibody and Vaccine Group, Centre for Cancer Immunology, School of Cancer Sciences, University of Southampton Faculty of Medicine, Southampton, United Kingdom, [2] Centre for Immunology and Infection, University of York, York, United Kingdom, [3] Nuffield Department of Orthopedics, Rheumatology and Musculoskeletal Sciences, Kennedy Institute of Rheumatology, University of Oxford, Oxford, United Kingdom, [4] Department of Cellular Pathology, Southampton University Hospital Trust, Southampton, United Kingdom

OPEN ACCESS

Edited by:
Fabio Malavasi, University of Turin, Italy

Reviewed by:
Zoltan Vereb, University of Szeged, Hungary
Gianluca Gaidano, Università degli Studi del Piemonte Orientale, Italy

***Correspondence:**
Stephen A. Beers
s.a.beers@soton.ac.uk
Mark S. Cragg
m.s.cragg@soton.ac.uk

†These authors share senior authorship

Specialty section:
This article was submitted to Cancer Immunity and Immunotherapy, a section of the journal Frontiers in Immunology

Received: *11 September 2020*
Accepted: *16 December 2020*
Published: *08 February 2021*

Citation:
Foxall R, Narang P, Glaysher B, Hub E, Teal E, Coles MC, Ashton-Key M, Beers SA and Cragg MS (2021) Developing a 3D B Cell Lymphoma Culture System to Model Antibody Therapy. Front. Immunol. 11:605231. doi: 10.3389/fimmu.2020.605231

Diffuse large cell B cell lymphoma (DLBCL) accounts for approximately 30%–40% of all non-Hodgkin lymphoma (NHL) cases. Current first line DLBCL treatment results in long-term remission in more than 60% of cases. However, those patients with primary refractory disease or early relapse exhibit poor prognosis, highlighting a requirement for alternative therapies. Our aim was to develop a novel model of DLBCL that facilitates *in vitro* testing of current and novel therapies by replicating key components of the tumor microenvironment (TME) in a three-dimensional (3D) culture system that would enable primary DLBCL cell survival and study *ex vivo*. The TME is a complex ecosystem, comprising malignant and non-malignant cells, including cancer-associated fibroblasts (CAF) and tumor-associated macrophages (TAM) whose reciprocal crosstalk drives tumor initiation and growth while fostering an immunosuppressive milieu enabling its persistence. The requirement to recapitulate, at least to some degree, this complex, interactive network is exemplified by the rapid cell death of primary DLBCL cells removed from their TME and cultured alone *in vitro*. Building on previously described methodologies to generate lymphoid-like fibroblasts from adipocyte derived stem cells (ADSC), we confirmed lymphocytes, specifically B cells, interacted with this ADSC-derived stroma, in the presence or absence of monocyte-derived macrophages (MDM), in both two-dimensional (2D) cultures and a 3D collagen-based spheroid system. Furthermore, we demonstrated that DLBCL cells cultured in this system interact with its constituent components, resulting in their improved viability as compared to *ex-vivo* 2D monocultures. We then assessed the utility of this system as a platform to study therapeutics in the context of antibody-directed phagocytosis, using rituximab as a model

immunotherapeutic antibody. Overall, we describe a novel 3D spheroid co-culture system comprising key components of the DLBCL TME with the potential to serve as a testbed for novel therapeutics, targeting key cellular constituents of the TME, such as CAF and/or TAM.

Keywords: diffuse large B cell lymphoma, antibody therapy, adipocyte derived stem cell, cancer associated fibroblast, tumor associated macrophage, 3D co-culture model

INTRODUCTION

Diffuse large cell B cell lymphoma (DLBCL) is the most common type of non-Hodgkin lymphoma (NHL); accounting for approximately 30%–40% of cases (1). Classically, it is sub-categorized into germinal-center B cell-like (GCB) and activated B cell-like (ABC) entities, based on cell-of-origin and gene expression profiling (GEP) (2), with ABC DLBCL associated with substantially worse outcomes with current treatments (3). Recently, more detailed genetic analyzes, indicate a third sub-type (type 3/unclassified) (2) suggesting DLBCL is actually a constellation of related, but genetically disparate diseases (4, 5). Current first line treatment for DLBCL involves Immunochemotherapy, with an anti-CD20 monoclonal antibody (mAb), usually rituximab, in combination with cyclophosphamide, doxorubicin, vincristine and prednisolone (R-CHOP) (1) which results in long-term remission in more than 60% of cases. However, in a subset of patients, the prognosis remains poor, highlighting an unmet need for alternative therapeutic approaches (6, 7). Furthermore, despite growing knowledge of the under-pinning mutations and oncogenic drivers in DLBCL, new targeted therapeutics have so far failed to deliver improved clinical outcomes, highlighting a need for better models to study DLBCL.

Our aim was to develop a 3D model that was both able to recreate *in vitro*, to some degree, the DLBCL tumor environment (TME), and provide a suitable platform for the testing of therapeutic agents. It is important to note that the TME is a complex ecosystem comprising a mixture of malignant and non-malignant cells residing within an extracellular matrix (ECM). Regarding lymphomas, the complexity of the TME varies according to type. Scott and Gascoyne (8) proposed three models to describe these differences, with DLBCL falling between the re-education model typified by follicular lymphoma (FL) and the effacement model exemplified by Burkitt lymphoma (BL).

Key cellular components of the TME include cancer-associated fibroblasts (CAF) and tumor-associated macrophages (TAM) whose reciprocal cross-talk, combined with their interaction with other TME constituents, sculpt the natural history of the disease. CAF comprise an heterogeneous cell population originating from a variety of sources (9, 10). The interactions between CAF and other cellular constituents of the TME, mediated *via* chemical and mechanical signaling, are key to tumor establishment and maintenance (9). Under normal conditions, a clear inter-relationship exists between B cells and the fibro-reticular network, (FRN) of secondary lymphoid organs. This is also observed in pathological conditions (11), particularly in lymphoma and during the formation of tertiary lymphoid structures in the context of inflammation (12). In the case of FL, cross talk between tumor cells and cells of the local FRN drives their differentiation into tumor-supporting lymphoid stroma (13). Similarly in DLBCL, malignant cells and non-malignant TME components have been shown to induce cells of the FRN, specifically Fibroblastic Reticular cells (FRC), to adopt a CAF-like phenotype (14, 15). Furthermore, CAF can promote survival of primary lymphoma cells *in-vitro* (14, 16), further highlighting the intimate inter-relationship between CAF and tumor cells in the DLBCL TME. Similarities between CAF and normal lymphoid fibroblasts have also been reported (17), with human tonsil derived primary stromal cell cultures shown to support the survival and proliferation of DLBCL cell lines (18). We selected adipocyte derived stem cells (ADSC) as our source of primary human lymphoid-like fibroblasts, as they have previously been utilized as an *in vitro* model of the lymphoid-stroma polarization associated with follicular lymphoma (FL) (13).

Macrophages are myeloid cells that play key roles in immunity and tissue homeostasis (19). In solid tumors, TAM can originate *via* local proliferation of tissue resident macrophages or from monocytes recruited to it (20, 21). In DLBCL, the origin of TAM remains unclear, although several studies have linked increased circulating monocyte frequencies with poor prognosis (22), suggesting a role for monocytes as TAM precursors. Although an over-simplification, it has been proposed that in established tumors, TAM feature an M2/anti-inflammatory-like phenotype supporting tumor growth and suppressing immune responses; while soluble factors produced by both malignant and non-malignant cells and constituents of the ECM within the TME provide reciprocal support for the TAM [as recently reviewed, (23)]. Of relevance to treatment of DLBCL, it has previously been shown that M2-like macrophages typically feature a lower ratio of activatory:inhibitory (A:I) Fc gamma receptor (FcγR) expression than their pro-inflammatory "M1-like" counterparts (24). Engagement of activatory FcγR on macrophages by mAb such as rituximab is proposed to play a key role in determining their anti-tumor efficacy (25, 26). Therefore, treatments that can increase the A:I FcγR expression ratio have the potential to augment mAb immunotherapy and overcome tumor suppression as we recently demonstrated with STING agonists (24) in mouse models.

Modeling the complex interactions of the TME *in vitro* with primary human material is challenging. Nevertheless, 3D co-culture systems are attractive, allowing the combination of key

cellular populations in an environment that can also recreate, to some degree, the *in vivo* spatial inter-relationships. Several different 3D techniques have been developed, each with their own limitations (27, 28). Scaffolding-based systems offer the flexibility of combining pre-selected cell populations in the context of a 3D matrix. Therefore, we elected to develop a scaffold-based system that would allow the combination of human primary cell populations, including fibroblasts, myeloid cells and tumor cells, within a Type I collagen-based 3D extracellular matrix, with the aim of recapitulating a DLBCL-like TME featuring key cell populations implicated in mediating and modulating the activity of anti-CD20 mAb.

Using this system, we demonstrated that normal and malignant human B cells interact with ADSC-derived human lymphoid-like fibroblasts, in the presence or absence of human monocyte-derived macrophages (MDM), in both 2D and 3D spheroid co-cultures. The latter system augmented DLBCL viability and provided a means to assess immune effector assays using therapeutic mAb. Our data indicate this system has the potential to serve as a testbed for novel therapeutics, targeting key cellular constituents of the TME, such as CAF and/or TAM.

MATERIALS AND METHODS

Primary Human Samples

Ethical approval for the use of human tumor samples was obtained by Southampton University Hospitals NHS Trust from Southampton and South West Hampshire Research Ethics Committee (REC reference 10/H0504/32). Diffuse large B cell lymphoma (DLBCL) cells were acquired from the Human Tissue Authority-licensed School of Cancer Sciences tissue bank at the University of Southampton under ethically approved study (REC reference 228/02/t). Peripheral blood mononuclear cells (PBMC) were obtained from anonymized leucocyte cones from the National Blood Service (Southampton U.K.) and processed within 4 h of preparation. Ethical approval for using human leukocyte cones was obtained by the Southampton University Hospitals NHS Trust from the East of Scotland Research Ethics Committee (REC reference 16/ES/0048). Informed consent was provided in accordance with the Declaration of Helsinki for all samples.

Cell Preparation

PBMC were isolated from leukocyte cones by density gradient centrifugation (Lymphoprep, Axis-Shield, UK). For some experiments, B and T cells were isolated from PBMC using untouched B cell, or Pan-T cell kits, respectively (Miltenyi Biotec, UK). A proportion of PBMC were frozen down in 10% Dimethyl sulfoxide (DMSO) and 90% Fetal Calf serum (FCS, both from Sigma, UK) and stored in liquid nitrogen until required. Frozen PBMC were thawed, washed and counted. Cell viability, determined with trypan blue (Sigma, UK), was typically >90%. Primary human monocyte derived macrophages (MDM) were generated from fresh PBMC as previously described (26). Primary DLBCL samples were thawed, washed, then rested for 1 h at 37°C/5% CO_2 prior to dead cell removal *via* density gradient centrifugation. Recovered cells were counted and viability determined with trypan blue (typically >95%). StemPro™ Human Adipose-Derived Stem Cells (ADSC) were purchased from Thermofisher scientific, UK and stored in liquid nitrogen until use. ADSC were cultured in MesenPRO RS™ medium containing the provided supplement (MesenPRO, GIBCO™, Thermofisher Scientific, UK) according to the manufacturer's instructions. Low passage number ADSC were generated for use in subsequent experiments, frozen down and stored in liquid nitrogen until required. TrypLE™ Express enzyme (GIBCO™, Thermofisher Scientific, UK) was used to detach ADSC from flasks/wells (see **Supplementary Table 1** for volume). The number of cells used to seed flasks/plates (obtained from Corning, UK) is provided in **Supplementary Table 1**.

Cell Staining and Flow Cytometry

Cells were washed and stained with combinations of fluorescently-labeled antibodies (see **Supplementary Table 2** for details of antibody clones and suppliers) on ice for 30 min, washed, fixed (in a 1:10 dilution of red blood cell lysis solution, Biorad, UK), and washed again. Labeled cells were stored at +4°C, protected from light, and run on the indicated flow cytometer within 24 h of staining.

Flow Cytometry Analysis

Harvested cells were washed, stained with Fluorochrome-labeled antibodies and run on a FACSCANTO II (BD Biosciences, UK). Doublets were excluded using side scatter (SSC) and Forward scatter (FSC) height and width, and single cells gated for further analysis.

ADSC-derived fibroblasts were identified as CD45- single cells; differentiation of ADSC in response to each cytokine alone or in combination was determined by the expression of the lymphoid fibroblast markers podoplanin, vascular cell adhesion molecule 1 (VCAM-1, CD106) and intercellular adhesion molecule 1 (ICAM-1, CD54) relative to untreated ADSC. Results are shown as geometric mean fluorescent intensity (MFI).

All flow cytometry analysis was carried out using the FCS express software package (Version 3 Research Edition, Denovo software, USA).

Adipocyte-Derived Stem Cell Differentiation

Adipocyte derived stem cells (ADSC) were differentiated into lymphoid-like fibroblasts according to the protocol designed by Mark Coles and Bridget Glaysher (29) and subsequently developed as an *in vitro* model of Follicular Lymphoma (FL)-associated lymphoid-stroma polarization (13). ADSC were thawed and cultured until approximately 90% confluent. Cells were harvested and re-plated in 6wp or 12wp in either MesenPRO alone (untreated ADSC) or MesenPRO supplemented with 50 ng/ml IL-4 (in-house), 10 ng/ml TNF-α (Peprotech, UK) or 50 ng/ml Lymphotoxin-α/β (R&D systems, Biotechne, UK), alone or in combination. Plates were cultured for 6 days at 37°C/5% CO_2 and refed at day 3. For immunofluorescence studies 1×10^4 ADSC

were cultured on 13 mm coverslips (Cellpath, UK) in 24 well-plates (wp) for 5 days in MesenPRO medium with/without cytokines (37°C/5% CO_2); immunofluorescent staining was carried out, and images acquired as described below.

Attachment Assay

ADSC were plated in 12wp and cultured for 7 days with/without cytokines. A vial of PBMC was then thawed, washed, counted and viability determined using Trypan blue; only samples with viability ≥80% were used. PBMC were rested for 1 h at 37°C/5% CO_2 prior to use. ADSC cultures were washed, 2×10^6 PBMC/well added and the plates incubated for 2 h (37°C/5% CO_2). After incubation the plates were imaged using phase contrast microscopy (4× and 10× magnification, Olympus CKX41). Plates were gently washed, and their contents harvested using TrypLE™ express. Recovered cells were stained with antibodies against lymphoid fibroblast markers and CD45 and samples run on a FACSCANTO II. Doublets were excluded and single cells gated as described above. The proportion of CD45+ cells in the samples from co-culture wells was determined using a histogram plot, with the cut-off set with isotype control antibodies. ADSC differentiation into lymphoid-like fibroblasts was confirmed by analyzing ADSC cultured with or without cytokines (see **Supplementary Figure 3**).

2D and 3D Co-Culture Assays

ADSC were thawed, washed and counted. T75 Flasks were seeded with ADSC (**Supplementary Table 1**) and cultured for 3 days (37°C/5% CO_2). On day −1 ADSC were harvested, washed, resuspended in MesenPRO, plated in 6wp and cultured overnight (37°C/5% CO_2). On day 0 the various cellular constituents for the co-cultures were prepared (see above) and resuspended in MesenPRO +/− cytokines, to give the required concentrations (see below) and then placed on ice. ADSC cultures were washed once and 10^6 of the previously prepared lymphocytes/primary DLBCL cells added to give a lymphocyte/DLBCL to ADSC ratio of 100:1. In some instances, increasing numbers of MDM were also added to give MDM to ADSC ratios of 1, 5, or 10:1. Differentiation controls of ADSC alone cultured with MesenPRO +/− cytokines were set up in parallel. On day 3, plates for 2D culture were refed with fresh MesenPRO +/− cytokines as appropriate. In some cases, a well per condition was harvested and the recovered cells stained with combinations of fluorescently labeled antibodies, and samples run on a FACSCANTO II. All wells to be used for 3D co-culture, were harvested using TrypLE™ express, the cells pelleted (400g, 5 min, full brake), all supernatant removed, and the cells placed on ice. Type I collagen (Scientific Laboratory Supplies, UK) and 10× DMEM (Sigma, UK), were mixed on ice; 1M NaOH (Sigma, UK) was added incrementally until the solution turned bright pink (neutral pH). The collagen solution was further diluted with ice cold MesenPRO +/− cytokines to obtain a 1 or 2 mg/ml collagen solution. Working on ice, each cell pellet was resuspended in 120 µl of ice-cold collagen solution and mixed well. Twelve microliters of this cell mixture was transferred to the reverse of a 6wp lid, generating 10 spheroids. The lid was then carefully inverted and placed over the base of a 6wp containing MesenPRO +/− cytokines, as required, and incubated for 30 min at 37°C/5%CO_2 to allow the collagen to set. Once set, the spheroids were gently lifted with forceps (Fisher Scientific, UK), and transferred to the appropriate well. These plates were transferred to an incubator (37°C/5% CO_2). On day 4, the 3D collagen spheroid cultures were transferred to new 6wp containing fresh MesenPRO +/− cytokines. 2D and 3D cultures were re-fed on Day 6; in some cases, 10 µg/ml of an irrelevant isotype control (trastuzumab) or rituximab was added to 3D spheroid co-cultures at 44 or 20 h prior to the end of the culture. At the end of the culture, a proportion of spheroids were prepared for either immunofluorescence microscopy or embedding in paraffin (see below). The remaining spheroids were washed 3 times, transferred to microcentrifuge tubes and pulsed briefly (Eppendorf Microfuge, 2000g). The supernatant was discarded and 250 µl/tube of 0.4 mg/ml Liberase TL (Roche, UK), added. Samples were incubated in a shaking heated block (Eppendorf, UK) for 10 min at 37°C. Up to 3 further 5-min incubations were performed, where necessary, to ensure spheroids were completely digested. The reaction was quenched by adding 1 ml of complete RPMI (cRPMI: RPMI supplemented with 2mM Glutamine, 1mM Pyruvate, and 100 IU/ml Penicillin/Streptomycin (all from GIBCO, UK) and 10% FCS). Cells were spun down (Eppendorf microcentrifuge, 5 min, 500g, room temperature) and washed twice in 1 ml of PBS (Severn Biotech Ltd, UK) supplemented with 2mM EDTA (VWR, UK). In some experiments, cells recovered from 2D cultures and 3D collagen spheroids were stained with the eBioscience fixable live/dead stain (Invitrogen, UK) according to the manufacturer's instructions prior to staining with combinations of fluorescently labeled antibodies. All samples were run on a FACSCANTO II. Doublets were excluded, and single cells gated for further analysis. ADSC-derived fibroblasts were identified as CD45- single cells; the degree of differentiation of ADSC in the various 2D and 3D mono and co-culture conditions was assessed by the expression of the fibroblast markers podoplanin, VCAM-1 and ICAM-1 relative to untreated ADSC. Results are shown as geometric mean fluorescent intensity (MFI). Cell viability was determined as the proportion of cells that were live/dead viability stain negative. For a given experiment, all 2D and 3D mono and co-cultures were set up in parallel, using the same cell constituents. For 2D immunofluorescence studies 1×10^6 primary human B cells or primary DLBCL cells were co-cultured with 1×10^4 ADSC to give a ratio of 100 B cells/primary DLBCL cells: 1 ADSC on coverslips as described above. Immunofluorescent staining and imaging were carried out as described below.

CFSE-Labeling

Primary DLBCL cells were resuspended at 10×10^6 cells/ml in warm PBS and labeled with 2.5 µM or 5 µM CFSE (Molecular probes, UK) for 15 min at room temperature, protected from light. 5 volumes cRPMI was added and the cells incubated on ice for 5 min. Cells were washed twice in 5 volumes of cRPMI, prior to resuspension at 5.0 x10^6 cells/ml.

2D Antibody-Dependent Cell Phagocytosis (ADCP) Assay

CFSE-labeled primary DLBCL cells were used as the target cell population and MDM as the effector cell population in standard ADCP assays, performed as previously described (30). Briefly, CFSE-labeled primary DLBCL cells were, washed, and opsonized with 10 μg/ml of an irrelevant antibody control (trastuzumab) or rituximab. Opsonized target cells were co-cultured with pre-plated MDM at a target:effector ratio of 5:1 for 60 min (37°C/5% CO_2). 1.5 μl of an in-house labeled anti-FcγRIII APC mAb (see **Supplementary Table 2**) was then added to the required wells, and the plate incubated at room temperature for 20 min protected from light. The plates were then gently washed, 140 μl of cold PBS added per well, and the plate incubated on ice for 30 min to 1 h, protected from light. Working on ice, each well was scraped, and its contents transferred to a flow cytometry tube (BD Biosciences, UK), prior to running on a FACSCalibur (BD Biosciences, UK). A minimum of 1,000 events/tube were collected. A macrophage gate was drawn according to Forward and Side scatter characteristics and the degree of ADCP determined as the % of FcγRIII+ macrophages co-staining with CFSE.

3D ADCP Assay

ADCP in 3D collagen spheroid co-cultures treated with 10 μg/ml of rituximab or isotype control (trastuzumab) was determined as follows. Cell suspensions recovered from 3D co-cultures containing ADSC, CFSE-labeled DLBCL and MDM were stained with an antibody panel including CD45 and CD11b and run on a FACSCanto II. Following doublet exclusion, the proportion of CFSE+ CD11b+ cells within an SSC high CD45+ gate was determined; the CFSE cut off was set using unlabeled DLBCL recovered from spheroids cultured in parallel, while an isotype control was used to set the cut off for CD11b. The proportion of DLBCL cells recovered from mAb-treated spheroids was identified as the percentage of SSC low CD45+ single cells. The expression of CD19, CD20 and FcγRIIB on these cells was assessed by flow cytometry in three experiments. The expression levels of these markers on DLBCL recovered from treated spheroids were normalized relative to those on DLBCL recovered from their untreated counterparts, run in parallel.

Immunofluorescence Staining

Coverslip mono and co-cultures: coverslips were washed, fixed with 4% paraformaldehyde (PFA (Sigma, UK), prepared in house) for 20 min at room temperature, then washed again. Coverslips were blocked with a 2.5% solution of normal goat serum (NGS, Thermofisher Scientific, UK) in PBS for 2 h at room temperature, or overnight at +4°C. When required, permeabilization with PBS/0.15% Triton X-100 (Sigma, UK) for 10 min, followed by a PBS wash was carried out prior to blocking. After blocking, coverslips were washed and incubated with anti-human VCAM-1 and anti-human podoplanin (see **Supplementary Table 2** for details) for 1 h at room temperature. Samples were then washed and stained with the species-appropriate secondary antibodies (**Supplementary Table 2**) for 45 min, protected from light. Samples were washed blocked in PBS/2.5% normal mouse serum (NMS, Thermofisher Scientific, UK) for 30 min, then stained with directly conjugated anti-human ICAM-1 Alexa 647 (**Supplementary Table 2**) for 1 h at room temperature protected from light. After incubation, coverslips were washed, and stained with DAPI (1μg/ml, Molecular probes, UK) in PBS for 10 min at room temperature protected from light, washed twice more and mounted on slides (2 coverslips/slide) in Vectashield (Vector Labs, UK). Slides were left for 15 min to allow the Vectashield to permeate cells, and then sealed. Slides were stored for no more than 8 days at +4°C, protected from light, prior to imaging on a confocal microscope (Leica SP5, Leica, UK) with a 40× oil immersion objective. Images were acquired and processed using LAS-AF Lite software version 4.0 (Leica UK, free download).

Whole Mount Staining of 3D Spheroid Cultures

Three to four collagen spheroids per culture condition were fixed in 4% PFA for 20–30 min at room temperature, washed three times with PBS and then stored at 4°C until staining. Prior to staining, one to two spheroids/condition were transferred to a flat-bottomed 96wp (Corning, UK), with all subsequent steps carried out in the plate. Spheroids were permeabilized with PBS/0.15% Triton X-100, washed three times with PBS and then blocked with PBS/2.5% of the appropriate animal serum at room temperature for 2 h protected from light. Following blocking, spheroids were stained with a primary antibody diluted to the appropriate concentration in PBS/2.5% appropriate animal serum/0.15% Triton-X-100 (**Supplementary Table 2**). After overnight incubation at 4°C, protected from light, spheroids were washed 4 times with PBS and stained with the appropriate fluorochrome-labeled secondary antibody diluted in PBS + 2.5% of the appropriate species-specific serum (**Supplementary Table 2**). For CD68 staining a 1:100 dilution of CD68 in PBS/2.5% NGS/0.15% Triton X-100 was added to the spheroid containing wells and incubated overnight at +4°C. Wells were washed and the appropriate secondary antibody, diluted in PBS+2.5% NGS, was added and the plate incubated for 1 h at room temperature, protected from light. Wells were washed with PBS. Where applicable, staining for ICAM-1 was performed after this step. Spheroids were blocked with PBS/2.5% NMS for 30 min, washed and stained with 1:50 dilution of mouse anti-human ICAM-1 Alexa 647 in PBS/2.5% NMS for 1 to 2 h. Following staining, cells were washed 3 times with PBS. Spheroids were counterstained with 10 μg/ml DAPI for 10–15 min, washed with PBS and the spheroids stored in PBS at 4°C until imaged. Spheroids were transferred to ibidi glass bottomed slides (Thistle Scientific, UK) prior to imaging on a confocal microscope (Leica SP5 or SP8, Leica, UK) with a 63× oil immersion objective. Images were acquired and processed using LAS-AF Lite software, version 4.0 (Leica, UK, free download).

Immunohistochemical Staining

Formaldehyde fixed paraffin embedded (FFPE) sections of normal human tonsil tissues and tissue microarrays (TMA)

constructed from archival ABC and GCB DLBCL diagnostic biopsy samples were provided by the Research Histology Unit, University Hospital Southampton NHS Foundation Trust. Several collagen spheroids per culture condition were randomly selected for formalin fixation and subsequent paraffin embedding. Spheroids were washed in PBS and fixed in a 10% formalin solution (Sigma, UK). Paraffin embedding and sectioning was carried out by the Histochemistry Research Unit, University Hospital Southampton NHS Foundation Trust. Three-micrometer sections were cut and transferred to slides. Collagen spheroid and TMA sections were stained by immunohistochemistry (IHC) using the fully automated BOND MAX or BOND RX IHC staining instruments (Leica Biosystems, U.K.) using BOND reagents (Leica Biosystems, U.K.) according to the manufacturer's instructions. Antibodies were diluted in BOND™ Primary Antibody Diluent (Leica Biosystems, UK). Briefly, sections were deparaffinized, pre-treated for heat-induced Ag retrieval (BOND ER1, or ER2 protocol), and incubated with hydrogen peroxide followed by the indicated antibody. The antibody was subsequently bound to the Poly-HRP IgG reagent before incubation with 3,3′-diaminobenzidine (DAB). The sections were subsequently incubated with the indicated antibody, which was then bound to the Post Primary IgG linker reagent. The substrate chromogen Fast Red was then applied. All sections were counterstained using hematoxylin and mounted in CV Ultra mounting media (Leica Biosystems, UK). Slides were imaged at 4×, 10×, and 40× magnification with an Olympus CKX41 microscope. Single color IHC DAB staining of normal human tonsil tissue sections was carried out to validate antibodies and confirm the expression/co-localization of fibroblast markers in lymphoid tissue (**Supplementary Figure 1**).

Cluster Count and Average Cluster Size Analysis

Phase contrast images of 2D co-cultures of ADSC and B cells or primary DLBCL cells were taken with an Olympus CKX41 microscope. Cluster numbers and average size were analyzed using ImageJ (31). Briefly, images were converted to binary and a size exclusion of 1,000 pixel units was applied to eliminate small clusters of B/DLBCL cells. The clusters were then manually counted, and their area measured using ImageJ.

Statistical Analysis

All statistical analyzes were performed using Graphpad Prism Version 8.2.1. Two group comparisons were made with unpaired or paired t tests. One-way analysis of variance (ANOVA) was used to compare the expression of markers on ADSC-derived fibroblasts recovered from 2D and 3D mono and co-cultures. Each experiment utilized a single batch of PBMC/DLBCL and MDM combined with ADSC, thus data sets from a single experiment were treated as paired data. We assumed a Gaussian distribution. If a data set was missing from an experiment, a mixed effects model was applied. The recommended Sidak test for multiple comparisons was applied, to both one-way ANOVA and mixed effects tests. p values <0.05 were considered significant; statistical significance was denoted as follows: *$p<0.05$, **$p<0.01$ ***$p<0.001$ and ****$p<0.0001$.

RESULTS

Primary DLBCL Cells Die *In Vitro*

The DLBCL TME is complex, with tumor cells interacting with stroma and immune cells (32). To assess TME cellular architecture in more detail we constructed tissue microarrays (TMA) from archival ABC and GCB DLBCL diagnostic biopsy samples and applied IHC for appropriate cell-specific targets. Prior to this, staining of tonsil tissue was used to validate antibodies and determine the expression/co-localization of fibroblast markers in normal lymphoid tissue (**Supplementary Figure 1**). Both lymphoid fibroblasts, positive for alpha-smooth muscle actin (α-SMA), podoplanin and VCAM-1, and CD20+ DLBCL cells were observed in close proximity to CD68+ macrophages (**Figure 1A**). These observations demonstrate the complex nature of the DLBCL microenvironment and confirm the presence of a heterogeneous network of cell-cell interactions. Next, we assessed the dependence of primary DLBCL cells on their microenvironment for survival. Primary DLBCL were thawed and, following dead cell removal, cultured for 7 days *in vitro*. Over this time, nearly all the DLBCL cells died (viability <2%, **Figure 1B**). In contrast, the relative proportion of CD3+ T cells significantly increased in these cultures, reflecting the specific loss of DLBCL cells during culture (**Figure 1C**). These observations confirm that a more complex *in vitro* multicellular model, better recapitulating the *in vivo* microenvironment, is required to support primary DLBCL cell survival *in vitro*.

Human Adipocyte-Derived Stem Cells Can Be Differentiated Into Lymphoid Stroma

Human ADSC are multi-potent mesenchymal stem cells, isolated from human adipose tissue, with the capacity to differentiate into different cell types dependent upon their cytokine milieu (33, 34). Data from animal studies indicate a key role for LT-β in driving the differentiation of adipocyte precursors into lymph node stromal cells (35). Similarly, in an *in vitro* model of FL, Pandey et al. (13) showed stimulation of human ADSC with LT-α/β and TNF-α resulted in their differentiation into lymphoid fibroblasts expressing VCAM-1 and ICAM-1, with subsequent addition of IL-4 modulating the phenotype of these cells. Simultaneous treatment of ADSC with all three cytokines has been shown to upregulate cell-surface markers typical of lymphoid fibroblasts, such as α-SMA, podoplanin and the adhesion molecules ICAM-1 and VCAM-1 (29). Therefore, we attempted to develop these cells as a route toward reconstructing the DLBCL TME.

Under standard culture conditions, ADSC expressed low levels of podoplanin and ICAM-1 and lacked expression of VCAM-1, as confirmed by Flow cytometry and IF microscopy (**Figure 2A**). Treatment of ADSC with LT-α/β, TNF-α, and IL-4 alone or in combination confirmed that all three cytokines were required to drive differentiation into lymphoid-like fibroblasts, as indicated by increased podoplanin and ICAM-1 expression and induction of VCAM-1 expression (**Figure 2B**). Immunofluorescence microscopy of ADSC treated with the cytokine combination confirmed our flow cytometry data (**Figure 2C**). We also demonstrated that these cells are highly dynamic with respect to

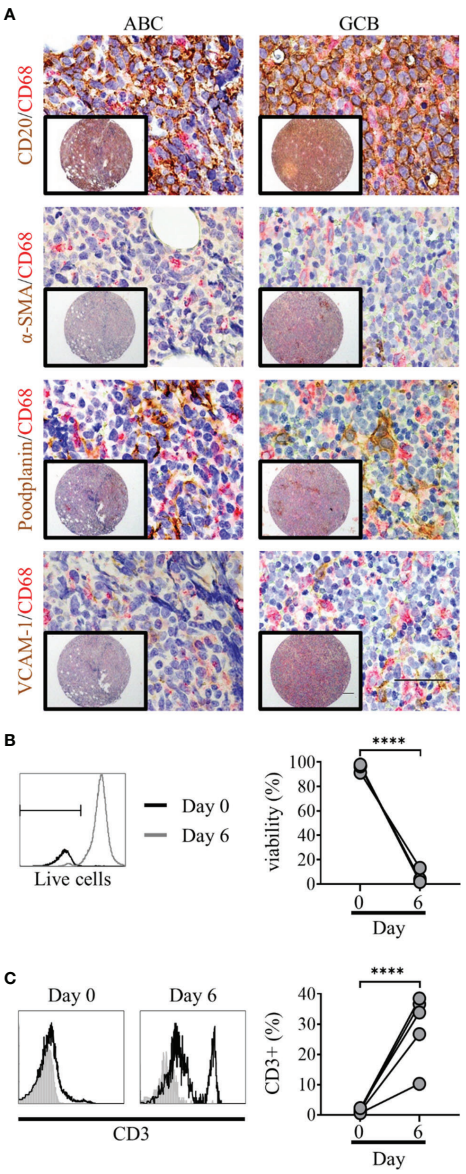

FIGURE 1 | Primary diffuse large cell B cell lymphoma (DLBCL) cells exist within a complex multicellular environment and die *in vitro*. **(A)** Double immunohistochemistry (IHC) staining of DLBCL cells (CD20, brown) or lymphoid fibroblasts [alpha smooth muscle Actin (α-SMA), podoplanin, and VCAM-1 (brown)] and macrophages (CD68, red) of activated B cell-like (ABC) (left hand panels) and germinal-center B cell-like (GCB) (right-hand panels) DLBCL tumor micro-array samples, demonstrating the close interaction of all three cell types within the tumor microenvironment. Scale bars: 200 μm, inset image, 50 μm main image. **(B)** Representative histograms of live/dead viability staining of primary DLBCL cells pre (day 0, black line) and post 6 days of *in vitro* culture (grey line); marker denotes the cut-off for live staining (dead cells stain more intensely). Graph shows pre- and post-culture viability, each filled circle represents an independent experiment. Statistical significance between groups was assessed using a paired two tailed t-tests, ****$p < 0.0001$. **(C)** Representative histograms showing CD3 staining in primary DLBCL cell suspensions before (day 0) and after 6 days of *in vitro* culture. Graph shows pre- and post-culture percentages of CD3+ lymphocytes, each filled circle represents an independent experiment. Statistical significance between groups was assessed using a paired two tailed t-tests, ****$p < 0.0001$.

their differentiation, whereby removal of cytokines resulted in their de-differentiation with a phenotypic switch back to untreated ADSC. Conversely, re-exposure to cytokines resulted in re-expression of the phenotypic markers akin to the original cytokine treated ADSC (**Supplementary Figure 2**), highlighting the dynamic nature of these cells.

ADSC-Derived Fibroblasts Interact With PBMC in Standard 2D *In Vitro* Cultures

As an initial step in producing successful co-cultures, we assessed whether lymphocytes could interact with ADSC-derived fibroblasts. Using a previously published protocol as a basis (18), we cultured PBMC for 2 h with ADSC, previously cultured in the presence or absence of cytokines for 7 days, (differentiation confirmed by flow cytometry; **Supplementary Figure 3**), after which wells were imaged using phase contrast microscopy (**Figure 3A**) and the recovered cells analyzed by flow cytometry (right-hand panel). The proportion of harvested cells expressing CD45 was higher for cytokine treated ADSC compared to their unstimulated counterparts indicating that PBMC were better able to interact with the former. Next, we added PBMC to ADSC at a ratio of 100:1 and cultured them for 3 days in medium supplemented with cytokines, with ADSC cultured +/− cytokines serving as controls. We noted that expression of lymphoid fibroblast was similarly increased in treated ADSC +/− PBMC relative to non-treated controls (**Figure 3B**). Given the highly complex cellular make-up of the DLBCL TME (32) and the presence of TAM which has been linked with overall patient prognosis (36, 37) and response to standard of care immunochemotherapy (38, 39), we next assessed the impact of adding increasing numbers of donor-matched MDM (0.1×, 0.5×, and 10 × 10^5 MDM), to our PBMC/ADSC co-culture system. Increasing numbers of MDM did not significantly impact the expression of lymphoid fibroblast markers on the recovered ADSC-derived fibroblasts (**Figure 3B**).

Next, we isolated B or T cells from PBMC and co-cultured them with ADSC at a ratio of 100:1 for 5 days in the presence or absence of cytokines. The images show that B cells form clusters with ADSC, while T cells are restricted to inter-ADSC spaces (**Figure 4A**); IF microscopy confirmed that B cells closely associate with ADSC-derived fibroblasts (**Figure 4B**, B cells indicated by white arrows). We also assessed the impact of B cell co-culture on the ability of cytokines to modulate lymphoid stromal marker expression on ADSC. Co-culture of B cells with cytokine treated ADSC did not significantly alter the expression of lymphoid fibroblast markers compared to cytokine treated ADSC alone (**Figure 4C**). Overall, these data support the assertion that ADSC differentiated with this cytokine cocktail become B cell supportive.

Primary DLBCL Cells Interact With ADSC-Derived Fibroblasts and Modulate Expression of Lymphoid Fibroblast Markers

Given our goal to generate a model of the DLBCL TME, we next established co-cultures combining ADSC with primary DLBCL tumor cells +/− MDM. DLBCL were rested for 1 h, prior to dead

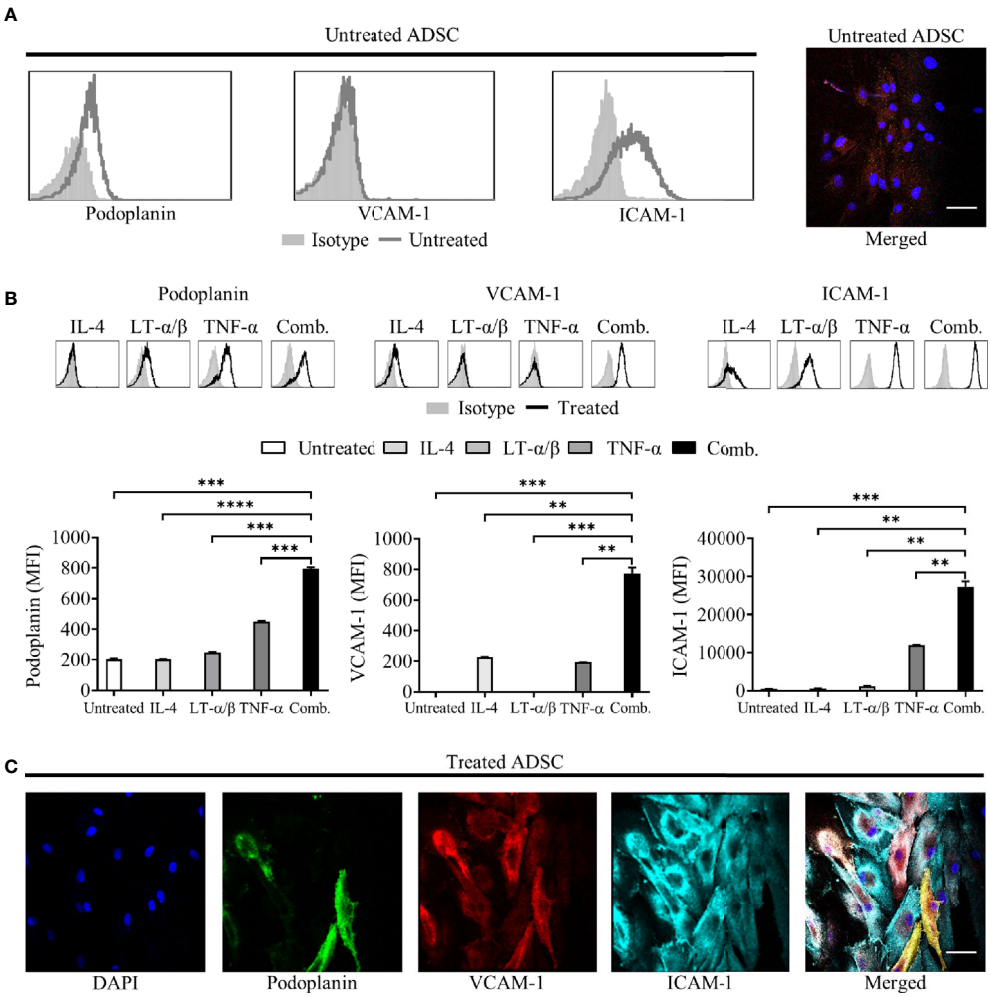

FIGURE 2 | Adipocyte derived stem cells (ADSC) can be differentiated into lymphoid fibroblasts. **(A)** Representative histogram overlays of podoplanin, vascular cell adhesion molecule 1 (VCAM-1) and intercellular adhesion molecule 1 (ICAM-1) expression on untreated ADSC after 6 days of culture, isotype controls are shown as filled silver histograms. Right-hand image depicts immunofluorescent staining of ADSC cultured on coverslips in media alone for 5 days, then stained with fluorescently labeled antibodies to podoplanin (green), VCAM-1 (red) and ICAM-1 (cyan), and counterstained with DAPI nuclear stain (blue); the panel depicts the merged image, scale bar, 50 μm. **(B)** Representative histogram overlays of podoplanin, vascular cell adhesion molecule 1 (VCAM-1) and intercellular adhesion molecule 1 (ICAM-1) expression on ADSC after 6 days of culture with IL-4, LT-α/β, or TNF-α alone, or in combination, isotype controls are shown as filled silver histograms. Graphs show surface expression of ICAM-1, VCAM-1 and podoplanin [Geomean Fluorescence intensity (MFI)] on ADSC cultured under the indicated conditions at day 6 of culture. The mean +/− SD are shown for three independent experiments with each condition performed in triplicate. Statistical significance between groups was assessed using a paired two tailed t-tests, $^{**}p < 0.01$ $^{***}p < 0.001$, and $^{****}p < 0.0001$. **(C)** Images depict immunofluorescent staining of ADSC cultured on coverslips in media supplemented with IL-4, LT-α/β, and TNF-α for 5 days, then stained with fluorescently labeled antibodies against the indicated markers, and counterstained with DAPI; panels depict each channel alone, with the final panel showing the merged channels, scale bar, 50 μm.

cell removal. DLBCL were added at the same ratio as PBMC; in some cases, 1×10^5 MDM were also added. Cells were then cultured in the presence of the cytokine cocktail for up to 8 days. DLBCL interacted with ADSC-derived fibroblasts as determined by IF (merged image panel, **Figure 5A**, DLBCL indicated by white arrows). Unlike PBMC/ADSC co-cultures, expression of lymphoid fibroblast markers differed in DLBCL/ADSC co-cultures at day 3, with podoplanin expression being significantly increased and ICAM-1 levels significantly decreased as compared to cytokine-treated ADSC alone (**Figure 5B**). Furthermore, addition of MDM to the co-culture system resulted in increased expression of all three lymphoid fibroblast markers. This pattern of expression was maintained for podoplanin after a further 5 days of culture, whereas VCAM-1 levels increased in DLBCL/ADSC co-cultures and ICAM-1 expression was similarly reduced in both DLBCL/ADSC and DLBCL/ADSC/MDM co-cultures compared to cytokine treated ADSC monocultures (**Supplementary Figure 4A**). We then analyzed bright field images of cytokine treated ADSC cultured with either B cells or DLBCL and observed that the frequency of clusters in B cell/ADSC co-cultures was significantly higher, and the average cluster size significantly lower, at day 5 than in in

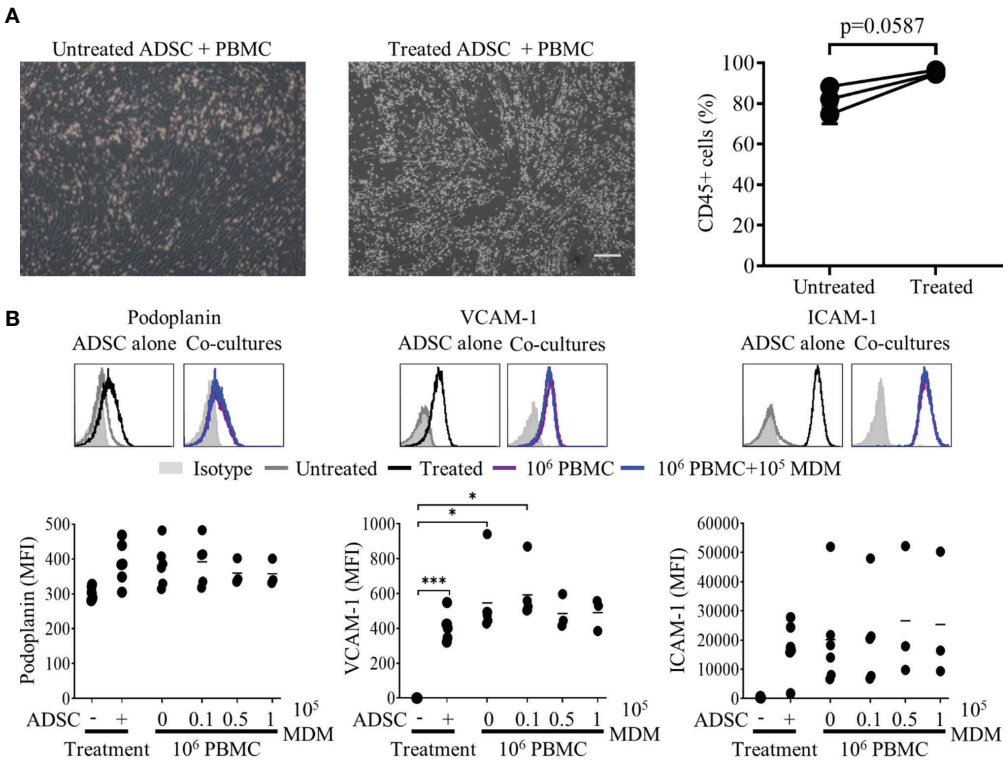

FIGURE 3 | Lymphocytes interact with adipocyte derived stem cells (ADSC)-derived lymphoid fibroblasts. **(A)** Peripheral blood mononuclear cell (PBMC) were co-cultured with untreated or cytokine treated ADSC for 2 h then washed; post-wash phase contrast images are shown, scale bar, 200 µm. The graph shows the percentage of CD45+ lymphocytes recovered from wells containing untreated or cytokine-treated ADSC after 2 h of co-culture, mean +/– SD of two replicates for three independent experiments is shown. Two group comparisons were made using a paired two-tailed t-test. **(B)** Representative histogram overlays of podoplanin, vascular cell adhesion molecule 1 (VCAM-1) and intercellular adhesion molecule 1 (ICAM-1) staining at day 3 of culture for untreated and cytokine treated ADSC alone or treated ADSC co-cultured with total PBMC +/– 1 × 10^5 autologous monocyte-derived macrophages (MDM). Isotype controls are shown as filled silver histograms. Graphs show surface expression of ICAM-1, VCAM-1 and podoplanin for each culture condition at day 3 of culture. Each solid circle represents an independent experiment, bars represent the mean. Two group comparisons were made using one-way ANOVA with Sidak correction for multiple comparisons applied, *p < 0.05, ***p < 0.001.

DLBCL/ADSC co-cultures (**Figure 5C**), indicating that fewer, larger clusters are formed in the latter, possibly due to increased migration of DLBCL toward ADSC-derived fibroblasts. Notably, cell viability was maintained at day 3 of culture (**Figure 5D**) and did not significantly change between day 3 and day 8 across all samples assessed, indicating the pro-survival impact of these co-cultures compared to DLBCL monocultures (**Supplementary Figure 4B** versus **Figure 1B**).

Given our observation of phenotypic alterations in cytokine-treated ADSC co-cultured with DLBCL and MDM, we next assessed whether the impact of cytokine withdrawal on ADSC-derived fibroblast phenotype would be lessened in this context. At day 3 co-culture, wells were either maintained in cytokine-supplemented media or switched to media alone for a further 5 days. The phenotype of ADSC-derived lymphoid fibroblasts was then assessed by flow cytometry. Removal of cytokines in the context of 2D co-cultures resulted in a reduction, but not total loss of lymphoid fibroblast marker expression on ADSC with podoplanin being the only marker significantly lower following cytokine withdrawal compared to co-cultures treated with cytokines throughout. Moreover, all three lymphoid fibroblast markers were maintained at higher levels in 2D co-culture following cytokine removal than in unstimulated ADSC (**Supplementary Figure 4C**). These data suggest that the phenotype of ADSC-derived lymphoid fibroblasts can be partially stabilized by primary DLBCL cells and MDM upon cytokine removal, indicating 2D co-culture generates, to some degree, a mutually supportive environment.

Overall, our data indicate that interactions between ADSC-derived lymphoid fibroblasts and primary DLBCL cells are qualitatively different from those observed in PBMC/ADSC co-cultures. A marked increase in podoplanin, a recognized marker of CAF, suggests interactions between ADSC-derived lymphoid fibroblasts and DLBCL drive the former toward a more CAF-like phenotype. The observed reduction in ICAM-1 expression in co-cultures suggests this adhesion molecule may be involved in the observed inter-cellular interactions, particularly as its expression decreased during culture.

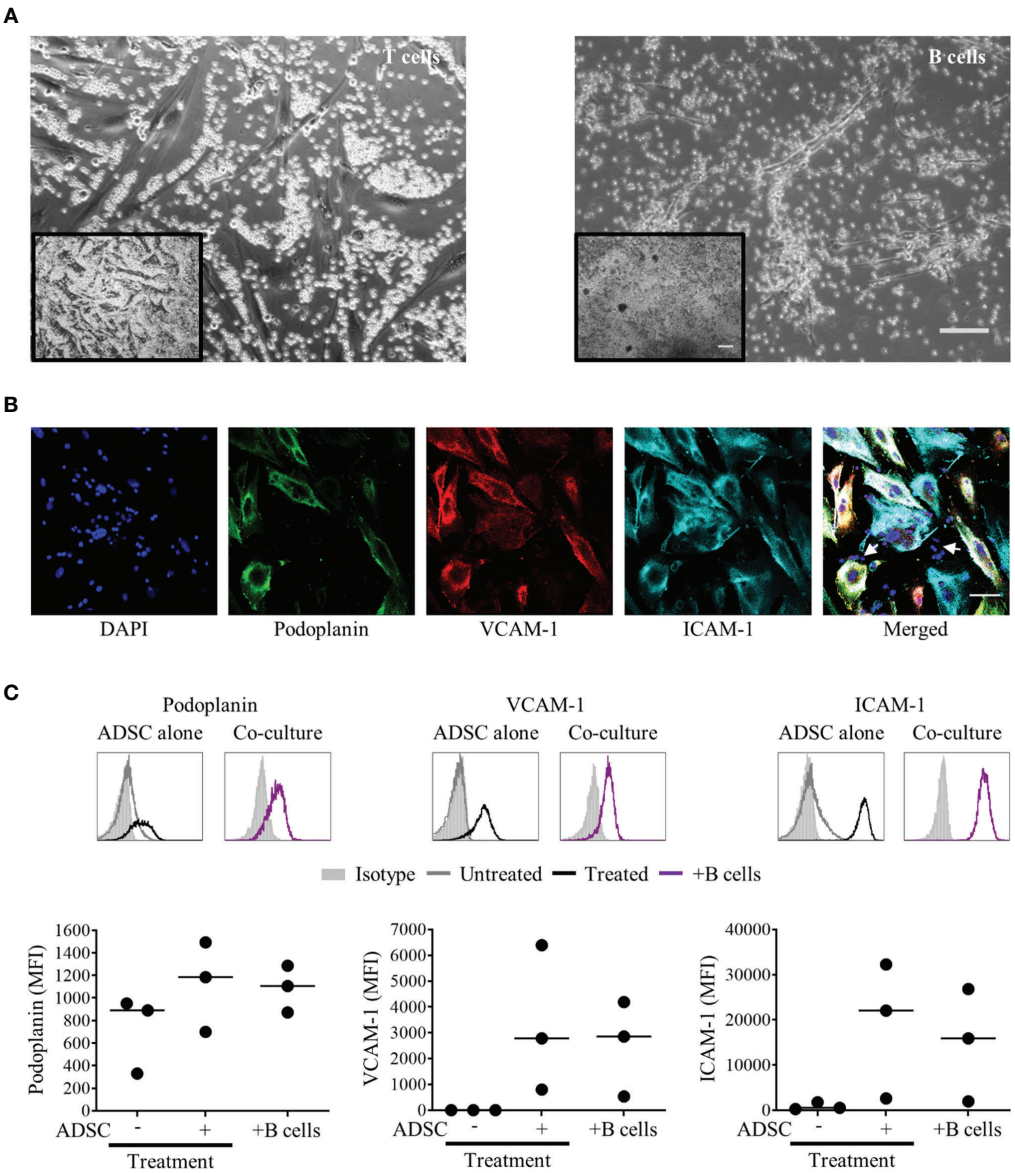

FIGURE 4 | B cells rather than T cells interact with adipocyte derived stem cells (ADSC)-derived lymphoid fibroblasts. **(A)** MACS-purified T or B cells were co-cultured with ADSC in the presence of cytokines for 5 days; phase contrast images are shown. Scale bars: 200 µm, inset image, 100 µm main image. **(B)** Immunofluorescent staining of ADSC cultured on coverslips in cytokine-supplemented media in the presence of purified B cells, stained with fluorescently labeled antibodies against the indicated markers, and counterstained with DAPI; panels depict each channel alone, with the final panel showing the merged channels, with white arrows indicating nuclei of B cells in close proximity to ADSC-derived lymphoid fibroblasts, scale bar, 50 µm. **(C)** Representative histogram overlays of podoplanin, vascular cell adhesion molecule 1 (VCAM-1) and intercellular adhesion molecule 1 (ICAM-1) staining at day 6 of untreated and cytokine treated ADSC alone and cytokine treated ADSC co-cultured with MACS-purified B cells, isotype controls are shown as filled silver histograms. Graphs show surface expression of ICAM-1, VCAM-1, and podoplanin for each culture condition at day 5 of culture. Each closed circle represents an independent experiment, and bars represent mean values. Comparisons between groups were made using one-way ANOVA with Sidak correction for multiple comparisons applied, p values < 0.05 were considered significant.

Generation of 3D Collagen Spheroid Co-Cultures

Having shown that both PBMC and DLBCL cells differentially interact with ADSC-derived lymphoid stroma in standard 2D tissue culture, we next investigated whether these interactions would be maintained and potentially enhanced in the context of 3D cultures. We chose a scaffold-based system that would allow the incorporation of the previously tested 2D co-cultures into a Type I collagen-based extracellular matrix, generating 3D spheroids that could be subsequently cultured. **Figure 6A** illustrates the steps involved. Post-culture, the recovered spheroids were subdivided and either disaggregated and analyzed by flow cytometry, directly

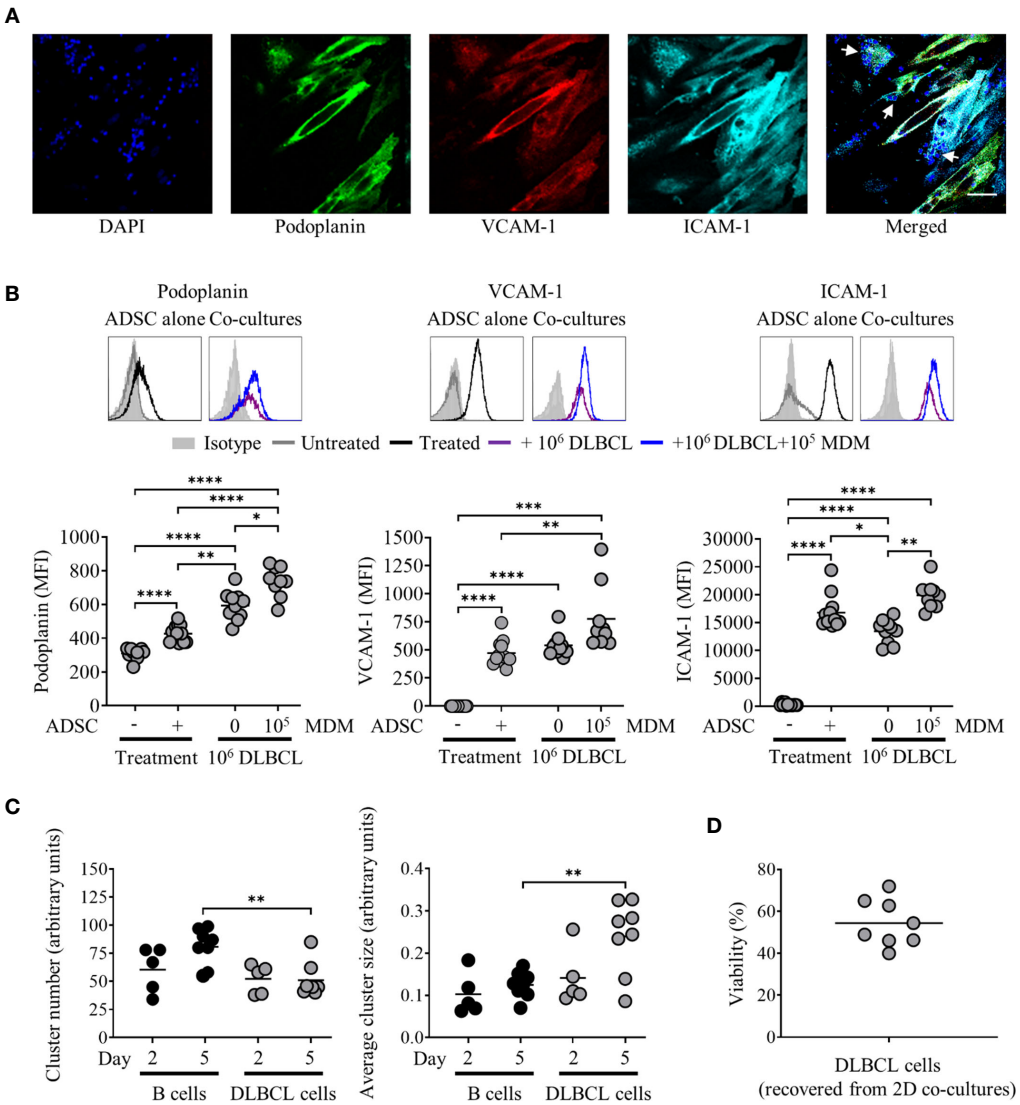

FIGURE 5 | Primary diffuse large cell B cell lymphoma (DLBCL) cells interact with adipocyte derived stem cell (ADSC)-derived lymphoid fibroblasts and modulate expression of lymphoid fibroblast markers. **(A)** ADSC co-cultured with primary DLBCL on coverslips in cytokine-supplemented media were stained with fluorescently labeled antibodies against the indicated markers, and counterstained with DAPI, panels depict each channel alone. The final panel shows the merged channels, with white arrows indicating nuclei of DLBCL cells in close proximity to ADSC-derived lymphoid fibroblasts, scale bar, 50 μm. **(B)** Representative histogram overlays of podoplanin, vascular cell adhesion molecule 1 (VCAM-1) and intercellular adhesion molecule 1 (ICAM-1) staining at day 3 for untreated and cytokine treated ADSC alone or treated ADSC co-cultured with primary DLBCL cells +/– 1×10^5 monocyte-derived macrophages (MDM). Isotype controls are shown as filled silver histograms. Graphs show surface expression of podoplanin, VCAM-1 and ICAM-1 for each culture condition after 3 days of culture. Each closed circle represents an independent experiment, bars represent the mean. Group comparisons were made using the one-way ANOVA test with Sidak correction for multiple comparisons, $^*p < 0.05$, $^{**}p < 0.01$, $^{***}p < 0.001$, $^{****}p < 0.0001$. **(C)** Graphs show cell cluster data calculated using ImageJ, specifically the number of cell clusters (left-hand graph) and average cluster size (right-hand graph). Pooled data from three independent experiments are shown, group comparisons were made using one-way ANOVA with Sidak correction for multiple comparisons, $^{**}p < 0.01$. **(D)** Graph depicting percentage viability of primary DLBCL after 3 days of culture with ADSC-derived lymphoid fibroblasts, each symbol represents data from an independent experiment, bar represents the mean.

stained for immunofluorescence, or fixed in formaldehyde prior to embedding in paraffin and sectioning, for subsequent staining by IHC.

3D collagen spheroid co-cultures, stained and analyzed by IF microscopy, revealed ADSC-derived lymphoid fibroblasts (ICAM-1-positive cells) and B cells (CD20 positive cells) were in close proximity to each other (**Figure 6A**, left-hand panel, white arrows). IHC of 3 μm sections generated from FFPE 3D spheroids, stained for MDM (CD68) and lymphoid fibroblast markers (podoplanin and VCAM-1) showed that these populations also interacted with each other in a 3D context (**Figure 6B**, right-hand panel). The pattern of fibroblast marker expression on ADSC-derived lymphoid fibroblasts isolated from 3D spheroid PBMC co-cultures, as determined by flow

cytometry (**Figure 6C**), differed to that seen in 2D co-cultures (see **Figure 3B**). Notably we were unable to detect VCAM-1 post-disaggregation, irrespective of the anti-human VCAM-1 antibody used (**Supplementary Figure 5A**), although IHC revealed the presence of VCAM-1 positive cells in sections from cytokine-treated 3D collagen spheroid cultures (**Figures 6B** and **7A**, and **Supplementary Figure 5B**). Although podoplanin expression on ADSC-derived lymphoid fibroblasts recovered from cytokine-treated 3D collagen spheroids was significantly higher compared to those from untreated controls, its expression on ADSC-derived lymphoid fibroblasts recovered from 3D PBMC/ADSC spheroid co-cultures, irrespective of the presence of MDM, was similar to that of untreated controls. ICAM-1 expression levels on ADSC-derived lymphoid fibroblasts recovered from cytokine-treated 3D spheroids were lower than seen in their 2D counterparts, but the pattern was similar, with significantly increased expression on cells recovered from cytokine treated 3D ADSC monocultures and 3D PBMC/ADSC co-cultures (**Figure 6C**). Overall, these flow cytometry data suggest a qualitative difference in the interaction of cell populations in 3D versus 2D ADSC/PBMC co-cultures.

Interactions Between Primary DLBCL Cells and ADSC-Derived Fibroblasts Persist in 3D Collagen Spheroids

We next applied our 3D collagen spheroid protocol to primary DLBCL cells. Fluorescence microscopy of immunostained 3D collagen spheroid co-cultures revealed ADSC-derived lymphoid fibroblasts (ICAM-1), DLBCL cells (CD20) and MDM (CD68) in close proximity to each other (**Figure 7A**, left-hand panel, white arrows). IHC corroborated the close interaction of these populations in 3D collagen spheroid co-cultures (**Figure 7A**, right-hand panels). Of note, the pattern of both podoplanin and ICAM-1 expression on ADSC-derived lymphoid fibroblasts recovered from 3D spheroid co-cultures (**Figure 7B**) was very similar to that observed in day 8 2D co-cultures (**Supplementary Figure 4**). The viability of DLBCL recovered from 3D collagen ADSC/DLBCL/MDM spheroid co-cultures was also maintained (**Figure 7C**). Moreover, there was no significant difference between the viability of cells recovered from 3D and parallel 2D co-cultures harvested at this time point (**Figure 7D**).

To assess the impact of cytokine withdrawal on ADSC-derived lymphoid fibroblast phenotype in the context of 3D spheroid co-cultures, we generated 3D DLBCL/ADSC/MDM spheroid co-cultures as previously described, and then cultured them in medium +/− cytokines for 5 days. Cultures were then stopped, and the phenotype of the recovered ADSC-derived fibroblasts assessed by flow cytometry. Unlike 2D co-cultures where cytokine removal resulted in a reduction, but not total loss of lymphoid fibroblast marker expression (**Supplementary Figure 4C**), ADSC-derived lymphoid fibroblasts recovered from 3D collagen spheroid co-cultures cultured in medium alone maintained lymphoid fibroblast marker expression at similar levels to those of cells recovered from 3D spheroids cultured in cytokine-supplemented medium (**Supplementary Figure 6A**). Furthermore, IHC of spheroids cultured in medium +/− cytokines also showed similar patterns of podoplanin and CD68 expression (**Supplementary Figure 6B**). These data indicate that the ADSC-derived lymphoid fibroblast phenotype is maintained in the 3D co-culture environment even in the absence of cytokines. Overall, these data provide further evidence that ADSC-derived lymphoid fibroblasts, DLBCL cells and MDM can interact and that, in the context of 3D collagen spheroid co-cultures, generate a self-sustainable environment. The maintenance of primary DLBCL cell viability in the context of the 3D co-culture system further supports this observation and indicates that the system could be adapted to study the impact of therapeutic agents.

DLBCL Are Targets for Antibody Dependent Cellular Phagocytosis in 2D and 3D Models

Current standard of care for many lymphomas, including DLBCL, involves anti-CD20 mAb (40), with ADCP being one of its main modes of action. Therefore, we next explored the suitability of primary DLBCL as targets for phagocytosis in our model systems, comparing conventional 2D and 3D cultures. To this end, DLBCL were labeled with CFSE, and treated with either 10 μg/ml of irrelevant control or anti-CD20 mAb (rituximab) and phagocytosis assessed in a standard 2D ADCP assay (30). In this assay rituximab opsonized DLBCL were preferentially phagocytosed compared to controls (**Supplementary Figure 7A**). Having established the suitability of DLBCL as targets for rituximab mediated ADCP, we next assessed whether we could measure this activity in our standard 3D collagen spheroid co-culture system. Thus, we generated spheroid co-cultures as described, using CFSE-labeled primary DLBCL cells; cultured them as before, with the addition 10 μg/ml of control or rituximab mAb 44 h prior to the end of culture. Cells were recovered and assessed by flow cytometry; following doublet exclusion, SSC high CD45+ cells were gated, and the proportion of CD11b+ CFSE+ cells within this population used to determine the level of phagocytosis. Only 1 of the 5 rituximab-treated spheroid co-cultures demonstrated increased ADCP, relative to their control-treated counterparts (data not shown). Nevertheless, IHC of FFPE sections from control- or rituximab-treated 3D collagen spheroid co-cultures, stained for DLBCL cells (CD20) and MDM (CD68) showed that these cell populations clearly interacted with each other (**Figure 8A**). As a next step, we assessed ADCP in spheroids generated with a lower collagen concentration (1 mg/ml) to determine whether this would generate a less rigid matrix that might facilitate higher levels of phagocytosis. We showed that ADSC recovered from cytokine-treated spheroids composed of 1 mg/ml collagen featured significantly increased levels of podoplanin and ICAM-1 compared to unstimulated controls (**Supplementary Figure 7B**).

We next assessed ADCP in these 3D spheroid co-cultures (1 mg/ml collagen) treated with mAb for the last 20 h of culture. We observed moderately increased ADCP following rituximab versus control mAb treatment in three of four experiments (**Figure 8B**), suggesting that the reduced collagen

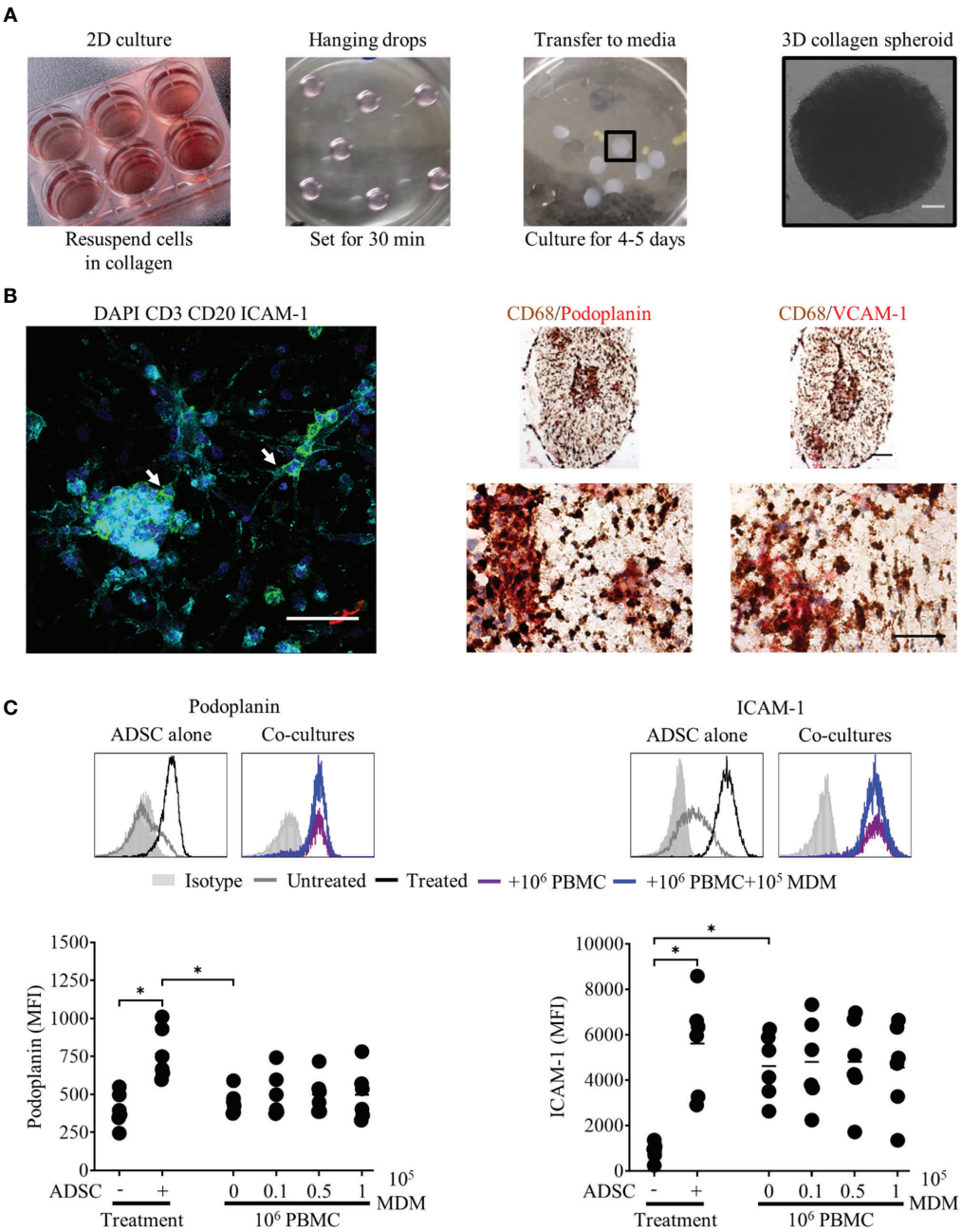

FIGURE 6 | Peripheral blood mononuclear cell (PBMC) interact with adipocyte derived stem cell (ADSC)-derived fibroblasts in 3D collagen spheroid co-cultures. **(A)** Images demonstrating the culture techniques used to generate 3D collagen spheroid co-cultures. Day 3 ADSC, PBMC monocyte-derived macrophage (MDM) 2D co cultures (first panel), 12 µl droplets of cells suspended in Type-I collagen (second panel), 3D collagen spheroid co-cultures in six well-plate (third panel). The final panel depicts a phase contrast image of a 3D collagen spheroid co-culture at day 8 of culture, scale bar 200 µm. **(B)** Left-hand panel: Whole-mount staining of a 3D collagen spheroid co-culture containing ADSC (ICAM-1, cyan) and PBMC [B cells, CD20 (green), T cells, CD3 (red)], counterstained with DAPI nuclear stain (blue). White arrows indicate B cells in close association with ADSC-derived lymphoid-like fibroblasts, scale bar, 50 µm. Right-hand panel; representative double immunohistochemistry (IHC) staining of formaldehyde fixed paraffin embedded (FFPE) sections of collagen spheroid co-cultures containing ADSC-derived lymphoid fibroblasts (podoplanin and VCAM-1, red), PBMC, and MDM (CD68, brown), scale bars 100 µm and 50 µm for upper and lower images, respectively. **(C)** Representative histogram overlays of podoplanin and ICAM-1 staining of untreated and cytokine treated ADSC alone or cytokine treated ADSC co-cultured with PBMC +/– 10^5 autologous MDM recovered from 3D collagen spheroid cultures after 8 days of culture, isotype controls are shown as filled silver histograms. Graphs show surface expression of podoplanin and ICAM-1 on lymphoid fibroblasts for each culture condition at day 8 of culture. Each closed circle represents data from an independent experiment, bars represent the mean. Group comparisons were made using the one-way ANOVA test with Sidak correction for multiple comparisons; p values < 0.05 were considered significant, *p < 0.05.

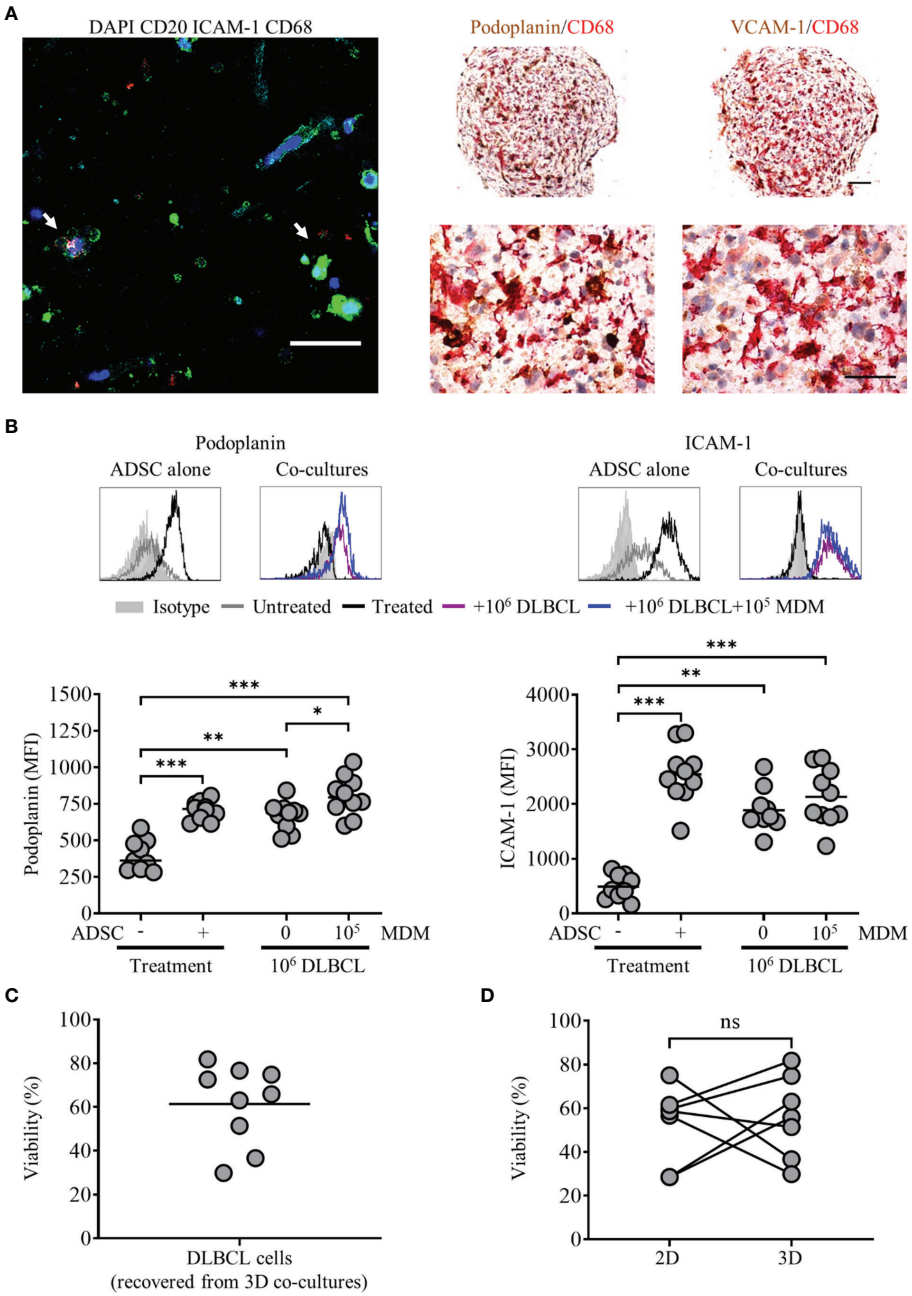

FIGURE 7 | Primary diffuse large cell B cell lymphoma (DLBCL) cells interact with adipocyte derived stem cell (ADSC)-derived fibroblasts in 3D collagen spheroid co-cultures. **(A)** Left-hand panel: Whole-mount staining of a 3D collagen spheroid co-culture containing ADSC (ICAM-1, cyan), primary DLBCL cells (CD20, green), and monocyte-derived macrophages (MDM) (CD68, red), counterstained with DAPI (blue). White arrows indicate DLBCL cells in close association with ADSC-derived lymphoid-like fibroblasts and MDM, scale bar, 50 µm. Right-hand panel; representative double IHC staining of FFPE sections of 3D spheroid co-cultures containing ADSC-derived lymphoid fibroblasts (podoplanin and VCAM-1, brown), primary DLBCL cells and MDM (CD68, red), scale bars 100 µm and 50 µm for upper and lower images, respectively. **(B)** Representative histogram overlays of podoplanin and ICAM-1 staining of untreated and cytokine treated ADSC alone or treated ADSC co-cultured with primary DLBCL cells +/– 1 × 10^5 MDM recovered from 3D collagen spheroid cultures after 8 days of culture, isotype controls are shown as filled silver histograms. Graphs show surface expression of podoplanin and ICAM-1 for each culture condition at day 8 of culture. Each closed circle represents an independent experiment, bars represent the mean. Group comparisons were made using a one-way ANOVA with Sidak correction for multiple comparisons; p values < 0.05 were considered significant, *p < 0.05, **p < 0.01, ***p < 0.001. **(C)** Viability of primary DLBCL cells recovered from 3D collagen spheroid co-cultures after 8 days of culture, each symbol represents data from an independent experiment, bars represent the mean (left-hand graph). **(D)** Comparison of the viability of primary DLBCL recovered from 2D co-cultures or 3D spheroid co-cultures cultured in parallel for 8 days (right-hand graph). Each pair of linked filled circles represents data from an independent experiment. Two group comparisons were made using a paired t-test; p values <0.05 were considered significant, ns, not significant.

concentration had resulted in conditions more favorable for ADCP. Furthermore, we observed a reduction in the proportion of DLBCL, defined as the percentage of SSC low CD45+ single cells, recovered from rituximab-treated 1 mg/ml collagen spheroids as compared to their control-treated counterparts (**Figure 8C**).

Finally, to assess rituximab's ability to enter collagen spheroid co-cultures and subsequently target the DLBCL cells within them, we assessed levels of two molecules expressed by DLBCL cells that interact with rituximab, its target molecule CD20 and the inhibitory FcγRIIB (CD32B) able to bind rituximab's Fc region (30). Both CD20 and FcγRIIB staining were reduced on DLBCL recovered from rituximab-treated compared to control-treated spheroids (**Figure 8D**), confirming that Rituximab was able to access spheroids and interact with the primary DLBCL cells within them. Overall, these data suggest that 3D spheroid co-cultures, generated using 1 mg/ml collagen offer a potential platform to investigate therapeutic agents targeting either DLBCL cells, or the TME itself.

DISCUSSION

Our aim was to generate a model of the DLBCL-like TME with the potential to serve as a platform to assess therapies targeting this clinically relevant lymphoma. We chose not to focus on traditional 2D culture techniques, as the complex nature of the DLBCL microenvironment, confirmed by IHC in **Figure 1A**, would be difficult to recapitulate using this approach. Moreover, our observation that 98% of primary DLBCL cells died when cultured alone *in vitro* (**Figure 1B**) indicates that these cells require a culture system that effectively mimics the complex multicellular TME to support tumor cell survival *in vitro*. One way to achieve this is by using a 3D co-culture approach. Such systems have already been used as tools to study immune function *ex vivo* (41) and specific cellular constituents of the solid tumor TME, such as macrophages (42, 43), and CAF (44, 45).

Regarding lymphomas, a 3D model of FL combining lymphoma cell lines with dermal fibroblasts on a polystyrene matrix demonstrated enhancement of malignant B cell proliferative capacity compared to 2D stromal cell co-cultures (46). A cell aggregate-based system, utilizing lymphoma cell-lines, has been used to assess the efficacy of anti-CD20 mAb and Natural Killer (NK) cell-mediated ADCC (47–49). Other groups have developed models of the bone-marrow and vascular niches (50, 51) to study resistance to drug-induced apoptosis, while a recent 3D chip-based model of DLBCL, utilizing a variety of primary murine cells, enabled the *in vitro* modeling of the DLBCL TME and associated microvasculature (52). 3D Bioprinting is another technology currently being explored as a resource to recreate the tumor microenvironment, [recently reviewed by Mao et al. (53)]. Its ability to combine multiple cell types in pre-defined spatial arrays, coupled with the capacity to produce standardized 3D tumor environments lends itself to a precision medicine approach to tumor modeling. None of these models to date exclusively incorporate key primary human cell populations in a biologically relevant 3D matrix. Therefore, we elected to develop a scaffold-based 3D culture system in which cells are seeded on, or encapsulated within, natural or synthetic biomaterials (54) that mimic the ECM of solid tissues (55). This offers the flexibility of combining primary human cell populations identified as relevant for the DLBCL TME, specifically fibroblasts, and those implicated in mediating and modulating the activity of anti-CD20 mAb, macrophages, with primary tumor cells, within a Type I collagen-based 3D extracellular matrix, with the aim of recapitulating a DLBCL-like TME. We favor this approach as the encapsulation of cellular components within a 3D structure enables their recovery as single cell suspensions for downstream processing, as well as facilitating sample preparation for microscopy (FFPE for IHC, and/or whole mount staining for IF microscopy).

We confirmed that 2D culture of commercially obtained ADSC with IL-4, TNF-α and LT-α/β resulted in the generation of fibroblast-like cells, expressing markers associated with lymphoid fibroblasts (29), and that all three cytokines were not only required to drive this process (**Figures 2B, C**), but also to maintain it (**Supplementary Figure 2**). Although PBMC preferentially adhered to 2D cultures of cytokine stimulated ADSC (**Figure 3A**), addition of PBMC, either alone or together with increasing numbers of MDM, did not significantly alter the expression of lymphoid fibroblast markers on cytokine treated ADSC (**Figure 3B**). Furthermore, though we identified B cells as the lymphocyte population interacting directly with ADSC-derived lymphoid fibroblasts (**Figure 4A**), B cell/ADSC co-cultures did not alter the phenotype of the recovered ADSC-derived lymphoid fibroblasts (**Figure 4B**). In contrast, co-culturing cytokine treated ADSC with primary DLBCL cells clearly impacted the expression of podoplanin, VCAM-1, and ICAM-1 on the recovered ADSC, with addition of MDM further modulating this effect (**Figure 5B**, **Supplementary Figure 4A**), suggesting that MDM may foster unique interactions between these cells, stroma and primary DLBCL cells. The reduced ICAM-1 expression at both day 3 and 8 of 2D co-culture suggest that this adhesion molecule plays a role in mediating interactions between the three cellular constituents in this context. The observed increase in podoplanin expression was also a characteristic feature of both DLBCL/ADSC and/DLBCL/ADSC/MDM 2D co-cultures, which is notable, given the reported enrichment of the DLBCL stromal-1 gene signature in podoplanin expressing cells, including lymph node FRC (56). The viability of primary DLBCL cells was also maintained in 2D co-cultures for up to 8 days, supporting the ability of our tri-partite co-culture system to provide signals necessary to maintain DLBCL cell survival.

Our next step was to incorporate 2D co-cultures into a Type-I collagen matrix, to generate 3D spheroids (**Figure 6A**). Enzymatic digestion of these spheroids impacted upon the ability to detect adhesion molecule expression on the recovered ADSC by flow cytometry, reducing ICAM-1 MFI, and rendering VCAM-1 undetectable, indicating that these molecules likely

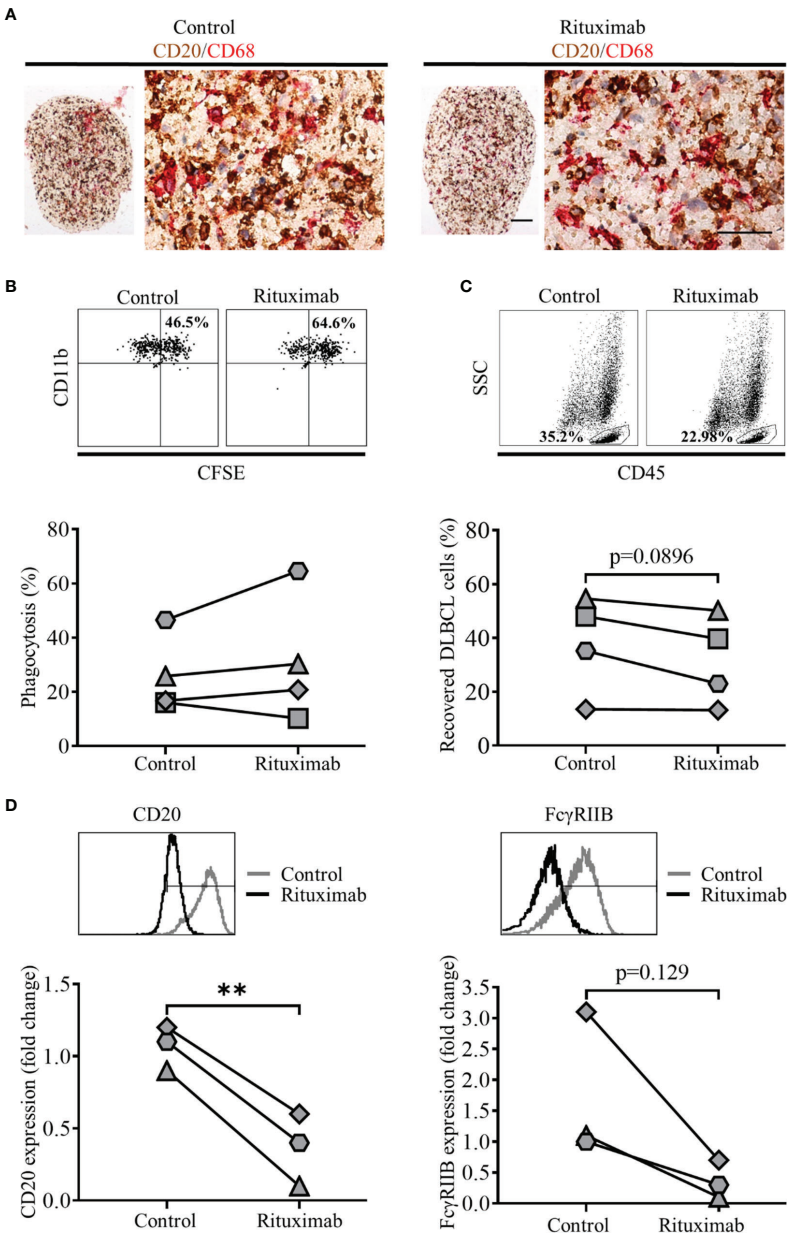

FIGURE 8 | Treatment of 3D spheroid co-cultures with rituximab can induce antibody dependent cell phagocytosis (ADCP). **(A)** Representative double immunohistochemistry (IHC) staining of formaldehyde fixed paraffin embedded (FFPE) sections of 2 mg/ml collagen spheroid co-cultures containing adipocyte derived stem cell (ADSC)-derived lymphoid fibroblasts, primary diffuse large cell B cell lymphoma (DLBCL) cells (CD20, brown), and monocyte-derived macrophages (MDM) (CD68, red) cultured with 10 μg/ml of a control antibody (trastuzumab, left-hand panel) or rituximab (right-hand panel) for 44 h prior to harvest, scale bars 100 and 50 μm for upper and lower images, respectively. **(B)** Representative dot plots illustrating the percentage phagocytosis in cells recovered from 1 mg/ml collagen spheroid co-cultures treated with 10 μg/ml of control antibody (left-hand panel) or rituximab (right-hand panel) for 20 h prior to harvest; the graph shows the % phagocytosis in cells recovered from control antibody-treated and rituximab-treated 3D collagen spheroid co-cultures, each pair of linked filled circles represents data from an independent experiment. Two group comparisons were made using a paired two-tailed t test. **(C)** Representative dot plots illustrating the percentage of DLBCL recovered from 1 mg/ml collagen spheroid co-cultures treated with 10 μg/ml of control antibody (left-hand panel) or rituximab (right-hand panel) for 20 h prior to harvest; the graph shows the % of DLBCL cells recovered from control- and rituximab-treated 3D collagen spheroid co-cultures, each pair of linked filled circles represents data from an independent experiment. Two group comparisons were made using a paired two-tailed t test, p values <0.05 were considered significant. **(D)** Representative histograms showing the expression of CD20 (left-hand panel) and FcγRIIB (right-hand panel) on primary DLBCL recovered from 1 mg/ml collagen spheroid co-cultures treated with 10 ug/ml of control antibody (trastuzumab) or rituximab for 20 h prior to harvest. Graph shows the fold-change in the expression of CD20 (left-hand graph) and FcγRIIB (right-hand graph) on primary DLBCL recovered from rituximab-treated spheroid co-cultures relative to those recovered from control mAb-treated spheroids, values have been normalized relative to untreated controls. Each filled circle represents a single independent experiment. Two group comparisons were made using a paired t-test; p values < 0.05 were considered significant, **p < 0.01.

mediate interactions between the ADSC-derived lymphoid fibroblasts and the 3D collagen scaffold. Microscopic assessment of 3D PBMC/ADSC spheroid co-cultures demonstrated that B cells and MDM maintain a close association with ADSC-derived fibroblasts in this context. Expression of lymphoid fibroblast markers on ADSC-derived fibroblasts recovered from 3D spheroid co-cultures differed to that observed for 2D co-cultures (**Figures 6C** and **3B**, respectively), suggesting that the 3D PBMC/ADSC/MDM spheroid co-cultures were qualitatively different to their 2D counterparts. 3D DLBCL/ADSC/MDM spheroid co-cultures also featured close interaction between all three cell populations in the 3D environment, with these associations comparable to those observed in clinical samples (**Figure 7A**, right-hand panels, and **Figure 1A**, respectively). Similar to 2D co-cultures, ADSC-derived fibroblasts recovered from 3D collagen spheroid co-cultures featured increased podoplanin expression and decreased ICAM-1 (**Supplementary Figure 4A** and **Figure 7B**, respectively). The viability of DLBCL cells recovered from 3D collagen spheroid co-cultures and 2D co-cultures ran in parallel, was similar suggesting that the 3D co-culture system generated an environment compatible for DLBCL cell survival (**Figures 7C, D**). Interestingly, recent data indicate that BAFF-expressing FRC promote the survival of DLBCL cells in 3D matrix gel co-cultures (14), highlighting a key support role for lymphoid fibroblasts in the DLBCL TME. However, a role for MDM in the improved survival of DLBCL in our system cannot be excluded, given the reported supportive role of monocytes in DLBCL survival and proliferation (57). Further evidence that the 3D spheroid co-culture environment featured supportive interactions between its constituents was provided by the preservation of podoplanin and ICAM-1 expression on ADSC-derived lymphoid fibroblasts recovered from 3D DLBCL/ADSC/MDM spheroid co-cultures following cytokine removal (**Supplementary Figure 6A**). This ability to compensate for the loss of extrinsic cytokine-derived signals is supported by recent data showing that co-culture of DLBCL cells with human lymph node-derived FRC increased their expression of podoplanin, a process linked to lymphoma secreted lymphotoxins and TNF-α (14).

Although our model is a simplistic representation of the *in vivo* DLBCL TME, it does include macrophages; these cells usually represent the highest proportion of inflammatory cells in the TME, sometimes as much as 50%, depending on tumor type (58). They are also key effector cells involved in delivering anti-tumor effects through mAb therapy.

Using rituximab as a model therapeutic agent in our 3D co-culture system, we noted increased phagocytosis in rituximab vs control-treated spheroids in three of four experiments (**Figure 8B**). Furthermore, there was a reduction in the percentage of DLBCL cells recovered from the rituximab-treated spheroids compared to their control-treated counterparts (**Figure 8C**).

The primary DLBCL cells we used in all our assays, from a single donor, expressed FcγRIIB (**Figure 8D**), a receptor known to bind the Fc portion of rituximab at the lymphoma cell surface resulting in its internalization and/or trogocytosis (30). The observation of down-regulation of both CD20 and FcγRIIB in rituximab-treated cultures (**Figure 8D**) suggests that this process may underlie the observed low levels of ADCP. It must be noted that CD20 expression was assessed using an in-house labeled rituximab, so we cannot exclude a competition effect underlying this reduction in CD20 expression. However, the concurrent reduction in CD19 expression on these cells (data not shown) suggests that CD20 and its associated B cell receptor components such as CD19 (59) are being internalized. Blocking of FcγRIIB could potentially overcome this issue (60). Alternatively using a type II anti-CD20 antibody such as obinutuzumab, which is not subject to such marked internalization (26, 30) could result in improved ADCP in our system.

The levels of rituximab mediated ADCP observed in our 3D spheroid co-cultures were low, suggesting that they are potentially antagonistic to ADCP, given the activity of the MDM in 2D cultures (**Supplementary Figure 7A**). This raises the possibility that a similar environment may exist in the DLBCL TME *in vivo*. The limited ADCP that we observed does, however, provide the opportunity to test agents that repolarize macrophages to a more phagocytic phenotype. Ligands that target pattern recognition receptors expressed by macrophages such as Pam3CSK4, as well as STING agonists, have been shown to enhance ADCP by altering the relative expression of activatory and inhibitory FcγRs (A:I ratio) (24) and so such reagents and strategies could be tested in follow on studies, and extended to include novel therapeutic approaches directly targeting other TME constituents.

Overall, we demonstrated that 3D collagen spheroids incorporating ADSC-derived fibroblasts co-cultured with primary DLBCL cells and MDM can be generated and are amenable to subsequent manipulation and downstream analysis by flow cytometry and microscopy. These spheroids recreate the spatial relationship of the cell populations observed in the DLBCL TME, and, to some degree, the inter cell communication that occurs within it, as evidenced by the maintenance of DLBCL viability and impact upon ADSC-derived lymphoid fibroblast phenotype. Although our current system is labor-intensive, the application of microfluidic technologies could help ameliorate this issue. Furthermore, the ability to combine multiple cell types in a 3D scaffold means it has the capacity to be modified to study other lymphomas and/or solid tumors. The modular nature of system further lends itself to personalized medicine; for example, Majudmer et al. (61) recently developed an *ex vivo* system comprising tumor sections cultured on grade-matched tumor matrix in the presence of autologous serum. Similarly, our system could be adapted to incorporate patient-derived CAF and/or TAM with the corresponding primary tumor cells in a 3D scaffold based upon the matrix within the patient's tumor. Regardless of the precise format, it is clear that more sophisticated model systems are required to address the complexities of cancer. Hopefully such systems will elicit more effective therapies in the future.

DATA AVAILABILITY STATEMENT

The raw data supporting the conclusions of this article will be made available by the authors without undue reservation.

ETHICS STATEMENT

Ethical approval for the use of human tumor samples was obtained by Southampton University Hospitals NHS Trust from Southampton and South West Hampshire Research Ethics Committee. Informed consent was provided in accordance with the Declaration of Helsinki. DLBCL samples were obtained from Human Tissue Authority Licensed University of Southampton, Cancer Sciences Unit Tissue Bank. Use of human blood samples was approved by the East of Scotland Research ethics service. Blood donors provided their informed consent to participate in research studies.

AUTHOR CONTRIBUTIONS

RF, PN, ET performed the experiments. RF, PN, BG, EH, MCC, SB, and MSC designed the experiments. RF, PN, MAK, SB, and MSC analysed the data. RF, SB, and MSC wrote the manuscript. All authors contributed to the article and approved the submitted version.

FUNDING

This work was supported by Bloodwise (Award number: 12050) and CRUK programme grants awarded to MC and SB (Award number: 24721), CRUK ECMC grant (Award number: A25171) and CRUK centre grant (Award number: A25139).

ACKNOWLEDGMENTS

We are grateful to Jenny Norman in the Histochemistry Research Unit, University Hospital Southampton, Maria Fernandes, in the Research Pathology, University Hospital Southampton and Dave Johnston in the Biomedical Imaging Unit, University Hospital Southampton for the assistance they provided.

SUPPLEMENTARY MATERIAL

The Supplementary Material for this article can be found online at: https://www.frontiersin.org/articles/10.3389/fimmu.2020.605231/full#supplementary-material

REFERENCES

1. Chaganti S, Illidge T, Barrington S, McKay P, Linton K, Cwynarski K, et al. Guidelines for the management of diffuse large B-cell lymphoma. *Br J Haematol* (2016) 174:43–56. doi: 10.1111/bjh.14136
2. Alizadeh AA, Eisen MB, Davis RE, Ma C, Lossos IS, Rosenwald A, et al. Distinct types of diffuse large B-cell lymphoma identified by gene expression profiling. *Nature* (2000) 403:503–11. doi: 10.1038/35000501
3. Rosenwald A, Wright G, Leroy K, Yu X, Gaulard P, Gascoyne RD, et al. Molecular diagnosis of primary mediastinal B cell lymphoma identifies a clinically favorable subgroup of diffuse large B cell lymphoma related to Hodgkin lymphoma. *J Exp Med* (2003) 198:851–62. doi: 10.1084/jem.20031074
4. Chapuy B, Stewart C, Dunford AJ, Kim J, Kamburov A, Redd RA, et al. Molecular subtypes of diffuse large B cell lymphoma are associated with distinct pathogenic mechanisms and outcomes. *Nat Med* (2018) 24:679–90. doi: 10.1038/s41591-018-0016-8
5. Schmitz R, Wright GW, Huang DW, Johnson CA, Phelan JD, Wang JQ, et al. Genetics and Pathogenesis of Diffuse Large B-Cell Lymphoma. *N Engl J Med* (2018) 378:1396–407. doi: 10.1056/NEJMoa1801445
6. Crump M, Neelapu SS, Farooq U, Van Den Neste E, Kuruvilla J, Westin J, et al. Outcomes in refractory diffuse large B-cell lymphoma: results from the international SCHOLAR-1 study. *Blood* (2017) 130:1800–8. doi: 10.1182/blood-2017-03-769620
7. Cummin TC, Cragg MS, Friedberg JW, Johnson PWM. "Targeted Therapeutics for Lymphoma: Using Biology to Inform Treatment". In: GS Lenz, G Salles, editors. *Aggressive lymphomas*. Switzerland: Springer International Publishing (2018). p. 343–60. doi: 10.1007/978-3-030-00362-3
8. Scott DW, Gascoyne RD. The tumour microenvironment in B cell lymphomas. *Nat Rev Cancer* (2014) 14:517–34. doi: 10.1038/nrc3774
9. Liu T, Zhou L, Li D, Andl T, Zhang Y. Cancer-Associated Fibroblasts Build and Secure the Tumor Microenvironment. *Front Cell Dev Biol* (2019) 7:60. doi: 10.3389/fcell.2019.00060
10. Bu L, Baba H, Yoshida N, Miyake K, Yasuda T, Uchihara T, et al. Biological heterogeneity and versatility of cancer-associated fibroblasts in the tumor microenvironment. *Oncogene* (2019) 38:4887–901. doi: 10.1038/s41388-019-0765-y
11. Lamaison C, Tarte K. Impact of B cell/lymphoid stromal cell crosstalk in B-cell physiology and malignancy. *Immunol Lett* (2019) 215:12–8. doi: 10.1016/j.imlet.2019.02.005
12. Nayar S, Campos J, Smith CG, Iannizzotto V, Gardner DH, Mourcin F, et al. Immunofibroblasts are pivotal drivers of tertiary lymphoid structure formation and local pathology. *Proc Natl Acad Sci U S A* (2019) 116:13490–7. doi: 10.1073/pnas.1905301116
13. Pandey S, Mourcin F, Marchand T, Nayar S, Guirriec M, Pangault C, et al. IL-4/CXCL12 loop is a key regulator of lymphoid stroma function in follicular lymphoma. *Blood* (2017) 129:2507–18. doi: 10.1182/blood-2016-08-737239
14. Apollonio B, Jarvis P, Phillips E, Kuhnl A, Salisbury J, Zacharioudakis G, et al. Diffuse large B-cell lymphoma remodels the fibroblastic reticular network that acquires aberrant immunosuppressive capabilities; implications for the regulation of anti-tumor immunity in the immuno-oncology era. *Br J Haematol* (2019) 185(Suppl. 1):26. doi: 10.1111/bjh.15854
15. Apollonio B, Nicholas NS, Sutton LA, Salisbury J, Patten PE, Kassam S, et al. Diffuse Large B-Cell Lymphoma (DLBCL) Tumor Cells Reprogram Lymphatic Fibroblasts into Cancer-Associated Fibroblasts (CAFs) That Contribute to Tumor Microenvironment (TME)-Driven Immune Privilege. *Blood* (2015) 126(23):1474. doi: 10.1182/blood.V126.23.1474.1474
16. Sakamoto A, Kunou S, Shimada K, Tsunoda M, Aoki T, Iriyama C, et al. Pyruvate secreted from patient-derived cancer-associated fibroblasts supports survival of primary lymphoma cells. *Cancer Sci* (2019) 110:269–78. doi: 10.1111/cas.13873
17. Shields JD, Kourtis IC, Tomei AA, Roberts JM, Swartz MA. Induction of lymphoidlike stroma and immune escape by tumors that express the chemokine CCL21. *Science* (2010) 328:749–52. doi: 10.1126/science.1185837
18. Ame-Thomas P, Maby-El Hajjami H, Monvoisin C, Jean R, Monnier D, Caulet-Maugendre S, et al. Human mesenchymal stem cells isolated from bone marrow and lymphoid organs support tumor B-cell growth: role of stromal cells in follicular lymphoma pathogenesis. *Blood* (2007) 109:693–702. doi: 10.1182/blood-2006-05-020800
19. Murray PJ, Wynn TA. Protective and pathogenic functions of macrophage subsets. *Nat Rev Immunol* (2011) 11:723–37. doi: 10.1038/nri3073
20. DeNardo DG, Ruffell B. Macrophages as regulators of tumour immunity and immunotherapy. *Nat Rev Immunol* (2019) 19:369–82. doi: 10.1038/s41577-019-0127-6
21. Gok Yavuz B, Gunaydin G, Gedik ME, Kosemehmetoglu K, Karakoc D, Ozgur F, et al. Cancer associated fibroblasts sculpt tumour microenvironment by recruiting monocytes and inducing immunosuppressive PD-1(+) TAMs. *Sci Rep* (2019) 9:3172. doi: 10.1038/s41598-019-39553-z
22. Li YL, Shi ZH, Wang X, Gu KS, Zhai ZM. Tumor-associated macrophages predict prognosis in diffuse large B-cell lymphoma and correlation with

peripheral absolute monocyte count. *BMC Cancer* (2019) 19:1049. doi: 10.1186/s12885-019-6208-x
23. Long KB, Collier AI, Beatty GL. Macrophages: Key orchestrators of a tumor microenvironment defined by therapeutic resistance. *Mol Immunol* (2019) 110:3–12. doi: 10.1016/j.molimm.2017.12.003
24. Dahal LN, Dou L, Hussain K, Liu R, Earley A, Cox KL, et al. STING Activation Reverses Lymphoma-Mediated Resistance to Antibody Immunotherapy. *Cancer Res* (2017) 77:3619–31. doi: 10.1158/0008-5472.CAN-16-2784
25. Nimmerjahn F, Ravetch JV. Fcgamma receptors as regulators of immune responses. *Nat Rev Immunol* (2008) 8:34–47. doi: 10.1038/nri2206
26. Tipton TR, Roghanian A, Oldham RJ, Carter MJ, Cox KL, Mockridge CI, et al. Antigenic modulation limits the effector cell mechanisms employed by type I anti-CD20 monoclonal antibodies. *Blood* (2015) 125:1901–9. doi: 10.1182/blood-2014-07-588376
27. Di Modugno F, Colosi C, Trono P, Antonacci G, Ruocco G, Nistico P. 3D models in the new era of immune oncology: focus on T cells, CAF and ECM. *J Exp Clin Cancer Res* (2019) 38:117. doi: 10.1186/s13046-019-1086-2
28. Hoarau-Vechot J, Rafii A, Touboul C, Pasquier J. Halfway between 2D and Animal Models: Are 3D Cultures the Ideal Tool to Study Cancer-Microenvironment Interactions? *Int J Mol Sci* (2018) 19(1):181. doi: 10.3390/ijms19010181
29. Coles M, Glaysher B. Composition used for differentiating mesenchymal stem cells into lymphoid stromal cells, comprises cytokine receptor ligands, where the ligands bind and activate interleukin 4 receptor, TNF receptor and lymphotoxin beta receptor, Univ York (Uyyk-C.). WO/2013/041843 CELL DIFFERENTIATION - Patentscope, 28.03.2013.
30. Lim SH, Vaughan AT, Ashton-Key M, Williams EL, Dixon SV, Chan HT, et al. Fc gamma receptor IIb on target B cells promotes rituximab internalization and reduces clinical efficacy. *Blood* (2011) 118:2530–40. doi: 10.1182/blood-2011-01-330357
31. Schneider CA, Rasband WS, Eliceiri KW. NIH Image to ImageJ: 25 years of image analysis. *Nat Methods* (2012) 9:671–5. doi: 10.1038/nmeth.2089
32. Opinto G, Vegliante MC, Negri A, Skrypets T, Loseto G, Pileri SA, et al. The Tumor Microenvironment of DLBCL in the Computational Era. *Front Oncol* (2020) 10:351. doi: 10.3389/fonc.2020.00351
33. Gronthos S, Franklin DM, Leddy HA, Robey PG, Storms RW, Gimble JM. Surface protein characterization of human adipose tissue-derived stromal cells. *J Cell Physiol* (2001) 189:54–63. doi: 10.1002/jcp.1138
34. Walmsley GG, Atashroo DA, Maan ZN, Hu MS, Zielins ER, Tsai JM, et al. High-Throughput Screening of Surface Marker Expression on Undifferentiated and Differentiated Human Adipose-Derived Stromal Cells. *Tissue Engineering Part A* (2015) 21:2281–91. doi: 10.1089/ten.tea.2015.0039
35. Benezech C, Mader E, Desanti G, Khan M, Nakamura K, White A, et al. Lymphotoxin-beta receptor signaling through NF-kappaB2-RelB pathway reprograms adipocyte precursors as lymph node stromal cells. *Immunity* (2012) 37:721–34. doi: 10.1016/j.immuni.2012.06.010
36. Marchesi F, Cirillo M, Bianchi A, Gately M, Olimpieri OM, Cerchiara E, et al. High density of CD68+/CD163+ tumour-associated macrophages (M2-TAM) at diagnosis is significantly correlated to unfavorable prognostic factors and to poor clinical outcomes in patients with diffuse large B-cell lymphoma. *Hematol Oncol* (2015) 33:110–2. doi: 10.1002/hon.2142
37. Xu XX, Li ZX, Liu J, Zhu FF, Wang ZT, Wang JY, et al. The prognostic value of tumour-associated macrophages in Non-Hodgkin's lymphoma: A systematic review and meta-analysis. *Scand J Immunol* (2020) 91(1):1–9. doi: 10.1111/sji.12814
38. Nam SJ, Go H, Paik JH, Kim TM, Heo DS, Kim CW, et al. An increase of M2 macrophages predicts poor prognosis in patients with diffuse large B-cell lymphoma treated with rituximab, cyclophosphamide, doxorubicin, vincristine and prednisone. *Leukemia Lymphoma* (2014) 55:2466–76. doi: 10.3109/10428194.2013.879713
39. Riihijarvi S, Fiskvik I, Taskinen M, Vajavaara H, Tikkala M, Yri O, et al. Prognostic influence of macrophages in patients with diffuse large B-cell lymphoma: a correlative study from a Nordic phase II trial. *Haematologica* (2015) 100:238–45. doi: 10.3324/haematol.2014.113472
40. Sopp J, Cragg MS. Deleting Malignant B Cells With Second-Generation Anti-CD20 Antibodies. *J Clin Oncol* (2018) 36:2323–5. doi: 10.1200/JCO.2018.78.7390
41. Purwada A, Shah SB, Beguelin W, August A, Melnick AM, Singh A. Ex vivo synthetic immune tissues with T cell signals for differentiating antigen-specific, high affinity germinal center B cells. *Biomaterials* (2019) 198:27–36. doi: 10.1016/j.biomaterials.2018.06.034
42. Kuen J, Darowski D, Kluge T, Majety M. Pancreatic cancer cell/fibroblast co-culture induces M2 like macrophages that influence therapeutic response in a 3D model. *PLoS One* (2017) 12:e0182039. doi: 10.1371/journal.pone.0182039
43. Rebelo SP, Pinto C, Martins TR, Harrer N, Estrada MF, Loza-Alvarez P, et al. 3D-3-culture: A tool to unveil macrophage plasticity in the tumour microenvironment. *Biomaterials* (2018) 163:185–97. doi: 10.1016/j.biomaterials.2018.02.030
44. Nakamura H, Sugano M, Miyashita T, Hashimoto H, Ochiai A, Suzuki K, et al. Organoid culture containing cancer cells and stromal cells reveals that podoplanin-positive cancer-associated fibroblasts enhance proliferation of lung cancer cells. *Lung Cancer* (2019) 134:100–7. doi: 10.1016/j.lungcan.2019.04.007
45. Wessels DJ, Pradhan N, Park YN, Klepitsch MA, Lusche DF, Daniels KJ, et al. Reciprocal signaling and direct physical interactions between fibroblasts and breast cancer cells in a 3D environment. *PLoS One* (2019) 14:e0218854. doi: 10.1371/journal.pone.0218854
46. Caicedo-Carvajal CE, Liu Q, Remache Y, Goy A, Suh KS. Cancer Tissue Engineering: A Novel 3D Polystyrene Scaffold for In Vitro Isolation and Amplification of Lymphoma Cancer Cells from Heterogeneous Cell Mixtures. *J Tissue Eng* (2011) 2011:362326. doi: 10.4061/2011/362326
47. Decaup E, Jean C, Laurent C, Gravelle P, Fruchon S, Capilla F, et al. Anti-tumor activity of obinutuzumab and rituximab in a follicular lymphoma 3D model. *Blood Cancer J* (2013) 3:e131. doi: 10.1038/bcj.2013.32
48. Decaup E, Rossi C, Gravelle P, Laurent C, Bordenave J, Tosolini M, et al. A Tridimensional Model for NK Cell-Mediated ADCC of Follicular Lymphoma. *Front Immunol* (2019) 10:1943. doi: 10.3389/fimmu.2019.01943
49. Gravelle P, Jean C, Familiades J, Decaup E, Blanc A, Bezombes-Cagnac C, et al. Cell growth in aggregates determines gene expression, proliferation, survival, chemoresistance, and sensitivity to immune effectors in follicular lymphoma. *Am J Pathol* (2014) 184:282–95. doi: 10.1016/j.ajpath.2013.09.018
50. Aljitawi OS, Li D, Xiao Y, Zhang D, Ramachandran K, Stehno-Bittel L, et al. A novel three-dimensional stromal-based model for in vitro chemotherapy sensitivity testing of leukemia cells. *Leukemia Lymphoma* (2014) 55:378–91. doi: 10.3109/10428194.2013.793323
51. Bray LJ, Binner M, Korner Y, von Bonin M, Bornhauser M, Werner C. A three-dimensional ex vivo tri-culture model mimics cell-cell interactions between acute myeloid leukemia and the vascular niche. *Haematologica* (2017) 102:1215–26. doi: 10.3324/haematol.2016.157883
52. Mannino RG, Santiago-Miranda AN, Pradhan P, Qiu Y, Mejias JC, Neelapu SS, et al. 3D microvascular model recapitulates the diffuse large B-cell lymphoma tumor microenvironment in vitro. *Lab chip* (2017) 17:407–14. doi: 10.1039/C6LC01204C
53. Mao S, Pang Y, Liu T, Shao Y, He J, Yang H, et al. Bioprinting of in vitro tumor models for personalized cancer treatment: a review. *Biofabrication* (2020) 12:042001. doi: 10.1088/1758-5090/ab97c0
54. Nyga A, Cheema U, Loizidou M. 3D tumour models: novel in vitro approaches to cancer studies. *J Cell Commun Signal* (2011) 5:239–48. doi: 10.1007/s12079-011-0132-4
55. Ferreira LP, Gaspar VM, Mano JF. Design of spherically structured 3D in vitro tumor models -Advances and prospects. *Acta Biomater* (2018) 75:11–34. doi: 10.1016/j.actbio.2018.05.034
56. Haro M, Orsulic S. A Paradoxical Correlation of Cancer-Associated Fibroblasts With Survival Outcomes in B-Cell Lymphomas and Carcinomas. *Front Cell Dev Biol* (2018) 6:98. doi: 10.3389/fcell.2018.00098
57. Mueller CG, Boix C, Kwan WH, Daussy C, Fournier E, Fridman WH, et al. Critical role of monocytes to support normal B cell and diffuse large B cell lymphoma survival and proliferation. *J Leukoc Biol* (2007) 82:567–75. doi: 10.1189/jlb.0706481
58. Yang L, Zhang Y. Tumor-associated macrophages: from basic research to clinical application. *J Hematol Oncol* (2017) 10:58. doi: 10.1186/s13045-017-0430-2
59. Fujimoto M, Poe JC, Inaoki M, Tedder TF. CD19 regulates B lymphocyte responses to transmembrane signals. *Semin Immunol* (1998) 10:267–77. doi: 10.1006/smim.1998.9999
60. Roghanian A, Teige I, Martensson L, Cox KL, Kovacek M, Ljungars A, et al. Antagonistic human FcgammaRIIB (CD32B) antibodies have anti-tumor activity and overcome resistance to antibody therapy in vivo. *Cancer Cell* (2015) 27:473–88. doi: 10.1016/j.ccell.2015.03.005

61. Majumder B, Baraneedharan U, Thiyagarajan S, Radhakrishnan P, Narasimhan H, Dhandapani M, et al. Predicting clinical response to anticancer drugs using an ex vivo platform that captures tumour heterogeneity. *Nat Commun* (2015) 6:6169. doi: 10.1038/ncomms7169

Conflict of Interest: MSC is a retained consultant for BioInvent International and has performed educational and advisory roles for Baxalta, Boehringer Ingleheim and Merck GdA. He has received research funding from Roche, Gilead, iTeos, UCB, Bioinvent International and GSK. SB has received institutional support from BioInvent for grants and patents.

The remaining authors declare that the research was conducted in the absence of any commercial or financial relationships that could be construed as a potential conflict of interest.

frontiers in Immunology

MINI REVIEW
published: 10 February 2021
doi: 10.3389/fimmu.2020.614300

Advances in Modeling the Immune Microenvironment of Colorectal Cancer

Paul Sukwoo Yoon[1†], Nuala Del Piccolo[2†], Venktesh S. Shirure[2], Yushuan Peng[2], Amanda Kirane[1], Robert J. Canter[1], Ryan C. Fields[3], Steven C. George[2] and Sepideh Gholami[1]*

[1] Department of Surgery, University of California, Davis, Sacramento, CA, United States, [2] Department of Biomedical Engineering, University of California, Davis, Davis, CA, United States, [3] Department of Surgery, The Alvin J. Siteman Cancer Center, Washington University School of Medicine, St. Louis, MO, United States

Colorectal cancer (CRC) is the third most common cancer and second leading cause of cancer-related death in the US. CRC frequently metastasizes to the liver and these patients have a particularly poor prognosis. The infiltration of immune cells into CRC tumors and liver metastases accurately predicts disease progression and patient survival. Despite the evident influence of immune cells in the CRC tumor microenvironment (TME), efforts to identify immunotherapies for CRC patients have been limited. Here, we argue that preclinical model systems that recapitulate key features of the tumor microenvironment—including tumor, stromal, and immune cells; the extracellular matrix; and the vasculature—are crucial for studies of immunity in the CRC TME and the utility of immunotherapies for CRC patients. We briefly review the discoveries, advantages, and disadvantages of current *in vitro* and *in vivo* model systems, including 2D cell culture models, 3D culture systems, murine models, and organ-on-a-chip technologies.

Keywords: colorectal cancer, tumor microenvironment, cancer immunology, tissue engineering, organ-on-a-chip (OOC)

OPEN ACCESS

Edited by:
Benjamin Frey,
University Hospital Erlangen, Germany

Reviewed by:
Nathalie Britzen-Laurent,
University Hospital Erlangen, Germany
Laura Bracci,
National Institute of Health (ISS), Italy

****Correspondence:***
Sepideh Gholami
sgholami@ucdavis.edu

[†]These authors have contributed equally to this work

Specialty section:
This article was submitted to Cancer Immunity and Immunotherapy, a section of the journal Frontiers in Immunology

Received: *05 October 2020*
Accepted: *29 December 2020*
Published: *10 February 2021*

Citation:
Yoon PS, Del Piccolo N, Shirure VS, Peng Y, Kirane A, Canter RJ, Fields RC, George SC and Gholami S (2021) Advances in Modeling the Immune Microenvironment of Colorectal Cancer. Front. Immunol. 11:614300. doi: 10.3389/fimmu.2020.614300

INTRODUCTION

In the US, colorectal cancer (CRC) is the third most common cancer and second leading cause of cancer-related death (1). CRC is largely asymptomatic until it has progressed to advanced stages (2), with 5 year survival rates of 90% and 14% for localized and metastatic cases, respectively (1). Population-wide screening campaigns in the last two decades have led to earlier diagnoses and boosted the overall 5 year survival rate to ~65% (1). Due to anatomical proximity, CRC often metastasizes to the liver: 20%–25% of patients present with colorectal liver metastases (CRLM) at initial diagnosis and 50-60% of CRC patients will develop CRLM at some point (2–4). Hepatectomy is currently the best course of action for CRLM patients, offering a 5 year survival rate of up to 60% (3–5). Unfortunately, only 20%–25% of CRLM patients are eligible for resection at time of diagnosis, leaving a large majority of patients to succumb to progressive metastatic cancer (3, 5).

Recent research has demonstrated the role of immunity on CRC progression, prognosis, and response to therapy. For example, immune cell infiltration into tumors correlates with clinical outcomes: T cells (6–10), Tregs (11), and NK cells (10) in primary CRC or CRLM lesions correlate

with better prognoses, while the presence of tumor-associated macrophages (TAMs) has been alternately associated with pro- (12, 13) and anti-tumor (13–15) effects. In 2006, Galon and colleagues introduced the ImmunoScore. This measure of the density of immune cells in the invasive margin and core of a lesion (9, 16–18) provides more accurate predictions of recurrence, overall survival, and disease-free survival than traditional TNM staging for both CRC (7, 16, 18) and CRLM patients (6, 8, 11, 16).

Based on ImmunoScore's prognostic success, clinicians are actively pursuing immunotherapies for CRC and CRLM patients. Checkpoint blockade therapies have shown particular promise for mismatch repair deficient (dMMR)/microsatellite instability-high (MSI-H) CRC tumors (19–21). In a 2015 Phase II clinical trial, dMMR/MSI-H patients treated with pembrolizumab (PD-1 inhibitor) exhibited a 40% response rate and 78% 12-month progression free survival (22); the FDA approved this course of treatment in 2017 (19). More recent work has probed the utility of combining nivolumab (PD-1 inhibitor) with ipilimumab (CTLA-4 inhibitor) (23). Results from this Phase II trial are still maturing, but preliminary results suggest a response rate as high as 55% (19, 23). Unfortunately, only 15% of CRC tumors are classified as dMMR/MSI-H (19), and there are currently no immunotherapies available to the remaining 85% of CRC patients. Pre-clinical work addressing this gap is focused on adoptive cell therapies, vaccines, immunostimulatory cytokines, and combinations thereof, and early studies have produced promising results (19–21).

The development of more efficacious cancer therapeutics is hindered by the limitations of current preclinical model systems, which do not recapitulate the whole tumor microenvironment (TME) (**Table 1**) (24, 25). The TME is crucial for investigating tumor-immune cell crosstalk, modeling tumor heterogeneity within and between patients, recapitulating events in the metastatic cascade, and simulating responses to therapeutics (24–28). 2D *in vitro* models of cells growing in tissue culture plates lend themselves to the study of tumor growth and cell migration, but lack complex tissue features like the vasculature and extracellular matrix (ECM) (24, 25, 28–31). In 3D *in vitro* models, multiple cell types can be co-cultured in ECM scaffolds, enabling the study of cell-cell interactions and nutrient/waste transport over small distances; however, these models lack key biomechanical features of the TME, including vascular and interstitial perfusion (24, 25, 28–31). Animal models are capable of simulating the dynamic, multi-cellular/organ nature of the TME, but are expensive, difficult to manipulate, and limited in their ability to recreate human immunobiology (24, 32–34).

TABLE 1 | Advances in modeling colorectal cancer.

Model	Application	Advantages	Disadvantages
2D *In vitro*			
Culture plate	• Adhesion • Gene expression • Drug screening	• Simple • Low cost • High throughput	• Low predictive power • Lack of native architecture • Loss of tumor heterogeneity
Wound healing	• Migration		
3D *In vitro*			
Organoid/ Spheroid	• Proliferation • Migration • Gene expression • Drug screening	• Retain native tumor geometry • Cell-cell/ECM interaction • Tumor heterogeneity	• Avascular • High cost • Low scalability • Low reproducibility
Co-culture	• Stromal crosstalk • Immune crosstalk		
In vivo			
Patient-derived xenografts	• Proliferation • Migration • Invasion • Angiogenesis • Gene expression • Drug screening	• Tumor heterogeneity	• High cost • Laborious • Low predictive power • Immunocompromised • Limited metastasis
Humanized mice		• Tumor microenvironment • Tumor heterogeneity • Immunocompetent	• High cost • Laborious • Incomplete immune function • Engraftment difficulties
Genetically engineered mice		• Tumor microenvironment • Tumor heterogeneity • Immunocompetent • Natural disease progression	• High cost • Laborious • Time consuming
Organ-on-a-chip	• Proliferation Migration • Intravasation Extravasation • Invasion • Angiogenesis • Stromal crosstalk • Immune crosstalk • Gene expression • Drug screening	• Tumor microenvironment • Tumor heterogeneity • Vascular • Hydrodynamic properties • Biochemical gradient • Precise control • Easy visualization	• Lack of standardization • High cost • Laborious • Low reproducibility

Model systems that combine tissue engineering with microfluidic technology represent a new frontier for the study of cancer development, progression, immunity, and metastasis. Dubbed "organ-on-a-chip" (OOC) systems, these models incorporate many features of the TME, including multiple cell types, matrix components, biochemical cues, spatiotemporal distribution of soluble mediators and oxygen, and perfusable vascular networks (24, 26, 35–37). Thus, OOC platforms offer great potential as a preclinical tool for precision therapy. This review will highlight recent advances in the utility of OOC devices to model immunity in the CRC/CRLM TME and compare this work with conventional model systems (**Figure 1A**).

TWO-DIMENSIONAL (2D) CULTURES

Cell cultures in 2D (**Figure 1A**) are a standard and well-established model system because they are simple, inexpensive, and easy to manipulate, and enable imaging with high spatiotemporal resolution (**Table 1**) (24, 31). 2D cultures rely on cells adhering to a flat surface—generally a flask or plate—which does not reflect the natural 3D architecture of tissues or tumors. Furthermore, cells in 2D cultures receive relatively uniform and often excessive levels of oxygen, nutrients, and growth factors, compromising their ability to faithfully capture the *in vivo* TME (28–31). Despite these drawbacks, 2D experiments have revealed multiple mechanisms driving the behavior of epithelial sheets of cells (30) and epithelial-derived tumors like CRC and CRLM (40–50).

2D cultures are conducive to studies of tumor-immune cell crosstalk in the TME. For example, 2D *in vitro* systems have been used to examine the role of the CRC TME's atypically high number of macrophages, a topic of active debate. These studies show that macrophages differentiate towards an M2-like phenotype in response to tumor cells or tumor cell-conditioned media (51–55) and migrate towards tumor cells (54, 55). TAMs in CRC have also been shown to modify the tumor cell response to chemotherapy (56, 57); support tumor cell proliferation, migration, and invasion (53–55); and limit tumor cell survival in a cell contact-dependent manner (13). Additionally, Yu and co-authors showed that mast cells migrate towards CRC tumor cell-conditioned media in a Transwell assay and that co-culture of mast and tumor cells increases tumor cell proliferation; the results of these 2D culture experiments were verified in a 3D spheroid model (58). Studies with primary patient samples have demonstrated i) an HLA-mediated T cell response to the survivin protein in CRC tumor cells (59), and ii) NK cell cytotoxicity directed against CRC tumor cells following immune cell activation or tumor cell priming (60).

THREE-DIMENSIONAL (3D) CULTURES

3D cell cultures (**Figure 1A**) are comprised of cells distributed in synthetic or naturally-occurring scaffolds or hydrogels to mimic *in vivo* tissue architecture and can be cultured under static or perfused conditions (28–30). Compared to 2D cell culture systems, 3D *in vitro* systems more accurately model *in vivo* biochemical factor distribution and transport (28, 30); cell morphology, polarity, and gene expression (61–66); heterogeneity in cell types (62, 64, 67); and sensitivity to cancer therapeutics (61, 64, 67, 68). This accuracy is more pronounced under perfused culture conditions (61, 67–69) (**Table 1**). The challenges facing 3D cell culture systems include: i) uncertainty introduced by the underdefined, variable composition of popular scaffold materials (including the gold standard Matrigel); ii) the absence of vascular flow, which is responsible for cancer cell dissemination, trafficking of some immune cells, and delivery of therapeutics; iii) the inability to replicate the long-range interactions between tumors and other organs in the body that govern metastasis and the immune response (24, 29, 35, 70); and iv) limited reproducibility, scalability, and ease of use.

A handful of recent reports demonstrate the utility of 3D models systems for the study of immunity in the CRC TME. In a 2018 paper, Dijkstra et al. co-cultured organoids from dMMR CRC patients with autologous peripheral blood lymphocytes (71). In this novel culture system, the team generated patient-specific, cancer-reactive T cells from 4 of 8 patients, characterized the specificity of T cells for tumor versus healthy tissue, and measured the efficiency of T cell mediated tumor cell killing. A 2019 report by Courau and colleagues demonstrated that primary T and NK cells infiltrate into cell line-derived CRC spheroids, where they kill tumor cells and degrade the 3D structure of the spheroid, and that these effects can be enhanced by stimulating the immune response with IL-15 plus anti-NKG2D and/or anti-MICA/B antibodies (72). The authors also showed that stimulation of the immune response is necessary for infiltration of autologous T and NK cells into patient-matched CRC spheroids. Another recent study found that CAR-NK-92 cells engineered to recognize the universal antigen EPCAM, the neoantigen EGFRvIII, or the tumor-associated antigen FRIZZLED can identify and lyse cells in murine- and patient-derived normal colon and CRC organoids, but the effects are reduced by limited immune cell infiltration into organoids (73). Further, a 2019 report showed that primary CRC samples cultured under perfused conditions retained native tissue architecture, tumor cell density, and immune and stromal cell viability better than samples cultured under static conditions (69).

IN VIVO MODELS

In vivo models (**Figure 1A**) are integral tools in cancer research because they recapitulate several features of the TME not available in *in vitro* models, including vascular flow and communication between the tumor and distant organs (74–79). There are five types of mouse models of cancer: 1) xenograft, 2) allograft, 3) patient-derived xenograft (PDX), 4) humanized, and 5) genetically modified mouse (GEMM). Though murine models are labor intensive, expensive, low-throughput, and susceptible to cross-species incompatibilities, they have produced numerous insights into CRC response to drug treatment (76, 77, 80–87) and metastasis (85, 88–90) (**Table 1**).

Though transplant mouse models (xenograft, allograft, and PDX) accurately replicate the response to therapeutics

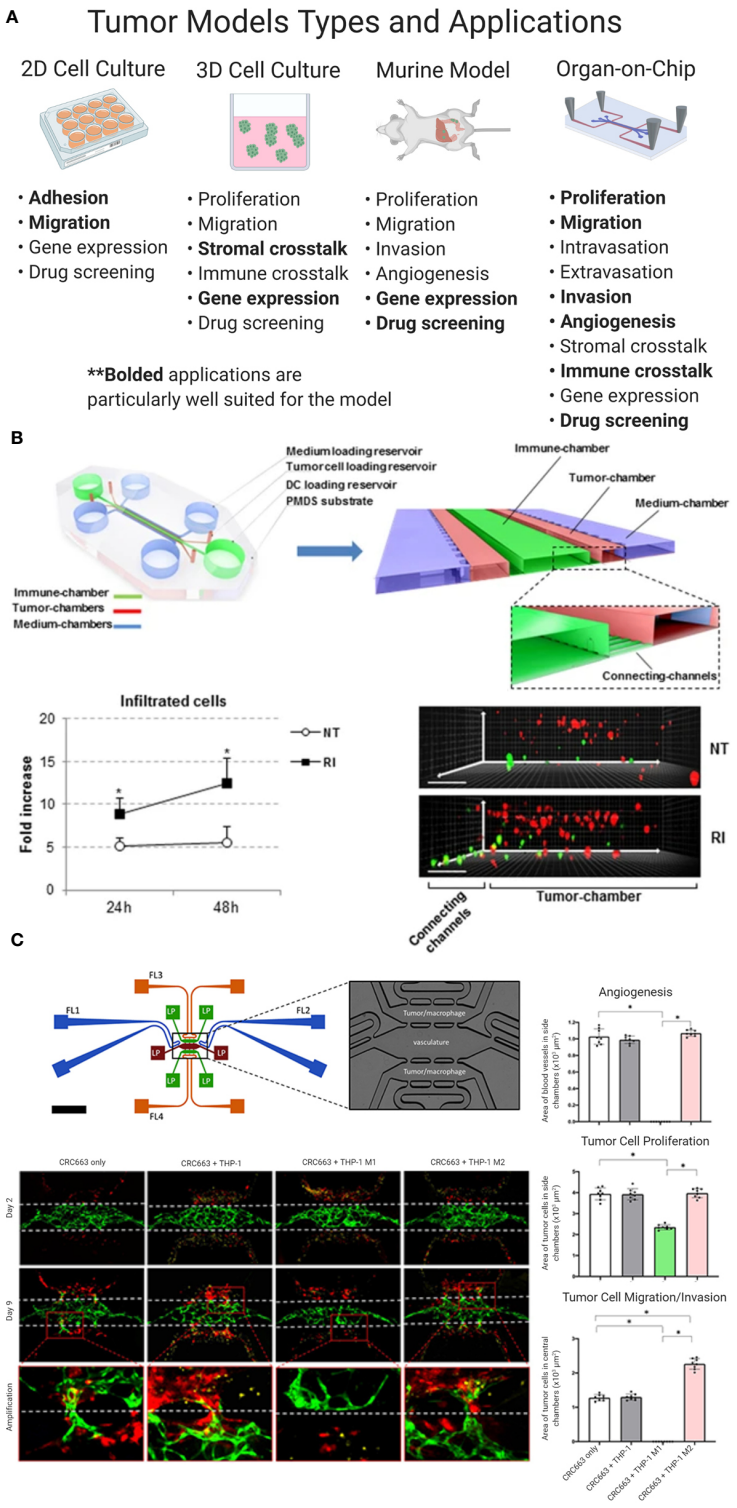

FIGURE 1 | **(A)** Colorectal liver metastasis models. Bolded applications are particularly well suited for the model. Even in the same category of model, constituent models can vary greatly, based on design, method, and study goals. **(B, C)** Colorectal cancer (CRC) "organ-on-a-chip" (OOC) platforms can model the immune response to tumors. **(B)** CRC cells (red) and IFN-DCs (green) are cultured in an OOC device (see cartoon) to simulate immune crosstalk. IFN-DCs migrate towards and phagocytose CRC cells following treatment with interferon-α and romidepsin. Images have been adapted from Parlato et al's 2017 *Scientific Reports* article (38). **(C)** M1 and M2 macrophages (red) cultured with CRC cell lines (not shown) in a vascularized OOC platform (vessels shown in green) display anti- and pro-tumor effects, respectively. Figure was originally published in Bi et al's 2020 *Integrative Biology* report (39).

(76, 77, 80–84), they struggle to retain the genetic and cellular features of native tumors (76, 79), recreate the metastatic cascade (with the possible exception of orthotopic transplant models) (89), and mimic the immune response to a tumor (note that xenograft and PDX models are both necessarily immunocompromised to enable inoculation with human cell lines and primary human tumor cells, respectively) (76, 79). Hence, humanized mouse models and GEMMs are more useful for studies of immunity in the TME. Humanized mice are generated by engrafting specific mouse strains with human leukocytes (hematopoietic stem cells or peripheral blood mononuclear cells). These mice produce a human immune response and are available commercially (91, 92), but sometimes suffer from xenoreactive complications and do not mount a full humoral immune response (74). In the context of CRC, humanized mouse models have been used to study tumor response to checkpoint blockade therapies (93, 94). In a 2015 report, humanized mice engrafted with a CRC cell line and treated with urelumab (CD137 inhibitor), nivolumab (PD-1 inhibitor), or a combination of the two demonstrated limited tumor growth and high infiltration of tumors by lymphocytes (93). Capasso and co-authors created humanized PDX mouse models by implanting patient-derived MSI-H or microsatellite stable (MSS) tumor cells and then treated the mice with nivolumab (PD-1 inhibitor) (94). Mice bearing MSI-H tumors showed high T cell infiltration into tumors and inhibited tumor growth compared to mice bearing MSS tumors; these results match clinical observations.

GEMMs are created by activating or deactivating specific genes using genome editing technology (75, 89, 95). These models retain a natural murine immune system; can simulate the natural development of CRC tumors from adenoma to carcinoma to metastasis (85, 88, 90); and can reproduce tumor response to therapy (75, 85–87, 95). Drawbacks to GEMMs include that they are time consuming and expensive to generate and characterize, and have a long time course of disease progression compared to other model systems (75, 89, 95). Tauriello and colleagues reported a set of GEMMs with mutations in one or more of the CRC-associated genes *Apc*, *Kras*, *Tgfbr2*, and *Trp53* (87); these models recreate many features of the human TME, including well-differentiated cancer cells, desmoplasia, and metastasis to the lung and liver. In subsequent experiments, the research team transplanted organoids from these CRC GEMMs into C57BL/6J mice to produce a model of advanced disease characterized by immune cell exclusion, increased TGFβ activity, and metastasis. Treatment with galunisertib (TGFBR1 inhibitor) reduced tumor growth and metastasis, increased immune cell infiltration and activation, and rendered tumors more responsive to anti-PD-L1 immunotherapy. Kostic et al. used a CRC GEMM model with a mutation in one copy of the *Apc* gene to explore the idea that the microbiome plays a role in CRC development (96). Mice were fed either a *Streptococcus* species or *Fusobacterium nucleatum*. The latter bacteria is found at higher levels in CRC tumor tissue than healthy colon tissue; indeed, mice fed *F. nucleatum* developed tumors more quickly and these tumors were infiltrated with high levels of pro-tumor immune cells, including myeloid-derived suppressor cells, granulocytes, neutrophils, TAMs, and M2-like macrophages. Some CRC cases are associated with colitis, a state of constant inflammation in the colon; colitis can be modeled in mice through treatment with azoxymethane and/or dextran sodium sulfate. Through comparisons of wild-type and knockout GEMM colitis mouse models, researchers have demonstrated the critical role of *p53* (97), IL-6 and Stat3 (98), TLR4 (99), *Pycard*, *Casp1*, and *Nlrp3* (100), and Nod1 (101) on tumor formation and growth; all of these factors are implicated in regulation of the immune response.

ORGAN-ON-A-CHIP MODELS

OOC models (**Figure 1A**) utilize microfluidic technology and tissue engineering to mimic and monitor dynamic 3D tissue microenvironments, including epithelial barriers, parenchymal tissues, perfused microvasculature, multiple organ interactions, and the immune response (24, 37). An OOC platform consists of an interconnected series of 3D channels and chambers filled with cells suspended in hydrogels. The geometry of these channels and chambers can be precisely selected to match a variety of tissue architectures and mechanical forces, has a scale of tens to hundreds of microns, and is carved into an optically clear polymer using microfabrication or 3D printing (24, 102). Strengths of OOC systems include the ability to incorporate multiple human cell types at physiologically-relevant ratios; control hydrogel composition and spatial distribution; customize the physiochemical properties of the tissue microenvironment; and image tissues with high spatiotemporal resolution. Drawbacks of this emerging technology include difficulties transferring technology between labs, a lack of standardized benchmarks of success, and low-throughput experiments (**Table 1**).

Recent studies in CRC OOC models have successfully reproduced disease progression (103–106), immunity (38, 107–109), metastasis (110–112), and response to therapy (38, 103, 105–107, 110, 113). Biochemical gradients of growth factors, cytokines, and chemokines influence cell migration, tissue phenotype, and angiogenesis in the TME (114), and can be established, monitored, and perturbed using OOC technologies (24, 114–116). Emerging methods also enable the manipulation of hypoxia in OOC devices (117, 118); this property regulates gene transcription and alters physiological and pathological immunity (119, 120). Our group has also pioneered methods to vascularize tissues, including CRC, in OOC devices (39, 103, 106, 113, 121, 122). These blood vessel networks self-assemble when endothelial cells and stromal cells are mixed, suspended in hydrogels, and cultured under perfusion conditions. These microvasculature models mimic transport of cells, nutrients, waste, and therapies through tissues; and can be engineered from autologous cell sources.

OOC platforms can mimic the immune-tumor cell crosstalk found in the CRC TME. For example, Parlato et al. monitored the interactions between untreated and treated CRC tumor cells

and interferon-α-conditioned dendritic cells (IFN-DCs)—a potential cancer therapeutic with the ability to uptake cancer antigens, stimulate a T cell response, and phagocytose tumor cells—in a 3D microfluidic model (**Figure 1B**). They observed that IFN-DCs preferentially migrate towards and phagocytose tumor cells that have been treated with interferon-α and romidepsin, thereby demonstrating the utility of the model for tracking immune-tumor cell interactions in real time and examining novel combination therapies. In a series of papers, an interdisciplinary team reported that patient- and murine-derived organotypic tumor spheroids cultured in microfluidic devices retain the tumor, stromal, and immune cell populations for multiple cancers, including CRC (107–109). The team also demonstrated that this model system recreates the tumor response to checkpoint blockade therapy more accurately than 3D *in vitro* systems and can be used to screen novel therapeutics for efficacy. A 2020 report from our group probed the role of M1 and M2 macrophages in the TME using a vascularized CRC OOC model (39) (**Figure 1C**). Our results showed that M1 macrophages inhibit angiogenesis and tumor cell growth and migration, while M2 macrophages have the reverse effect. Further, we showed that these outcomes are mediated by macrophage-derived soluble factors, suggesting new therapeutic targets and demonstrating the utility of the OOC platform to characterize the CRC TME.

FUTURE DIRECTIONS

Improvement of CRC and CRLM patient outcomes requires the development of efficacious, targeted therapies. Immune-mediated therapeutic strategies are particularly promising but remain unrealized, which can be partially attributed to the inability of current *in vitro* and *in vivo* models to fully recapitulate immunity in the TME. 2D culture experiments provide an informative picture of tumor-immune cell crosstalk, but are limited in the number of cell types that can be examined simultaneously and cannot mimic *in vivo* transport of cells and secreted factors. 3D culture systems can support multiple cell types, mimic transport of biochemical factors through tumor tissue, and reproduce tumor response to immunotherapy, but lack the vascular supply necessary to mimic *in vivo* transport of immune cells to and through the tumor. Murine models have been critical to characterizing the immunobiology of the CRC TME, but these models struggle to accurately recapitulate metastasis; further, successful transition of therapeutics from murine studies to clinical practice remains quite limited. OOC platforms are capable of recapitulating the CRC TME, characterizing tumor-immune cell crosstalk, and mimicking patient-specific tumor response to therapy, but remain limited in their ability to model metastasis.

In contrast to the extensively characterized and utilized 2D culture, 3D culture, and mouse model systems, OOC platforms remain in early-stage development with untapped potential. Future work with OOC technology should focus on recreating colon-specific biological and physiochemical features of the primary CRC and metastatic CRLM TME. In particular, these models should seek to: i) incorporate tumor, stromal, and immune cells at the ratios found in the native TME; ii) mimic both MSS and MSI-H tumors; iii) utilize patient-specific cell sources; and iv) recreate the metastatic cascade by connecting CRC tissue models to liver tissue models using microfluidics. These advances in experimental modeling, especially when coupled with unforeseen progress, will produce additional knowledge regarding immunity in the CRC and CRLM TMEs and tumor response to immunotherapies, which may inform future clinical strategies and patient outcomes.

AUTHOR CONTRIBUTIONS

PSY, NDP, VSS, and YP performed the literature review. PSY and NDP wrote the manuscript. VSS, YP, AK, RJC, RCF, SCG, and SG critically reviewed and edited the manuscript. YP, VSS, and NDP created the figure. PSY compiled the table. RCF, SCG, and SG received the funding sources. All authors contributed to the article and approved the submitted version.

FUNDING

This work is supported in part by grants from the National Institutes of Health (R21 CA223836, Fields and George), the Cancer Research Coordinating Committee (CRCC, University of California System, Gholami and George).

ACKNOWLEDGMENTS

Figure 1 was created with Biorender.com.

REFERENCES

1. Siegel RL, Miller KD, Goding Sauer A, Fedewa SA, Butterly LF, Anderson JC, et al. Colorectal cancer statistics, 2020. *CA Cancer J Clin* (2020) 70 (3):145–64. doi: 10.3322/caac.21601
2. Dekker E, Tanis PJ, Vleugels JLA, Kasi PM, Wallace MB. Colorectal cancer. *Lancet* (2019) 394(10207):1467–80. doi: 10.1016/S0140-6736(19)32319-0
3. Chow FC, Chok KS. Colorectal liver metastases: An update on multidisciplinary approach. *World J Hepatol* (2019) 11(2):150–72. doi: 10.4254/wjh.v11.i2.150
4. Misiakos EP, Karidis NP, Kouraklis G. Current treatment for colorectal liver metastases. *World J Gastroenterol* (2011) 17(36):4067–75. doi: 10.3748/wjg.v17.i36.4067
5. Pathak S, Jones R, Tang JM, Parmar C, Fenwick S, Malik H, et al. Ablative therapies for colorectal liver metastases: a systematic review. *Colorectal Dis* (2011) 13(9):e252–65. doi: 10.1111/j.1463-1318.2011.02695.x
6. Katz SC, Pillarisetty V, Bamboat ZM, Shia J, Hedvat C, Gonen M, et al. T cell infiltrate predicts long-term survival following resection of colorectal cancer liver metastases. *Ann Surg Oncol* (2009) 16(9):2524–30. doi: 10.1245/s10434-009-0585-3

7. Pages F, Galon J, Dieu-Nosjean MC, Tartour E, Sautes-Fridman C, Fridman WH. Immune infiltration in human tumors: a prognostic factor that should not be ignored. *Oncogene* (2010) 29(8):1093–102. doi: 10.1038/onc.2009.416
8. Maker AV, Ito H, Mo Q, Weisenberg E, Qin LX, Turcotte S, et al. Genetic evidence that intratumoral T-cell proliferation and activation are associated with recurrence and survival in patients with resected colorectal liver metastases. *Cancer Immunol Res* (2015) 3(4):380–8. doi: 10.1158/2326-6066.CIR-14-0212
9. Mlecnik B, Tosolini M, Kirilovsky A, Berger A, Bindea G, Meatchi T, et al. Histopathologic-based prognostic factors of colorectal cancers are associated with the state of the local immune reaction. *J Clin Oncol* (2011) 29(6):610–8. doi: 10.1200/JCO.2010.30.5425
10. Donadon M, Hudspeth K, Cimino M, Di Tommaso L, Preti M, Tentorio P, et al. Increased Infiltration of Natural Killer and T Cells in Colorectal Liver Metastases Improves Patient Overall Survival. *J Gastrointest Surg* (2017) 21 (8):1226–36. doi: 10.1007/s11605-017-3446-6
11. Nakagawa K, Tanaka K, Homma Y, Nojiri K, Kumamoto T, Takeda K, et al. Low infiltration of peritumoral regulatory T cells predicts worse outcome following resection of colorectal liver metastases. *Ann Surg Oncol* (2015) 22 (1):180–6. doi: 10.1245/s10434-014-3974-1
12. Grossman JG, Nywening TM, Belt BA, Panni RZ, Krasnick BA, DeNardo DG, et al. Recruitment of CCR2(+) tumor associated macrophage to sites of liver metastasis confers a poor prognosis in human colorectal cancer. *Oncoimmunology* (2018) 7(9):e1470729. doi: 10.1080/2162402X.2018.1470729
13. Forssell J, Oberg A, Henriksson ML, Stenling R, Jung A, Palmqvist R. High macrophage infiltration along the tumor front correlates with improved survival in colon cancer. *Clin Cancer Res* (2007) 13(5):1472–9. doi: 10.1158/1078-0432.CCR-06-2073
14. Cavnar MJ, Turcotte S, Katz SC, Kuk D, Gonen M, Shia J, et al. Tumor-Associated Macrophage Infiltration in Colorectal Cancer Liver Metastases is Associated With Better Outcome. *Ann Surg Oncol* (2017) 24(7):1835–42. doi: 10.1245/s10434-017-5812-8
15. Zhou Q, Peng RQ, Wu XJ, Xia Q, Hou JH, Ding Y, et al. The density of macrophages in the invasive front is inversely correlated to liver metastasis in colon cancer. *J Transl Med* (2010) 8:13. doi: 10.1186/1479-5876-8-13
16. Galon J, Costes A, Sanchez-Cabo F, Kirilovsky A, Mlecnik B, Lagorce-Pages C, et al. Type, density, and location of immune cells within human colorectal tumors predict clinical outcome. *Science* (2006) 313(5795):1960–4. doi: 10.1126/science.1129139
17. Galon J, Pages F, Marincola FM, Thurin M, Trinchieri G, Fox BA, et al. The immune score as a new possible approach for the classification of cancer. *J Transl Med* (2012) 10:1. doi: 10.1186/1479-5876-10-1
18. Pages F, Mlecnik B, Marliot F, Bindea G, Ou FS, Bifulco C, et al. International validation of the consensus Immunoscore for the classification of colon cancer: a prognostic and accuracy study. *Lancet* (2018) 391(10135):2128–39. doi: 10.1016/S0140-6736(18)30789-X
19. Ganesh K, Stadler ZK, Cercek A, Mendelsohn RB, Shia J, Segal NH, et al. Immunotherapy in colorectal cancer: rationale, challenges and potential. *Nat Rev Gastroenterol Hepatol* (2019) 16(6):361–75. doi: 10.1038/s41575-019-0126-x
20. Kalyan A, Kircher S, Shah H, Mulcahy M, Benson A. Updates on immunotherapy for colorectal cancer. *J Gastrointest Oncol* (2018) 9 (1):160–9. doi: 10.21037/jgo.2018.01.17
21. Tintelnot J, Stein A. Immunotherapy in colorectal cancer: Available clinical evidence, challenges and novel approaches. *World J Gastroenterol* (2019) 25 (29):3920–8. doi: 10.3748/wjg.v25.i29.3920
22. Le DT, Uram JN, Wang H, Bartlett BR, Kemberling H, Eyring AD, et al. PD-1 Blockade in Tumors with Mismatch-Repair Deficiency. *N Engl J Med* (2015) 372(26):2509–20. doi: 10.1056/NEJMoa1500596
23. Overman MJ, Lonardi S, Wong KYM, Lenz HJ, Gelsomino F, Aglietta M, et al. Durable Clinical Benefit With Nivolumab Plus Ipilimumab in DNA Mismatch Repair-Deficient/Microsatellite Instability-High Metastatic Colorectal Cancer. *J Clin Oncol* (2018) 36(8):773–9. doi: 10.1200/JCO.2017.76.9901
24. Hachey SJ, Hughes CCW. Applications of tumor chip technology. *Lab Chip* (2018) 18(19):2893–912. doi: 10.1039/C8LC00330K
25. Stock K, Estrada MF, Vidic S, Gjerde K, Rudisch A, Santo VE, et al. Capturing tumor complexity in vitro: Comparative analysis of 2D and 3D tumor models for drug discovery. *Sci Rep* (2016) 6:28951. doi: 10.1038/srep28951
26. Kumar V, Varghese S. Ex Vivo Tumor-on-a-Chip Platforms to Study Intercellular Interactions within the Tumor Microenvironment. *Adv Healthc Mater* (2019) 8(4):e1801198. doi: 10.1002/adhm.201801198
27. Binnewies M, Roberts EW, Kersten K, Chan V, Fearon DF, Merad M, et al. Understanding the tumor immune microenvironment (TIME) for effective therapy. *Nat Med* (2018) 24(5):541–50. doi: 10.1038/s41591-018-0014-x
28. Edmondson R, Broglie JJ, Adcock AF, Yang L. Three-dimensional cell culture systems and their applications in drug discovery and cell-based biosensors. *Assay Drug Dev Technol* (2014) 12(4):207–18. doi: 10.1089/adt.2014.573
29. Asghar W, El Assal R, Shafiee H, Pitteri S, Paulmurugan R, Demirci U. Engineering cancer microenvironments for in vitro 3-D tumor models. *Mater Today (Kidlington)* (2015) 18(10):539–53. doi: 10.1016/j.mattod.2015.05.002
30. Duval K, Grover H, Han LH, Mou Y, Pegoraro AF, Fredberg J, et al. Modeling Physiological Events in 2D vs. 3D Cell Culture. *Physiology (Bethesda)* (2017) 32(4):266–77. doi: 10.1152/physiol.00036.2016
31. Kapałczyńska M, Kolenda T, Przybyła W, Zajączkowska M, Teresiak A, Filas V, et al. 2D and 3D cell cultures - a comparison of different types of cancer cell cultures. *Arch Med Sci* (2018) 14(4):910–9. doi: 10.5114/aoms.2016.63743
32. Mestas J, Hughes CC. Of mice and not men: differences between mouse and human immunology. *J Immunol* (2004) 172(5):2731–8. doi: 10.4049/jimmunol.172.5.2731
33. Frese KK, Tuveson DA. Maximizing mouse cancer models. *Nat Rev Cancer* (2007) 7(9):645–58. doi: 10.1038/nrc2192
34. Guerin MV, Finisguerra V, Van den Eynde BJ, Bercovici N, Trautmann A. Preclinical murine tumor models: a structural and functional perspective. *Elife* (2020) 9:e50740. doi: 10.7554/eLife.50740
35. Caballero D, Kaushik S, Correlo VM, Oliveira JM, Reis RL, Kundu SC. Organ-on-chip models of cancer metastasis for future personalized medicine: From chip to the patient. *Biomaterials* (2017) 149:98–115. doi: 10.1016/j.biomaterials.2017.10.005
36. Huang YL, Segall JE, Wu M. Microfluidic modeling of the biophysical microenvironment in tumor cell invasion. *Lab Chip* (2017) 17(19):3221–33. doi: 10.1039/C7LC00623C
37. Heylman C, Sobrino A, Shirure VS, Hughes CC, George SC. A strategy for integrating essential three-dimensional microphysiological systems of human organs for realistic anticancer drug screening. *Exp Biol Med (Maywood)* (2014) 239(9):1240–54. doi: 10.1177/1535370214525295
38. Parlato S, De Ninno A, Molfetta R, Toschi E, Salerno D, Mencattini A, et al. 3D Microfluidic model for evaluating immunotherapy efficacy by tracking dendritic cell behaviour toward tumor cells. *Sci Rep* (2017) 7(1):1093. doi: 10.1038/s41598-017-01013-x
39. Bi Y, Shirure VS, Liu R, Cunningham C, Ding L, Meacham JM, et al. Tumor-on-a-chip platform to interrogate the role of macrophages in tumor progression. *Integr Biol (Camb)* (2020) 12(9):221–32. doi: 10.1101/2020.05.27.119636
40. Pouliot N, Connolly LM, Moritz RL, Simpson RJ, Burgess AW. Colon cancer cells adhesion and spreading on autocrine laminin-10 is mediated by multiple integrin receptors and modulated by EGF receptor stimulation. *Exp Cell Res* (2000) 261(2):360–71. doi: 10.1006/excr.2000.5065
41. Bartolomé RA, Barderas R, Torres S, Fernandez-Aceñero MJ, Mendes M, García-Foncillas J, et al. Cadherin-17 interacts with α2β1 integrin to regulate cell proliferation and adhesion in colorectal cancer cells causing liver metastasis. *Oncogene* (2014) 33(13):1658–69. doi: 10.1038/onc.2013.117
42. Barbazan J, Alonso-Alconada L, Elkhatib N, Geraldo S, Gurchenkov V, Glentis A, et al. Liver Metastasis Is Facilitated by the Adherence of Circulating Tumor Cells to Vascular Fibronectin Deposits. *Cancer Res* (2017) 77(13):3431–41. doi: 10.1158/0008-5472.CAN-16-1917
43. Wang H, Wang HS, Zhou BH, Li CL, Zhang F, Wang XF, et al. Epithelial-mesenchymal transition (EMT) induced by TNF-α requires AKT/GSK-3β-mediated stabilization of snail in colorectal cancer. *PloS One* (2013) 8(2):e56664. doi: 10.1371/journal.pone.0056664
44. Kahlert C, Lahes S, Radhakrishnan P, Dutta S, Mogler C, Herpel E, et al. Overexpression of ZEB2 at the invasion front of colorectal cancer is an independent prognostic marker and regulates tumor invasion in vitro. *Clin Cancer Res* (2011) 17(24):7654–63. doi: 10.1158/1078-0432.CCR-10-2816

45. Deng JJ, Zhang W, Xu XM, Zhang F, Tao WP, Ye JJ, et al. Twist mediates an aggressive phenotype in human colorectal cancer cells. *Int J Oncol* (2016) 48 (3):1117–24. doi: 10.3892/ijo.2016.3342
46. Jackstadt R, Röh S, Neumann J, Jung P, Hoffmann R, Horst D, et al. AP4 is a mediator of epithelial-mesenchymal transition and metastasis in colorectal cancer. *J Exp Med* (2013) 210(7):1331–50. doi: 10.1084/jem.20120812
47. Han X, Fang X, Lou X, Hua D, Ding W, Foltz G, et al. Silencing SOX2 induced mesenchymal-epithelial transition and its expression predicts liver and lymph node metastasis of CRC patients. *PloS One* (2012) 7(8):e41335. doi: 10.1371/journal.pone.0041335
48. Dai X, Ge J, Wang X, Qian X, Zhang C, Li X. OCT4 regulates epithelial-mesenchymal transition and its knockdown inhibits colorectal cancer cell migration and invasion. *Oncol Rep* (2013) 29(1):155–60. doi: 10.3892/or.2012.2086
49. Cui YM, Jiao HL, Ye YP, Chen CM, Wang JX, Tang N, et al. FOXC2 promotes colorectal cancer metastasis by directly targeting MET. *Oncogene* (2015) 34(33):4379–90. doi: 10.1038/onc.2014.368
50. Bartolome RA, Pintado-Berninches L, Jaen M, de Los Rios V, Imbaud JI, Casal JI. SOSTDC1 promotes invasion and liver metastasis in colorectal cancer via interaction with ALCAM/CD166. *Oncogene* (2020) 39(38):6085–98. doi: 10.1038/s41388-020-01419-4
51. Lundholm M, Hagglof C, Wikberg ML, Stattin P, Egevad L, Bergh A, et al. Secreted Factors from Colorectal and Prostate Cancer Cells Skew the Immune Response in Opposite Directions. *Sci Rep* (2015) 5:15651. doi: 10.1038/srep15651
52. Edin S, Wikberg ML, Rutegard J, Oldenborg PA, Palmqvist R. Phenotypic skewing of macrophages in vitro by secreted factors from colorectal cancer cells. *PloS One* (2013) 8(9):e74982. doi: 10.1371/journal.pone.0074982
53. Patel SA, Gooderham NJ. IL6 Mediates Immune and Colorectal Cancer Cell Cross-talk via miR-21 and miR-29b. *Mol Cancer Res* (2015) 13(11):1502–8. doi: 10.1158/1541-7786.MCR-15-0147
54. Zhang Y, Sime W, Juhas M, Sjolander A. Crosstalk between colon cancer cells and macrophages via inflammatory mediators and CD47 promotes tumour cell migration. *Eur J Cancer* (2013) 49(15):3320–34. doi: 10.1016/j.ejca.2013.06.005
55. Wei C, Yang C, Wang S, Shi D, Zhang C, Lin X, et al. Crosstalk between cancer cells and tumor associated macrophages is required for mesenchymal circulating tumor cell-mediated colorectal cancer metastasis. *Mol Cancer* (2019) 18(1):64. doi: 10.1186/s12943-019-0976-4
56. Kaminski BM, Weigert A, Scherzberg MC, Ley S, Gilbert B, Brecht K, et al. Resveratrol-induced potentiation of the antitumor effects of oxaliplatin is accompanied by an altered cytokine profile of human monocyte-derived macrophages. *Apoptosis* (2014) 19(7):1136–47. doi: 10.1007/s10495-014-0988-x
57. Yin Y, Yao S, Hu Y, Feng Y, Li M, Bian Z, et al. The Immune-microenvironment Confers Chemoresistance of Colorectal Cancer through Macrophage-Derived IL6. *Clin Cancer Res* (2017) 23(23):7375–87. doi: 10.1158/1078-0432.CCR-17-1283
58. Yu Y, Blokhuis B, Derks Y, Kumari S, Garssen J, Redegeld F. Human mast cells promote colon cancer growth via bidirectional crosstalk: studies in 2D and 3D coculture models. *Oncoimmunology* (2018) 7(11):e1504729. doi: 10.1080/2162402X.2018.1504729
59. Casati C, Dalerba P, Rivoltini L, Gallino G, Deho P, Rini F, et al. The apoptosis inhibitor protein survivin induces tumor-specific CD8+ and CD4+ T cells in colorectal cancer patients. *Cancer Res* (2003) 63(15):4507–15.
60. Turin I, Delfanti S, Ferulli F, Brugnatelli S, Tanzi M, Maestri M, et al. In Vitro Killing of Colorectal Carcinoma Cells by Autologous Activated NK Cells is Boosted by Anti-Epidermal Growth Factor Receptor-induced ADCC Regardless of RAS Mutation Status. *J Immunother* (2018) 41(4):190–200. doi: 10.1097/CJI.0000000000000205
61. Hirt C, Papadimitropoulos A, Muraro MG, Mele V, Panopoulos E, Cremonesi E, et al. Bioreactor-engineered cancer tissue-like structures mimic phenotypes, gene expression profiles and drug resistance patterns observed "in vivo". *Biomaterials* (2015) 62:138–46. doi: 10.1016/j.biomaterials.2015.05.037
62. Devarasetty M, Dominijanni A, Herberg S, Shelkey E, Skardal A, Soker S. Simulating the human colorectal cancer microenvironment in 3D tumor-stroma co-cultures in vitro and in vivo. *Sci Rep* (2020) 10(1):9832. doi: 10.1038/s41598-020-66785-1
63. Tsunoda T, Takashima Y, Yoshida Y, Doi K, Tanaka Y, Fujimoto T, et al. Oncogenic KRAS regulates miR-200c and miR-221/222 in a 3D-specific manner in colorectal cancer cells. *Anticancer Res* (2011) 31(7):2453–9.
64. Zoetemelk M, Rausch M, Colin DJ, Dormond O, Nowak-Sliwinska P. Short-term 3D culture systems of various complexity for treatment optimization of colorectal carcinoma. *Sci Rep* (2019) 9(1):7103. doi: 10.1038/s41598-019-42836-0
65. Stankevicius V, Vasauskas G, Noreikiene R, Kuodyte K, Valius M, Suziedelis K. Extracellular Matrix-dependent Pathways in Colorectal Cancer Cell Lines Reveal Potential Targets for Anticancer Therapies. *Anticancer Res* (2016) 36 (9):4559–67. doi: 10.21873/anticanres.11004
66. Luca AC, Mersch S, Deenen R, Schmidt S, Messner I, Schäfer KL, et al. Impact of the 3D microenvironment on phenotype, gene expression, and EGFR inhibition of colorectal cancer cell lines. *PloS One* (2013) 8(3):e59689. doi: 10.1371/journal.pone.0059689
67. Devarasetty M, Wang E, Soker S, Skardal A. Mesenchymal stem cells support growth and organization of host-liver colorectal-tumor organoids and possibly resistance to chemotherapy. *Biofabrication* (2017) 9(2):021002. doi: 10.1088/1758-5090/aa7484
68. Wan X, Li Z, Ye H, Cui Z. Three-dimensional perfused tumour spheroid model for anti-cancer drug screening. *Biotechnol Lett* (2016) 38(8):1389–95. doi: 10.1007/s10529-016-2035-1
69. Manfredonia C, Muraro MG, Hirt C, Mele V, Governa V, Papadimitropoulos A, et al. Maintenance of Primary Human Colorectal Cancer Microenvironment Using a Perfusion Bioreactor-Based 3D Culture System. *Adv Biosyst* (2019) 3(4):e1800300. doi: 10.1002/adbi.201800300
70. Fang Y, Eglen RM. Three-Dimensional Cell Cultures in Drug Discovery and Development. *SLAS Discov* (2017) 22(5):456–72. doi: 10.1177/1087057117696795
71. Dijkstra KK, Cattaneo CM, Weeber F, Chalabi M, van de Haar J, Fanchi LF, et al. Generation of Tumor-Reactive T Cells by Co-culture of Peripheral Blood Lymphocytes and Tumor Organoids. *Cell* (2018) 174(6):1586–98.e12. doi: 10.1016/j.cell.2018.07.009
72. Courau T, Bonnereau J, Chicoteau J, Bottois H, Remark R, Assante Miranda L, et al. Cocultures of human colorectal tumor spheroids with immune cells reveal the therapeutic potential of MICA/B and NKG2A targeting for cancer treatment. *J Immunother Cancer* (2019) 7(1):74. doi: 10.1186/s40425-019-0553-9
73. Schnalzger TE, de Groot MH, Zhang C, Mosa MH, Michels BE, Roder J, et al. 3D model for CAR-mediated cytotoxicity using patient-derived colorectal cancer organoids. *EMBO J* (2019) 38(12):e100928. doi: 10.15252/embj.2018100928
74. Morton JJ, Bird G, Refaeli Y, Jimeno A. Humanized Mouse Xenograft Models: Narrowing the Tumor-Microenvironment Gap. *Cancer Res* (2016) 76(21):6153–8. doi: 10.1158/0008-5472.CAN-16-1260
75. Kersten K, de Visser KE, van Miltenburg MH, Jonkers J. Genetically engineered mouse models in oncology research and cancer medicine. *EMBO Mol Med* (2017) 9(2):137–53. doi: 10.15252/emmm.201606857
76. Yoshida GJ. Applications of patient-derived tumor xenograft models and tumor organoids. *J Hematol Oncol* (2020) 13(1):4. doi: 10.1186/s13045-019-0829-z
77. Izumchenko E, Paz K, Ciznadija D, Sloma I, Katz A, Vasquez-Dunddel D, et al. Patient-derived xenografts effectively capture responses to oncology therapy in a heterogeneous cohort of patients with solid tumors. *Ann Oncol* (2017) 28(10):2595–605. doi: 10.1093/annonc/mdx416
78. Morton CL, Houghton PJ. Establishment of human tumor xenografts in immunodeficient mice. *Nat Protoc* (2007) 2(2):247–50. doi: 10.1038/nprot.2007.25
79. Zhong W, Myers JS, Wang F, Wang K, Lucas J, Rosfjord E, et al. Comparison of the molecular and cellular phenotypes of common mouse syngeneic models with human tumors. *BMC Genomics* (2020) 21(1):2. doi: 10.1186/s12864-019-6344-3
80. Bertotti A, Migliardi G, Galimi F, Sassi F, Torti D, Isella C, et al. A molecularly annotated platform of patient-derived xenografts ("xenopatients") identifies HER2 as an effective therapeutic target in

cetuximab-resistant colorectal cancer. *Cancer Discov* (2011) 1(6):508–23. doi: 10.1158/2159-8290.CD-11-0109
81. Kavuri SM, Jain N, Galimi F, Cottino F, Leto SM, Migliardi G, et al. HER2 activating mutations are targets for colorectal cancer treatment. *Cancer Discov* (2015) 5(8):832–41. doi: 10.1158/2159-8290.CD-14-1211
82. Nunes M, Vrignaud P, Vacher S, Richon S, Lièvre A, Cacheux W, et al. Evaluating patient-derived colorectal cancer xenografts as preclinical models by comparison with patient clinical data. *Cancer Res* (2015) 75(8):1560–6. doi: 10.1158/0008-5472.CAN-14-1590
83. Zanella ER, Galimi F, Sassi F, Migliardi G, Cottino F, Leto SM, et al. IGF2 is an actionable target that identifies a distinct subpopulation of colorectal cancer patients with marginal response to anti-EGFR therapies. *Sci Transl Med* (2015) 7(272):272ra12. doi: 10.1126/scitranslmed.3010445
84. Bardelli A, Corso S, Bertotti A, Hobor S, Valtorta E, Siravegna G, et al. Amplification of the MET receptor drives resistance to anti-EGFR therapies in colorectal cancer. *Cancer Discov* (2013) 3(6):658–73. doi: 10.1158/2159-8290.CD-12-0558
85. Hung KE, Maricevich MA, Richard LG, Chen WY, Richardson MP, Kunin A, et al. Development of a mouse model for sporadic and metastatic colon tumors and its use in assessing drug treatment. *Proc Natl Acad Sci U S A* (2010) 107(4):1565–70. doi: 10.1073/pnas.0908682107
86. Coffee EM, Faber AC, Roper J, Sinnamon MJ, Goel G, Keung L, et al. Concomitant BRAF and PI3K/mTOR blockade is required for effective treatment of BRAF(V600E) colorectal cancer. *Clin Cancer Res* (2013) 19 (10):2688–98. doi: 10.1158/1078-0432.CCR-12-2556
87. Tauriello DVF, Palomo-Ponce S, Stork D, Berenguer-Llergo A, Badia-Ramentol J, Iglesias M, et al. TGFβ drives immune evasion in genetically reconstituted colon cancer metastasis. *Nature* (2018) 554(7693):538–43. doi: 10.1038/nature25492
88. Boutin AT, Liao WT, Wang M, Hwang SS, Karpinets TV, Cheung H, et al. Oncogenic Kras drives invasion and maintains metastases in colorectal cancer. *Genes Dev* (2017) 31(4):370–82. doi: 10.1101/gad.293449.116
89. Burtin F, Mullins CS, Linnebacher M. Mouse models of colorectal cancer: Past, present and future perspectives. *World J Gastroenterol* (2020) 26 (13):1394–426. doi: 10.3748/wjg.v26.i13.1394
90. Romano G, Chagani S, Kwong LN. The path to metastatic mouse models of colorectal cancer. *Oncogene* (2018) 37(19):2481–9. doi: 10.1038/s41388-018-0155-x
91. Ishikawa F, Yasukawa M, Lyons B, Yoshida S, Miyamoto T, Yoshimoto G, et al. Development of functional human blood and immune systems in NOD/SCID/IL2 receptor {gamma} chain(null) mice. *Blood* (2005) 106 (5):1565–73. doi: 10.1182/blood-2005-02-0516
92. *Humanized Mice Services*. Bar Harbor, ME: The Jackson Laboratory. Available at: https://www.jax.org/jax-mice-and-services/in-vivo-pharmacology/humanized-mice#.
93. Sanmamed MF, Rodriguez I, Schalper KA, Onate C, Azpilikueta A, Rodriguez-Ruiz ME, et al. Nivolumab and Urelumab Enhance Antitumor Activity of Human T Lymphocytes Engrafted in Rag2-/-IL2Rgammanull Immunodeficient Mice. *Cancer Res* (2015) 75(17):3466–78. doi: 10.1158/0008-5472.CAN-14-3510
94. Capasso A, Lang J, Pitts TM, Jordan KR, Lieu CH, Davis SL, et al. Characterization of immune responses to anti-PD-1 mono and combination immunotherapy in hematopoietic humanized mice implanted with tumor xenografts. *J Immunother Cancer* (2019) 7(1):37. doi: 10.1186/s40425-019-0518-z
95. Oh BY, Hong HK, Lee WY, Cho YB. Animal models of colorectal cancer with liver metastasis. *Cancer Lett* (2017) 387:114–20. doi: 10.1016/j.canlet.2016.01.048
96. Kostic AD, Chun E, Robertson L, Glickman JN, Gallini CA, Michaud M, et al. Fusobacterium nucleatum potentiates intestinal tumorigenesis and modulates the tumor-immune microenvironment. *Cell Host Microbe* (2013) 14(2):207–15. doi: 10.1016/j.chom.2013.07.007
97. Schwitalla S, Ziegler PK, Horst D, Becker V, Kerle I, Begus-Nahrmann Y, et al. Loss of p53 in enterocytes generates an inflammatory microenvironment enabling invasion and lymph node metastasis of carcinogen-induced colorectal tumors. *Cancer Cell* (2013) 23(1):93–106. doi: 10.1016/j.ccr.2012.11.014
98. Grivennikov S, Karin E, Terzic J, Mucida D, Yu GY, Vallabhapurapu S, et al. IL-6 and Stat3 are required for survival of intestinal epithelial cells and development of colitis-associated cancer. *Cancer Cell* (2009) 15(2):103–13. doi: 10.1016/j.ccr.2009.01.001
99. Fukata M, Chen A, Vamadevan AS, Cohen J, Breglio K, Krishnareddy S, et al. Toll-like receptor-4 promotes the development of colitis-associated colorectal tumors. *Gastroenterology* (2007) 133(6):1869–81. doi: 10.1053/j.gastro.2007.09.008
100. Allen IC, TeKippe EM, Woodford RM, Uronis JM, Holl EK, Rogers AB, et al. The NLRP3 inflammasome functions as a negative regulator of tumorigenesis during colitis-associated cancer. *J Exp Med* (2010) 207 (5):1045–56. doi: 10.1084/jem.20100050
101. Chen GY, Shaw MH, Redondo G, Nunez G. The innate immune receptor Nod1 protects the intestine from inflammation-induced tumorigenesis. *Cancer Res* (2008) 68(24):10060–7. doi: 10.1158/0008-5472.CAN-08-2061
102. Low LA, Mummery C, Berridge BR, Austin CP, Tagle DA. Organs-on-chips: into the next decade. *Nat Rev Drug Discov* (2020). doi: 10.1038/s41573-020-0079-3
103. Shirure VS, Bi Y, Curtis MB, Lezia A, Goedegebuure MM, Goedegebuure SP, et al. Tumor-on-a-chip platform to investigate progression and drug sensitivity in cell lines and patient-derived organoids. *Lab Chip* (2018) 18 (23):3687–702. doi: 10.1039/C8LC00596F
104. Jeong SY, Lee JH, Shin Y, Chung S, Kuh HJ. Co-Culture of Tumor Spheroids and Fibroblasts in a Collagen Matrix-Incorporated Microfluidic Chip Mimics Reciprocal Activation in Solid Tumor Microenvironment. *PloS One* (2016) 11(7):e0159013. doi: 10.1371/journal.pone.0159013
105. Carvalho MR, Barata D, Teixeira LM, Giselbrecht S, Reis RL, Oliveira JM, et al. Colorectal tumor-on-a-chip system: A 3D tool for precision onco-nanomedicine. *Sci Adv* (2019) 5(5):eaaw1317. doi: 10.1126/sciadv.aaw1317
106. Sobrino A, Phan DT, Datta R, Wang X, Hachey SJ, Romero-López M, et al. 3D microtumors in vitro supported by perfused vascular networks. *Sci Rep* (2016) 6:31589. doi: 10.1038/srep31589
107. Aref AR, Campisi M, Ivanova E, Portell A, Larios D, Piel BP, et al. 3D microfluidic ex vivo culture of organotypic tumor spheroids to model immune checkpoint blockade. *Lab Chip* (2018) 18(20):3129–43. doi: 10.1039/C8LC00322J
108. Deng J, Wang ES, Jenkins RW, Li S, Dries R, Yates K, et al. CDK4/6 Inhibition Augments Antitumor Immunity by Enhancing T-cell Activation. *Cancer Discov* (2018) 8(2):216–33. doi: 10.1158/2159-8290.CD-17-0915
109. Jenkins RW, Aref AR, Lizotte PH, Ivanova E, Stinson S, Zhou CW, et al. Ex Vivo Profiling of PD-1 Blockade Using Organotypic Tumor Spheroids. *Cancer Discov* (2018) 8(2):196–215. doi: 10.1158/2159-8290.CD-17-0833
110. Skardal A, Devarasetty M, Forsythe S, Atala A, Soker S. A reductionist metastasis-on-a-chip platform for in vitro tumor progression modeling and drug screening. *Biotechnol Bioeng* (2016) 113(9):2020–32. doi: 10.1002/bit.25950
111. Aleman J, Skardal A. A multi-site metastasis-on-a-chip microphysiological system for assessing metastatic preference of cancer cells. *Biotechnol Bioeng* (2019) 116(4):936–44. doi: 10.1002/bit.26871
112. Sung JH, Shuler ML. A micro cell culture analog (microCCA) with 3-D hydrogel culture of multiple cell lines to assess metabolism-dependent cytotoxicity of anti-cancer drugs. *Lab Chip* (2009) 9(10):1385–94. doi: 10.1039/b901377f
113. Weng KC, Kurokawa YK, Hajek BS, Paladin JA, Shirure VS, George SC. Human Induced Pluripotent Stem-Cardiac-Endothelial-Tumor-on-a-Chip to Assess Anticancer Efficacy and Cardiotoxicity. *Tissue Eng Part C Methods* (2020) 26(1):44–55. doi: 10.1089/ten.tec.2019.0248
114. Oudin MJ, Weaver VM. Physical and Chemical Gradients in the Tumor Microenvironment Regulate Tumor Cell Invasion, Migration, and Metastasis. *Cold Spring Harb Symp Quant Biol* (2016) 81:189–205. doi: 10.1101/sqb.2016.81.030817
115. Shirure VS, Lezia A, Tao A, Alonzo LF, George SC. Low levels of physiological interstitial flow eliminate morphogen gradients and guide angiogenesis. *Angiogenesis* (2017) 20(4):493–504. doi: 10.1007/s10456-017-9559-4
116. Hwang PY, Brenot A, King AC, Longmore GD, George SC. Randomly Distributed K14(+) Breast Tumor Cells Polarize to the Leading Edge and Guide Collective Migration in Response to Chemical and Mechanical Environmental Cues. *Cancer Res* (2019) 79(8):1899–912. doi: 10.1158/0008-5472.CAN-18-2828
117. Lam SF, Shirure VS, Chu YE, Soetikno AG, George SC. Microfluidic device to attain high spatial and temporal control of oxygen. *PloS One* (2018) 13(12): e0209574. doi: 10.1371/journal.pone.0209574

118. Shirure VS, Lam SF, Shergill B, Chu YE, Ng NR, George SC. Quantitative design strategies for fine control of oxygen in microfluidic systems. *Lab Chip* (2020) 20(16):3036–50. doi: 10.1039/D0LC00350F
119. Semenza GL. Hypoxia-inducible factors in physiology and medicine. *Cell* (2012) 148(3):399–408. doi: 10.1016/j.cell.2012.01.021
120. Taylor CT, Colgan SP. Regulation of immunity and inflammation by hypoxia in immunological niches. *Nat Rev Immunol* (2017) 17(12):774–85. doi: 10.1038/nri.2017.103
121. Moya ML, Alonzo LF, George SC. Microfluidic device to culture 3D in vitro human capillary networks. *Methods Mol Biol* (2014) 1202:21–7. doi: 10.1007/7651_2013_36
122. Hsu YH, Moya ML, Hughes CC, George SC, Lee AP. A microfluidic platform for generating large-scale nearly identical human microphysiological vascularized tissue arrays. *Lab Chip* (2013) 13(15):2990–8. doi: 10.1039/c3lc50424g

Conflict of Interest: SCG is co-founder of Aracari Biosciences, a start-up company focused on the commercialization of vascularized OOC technology.

The remaining authors declare that the research was conducted in the absence of any commercial or financial relationships that could be construed as a potential conflict of interest.

frontiers in Immunology

ORIGINAL RESEARCH
published: 16 August 2021
doi: 10.3389/fimmu.2021.719116

Co-Stimulatory Bispecific Antibodies Induce Enhanced T Cell Activation and Tumor Cell Killing in Breast Cancer Models

*Karsten M. Warwas[1,2], Marten Meyer[1,2], Márcia Gonçalves[1,2], Gerhard Moldenhauer[3], Nadja Bulbuc[2], Susanne Knabe[1], Claudia Luckner-Minden[4], Claudia Ziegelmeier[4], Claus Peter Heussel[5,6,7], Inka Zörnig[4], Dirk Jäger[1,4] and Frank Momburg[2,4]**

[1] Clinical Cooperation Unit Applied Tumor Immunity, German Cancer Research Center (DKFZ), Heidelberg, Germany, [2] Antigen Presentation and T/NK Cell Activation Group, DKFZ, Heidelberg, Germany, [3] Department of Translational Immunology, DKFZ, Heidelberg, Germany, [4] Department of Medical Oncology, National Center for Tumor Diseases (NCT), University Hospital, Heidelberg, Germany, [5] Diagnostic and Interventional Radiology With Nuclear Medicine, Thoraxklinik at Heidelberg University Hospital, Heidelberg, Germany, [6] Department of Diagnostic and Interventional Radiology, University Hospital, Heidelberg, Germany, [7] Translational Lung Research Center Heidelberg (TLRC), German Lung Research Center (DZL), Heidelberg, Germany

OPEN ACCESS

Edited by:
Sebastian Kobold,
LMU Munich University Hospital, Germany

Reviewed by:
Johannes vom Berg,
University of Zurich, Switzerland
Bruno L. Cadilha,
Ludwig Maximilian University of Munich, Germany

***Correspondence:**
Frank Momburg
f.momburg@dkfz-heidelberg.de

Specialty section:
This article was submitted to Cancer Immunity and Immunotherapy, a section of the journal Frontiers in Immunology

Received: 01 June 2021
Accepted: 27 July 2021
Published: 16 August 2021

Citation:
Warwas KM, Meyer M, Gonçalves M, Moldenhauer G, Bulbuc N, Knabe S, Luckner-Minden C, Ziegelmeier C, Heussel CP, Zörnig I, Jäger D and Momburg F (2021) Co-Stimulatory Bispecific Antibodies Induce Enhanced T Cell Activation and Tumor Cell Killing in Breast Cancer Models. Front. Immunol. 12:719116. doi: 10.3389/fimmu.2021.719116

Although T cell-recruiting CD3-binding bispecific antibodies (BiMAb) have been proven to be clinically effective for hematologic malignancies, the success of BiMAb targeting solid tumor-associated antigens (TAA) in carcinomas so far remains poor. We reasoned that provision of co-stimulatory BiMAb in combination with αTAA–αCD3 BiMAb would boost T cell activation and proliferative capacity, and thereby facilitate the targeting of weakly or heterogeneously expressed tumor antigens. Various αTAA–αCD3 and αTAA–αCD28 BiMAb in a tetravalent IgG1-Fc based format have been analyzed, targeting multiple breast cancer antigens including HER2, EGFR, CEA, and EpCAM. Moreover, bifunctional fusion proteins of αTAA–tumor necrosis factor ligand (TNFL) superfamily members including 4-1BBL, OX40L, CD70 and TL1A have been tested. The functional activity of BiMAb was assessed using co-cultures of tumor cell lines and purified T cells in monolayer and tumor spheroid models. Only in the presence of tumor cells, αTAA–αCD3 BiMAb activated T cells and induced cytotoxicity *in vitro*, indicating a strict dependence on cross-linking. Combination treatment of αTAA–αCD3 BiMAb and co-stimulatory αTAA–αCD28 or αTAA–TNFL fusion proteins drastically enhanced T cell activation in terms of proliferation, activation marker expression, cytokine secretion and tumor cytotoxicity. Furthermore, BiMAb providing co-stimulation were shown to reduce the minimally required dose to achieve T cell activation by at least tenfold. Immuno-suppressive effects of TGF-β and IL-10 on T cell activation and memory cell formation could be overcome by co-stimulation. BiMAb-mediated co-stimulation was further augmented by immune checkpoint-inhibiting antibodies. Effective co-stimulation could be achieved by targeting a second breast cancer antigen, or by targeting fibroblast activation protein (FAP) expressed on another target cell. In tumor spheroids derived from pleural effusions of breast cancer patients, co-stimulatory BiMAb were essential for the activation tumor-

infiltrating lymphocytes and cytotoxic anti-tumor responses against breast cancer cells. Taken together we showed that co-stimulation significantly potentiated the tumoricidal activity of T cell-activating BiMAb while preserving the dependence on TAA recognition. This approach could provide for a more localized activation of the immune system with higher efficacy and reduced peripheral toxicities.

Keywords: T cells, co-stimulation, tumor cell spheroids, tumor therapy, cytotoxicity, bispecific antibodies

INTRODUCTION

Cancer immunotherapies have demonstrated remarkable clinical benefits in the past years and have changed the paradigm of cancer treatment. Especially, monoclonal antibodies mediating immune checkpoint inhibition (ICI) have shown promising clinical responses in a broad range of solid tumors, including late-stage cancers (1, 2). The number of patients with a benefit from ICI is, however, still limited and success varies depending on the cancer type (3). Crucial for the anti-tumor effect of ICI are endogenous T cells recognizing and eliminating cancer cells after recognition of MHC molecules loaded with cancer-derived peptides. While exhaustion of a subset of tumor-reactive T cell clones can potentially be prevented by ICI, the approach is generally limited by tumor immune escape mechanism such as loss of MHC class I molecules or lack of immunogenic mutant T cell epitopes.

T cell-recruiting bispecific monoclonal antibodies (BiMAb) are an alternative approach to redirect immune effector cells to the proximity of cancer cells in order to induce tumor regression. BiMAb that have been engineered in a large variety of different formats combine variable fragments from two different antibodies (4–8). One antibody binds to a tumor-associated antigen (TAA) and the other usually targets the CD3ϵ chain in the T cell receptor complex, forming an MHC-unrestricted surrogate immune synapse between target cells and T cells independent of phenotype, maturation or antigen specificity. BiMAb-mediated cross-linking of target cell and T cell triggers T cell activation and proliferation as well as the release of cytotoxic molecules and cytokines. T cell-recruiting BiMAb have the potential to overcome tumor evasion due to MHC molecule downmodulation. However, they require cell surface-expressed target proteins or glycans having high selectivity for the malignant cell population in order to spare corresponding healthy tissues from T cell attack. While this goal is very difficult to achieve for carcinomas, melanomas and sarcomas, in hematological malignancies such as B cell leukemia, normal B cell differentiation antigens such CD20 or CD19 can serve as tumor targets because B cells can be replenished from hematopoietic stem cells.

For efficient T cell activation, clonal expansion and memory formation, co-stimulatory signals through CD28 or members of the tumor necrosis factor ligand (TNFL) superfamily are required (9, 10). However, systemic and cancer cell-independent co-stimulation by agonistic co-stimulatory antibodies can lead to severe off-target toxicities (11–13). With the aim to provide a target-dependent co-stimulation, a number of bifunctional reagents have been developed that combine tumor targeting by anti-TAA antibodies with co-stimulation by TNFL proteins or anti-CD28 antibodies (14–21).

While the first approved single-chain variable fragment (scFv) bispecific T cell engager, blinatumomab, has demonstrated substantial clinical efficacy for the treatment of $CD19^+$ B cell leukemia/lymphoma (22, 23), the clinical benefit of BiMAb targeting TAAs in carcinomas is controversially discussed (24, 25). Major limitations are imposed by the limited physical accessibility of solid tumors for antibodies, the immunosuppressive microenvironment and dose-limiting toxicities. As most targets are not strictly tumor-specific, being expressed to various degrees in normal epithelial tissues as well, "on-target, off-tumor" effects might limit therapeutic efficacy.

To overcome these limitations, we developed BiMAb and bifunctional TNFL fusion proteins to provide targeted co-stimulation at the tumor site. We hypothesized that co-stimulation in combination with anti-CD3 BiMAb would boost T cell activation, thereby reducing the minimally required effective dose of anti-CD3 BiMAb and potentially limiting systemic toxicities. Furthermore, we propose an approach to treat solid tumors by simultaneously engaging two tumor-associated antigens, where co-stimulatory bispecific proteins should target a second antigen on the malignant cell population, or an antigen expressed on tumor stromal cells. This split co-stimulation approach should trigger full T cell activation predominantly at the tumor site, theoretically increasing specificity and enhancing anti-tumor activity.

Here, we report the engineering and testing of BiMAb and bifunctional TNFL fusion proteins targeting various well-established breast cancer-associated TAAs, including EGFR, HER2, CEA, EpCAM, and the tumor stroma antigen FAP. We provide evidence that only in the presence of tumor cells, tetravalent (anti-TAA scFv-hIgG1-Fc-anti-CD3ε scFv)$_2$ BiMAb studied in this work activated T cells and induced cytotoxicity in adherent cell and tumor spheroid cultures *in vitro*, suggesting that T cell activation strictly depended on cross-linking. Addition of co-stimulatory bispecifics greatly enhanced T cell activation

Abbreviations: ICI, immune checkpoint inhibition; BiMAb, bispecific monoclonal antibody(ies); TAA, tumor-associated antigen(s), TNFL, tumor necrosis factor ligand superfamily member(s); scFv, single-chain variable fragment; FAP, fibroblast activation protein-α; GSL, glycine-serine-rich linker; CHO, Chinese hamster ovary cells; FCS, fetal calf serum; LDH, lactate dehydrogenase; CTV, CellTrace™ Violet; ELISA, enzyme-linked immunosorbent assay; HRP, horseradish peroxidase; ns, not significant; PBMC, peripheral blood mononuclear cells; TMB, 3,3',5,5'-tetramethyl benzidine; ANOVA, analysis of variance; TL1A, TNF-like ligand 1A.

and tumor cell lysis. Finally, the anti-tumor potential was confirmed in an *ex-vivo* patient-derived spheroid model.

MATERIALS AND METHODS

BiMAb and TNFL Fusion Protein Cloning

The binding moieties of tetravalent BiMAb are V_H–$(Gly_4Ser)_3$-V_L scFv derived from monoclonal antibodies, anti(α)-EpCAM, HEA125 (US20120213805A1); αHER2 Trastuzumab (PDB:4HJG_B, PDB:4HJG_A); αEGFR Cetuximab (PDB:1YY8_B, PDB:1YY8_A); αCEA, Mfe-23 (PDB:1QOK_A), anti-fibroblast activation protein-α (FAP), BIBH1/Sibrotuzumab, (US20090304718A1); αPD-L1, Avelumab (PDB:5GRJ_H, PDB:5GRJ_L); αCD3ϵ OKT3 (PDB:1SY6_H, PDB:1SY6_L); αCD28, 9.3 (V_H GenBank : CAD30987.1, V_L GenBank : CAD30986.1). cDNAs coding for the mentioned scFv with tumor antigen specificity were cloned 3' of an hIg-κ ER leader sequence followed by a glycine-serine-rich linker ["*GSL*", $GNS(G_4S)_3AS$] and the hinge-CH2-CH3 domains of hIgG1 (E216–K447) harboring the mutations C220S, E233P, L234A, L235A, ΔG236, N297Q, K322A, A327G, P329A, A330S, P331S to abolish Fc receptor and complement binding (26). Instead of the stop codon, a StrepTag-II sequence [DPG**WSHPQFEK**SR] flanked by restriction sites was inserted. The C-terminal scFv OKT3 and 9.3 sequences were cloned 3' of the StrepTag-II sequence (preceded by a $(Gly)_4$ linker). The resulting BiMAb constructs assemble to covalently linked homodimers due to two intermolecular disulfide bonds in the hIgG1 hinge region. In scFv–hIgG1-$Fc^{FcR\text{-}KO}$–TNFL constructs, C-terminal scFv were replaced by the ectodomains of h4-1BBL (NP_003802.1, a.a. A58-E254), hOX40L (NP_003317.1, a.a. Q51-L183), hTL1A (NP_005109.2, a.a. L72-L251) or hCD70 (NP_001243.1, a.a. Q39-P193), respectively. All constructs were cloned between XhoI and NotI sites of expression vector pcDNA3.1 (–) (ThermoFisher/Invitrogen, Waltham, USA).

Production of BiMAb and TNFL Bifunctional Fusion Proteins

Suspension-adapted Freestyle Chinese hamster ovary cells (CHO-S; Invitrogen) were used for transient gene expression as previously described (26, 27). CHO-S were routinely cultured in PowerCHO-2 CD (Lonza, Basel, Switzerland), supplemented with 8 mM Ultraglutamine (Lonza) in 500 ml round glass bottles at 37°C, 8% CO_2 and 130 rpm. For transfection CHO-S cells were resuspend at $3x10^6$ cells/ml in ProCHO4 medium (Lonza) supplemented with 4 mM Ultraglutamin followed by the sequential addition of 2.5 µg 25-kDa linear polyethyleneimine (PEI; Polysciences Europe GmbH, Germany) and 0.625 µg plasmid DNA per $1x10^6$ cells. After 6 days in culture at 32°C, 5% CO_2 and rotation at 130 rpm the supernatants of the transfected cultures were harvested and purified using the Strep-Tactin® system (IBA Lifesciences, Göttingen, Germany) according to the manufacturer's instructions. The harvested supernatant was applied to a Strep-Tactin® column using a peristaltic pump and washed with PBS. Elution of purified proteins was performed by addition of PBS, supplemented with 5 mM desthiobiotin (IBA Lifesciences). Eluted proteins were dialyzed against PBS and purity was verified by reducing and non-reducing 10% SDS-PAGE prior to functional testing. Binding of purified BiMAb and TNFL bifunctional fusion proteins was validated on target positive tumor cell lines (MCF-7, HT-1080/FAP). Purified proteins were stored at 2–8°C.

Cell Lines and Culture Conditions

The human breast adenocarcinoma cell line MCF-7 (ATCC® HTB-22) was used as an EpCAM, HER2, EGFR and CEA expressing cell line. As FAP, EGFR and PD-L1 expressing cells, the FAP-transfected human fibrosarcoma cell line HT-1080/FAP [kindly provided by A. Loktev, University of Heidelberg (28)] was used. Cell lines were cultured in RPMI-1640 (ThermoFisher Scientific/Gibco), supplemented with 10% heat-inactivated fetal calf serum (FCS, Gibco), 1% penicillin/streptomycin (Sigma-Aldrich) and 2 mM glutamine (Lonza) and passaged every 3-4 days.

Human *Ex Vivo* Breast Cancer Patients' Samples

Pleural effusions as well as autologous blood samples were collected from 8 patients suffering from pleural carcinosis due to breast cancer after informed consent. Cells from pleural effusions were collected by centrifugation. In a culture flask, a monocyte adherence step was performed for 1.5 hours. Non-adherent cells were transferred to a new culture flask, resuspended in "conditioned" medium (RPMI-1640 mixed with supernatant of punctate at a 1:1 ratio) and tumor cells were enriched by overnight adherence to tissue culture flasks and harvested by trypsinization. Prior to functional experiments, breast cancer samples were characterized by flow cytometry for antigen expression.

T Cell Isolation

$CD3^+$ T cells were isolated from human PBMC purified from buffy coats from healthy donors or from breast cancer patients by negative selection using the Pan-T cell Isolation Kit (Miltenyi Biotec, Bergisch Gladbach, Germany) according to the manufacturer's protocol. Cell purity was routinely >95%. Purified T cells were maintained in complete RPMI medium and incubated at 37°C in a humidified 5% CO_2 atmosphere.

In Vitro Cytotoxicity Assay

Adherent tumor cells (MCF-7, HT-1080/FAP) were trypsinized (0.05% trypsin/EDTA; Gibco) and collected. $2.5x10^4$ cells/well were seeded in 96-well flat-bottom plates in complete RPMI medium and incubated overnight at 37°C in a humidified 5% CO_2 atmosphere. Target cells were preincubated with BiMAb and/or TNFL bifunctional fusion proteins for 60 minutes at 37°C, 5% CO_2, before purified T cells were added in a 2:1 E/T ratio ($1x10^5$ cells/well) and incubated for 48 hours. Cellular cytotoxicity based on lactate dehydrogenase (LDH) release into supernatants by dead target cells was quantified according to the manufacturer's instructions (CyQUANT™ LDH Cytotoxicity Assay; ThermoFisher). Maximal lysis of target cells was achieved by incubation of target cells with lysis buffer. Spontaneous LDH release refers to target and effector cells

without BiMAb or TNFL bifunctional proteins. The calculated percentage of specific cell lysis is based on the following equation:

$$\%\,Cytotoxicity = \frac{Experimental\ Value - Effector\ Cells\ Spontaneous\ Control - Target\ Cells\ Spontaneous\ Control}{Target\ Cell\ Maximum\ Control - Target\ Cells\ Spontaneous\ Control} \times 100$$

Proliferation Assay

To measure proliferation purified T cells were labelled with 1 μM Cell Trace Violet (CTV; ThermoFisher) according to the manufacturer's instructions. Target cells and CTV-labelled T cells were co-cultured with BiMAb and/or TNFL bifunctional fusion proteins as described above for 5 days. Proliferation of $CD4^+$ and $CD8^+$ T cells based on CTV dilution was analyzed by flow cytometry using a FACS Canto-II™ cell analyser (BD Biosciences, Heidelberg, Germany).

Flow Cytometry

Tumor cells were stained with αTAA-hIgGFc–αCD3/αCD28 BiMAb [5 μg/ml in FACS buffer (Dulbecco's PBS/2% FCS)] followed by goat anti-human Ig-PE (Dianova, Hamburg, #109-115-098). αEpCAM-A488 (9C4), αHER2-PE (24D2), αCEA-PE (ASL-32), αPD-L1-PE (29E.2A3) and isotype control antibodies mIgG2b-A488/PE (MPC-11), mIgG1-APC/PE (MOPC-21), mIgG2a-APC (MOPC-173) were all from BioLegend (San Diego, CA, USA), and αFAP-APC from R&D Systems (#427819). T cells from cytotoxicity or proliferation assays were harvested to measure activation marker expression or T cell subpopulations by flow cytometry after 48 hours or 5 days of co-culture, respectively. Briefly, T cells were transferred into 96-well round-bottom plates and washed once with PBS. Dead cells were stained with the Zombie Aqua Fixable Viability Kit (BioLegend) according to the manufacturer's protocol. Next, Fc receptors were blocked with Human TruStain FcX (BioLegend) and incubated in FACS buffer containing fluorescently labelled monoclonal antibodies αCD3-APC-Cy7 (HIT3a), αCD4-A488/PE (RPA-T4), αCD8-PB (SK1), αCD8-APC (RPA-T8), αCD14-BV510 (M5E2), αCD19-BV510 (HIB19), αCD25-A647 (BC96), αCD45RA-A488 (HI100), αCD56-BV510 (HCD56) αCD62L-PerCP-Cy5.5 (DREG-56), αCD134/OX40-PE-Cy7 (ACT35), αCD137/4-1BB-PE (4B4-1), αCD274/PD-L1-PE (29E.2A3), αCD279/PD-1-APC (EH12.2H7) (all from BioLegend) for 25 min at 4°C protected from light. Cells were washed twice and fixed prior to flow cytometric measurement. FlowJo software (TreeStar Inc., Ashland, OR, USA) was used for analysis. A minimum of $1x10^4$ living $CD3^+$ T-cells were acquired for each sample.

Cytokine Measurement

Cytokine release was assessed 48 hours after incubation of target cells with BiMAb, TNFL fusion proteins and purified T cells as described above. Cytokines were measured by enzyme-linked immunosorbent assay (ELISA). Anti-human IFN-γ (MD-1, BioLegend), anti-human IL-2 (MQ1-17H12, BioLegend) capture antibodies were coated on a 96-well Nunc MaxiSorp™ (ThermoFisher) flat-bottom plates and incubated overnight at 4°C protected from light. After washing, blocking was performed to reduce unspecific binding. Supernatant of the cytotoxicity assay was added and incubated for 90 minutes at room temperature. For detection, biotinylated anti-human IFN-γ (4S.B3, BioLegend) or anti-human IL-2 (Poly5176, BioLegend) antibodies were used in combination with streptavidin-horseradish peroxidase (HRP; BioLegend) and TMB (3,3',5,5'-tetramethyl benzidine) substrate solution. The reaction was stopped with H_2SO_4 and the absorbance was measured at 450 and 540 nm. Cytokine concentrations were calculated based on reference cytokine standards (BioLegend).

Three-Dimensional Spheroid Generation and Culture

MCF-7, HT-1080/FAP or *ex vivo* human breast cancer cells derived from pleural effusion were grown in 100 μl DMEM supplemented with B-27 supplement and 1% Matrigel. Multicellular tumor spheroids were generated as described elsewhere (29). Briefly, $5x10^4$ cells/well were seeded in low-adhesion 96-well round bottom plates (ThermoFisher), centrifuged at 100 x g for 5 minutes and maintained at 37°C, 5% CO_2 in a humidified incubator. In mixed tumor cell spheroids MCF-7 and HT-1080/FAP cells were blended in a 1:1 ratio. Spheroids were observed to form overnight after seeding and incubated for 2 days prior to functional experiments. In some experiments, spheroids were formed with CTV-labeled tumor cells, co-cultured for 48 h with T cells labelled with 1 μM carboxyfluorescein succinimidyl ester (CFSE) and analyzed by fluorescence microscopy using an Olympus CKX41 inverted microscope quickly after addition of propidium iodide (PI, 4 μg/ml final concentration). BiMAb at 10 nM final concentration were added in 50 μl DMEM medium supplemented with 10% FCS and B-27 supplement. 10^5 T cells were added in 50 μl of the same medium and cultured for 48 h to measure cytoxicity *via* LDH release, T cell activation and cytokine secretion or for 5 days to measure T cell proliferation.

Statistical Analysis

Unless otherwise stated, all results are expressed as mean ± SEM. Analysis and graphical representations were conducted using GraphPad Prism 8 software (GraphPad Software Inc., USA). Experiments containing more than 2 experimental groups were analyzed using a one- or two-way analysis of variance (ANOVA) with Tukey's multiple comparison test or Dunnett's follow-up test where appropriate. The number of donors and experiments, as well as the statistical analysis is stated in the respective figure legends with p values <0.05 considered statistically significant (not significant (ns), $p > 0.05$; *$p < 0.05$; **$p < 0.01$; ***$p < 0.001$; ****$p < 0.0001$).

RESULTS

Enhanced Potency of T Cell-Stimulatory BiMAb Through Co-Stimulation

We engineered a variety of bispecific T cell-engaging antibodies, produced them in CHO-S cells and purified them by StrepTag immunoaffinity chromatography (**Figures 1A, B**). scFv antibodies in the used tetravalent bispecific (scFv1-linker-

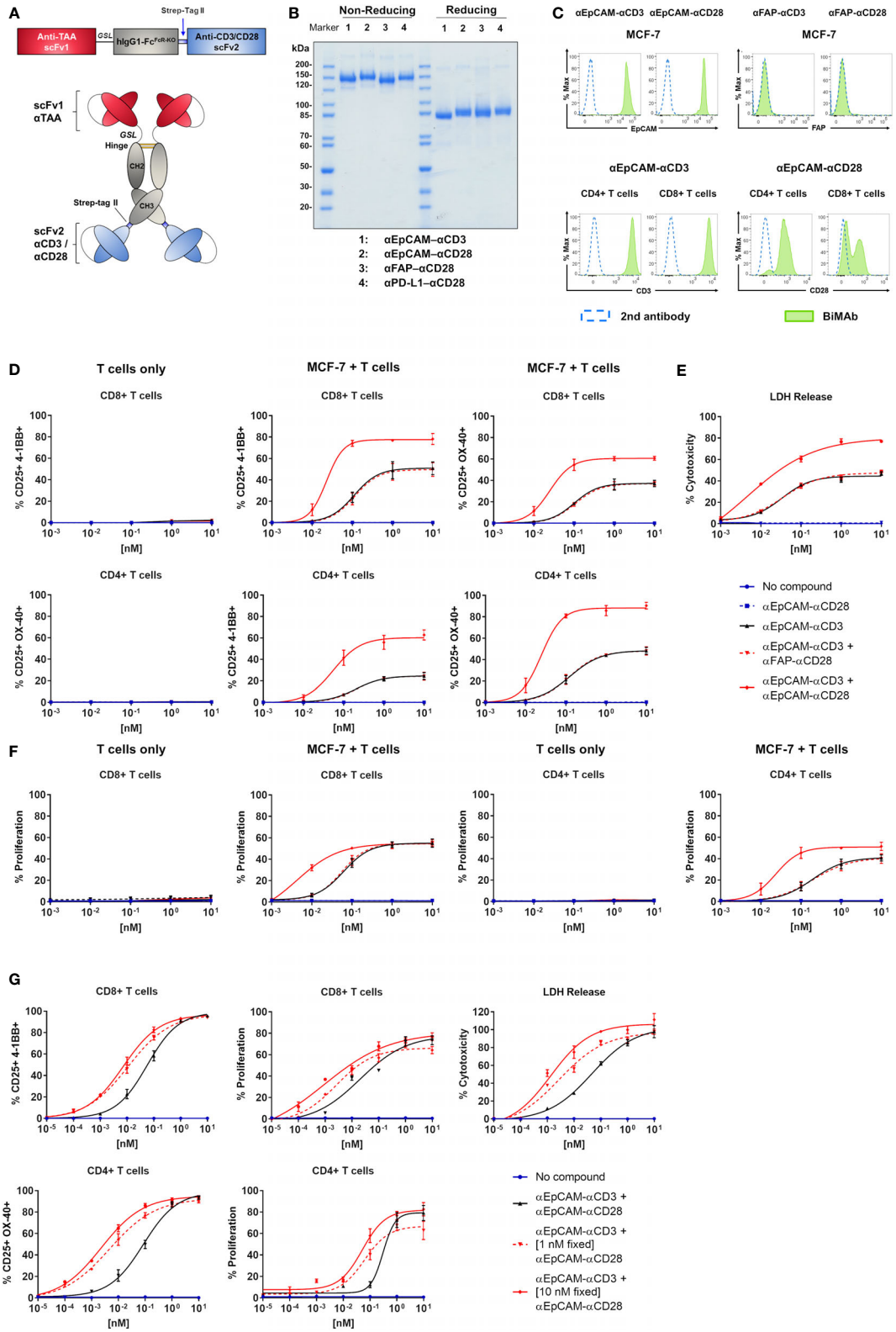

FIGURE 1 | Continued

FIGURE 1 | Co-stimulatory BiMAb enhance *in vitro* T cell activation, proliferation, and cytotoxicity against MCF-7 cells upon bidirectional binding. **(A)** Schematic representation of the tetravalent bispecific BiMAb format. A single chain variable fragment (scFv) antibody 1 specific for a tumor-associated antigen (TAA) is conjugated with the hinge–CH2–CH3 domains of hIgG1 *via* a flexible glycine-serine linker (*GSL*). The Fc domain contains multiple point mutations to abrogate Fc receptor and complement binding. At the C-terminal end of the CH3 domain a Strep-tag II is added for immunoaffinity purification followed by an scFv antibody 2 recognizing either CD3ε or CD28. **(B)** SDS-PAGE analysis (10%) and Coomassie staining of examples of purified bispecific antibodies under non-reducing and reducing conditions. **(C)** Binding of BiMAb to MCF-7 cells (top panel) and T cells (bottom panel) was detected *via* flow cytometry using PE-conjugated goat anti-human IgG secondary antibody. Staining with BiMAb (green filled), GaHIgG-PE control (dotted blue line). **(D–F)** Assays were performed in 2D adherent cell cultures using serial dilutions of either αEpCAM–αCD3 +/– co-stimulatory αEpCAM–αCD28 used at equimolar concentrations, purified unstimulated T cells isolated from healthy donors as effector cells and MCF-7 as target cells (E:T ratio 2:1). **(D)** After 48 h of co-culture, BiMAb-mediated $CD8^+$ and $CD4^+$ T cell activation indicated by CD25 and 4-1BB, or CD25 and OX40 surface co-expression was measured by flow cytometry. T cells only (left panel) *vs*. MCF-7/T cell co-culture (middle and right panel). **(E)** Supernatants were collected after 48 h from co-culture assays and cytotoxicity was measured based on lactate dehydrogenase (LDH) release from lysed cells. **(F)** CTV-labelled T cells were used for co-culture and after 5 days of incubation $CD8^+$ or $CD4^+$ T cell proliferation was measured by flow cytometry based on CTV dilution (see **Supplementary Figure 1E**). T cells only *vs*. MCF-7/T cell co-culture. The legend refers to **(D–F)**. **(G)** Co-culture assays were repeated using serial dilutions of αCD3 BiMAb +/- fixed concentrations (1 and 10 nM) of co-stimulatory αCD28 BiMAb, respectively. Top, frequencies of $CD25^+$/4-$1BB^+$ $CD8^+$ T cells (left) and proliferating $CD8^+$ T cells (middle) were analyzed by flow cytometry after 48 h and 5 days, respectively. Tumor cell lysis was measured after 48 h *via* LDH release assay (right). Bottom, frequencies of $CD25^+$/$OX40^+$ $CD4^+$ T cells (left) and proliferating $CD4^+$ T cells (right) were analyzed by flow cytometry after 48 h and 5 days, respectively. Diagrams show mean values ± SEM from 3 independent experiments performed in triplicates. EC_{50} values are listed in **Table 1**.

hIgG1-Fc-StrepTag-scFv2)$_2$ format recognized tumor-associated antigens with the N-terminal scFv1 and either CD3ϵ or CD28 receptors with the C-terminal scFv2 (26). The Fc portion harbored several mutations to abolish Fc receptor and complement binding. We first sought to validate binding properties of our bispecific antibodies. Analysis by flow cytometry showed binding of the αEpCAM–αCD3 and αEpCAM–αCD28 BiMAb to EpCAM-positive MCF-7 breast cancer cells, whereas irrelevant FAP-specific BiMAb did not bind, as this antigen was not expressed on MCF-7 cells (**Figures 1C**, **4B**). Similarly, our αCD3 and αCD28 BiMAb exhibited binding to $CD4^+$ and $CD8^+$ T cells. As shown previously (26), we observed two distinct peaks of αEpCAM–αCD28 BiMAb binding to cytotoxic $CD8^+$ T cells, which is consistent with reports that, depending on the donor, CD28 can be variably expressed on $CD8^+$ cells from peripheral blood (30). We next determined the dose response of αCD3 and αCD28 bispecific antibodies driving T cell activation and proliferation *in vitro*. Addition of αEpCAM–αCD3 to the co-culture of MCF-7 and purified T cells elicited T cell activation in terms of enhanced CD25 and 4-1BB (or OX40) co-expression on $CD8^+$ T cells (**Figure 1D** and **Supplementary Figure 1D**), or of CD25 and OX40 (or 4-1BB) co-expression on $CD4^+$ T cells (**Figure 1D**), in a dose-dependent manner. Since 4-1BB upregulation on $CD8^+$ cells and OX40 upregulation on $CD4^+$ T cells were more prominent, respectively, $CD8^+$/$CD25^+$/4-$1BB^+$ and $CD4^+$/$CD25^+$/$OX40^+$ T cells will be reported for the following experiments. Combination with co-stimulatory αEpCAM–αCD28 bispecific antibodies added in equimolar amounts enhanced the potency of the αEpCAM–αCD3 BiMAb, reducing EC_{50} values in dose response curves of $CD8^+$ and $CD4^+$ T cell activation by about 5-fold (**Figure 1D** and **Table 1**). Increased T cell activation in the presence of co-stimulatory BiMAb also translated into enhanced cytotoxicity as measured by LDH release and $CD8^+$/$CD4^+$ T cell proliferation (**Figures 1E, F**, **Table 1** and **Supplementary Figure 1E**). Importantly, when used as a single agent, even at the highest dose of 10 nM, the co-stimulatory αCD28 BiMAb elicited no T cell stimulating effect (**Figures 1D–F**). Furthermore, it is shown that BiMAb activity was strictly dependent on expression of the appropriate TAA on the target cell, since the irrelevant αFAP–αCD3 bispecific antibody was unable to activate T cells and elicit cytotoxicity or proliferation when co-cultured with FAP-negative MCF-7 (**Supplementary Figures 1A–C**). When comparing αEpCAM–αCD3 BiMAb alone with the combination of αEpCAM–αCD3 and αFAP–αCD28 BiMAb, no substantial differences were seen for EC_{50} values across all assays (**Table 1**), indicating that also for co-stimulation binding of the respective BiMAb to a target cell antigen was required. When combinations of αEpCAM and αFAP BiMAb were cultured with T cells in the absence of MCF-7 cells, no activation or proliferation was observed (**Figures 1D, F** and **Supplementary Figures 1A, C**),

TABLE 1 | EC_{50} values of stimulatory and co-stimulatory BiMAb in functional T cell assays.

EC_{50} [pM]	αEpCAM–αCD3	αEpCAM–αCD3 + αFAP–αCD28	αEpCAM–αCD3 + αEpCAM–αCD28	αEpCAM–αCD3 titrated + 1 nM αEpCAM–αCD28	αEpCAM–αCD3 titrated + 10 nM αEpCAM–αCD28
Cytotoxicity	33.5	35.1	4.6	2.7	1.4
$CD4^+$ T cell Activation	125.4	122.6	24.6	4.7	2.3
$CD8^+$ T cell Activation	110.9	114.9	22.8	10.9	7.2
$CD4^+$ T cell Proliferation	193.4	197.8	23.6	6.2	5.2
$CD8^+$ T cell Proliferation	62.1	55.2	4.3	2.6	0.9

EC_{50} values in pM were calculated with GraphPad Prism™ Software using non-linear regression log (agonist) vs. response variable slope with a robust fit.

further supporting the conjecture that T cell-activating effects of tetravalent bispecific antibodies analyzed here were strictly dependent on T cell–tumor cell cross-linking.

When using a fixed dose of 1 nM or 10 nM αEpCAM–αCD28 in combination with decreasing amounts of αEpCAM–αCD3 BiMAb, the dose response curves of $CD8^+$ and $CD4^+$ T cells shifted to lower concentrations (**Figure 1G** and **Table 1**). In the presence of 0.1-1 pM concentrations (ca. 3.5–35 pg antibody/200 µl assay volume) of the αEpCAM–αCD3 BiMAb, addition of 1 nM or 10 nM of co-stimulatory αCD28 BiMAb still triggered measurable T cell responses. Consistently, EC_{50} values dropped to the low picomolar range in activation, proliferation and cytotoxicity assays using fixed concentrations of co-stimulatory BiMAb, suggesting that at very low concentrations of stimulatory BiMAb, equimolar quantities of co-stimulatory BiMAb became rate-limiting (**Table 1**).

We then investigated whether pre-activated T cells could be stimulated by a timely separated treatment with a tumor cell-binding αCD28 BiMAb. T cells were first co-cultured with MCF-7 or HT-1080/FAP cells for 48h in the presence 1 nM αEpCAM–αCD3 or αFAP–αCD3, respectively. After this pre-treatment, T cells were harvested and co-cultured again with or without fresh MCF-7 or HT-1080/FAP tumor cells and BiMAb as indicated in **Supplementary Figure 1F**. We observed no stimulation of αCD3-preactivated T cells when sequentially treated with an αCD28 BiMAb alone, while secondary treatment with αCD3 BiMAb or αCD3 plus αCD28 BiMAb elicited potent activation of $CD4^+$ and $CD8^+$ T cells. Secondary activation through BiMAb was dependent on the presence of tumor cells (see part "T cells only" in **Supplementary Figure 1F**).

Together, we demonstrated that our co-stimulatory αCD28 bispecific antibodies considerably enhanced the anti-tumor immune response when applied in combination with αCD3 BiMAb. Regarding potential safety issues, our αCD28 BiMAb completely lacked activating activity on its own, but relied on antigen-dependent cross-linking and simultaneous signaling delivered through αCD3 BiMAb.

Co-Stimulation Overrides Immunosuppression Imposed by the Microenvironment

The tumor microenvironment is known to restrain T cell effector functions while driving T cell exhaustion. In order to mimic an immunosuppressive environment, we assessed the functionality of our BiMAb in co-cultures of tumor cells with $CD3^+$ T cells and titrated amounts of exogenous IL-10 and TGF-β. Addition of IL-10 and TGF-β significantly reduced BiMAb-mediated cytotoxicity in a dose-dependent manner, confirming the known immunosuppressive properties of these cytokines (**Figure 2A**). When testing the αEpCAM–αCD3 BiMAb as single agent, 100 ng/ml of each IL-10 and TGF-β completely abrogated cytotoxicity. In combination with the αCD28 BiMAb we also observed a reduction of tumor cell lysis by IL-10/TGF-β, however, this decrease was significantly less pronounced compared to αCD3 BiMAb alone. In the presence of αEpCAM–αCD28 BiMAb, 72.5% cytotoxicity was still observed at the highest IL-10/TGF-β dose (**Figure 2A**).

Similar inhibitory effects on $CD8^+$ and $CD4^+$ T cell activation (**Figure 2B** and **Supplementary Figure 2A**), proliferation (**Figure 2C** and **Supplementary Figure 2B**) and IFN-γ/IL-2 secretion (**Figure 2D**) were noted with high concentrations of IL-10 and TGF-β. In contrast, there was no significant immunosuppressive effect when additional αCD28 BiMAb was present, maintaining a high frequency of $CD25^+$/4-1BB$^+$ $CD8^+$ T cells and high proliferation rates. Moreover, immunosuppressive cytokines impaired the maturation of $CD8^+$ and $CD4^+$ T cells into effector and memory phenotypes (**Figure 2E**). When using αCD3 BiMAb alone, IL-10 and TGF-β preserved a naïve T cell phenotype in a dose-dependent manner. Compared to no-cytokine controls, the highest concentrations of IL-10 and TGF-β apparently prevented differentiation/maturation so that relative frequencies of naïve $CD4^+$ and $CD8^+$ T cells were increased by factors of 5.9 and 27.1, respectively. With the addition of the αEpCAM–αCD28 BiMAb, naïve T cells remained at low frequencies, while the central memory effector T cell pool was expanded (**Figure 2E**). Using 100 ng/ml IL-10 and TGF-β we observed no significant changes regarding the frequencies of $CD62L^+CD45RA^+$ naïve or $CD62L^+CD45RA^-$ central memory $CD8^+$ T cells when treating with αCD3 BiMAb alone compared to no-compound controls (**Figure 2F**). However, addition of co-stimulation elicited a significant decrease (factor 8.4) in naïve $CD8^+$ T cells, while significantly enhancing the frequency of central memory cytotoxic T cells (factor 4.4).

Thus, co-stimulatory αCD28 bispecific antibodies were demonstrated to efficiently counteract immunosuppressive effects of IL-10 and TGF-β on anti-tumor cytotoxic responses as well as on T cell activation, proliferation, cytokine secretion and expansion of central memory effector T cells.

BiMAb Enhance T Cell Activation and Cytotoxicity Depending on TAA Expression Levels

To further analyze the potential and limitations of co-stimulatory BiMAb in the tetravalent format, we tested pairs of αCD3 and αCD28 BiMAb targeting TAA expressed at different levels on tumor cells. MCF-7 cells displayed substantial surface expression of EpCAM and HER2, while expression was intermediate for CEA and low EGFR (**Figure 3A**). Consistent with results shown above, as a single agent, co-stimulatory αTAA–αCD28 BiMAb elicited no cytotoxicity, regardless of the chosen target (**Figure 3B**). In contrast, single use of αTAA–αCD3 BiMAb showed target-dependent effects. The highest cytotoxicity was elicited with BiMAb directed against EpCAM or HER2, with 47.2% and 36.1% of MCF-7 cells lysed, respectively. Targeting TAAs with lower surface expression such as CEA or EGFR elicited no notable cytotoxic effects. When directed against strongly expressed antigens, the combination of αCD3 and αCD28 BiMAb further enhanced the anti-tumor response in terms of cytotoxicity (**Figure 3B**). Compared to treatment with EpCAM-binding αCD3 bispecific antibodies alone, the addition of αEpCAM–αCD28 significantly enhanced tumor cell lysis by 1.9-fold. Similarly, αCD28 BiMAb directed

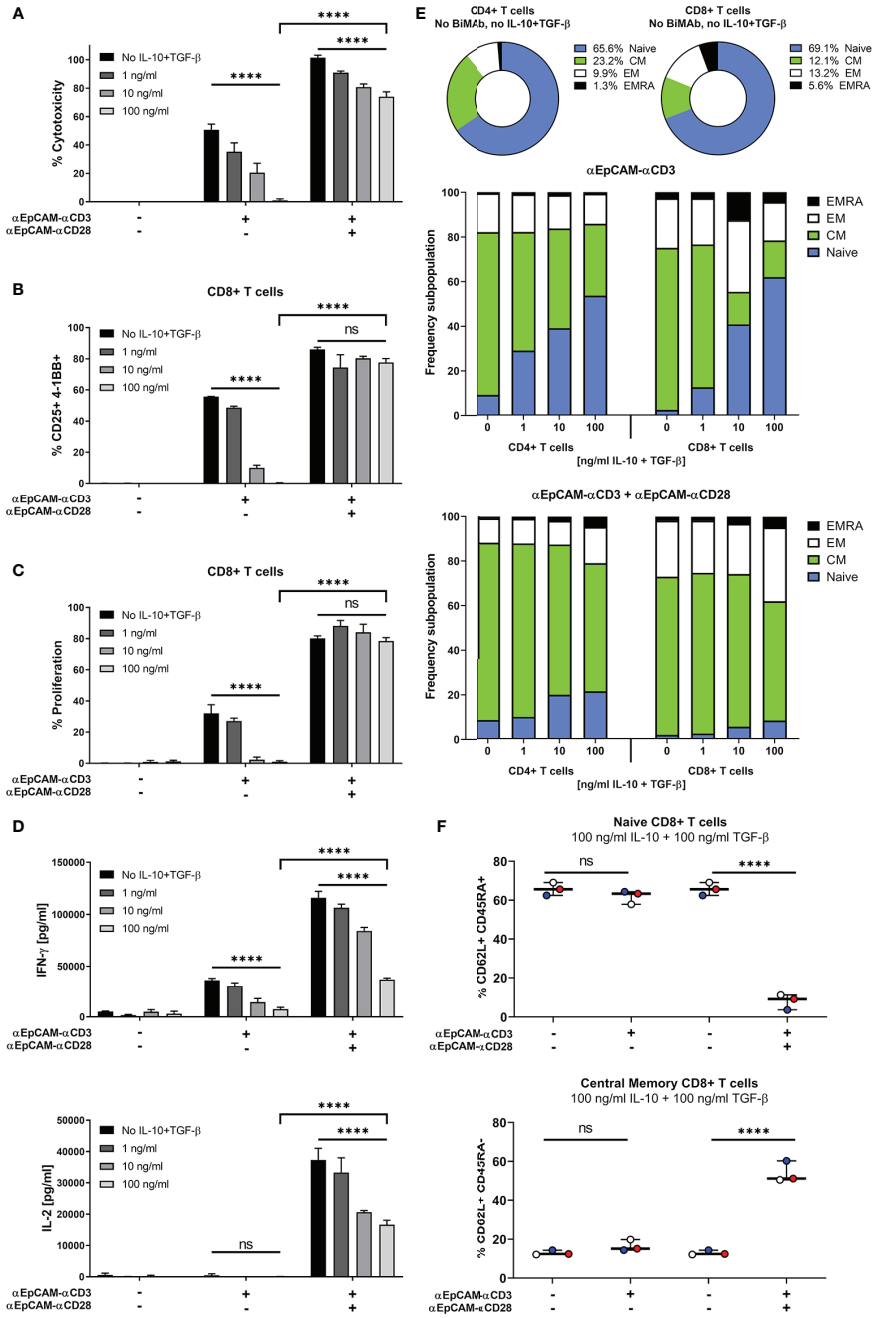

FIGURE 2 | Co-stimulation overrides immunosuppressive effects of exogenous IL-10 and TGF-β. MCF-7 cells were co-cultured with purified $CD3^+$ T cells and serial dilutions of human IL-10 and TGF-β (0, 1, 10, 100 ng/ml each) in the presence or absence of 1 nM αCD3 +/- αCD28 EpCAM-targeting BiMAb. **(A)** MCF-7 tumor cell lysis was measured by LDH release assay after 48 h of co-culture. **(B)** $CD8^+$ T cell activation was determined by flow cytometry and shown as percentages of $CD25^+$/4-1BB$^+$ T cells. **(C)** Frequencies of proliferating $CD8^+$ T cells were measured by flow cytometry based on CTV dilution after 5d of incubation. **(D)** IFN-γ (top panel) and IL-2 secretion (bottom panel) by T cells co-cultured with MCF-7 cells and αEpCAM–αCD3 +/- αEpCAM–αCD28 in the presence of the indicated concentrations of IL-10 and TGF-β. **(E)** Subpopulations of $CD4^+$ and $CD8^+$ T cells were characterized by flow cytometry based on CD62L and CD45RA surface expression: Naïve ($CD62L^+$/$CD45RA^+$), central memory (CM, $CD62L^+$/$CD45RA^-$), effector memory (EM, $CD62L^-$/$CD45RA^-$) and effector memory cells re-expressing CD45RA (EMRA, $CD62L^-$/$CD45RA^+$). Frequencies of subpopulations in untreated controls are shown for $CD4^+$ and $CD8^+$ T cells, respectively (top). Bar diagrams show the effects of BiMAb on $CD4^+$ and $CD8^+$ T cell subpopulations with increasing concentrations of IL-10 and TGF-β (middle and bottom panel). **(F)** Frequencies of naïve and central memory $CD8^+$ T cells after treatment with 100 ng/ml IL-10, 100 ng/ml TGF-β and αEpCAM–αCD3 +/- αEpCAM–αCD28 (1 nM), or without BiMAb treatment for control, with each individual data point representing the mean value of an individual donor. Data represent mean values ± SEM from 3 independent experiments each done in duplicates that were statistically analyzed by two-way ANOVA followed by Tukey's multiple comparison test **(A–D)** or one-way ANOVA with Dunnett's follow-up test for comparison with no compound control **(F)**, ns, not significant; ****$p < 0.0001$.

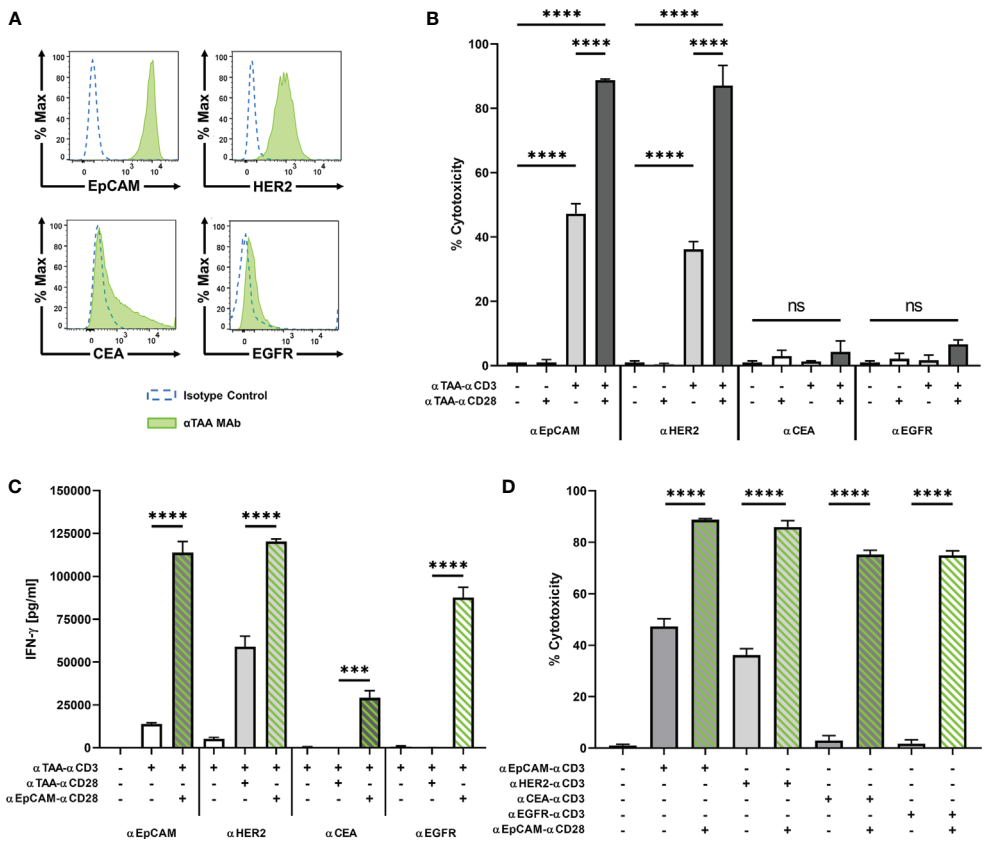

FIGURE 3 | BiMAb induce T cell activation in a target antigen-dependent manner. MCF-7 cells were co-cultured with purified unstimulated T cells in the presence or absence of 1 nM αCD3 +/- αCD28 BiMAb targeting the tumor-associated antigens (TAA), EpCAM, HER2, CEA, or EGFR as indicated. **(A)** TAA cell surface expression on MCF-7 cells was analyzed by flow cytometry using αTAA monoclonal antibodies (green filled lines) and isotype control antibodies (dotted blue lines). Mean fluorescence intensities for EpCAM, HER2, CEA and EGFR were 8523, 828, 733 and 71, respectively. **(B)** Tumor cell lysis based on LDH release was measured in supernatants collected after 48h of co-culture of T cells in the presence of the indicated stimulatory and co-stimulatory BiMAb. Co-stimulatory αEpCAM–αCD28 BiMAb rescue T cell activation. **(C)** IFN-γ secretion (in pg/ml) in T cell co-cultures with MCF-7 cells and the indicated αTAA–αCD3 ± αTAA–αCD28 BiMAb was measured after 48 h by ELISA. **(D)** 2D co-culture assays were performed using combinations of αTAA–αCD3 with αEpCAM–αCD28 BiMAb to validate a split co-stimulation approach. Cytotoxicity measurements were based on LDH released by lysed tumor cells after 48 h. Data represent mean values ± SEM from 3 independent experiments in triplicates with statistical analysis by one-way ANOVA test followed by Tukey's multiple comparison test **(B–D)**, ns, not significant; ***$p < 0.001$; ****$p < 0.0001$.

against HER2 lead to a significant 2.4-fold increase in cytotoxicity compared to αHER2–αCD3 alone. For co-stimulatory bispecific antibodies targeting CEA or EGFR, the observed minor increases did not reach significance. The 4 pairs of αTAA BiMAb showed similar effects in terms of $CD8^+$ and $CD4^+$ T cell activation (**Supplementary Figure 3A**). Again, TAA surface expression correlated with responses, as addition of co-stimulatory BiMAb targeting EpCAM or HER2 lead to a significant upregulation of CD25/4-1BB on $CD8^+$ T cells and CD25/OX40 on $CD4^+$ T cells, respectively. However, αCEA or αEGFR co-stimulatory bispecifics did not further enhance the frequency of activated $CD8^+$ and $CD4^+$ T cells. In the same line, proliferation of either $CD8^+$ and $CD4^+$ T cells was significantly stimulated by the combination of stimulatory and co-stimulatory BiMAb recognizing either EpCAM or HER2 but not CEA nor EGFR (**Supplementary Figure 3B**). Furthermore, IFN-γ and IL-2 secretion by responding T cells could not be elicited by CEA nor EGFR BiMAb while αEpCAM–αCD28 significantly induced cytokine secretion (**Figure 3C** and **Supplementary Figure 3F**). These results suggest that stimulation and co-stimulation through the same, weakly expressed tumor antigen may be inefficient.

We therefore combined αTAA–αCD3 bispecific antibodies with co-stimulatory αEpCAM–αCD28 BiMAb addressing a separate, highly expressed antigen on the same tumor target cell. In this case, co-stimulation significantly enhanced cytotoxicity of all tested αCD3 BiMAb regardless of the targeted tumor antigen (**Figure 3D**). The co-stimulatory effect was conspicuous when we combined αCEA–αCD3 or αEGFR–αCD3 with the αEpCAM–αCD28 BiMAb, which improved cytotoxicity by 25.5- and 44.3-fold, respectively. The presence of αEpCAM–αCD28 significantly enhanced the frequency of activated $CD8^+$ and $CD4^+$ T cells in combination with αCEA–αCD3 or αEGFR–αCD3 BiMAb, respectively

(**Supplementary Figures 3C, D**). In terms of T cell proliferation, we observed the same TAA-independent effects in the presence of αEpCAM–αCD28 co-stimulation (**Supplementary Figure 3E**). Increased proliferation was more pronounced in $CD8^+$ than in $CD4^+$ T cells. Likewise, αEpCAM–αCD28 rescued T cell proliferation triggered by αCEA–αCD3 and αEGFR–αCD3 BiMAb. Only in combination with the αEpCAM–αCD28 BiMAb, αCEA–αCD3 and αEGFR–αCD3 BiMAb elicited sizable secretion of IFN-γ and IL-2 (**Figure 3C** and **Supplementary Figure 3F**).

We next evaluated dose responses of αCEA or αEGFR-reactive αCD3 BiMAb in combination with αEpCAM–αCD28 (**Supplementary Figures 3G, H**). In accordance with the BiMAb titration data shown in **Figure 1**, co-stimulation through EpCAM greatly augmented $CD8^+$ and $CD4^+$ T cell cytotoxicity, activation and proliferation. While combinations of CEA-reactive (**Supplementary Figure 3G**) and EGFR-reactive (**Supplementary Figure 3H**) stimulatory and co-stimulatory BiMAb induced quantitatively weak and non-saturating responses (up to 10 nM), the combinatory use with αEpCAM–αCD28 elicited considerable activating effects with EC_{50} values in these assays ranging from ~100-200 pM.

We next analysed to which extent BiMAb-mediated co-stimulation was influenced by receptor density on the target cell. To that end we pre-incubated MCF-7 cells with titrated amounts of trastuzumab antibody before addition of purified T cells and αEpCAM–αCD3 +/- αHER2–αCD28 BiMAb in co-culture experiments for 48 h (**Supplementary Figures 4A, B**) or 5 days (**Supplementary Figure 4C**). Pre-incubation with 0.1 nM trastuzumab (i.e. ~3 x 10^5 antibody molecules offered per MCF-7 cell) did not block $CD8^+$/$CD4^+$ T cell activation measured by CD25/4-1BB or CD25/OX40 co-expression (**Supplementary Figure 4A**), respectively, as well as cytotoxicity measured in the LDH release assay (**Supplementary Figure 4B**). 1, 10 and 100 nM trastuzumab fully abrogated co-stimulation by the αHER2–αCD28 BiMab (containing trastuzumab V_H and V_L sequences in the scFv format). The proliferation of $CD4^+$ T cells, and to a lesser extent of $CD8^+$ T cells, was also inhibited with increasing amounts of trastuzumab (**Supplementary Figure 4C**).

Taken together, a co-stimulatory αCD28 BiMAb engaging the highly expressed antigen EpCAM enhanced the efficacy of αCD3 BiMAb recognizing a second TAA on the same tumor cell. This approach appears to be particularly useful for αCD3 BiMAb targeting tumor antigens expressed at low levels.

Split Co-Stimulation in Multicellular Tumor Spheroids

Multicellular, three-dimensional organoid models are suitable to recapitulate *in vivo* cell-cell interactions (31, 32). We generated *in vitro* tumor spheroids from MCF-7 breast cancer cells to further evaluate the capacity of our BiMAb to mediate anti-tumor responses in a more challenging 3D model. Tumor cells formed clusters within 24 h after seeding in Matrigel and formed compact spheroids reaching about 1 mm diameter after 2-3 days. T cell infiltration and tumor cell lysis mediated by BiMAb were investigated by fluorescence microscopy. MCF-7 tumor spheroids formed with CTV-labeled MCF-7 cells were co-cultured with CFSE-labelled T cells and bispecific antibodies (**Figure 4A**). $CFSE^+$ T cells accumulated in a dense layer around spheroids. Upon combined treatment with αEpCAM–αCD3 and αEpCAM–αCD28 BiMAb, an extensive T cell infiltration throughout spheroid masses was observed, whereas with singly used αCD3 or αCD28 BiMAb spheroids were microscopically comparable to untreated controls displaying a low degree of spontaneous T cell infiltration as indicated by small scattered $CFSE^+$ cell clusters appearing inside spheroids. Single use of the αCD3 BiMAb, but not the αCD28 BiMAb, elicited a minor degree of cytotoxicity as evidenced by propidium iodide staining. However, this tumor cell lysis appeared to be confined to the outer rim of spheroids, whereas the addition of co-stimulatory αCD28 BiMAb resulted in an intense and permeating PI staining, indicative of a high degree of tumor cell lysis caused by spheroid-infiltrating cytotoxic T cells. Cell death visualized by PI staining was quantified by LDH release into the supernatant as shown in **Figure 4C**.

Next, we examined the possibility of an extended split co-stimulation approach by targeting distinct antigens on two different tumor cells in order to deliver activating and co-stimulatory signaling to T cells. Based on the surface expression levels of EpCAM, HER2, FAP and PD-L1, we chose to generate mixed multicellular tumor spheroids by blending the MCF-7 breast cancer cell line and FAP-transfected HT-1080 fibrosarcoma cells serving as a surrogate for FAP-expressing cancer-associated fibroblasts in tumor stroma. MCF-7 expressed EpCAM and HER2 but were negative for FAP and PD-L1, while HT-1080/FAP cells displayed the opposite phenotype (**Figure 4B**). Single use of either of the three αTAA–αCD3 BiMAb demonstrated no significant effect on cytotoxicity as measured by LDH release, whereas the combination of activating and co-stimulatory BiMAb significantly enhanced tumor cell lysis compared to treatment with αCD3 BiMAb alone (**Figure 4C**). The highest cytotoxicity was observed using a combination of αCD3 and αCD28 BiMAb targeting EpCAM. The αCD28 bispecific antibodies directed against HER2, FAP or PD-L1 also promoted significant cytotoxic effects in combination with αEpCAM–αCD3, albeit slightly weaker compared to αEpCAM–αCD28. Remarkably, we observed significant co-stimulatory effects exerted by αFAP–αCD28 and αPD-L1–αCD28 BiMAb when using αEpCAM–αCD3 or αHER2–αCD3 stimulatory BiMAb. V*ice versa*, co-stimulation through EpCAM or HER-2 significantly enhanced FAP-mediated tumor cell lysis, suggesting that T cells engaged carcinoma and sarcoma cells concomitantly. Similar results were observed for $CD8^+$ T cell activation assessed by CD25/4-1BB co-expression (**Figure 4D**) and $CD4^+$ T cells (**Supplementary Figure 5A**). Regarding T cell proliferation, treatment with αCD3 BiMAb alone induced only a minor degree of $CD4^+$ and $CD8^+$ T cells proliferation which was not significant (**Figure 4E**). Addition of αCD28 BiMAb clearly enhanced T cell proliferation when compared to αCD3 single use. Interestingly, αCD28 BiMAb

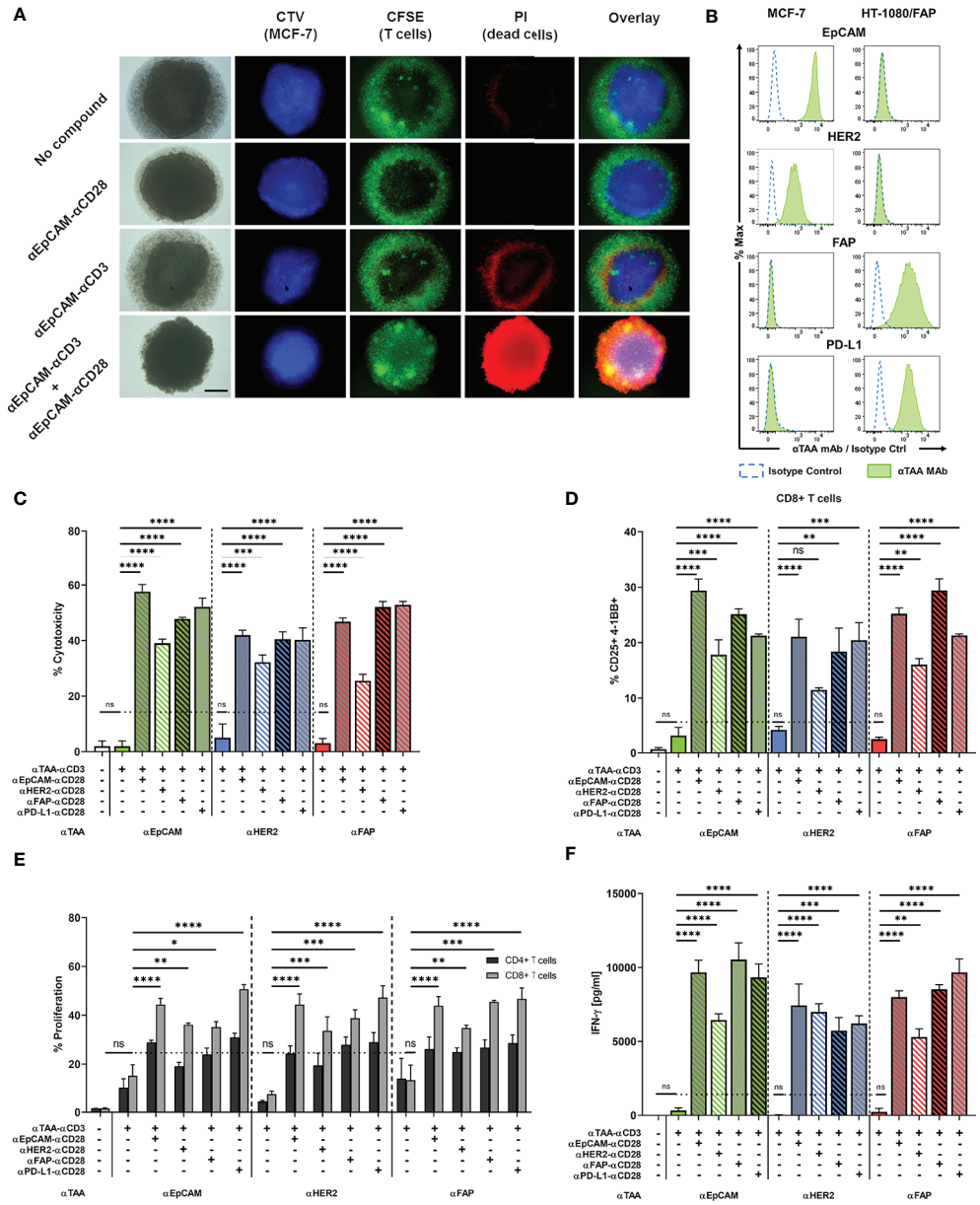

FIGURE 4 | A split co-stimulation approach targeting TAAs on different target cells enhances T cell activation in a mixed MCF-7 + HT-1080/FAP tumor spheroid model. **(A)** Fluorescence microscopy of MCF-7 spheroids after incubation with or without 10 nM of αCD3 +/- αCD28 BiMAb. Representative images of CTV-labelled MCF-7 spheroids. Purified T cells were labeled with carboxyfluorescein succinimidyl ester (CFSE). Cell death was visualised by PI staining. The scale bar represents 250 µm. **(B)** EpCAM, HER2, FAP and PD-L1 surface expression on MCF-7 and HT-1080/FAP cells, respectively, analyzed by flow cytometry. Cell surface staining with isotype control antibodies (dotted blue line) and αTAA mAb (green filled). **(C–F)** Tumor spheroids from $5x10^4$ mixed MCF-7 and HT-1080/FAP cells (1:1 ratio) were co-cultured with purified unstimulated T cells (10^5 cells per 96-well) and combinations of αTAA–αCD3 +/- αTAA–αCD28 BiMAb at 10 nM final concentration. TAA reactivities included EpCAM, HER2, FAP and PD-L1. **(C)** Supernatants were collected after 48h of co-culture and tumor cell lysis was assessed *via* LDH release assay. **(D)** BiMAb-mediated $CD8^+$ T cell activation was detected by flow cytometry based on surface co-expression of CD25 and 4-1BB. **(E)** Frequencies of proliferating $CD4^+$ and $CD8^+$ T cells were measured by flow cytometry (dilution of CTV labeling) after 5 days of incubation. αTAA–αCD3 treatment was statistically compared with the no compound control, αTAA–αCD3 + αTAA–αCD28 combinations were compared with αTAA–αCD3. Co-stimulation significantly enhanced $CD8^+$ T cell proliferation for all settings (statistics indicated in figure). Enhancement of $CD4^+$ T cell proliferation was significant only for the combinations αEpCAM–αCD3 + αEpCAM–αCD28 (*), αEpCAM–αCD3 + αPD-L1–αCD28 (*), αHER2–αCD3 + αEpCAM–αCD28 (*), αHER2–αCD3 + αFAP–αCD28 (**), and αHER2-αCD3 + αPD-L1-αCD28 (***). **(F)** Concentrations of IFN-γ (in pg/ml) in cell culture supernatants after 48 h of co-culture were determined by ELISA. Data represent mean values ± SEM from 3 independent experiments done in duplicates. Statistical analysis by one-way ANOVA **(C, D, F)** or two-way ANOVA **(E)**, both followed by Tukey's multiple comparison test; ns, not significant; *$p < 0.05$; **$p < 0.01$; ***$p < 0.001$; ****$p < 0.0001$.

particularly induced proliferation of $CD8^+$ T cells, as the frequencies of those cells increased by at least 2-fold in comparison to αCD3 BiMAb treatment alone, regardless of the examined TAA combination. For $CD4^+$ T cells, only some combinations of (co)-stimulatory BiMAb significantly enhanced proliferation (see legend to **Figure 4**). Treatment with αTAA–αCD3 BiMAb alone did not trigger notable IFN-γ secretion (**Figure 4F**). In contrast, addition of co-stimulatory αTAA x αCD28 BiMAb induced a highly significant release of IFN-γ, regardless of the chosen target antigen. A comparable enhancement was observed for IL-2 release (**Supplementary Figure 5B**). We conclude that co-stimulatory BiMAb targeting a second tumor-associated antigen on either the same or on a second distinct tumor cells in mixed tumor cell spheroids demonstrated considerable efficacy in combination with a panel of αCD3 BiMAb.

We also asked whether bystander cytotoxicity would occur in adherent cell co-culture assays with confluent $EpCAM^+$ MCF-7 and $EpCAM^-$ HT-1080/FAP target cells (**Figure 4B**) mixed in a 1:1 ratio. Using αEpCAM–αCD3 BiMAb to stimulate T cells and αEpCAM–αCD28 or αFAP–αCD28 BiMAb for co-stimulation, we confirmed that cytoxicity against MCF-7 could be co-stimulated by either of the two CD28 BiMAb (**Supplementary Figure 5C**). ~25%-30% dead $EpCAM^-$ HT-1080/FAP target cells were observed when co-stimulatory αFAP–αCD28 and αEpCAM–αCD28 BiMAb were present in the assay, suggesting that release of cytotoxic granules by activated T cells was not strictly focussed on MCF-7 targets.

Split Co-Stimulation With TNFL Bifunctional Fusion Proteins

In addition to αCD28 bispecific antibodies, we evaluated the capacity of four members of the TNF ligand superfamily, 4-1BBL (TNFSF9), OX40L (TNFSF4), CD70 (TNFSF7), and TL1A (TNFSF15) to provide co-stimulation to T cells in the context of bifunctional reagents. We generated bifunctional fusion proteins containing N-terminal αFAP or αEpCAM scFv antibodies as in tetravalent hIgG1-Fc-based BiMAb, however, replaced the C-terminal αCD28 scFv by a single extracellular domain of either 4-1BBL, OX40L, CD70 or TL1A. The co-stimulatory capacities of αEpCAM–TNFL fusion proteins were first examined with 2D adherent MCF-7 cells with regard to cytotoxicity elicited by the weakly expressed tumor antigens CEA and EGFR. In line with results shown above (**Figure 3**), the co-stimulation-dependent αCEA–αCD3 and αEGFR–αCD3 BiMAb alone did not trigger cytotoxicity against MCF-7 targets and could not be rescued by co-stimulation through αCEA–αCD28 or αEGFR–αCD28, respectively (**Figure 5A**). Highly significant enhancement of cytotoxicity, however, was achieved by inclusion of αEpCAM–αCD28 and either of the four αEpCAM–TNFL fusion proteins.

The four αFAP–TNFL bifunctional reagents were studied in the 3D tumor spheroid model with MCF-7 and HT-1080/FAP cells blended in a 1:1 ratio. Consistent with absent T cell stimulation by the αFAP–αCD28 BiMAb alone, αFAP–TNFL fusion proteins displayed no effect regarding tumor cell lysis when used as single reagents (**Figure 5B**). Again, the αEpCAM–αCD3 BiMAb alone elicited only an insignificant degree of cytotoxicity. High levels of cytotoxicity were induced by the combination of αEpCAM–αCD3 and co-stimulatory αFAP–αCD28 with approximately 50% of tumor cells being lysed. When combining αFAP–TNFL fusion proteins with αEpCAM–αCD3, we observed a significant augmentation of cytotoxicity for all four constructs, suggesting that they were able to deliver co-stimulation for cytotoxic effector functions by engaging the FAP antigen expressed on admixed fibrosarcoma cells. Among the TNFL members investigated, OX40L and CD70 displayed the weakest cytotoxic effect (30% and 24.5% tumor cell death, respectively). 4-1BBL and TL1A induced comparable cytotoxic effects with 36.2% and 38.2% of tumor cells lysed, respectively, when used at an equimolar concentration of 10 nM. We observed a similar pattern regarding activation marker expression on $CD8^+$ T cells. Combination of αEpCAM–αCD3 with αCD28, 4-1BBL or TL1A fusion proteins significantly enhanced co-expression of CD25/4-1BB on $CD8^+$ T cells (**Figure 5C**) or CD25/OX40 on $CD4^+$ T cells (**Supplementary Figure 5D**).

$CD8^+$ T cell proliferation which was significantly enhanced compared to solely used αEpCAM–αCD3 by αFAP–αCD28 BiMAb and αFAP–TNFL fusion proteins containing 4-1BBL, OX40L or TL1A whereas there were only tendencies to increase proliferation of $CD4^+$ T cells (**Figure 5D**). Regarding cytokine release, the TNFL bispecific fusion proteins displayed weaker co-stimulatory effects compared to the αFAP–αCD28 BiMAb (**Figures 5E, F**) with only 4-1BBL inducing a significant rise in IL-2 secretion and 4-1BBL and TL1A in IFN-γ secretion, in comparison to treatment with αEpCAM–αCD3 only. Together, the results suggest a hierarchy in the co-stimulatory capacity of the herein used αFAP–TNFL fusion proteins in the order 4-1BBL, TL1A, OX40L, and CD70.

ICI Antibodies Enhance Anti-Tumor Effects of BiMAb-Induced Co-Stimulation

We next investigated the question whether a combination of αCD3/αCD28 BiMAb with immune checkpoint inhibitor antibodies would further augment anti-tumor effects. The rationale to examine this combinatory approach was based on our observation of enhanced checkpoint receptor expression on T cells activated by BiMAb. In 2D co-culture experiments of MCF-7 with T cells, treatment with the αEpCAM–αCD3 BiMAb alone led to a rapid upregulation of PD-1 (**Figure 6A**) and PD-L1 (**Figure 6B**) on $CD8^+$ and $CD4^+$ T cells. Addition of the co-stimulatory αEpCAM–αCD28 BiMAb further enhanced PD-1 and PD-L1 expression, whereas αEpCAM–αCD28 BiMAb alone had no effect on immune checkpoint receptor expression. Upregulation of PD-1 and PD-L1 surface expression in the presence of αEpCAM–αCD28 co-stimulation persisted on $CD4^+$ and $CD8^+$ T cells over 7 days, while PD-1 and PD-L1 expression declined after 72 h when only the αEpCAM–αCD3 BiMAb was present (**Figures 6A, B**). Notably, we found a similar induction of PD-L1 on tumor cells. In response to BiMAb-mediated T cell activation, PD-L1-deficient MCF-7 cells significantly increased PD-L1 surface expression (**Figure 6C**). Again, PD-L1 upregulation was

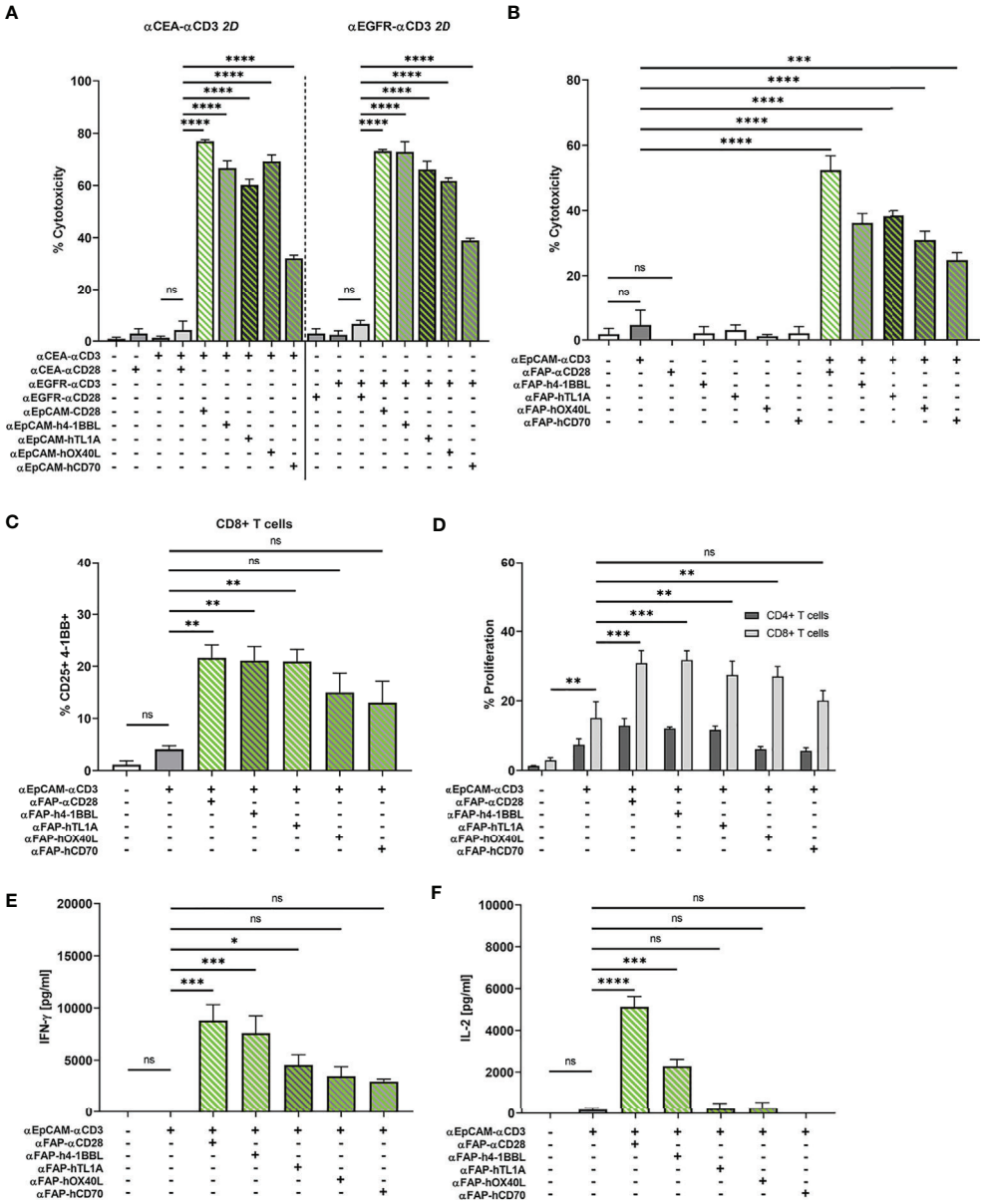

FIGURE 5 | **(A)** Split co-stimulation with αEpCAM–TNFL fusion proteins in the 2D adherent cell model. αCEA–αCD3 (1 nM, left) or αEGFR–αCD3 BiMAb (1 nM, right) were used in cytoxicity assays (LDH release) with MCF-7 target cells (E:T ratio 2:1) +/- the indicated αEpCAM–TNFL fusion proteins (1 nM) or αCEA/EGFR–αCD28 BiMAb (1 nM) that were used for statistical comparison by one-way ANOVA with Dunnett's follow-up test. **(B–F)** Bifunctional αTAA scFv–TNFL fusion proteins provide co-stimulation to αCD3 BiMAb-activated T cells in a split co-stimulation approach in the 3D spheroid model. Tumor spheroids containing MCF-7 + HT-1080/FAP cells in a 1:1 ratio were co-cultured with purified unstimulated T cells and combinations of αEpCAM–αCD3 BiMAb +/- 10 nM αFAP–αCD28 BiMAb or 10 nM fusion proteins of αFAP scFv-hIgG-Fc and ectodomains of tumor necrosis factor superfamily ligands (TNFL) 4-1BBL, CD70, OX40L or TL1A. **(B)** Cytotoxicity based on LDH release, measured in supernatants collected after 48h of co-culture. **(C)** Frequencies of CD25 and 4-1BB double positive $CD8^+$ T cells analyzed by flow cytometry. **(D)** Proliferation of CTV-labelled $CD4^+$ and $CD8^+$ T cells measured by flow cytometry after 5 days of co-culture. Proliferation of $CD4^+$ T cells was not significantly enhanced. Cytokine release (in pg/ml) of IFN-γ **(E)** and IL-2 **(F)** was measured after 48 h of co-culture by ELISA. Data represent the mean ± SEM from 3 independent experiments in duplicates. Statistical analysis *vs*. αEpCAM-αCD3 groups by one-way ANOVA **(B, C, E, F)** or two-way ANOVA **(D)**, both with Dunnett's follow-up test; ns, not significant; $^*p < 0.05$; $^{**}p < 0.01$; $^{***}p < 0.001$; $^{****}p < 0.0001$.

further enhanced by the αCD3 and αCD28 BiMAb combination, resulting in a frequency of approximately 60% PD-L1$^+$ MCF-7 cells. Small subpopulations of $CD8^+$ and $CD4^+$ T cells upregulated CTLA-4 expression in co-cultures with MCF-7 cells in the presence of αEpCAM–αCD3 BiMAb and the αEpCAM–αCD3/CD28 BiMAb combination (data not shown).

Subsequently, we examined the effect of immune checkpoint inhibitors targeting CTLA-4 and the PD-1/PD-L1 axis to further

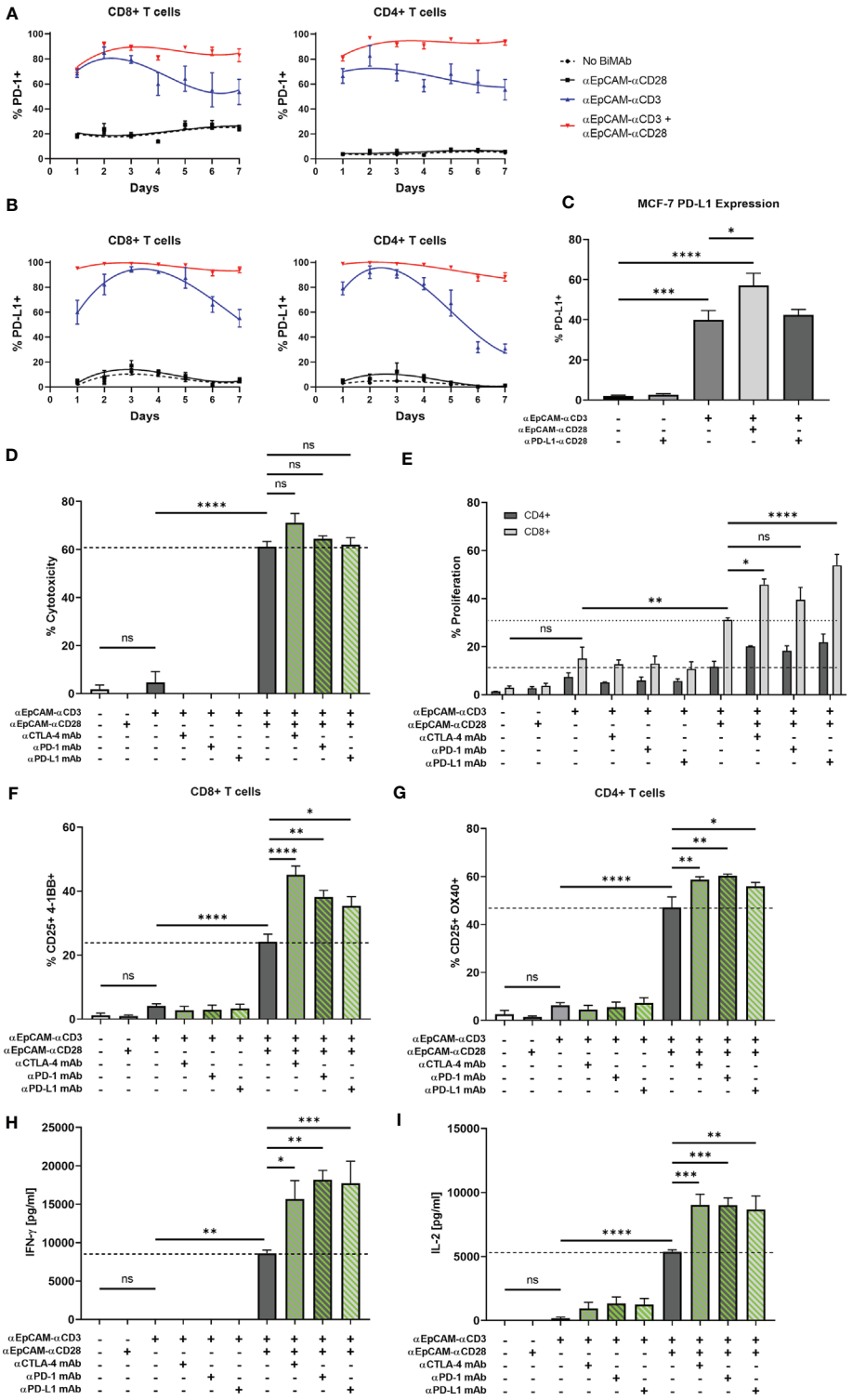

FIGURE 6 | Continued

FIGURE 6 | BiMAb-mediated T cell activation induces expression of PD-1 and PD-L1; blockade of immune checkpoints enhances the efficacy of BiMAb in MCF-7 + HT-1080/FAP tumor spheroids. Time course of PD-1 **(A)** and PD-L1 **(B)** expression on $CD8^+$ and $CD4^+$ T cell subsets co-cultured with MCF-7 in the presence of αEpCAM–αCD28, αEpCAM–αCD3 or a combination of both at 1 nM concentration for 7 days. Means ± SEM from 3 independent donors are shown. Co-stimulation leads to a rapid and permanent induction of PD-1 and PD-L1. **(C)** After 48 h of co-culture with $CD3^+$ T cells and the indicated BiMAb, upregulation of PD-L1 on MCF-7 cells was detected *via* flow cytometry. **(D–I)** MCF-7 + HT-1080/FAP tumor spheroids were co-cultured with purified unstimulated T cells and combinatory settings of EpCAM-targeting αCD3 +/- αCD28 BiMAb in the presence or absence of immune checkpoint inhibitor (ICI) antibodies, ipilimumab (αCTLA-4), nivolumab (αPD-1) or durvalumab (αPD-L1). Concentrations of bispecific and ICI antibodies were 10 nM and 100 nM, respectively. **(D)** Supernatants were collected after 48 h of co-culture and tumor cell lysis was measured *via* LDH release assay. **(E)** Frequencies of proliferating $CD4^+$ and $CD8^+$ T cells were measured by flow cytometry (CTV dilution) after 5 days of incubation. $CD4^+$ T cell proliferation was not significantly enhanced by ICI antibodies. **(F)** BiMAb-mediated T cell activation was detected by flow cytometry based on surface co-expression of CD25 and 4-1BB for $CD8^+$ T cells and **(G)** CD25 and OX40 for $CD4^+$ T cells, respectively. Cytokine release (in pg/ml) of IFN-γ **(H)** and IL-2 **(I)** was measured after 48 h of co-culture by ELISA. Data represent mean values ± SEM from 3 independent experiments performed in duplicates. Statistical analysis by one-way ANOVA **(C, D, F–I)** or two-way ANOVA **(E)**. Analysis of **(D–I)** included Dunnett's follow-up test for comparison with αEpCAM-αCD3 + αEpCAM-αCD28 groups without ICI antibodies; ns, not significant; $^*p < 0.05$; $^{**}p < 0.01$; $^{***}p < 0.001$; $^{****}p < 0.0001$.

enhance the anti-tumor response using MCF-7 tumor spheroids. Although a minor but non-significant increase in tumor cell lysis was observed with the αCTLA-4 monoclonal antibody ipilimumab, the combinatorial setting of αCD3 BiMAb, αCD28 BiMAb and clinically used ICI antibodies resulted in no significant impact on cytotoxicity as measured after 48 h by LDH release (**Figure 6D**). ICI antibodies ipilimumab, nivolumab (αPD-1) and durvalumab (αPD-L1) significantly enhanced $CD8^+$ T cell activation and to lesser extent also $CD4^+$ T cell activation above the levels achieved by αCD3 plus αCD28 BiMAb (**Figures 6F, G**). Further we examined whether T cell proliferation could also benefit from checkpoint inhibition (**Figure 6E**). Enhancement of proliferation was detected in $CD8^+$ T cells where the αPD-L1 mAb had the most pronounced effects whereas the proliferation of $CD4^+$ cells was not significantly augmented by ICI antibodies. Finally, we observed stimulating effects of ICI antibodies on the release of IFN-γ and IL-2. Targeting the PD-1/PD-L1 axis with monoclonal antibodies in combination with αCD3/αCD28 BiMAb resulted in a ~2-fold increase in IFN-γ secretion, compared to BiMAb treatment alone (**Figure 6H**). Similarly, addition of αCTLA-4 mAb significantly increased IFN-γ release by factor 1.8. All checkpoint inhibitor mAbs significantly enhanced IL-2 secretion by a comparable ~1.7-fold increase (**Figure 6I**). Of note, when we applied ICI antibodies together with the αEpCAM–αCD3 BiMAb alone, in none of the functional assays a significant enhancement of T cell effector functions was detected (**Figures 6D–I**). Hence, immune checkpoint inhibitors were demonstrated to be specifically effective in combination with co-stimulatory αCD28 BiMAb.

Ex Vivo Patient-Derived Tumor Spheroids

We developed an *ex-vivo* patient-derived spheroid model to assess the efficacy of our co-stimulatory BiMAb on primary tumor cells enriched from malignant pleural effusions that were obtained from advanced stage breast cancer patients. Prior to the spheroid generation, target antigen expression of patient-derived breast cancer cells was characterized by flow cytometry inasmuch as sufficient material was available. Since we detected substantial surface expression of HER2 on all patient tumor cell samples we decided to use αHER2–αCD3 as stimulatory BiMAb. As shown in a representative manner for patient #6 (**Figure 7A**), PD-L1, EGFR and EpCAM were expressed to a lower degree or on subsets of tumor cells while FAP expression was absent. *Ex-vivo* spheroids were co-cultured with autologous PBMC obtained from each patient. Due to low amounts of breast cancer cells isolated from some pleural effusions, we could not conduct a comprehensive analysis of target antigens, examine every experimental condition with all patient samples nor study effects of ICI antibodies.

Regarding cytotoxicity, treatment with αHER2–αCD3 alone demonstrated a weak and non-significant increase in tumor cell lysis compared to no-antibody controls (mean 8.4% *vs*. 1.8% specific LDH release) (**Figure 7B**). However, combination with co-stimulatory αCD28 BiMAb recognizing HER2, EpCAM, EGFR or PD-L1 significantly enhanced the anti-tumor immune response compared to no-antibody controls as well as to single treatment with αHER2–αCD3. With approximately 42% of cancer cells being lysed, the most prominent cytotoxic effect was observed with αHER2–αCD28 compared to treatment with αCD3 BiMAb alone, followed by αPD-L1–αCD28 and αEpCAM–αCD28. Regarding the activation of autologous $CD4^+$ and $CD8^+$ T cells, we observed a comparable pattern (**Figure 7C**). Treatment with αHER2–αCD3 alone significantly increased the frequency of activated $CD4^+/CD25^+/OX40^+$ and $CD8^+/CD25^+/4\text{-}1BB$ T cells. Furthermore, a significant upregulation of activation markers was achieved by combinatorial use of αHER2–αCD3 with either αCD28 BiMAb as compared with no-antibody controls. However, compared to αHER2–αCD3 single treatment, significance of the co-stimulatory setting was reached only for combinations with αCD28 BiMAb binding HER2 or PD-L1. (**Figure 7C**). Due to limiting amounts of tumor cells, we could only examine BiMAb-mediated effects on proliferation with ≤ 5 patient samples for most conditions (**Figure 7D**). αHER2–αCD3 alone significantly stimulated proliferation of $CD8^+$ but not of $CD4^+$ T cells. Except for αHER2–αCD28 in $CD4^+$ T cells, the addition of αCD28 BiMAb further significantly enhanced proliferation of both T cell subsets as compared to no-antibody controls. Notably, the greatest enhancement of proliferation was observed in combination with αPD-L1–αCD28 BiMAb. Compared to αHER2–αCD3 alone, addition of αPD-L1–αCD28 promoted 3.5-fold and 5.2-fold increases in

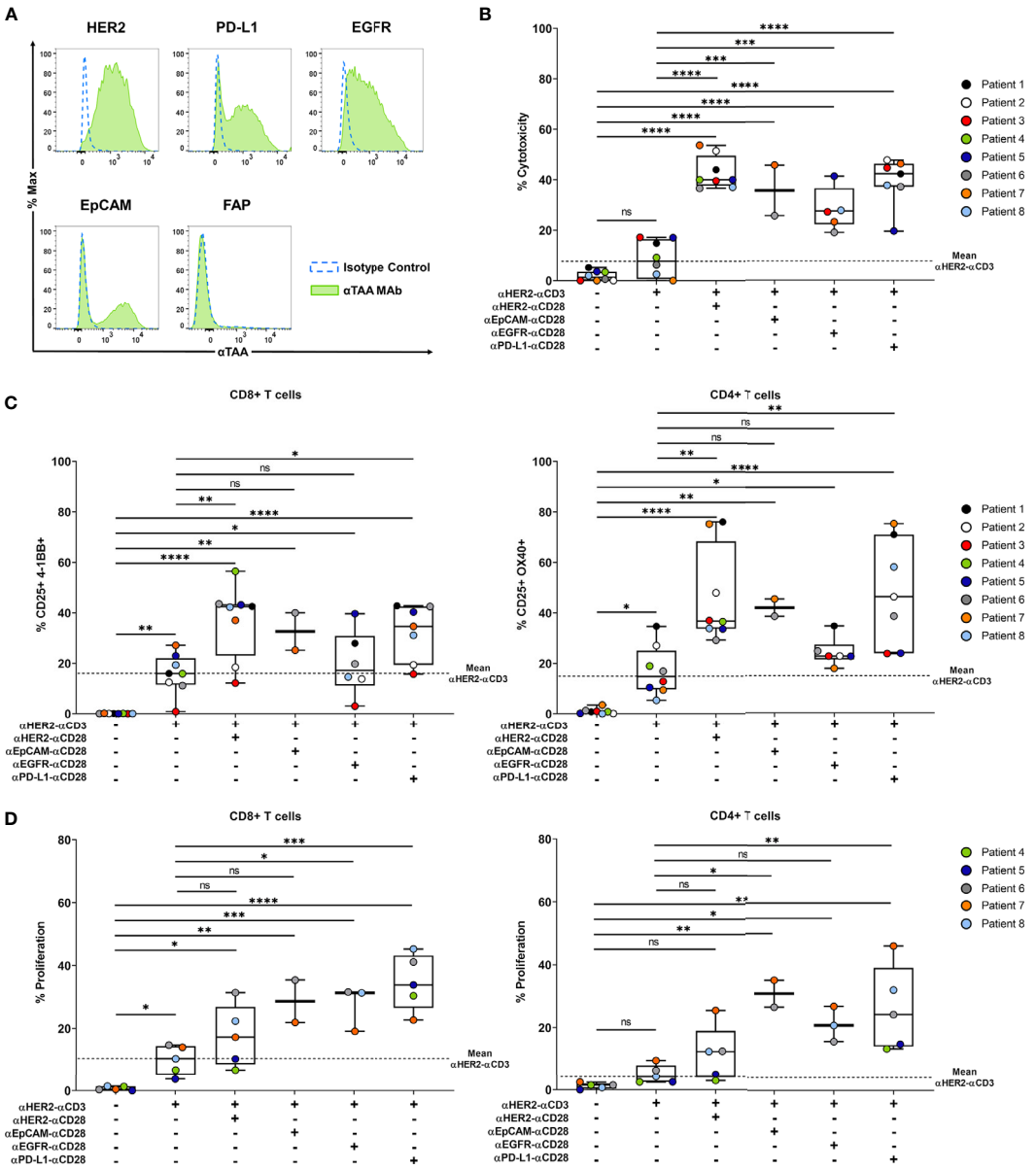

FIGURE 7 | Co-stimulatory BiMAb enhance activation of autologous T cells and induce tumor cell lysis in patient-derived tumor spheroids *in vitro*. Patient-derived tumor spheroids were generated *in vitro* with breast cancer cells purified from pleural effusions and co-cultured with autologous PBMC in the presence or absence of 10 nM αHER2– αCD3 +/- 10 nM αTAA–αCD28 BiMAb. TAA targeted by co-stimulatory BiMAb were HER2, EGFR, EpCAM and PD-L1. **(A)** TAA surface expression on purified tumor cells from a representative patient (#6) was analyzed by flow cytometry, staining with isotype control antibodies (dotted blue line) and αTAA mAb (green filled line). Examined TAA included HER2, PD-L1, EGFR, EpCAM and FAP. **(B)** Supernatants were collected after 48 h of co-culture and tumor cell lysis was measured by LDH release assay. **(C)** Frequencies of $CD25^+/4\text{-}1BB^+$ $CD8^+$ T cells (left panel) and $CD25^+/OX40^+$ $CD4^+$ T cells (right panel) analyzed *via* flow cytometry after 48 h of incubation. **(D)** T cell proliferation (CTV dilution) of $CD8^+$ (left panel) and $CD4^+$ (right panel) T cells, analyzed after 5 days of co-culture by flow cytometry. Results are shown as box and whisker plots with individual data points of n ≤ 8 patients. Statistical analysis by one-way ANOVA **(B–D)** with Tukey's multiple comparison test, ns, not significant; $^*p < 0.05$; $^{**}p < 0.01$; $^{***}p < 0.001$; $^{****}p < 0.0001$.

proliferating $CD8^+$ and $CD4^+$ T cells, respectively. In sum, we showed that also for tumor cell spheroids generated from patient-derived malignant effusions, the combinatory use of stimulatory and co-stimulatory BiMAb augmented tumor cell lysis by autologous T cells and enabled a more pronounced *in vitro* T cell activation and proliferation.

DISCUSSION

We studied the characteristics and efficacy of bispecific constructs providing co-stimulatory signals to T cells, that receive an activating signal through BiMAb-mediated cross-linking of the CD3ε molecule serving as surrogate for the

canonical TCR α/β–MHC-I/II interaction. For bispecific antibodies we utilized a tetravalent (scFv1-Fc^{KO}-scFv2)$_2$ format that was recently shown by us to be efficacious for the targeting of HBsAg expressed by HBV-infected or HBVenv-transfected hepatoma cells (26). To overcome the issue of Fc receptor engagement and inadvertent bystander T cell activation in the absence of tumor antigen recognition, we introduced mutations to silence the Fc domain in our constructs (26). Thus, the activity of our bispecific agents is independent of FcγR binding, but solely relies on cross-linking between tumor cells and T cells in an antigen-dependent manner. We demonstrated that our αTAA–αCD3 BiMAb are unable to stimulate T cells in the absence of tumor cells or when the relevant tumor-associated antigen is not expressed on the surface of a tumor cell. Importantly, we showed that our co-stimulatory αCD28 BiMAb and TNFL bispecific fusion proteins have no activity as single agents in the absence of TCR complex triggering, but drastically enhanced the magnitude of T cell activation and further boosted the anti-tumor response in combination with αCD3 bispecifics. We demonstrated that the co-stimulatory signal needs to be delivered in an appropriate spatiotemporal context since T cells pretreated with αCD3 BiMAb become refractory to the co-stimulatory activity of αCD28 BiMAb when administered temporally delayed, even when the αTAA–αCD28 BiMAb was suited to cross-link T cells and tumor cells. This feature provides for an important safety aspect diminishing T cell activation outside of tumor tissue, however, requires synchronous administration of two BiMAb.

Moreover, tumor-targeted co-stimulation was shown to reduce the required dose of αCD3 BiMAb to achieve T cell activation by at least 10-fold. Enhancement of T cell activation through co-stimulation was particular effective if the concentration of the αCD28 BiMAb was fixed at 10 nM (~1.68 mg/l) (see **Figure 1G** and **Table 1**). In that case, the EC_{50} for the αCD3 BiMAb regarding cytotoxicity against MCF-7 targets was 1.4 pM (~235 ng/l) and hence ~7000-fold lower than the αCD28 BiMAb concentration (10 nM). Thus, to best avoid unspecific T cell activation it could be advantageous to work with two independently titratable, stimulatory and co-stimulatory BiMAb rather than with a trispecific αTAA/αCD3/αCD28 antibody (33). Due to the complete lack of stimulatory activity of the αCD28 BiMAb, increasing its concentration appears to be an acceptable strategy.

It is of interest to discuss the tetravalent (scFv1-Fc^{KO}-scFv2)$_2$ format used in this report in the context of BiMAb formats with other valencies of target antigen and T cell recognition (4–8, 24, 25). In a recent study (26), we carefully analyzed αHBsAg–αCD3/CD28 BiMAb of exactly the same molecular architecture as the TAA-reactive BiMAb used here representing a 2:2 ratio in terms of TAA and CD3ε/CD28 recognition, side by side with αHBsAg F(ab)–αCD3/28 scFv fusion proteins (FabMAb) with an 1:1 target/T cell ratio, which is also present in the BiTE/SMITE tandem di-scFv format (20, 22, 23). Both 2:2 BiMAb and 1:1 FabMAb formats proved to be highly similar in terms of HBsAg binding, T cell binding, T cell activation, dependence of CD28-mediated co-stimulation, induction of proliferation, cytokine release and cytotoxicity against HBsAg-positive targets. The major difference consisted in the *in vivo* half-life that was <6 h for the FabMAb (~78 kDa) and >72 h for the BiMAb (~170 kDa). The findings indicated that the BiMAb format containing an Fc portion that allows recycling through the neonatal Fc receptor, has advantageous pharmacokinetic properties *in vivo*. While it seems reasonable that the reported comparable potencies of HBsAg BiMAb of 2:2 and 1:1 formats can be extrapolated to the αEpCAM/HER2/EGFR/CEA/FAP/PD-L1 BiMAbs used here, it still needs to be tested how a 2:1 bispecific IgG antibody format (34) would perform in comparison with the 2:2 BiMAb format.

Our experiments revealed a slightly weaker anti-tumor response in the *in vitro* spheroid model as compared to monolayer cultures which is likely due to the fact that, similar to naturally grown tumor masses, cytotoxic T cells need to infiltrate spheroids formed in Matrigel and BiMAb enter by diffusion or are carried on the surface of infiltrating T cells. Notably, solely administered αCD3 bispecific antibodies displayed no significant efficacy in functional T cell assays involving spheroids except for inducing a minor degree of T cell proliferation. Based on these observations, BiMAb providing co-stimulation demonstrated to be essential in promoting robust anti-tumor immune responses in breast cancer and mixed tumor organoids.

The success of treating hematological malignancies with bispecific antibody formats such as blinatumomab fueled efforts to expand this approach to the more challenging treatment of solid tumors (7, 8). One obstacle is the choice of an appropriate target, as most conventional solid tumor antigens such as EpCAM, HER2 or EGFR are not tumor-specific, being expressed to various degrees in healthy tissues as well. Therefore, T cell-recruiting bispecific antibodies would require TAA having a high selectivity for the malignant cell population in order to spare vital, healthy tissues from destruction by activated T cells as much as possible. By targeting various TAA on different tumor cells, our studies demonstrated that split co-stimulation, even involving antigens individually expressed by mixed breast carcinoma and fibrosarcoma cells, is a valid approach to enhance immune responses. We showed that targeting FAP on a second distinct cell line allowed to deliver co-stimulatory signals to T cells targeting a conventional TAA on other tumor cells. Such a split co-stimulation approach could potentially limit systemic toxicities, while increasing T cell activation and effector functions predominantly at the tumor site. These promising results are in full agreement with recent reports demonstrating the feasibility of split co-stimulation using different molecular architectures of αCD28 BiMAb and target antigens (20, 21). Provided that an αCD3 BiMAb shows no tumor-independent activation of T cells and an αCD28 BiMAb acts in a strictly co-stimulatory manner, a pan-epithelial cell surface antigen should be usable for split co-stimulation against carcinoma cells. The results presented in this work suggest that the αEpCAM–αCD28 BiMAb could fulfill these requirements in combination with, e.g., αCEA–αCD3 or αEGFR–αCD3 BiMAb.

The same consideration holds for the FAP antigen that is consistently expressed on activated cancer-associated fibroblasts (35, 36). Extending reports on αFAP–B7.1 and αFAP–4-1BBL fusion proteins (16–19) we show here that a tetravalent bispecific αFAP–αCD28 antibody can provide efficient co-stimulation in our mixed MCF-7/HT-1080-FAP tumor cell spheroids for T cell activation that is delivered through e.g., αEpCAM–αCD3 or αHER2–αCD3 BiMAb. Preliminary experiments using adherent MCF-7 and HT-1080/FAP cells seeded at high and low cell densities demonstrated that co-stimulation *via* a second target cell required (sub)confluent monolayers, suggesting that responding T cells simultaneously contacted both types of tumor cells for stimulation and co-stimulation, respectively. In our model of mixed tumor cell spheroids close contacts between carcinoma and fibrosarcoma cells are expected to occur that might even lead to a minor degree of plasma membrane exchange and bystander killing of cells not expressing the TAA targeted by the αTAA–αCD3 BiMAb as demonstrated in **Supplementary Figure 5C** and previously shown for EGFR/CD3 BiTEs (37). We are presently studying these possibilities also in mixed tumor spheroids with different cellular compositions that could be developed as a model for the effect of BiMAb-mediated T cell activation in de-differentiated carcinomas with high contents of stroma cells.

A number of previous studies addressed co-stimulatory properties of members of the TNF ligand superfamily including 4-1BBL, OX40L, GITRL and LIGHT using (αTAA scFv–TNFL)$_3$ homotrimers or fusion proteins of αTAA scFv antibodies with single chain TNFL (14–17), or studied a heterodimeric knob-in-hole IgG-like F(ab)-Fc/(4-BBL)$_3$-Fc fusion protein (18, 19). To maintain a bivalent interaction with the tumor antigen of choice, we chose to replace the C-terminal scFv antibody in homodimeric tetravalent BiMAb by the ectodomain of either 4-1BBL, OX40L, TL1A or CD70. We compared co-stimulation by αTAA–αCD28 with αTAA–TNFL fusion proteins side by side. In keeping with earlier reports (15–18) we observed a considerable co-stimulatory activity of 4-1BBL and OX40L ectodomains in fusion proteins with αEpCAM or αFAP scFv antibodies that was, however, slightly inferior to αCD28 BiMAb when used in equimolar amounts.

In this work, we further expanded the scope of co-stimulatory agents. We present, to our knowledge, the first bifunctional TNF-like ligand 1A (TL1A/TNFSF15) fusion proteins to deliver tumor-targeted co-stimulation. TL1A fusion proteins co-stimulated robust anti-tumor responses comparable to 4-1BBL. TL1A is a member of the TNF superfamily that attracted less attention than the co-stimulatory receptors mentioned above and is found mainly on the surface of DCs, B cells and macrophages (38). TL1A binds to death receptor 3 (DR3/TNFRSF25) that is upregulated on activated T cells, B cells and NK cells (39). The TL1A-DR3 interaction supports T cells in the late phase of an immune response, promoting proliferation and cytokine production (40). T_{reg} constitutively express DR3 on their surface, however, TL1A has been shown to diminish the immunosuppressive capacity in pre-clinical studies (41). The number of reports evaluating the role of TL1A in anti-tumor responses remains rather limited to date. Nevertheless, the co-stimulatory effects of the TL1A-DR3 axis could potentially be used to support anti-tumor responses and deserves further investigation. Since TL1A, also named VEGI, suppresses the growth of vascular endothelial cells (42), targeted delivery of co-stimulatory TL1A fusion proteins could serve as an inhibitor of tumor neo-angiogenesis.

Also CD70 (TNFSF7) as the ligand for the CD27 receptor that is constitutively expressed on resting lymphocytes has not been analyzed in bifunctional fusion proteins. The CD27-CD70 interaction induces T cell survival, clonal expansion and enhanced effector functions (43, 44). As compared with three other TNFL studied here, CD70 showed, however, the lowest co-stimulatory capacity.

Clinical trial designs evaluating new cancer treatments often include a combination with immune checkpoint inhibitors (1, 2). A combinatorial setting of bispecific antibodies and checkpoint inhibitors may be beneficial as well to improve the anti-tumor response. Indeed, our work using mixed MCF-7 + HT-1080/FAP tumor spheroids demonstrated further enhancement of T cell stimulation by ICI. Blocking CTLA-4 or the PD-L1/PD-1 axis increased the efficacy of αCD3/αCD28 BiMAb in terms of T cell activation, proliferation, and cytokine secretion (see **Figure 6**). Combination of co-stimulation and checkpoint inhibition can be achieved by simple addition of ICI antibodies (45, 46) or by inclusion of ICI antibody specificities in BiMAb (20, 47). In line with a previous report (20) using a tandem di-scFv format, we demonstrated a significant capacity of a tetravalent αPD-L1–Fc–αCD28 BiMAb to co-stimulate T cell activation triggered by αEpCAM–αCD3, αHER2–αCD3 or αFAP–αCD3 (see **Figures 4**, **7**). While PD-L1 can constitutively be expressed on tumor cells (see **Figures 4B**, **7A**), or be upregulated on tumor cells during co-culture with activated T cells (see **Figure 6C**), it is important to note that cytotoxic T cells consistently upregulated PD-L1 themselves upon activation with αCD3/αCD28 BiMAb (see **Figure 6B**). Therefore, we cannot exclude that co-stimulation by the αPD-L1–αCD28 BiMAb was in part related to PD-L1 and CD28 cross-linking in *cis* on the cell surface of an individual T cell or in *trans* between T cells. Since this could lead to bystander T cell activation independent of tumor antigen binding, the clinical application of αPD-L1–αCD28 co-stimulatory BiMAb should be considered with caution.

Sustained effector T cell activation in the tumor microenvironment is difficult to achieve due immunosuppressive cytokines secreted by the malignant cell population and tumor-associated myeloid-derived suppressor cells (48). We have shown that two relevant immunosuppressive factors, IL-10 and TGF-β, in high concentrations can extensively block cytotoxicity, $CD8^+$ and $CD4^+$ T cell activation, cytokine secretion, proliferation and differentiation of naïve T cells into central and effector memory cells *in vitro* (see **Figure 2**) when activated through an αCD3 BiMAb in the presence of MCF-7 tumor cells. Immunosuppressive effects of IL-10 and TGF-β in combination were almost completely rescued by addition of 1 nM of co-stimulatory αEpCAM–αCD28 BiMAb for all assay parameters

examined, except for IFN-γ and IL-2 secretion that were only partially rescued. In line with an earlier report employing TNFL fusion proteins for co-stimulation (17), the impressive effects of co-stimulation shown here advocate the use of suitable BiMAb to maintain effector T cells in tumor tissues and to invigorate the response of circulating central memory T cells.

Several clinical trials evaluated safety and efficacy of CD3-based bispecific antibodies. However, dose-limiting toxicities often impaired therapeutic success. A phase I study examining an αEpCAM–αCD3 BiMAb (solitomab/AMG 110) in patients with refractory solid tumors revealed persistent dose-dependent gastrointestinal toxicities (49). Endoscopic examination of the duodenum exposed widespread mucosal atrophy, as EpCAM is also found on the epithelia of the colon and intestine. Confirmed stable disease was the best overall response achieved in this study, as target-related side effects prevented dose escalation to therapeutic levels. Other phase I trials targeting CEA or HER2 with αCD3 bispecific antibodies in patients with advanced solid tumors showed manageable treatment-related toxicities, while disease stabilization was observed in a minority of patients with one partial response (50, 51). A recently published dose escalation study evaluated pasotuximab, an αPSMA–αCD3 BiTE, in patients with castration-resistant prostate cancer. Serious treatment-related adverse events were reported in more than 70% of patients (52). According to RECIST criteria the best overall response was disease stabilization. However, two patients had long-term responses, of which one with significant regression of lymph node and bone metastases. Nevertheless, the therapeutic efficacy of αCD3 BiMAb in solid tumors evidently lags behind hematological malignancies. Dose-limiting toxicities, mostly reversible upon treatment discontinuation, further obstruct broad clinical applications. As currently no other bispecific construct achieved regulatory approval, the αCD19–αCD3 BiTE, blinatumomab, remains the only BiMAb being successfully applied in the clinic (22, 23).

A combinatory approach using separate αTAA1–αCD3 and αTAA2–αCD28 BiMAb could help to focus immune responses at the tumor site and thereby allow to use low doses of αTAA1–αCD3 BiMAb in order to limit inadvertent T cell activation in the periphery and resulting systemic toxicities due to excessive cytokine release. We demonstrated that αCD3 BiMAb have rather limited efficacy in our *ex-vivo* patient-derived breast cancer spheroid model but promoted substantial tumor cell killing in combination with co-stimulatory bispecific antibodies. In this work we showed that bispecific antibodies with an (scFv-Fc^{KO}-scFv)$_2$ molecular architecture have substantial efficacy against human cancer cells, with co-stimulatory BiMAb playing an essential role in the anti-tumor responses. Combined use of αCD3 and co-stimulatory αCD28 BiMAb was shown here to efficiently activate autologous T cells in an *ex-vivo* spheroid model leading to remarkable tumor cell eradication. Thus, the ability of BiMAb to stimulate the patient's immune system against their own cancer was demonstrated, while emphasizing the importance and potential of targeted co-stimulation. Like chimeric antigen receptor (CAR)-transduced T cells, expressing receptors providing both stimulatory and co-stimulatory signals, we believe that a similar approach, combining stimulatory and co-stimulatory BiMAb, may be beneficial for treating solid tumors especially when co-stimulation involves a second tumor-associated antigen or a tumor stromal antigen.

DATA AVAILABILITY STATEMENT

The original contributions presented in the study are included in the article/**Supplementary Material**. Further inquiries can be directed to the corresponding author.

ETHICS STATEMENT

The studies involving human participants were reviewed and approved by the ethics committee of the Heidelberg University Faculty of Medicine (approval S-022/2013 and S-207/2005, renewed on 10 September 2018). The patients/participants provided their written informed consent to participate in this study.

AUTHOR CONTRIBUTIONS

KW and FM: conceptualization. KW, MM, GM, NB, CL-M, CZ, CPH, IZ, and FM: methodology. KW, MM, MG, and SK: investigation. FM and MM: supervision. KW and FM: writing. IZ, DJ, and FM: funding acquisition. All authors contributed to the article and approved the submitted version.

FUNDING

This work was in part supported by the Helmholtz Validation Funds (grant number HVF-0078).

ACKNOWLEDGMENTS

The authors would like to thank P. Hill, I. Kaiser, J. Funk and A. Köster for their technical assistance regarding the collection of tumor cells from pleural effusions and isolation of patient-derived peripheral blood mononuclear cells.

SUPPLEMENTARY MATERIAL

The Supplementary Material for this article can be found online at: https://www.frontiersin.org/articles/10.3389/fimmu.2021.719116/full#supplementary-material

Supplementary Figure 1 | (A–C) Assays were performed in 2D adherent cell cultures using serial dilutions of control αFAP–αCD3 BiMAb +/– co-stimulatory control αFAP–αCD28 BiMAb used at equimolar concentrations, purified unstimulated T cells isolated from healthy donors as effector cells and MCF-7 as

target cells (E:T ratio 2:1). **(A–C)** share the legend. **(A)** After 48 h of co-culture, BiMAb-mediated $CD8^+$ (top) and $CD4^+$ (bottom) T cell activation indicated by CD25 and 4-1BB, or CD25 and OX40 surface co-expression was measured by flow cytometry. T cells only (left) *vs*. MCF-7/T cell co-culture (right). **(B)** CTV-labelled T cells were used for co-culture and after 5 days of incubation $CD8^+$ (top) or $CD4^+$ (bottom) T cell proliferation was measured by flow cytometry based on CTV dilution. **(C)** Supernatants were collected after 48 h from co-culture assays and cytotoxicity was measured based on lactate dehydrogenase (LDH) release from lysed cells. **(D)** Representative FACS plots showing CD25 and 4-1BB surface expression on $CD8^+$ T cells (top) and CD25 and OX40 surface expression on $CD4^+$ T cells (bottom) after co-culture with MCF-7 cells and 1 nM αEpCAM–αCD3 +/- αEpCAM–αCD28 BiMAb. **(E)** Representative histograms of BiMAb-induced proliferation of CTV-labelled $CD4^+$ T cells incrementally losing CTV staining with each cell division. No compound control (blue filled), BiMAb treatment (1 nM) as indicated (green filled). Fraction of proliferating cells is indicated. **(F)** Consecutive co-stimulation does not stimulate T cells with pre-bound αCD3 BiMAb. T cells in MCF-7 and HT-1080/FAP co-cultures or purified T cells alone were pre-incubated with 1 nM of αEpCAM–αCD3 (MCF-7, T cells only) or αFAP–αCD3 (HT-1080/FAP) BiMAb for 48 h (1^{st} incubation). T cells were collected and co-cultured again for 48h in the presence or absence of fresh MCF-7, HT1080-FAP or no target cells and 1 mM αCD3 +/- αCD28 BiMAb as indicated (2^{nd} incubation). Activation based on CD25 and OX40/4-1BB co-expression on $CD8^+$ (left panel) and $CD4^+$ (right panel) was analyzed by flow cytometry. Temporally separated T cell co-stimulation by αEpCAM–αCD28, αFAP–αCD28 or αPD-L1–αCD28 BiMAb in the presence of TAA-expressing tumor cells did not lead to activation while this required newly added αCD3 BiMAb. Data represent mean values ± SEM from 3 independent experiments each performed in triplicates. Statistics were performed by one-way ANOVA test with Dunnett's follow-up test *vs*. no compound control, $^{****}p < 0.0001$.

Supplementary Figure 2 | Co-stimulation overrides immunosuppressive effects of exogenous IL-10 and TGF-β. **(A)** $CD4^+$ T cell activation was determined by flow cytometry and shown as percentages of $CD25^+/OX40^+$ T cells. **(B)** Frequencies of proliferating $CD4^+$ T cells was measured by flow cytometry based on CTV dilution after 5d of incubation. Data represent mean values ± SEM from 3 independent experiments each done in duplicates that were statistically analyzed by two-way ANOVA followed by Tukey's multiple comparison test **(A, B)**, ns, not significant; $^*p < 0.05$; $^{****}p < 0.0001$.

Supplementary Figure 3 | Co-stimulatory αEpCAM–αCD28 BiMAb rescue failing T cell activation by αCD3 BiMAb recognizing a second, weakly expressed TAA on MCF-7 target cells. **(A)** $CD8^+$ and $CD4^+$ T cell activation after 48h of incubation was analyzed by flow cytometry based on surface co-expression of CD25/4-1BB and CD25/OX40, respectively. **(B, E)** After 5 days of co-culture, frequencies of proliferating CTV-labelled $CD4^+$ and $CD8^+$ T cells were detected by flow cytometry. **(C)** Percentages of CD25/4-1BB-expressing $CD8^+$ T cells and **(D)** CD25/OX40-expressing $CD4^+$ T cells were determined by flow cytometry after 48 h of co-culture.
(F) IL-2 secretion (in pg/ml) in T cell co-cultures with MCF-7 cells and the indicated αTAA–αCD3 +/- αTAA–αCD28 BiMAb was measured after 48 h by ELISA. Titrations of αCEA **(G)** and αEGFR-binding **(H)** αCD3 BiMAb with either co-stimulatory αTAA–αCD28 or αEpCAM–αCD28 BiMAb. Cytotoxicity measurements were based on LDH released by lysed tumor cells after 48 h (left). BiMAb-mediated T cell activation was assessed by flow cytometry based on the co-expression of CD25/4-1BB for $CD8^+$ T cells and CD25/OX40 for $CD4^+$ T cells, respectively. Proliferation was analyzed by flow cytometry based on CTV dilution. Data represent the mean ± SEM from 3 independent experiments done in triplicates with statistical analysis by one-way ANOVA **(A, C, D, F)** or two-way ANOVA tests **(B, E)**, followed by Tukey's multiple comparison test **(A, C–F)** or Dunnett's follow-up test for comparison with no compound control **(B)**: ns, not significant; $^{***}p < 0.001$; $^{****}p < 0.0001$. EC_{50} values were calculated with GraphPad Prism™ Software using non-linear regression log (agonist) *vs*. response variable slope with a robust fit. EC_{50} values are only shown for αCEA/αEGFR–αCD3 + αEpCAM–αCD28 BiMAb since αCEA/EGFR–αCD28 BiMAb did show co-stimulatory effects or lacked saturation at 10 nM.

Supplementary Figure 4 | MCF-7 cells were pre-incubated with serial dilutions of the HER2-targeting monoclonal antibody trastuzumab (0, 0.1, 1, 10, 100 nM). After 24 h, purified $CD3^+$ T cells and 1 nM αEpCAM-αCD3 +/- αCD28 HER2-targeting BiMAb were added to the culture and further incubated for 48h or 5 days, respectively. **(A)** $CD8^+$ (left) and $CD4^+$ (right) T cell activation after 48h of incubation was analyzed by flow cytometry based on surface co-expression of CD25/4-1BB and CD25/OX40, respectively. **(B)** Cytotoxicity based on LDH release, measured in supernatants collected after 48 h of co-culture. **(C)** After 5 days of co-culture, frequencies of proliferating $CD4^+$ and $CD8^+$ T cells were detected by flow cytometry based on CTV dilution. Data represent the mean ± SEM from 3 independent experiments done in duplicates. Statistical analysis in **(A–C)** was conducted by one-way ANOVA followed by Dunnett's multiple comparison test for comparison with the αEpCAM-αCD3 + αEpCAM-αCD28 condition, ns, not significant; $^{**}p < 0.01$, $^{***}p < 0.001$, $^{****}p < 0.0001$.

Supplementary Figure 5 | Split co-stimulation of T cells by αCD28 BiMAbs or αFAP–TNFL fusion proteins targeting TAAs on different target cells in mixed MCF-7 + HT-1080/FAP tumor spheroids. **(A)** BiMAb-mediated $CD4^+$ T cell activation was detected by flow cytometry based on surface co-expression of CD25 and OX40. **(B)** Concentrations of IL-2 (in pg/ml) in cell culture supernatants of co-culture were determined by ELISA. **(C)** Mixed co-cultures of CellTrace Violet-labelled MCF-7 and CellTrace FarRed-labelled HT-1080/FAP cells (1:1 ratio) were established in 24-well plates, with a total cell number of $5x10^5$ per well. Purified unstimulated T cells ($2.5x10^5$ cells per 24-well) and combinations of αEpCAM–αCD3 +/- αTAA–αCD28 BiMAb at 1 nM final concentration were added to the culture and incubated for 48 h. Frequencies of living/dead tumor cells were assessed using Zombie Aqua viability staining by flow cytometry. MCF-7 and HT-1080/FAP cells were distinguished based on CellTrace Violet or CellTrace FarRed dyes, respectively. **(D)** Tumor spheroids containing MCF-7 + HT-1080/FAP cells in a 1:1 ratio were co-cultured with purified unstimulated T cells and 10 nM fusion proteins of αFAP scFv-hIgG-Fc with ectodomains of tumor necrosis factor superfamily ligands (TNFL) 4-1BBL, CD70, OX40L or TL1A. Frequencies of CD25 and OX40 double positive $CD4^+$ T cells analyzed by flow cytometry. Data represent the mean ± SEM from 3 independent experiments in duplicates **(A, B, D)** or triplicates **(C)**. Statistical analysis *vs*. αTAA-αCD3 groups **(A, B)** or αEpCAM-αCD3 group **(D)** by one-way ANOVA followed by Tukey's multiple comparison test **(A, B)** or Dunnett's follow-up test **(D)** ns, not significant, $^*p < 0.05$, $^{**}p < 0.01$, $^{***}p < 0.001$, $^{****}p < 0.0001$.

REFERENCES

1. Sharma P, Allison JP. The Future of Immune Checkpoint Therapy. *Science* (2015) 348:56–61. doi: 10.1126/science.aaa8172
2. Wilson RAM, Evans TRJ, Fraser AR, Nibbs RJB. Immune Checkpoint Inhibitors: New Strategies to Checkmate Cancer. *Clin Exp Immunol* (2018) 191:133–48. doi: 10.1111/cei.13081
3. Fujiwara Y, Mittra A, Naqash AR. Takebe N. A Review of Mechanisms of Resistance to Immune Checkpoint Inhibitors and Potential Strategies for Therapy. *Cancer Drug Resist* (2020) 3:252–75. doi: 10.20517/cdr.2020.11
4. Kontermann RE, Brinkmann U. Bispecific Antibodies. *Drug Discov Today* (2015) 20:838–47. doi: 10.1016/j.drudis.2015.02.008
5. Spiess C, Zhai Q, Carter PJ. Alternative Molecular Formats and Therapeutic Applications for Bispecific Antibodies. *Mol Immunol* (2015) 67:95–106. doi: 10.1016/j.molimm.2015.01.003
6. Zhukovsky EA, Morse RJ, Maus MV. Bispecific Antibodies and CARs: Generalized Immunotherapeutics Harnessing T Cell Redirection. *Curr Opin Immunol* (2016) 40:24–35. doi: 10.1016/j.coi.2016.02.006
7. Yu S, Li A, Liu Q, Yuan X, Xu H, Jiao D, et al. Recent Advances of Bispecific Antibodies in Solid Tumors. *J Hematol Oncol* (2017) 10:155. doi: 10.1186/s13045-017-0522-z
8. Runcie K, Budman DR, John V, Seetharamu N. Bi-Specific and Tri-Specific Antibodies- the Next Big Thing in Solid Tumor Therapeutics. *Mol Med* (2018) 24:50. doi: 10.1186/s10020-018-0051-4

9. Chen L, Flies DB. Molecular Mechanisms of T Cell Co-Stimulation and Co-Inhibition. *Nat Rev Immunol* (2013) 13:227–42. doi: 10.1038/nri3405
10. Esensten JH, Helou YA, Chopra G, Weiss A, Bluestone JA. CD28 Costimulation: From Mechanism to Therapy. *Immunity* (2016) 44:973–88. doi: 10.1016/j.immuni.2016.04.020
11. Suntharalingam G, Perry MR, Ward S, Brett SJ, Castello-Cortes A, Brunner MD, et al. Cytokine Storm in a Phase 1 Trial of the Anti-CD28 Monoclonal Antibody TGN1412. *N Engl J Med* (2006) 355:1018–28. doi: 10.1056/NEJMoa063842
12. Dubrot J, Milheiro F, Alfaro C, Palazón A, Martinez-Forero I, Perez-Gracia JL, et al. Treatment With Anti-CD137 Mabs Causes Intense Accumulations of Liver T Cells Without Selective Antitumor Immunotherapeutic Effects in This Organ. *Cancer Immunol Immunother* (2010) 59:1223–33. doi: 10.1007/s00262-010-0846-9
13. Melero I, Hirschhorn-Cymerman D, Morales-Kastresana A, Sanmamed MF, Wolchok JD. Agonist Antibodies to TNFR Molecules That Costimulate T and NK Cells. *Clin Cancer Res* (2013) 19:1044–53. doi: 10.1158/1078-0432.CCR-12-2065
14. Müller D, Frey K, Kontermann RE. A Novel Antibody-4-1BBL Fusion Protein for Targeted Costimulation in Cancer Immunotherapy. *J Immunother* (2008) 31:714–22. doi: 10.1097/CJI.0b013e31818353e9
15. Hornig N, Reinhardt K, Kermer V, Kontermann RE, Müller D. Evaluating Combinations of Costimulatory Antibody-Ligand Fusion Proteins for Targeted Cancer Immunotherapy. *Cancer Immunol Immunother* (2013) 62:1369–80. doi: 10.1007/s00262-013-1441-7
16. Fellermeier S, Beha N, Meyer JE, Ring S, Bader S, Kontermann RE, et al. Advancing Targeted Co-Stimulation With Antibody-Fusion Proteins by Introducing TNF Superfamily Members in a Single-Chain Format. *Oncoimmunology* (2016) 5:e1238540. doi: 10.1080/2162402X.2016.1238540
17. Sapski S, Beha N, Kontermann R, Müller D. Tumor-Targeted Costimulation With Antibody-Fusion Proteins Improves Bispecific Antibody-Mediated Immune Response in Presence of Immunosuppressive Factors. *Oncoimmunology* (2017) 6:e1361594. doi: 10.1080/2162402X.2017.1361594
18. Claus C, Ferrara C, Xu W, Sam J, Lang S, Uhlenbrock F, et al. Tumor-Targeted 4-1BB Agonists for Combination With T Cell Bispecific Antibodies as Off-the-Shelf Therapy. *Sci Transl Med* (2019) 11:eaav5989. doi: 10.1126/scitranslmed.aav5989
19. Trüb M, Uhlenbrock F, Claus C, Herzig P, Thelen M, Karanikas V, et al. Fibroblast Activation Protein-Targeted-4-1BB Ligand Agonist Amplifies Effector Functions of Intratumoral T Cells in Human Cancer. *J Immunother Cancer* (2020) 8:e000238. doi: 10.1136/jitc-2019-000238
20. Correnti CE, Laszlo GS, de van der Schueren WJ, Godwin CD, Bandaranayake A, Busch MA, et al. Simultaneous Multiple Interaction T-Cell Engaging (SMITE) Bispecific Antibodies Overcome Bispecific T-Cell Engager (BiTE) Resistance *via* CD28 Co-Stimulation. *Leukemia* (2018) 32:1239–43. doi: 10.1038/s41375-018-0014-3
21. Skokos D, Waite JC, Haber L, Crawford A, Hermann A, Ullman E, et al. A Class of Costimulatory CD28-Bispecific Antibodies That Enhance the Antitumor Activity of CD3-Bispecific Antibodies. *Sci Transl Med* (2020) 12:eaaw7888. doi: 10.1126/scitranslmed.aaw7888
22. Bargou R, Leo E, Zugmaier G, Klinger M, Goebeler M, Knop S, et al. Tumor Regression in Cancer Patients by Very Low Doses of a T Cell-Engaging Antibody. *Science* (2008) 321:974–7. doi: 10.1126/science.1158545
23. Kantarjian H, Stein A, Gökbuget N, Fielding AK, Schuh AC, Ribera JM, et al. Blinatumomab Versus Chemotherapy for Advanced Acute Lymphoblastic Leukemia. *N Engl J Med* (2017) 376:836–47. doi: 10.1056/NEJMoa1609783
24. Goebeler ME. Bargou RC. T Cell-Engaging Therapies - BiTEs and Beyond. *Nat Rev Clin Oncol* (2020) 17:418–34. doi: 10.1038/s41571-020-0347-5
25. Middelburg J, Kemper K, Engelberts P, Labrijn AF, Schuurman J, van Hall T. Overcoming Challenges for CD3-Bispecific Antibody Therapy in Solid Tumors. *Cancers (Basel)* (2021) 13:287. doi: 10.3390/cancers13020287
26. Quitt O, Luo S, Meyer M, Zhe X, Golsaz-Shirazi F, Loffredo-Verde E, et al. T-Cell Engager Antibodies Enable T Cells to Control Hepatitis B Virus Infection and to Target HBsAg-Positive Hepatoma in Mice. *J Hepatol* (2021). doi: 10.1016/j.jhep.2021.06.022 Online ahead of print.
27. Rölle A, Meyer M, Calderazzo S, Jäger D, Momburg F. Distinct HLA-E Peptide Complexes Modify Antibody-Driven Effector Functions of Adaptive NK Cells. *Cell Rep* (2018) 24:1967–1976.e4. doi: 10.1016/j.celrep.2018.07.069
28. Loktev A, Lindner T, Mier W, Debus J, Altmann A, Jäger D, et al. A Tumor-Imaging Method Targeting Cancer-Associated Fibroblasts. *J Nucl Med* (2018) 59:1423–9. doi: 10.2967/jnumed.118.210435
29. Stebbing J, Shah K, Lit LC, Gagliano T, Ditsiou A, Wang T, et al. LMTK3 Confers Chemo-Resistance in Breast Cancer. *Oncogene* (2018) 37:3113–30. doi: 10.1038/s41388-018-0197-0
30. Arosa FA. CD8+CD28- T Cells: Certainties and Uncertainties of a Prevalent Human T-Cell Subset. *Immunol Cell Biol* (2002) 80:1–13. doi: 10.1046/j.1440-1711.2002.01057.x
31. Jeppesen M, Hagel G, Glenthoj A, Vainer B, Ibsen P, Harling H, et al. Short-Term Spheroid Culture of Primary Colorectal Cancer Cells as an *In Vitro* Model for Personalizing Cancer Medicine. *PloS One* (2017) 12:e0183074. doi: 10.1371/journal.pone.0183074
32. Weeber F, Ooft SN, Dijkstra KK, Voest EE. Tumor Organoids as a Pre-Clinical Cancer Model for Drug Discovery. *Cell Chem Biol* (2017) 24:1092–100. doi: 10.1016/j.chembiol.2017.06.012
33. Wu L, Seung E, Xu L, Rao E, Lord DM, Wei RR, et al. Trispecific Antibodies Enhance the Therapeutic Efficacy of Tumor-Directed T Cells Through T Cell Receptor Co-Stimulation. *Nat Cancer* (2020) 1:86–98. doi: 10.1038/s43018-019-0004-z
34. Bacac M, Klein C, Umana P. CEA TCB: A Novel Head-to-Tail 2:1 T Cell Bispecific Antibody for Treatment of CEA-Positive Solid Tumors. *Oncoimmunology* (2016) 5:e1203498. doi: 10.1080/2162402X.2016.1203498
35. Park JE, Lenter MC, Zimmermann RN, Garin-Chesa P, Old LJ, Rettig WJ. Fibroblast Activation Protein, a Dual Specificity Serine Protease Expressed in Reactive Human Tumor Stromal Fibroblasts. *J Biol Chem* (1999) 274:36505–12. doi: 10.1074/jbc.274.51.36505
36. Juillerat-Jeanneret L, Tafelmeyer P, Golshayan D. Fibroblast Activation Protein-α in Fibrogenic Disorders and Cancer: More Than a Prolyl-Specific Peptidase? *Expert Opin Ther Targets* (2017) 21:977–91. doi: 10.1080/14728222.2017.1370455
37. Ross SL, Sherman M, McElroy PL, Lofgren JA, Moody G, Baeuerle PA, et al. Bispecific T Cell Engager (BiTE®) Antibody Constructs Can Mediate Bystander Tumor Cell Killing. *PloS One* (2017) 12:e0183390. doi: 10.1371/journal.pone.0183390
38. Richard AC, Ferdinand JR, Meylan F, Hayes ET, Gabay O, Siegel RM. The TNF-Family Cytokine TL1A: From Lymphocyte Costimulator to Disease Co-Conspirator. *J Leukoc Biol* (2015) 98:333–45. doi: 10.1189/jlb.3RI0315-095R
39. Aiba Y, Nakamura M. The Role of TL1A and DR3 in Autoimmune and Inflammatory Diseases. *Mediators Inflamm* (2013) 2013:258164. doi: 10.1155/2013/258164
40. Meylan F, Richard AC, Siegel RM. TL1A and DR3, a TNF Family Ligand-Receptor Pair That Promotes Lymphocyte Costimulation, Mucosal Hyperplasia, and Autoimmune Inflammation. *Immunol Rev* (2011) 244:188–96. doi: 10.1111/j.1600-065X.2011.01068.x
41. Taraban VY, Slebioda TJ, Willoughby JE, Buchan SL, James S, Sheth B, et al. Sustained TL1A Expression Modulates Effector and Regulatory T-Cell Responses and Drives Intestinal Goblet Cell Hyperplasia. *Mucosal Immunol* (2011) 4:186–96. doi: 10.1038/mi.2010.70
42. Zhai Y, Ni J, Jiang GW, Lu J, Xing L, Lincoln C, et al. VEGI, a Novel Cytokine of the Tumor Necrosis Factor Family, is an Angiogenesis Inhibitor That Suppresses the Growth of Colon Carcinomas *In Vivo*. *FASEB J* (1999) 13:181–9. doi: 10.1096/fasebj.13.1.181
43. van de Ven K, Borst J. Targeting the T-Cell Co-Stimulatory CD27/CD70 Pathway in Cancer Immunotherapy: Rationale and Potential. *Immunotherapy* (2015) 7:655–67. doi: 10.2217/imt.15.32
44. Sanmamed MF, Pastor F, Rodriguez A, Perez-Gracia JL, Rodriguez-Ruiz ME, Jure-Kunkel M, et al. Agonists of Co-Stimulation in Cancer Immunotherapy Directed Against CD137, OX40, GITR, CD27, CD28, and ICOS. *Semin Oncol* (2015) 42:640–55. doi: 10.1053/j.seminoncol.2015.05.014
45. Kobold S, Pantelyushin S, Rataj F, Vom Berg J. Rationale for Combining Bispecific T Cell Activating Antibodies With Checkpoint Blockade for Cancer Therapy. *Front Oncol* (2018) 8:285. doi: 10.3389/fonc.2018.00285
46. Sam J, Colombetti S, Fauti T, Roller A, Biehl M, Fahrni L, et al. Combination of T-Cell Bispecific Antibodies With PD-L1 Checkpoint Inhibition Elicits Superior Anti-Tumor Activity. *Front Oncol* (2020) 10:575737. doi: 10.3389/fonc.2020.575737
47. Koopmans I, Hendriks D, Samplonius DF, van Ginkel RJ, Heskamp S, Wierstra PJ, et al. A Novel Bispecific Antibody for EGFR-Directed Blockade

of the PD-1/PD-L1 Immune Checkpoint. *Oncoimmunology* (2018) 7: e1466016. doi: 10.1080/2162402X.2018.1466016

48. Vesely MD, Kershaw MH, Schreiber RD, Smyth MJ. Natural Innate and Adaptive Immunity to Cancer. *Annu Rev Immunol* (2011) 29:235–71. doi: 10.1146/annurev-immunol-031210-101324
49. Kebenko M, Goebeler ME, Wolf M, Hasenburg A, Seggewiss-Bernhardt R, Ritter B, et al. A Multicenter Phase 1 Study of Solitomab (MT110, AMG 110), a Bispecific EpCAM/CD3 T-Cell Engager (BiTE®) Antibody Construct, in Patients With Refractory Solid Tumors. *Oncoimmunology* (2018) 7:e1450710. doi: 10.1080/2162402X.2018.1450710
50. Haense N, Atmaca A, Pauligk C, Steinmetz K, Marmé F, Haag GM, et al. A Phase I Trial of the Trifunctional Anti Her2 × Anti CD3 Antibody Ertumaxomab in Patients With Advanced Solid Tumors. *BMC Cancer* (2016) 16:420. doi: 10.1186/s12885-016-2449-0
51. Pishvaian M, Morse MA, McDevitt J, Norton JD, Ren S, Robbie GJ, et al. Phase 1 Dose Escalation Study of MEDI-565, a Bispecific T-Cell Engager That Targets Human Carcinoembryonic Antigen, in Patients With Advanced Gastrointestinal Adenocarcinomas. *Clin Colorectal Cancer* (2016) 15:345–51. doi: 10.1016/j.clcc.2016.07.009
52. Hummel HD, Kufer P, Grüllich C, Seggewiss-Bernhardt R, Deschler-Baier B, Chatterjee M, et al. Pasotuxizumab, a BiTE® Immune Therapy for Castration-Resistant Prostate CancerDose-Escalation Study Findings. *Immunotherapy* (2021) 13:125–41. doi: 10.2217/imt-2020-0256

Conflict of Interest: The authors declare that the research was conducted in the absence or any commercial of financial relationships that could be construed as a potential conflict of interest.

Publisher's Note: All claims expressed in this article are solely those of the authors and do not necessarily represent those of their affiliated organizations, or those of the publisher, the editors and the reviewers. Any product that may be evaluated in this article, or claim that may be made by its manufacturer, is not guaranteed or endorsed by the publisher.

frontiers in Immunology

ORIGINAL RESEARCH
published: 03 January 2022
doi: 10.3389/fimmu.2021.741634

Multi-Omics Analysis for Transcriptional Regulation of Immune-Related Targets Using Epigenetic Data: A New Research Direction

Chenshen Huang[1†], Na Zhang[2†], Hao Xiong[2†], Ning Wang[2†], Zhizhong Chen[3], Zhizhan Ni[1], Xiaohong Liu[2], Boxu Lin[2], Bujun Ge[1], Bing Du[2*] and Qi Huang[1*]*

[1] Department of General Surgery, Tongji Hospital, School of Medicine, Tongji University, Shanghai, China, [2] Shanghai Key Laboratory of Regulatory Biology, Institute of Biomedical Sciences and School of Life Sciences, East China Normal University, Shanghai, China, [3] Shengli Clinical Medical College of Fujian Medical University, Fujian Provincial Hospital, Fujian, China

Background: Currently, a comprehensive method for exploration of transcriptional regulation has not been well established. We explored a novel pipeline to analyze transcriptional regulation using co-analysis of RNA sequencing (RNA-seq), assay for transposase-accessible chromatin using sequencing (ATAC-seq), and chromatin immunoprecipitation with high-throughput sequencing (ChIP-seq).

Methods: The G protein-coupled receptors (GPCRs) possibly associated with macrophages were further filtered using a reduced-Cox regression model. ATAC-seq profiles were used to map the chromatin accessibility of the GPRC5B promoter region. Pearson analysis was performed to identify the transcription factor (TF) whose expression was correlated with open chromatin regions of GPRC5B promoter. ChIP-seq profiles were obtained to confirm the physical binding of GATA4 and its predicted binding regions. For verification, quantitative polymerase chain reaction (qPCR) and multidimensional database validations were performed.

Results: The reduced-Cox regression model revealed the prognostic value of GPRC5B. A novel pipeline for TF exploration was proposed. With our novel pipeline, we first identified chr16:19884686-19885185 as a reproducible open chromatin region in the GPRC5B promoter. Thereafter, we confirmed the correlation between GATA4 expression and the accessibility of this region, confirmed its physical binding, and proved *in vitro* how its overexpression could regulate GPRC5B. GPRC5B was significantly downregulated in colon adenocarcinoma (COAD) as seen in 28 patient samples. The correlation between GPRC5B and macrophages in COAD was validated using multiple databases.

OPEN ACCESS

Edited by:
Douglas Clayton Palmer, AstraZeneca, United States

Reviewed by:
Andrea Tangherloni, University of Bergamo, Italy
Hao Zhang, Xiangya Hospital Central South University, China
Yunfeng Wang, Université Paris-Saclay, France

****Correspondence:***
Bujun Ge
gebujun@126.com
Bing Du
bdu@bio.ecnu.edu.cn
Qi Huang
hqhq0078@163.com

†These authors have contributed equally to this work

Specialty section:
This article was submitted to Cancer Immunity and Immunotherapy, a section of the journal Frontiers in Immunology

Received: *15 July 2021*
Accepted: *10 December 2021*
Published: *03 January 2022*

Citation:
Huang C, Zhang N, Xiong H, Wang N, Chen Z, Ni Z, Liu X, Lin B, Ge B, Du B and Huang Q (2022) Multi-Omics Analysis for Transcriptional Regulation of Immune-Related Targets Using Epigenetic Data: A New Research Direction. Front. Immunol. 12:741634. doi: 10.3389/fimmu.2021.741634

Conclusion: GPRC5B, correlated with macrophages, was a key GPCR affecting COAD prognosis. Further, with our novel pipeline, TF GATA4 was identified as a direct upstream of GPRC5B. This study proposed a novel pipeline for TF exploration and provided a theoretical basis for COAD therapy.

Keywords: chromatin accessibility, ATAC-seq, ChIP-seq, multi-omics analysis, transcription factor

HIGHLIGHTS

- This study provides a novel pipeline to explore transcription factors based on multi-omics data, which is described adequately enough to be repeated and taken further.
- With our pipline, GATA4 was identified to be the direct upstream transcription factor regulating GPRC5B.
- GPRC5B may affect COAD patient prognosis, possibly by interacting with macrophages

INTRODUCTION

Colon cancer, a type of malignant tumor, is the third leading cause of cancer deaths worldwide (1–3). Colon adenocarcinoma (COAD) is the most common pathological subtype of colon cancer. Currently, the prognosis of advanced COAD patients remains poor. Accordingly, a better understanding of the molecular mechanisms involved in COAD is warranted.

In recent years, increasing evidence has revealed that immune infiltration might be an essential factor in COAD patient prognosis (4). Tumor-infiltrating macrophages of mixed origin are an important component of immune infiltration (5). Currently, several studies have indicated that tumor-infiltrating macrophages could impact COAD progression (6, 7). However, an improved understanding of the underlying mechanisms of action is still needed, and a search for potential macrophage-targeted therapeutic options is also required.

G protein-coupled receptors (GPCRs), a group of cell surface signaling proteins, represent the most prominent superfamily of pharmacological targets (8, 9). It has been confirmed that various GPCRs are involved in the progression of tumors (10), including colon cancer (11). Lysophosphatidic acid receptors (12), protease-activated receptor 1 (13), prostaglandin E2 receptors (14), and endothelin receptors (15) have all been identified as key players in colon cancer. Nevertheless, the functions of many GPCRs still remain unclear. Thus, an improved understanding of the involvement of GPCRs in colon cancer formation and progression might contribute to the development of a novel generation of antitumor therapeutics. Additionally, to date, a large number of GPCRs have been reported to influence tumor development through macrophages (16, 17). For example, our previous study demonstrated that LGR4 could maintain protumoral macrophages and thus play a vital role in tumor progression (18). Considering the information presented above, we inferred that macrophage-associated GPCRs could be a potential target for COAD therapy, and we employed bioinformatic methods for a more comprehensive investigation.

Currently, to explore the regulation of a target gene, various algorithms would be applied to transcriptome data for pathway quantization, followed by correlation analysis. If the target gene was statistically correlated with a quantized pathway, its involvement in the regulation of this pathway would be proposed. Besides analysis of transcriptome data from RNA sequencing (RNA-seq) profiles, our study further acquired epigenetic data to explore the target gene's regulation. Assay for transposase-accessible chromatin using sequencing (ATAC-seq) used Tn5 transposase to determine the nucleosome position and map the open chromatin regions (19, 20). The accessible chromatin sites in the promoter regions reflect the potential binding of transcription factors (TFs). Genes with chromatin accessibility in the promoters were more likely regulated by TFs. ATAC-seq profiles could detect the open chromatin regions of target genes and indicate their regulatory mechanism. Through co-analysis of ATAC-seq and transcriptome data, we could identify potential TFs, whose expressions were significantly correlated with the open promoter regions of the target gene. Next, chromatin immunoprecipitation (ChIP)-seq profiles were obtained to confirm the physical binding of potential TFs and the predicted binding regions.

Here, multi-omics bioinformatics was employed to discover the macrophage-correlated GPCRs that might play a key role in COAD. With transcriptome data from RNA-seq profiles, we explored the GPCRs that might be associated with tumor infiltrating macrophages. GPRC5B was eventually selected based on its clinical value. Moreover, epigenetic data from ATAC-seq profiles were also obtained to explore regulation mechanisms. The above-mentioned results were verified through quantitative polymerase chain reaction (qPCR), chromatin immunoprecipitation with high-throughput sequencing (ChIP-seq), and multidimensional databases.

Abbreviations: TF, Transcription factor; qPCR, Quantitative polymerase chain reaction; COAD, Colon adenocarcinoma; GPCR, G protein-coupled receptor; ATAC-seq, Assay for transposase-accessible chromatin using sequencing; ChIP-seq, Chromatin immunoprecipitation sequencing; FPKM, Fragments per kilobase per million mapped reads; ssGSEA, Single Sample Gene Set Enrichment Analysis; TSS, Transcription start site; GEO, Gene Expression Omnibus; TCGA, The Cancer Genome Atlas; TPM, Transcripts per million.

MATERIALS AND METHODS

Ethics

Our study was approved by Tongji Hospital, Shanghai, China (reference number 2018-LCYJ-005). Written consent was obtained from all participants/patients before the study.

Data Collection

The ATAC-seq profiles of 41 COAD samples were obtained from the NCI Genomic Data Commons (https://gdc.cancer.gov/about-data/publications/ATACseq-AWG). We acquired the Fragments Per Kilobase per Million mapped reads (FPKM) and htseq-count profiles of 514 samples from TCGA database (https://tcga-data.nci.nih.gov/), including 473 COAD samples and 41 solid normal tissue samples. Clinical demographic information of 426 COAD patients was also retrieved. The baseline information of all COAD patients is provided in **Supplemental Table S1**.

Infiltrating Immune Cells

The normalized gene expression matrix was obtained from the FPKM profiles. Further, based on the signature markers provided by Charoentong et al. (21), the Single Sample Gene Set Enrichment Analysis (ssGSEA) (22, 23) was applied to estimate the tumor-infiltrating immune cells in COAD. The signature markers are all listed in **Supplemental Table S2**. We applied the Wilcoxon rank-test to compare the difference in the abundances of immune cells between COAD samples and normal solid tissue samples.

Integrative Analysis of GPCRs and Tumor-Infiltrating Macrophage

The list of GPCRs was downloaded from the GPCR NaVa database (http://nava.liacs.nl) (24) and gene expression of recorded GPCRs were retrieved (**Supplemental Table S3**). To explore the GPCRs potentially correlated with tumor-infiltrating macrophages, we performed a Spearman correlation analysis. The filtered GPCRs were further included in the Lasso regression model and the reduced-Cox regression model. Eventually, based on the reduced-Cox model, a nomogram was constructed to predict COAD patient prognosis. Calibration curves were displayed to validate the accuracy and discrimination of the nomogram.

A Novel Pipeline for TF Exploration

Publicly available datasets were analyzed in this study, including 41 paired ATAC-seq and RNA-seq profiles of the same COAD patients. The sources of these profiles have been described in data collection section. The upstream analysis of ATAC-seq data was completed following the pipeline proposed by M. Ryan Corces et al. And a total of 122872 reproducible peaks were observed in 41 ATAC-seq profiles of COAD patients. In this study, we directly downloaded these peaks from the supplemental data file "cancer type-specific count matrices in normalized counts" (https://gdc.cancer.gov/about-data/publications/ATACseq-AWG).

With the data above, we proposed a novel pipeline to explore TF regulation based on multi-omics data. Our pipeline included: 1) Peak annotation. We used the R package "ChIPseeker" to annotate peaks (*annotatePeak* function with tssRegion from -2000 to 2000, TxDb equal to "TxDb.Hsapiens.UCSC.hg38.knownGene", and annoDb equal to "org.Hs.eg.db"). We obtained the 45377 peaks which were annotated as "Promoter (<=1kb)" or "Promoter (1-2kb)". 2) Getting the peaks located in the promoter region of target gene. We first used the R package "GenomicFeatures" to check the gene location of the target gene GPRC5B (*genes* function with x equal to "TxDb.Hsapiens.UCSC.hg38.knownGene"). Then, we search the above 45377 peaks, and we found the target peak (chr16:19884686-19885185) which had an overlap with the gene location of GPRC5B (chr16: 19856691-19886167). 3) Getting the mRNA expression of TFs. We downloaded the list of TFs from the Cistrome database (http://cistrome.org/). Based on the list, we can get the TF mRNA expression from RNA-seq profiles. 4) We used the R package "stats" (*cor.test* function) to perform the Pearson correlation analysis between the TF mRNA expression and the ATAC-seq peak accessibility of the target peak (chr16:19884686-19885185). The correlation threshold was set as an absolute value of $r > 0.2$, $p < 0.01$. In this study, the TF GATA4 expression was found to be most highly correlated with the target peak (chr16:19884686-19885185). 5) We used the Cistrome to browse the GATA4 ChIP-seq data (*Cistrome Data Browser* function with species equal to "Homo sapiens", and factors equal to "GATA4"), and we can check the overlap between the target peak (chr16:19884686-19885185) and the peaks of GATA4 ChIP-seq data. **Figure 1** presents an overview of the pipeline of our study.

Co-Analysis of ATAC-Seq and RNA-Seq Profiles

Chromatin accessibility analysis was performed based on ATAC-seq profiles. Peak regions over chromosomes were visualized through the R package karyoploteR (25). We also applied ChIPseeker (26) to map the tagMatrix, indicating the locations of peaks around the transcription start site (TSS) regions. The peaks near the TSS regions were annotated by TxDb. Hsapiens. UCSC. Hg38. knownGene. For visualization, we used a pie plot to better show the relationship between peak locations and promoter regions.

To explore the TF directly upstream of GPRC5B, the Pearson correlation analysis was performed for TF mRNA expression and chromatin accessibility of the GPRC5B promoter region. The potential TFs were further filtered by ChIP-seq profiles of colon cancer cells, which were obtained from the Cistrome database (http://cistrome.org/) (27, 28).

Multi-Database Validation

To minimize the bias of using a single database, we validated our results using multiple databases, including: Gene Expression Omnibus (GEO, ID: GSE85001, https://www.ncbi.nlm.nih.gov/geo/), Timer 2.0 database (http://timer.comp-genomics.org/) (29, 30), GEPIA database (http://gepia.cancer-pku.cn/) (31), Human Protein Atlas database (https://www.proteinatlas.org/) (32, 33), and LinkedOmics database (https://linkedomics.org/) (34). We also used four different algorithms (EPIC (35), XCELL (36), TIMER (37), and MCP-counter (38) algorithms) to confirm the significant correlation between tumor-infiltrating macrophages and GPRC5B. The EPIC and TIMER algorithms are partial deconvolution algorithms, while the XCELL and MCP-counter algorithms are scoring methods based on a set of marker genes (39).

qPCR Validation

We additionally validated the mRNA expression level of GPRC5B using fresh frozen tissue samples. COAD samples and paired normal

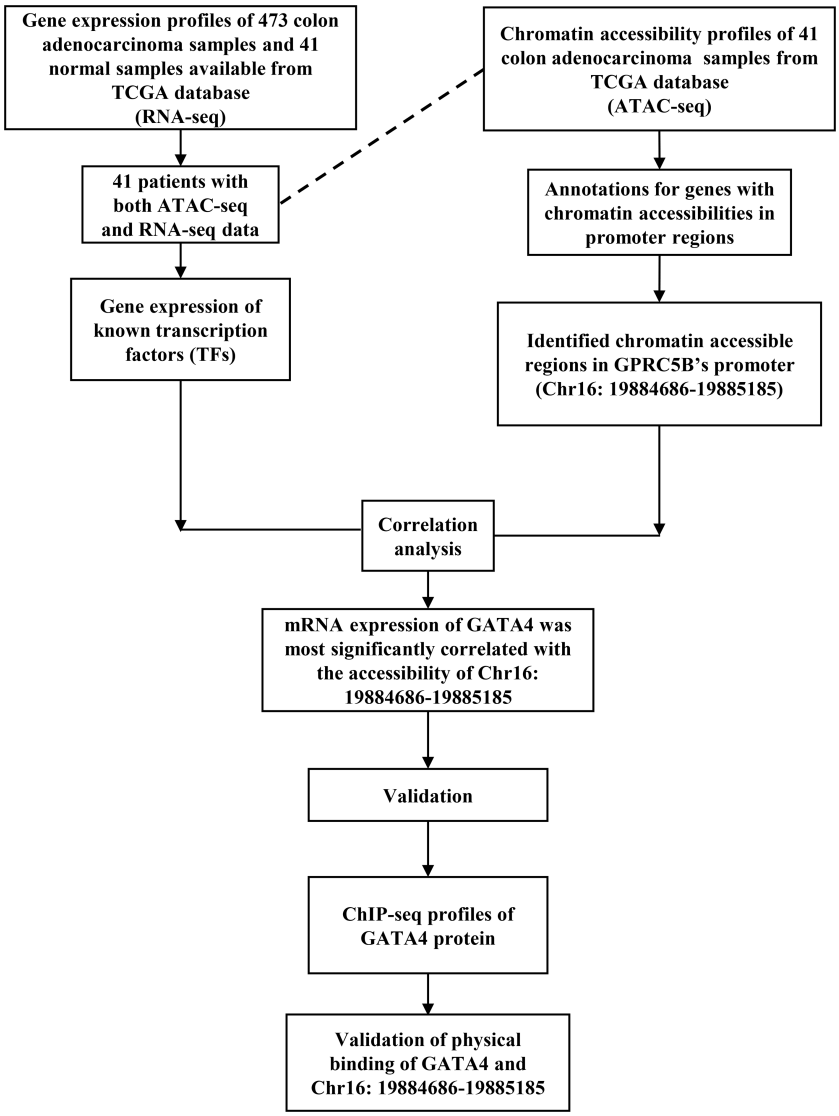

FIGURE 1 | An overview of the novel pipeline of our study.

tissues were obtained from 28 patients from Tongji Hospital, Shanghai, China. TRIzol reagent (Magen, R4801-01) was used for RNA extraction following the manufacturer's instructions. After reverse transcription, qPCR was performed using cDNA, SyberGreen (Yeasen, 11200ES08) and human GPRC5B primers (Forward: ACAATGCAGCTCTCCGAACAG, Reverse: TGATACACGTTGCTTCTAAACGG). The amplification program was set as follows: 95°C for 210 sec; 40 cycles at 95°C for 210 sec, 58°C for 30 sec, 63°C for 20 sec; melting curve from 58°C to 95°C. Every sample in the qPCR experiment was repeated in triplicate. Additionally, human GAPDH was selected as the internal control (Forward: GGAGCCAAAAGGGTCATCATCTC, Reverse: TGATGGCATGGACTGTGGTCATG). A paired *t*-test was applied to screen the significant differences.

Statistical Analysis

Statistical significance was set at $p < 0.05$. The correlation threshold was set as an absolute value of $r > 0.2$, $p < 0.01$ in Pearson or Spearman analysis. Variable normality was checked using Shapiro-Wilk normality test. For nonnormally distributed variables, the Wilcoxon rank-test was used for two independent group comparisons, while the Student's t-test was used to compare normally distributed variables. Paired data which were normally distributed were analyzed by paired t-test. In Kaplan-Meier survival analysis, to prevent the bias caused by non-tumor-related death, we obtained results only from patients who had a follow-up time of more than 90 days. The optimal cutoffs for Kaplan-Meier survival analysis were determined by R package survminer (Version 0.4.9; https://CRAN.R-project.org/

package=survminer). The differentially expressed genes were identified by R package edgeR (Version 3.28.1), and the statistical significance was set at adjusted $p < 0.05$. R (version 3.5.1; www.r-project.org) was the main analysis software.

RESULTS

Quantitation of Macrophages in COAD

We estimated the scaled proportion of tumor-infiltrating immune cells using the ssGSEA method to render the immune cells of each COAD patient comparable (**Figure 2A**). To make the results more reproducible and reliable, the whole ssGSEA process followed the signature markers from Charoentong et al. The detailed macrophage subsets, such as M0, M1, and M2, would be further analyzed in the final multi-database validation part. According to the violin plot in **Figure 2B**, total macrophage expression was significantly decreased in COAD samples. Kaplan-Meier plot of 5-year survival indicated that the COAD patients with higher macrophage infiltration displayed poorer prognosis ($p < 0.05$, **Figures 2C, D**).

Identifying GPCRs Significantly Correlated With Macrophages in COAD

To explore the potentially relevant GPCRs, we first filtered the recorded GPCRs by Spearman correlation analysis. The list of known GPCRs was obtained from the GPCR NaVa database, and GPCR expressions were retrieved from the RNA-seq profiles. Eventually, correlation analysis between GPCRs and macrophage expression was performed, identifying 190 GPCRs for further analysis (**Supplemental Table S4**).

Identification of the Potential Prognostic Biomarker GPRC5B

Considering that macrophages might influence COAD patient prognosis in a GPCR-related way, we aimed to identify a group of GPCRs correlated with macrophages and presented as prognostic predictors. Thus, all GPCRs obtained in the aforementioned results were further processed using the Cox regression model. We utilized LASSO regression to prevent overfitting (**Figure 3A**). According to the LASSO regression results, CRHR1 and GPRC5B were regarded as eligible and were included into the final reduced-Cox regression model

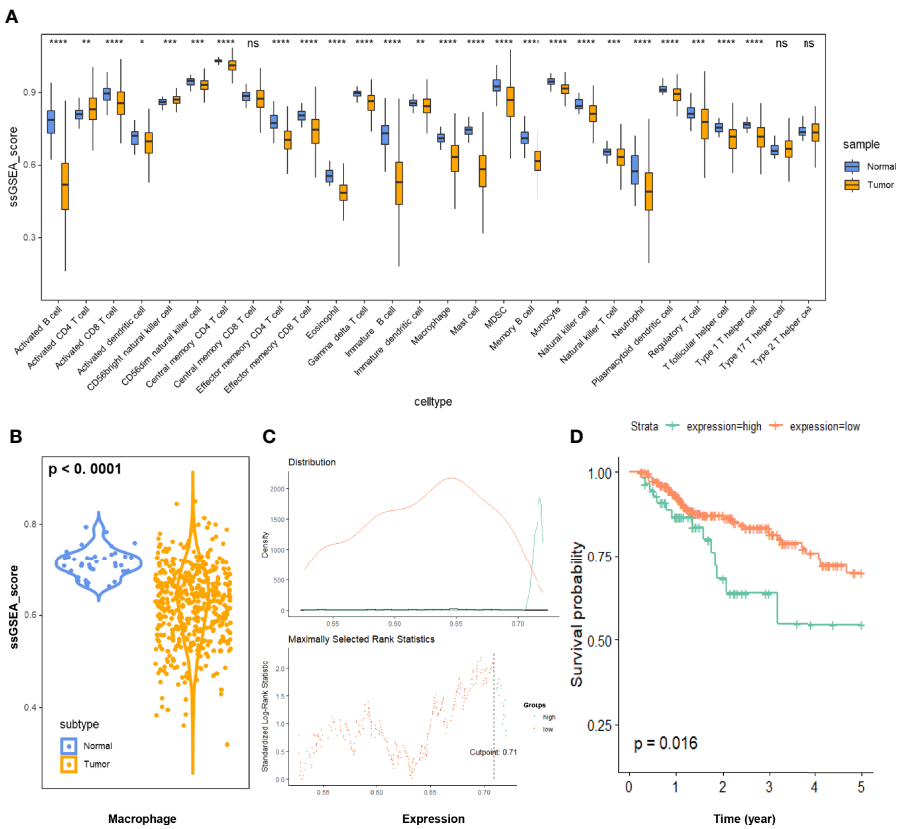

FIGURE 2 | **(A)** Immune infiltration of 28 immune cell subtypes was quantitated *via* the ssGSEA method in 473 COAD samples and 41 normal tissue samples. **(B)** The relative macrophage infiltration was significantly downregulated in COAD tissues ($p < 0.0001$). **(C)** Illustration of the optimal cutoff point identification for survival analysis in **(D)**. The cutoff point with the maximum standardized Log-rank statistical value was regarded as the optimal cutoff point. **(D)** Kaplan-Meier plot of 5-year survival of COAD patients with high vs. low ssGSEA scores of macrophage infiltration. The COAD patients with higher macrophage infiltration displayed poorer prognosis ($p < 0.05$). COAD, colon adenocarcinoma; ssGSEA, single sample gene set enrichment analysis. * $p \leq 0.05$; ** $p < 0.01$; *** $p < 0.001$; **** $p < 0.0001$; ns, not significant.

(C-index = 0.59, p < 0.05, **Figure 3B**). The reduced-Cox regression model indicated that CRHR1 (p = 0.003) and GPRC5B (p = 0.016) might evaluate the prognosis of COAD effectively. Furthermore, a nomogram was also constructed (**Figure 3C**), and the calibration curves indicated acceptable accuracy (**Figures 3D, E**).

Although both CRHR1 and GPRC5B might be important prognostic factors in COAD, we found that GPRC5B was more highly correlated with tumor-infiltrating macrophages [r = 0.49 (Spearman), p < 0.05, **Figures 4A, B**]. Further, as shown in **Figure 4C**, CRHR1 was only detected in part of the RNA-seq profiles, while GPRC5B was widely expressed in COAD patients. Collectively, we identified GPRC5B as a potential macrophage-related biomarker in COAD patients. More specifically, GPRC5B was a prognostic risk factor in COAD (**Figures 4D, E**).

Verification of GPRC5B Expression in COAD *via* qPCR

First, we applied the R package EdgeR (40) to the htseq-count profiles, identifying GPRC5B as a differentially expressed gene in COAD (p < 0.05, **Figure 4C**). To minimize the bias caused by bioinformatics, we also obtained clinical samples from Shanghai Tongji Hospital and

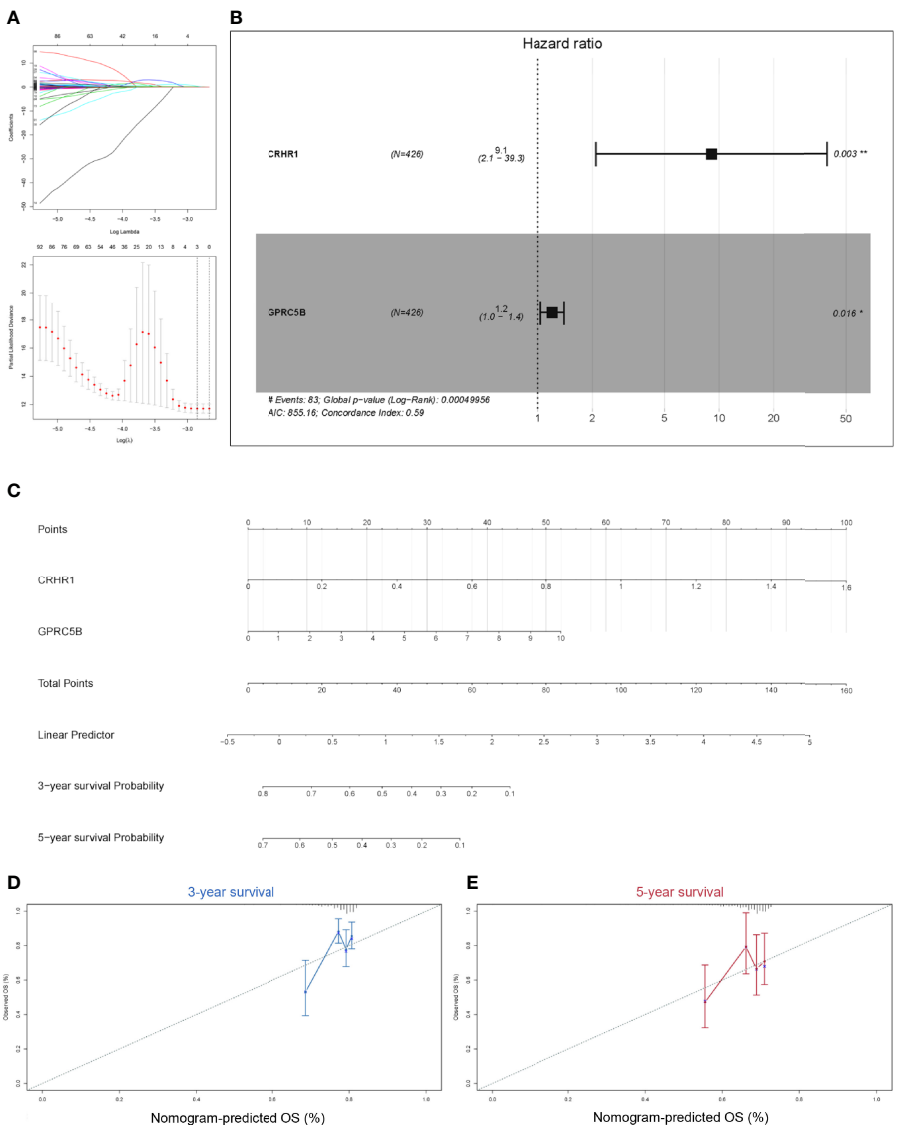

FIGURE 3 | **(A)** To prevent the bias caused by overfitting, LASSO regression was applied. **(B)** Based on the LASSO regression results, the reduced multi-Cox regression model was constructed. CRHR1 (p = 0.003) and GPRC5B (p = 0.016) were shown to be potentially correlated with COAD prognosis. **(C)** A nomogram based on the reduced-Cox model in **(B)** was constructed (p = 0.0005, AIC = 855.16, C-index = 0.6). **(D, E)** Calibration curves of 3-year survival **(D)** and 5-year survival **(E)** validated the acceptable accuracy of the model. LASSO, least absolute shrinkage and selection operator; CRHR1, corticotropin releasing hormone receptor 1; GPRC5B, G protein-coupled receptor class C group 5 member B; COAD, colon adenocarcinoma.

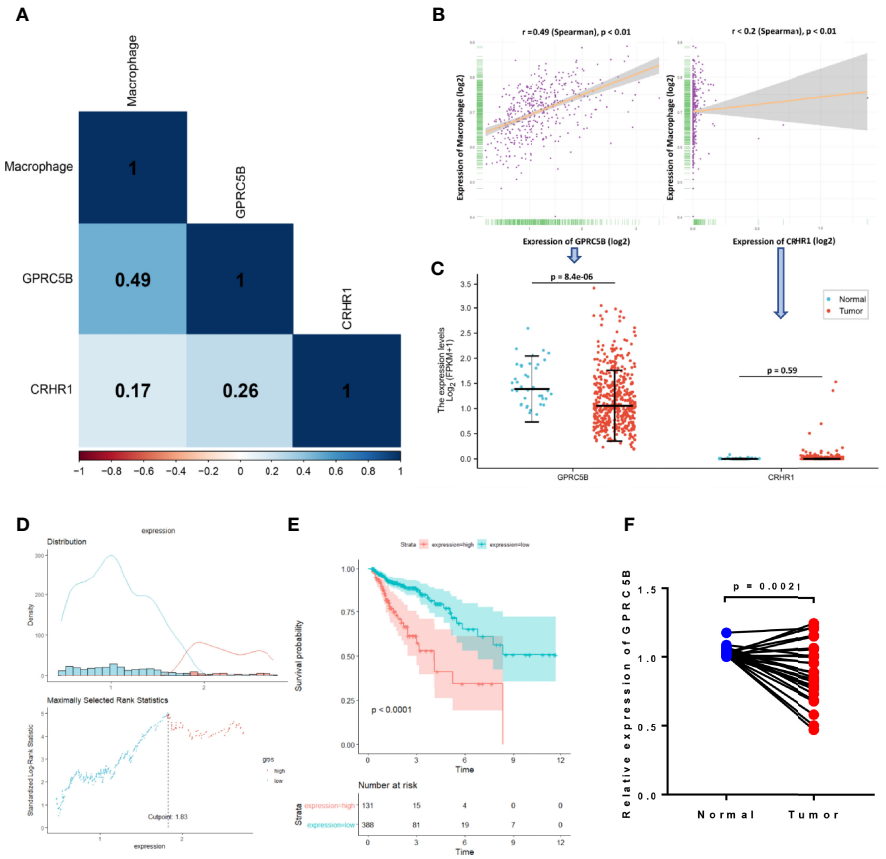

FIGURE 4 | **(A)** Correlation heatmap of macrophages and CRHR1 and GPRC5B expression. **(B)** GPRC5B was significantly correlated with macrophages (r = 0.49, Spearman, p < 0.01). CRHR1 was statistically, but weakly, correlated with macrophages (r < 0.2, Spearman, p < 0.01). **(C)** GPRC5B was a differentially expressed gene in COAD samples (p = 8.4e-06), whereas CRHR1 was only detected in a small number of samples. **(D)** An illustration of the optimal cutoff point identification for survival analysis in **(E)**. **(E)** GPRC5B was a potential prognostic risk factor in COAD patients (p < 0.0001). **(F)** For qPCR validation, clinical samples of 28 COAD tissues and paired normal tissues were acquired from Tongji Hospital, Shanghai, China. GPRC5B was significantly downregulated in COAD tissues (p = 0.0021). CRHR1, corticotropin releasing hormone receptor 1; GPRC5B, G protein-coupled receptor class C group 5 member B; COAD, colon adenocarcinoma.

performed qPCR on COAD tissues and the paired normal tissues from 28 patients. The qPCR result was consistent with our bioinformatic findings, indicating that GPRC5B was significantly downregulated in COAD tissues (**Figure 4F**).

Novel Pipeline Identified GATA4 as a Direct TF for GPRC5B

To further explore the regulation of GPRC5B, we combined ATAC-seq and RNA-seq profiles for co-analysis. It is well-known that TFs regulate genes by binding to the open regions around the promoter. Thus, we acquired the chromatin accessibility landscape of COAD patients from 41 ATAC-seq profiles. **Figure 5** showed that accessibilities were widely presented across the genome. Most open chromatin regions located around TSS regions (**Figures 6A, B**). For visualization, the pie plot indicated that the open chromatin regions were primarily located in the promoter regions (41%, **Figure 6C**). Across samples, we identified chr16:19884686-19885185 as the reproducible open chromatin region in the GPRC5B promoter.

Thereafter, according to the TF list from CISTROME database, we retrieved a TF expression matrix from the FPKM profiles. Correlation analysis was applied to TF expression and the identified accessible promoter regions (chr16:19884686-19885185) (**Supplemental Table S5**). GATA4 expression was found to be most highly correlated with the GPRC5B open promoter regions (p < 0.01), indicating that the TF GATA4 might regulate GPRC5B.

For validation, we then acquired the GATA4 ChIP-seq data from CISTROME. **Figure 6D** shows that the GATA4 protein specifically bonded to the identified promoter regions (Blue area, chr16:19884686-19885185) in colon cancer cells.

After confirming the physical combination between GATA4 and the GPRC5B promoter, we downloaded the RNA-seq profiles of GATA4-overexpressed cells from GEO (GSE85001). GPRC5B was identified as a differentially expressed gene and found to be upregulated in the treatment group (**Figure 6E**).

Collectively, the results showed that the TF GATA4 could bind to the GPRC5B promoter regions, regulating GPRC5B

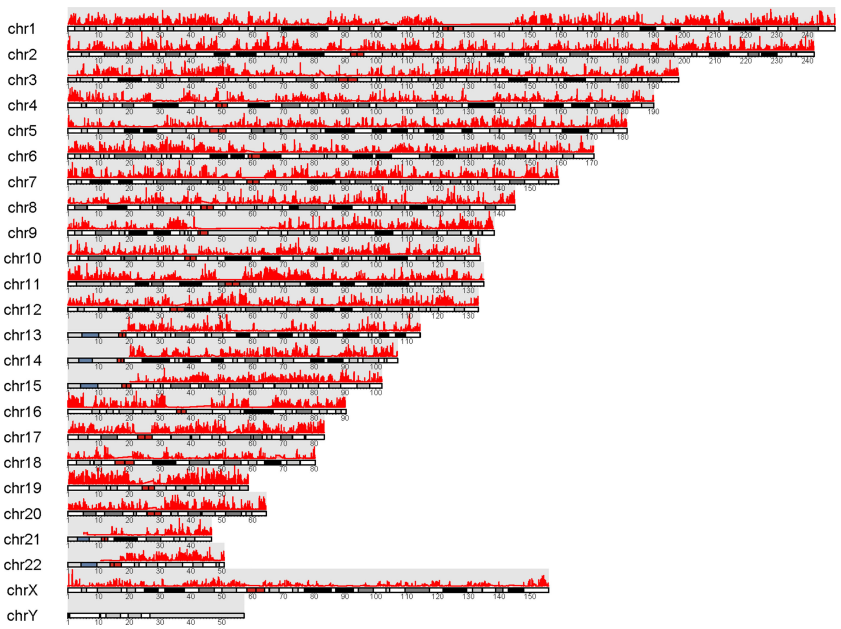

FIGURE 5 | Visualization of peaks (marked in red) over chromosomes. Chromatin accessibilities were widely present over the whole genome.

expression. Detailed steps of the novel pipeline above are visualized in **Figure 7**.

Multiple Database Validation

To prevent bias due to the use of a single database, multiple databases were used for validation. We confirmed that GPRC5B was significantly correlated with tumor-infiltrating macrophages using four algorithms (EPIC, XCELL, TIMER, and MCP-counter, **Figure 8A**). To be more exact, based on the CIBERSORT algorithm, we found that GPRC5B was more highly correlated with M2 macrophages ($r = 0.395$, $p < 0.01$, **Figure 8B**). Similar results were obtained from the GEPIA database (**Figure 8C**), indicating that GPRC5B was correlated with the surface marker CD163 ($r = 0.51$, $p < 0.01$) and MRC1 ($r = 0.54$, $p < 0.01$) of M2 macrophages.

Furthermore, according to the LinkedOmics database, there was a significant increase in GPRC5B expression with advancing T stage (**Figure 8D**). Patients with high GPRC5B expression tended to have poorer prognosis (**Figure 8E**). The Human Protein ATLAS database also confirmed the prognostic value of GPRC5B (**Figure 8F**). Moreover, according to Timer 2.0 database, GPRC5B was identified as a differentially expressed gene in various tumor types, including COAD (**Figure 8G**).

DISCUSSION

COAD is one of the most fatal malignant tumor types worldwide. In recent years, an increasing number of studies have indicated that tumor-infiltrating immune cells might play an important role in cancer development and progression (41–43). However, further study of the underlying mechanisms is still warranted. Conversely, although various GPCRs have been proven to be involved in tumor progression, the functions of many GPCRs remain unclear. As cell surface proteins, GPCRs could regulate a wide range of physiological processes and have always been important targets for drug development. Thus, we discovered that macrophage-associated GPCRs showed prognostic value in COAD. Our study aimed to explore potential pharmacological targets for COAD.

In this study, we found that GPRC5B was a key GPCR affecting COAD patient prognosis and could be a novel target of antitumor therapeutics. Also, considering the potential value of GPRC5B, we decided to further explore the regulation of GPRC5B through integrated bioinformatics. Combining RNA-seq and ATAC-seq profiles together, we identified GATA4 as a direct upstream TF of GPRC5B. The results above were verified through qPCR, ChIP, cell experiments, and multidimensional database validations.

GPRC5B belongs to type 3 GPCR family, characterized by a signature seven-transmembrane-domain motif. First identified in 2000 by Hans Brauner-Osborne and Povl Krogsgaard-Larsen (44), GPRC5B is currently an orphan heterotrimeric GPCR. It has been reported to modulate insulin secretion, and it might be associated with type 2 diabetes (45). Additionally, Carvalho et al. revealed that GPRC5B might regulate the membrane availability of the prostacyclin receptor (46). Furthermore, some studies indicated that GPRC5B might be involved in the regulation of obesity-associated inflammatory response and macrophage infiltration (47, 48). Some studies have indicated the role of GPRC5B in cancer, while its specific molecular mechanisms remain largely unknown (49–51). Our findings have supported the clinical value of GPRC5B in patients with COAD.

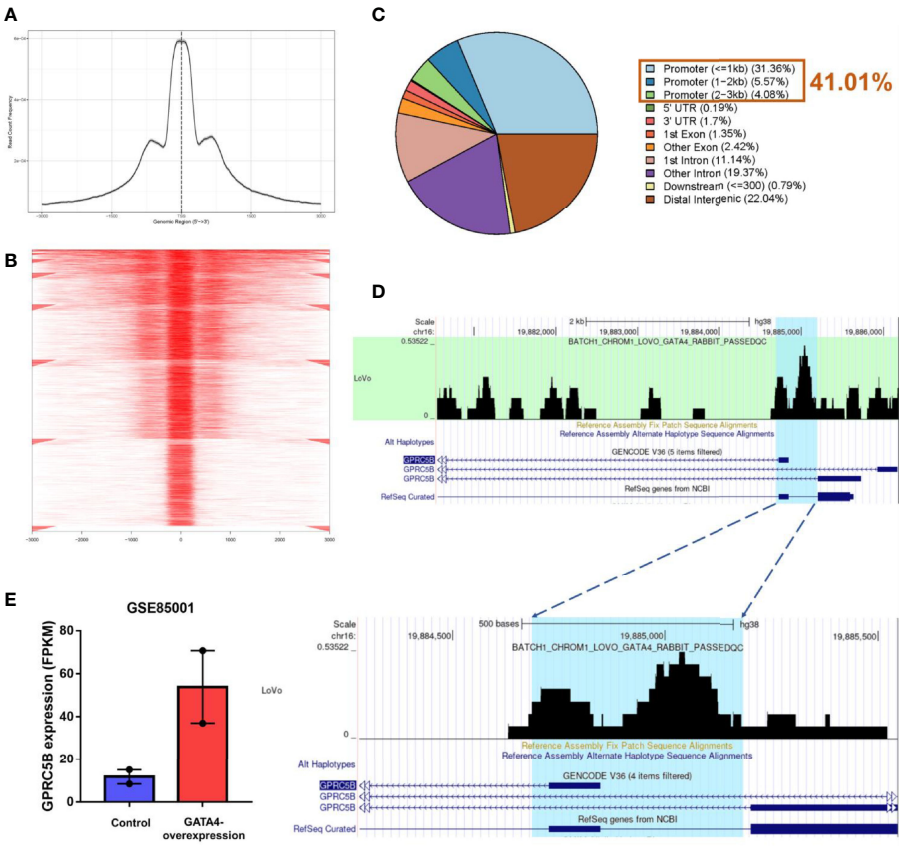

FIGURE 6 | **(A)** Visualization of read count frequency of peaks revealed that they were primarily located around the TSS. **(B)** Peaks are mapped to the TSS regions and further aligned in a tagMatrix, indicating that the majority of chromatin accessibilities were near the TSS. **(C)** Pie plot reveals that most of the open chromatin regions were located in promoters. **(D)** GATA4 ChIP-seq data show the strong overlap between the GATA4 protein binding regions and the predicted regions (highlighted in blue). GATA4 could physically bind to the GPRC5B promoter at chr16: 19884686-19885185. **(E)** According to the GEO database (GSE85001), GPRC5B was significantly upregulated in the GATA4-overexpression group. TSS, transcription start site; ChIP-seq, chromatin immunoprecipitation sequencing; GPRC5B, G protein-coupled receptor class C group 5 member B; GEO, Gene Expression Omnibus.

We identified GPRC5B as a differentially expressed gene in COAD through RNA-seq and qPCR of clinical samples. GPRC5B was significantly downregulated in COAD patients, while its expression would increase with the increase in tumor stages. Considering that GPRC5B was known as a cell surface protein, its expression pattern would make it an ideal pharmacological target. Next, according to the integrated analysis of GPRC5B and tumor-infiltrating immune cells, we also showed that GPRC5B was significantly associated with macrophages. As this correlation was primarily based on statistical methods, and the macrophages were quantized through the ssGSEA algorithm, we acquired multiple algorithms for validation. The classical algorithms, including EPIC, XCELL, TIMER, MCP-counter, and CIBERSORT, were all employed in this study to validate the result of ssGSEA algorithm. With the knowledge that macrophages are important in COAD development and progression, we hypothesized that the interactions between GPRC5B and tumor-infiltrating macrophages, potentially type M2, might be important in COAD and further affect the prognosis of patients with COAD. Based on the results above, we found that GPRC5B is a potential therapeutic target for COAD.

Moreover, a novel pipeline of multi-omics analysis was proposed in this study. Here, we applied this novel pipeline to explore the regulation of GPRC5B, identifying GATA4 as its direct upstream TF. The detailed workflow is displayed in **Figure 1**. In recent years, there have been various studies, which followed the classic pipeline to solve similar questions. However, most of these studies could only prove the correlation between the target genes and the algorithm-quantized pathways, primarily based on transcription data and Pearson/Spearman correlation analysis. Although multi-omics databases were used for validation, it was still hard to further explore the underlying mechanism. For example, Pearson/Spearman analysis could only tell the correlation degree based on statistics, instead of biological significance. Also, there were currently plenty of quantization algorithms, transferring the mRNA expression matrix into immune cell fractions, microenvironment scores, pathway expressions, and other key parameters. There was no doubt that these algorithms were effective and convincing. However, if we

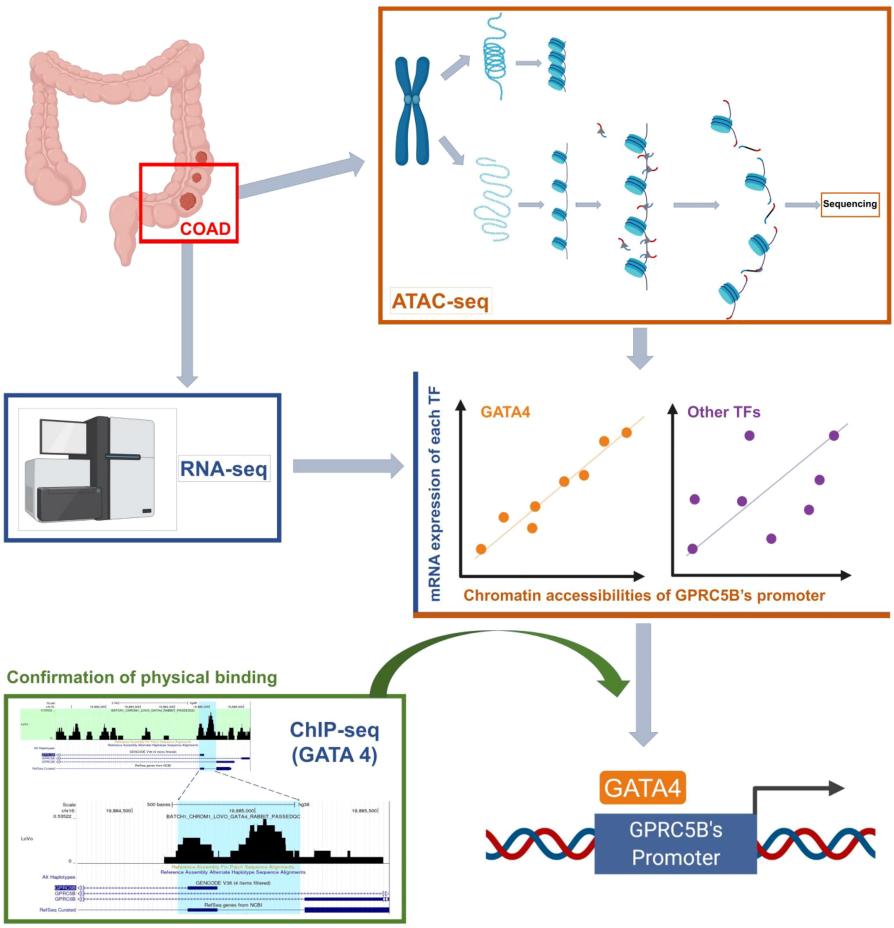

FIGURE 7 | Visualization of the detailed steps of our novel pipeline.

primarily focus on mRNA level and statistical screening, some important biological process might be ignored. To solve these problems, many researchers would apply laboratory experiments to confirm biological significances.

Considering the reasons above, we combined ATAC-seq, RNA-seq, and ChIP-seq profiles together for integrated analysis. ATAC-seq used Tn5 transposase to map the open chromatin regions, indicating the potential binding sites for TFs. It was known that genes with chromatin accessibility in the promoter regions are more likely to be regulated by TFs. The ChIP-seq profiles could ensure the physical binding between a specific TF and the target gene promoter region.

In our study, we first identified chr16:19884686-19885185 as the accessible chromatin region of the GPRC5B promoter through ATAC-seq profiles. Thereafter, we discovered that the mRNA expression of GATA4 was significantly associated with chr16:19884686-19885185. For confirmation, we acquired the ChIP-seq profiles of the GATA4 protein in colon cancer cells. The open chromatin region (chr16:19884686-19885185, highlighted in blue) was found to overlap with the GATA4 binding regions to a great extent. We also found that, with the upregulation and downregulation of GATA4 expression, GPRC5B would be regulated accordingly. Collectively, through this novel pipeline, we identified GATA4 as the direct upstream TF of GPRC5B.

Several inevitable limitations need to be addressed. First, our pipeline required paired ATAC-seq and RNA-seq profiles of the same samples, the amount of which was relatively small in public databases. However, despite the limited data sources, we acquired 41 eligible paired profiles to prove the effectiveness of our pipeline. Second, although we have identified GPRC5B as a key molecule in COAD prognosis through bioinformatics, we have not put forward any proof *in vivo*. Future studies should experimentally verify our findings.

Despite the limitations mentioned above, our study was the first to infer that GPRC5B, correlated with tumor-infiltrating macrophages, might be a key molecule affecting COAD prognosis. The interaction between GPRC5B and tumor-infiltrating macrophages could be a potential target for clinical therapy. We also proposed a novel pipeline, identifying GATA4 as a direct upstream TF of GPRC5B. This pipeline was based on the integration of multi-omics data, which was easy to apply and could be used to achieve a more convincing conclusion.

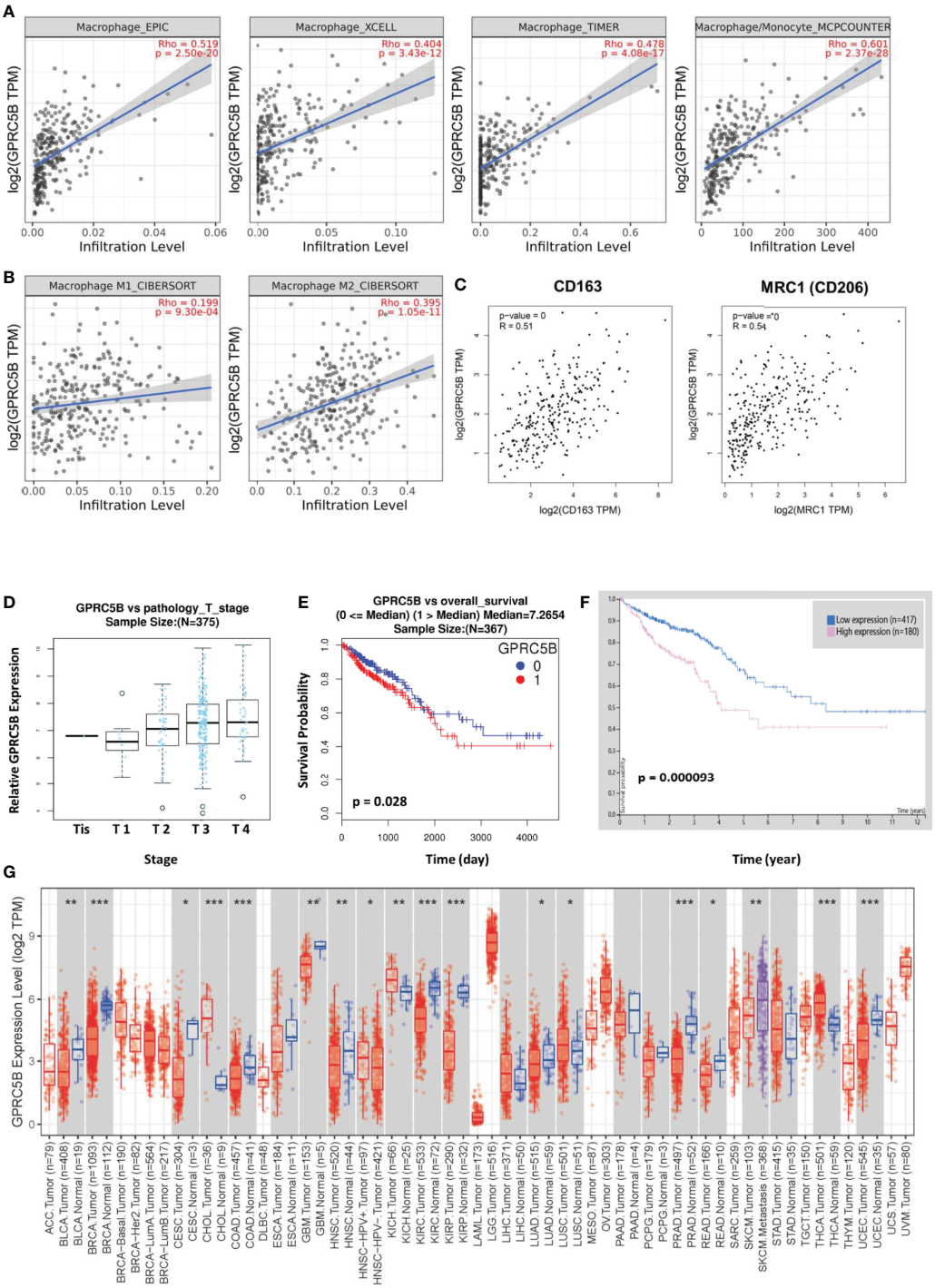

FIGURE 8 | **(A)** Based on the EPIC, XCELL, TIMER, and MCPcounter algorithms, GPRC5B was closely correlated with tumor-infiltrating macrophages in COAD. **(B)** The CIBERSORT algorithm indicated a closer correlation between GPRC5B and M2 macrophages ($r = 0.395$, $p < 0.01$), compared with M1 macrophages ($r = 0.199$, $p < 0.01$). **(C)** The GEPIA database showed that GPRC5B was significantly correlated with the M2 macrophage surface marker CD163 ($r = 0.51$, $p < 0.01$) and MRC1 ($r = 0.54$, $p < 0.01$). **(D)** The LinkedOmics database confirmed that GPRC5B was gradually upregulated following the progress of COAD development through different tumor stages. **(E)** The LinkedOmics database indicated that GPRC5B could be a potential risk factor for COAD ($p < 0.05$). **(F)** The Human Protein Atlas database indicated that GPRC5B could be a potential risk factor for COAD ($p < 0.05$). **(G)** The Timer 2.0 database showed the mRNA expression level of GPRC5B across various tumor types. GPRC5B was significantly downregulated in COAD samples ($p < 0.001$). GPRC5B, G protein-coupled receptor class C group 5 member B; COAD, colon adenocarcinoma; TPM, Transcripts per million. * $p \leq 0.05$; ** $p < 0.01$; *** $p < 0.001$.

CONCLUSIONS

GPRC5B, correlated with tumor-infiltrating macrophages, is a potential key molecule affecting COAD prognosis. Further, with our novel pipeline, TF GATA4 was identified as a direct upstream of GPRC5B. This study proposed a novel pipeline for TF exploration and provided a theoretical basis for COAD therapy.

DATA AVAILABILITY STATEMENT

Publicly available datasets were analyzed in this study. This data can be found here: https://portal.gdc.cancer.gov/, and https://gdc.cancer.gov/about-data/publications/ATACseq-AWG.

ETHICS STATEMENT

The studies involving human participants were reviewed and approved by Tongji Hospital, Shanghai, China (reference number 2018-LCYJ-005). The patients/participants provided their written informed consent to participate in this study.

AUTHOR CONTRIBUTIONS

Conception/design: CH, ZN, BG, BD, and QH. Collection and/or assembly of data: CH, NZ, HX, ZN, XL, BL, BG, BD, and QH. Data analysis and interpretation: CH, HX, NZ, NW, ZN, BL, BD, and QH. Manuscript writing: CH, NW, ZC, and QH. All authors read and approved the final manuscript.

FUNDING

This study was funded by Shanghai Science and Technology Innovation Action Plan (Grant No. 19441905700) and the Clinical Research and Cultivation Project of Shanghai Tongji Hospital (Grant No. ITJ (ZD) 1802, ITJ (ZD) 1804).

SUPPLEMENTARY MATERIAL

The Supplementary Material for this article can be found online at: https://www.frontiersin.org/articles/10.3389/fimmu.2021.741634/full#supplementary-material

REFERENCES

1. Jung G, Hernandez-Illan E, Moreira L, Balaguer F, Goel A. Epigenetics of Colorectal Cancer: Biomarker and Therapeutic Potential. *Nat Rev Gastroenterol Hepatol* (2020) 17(2):111–30. doi: 10.1038/s41575-019-0230-y
2. Siegel RL, Miller KD, Fuchs HE, Jemal A. Cancer Statistics, 2021. *CA Cancer J Clin* (2021) 71(1):7–33. doi: 10.3322/caac.21654
3. Siegel RL, Miller KD, Jemal A. Cancer Statistics, 2020. *CA Cancer J Clin* (2020) 70(1):7–30. doi: 10.3322/caac.21590
4. Angell HK, Bruni D, Barrett JC, Herbst R, Galon J. The Immunoscore: Colon Cancer and Beyond. *Clin Cancer Res* (2020) 26(2):332–9. doi: 10.1158/1078-0432.CCR-18-1851
5. Serini S, Ottes Vasconcelos R, Fasano E, Calviello G. Epigenetic Regulation of Gene Expression and M2 Macrophage Polarization as New Potential Omega-3 Polyunsaturated Fatty Acid Targets in Colon Inflammation and Cancer. *Expert Opin Ther Targets* (2016) 20(7):843–58. doi: 10.1517/14728222.2016.1139085
6. Fang M, Li Y, Huang K, Qi S, Zhang J, Zgodzinski W, et al. IL33 Promotes Colon Cancer Cell Stemness *via* JNK Activation and Macrophage Recruitment. *Cancer Res* (2017) 77(10):2735–45. doi: 10.1158/0008-5472.CAN-16-1602
7. Zhang L, Li Z, Skrzypczynska KM, Fang Q, Zhang W, O'Brien SA, et al. Single-Cell Analyses Inform Mechanisms of Myeloid-Targeted Therapies in Colon Cancer. *Cell* (2020) 181(2):442–59.e29. doi: 10.1016/j.cell.2020.03.048
8. Lappano R, Maggiolini M. G Protein-Coupled Receptors: Novel Targets for Drug Discovery in Cancer. *Nat Rev Drug Discov* (2011) 10(1):47–60. doi: 10.1038/nrd3320
9. Langenhan T. Adhesion G Protein-Coupled Receptors-Candidate Metabotropic Mechanosensors and Novel Drug Targets. *Basic Clin Pharmacol Toxicol* (2020) 126(Suppl 6):5–16. doi: 10.1111/bcpt.13223
10. Usman S, Khawer M, Rafique S, Naz Z, Saleem K. The Current Status of Anti-GPCR Drugs Against Different Cancers. *J Pharm Anal* (2020) 10(6):517–21. doi: 10.1016/j.jpha.2020.01.001
11. Ren SX, Cheng AS, To KF, Tong JH, Li MS, Shen J, et al. Host Immune Defense Peptide LL-37 Activates Caspase-Independent Apoptosis and Suppresses Colon Cancer. *Cancer Res* (2012) 72(24):6512–23. doi: 10.1158/0008-5472.CAN-12-2359
12. Contos JJ, Ishii I, Chun J. Lysophosphatidic Acid Receptors. *Mol Pharmacol* (2000) 58(6):1188–96. doi: 10.1124/mol.58.6.1188
13. Arora P, Ricks TK, Trejo J. Protease-Activated Receptor Signalling, Endocytic Sorting and Dysregulation in Cancer. *J Cell Sci* (2007) 120(Pt 6):921–8. doi: 10.1242/jcs.03409
14. Li X, Lv Y, Yuan A, Li Z. Gastrin-Releasing Peptide Links Stressor to Cancer Progression. *J Cancer Res Clin Oncol* (2010) 136(4):483–91. doi: 10.1007/s00432-010-0766-2
15. Growcott JW. Preclinical Anticancer Activity of the Specific Endothelin A Receptor Antagonist ZD4054. *Anticancer Drugs* (2009) 20(2):83–8. doi: 10.1097/CAD.0b013e328320791c
16. Bohn T, Rapp S, Luther N, Klein M, Bruehl TJ, Kojima N, et al. Tumor Immunoevasion *via* Acidosis-Dependent Induction of Regulatory Tumor-Associated Macrophages. *Nat Immunol* (2018) 19(12):1319–29. doi: 10.1038/s41590-018-0226-8
17. Pagano E, Elias JE, Schneditz G, Saveljeva S, Holland LM, Borrelli F, et al. Activation of the GPR35 Pathway Drives Angiogenesis in the Tumour Microenvironment. *Gut* (2021). doi: 10.1136/gutjnl-2020-323363
18. Tan B, Shi X, Zhang J, Qin J, Zhang N, Ren H, et al. Inhibition of Rspo-Lgr4 Facilitates Checkpoint Blockade Therapy by Switching Macrophage Polarization. *Cancer Res* (2018) 78(17):4929–42. doi: 10.1158/0008-5472.CAN-18-0152
19. Corces MR, Granja JM, Shams S, Louie BH, Seoane JA, Zhou W, et al. The Chromatin Accessibility Landscape of Primary Human Cancers. *Science* (2018) 362(6413). doi: 10.1126/science.362.6413.415-k
20. Ranzoni AM, Tangherloni A, Berest I, Riva SG, Myers B, Strzelecka PM, et al. Integrative Single-Cell RNA-Seq and ATAC-Seq Analysis of Human Developmental Hematopoiesis. *Cell Stem Cell* (2021) 28(3):472–87.e7. doi: 10.1016/j.stem.2020.11.015
21. Charoentong P, Finotello F, Angelova M, Mayer C, Efremova M, Rieder D, et al. Pan-Cancer Immunogenomic Analyses Reveal Genotype-Immunophenotype Relationships and Predictors of Response to Checkpoint Blockade. *Cell Rep* (2017) 18(1):248–62. doi: 10.1016/j.celrep.2016.12.019
22. Barbie DA, Tamayo P, Boehm JS, Kim SY, Moody SE, Dunn IF, et al. Systematic RNA Interference Reveals That Oncogenic KRAS-Driven Cancers Require TBK1. *Nature* (2009) 462(7269):108–12. doi: 10.1038/nature08460

23. Hanzelmann S, Castelo R, Guinney J. GSVA: Gene Set Variation Analysis for Microarray and RNA-Seq Data. *BMC Bioinf* (2013) 14:7. doi: 10.1186/1471-2105-14-7
24. Kazius J, Wurdinger K, van Iterson M, Kok J, Back T, Ijzerman AP. GPCR NaVa Database: Natural Variants in Human G Protein-Coupled Receptors. *Hum Mutat* (2008) 29(1):39–44. doi: 10.1002/humu.20638
25. Gel B, Serra E. Karyoploter: An R/Bioconductor Package to Plot Customizable Genomes Displaying Arbitrary Data. *Bioinformatics* (2017) 33(19):3088–90. doi: 10.1093/bioinformatics/btx346
26. Yu G, Wang LG, He QY. ChIPseeker: An R/Bioconductor Package for ChIP Peak Annotation, Comparison and Visualization. *Bioinformatics* (2015) 31 (14):2382–3. doi: 10.1093/bioinformatics/btv145
27. Yan J, Enge M, Whitington T, Dave K, Liu J, Sur I, et al. Transcription Factor Binding in Human Cells Occurs in Dense Clusters Formed Around Cohesin Anchor Sites. *Cell* (2013) 154(4):801–13. doi: 10.1016/j.cell.2013.07.034
28. Liu T, Ortiz JA, Taing L, Meyer CA, Lee B, Zhang Y, et al. Cistrome: An Integrative Platform for Transcriptional Regulation Studies. *Genome Biol* (2011) 12(8):R83. doi: 10.1186/gb-2011-12-8-r83
29. Li T, Fu J, Zeng Z, Cohen D, Li J, Chen Q, et al. TIMER2.0 for Analysis of Tumor-Infiltrating Immune Cells. *Nucleic Acids Res* (2020) 48(W1):W509–14. doi: 10.1093/nar/gkaa407
30. Li T, Fan J, Wang B, Traugh N, Chen Q, Liu JS, et al. TIMER: A Web Server for Comprehensive Analysis of Tumor-Infiltrating Immune Cells. *Cancer Res* (2017) 77(21):e108–10. doi: 10.1158/0008-5472.CAN-17-0307
31. Tang Z, Li C, Kang B, Gao G, Li C, Zhang Z. GEPIA: A Web Server for Cancer and Normal Gene Expression Profiling and Interactive Analyses. *Nucleic Acids Res* (2017) 45(W1):W98–W102. doi: 10.1093/nar/gkx247
32. Uhlen M, Fagerberg L, Hallstrom BM, Lindskog C, Oksvold P, Mardinoglu A, et al. Proteomics. Tissue-Based Map of the Human Proteome. *Science* (2015) 347(6220):1260419. doi: 10.1126/science.1260419
33. Uhlen M, Zhang C, Lee S, Sjostedt E, Fagerberg L, Bidkhori G, et al. A Pathology Atlas of the Human Cancer Transcriptome. *Science* (2017) 357 (6352). doi: 10.1126/science.aan2507
34. Vasaikar SV, Straub P, Wang J, Zhang B. LinkedOmics: Analyzing Multi-Omics Data Within and Across 32 Cancer Types. *Nucleic Acids Res* (2018) 46 (D1):D956–63. doi: 10.1093/nar/gkx1090
35. Racle J, Gfeller D. EPIC: A Tool to Estimate the Proportions of Different Cell Types From Bulk Gene Expression Data. *Methods Mol Biol* (2020) 2120:233–48. doi: 10.1007/978-1-0716-0327-7_17
36. Aran D, Hu Z, Butte AJ. Xcell: Digitally Portraying the Tissue Cellular Heterogeneity Landscape. *Genome Biol* (2017) 18(1):220. doi: 10.1186/s13059-017-1349-1
37. Li B, Severson E, Pignon JC, Zhao H, Li T, Novak J, et al. Comprehensive Analyses of Tumor Immunity: Implications for Cancer Immunotherapy. *Genome Biol* (2016) 17(1):174. doi: 10.1186/s13059-016-1028-7
38. Becht E, Giraldo NA, Lacroix L, Buttard B, Elarouci N, Petitprez F, et al. Estimating the Population Abundance of Tissue-Infiltrating Immune and Stromal Cell Populations Using Gene Expression. *Genome Biol* (2016) 17 (1):218. doi: 10.1186/s13059-016-1070-5
39. Finotello F, Trajanoski Z. Quantifying Tumor-Infiltrating Immune Cells From Transcriptomics Data. *Cancer Immunol Immunother* (2018) 67 (7):1031–40. doi: 10.1007/s00262-018-2150-z
40. Robinson MD, McCarthy DJ, Smyth GK. Edger: A Bioconductor Package for Differential Expression Analysis of Digital Gene Expression Data. *Bioinformatics* (2010) 26(1):139–40. doi: 10.1093/bioinformatics/btp616
41. Zhang H, Luo YB, Wu W, Zhang L, Wang Z, Dai Z, et al. The Molecular Feature of Macrophages in Tumor Immune Microenvironment of Glioma Patients. *Comput Struct Biotechnol J* (2021) 19:4603–18. doi: 10.1016/j.csbj.2021.08.019
42. Huang C, Huang R, Chen H, Ni Z, Huang Q, Huang Z, et al. Chromatin Accessibility Regulates Gene Expression and Correlates With Tumor-Infiltrating Immune Cells in Gastric Adenocarcinoma. *Front Oncol* (2020) 10:609940. doi: 10.3389/fonc.2020.609940
43. Zhang H, Dai Z, Wu W, Wang Z, Zhang N, Zhang L, et al. Regulatory Mechanisms of Immune Checkpoints PD-L1 and CTLA-4 in Cancer. *J Exp Clin Cancer Res* (2021) 40(1):184. doi: 10.1186/s13046-021-01987-7
44. Brauner-Osborne H, Krogsgaard-Larsen P. Sequence and Expression Pattern of a Novel Human Orphan G-Protein-Coupled Receptor, GPRC5B, a Family C Receptor With a Short Amino-Terminal Domain. *Genomics* (2000) 65 (2):121–8. doi: 10.1006/geno.2000.6164
45. Soni A, Amisten S, Rorsman P, Salehi A. GPRC5B a Putative Glutamate-Receptor Candidate Is Negative Modulator of Insulin Secretion. *Biochem Biophys Res Commun* (2013) 441(3):643–8. doi: 10.1016/j.bbrc.2013.10.099
46. Carvalho J, Chennupati R, Li R, Gunther S, Kaur H, Zhao W, et al. Orphan G Protein-Coupled Receptor GPRC5B Controls Smooth Muscle Contractility and Differentiation by Inhibiting Prostacyclin Receptor Signaling. *Circulation* (2020) 141(14):1168–83. doi: 10.1161/CIRCULATIONAHA.119.043703
47. Kim YJ, Sano T, Nabetani T, Asano Y, Hirabayashi Y. GPRC5B Activates Obesity-Associated Inflammatory Signaling in Adipocytes. *Sci Signal* (2012) 5 (251):ra85. doi: 10.1126/scisignal.2003149
48. von Samson-Himmelstjerna FA, Freundt G, Nitz JT, Stelter F, Luedde M, Wieland T, et al. The Orphan Receptor GPRC5B Modulates Inflammatory and Fibrotic Pathways in Cardiac Fibroblasts and Mice Hearts. *Biochem Biophys Res Commun* (2019) 514(4):1198–203. doi: 10.1016/j.bbrc.2019.05.038
49. Liu S, Xie F, Gan L, Peng T, Xu X, Guo S, et al. Integration of Transcriptome and Cistrome Analysis Identifies RUNX1-Target Genes Involved in Pancreatic Cancer Proliferation. *Genomics* (2020) 112(6):5343–55. doi: 10.1016/j.ygeno.2020.11.010
50. Liu J, Jiang C, Xu C, Wang D, Shen Y, Liu Y, et al. Identification and Development of a Novel Invasion-Related Gene Signature for Prognosis Prediction in Colon Adenocarcinoma. *Cancer Cell Int* (2021) 21(1):101. doi: 10.1186/s12935-021-01795-1
51. Dai S, Xu S, Ye Y, Ding K. Identification of an Immune-Related Gene Signature to Improve Prognosis Prediction in Colorectal Cancer Patients. *Front Genet* (2020) 11:607009. doi: 10.3389/fgene.2020.607009

Conflict of Interest: The authors declare that the research was conducted in the absence of any commercial or financial relationships that could be construed as a potential conflict of interest.

frontiers | Frontiers in Immunology

REVIEW
published: 05 April 2022
doi: 10.3389/fimmu.2022.770465

Organoid Models for Precision Cancer Immunotherapy

Cai-Ping Sun[1†], *Huan-Rong Lan*[2†], *Xing-Liang Fang*[3], *Xiao-Yun Yang*[4*] and *Ke-Tao Jin*[5*]

[1] Department of Medical Oncology, Shaoxing People's Hospital (Shaoxing Hospital, Zhejiang University School of Medicine), Shaoxing, China, [2] Department of Breast and Thyroid Surgery, Affiliated Jinhua Hospital, Zhejiang University School of Medicine, Jinhua, China, [3] Department of Hepatobiliary Surgery, Affiliated Hospital of Shaoxing University College of Medicine (Shaoxing Municipal Hospital), Shaoxing, China, [4] Department of Gastroenterology, Affiliated Jinhua Hospital, Zhejiang University School of Medicine, Jinhua, China, [5] Department of Colorectal Surgery, Affiliated Jinhua Hospital, Zhejiang University School of Medicine, Jinhua, China

OPEN ACCESS

Edited by:
Alessandro Poggi,
San Martino Hospital (IRCCS), Italy

Reviewed by:
Silvia Guil-Luna,
Maimonides Biomedical Research Institute of Cordoba (IMIBIC), Spain
Steven Forsythe,
Wake Forest School of Medicine, United States
Mikaela Grönholm,
University of Helsinki, Finland

***Correspondence:**
Ke-Tao Jin
jinketao2001@zju.edu.cn
Xiao-Yun Yang
yxy_zju@163.com

[†]These authors have contributed equally to this work

Specialty section:
This article was submitted to Cancer Immunity and Immunotherapy, a section of the journal Frontiers in Immunology

Received: 06 September 2021
Accepted: 15 March 2022
Published: 05 April 2022

Citation:
Sun C-P, Lan H-R, Fang X-L, Yang X-Y and Jin K-T (2022) Organoid Models for Precision Cancer Immunotherapy. Front. Immunol. 13:770465. doi: 10.3389/fimmu.2022.770465

Cancer immunotherapy is exploited for the treatment of disease by modulating the immune system. Since the conventional *in vivo* animal and 2D *in vitro* models insufficiently recapitulate the complex tumor immune microenvironment (TIME) of the original tumor. In addition, due to the involvement of the immune system in cancer immunotherapy, more physiomimetic cancer models, such as patient-derived organoids (PDOs), are required to evaluate the efficacy of immunotherapy agents. On the other hand, the dynamic interactions between the neoplastic cells and non-neoplastic host components in the TIME can promote carcinogenesis, tumor metastasis, cancer progression, and drug resistance of cancer cells. Indeed, tumor organoid models can properly recapitulate the TIME by preserving endogenous stromal components including various immune cells, or by adding exogenous immune cells, cancer-associated fibroblasts (CAFs), vasculature, and other components. Therefore, organoid culture platforms could model immunotherapy responses and facilitate the immunotherapy preclinical testing. Here, we discuss the various organoid culture approaches for the modeling of TIME and the applications of complex tumor organoids in testing cancer immunotherapeutics and personalized cancer immunotherapy.

Keywords: cancer, immunotherapy, organoid, precision medicine, tumor microenvironment

INTRODUCTION

Immunotherapy is a type of cancer therapy that boosts the body's immune system to fight cancer. The immune system uses a variety of mechanisms to identify and eradicate tumor cells, but many of them are inactivated in the tumor microenvironment (TME) during tumor development (1). Immunotherapy can be exploited to help the immune system for detection of neoplastic cells and triggering of the immune response, or promote an existing one against the tumor cells. Indeed, immunotherapies systemically boost the immune surveillance and/or locally regulate the tumor immune microenvironment (TIME) (2). These immunotherapies include oncolytic viruses, pattern recognition receptor (PRR)-targeted therapies, vaccines, tumor antigen-targeted monoclonal antibodies, adjuvants such as cytokines, or other cell signaling molecules (3–5). Immunotherapy approaches that have revolutionized conventional malignancy treatment include: 1) adoptive T cell

therapies (ACT), such as T cell receptor (TCR)- and chimeric antigen receptor (CAR)-T cells, also bulk tumor-infiltrating lymphocyte (TIL) therapy (6–8) and 2) immune checkpoint inhibitors (ICIs) (9–11) including anti-CTLA-4 monoclonal antibodies and anti-PD-1/PD-L1 monoclonal antibodies that boost CD8+ T cell effector functions. Since the immune system is involved in cancer immunotherapy, therefor, efficient cancer models are required to test the effect of immunotherapy agents in a context where there are immune cells and other TME components. In addition, the dynamic interactions between the neoplastic cells and non-neoplastic host components in the TME can affect carcinogenesis, tumor metastasis, cancer progression, and drug resistance of cancer cells. Hence, conventional *in vivo* animal and 2D *in vitro* models are not suitable for immunotherapy because these models insufficiently recapitulate the complex tumor (immune) microenvironment of original human tumors (2). Mice models, which are useful for studying classic drug's efficacy, cannot be used to evaluate all forms of immunotherapy, because of the considerable differences between the immune system of mice and humans (12). Patient-derived tumor xenografts (PDTX) models can properly recapitulate the interactions of cancer cells with surrounding elements, except the interactions with the immune system. Humanized immuno-oncology models have been generated to overcome this problem. These models bearing human immune cells, but cost, throughput, and complete immunocompatibility, remain challenges (13, 14). On the other hand, the generation of a successful PDTX model is time-consuming, about 4-8 months, therefore, these models cannot be a rational choice for real-time precision cancer therapy (15). The selection of effective transplanting approaches for various tumor tissues and the generation of specific subtypes of tumors are other limitations of PDTXs models (16–19). Given the role of the tumor (immune) microenvironment in the drug screening and immunotherapy studies (20, 21), the presence of pre-existing structural elements such as mouse stromal cells in TME of PDTX models can affect the validity of the study results (20). All the models mentioned above inadequately model the complex immunobiology and pathophysiology of the original parent tumors. In addition, animal models are expensive and time-consuming to develop and apply (22). Hence, it is necessary to develop an alternative model that can recapitulate the human TME while preserving the human immune system components. Therefore, using human tumor organoid models is necessary to tackle these limitations. Indeed, organoid models can properly recapitulate the tumor (immune) microenvironment by preserving tissue architecture, endogenous stromal components including various immune cells, or by adding exogenous immune cells, vasculature, and other components (23–29). Therefore, PDO culture systems could model immunotherapy responses and facilitate the immunotherapy preclinical testing. PDTXs accurately retain the heterogeneity of human tumors, but in contrast to PDTXs, PDOs can be cultured for a long time, expanded, and finally cryopreserved. The establishment of large organoid biobanks has been made possible by the propagation of tumor biopsies *in vitro*, that these tumor biobanks preserve the mutational diversity and histological properties of native human tumors (30–32). Here, we discuss the various organoid culture strategies for the modeling of TIME and the applications of complex PDOs in testing cancer immunotherapeutics and personalized cancer immunotherapy.

ORGANOID CULTURE TECHNIQUES FOR IMMUNOTHERAPY STUDIES

Various organoid culture approaches are utilized for modeling the TIME that are suitable for immunotherapy including 1) Reconstitution approaches, such as submerged Matrigel culture, because the typical submerged Matrigel organoids contain exclusively epithelial cells, any study on immunotherapy and TIME in this approach requires the addition of exogenous immune cells and other stromal cell types (2). 2) Holistic approaches, such as air-liquid interface (ALI) and microfluidic 3D culture that in these culture strategies the native TIME and small fragment of tumor tissue, as an intact unit without reconstitution, are preserved (2) (**Table 1**). Methods such as ALI, in which the tissue architecture is preserved, are also known as explant culture methods (48). In addition, 3D micro-sized cell aggregates that are generated as suspension or embedded within a 3D matrix are known as spheroids (49).

Submerged Matrigel Culture

The submerged Matrigel technique is widely used to culture dissociated cancer cells from tumor biopsies underneath tissue culture medium in a mixture with a dome or flat gel of 3D Matrigel. In this culture method, various growth factors and/or pathway inhibitors are added to the culture medium depending on the type of tumor tissue (25, 50–52). Customized culture conditions have been adapted for many different tissues (25, 32, 53–64), but often include ligands and additives, such as Wnt3a and/or R-spondin, bone morphogenetic (BMP) inhibitor Noggin, and epidermal growth factor (EGF) (25), which allow the stem cells to undergo long-term self-renewal and differentiation into various cell lineages (25). These niche factor requirements are mainly determined by genetic variations that increase tumorigenicity (51). These supplementations are also been utilized in other organoid culture strategies such as ALI (42). Dissociation of tissue during organoid preparation leads to activation of Rho kinase (ROCK)-dependent programmed cell death, therefore the addition of ROCK inhibitors to the medium can efficiently increase the success rates of organoid generation (25, 65, 66). It should be noted that conventional submerged Matrigel methods exclusively enrich epithelial tumor cells, but fail to preserve stromal components (25). Hence, TIME modeling in these techniques needs a co-culture of PDOs with exogenous (immune) cells. Seino et al. (50), by using this technique showed that co-culturing of human pancreatic ductal adenocarcinoma (PDAC) organoids with cancer-associated fibroblasts (CAFs), which shows immunosuppressive activity in TME (67), trigger organoid growth of WNT-nonproducing PDAC subtypes by CAF produced WNT (50). On the other hand, TGFβ and IL-1 ligands

TABLE 1 | Overview of organoid culture techniques in cancer research.

	Organoid culture techniques		
	Submerged Matrigel culture	**Air-liquid interface culture**	**Microfluidic 3D culture**
Tissue processing before culture	Tissues are dissociated mechanically or/and enzymatically	Tissue is minced into small fragments	Tissues are dissociated mechanically or/and enzymatically; by filtering 40–100 μm-sized tumor fragments are collected and pelleted in ultra-low-attachment plates
Culture matrix And Culture equipment	Matrigel Dish or plate	Collagen Inner dish, Outer dish (Transwell plates with permeable membrane inserts)	Collagen Microfluidic device
Plating condition	Cells culture underneath medium in mixture with 3D Matrigel	Mixture of tissue fragments and collagen plated on the inner dish with a bottom collagen layer; medium is added into an outer dish that can diffuse into the inner trans-well dish through a permeable membrane; top of collagen layer is exposed to air	Spheroid-collagen mixture is inoculated into central gel region of the device; medium is added into media channels on both sides
Preserved cell types of original tumor tissue in culture	Cancer cells exclusively	Cancer cells, tumor-infiltrating myeloid and lymphoid cells, native immune cells, and stromal cells	Cancer cells, tumor-infiltrating myeloid and lymphoid cells, native immune cells, and stromal cells
Modeling the tumor immune microenvironment	PBMCs, DCs and other immune cells can be added to the culture	Immune cells of tumor tissue are faithfully preserved	Immune cells can be added in the medium; immune cells of tumor tissue are faithfully preserved
Advantages	Organoid expansion is convenient	Cellular complexity and architecture of the tumor tissue are maintained as an intact *en bloc* unit without reconstitution	Cellular diversity and architecture of the tumor tissue are maintained; small amount of medium/reagents and small number of cells are required; it can be automated; mimicking physiological shear flow
Limitations	Stromal components and immune cells are usually not preserved in tissue processing stage, determining the growth factors and/or inhibitors required to maintain all subclones is the laborious and time-consuming process; does not reflect the native tumor-infiltrating immune cells, lack of immune components hinders immunotherapy assessment; allogeneic cultures will result in high background killing compared with autologous systems	Determining the growth factors and/or inhibitors required to maintain all subclones is the laborious and time-consuming process; necrosis and hypoxic cores of organoids; the immune components decline over time and do not persist beyond ~2 months	Determining the growth factors and/or inhibitors required to maintain all subclones is the laborious and time-consuming process; size limitation; requires specialized equipment; the immune components decline over time
Possible future improvements	Culture duration can be extended; establishing organoid biobanks for model standardization across laboratories; incorporating multiple organoid types into single microchips; using synthetic scaffolds with precise ECM composition that is essential for reproducible research; increase immune cellular complexity by both incorporated into, and preserved in; to overcome to the formation of a necrotic core, and better recapitulation of native TME organoid vascularization and perfusion are needed		
References	(33–41)	(42, 43)	(44–47)

secreted by PDAC organoids can increase CAF heterogeneity and induce distinct myofibroblast and inflammatory CAF subtypes, respectively (68). Therefore, selective targeting of tumor-promoting CAFs can be improved by understanding the CAF heterogeneity mechanisms (68). Chakrabarti et al, designed a complex submerged Matrigel culture system by co-culturing of mouse tumor organoids with cytotoxic T lymphocytes and bone marrow-derived dendritic cells pulsed by conditioned media (tumor antigen) collected from tumor organoids. The promotion of apoptosis by activated CTLs was observed in cancer cell in the presence of PD-L1 neutralizing antibody (69). This method, co-culture of immune cells and human tumor organoids, is also used for the generation of tumor-reactive T cells from autologous peripheral blood lymphocytes (33) and survey on the *Helicobacter pylori* infection process (34, 70). Forsythe et al. (71), utilized a collagen-based extracellular matrix (ECM, hydrogel) to fabricate PDOs. They generate immunocompetent organoids with coculturing of tumor cells with patient-matched immune cells derived from peripheral blood mononuclear cells (PBMC), spleen, and lymph nodes. They showed that immunocompetent organoids can be useful in the preclinical study of personalized immunotherapy efficacy.

Microfluidic 3D Culture

In microfluidic 3D devices, murine- or patient-derived organotypic tumor spheroids (MDOTS/PDOTS) are cultured in a mixture of collagen gel (72). For MDOTS/PDOTS culture (44), tumor tissues specimen is obtained from the patient and dissociated mechanically and enzymatically. This procedure ultimately gives a heterogeneous mixture of single cells,

spheroids, and macroscopic tumor fragments. Then, this mixture is filtered through 100 μm and 40 μm filters to obtain spheroids with 40–100 μm in diameter, afterward, this fraction is pelleted in ultra-low-attachment plates and mixed with collagen gel, and inoculated into the center region of the microfluidic device. To feed the spheroids, the culture medium is added into the media channels located on both sides of the central channel. In this approach, spheroids maintain the native cancer tissue complexity and cellular diversity such as autologous myeloid populations (tumor-associated macrophages [TAM], monocyte, DC, and MDSC), lymphocytes (B cell and T cell), and cancer cells without reconstitution (45). T cell infiltration into cancer spheroids and tumor-immune cell interactions and cross-talk can be studied in these devices by adding exogenous T cells such as Jurkat cells into the media channels (46, 73). The composition of the devices and the size of media and central channels are variables that can reduce the validity and reproducibility of studies (44). The composition of the devices such as PDMS (polydimethylsiloxane) is one of the interfering factors in testing immune checkpoint blockade (ICB) in a mixture with small molecules (generally prepared in dimethyl sulfoxide, DMSO), because PDMS can adsorb the small hydrophobic molecules (74) that prevent the drug delivery to tumor spheroids.

Air–Liquid Interface Culture

In this approach, two inner and outer dishes are used. The inner dish consists of two layers, bottom and top, for preparation of the bottom layer the collagen gel matrix was added to the inner dish (43). For the preparation of primary tissues, after obtaining the tissue specimen, it immediately are placed in an ice-cold medium (43). After rinsing the tissue, it mechanically dissociated into small fragments and then are cultured in a mixture with collagen gel as a top layer of the inner transwell dish by pouring the mixture onto the inner dish with the bottom layer gel matrix (43). Then prepared inner dish is placed into an outer dish, transferred to a 37°C incubator, and allowed the gel of the inner dish to solidify (43). Afterward, culture media is added to the outer dish that can diffuse into the inner dish through a permeable membrane. In addition, the top layer of culture is in direct air exposure that supply tissue organoid oxygen efficiently (26, 43, 75). ALI allows the growth of large multicellular tissue fragments that retain native tissue architecture, such as cancer cells *en bloc* with endogenous stromal and immune cells without reconstitution, which is different from submerged Matrigel culture (76). In addition, ALI PDOs preserve not only the architecture and complex cellular composition of the TME, but also the genetic alterations of the native tumor (42). These features of ALI, in contrast to submerged Matrigel Culture, make it suitable for TME modeling (32). It has been observed that in ALI, probably essential endogenous niche factors produced by stromal cells are sufficient to support tissue fragment growth without growth factor supplementation (26).

Organoid On-a-Chip

Organoid culture without physical restrictions resulted in organoid fragments with differences in shape, size, geometry, and cell number. As well, the mechanical factors such as fluid shear stress, tension, and compression are not recapitulated the native condition of tumor in 2D or 3D culture models. Therefore, these limitations lead to the non-reproducibility of results in organoid cultures (3). Organoid-on-a-chip models can overcome this challenge by increasing of uniformity of organoids and mimicking the physical conditions of the body such as providing perfusion of culture media. In addition, microfluidic devices can monitor and control the culture condition and assay variables by integrated sensors and actuators (77). The multi-organoid-on-a-chip have also been built (77, 78), nevertheless, optimization of culture media and mechanical condition for different tissue remain as a major challenge.

COMPLEX ORGANOIDS FOR IMMUNOTHERAPY

For various reasons, the TME is not fully recapitulated in most organoid culture methods. This drawback, especially the lack of immune cells, limits the application of organoids in immunotherapy studies. Nevertheless, many studies are underway to solve this issue.

Adding Immune Components

In some cases, immune cells are not added, but the immune cells within the organoid are maintained and expanded. Zumwalde et al. (79), showed the presence of immune cell populations and characterized the intraepithelial lymphocyte compartment within the organoid culture. They demonstrated that leukocyte populations of the breast organoid differed from those in peripheral blood, and conserved T lymphocytes can be expanded in response to the bisphosphonate. As noted above, cultured tumor spheroids in microfluidics devices are able to preserve autologous myeloid and lymphoid cell populations (45). The air-liquid interphase (ALI) culture strategy is another approach that retains native immune and stromal components. In ALI, the cancer epithelium and its complex microenvironment including fibroblasts, immune cells such as cytotoxic T lymphocytes (CTLs), helper T cells, TAMs, natural killer (NK) cells, B cells, and NK T cells are maintained for over a 1- to 2-month period (42). In addition, the T cell receptor (TCR) spectrum of the native tumor is accurately preserved in organoid culture (42).

In some organoid culture strategies, such as the submerged Matrigel technique, stromal and immune cells are not preserved. Therefore, to perform immunotherapy studies, it is necessary to add immune cells to the organoid. Tsai et al. (80), generated pancreatic cancer organoids using primary organoid co-culture with patient-matched peripheral blood lymphocytes and CAFs that were relevant to the immunotherapy and tumor-immune cell interaction studies. Activation of myofibroblast-like CAFs and tumor-dependent lymphocyte infiltration were detected in these complex organotypic models. In another study (33), co-cultures of autologous tumor organoids and peripheral blood lymphocytes were established for the enrichment of tumor-reactive T cells from peripheral blood of colorectal cancer

(CRC) and non-small-cell lung carcinoma (NSCLC) patients. Thus, this approach can be used to evaluate the efficiency of the killing of tumor organoids by autologous tumor-reactive T cells (33). Many factors can affect the outcome and our success in the generation of complex organoids. For instance, in some cancer immune cells located in the surrounding stroma of the tumor or completely lack in TME. Therefore, this will impact the immune cell population of primary organoid culture (3). Furthermore, the addition of exogenous immune components to organoids will not be able to recapitulate the complexity of the patient-specific immune cell composition within TME. If allogeneic immune cells are used as a source of exogenous immune components, because of interpersonal differences in HLA, it will lead to high background killing compared with patient-specific PBMCs (3). Ultimately, choosing the proper strategy for co-culture depend on the downstream assays.

Organoid Vascularization and Perfusion

Lack of perfusion flow and vascular networks in organoids remains a major challenge in the preparation of complex organoids as an ideal cancer model. The absence of vasculature limits the size of the organoid, and organoids larger than 100-200 μm in diameter suffer from the diffusion of nutrients, oxygen, and metabolites to the central region of the organoid. Furthermore, organoid fragments larger than 500 μm in diameter show necrosis (81, 82). Many studies have been performed to overcome this problem and establish perfusion flow in the organoid (23, 27–29). Wörsdörfer et al. (29), co-cultured the mesodermal progenitor cells (MPCs) with tissue-specific (progenitor) cell types for the establishment of complex neural as well as human tumor organoids. They showed the directed incorporation of MPCs into organoids and the formation of vascular networks in these organoids. They observed the expansion of vascular networks during organoid growth. In addition, this endothelial network was responsive to pro-angiogenic conditions and anti-angiogenic agents (29). Organoid vascularization has been previously well-reviewed by Grebenyuk and Ranga (28).

APPLICATION OF ORGANOIDS IN IMMUNOTHERAPY

For immunotherapies screening and studies, an ideal *ex vivo* model is needed to be able to fully recapitulate the heterogenicity of the native TME. For this reason, PDOs, which can preserve TIME as well as represent the stage and the treatment history of the patient, can be utilized. In the following, we will discuss the applications of organoids in immunotherapy (**Figure 1**).

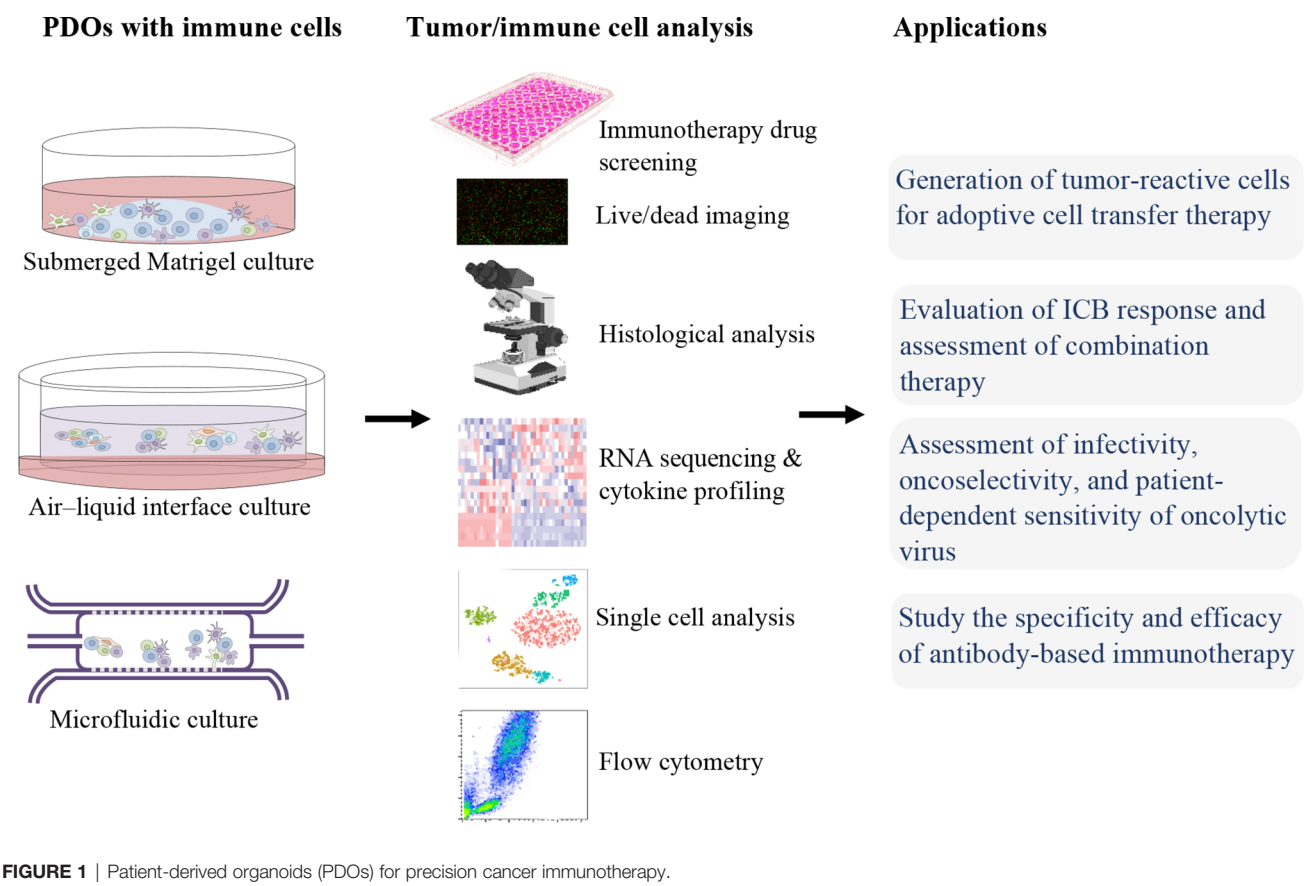

FIGURE 1 | Patient-derived organoids (PDOs) for precision cancer immunotherapy.

Adoptive Cell Transfer Therapy

In ACT immunotherapy, TILs or circulating lymphocytes are collected, high-affinity TCRs recognizing tumor antigens are selected or genetically engineered, subsequently, these cells expanded and activated *ex vivo* followed by reinfusion into patients (8, 83). CAR T cells are genetically modified T cells that produce an artificial T-cell receptor, targeting a specific antigen on the surface of tumor cells and circumventing MHC restriction (84). Studies have shown that PDOs are efficient platforms to evaluate the tumor-specific cytotoxicity of T cells (e.g., CAR T cell, TCR T cell). In the study of Michie et al. (85), PDOs were exploited to evaluate the effect of combination therapy of CAR T cells and birinapant, the inhibitor of apoptosis antagonist. They observed that the combination of CAR T cells with birinapant significantly reduce PDOs growth in a tumor necrosis factor (TNF)-dependent manner, while CAR T cells alone were relatively ineffective. Schnalzger et al. (35), developed a sensitive preclinical model, 3D PDOs, that allows assaying the CAR-mediated cytotoxicity in the native TIME mimicking model. Furthermore, they established a confocal live-cell imaging protocol for dynamic monitoring of cytotoxic activity toward organoids at a single organoid level. They demonstrated a stable effector-target cell interaction in the co-culture of NK cells with CRC or normal organoids on an ECM layer. In addition, CRC organoids were utilized to monitor the tumor antigen-specific cytotoxicity of EGFRvIII or FRIZZLED receptors-targeting CAR-engineered NK-92 cells. In sum, they established a sensitive platform to assay CAR efficacy and tumor specificity in a personalized manner (35). In addition, Epithelial-only PDOs, while lacking stromal and immune components, can be used for the selection of tumor-reactive T cells (33). This co-culture strategy can be served to enrichment, stimulation, and efficacy evaluation of tumor-reactive lymphocytes. Dijkstra et al. (33), cocultured CRC or NSCLC organoids with autologous circulating T cells (PBMCs), in medium supplemented with anti-PD1, anti-CD28, and IL-2 for generation of tumor-reactive $CD8^+$ populations. After two weeks of co-culture, T cell-mediated killing, MHC-dependent cytotoxicity, against autologous tumors organoids, and upregulation of CD107a and IFNγ secretion in $CD8^+$ T cells were observed. But, these tumor-reactive $CD8^+$ cells did not affect the survival of matched healthy organoids. Therefore, they established a platform for the expansion of tumor-reactive T cells and evaluation of the specificity and sensitivity of cancer cell killing by autologous T cells in a personalized manner. Additionally, tumor-reactive T cells can be isolated from TILs that are more specific than the non-infiltrating lymphocytes, subsequently, these cells can be infused back into the patient (86).

Immune Checkpoint Inhibitors

Clinical benefits of ICIs that target CTLA-4, PD1/PD-L1 have been observed in various advanced tumors, such as renal cell carcinoma (RCC) (87), cutaneous squamous cell cancer (88), melanoma (11), head and neck cancer (89), and NSCLC (10). Epithelial-only organoid biobanks have been established from diverse malignancies and are widely available through entities such as the Human Cancer Models Initiative (HCMI). But lack of immune compartments in these types of PDOs hinders their immunotherapy application. Some studies have been performed to overcome this issue. For instance, Kong and colleagues (36), cocultured epithelial-only submerged Matrigel organoids with autologous TILs and demonstrated the TILs migration toward organoids and cytotoxic activity of T cells. They also showed the rescue of TIL function after ICB. But since, co-culturing the epithelial only PDOs with exogenous immune cells, as a reconstitution approach, cannot fully recapitulate the complex interaction and crosstalk between diverse cell populations in the TME, especially when using immunomodulatory drugs. To tackle this problem, a holistic culture approach, such as 3D microfluidic and ALI culture strategies, can be utilized for TIME modeling. The dynamic response and resistance to ICB (such as PD-1 blockade) can be recapitulated using organotypic spheroids in a short-term 3D microfluidic culture that maintains autologous myeloid and lymphoid cell populations similar to the original donor human or mouse tumors (45). As well, the cytokine secretion profiles of PDOTS/MDOTS matched the profile of the donor tumors (45). Therefore, PDOTS/MDOTS profiling facilitates the evaluation of ICB using clinically relevant models. Neal et al. (42), utilized WENR (WNT3A, EGF, NOGGIN, and RSPO1) base medium to expand and serially passage physically processed cancer fragments as ALI organoids. They demonstrated that ALI PDOs, like the microfluidic approach, preserve the stromal and immune cell populations, and effectively recapitulate the expansion, activation, and tumor cytotoxicity of tumor antigen-specific TILs in response to PD-1/PD-L1 ICB. They observed the $CD8^+$ TIL expansion, activation, and tumor cell killing after 1 week of anti-PD-1 treatment of ALI PDOs from various human tumor biopsies, including RCC, NSCLC, and melanoma. It should also be noted that the material and composition of devices used in organoid culture can affect the results of immunotherapy such as ICB studies (74).

Other Immunotherapy Applications

PDOs can be used as predictive tools to study the specific infectivity, and cytotoxicity of the oncolytic virus alone or in combination with chemotherapy (90). In the study of Raimondi et al, Oncolytic adenovirus (OA) displayed a good selectivity of replication in PDAC organoids, but not in healthy pancreas tissue organoids. Patient-specific responses were also observed, indicating that PDOs are reliable *in vitro* tumor models to assay preclinical responses to oncolytic viruses.

Tumor organoids can also be utilized to study the specificity and efficacy of antibody-based immunotherapy. As mentioned in the previous section, many studies used the organoid models in antibody-based ICB therapies (42, 45, 69, 91). Courau et al. (92), showed that both NKG2D-MICA/B and NKG2A-HLA-E pathways are involved in the infiltration process of activated/memory T and NK cells into organoids, subsequently these activated cells can kill cancer cells and disrupt the 3D structure. They demonstrated that anti-MICA/B and a combination of both anti-MICA/B and anti-NKG2A antibodies were able to induce immune-mediated destruction of colorectal tumor organoids during cocultures with autologous TILs. Gonzalez-Exposito et al. (93), established seven PDOs from treatment-refractory metastatic

CRC and one from a treatment naïve primary CRC, to investigate on resistance and sensitivity mechanisms of cibisatamab, a bispecific monoclonal antibody that binds carcino-embryonic antigen (CEA) on tumor cells and CD3 on T cells. They designed a co-culture of organoids and allogeneic $CD8^+$ T cells to evaluate cibisatamab efficacy. Using this platform, they demonstrated that CEA_{low} PDOs were resistant whereas CEA_{high} PDOs were sensitive to cibisatamab. Indeed, CEA_{low} cells maintain tumor cell growth, and an increased WNT/β-catenin pathway activity was detected in CEA_{low} cells by RNA-sequencing. They suggested the use of WNT/β-catenin pathway inhibitors in combination with cibisatamab as a potential strategy to increase the treatment success.

CONCLUSIONS

Nowadays, the use of PDOs to study the dynamic interactions between cancer and the immune system has attracted increasing attention. In addition, the modeling of TME could facilitate immunotherapy screening in the preclinical setting. Lack of stromal components and vascular network are the major limitations of organoid technology for studying the influence of TIME on cancer behavior against immunotherapy agents. To overcome these restrictions, the complex organoids have been developed by co-culturing of organoids (or progenitor cells) with immune cells, CAFs, mesodermal progenitor cells. In addition, co-culturing of organoids with PBMCs or immune cells from lymph nodes can model the cancer-immunity cycles, including effector T cell priming/activation, T cell trafficking/infiltration into tumor tissues, and recognition/killing of cancer cells by T cells. For the long-term preservation of immune cells, using additional supplements such as anti-CD28, anti-CD3, and IL-2 antibodies has been suggested. As well, the culture media composition should be optimized in such a way that supports the growth of all clones without selective growth of specific colonies. Recapitulation of mechanical stress such as physiologic shear flow can improve the modeling of native TME. Using scaffolds with well-defined composition and control of size, shape, cell number, and relative arrangement of different cell types within organoids could improve the reproducibility of drug screening results. In comparison to animal models, establishing a research platform with organoid models take less time: it is feasible to establish a successful human organoid culture within a few weeks or months, as a result, it is possible for PDOs to be used for precision medicine to provide robust data on individual mutation profiles and drug responses (94). Numerous clinical trials are underway to evaluate the various applications of organoids and their effectiveness in precision cancer immunotherapy.

AUTHOR CONTRIBUTIONS

C-PS: Conceptualization, Writing-original draft, Writing-review and editing. H-RL: Validation, Writing-original draft, Writing-review and editing. X-LF: Funding acquisition, Validation, Writing-review and editing. X-YY: Supervision, Validation, Writing-review and editing. K-TJ: Funding acquisition, Supervision, Writing-review and editing. All authors contributed to the article and approved the submitted version.

FUNDING

This work was supported by National Natural Science Foundation of China (grant no. 82104445 to H-RL), Zhejiang Provincial Public Welfare Technology Application Research Project (grants no. LGF22H160046 to H-RL, and LGF21H160004 to X-LF), Jinhua Municipal Science and Technology Projects (grants no. 2021-3-040 to K-TJ, and 2021-3-046 to H-RL).

REFERENCES

1. Vinay DS, Ryan EP, Pawelec G, Talib WH, Stagg J, Elkord E, et al. Immune Evasion in Cancer: Mechanistic Basis and Therapeutic Strategies. *Semin Cancer Biol* (2015) 35:S185–98. doi: 10.1016/j.semcancer.2015.03.004
2. Yuki K, Cheng N, Nakano M, Kuo CJ. Organoid Models of Tumor Immunology. *Trends Immunol* (2020) 41:652–64. doi: 10.1016/j.it.2020.06.010
3. Grönholm M, Feodoroff M, Antignani G, Martins B, Hamdan F, Cerullo V. Patient-Derived Organoids for Precision Cancer Immunotherapy. *Cancer Res* (2021) 81:3149–55. doi: 10.1158/0008-5472.CAN-20-4026
4. Demaria O, Cornen S, Daëron M, Morel Y, Medzhitov R, Vivier E. Harnessing Innate Immunity in Cancer Therapy. *Nature* (2019) 574:45–56. doi: 10.1038/s41586-019-1593-5
5. Houot R, Kohrt HE, Marabelle A, Levy R. Targeting Immune Effector Cells to Promote Antibody-Induced Cytotoxicity in Cancer Immunotherapy. *Trends Immunol* (2011) 32:510–6. doi: 10.1016/j.it.2011.07.003
6. Tran E, Robbins PF, Lu Y-C, Prickett TD, Gartner JJ, Jia L, et al. T-Cell Transfer Therapy Targeting Mutant KRAS in Cancer. *N Engl J Med* (2016) 375:2255–62. doi: 10.1056/nejmoa1609279
7. Hammerl D, Rieder D, Martens JWM, Trajanoski Z, Debets R. Adoptive T Cell Therapy: New Avenues Leading to Safe Targets and Powerful Allies. *Trends Immunol* (2018) 39:921–36. doi: 10.1016/j.it.2018.09.004
8. Rosenberg SA, Restifo NP. Adoptive Cell Transfer as Personalized Immunotherapy for Human Cancer. *Science* (2015) 348:62–8. doi: 10.1126/science.aaa4967
9. Pardoll DM. The Blockade of Immune Checkpoints in Cancer Immunotherapy. *Nat Rev Cancer* (2012) 12:252–64. doi: 10.1038/nrc3239
10. Socinski MA, Jotte RM, Cappuzzo F, Orlandi F, Stroyakovskiy D, Nogami N, et al. Atezolizumab for First-Line Treatment of Metastatic Nonsquamous NSCLC. *N Engl J Med* (2018) 378:2288–301. doi: 10.1056/nejmoa1716948
11. Larkin J, Chiarion-Sileni V, Gonzalez R, Grob J-J, Rutkowski P, Lao CD, et al. Five-Year Survival With Combined Nivolumab and Ipilimumab in Advanced Melanoma. *N Engl J Med* (2019) 381:1535–46. doi: 10.1056/nejmoa1910836
12. Begley CG, Ellis LM. Drug Development: Raise Standards for Preclinical Cancer Research. *Nature* (2012) 483:531–3. doi: 10.1038/483531a
13. Jespersen H, Lindberg MF, Donia M, Söderberg EMV, Andersen R, Keller U, et al. Clinical Responses to Adoptive T-Cell Transfer can be Modeled in an Autologous Immune-Humanized Mouse Model. *Nat Commun* (2017) 8:1–10. doi: 10.1038/s41467-017-00786-z
14. Zhao Y, Shuen TWH, Toh TB, Chan XY, Liu M, Tan SY, et al. Development of a New Patient-Derived Xenograft Humanised Mouse Model to Study Human-Specific Tumour Microenvironment and Immunotherapy. *Gut* (2018) 67:1845–54. doi: 10.1136/gutjnl-2017-315201
15. Hidalgo M, Amant F, Biankin AV, Budinská E, Byrne AT, Caldas C, et al. Patient-Derived Xenograft Models: An Emerging Platform for Translational

Cancer Research. *Cancer Discov* (2014) 4:998–1013. doi: 10.1158/2159-8290.CD-14-0001
16. Zhang X, Claerhout S, Prat A, Dobrolecki LE, Petrovic I, Lai Q, et al. A Renewable Tissue Resource of Phenotypically Stable, Biologically and Ethnically Diverse, Patient-Derived Human Breast Cancer Xenograft Models. *Cancer Res* (2013) 73:4885–97. doi: 10.1158/0008-5472.CAN-12-4081
17. Marangoni E, Vincent-Salomon A, Auger N, Degeorges A, Assayag F, De Cremoux P, et al. A New Model of Patient Tumor-Derived Breast Cancer Xenografts for Preclinical Assays. *Clin Cancer Res* (2007) 13:3989–98. doi: 10.1158/1078-0432.CCR-07-0078
18. Derose YS, Wang G, Lin YC, Bernard PS, Buys SS, Ebbert MTW, et al. Tumor Grafts Derived From Women With Breast Cancer Authentically Reflect Tumor Pathology, Growth, Metastasis and Disease Outcomes. *Nat Med* (2011) 17:1514–20. doi: 10.1038/nm.2454
19. Tetteh PW, Kretzschmar K, Begthel H, Van Den Born M, Korving J, Morsink F, et al. Generation of an Inducible Colon-Specific Cre Enzyme Mouse Line for Colon Cancer Research. *Proc Natl Acad Sci USA* (2016) 113:11859–64. doi: 10.1073/pnas.1614057113
20. Klemm F, Joyce JA. Microenvironmental Regulation of Therapeutic Response in Cancer. *Trends Cell Biol* (2015) 25:198–213. doi: 10.1016/j.tcb.2014.11.006
21. Mcmillin DW, Negri JM, Mitsiades CS. The Role of Tumour-Stromal Interactions in Modifying Drug Response: Challenges and Opportunities. *Nat Rev Drug Discov* (2013) 12:217–28. doi: 10.1038/nrd3870
22. Lo YH, Karlsson K, Kuo CJ. Applications of Organoids for Cancer Biology and Precision Medicine. *Nat Cancer* (2020) 1:761–73. doi: 10.1038/s43018-020-0102-y
23. Nashimoto Y, Teraoka Y, Banan Sadeghian R, Nakamasu A, Arima Y, Hanada S, et al. Perfusable Vascular Network With a Tissue Model in a Microfluidic Device. *J Vis Exp* (2018) 2018:506–18. doi: 10.3791/57242
24. Fujii M, Matano M, Toshimitsu K, Takano A, Mikami Y, Nishikori S, et al. Human Intestinal Organoids Maintain Self-Renewal Capacity and Cellular Diversity in Niche-Inspired Culture Condition. *Cell Stem Cell* (2018) 23:787–93.e6. doi: 10.1016/j.stem.2018.11.016
25. Sato T, Vries RG, Snippert HJ, Van De Wetering M, Barker N, Stange DE, et al. Single Lgr5 Stem Cells Build Crypt-Villus Structures *In Vitro* Without a Mesenchymal Niche. *Nature* (2009) 459:262–5. doi: 10.1038/nature07935
26. Ootani A, Li X, Sangiorgi E, Ho QT, Ueno H, Toda S, et al. Sustained *In Vitro* Intestinal Epithelial Culture Within a Wnt-Dependent Stem Cell Niche. *Nat Med* (2009) 15:701–6. doi: 10.1038/nm.1951
27. Mansour AA, Gonçalves JT, Bloyd CW, Li H, Fernandes S, Quang D, et al. An *In Vivo* Model of Functional and Vascularized Human Brain Organoids. *Nat Biotechnol* (2018) 36:432–41. doi: 10.1038/nbt.4127
28. Grebenyuk S, Ranga A. Engineering Organoid Vascularization. *Front Bioeng Biotechnol* (2019) 7:39. doi: 10.3389/fbioe.2019.00039
29. Wörsdörfer P, Dalda N, Kern A, Krüger S, Wagner N, Kwok CK, et al. Generation of Complex Human Organoid Models Including Vascular Networks by Incorporation of Mesodermal Progenitor Cells. *Sci Rep* (2019) 9:1–13. doi: 10.1038/s41598-019-52204-7
30. Yan HHN, Siu HC, Law S, Ho SL, Yue SSK, Tsui WY, et al. A Comprehensive Human Gastric Cancer Organoid Biobank Captures Tumor Subtype Heterogeneity and Enables Therapeutic Screening. *Cell Stem Cell* (2018) 23:882–897.e11. doi: 10.1016/j.stem.2018.09.016
31. Van De Wetering M, Francies HE, Francis JM, Bounova G, Iorio F, Pronk A, et al. Prospective Derivation of a Living Organoid Biobank of Colorectal Cancer Patients. *Cell* (2015) 161:933–45. doi: 10.1016/j.cell.2015.03.053
32. Sachs N, de Ligt J, Kopper O, Gogola E, Bounova G, Weeber F, et al. A Living Biobank of Breast Cancer Organoids Captures Disease Heterogeneity. *Cell* (2018) 172:373–86.e10. doi: 10.1016/j.cell.2017.11.010
33. Dijkstra KK, Cattaneo CM, Weeber F, Chalabi M, van de Haar J, Fanchi LF, et al. Generation of Tumor-Reactive T Cells by Co-Culture of Peripheral Blood Lymphocytes and Tumor Organoids. *Cell* (2018) 174:1586–1598.e12. doi: 10.1016/j.cell.2018.07.009
34. Sebrell TA, Hashimi M, Sidar B, Wilkinson RA, Kirpotina L, Quinn MT, et al. Bimczok D. A Novel Gastric Spheroid Co-Culture Model Reveals Chemokine-Dependent Recruitment of Human Dendritic Cells to the Gastric Epithelium. *Cmgh* (2019) 8:157–171.e3. doi: 10.1016/j.jcmgh.2019.02.010
35. Schnalzger TE, Groot MH, Zhang C, Mosa MH, Michels BE, Röder J, et al. 3D Model for CAR -Mediated Cytotoxicity Using Patient-Derived Colorectal Cancer Organoids. *EMBO J* (2019) 38:e100928. doi: 10.15252/embj.2018100928
36. Kong JCH, Guerra GR, Millen RM, Roth S, Xu H, Neeson PJ, et al. Tumor-Infiltrating Lymphocyte Function Predicts Response to Neoadjuvant Chemoradiotherapy in Locally Advanced Rectal Cancer. *JCO Precis Oncol* (2018) 2:1–15. doi: 10.1200/po.18.00075
37. Vlachogiannis G, Hedayat S, Vatsiou A, Jamin Y, Fernández-Mateos J, Khan K, et al. Patient-Derived Organoids Model Treatment Response of Metastatic Gastrointestinal Cancers. *Science* (2018) 359:920–6. doi: 10.1126/science.aao2774
38. DeNardo DG, Barreto JB, Andreu P, Vasquez L, Tawfik D, Kolhatkar N, et al. CD4+ T Cells Regulate Pulmonary Metastasis of Mammary Carcinomas by Enhancing Protumor Properties of Macrophages. *Cancer Cell* (2009) 16:91–102. doi: 10.1016/j.ccr.2009.06.018
39. Ganesh K, Wu C, O'Rourke KP, Szeglin BC, Zheng Y, Sauvé CEG, et al. A Rectal Cancer Organoid Platform to Study Individual Responses to Chemoradiation. *Nat Med* (2019) 25:1607–14. doi: 10.1038/s41591-019-0584-2
40. Driehuis E, Kolders S, Spelier S, Lõhmussaar K, Willems SM, Devriese LA, et al. Oral Mucosal Organoids as a Potential Platform for Personalized Cancer Therapy. *Cancer Discov* (2019) 9:852–71. doi: 10.1158/2159-8290.CD-18-1522
41. Pasch CA, Favreau PF, Yueh AE, Babiarz CP, Gillette AA, Sharick JT, et al. Patient-Derived Cancer Organoid Cultures to Predict Sensitivity to Chemotherapy and Radiation. *Clin Cancer Res* (2019) 25:5376–87. doi: 10.1158/1078-0432.CCR-18-3590
42. Neal JT, Li X, Zhu J, Giangarra V, Grzeskowiak CL, Ju J, et al. Organoid Modeling of the Tumor Immune Microenvironment. *Cell* (2018) 175:1972–88.e16. doi: 10.1016/j.cell.2018.11.021
43. Li X, Ootani A, Kuo C. An Air-Liquid Interface Culture System for 3D Organoid Culture of Diverse Primary Gastrointestinal Tissues. *Methods Mol Biol* (2016) 1422:33–40. doi: 10.1007/978-1-4939-3603-8_4
44. Aref AR, Campisi M, Ivanova E, Portell A, Larios D, Piel BP, et al. 3D Microfluidic: Ex Vivo Culture of Organotypic Tumor Spheroids to Model Immune Checkpoint Blockade. *Lab Chip* (2018) 18:3129–43. doi: 10.1039/c8lc00322j
45. Jenkins RW, Aref AR, Lizotte PH, Ivanova E, Stinson S, Zhou CW, et al. Ex Vivo Profiling of PD-1 Blockade Using Organotypic Tumor Spheroids. *Cancer Discov* (2018) 8:196–215. doi: 10.1158/2159-8290.CD-17-0833
46. Kitajima S, Ivanova E, Guo S, Yoshida R, Campisi M, Sundararaman SK, et al. Suppression of STING Associated With Lkb1 Loss in KRAS-Driven Lung Cancer. *Cancer Discov* (2019) 9:34–45. doi: 10.1158/2159-8290.CD-18-0689
47. Kane KIW, Moreno EL, Hachi S, Walter M, Jarazo J, Oliveira MAP, et al. Automated Microfluidic Cell Culture of Stem Cell Derived Dopaminergic Neurons. *Sci Rep* (2019) 9:1–12. doi: 10.1038/s41598-018-34828-3
48. Powley IR, Patel M, Miles G, Pringle H, Howells L, Thomas A, et al. Patient-Derived Explants (PDEs) as a Powerful Preclinical Platform for Anti-Cancer Drug and Biomarker Discovery. *Br J Cancer* (2020) 122:735–44. doi: 10.1038/s41416-019-0672-6
49. Rodrigues T, Kundu B, Silva-Correia J, Kundu SC, Oliveira JM, Reis RL, et al. Emerging Tumor Spheroids Technologies for 3D *In Vitro* Cancer Modeling. *Pharmacol Ther* (2018) 184:201–11. doi: 10.1016/j.pharmthera.2017.10.018
50. Seino T, Kawasaki S, Shimokawa M, Tamagawa H, Toshimitsu K, Fujii M, et al. Human Pancreatic Tumor Organoids Reveal Loss of Stem Cell Niche Factor Dependence During Disease Progression. *Cell Stem Cell* (2018) 22:454–467.e6. doi: 10.1016/j.stem.2017.12.009
51. Fujii M, Shimokawa M, Date S, Takano A, Matano M, Nanki K, et al. A Colorectal Tumor Organoid Library Demonstrates Progressive Loss of Niche Factor Requirements During Tumorigenesis. *Cell Stem Cell* (2016) 18:827–38. doi: 10.1016/j.stem.2016.04.003
52. Drost J, Van Jaarsveld RH, Ponsioen B, Zimberlin C, Van Boxtel R, Buijs A, et al. Sequential Cancer Mutations in Cultured Human Intestinal Stem Cells. *Nature* (2015) 521:43–7. doi: 10.1038/nature14415
53. Bartfeld S, Bayram T, Van De Wetering M, Huch M, Begthel H, Kujala P, et al. *In Vitro* Expansion of Human Gastric Epithelial Stem Cells and Their Responses to Bacterial Infection. *Gastroenterology* (2015) 148:126–136.e6. doi: 10.1053/j.gastro.2014.09.042

54. Boj SF, Hwang C, Baker LA, Chio IIC, Engle DD, Corbo V, et al. Organoid Models of Human and Mouse Ductal Pancreatic Cancer. *Cell* (2015) 160:324–38. doi: 10.1016/j.cell.2014.12.021
55. Tata PR, Mou H, Pardo-Saganta A, Zhao R, Prabhu M, Law BM, et al. Dedifferentiation of Committed Epithelial Cells Into Stem Cells *In Vivo*. *Nature* (2013) 503:218–23. doi: 10.1038/nature12777
56. Ren W, Lewandowski BC, Watson J, Aihara E, Iwatsuki K, Bachmanov AA, et al. Single Lgr5- or Lgr6-Expressing Taste Stem/Progenitor Cells Generate Taste Bud Cells Ex Vivo. *Proc Natl Acad Sci U.S.A.* (2014) 111:16401–6. doi: 10.1073/pnas.1409064111
57. Sato T, Stange DE, Ferrante M, Vries RGJ, Van Es JH, Van Den Brink S, et al. Long-Term Expansion of Epithelial Organoids From Human Colon, Adenoma, Adenocarcinoma, and Barrett's Epithelium. *Gastroenterology* (2011) 141:1762–72. doi: 10.1053/j.gastro.2011.07.050
58. Huch M, Dorrell C, Boj SF, Van Es JH, Li VSW, Van De Wetering M, et al. *In Vitro* Expansion of Single Lgr5 + Liver Stem Cells Induced by Wnt-Driven Regeneration. *Nature* (2013) 494:247–50. doi: 10.1038/nature11826
59. Turco MY, Gardner L, Hughes J, Cindrova-Davies T, Gomez MJ, Farrell L, et al. Long-Term, Hormone-Responsive Organoid Cultures of Human Endometrium in a Chemically Defined Medium. *Nat Cell Biol* (2017) 19:568–77. doi: 10.1038/ncb3516
60. Kessler M, Hoffmann K, Brinkmann V, Thieck O, Jackisch S, Toelle B, et al. The Notch and Wnt Pathways Regulate Stemness and Differentiation in Human Fallopian Tube Organoids. *Nat Commun* (2015) 6:1–11. doi: 10.1038/ncomms9989
61. Karthaus WR, Iaquinta PJ, Drost J, Gracanin A, Van Boxtel R, Wongvipat J, et al. Identification of Multipotent Luminal Progenitor Cells in Human Prostate Organoid Cultures. *Cell* (2014) 159:163–75. doi: 10.1016/j.cell.2014.08.017
62. Kopper O, de Witte CJ, Lõhmussaar K, Valle-Inclan JE, Hami N, Kester L, et al. An Organoid Platform for Ovarian Cancer Captures Intra- and Interpatient Heterogeneity. *Nat Med* (2019) 25:838–49. doi: 10.1038/s41591-019-0422-6
63. Schutgens F, Rookmaaker MB, Margaritis T, Rios A, Ammerlaan C, Jansen J, et al. Tubuloids Derived From Human Adult Kidney and Urine for Personalized Disease Modeling. *Nat Biotechnol* (2019) 37:303–13. doi: 10.1038/s41587-019-0048-8
64. Nanduri LSY, Baanstra M, Faber H, Rocchi C, Zwart E, De Haan G, et al. Purification and Ex Vivo Expansion of Fully Functional Salivary Gland Stem Cells. *Stem Cell Rep* (2014) 3:957–64. doi: 10.1016/j.stemcr.2014.09.015
65. Watanabe K, Ueno M, Kamiya D, Nishiyama A, Matsumura M, Wataya T, et al. A ROCK Inhibitor Permits Survival of Dissociated Human Embryonic Stem Cells. *Nat Biotechnol* (2007) 25:681–6. doi: 10.1038/nbt1310
66. Bhaduri A, Andrews MG, Mancia Leon W, Jung D, Shin D, Allen D, et al. Cell Stress in Cortical Organoids Impairs Molecular Subtype Specification. *Nature* (2020) 578:142–8. doi: 10.1038/s41586-020-1962-0
67. Liu T, Han C, Wang S, Fang P, Ma Z, Xu L, et al. Cancer-Associated Fibroblasts: An Emerging Target of Anti-Cancer Immunotherapy. *J Hematol Oncol* (2019) 12:1–15. doi: 10.1186/s13045-019-0770-1
68. Biffi G, Oni TE, Spielman B, Hao Y, Elyada E, Park Y, et al. Il1-Induced Jak/STAT Signaling is Antagonized by Tgfβ to Shape CAF Heterogeneity in Pancreatic Ductal Adenocarcinoma. *Cancer Discovery* (2019) 9:282–301. doi: 10.1158/2159-8290.CD-18-0710
69. Chakrabarti J, Holokai L, Syu LJ, Steele NG, Chang J, Wang J, et al. Hedgehog Signaling Induces PD-L1 Expression and Tumor Cell Proliferation in Gastric Cancer. *Oncotarget* (2018) 9:37439–57. doi: 10.18632/oncotarget.26473
70. Holokai L, Chakrabarti J, Broda T, Chang J, Hawkins JA, Sundaram N, et al. Increased Programmed Death-Ligand 1 is an Early Epithelial Cell Response to Helicobacter Pylori Infection. *PloS Pathog* (2019) 15:e1007468. doi: 10.1371/journal.ppat.1007468
71. Forsythe SD, Erali RA, Sasikumar S, Laney P, Shelkey E, D'Agostino R, et al. Organoid Platform in Preclinical Investigation of Personalized Immunotherapy Efficacy in Appendiceal Cancer: Feasibility Study. *Clin Cancer Res* (2021) 27:5141–50. doi: 10.1158/1078-0432.CCR-21-0982
72. Sontheimer-Phelps A, Hassell BA, Ingber DE. Modelling Cancer in Microfluidic Human Organs-on-Chips. *Nat Rev Cancer* (2019) 19:65–81. doi: 10.1038/s41568-018-0104-6
73. Businaro L, De Ninno A, Schiavoni G, Lucarini V, Ciasca G, Gerardino A, et al. Cross Talk Between Cancer and Immune Cells: Exploring Complex Dynamics in a Microfluidic Environment. *Lab Chip* (2013) 13:229–39. doi: 10.1039/c2lc40887b
74. Halldorsson S, Lucumi E, Gómez-Sjöberg R, Fleming RMT. Advantages and Challenges of Microfluidic Cell Culture in Polydimethylsiloxane Devices. *Biosens Bioelectron* (2015) 63:218–31. doi: 10.1016/j.bios.2014.07.029
75. Li X, Nadauld L, Ootani A, Corney DC, Pai RK, Gevaert O, et al. Oncogenic Transformation of Diverse Gastrointestinal Tissues in Primary Organoid Culture. *Nat Med* (2014) 20:769–77. doi: 10.1038/nm.3585
76. Xia T, Du WL, Chen XY, Zhang YN. Organoid Models of the Tumor Microenvironment and Their Applications. *J Cell Mol Med* (2021) 25:5829–41. doi: 10.1111/jcmm.16578
77. Yu F, Hunziker W, Choudhury D. Engineering Microfluidic Organoid-on-a-Chip Platforms. *Micromachines* (2019) 10:165. doi: 10.3390/mi10030165
78. Bhatia SN, Ingber DE. Microfluidic Organs-on-Chips. *Nat Biotechnol* (2014) 32:760–72. doi: 10.1038/nbt.2989
79. Zumwalde NA, Haag JD, Sharma D, Mirrielees JA, Wilke LG, Gould MN, et al. Analysis of Immune Cells From Human Mammary Ductal Epithelial Organoids Reveals Vδ2+ T Cells That Efficiently Target Breast Carcinoma Cells in the Presence of Bisphosphonate. *Cancer Prev Res* (2016) 9:305–16. doi: 10.1158/1940-6207.CAPR-15-0370-T
80. Tsai S, McOlash L, Palen K, Johnson B, Duris C, Yang Q, et al. Development of Primary Human Pancreatic Cancer Organoids, Matched Stromal and Immune Cells and 3D Tumor Microenvironment Models. *BMC Cancer* (2018) 18:1–13. doi: 10.1186/s12885-018-4238-4
81. Langan LM, Dodd NJF, Owen SF, Purcell WM, Jackson SK, Jha AN. Correction: Direct Measurements of Oxygen Gradients in Spheroid Culture System Using Electron Paramagnetic Resonance Oximetry. *PloS One* (2016) 11:e0149492. doi: 10.1371/journal.pone.0160795
82. Hirschhaeuser F, Menne H, Dittfeld C, West J, Mueller-Klieser W, Kunz-Schughart LA. Multicellular Tumor Spheroids: An Underestimated Tool is Catching Up Again. *J Biotechnol* (2010) 148:3–15. doi: 10.1016/j.jbiotec.2010.01.012
83. Waldman AD, Fritz JM, Lenardo MJ. A Guide to Cancer Immunotherapy: From T Cell Basic Science to Clinical Practice. *Nat Rev Immunol* (2020) 20:651–68. doi: 10.1038/s41577-020-0306-5
84. Majzner RG, Mackall CL. Clinical Lessons Learned From the First Leg of the CAR T Cell Journey. *Nat Med* (2019) 25:1341–55. doi: 10.1038/s41591-019-0564-6
85. Michie J, Beavis PA, Freeman AJ, Vervoort SJ, Ramsbottom KM, Narasimhan V, et al. Antagonism of IAPs Enhances CAR T-Cell Efficacy. *Cancer Immunol Res* (2019) 7:183–92. doi: 10.1158/2326-6066.CIR-18-0428
86. Badalamenti G, Fanale D, Incorvaia L, Barraco N, Listì A, Maragliano R, et al. Role of Tumor-Infiltrating Lymphocytes in Patients With Solid Tumors: Can a Drop Dig a Stone? *Cell Immunol* (2019) 343:103753. doi: 10.1016/j.cellimm.2018.01.013
87. Motzer RJ, Escudier B, McDermott DF, George S, Hammers HJ, Srinivas S, et al. Nivolumab Versus Everolimus in Advanced Renal-Cell Carcinoma. *N Engl J Med* (2015) 373:1803–13. doi: 10.1056/nejmoa1510665
88. Migden MR, Rischin D, Schmults CD, Guminski A, Hauschild A, Lewis KD, et al. PD-1 Blockade With Cemiplimab in Advanced Cutaneous Squamous-Cell Carcinoma. *N Engl J Med* (2018) 379:341–51. doi: 10.1056/nejmoa1805131
89. Gonzalez-Rodriguez E, Rodríguez-Abreu D, Boronat M. Nivolumab for Squamous-Cell Cancer of Head and Neck. *N Engl J Med* (2017) 376:595–6. doi: 10.1056/nejmc1615565
90. Raimondi G, Mato-Berciano A, Pascual-Sabater S, Rovira-Rigau M, Cuatrecasas M, Fondevila C, et al. Patient-Derived Pancreatic Tumour Organoids Identify Therapeutic Responses to Oncolytic Adenoviruses. *EBioMedicine* (2020) 56:102786. doi: 10.1016/j.ebiom.2020.102786
91. Deng J, Wang ES, Jenkins RW, Li S, Dries R, Yates K, et al. CDK4/6 Inhibition Augments Antitumor Immunity by Enhancing T-Cell Activation. *Cancer Discovery* (2018) 8:216–33. doi: 10.1158/2159-8290.CD-17-0915
92. Courau T, Bonnereau J, Chicoteau J, Bottois H, Remark R, Assante Miranda L, et al. Cocultures of Human Colorectal Tumor Spheroids With Immune Cells Reveal the Therapeutic Potential of MICA/B and NKG2A Targeting for Cancer Treatment. *J Immunother Cancer* (2019) 7:1–14. doi: 10.1186/s40425-019-0553-9

93. Gonzalez-Exposito R, Semiannikova M, Griffiths B, Khan K, Barber LJ, Woolston A, et al. CEA Expression Heterogeneity and Plasticity Confer Resistance to the CEA-Targeting Bispecific Immunotherapy Antibody Cibisatamab (CEA-TCB) in Patient-Derived Colorectal Cancer Organoids. *J Immunother Cancer* (2019) 7:101. doi: 10.1186/s40425-019-0575-3
94. Kim J, Koo BK, Knoblich JA. Human Organoids: Model Systems for Human Biology and Medicine. *Nat Rev Mol Cell Biol* (2020) 21:571–84. doi: 10.1038/s41580-020-0259-3

Conflict of Interest: The authors declare that the research was conducted in the absence of any commercial or financial relationships that could be construed as a potential conflict of interest.

Publisher's Note: All claims expressed in this article are solely those of the authors and do not necessarily represent those of their affiliated organizations, or those of the publisher, the editors and the reviewers. Any product that may be evaluated in this article, or claim that may be made by its manufacturer, is not guaranteed or endorsed by the publisher.

frontiers | Frontiers in Immunology

TYPE Original Research
PUBLISHED 18 August 2022
DOI 10.3389/fimmu.2022.901662

OPEN ACCESS

EDITED BY
Tian Li,
Independent Researcher, Xi'an, China

REVIEWED BY
Yaozeng Xu,
The First Affiliated Hospital of Soochow University, China
Xing Huang,
Zhejiang University, China

*CORRESPONDENCE
Xiaodan Lai
461610115@qq.com
Zhe Wang
wangzhe@tmmu.edu.cn

†These authors have contributed equally to this work and share first authorship

SPECIALTY SECTION
This article was submitted to Cancer Immunity and Immunotherapy, a section of the journal Frontiers in Immunology

RECEIVED 22 March 2022
ACCEPTED 28 July 2022
PUBLISHED 18 August 2022

CITATION
Xie L, Wu S, He R, Li S, Lai X and Wang Z (2022) Identification of epigenetic dysregulation gene markers and immune landscape in kidney renal clear cell carcinoma by comprehensive genomic analysis. *Front. Immunol.* 13:901662. doi: 10.3389/fimmu.2022.901662

Identification of epigenetic dysregulation gene markers and immune landscape in kidney renal clear cell carcinoma by comprehensive genomic analysis

Linli Xie[1†], Shuang Wu[2†], Rong He[1], Sisi Li[3], Xiaodan Lai[4*] and Zhe Wang[2*]

[1]Department of Pharmacy, Southwest Hospital, Third Military Medical University (Army Medical University), Chongqing, China, [2]Department of Oncology and Southwest Cancer Center, Southwest Hospital, Third Military Medical University (Army Medical University), Chongqing, China, [3]Institute of Pathology and Southwest Cancer Center, Southwest Hospital, Third Military Medical University (Army Medical University), Chongqing, China, [4]Department of Pharmacy, No. 958 Hospital of Chinese People's Liberation Army (PLA), Chongqing, China

Kidney cancer is one the most lethal cancers of the urinary system, but current treatments are limited and its prognosis is poor. This study focused on kidney renal clear cell carcinoma (KIRC) and analyzed the relationship between epigenetic alterations and KIRC prognosis, and explored the prognostic significance of these findings in KIRC patients. Based on multi-omics data, differentially expressed histone-modified genes were identified using the R package limma package. Gene enhancers were detected from data in the FANTOM5 database. Gene promoters were screened using the R package ChIPseeker, and the Bumphunter in the R package CHAMP was applied to screen differentially methylated regions (DMR). Kyoto Encyclopedia of Genes and Genomes (KEGG) pathway analysis and Gene Ontology (GO) functional enrichment analysis of genes was performed using the R package clusterProfiler. We identified 51 dysregulated epigenetic protein coding genes (epi-PCGs) from 872 epi-PCGs, and categorized three molecular subtypes (C1, C2, and C3) of KIRC samples with significantly different prognosis. Notably, among the three molecular subtypes, we found a markedly differential immune features in immune checkpoints, cytokines, immune signatures, and immune cell distribution. C2 subtype had significantly lower enrichment score of IFNγ, cytotoxic score (CYT), and angiogenesis. In addition, an 8-gene signature containing 8 epi-PCGs (ETV4, SH2B3, FATE1, GRK5, MALL, HRH2, SEMA3G, and SLC10A6) was developed for predicting KIRC prognosis. Prognosis of patients with a high 8-gene signature score was significantly worse than those with a low 8-gene signature score, which was also validated by the independent validation data. The 8-gene signature had a better performance compared with previous signatures of KIRC. Overall, this study highlighted the important role of epigenetic regulation

in KIRC development, and explored prognostic epi-PCGs, which may provide a guidance for exploiting further pathological mechanisms of KIRC and for developing novel drug targets.

KEYWORDS

kidney cancer, multi-omics data, prognosis, histone-modified genes, epigenetic modification

Introduction

Kidney cancer is the most lethal cancer of the urinary system, and shows an increasing incidence in recent years (1, 2). Due to a lack of specific clinical manifestations of kidney cancer, about 20-25% of patients have already developed distant metastasis by the time of diagnosis (3). For localized kidney cancer, local surgical resection in the form of partial or radical nephrectomy offers the possibility of partial cure. However, patients who have developed local recurrence or distant metastases are relatively resistant to conventional chemotherapy and radiotherapy and have a low 5-year survival rate (4, 5). Immunotherapy, especially immune checkpoint inhibitors, creates the hope for treating metastatic kidney cancer. For instance, monotherapy (nivolumab) or combined therapy (nivolumab and ipilimumab) shows favorable results on prolonged oval survival (6). Combined with other therapeutics such as tyrosine kinase inhibitors (TKIs), prolonged progression-free survival can be also realized in early phase trials (7). Nevertheless, a large proportion of kidney cancer patients still could not benefit from the immunotherapy due to individual differences. Therefore, to benefit more patients from immunotherapy, molecular subtyping may serve a role for assisting personalized therapies and reducing unnecessary treatment. So far, we face a lack of biomarkers for prognosis prediction and drug targets for therapeutic intervention, target-specific precision therapy for kidney cancer treatment, and KIRC patients often develop a poor prognosis. Therefore, there is an urgent need to find reliable new biomarkers to better understand the mechanisms of kidney cancer progression and to further develop new therapeutic strategies.

The essence of tumor occurrence and development is the inactivation of tumor suppressor genes and the activation of tumor-promoting genes. It takes a long time from the initial genetic change to evolve to a solid tumor. There is an epigenetic change prior to genetic change, or it is said that dysregulated gene expressions are caused by epigenetic changes. Studies have shown that epigenetic changes can regulate gene expression. Common epigenetic modifications include DNA methylation and acetylation, histone methylation and acetylation. Especially, histones modification, which commonly refers to methylation and acetylation, plays an important role in abnormal expression of genes. The modification of histone acetylation is based on the acetylation modification of histone lysine residues, which is largely related to transcriptional activation (8), and such a transcriptional activation is closely associated with the phenotype of a variety of tumors (9). When hyperacetylation occurs, particularly in proto-oncogenes, gene expression may be activated, and the hypoacetylation of tumor suppressor genes is usually located in the promoter, which will cause gene silencing when co-occurring with DNA methylation (10). The function of histone methylation modification is more complicated than that of histone acetylation modification in tumors (11, 12), but it is generally believed that the modification of histone methylation will reduce the transcription of target genes (13). Still, the relationship between such a modification and tumor development needs further research.

Current studies have shown that abnormal histone methylation is an independent prognostic marker of kidney cancer and a potential clinical target of kidney cancer (14–16). Various gene signatures related to epigenetic dysregulation have been developed for predicting the prognosis of renal cell carcinoma. For example, Zhou et al. analyzed the copy number variations (CNVs) of N6-methyladenosine (m6A) regulatory genes in clear cell renal cell carcinoma (ccRCC) samples, and observed a significant correlation between their CNVs and either overall survival or disease-free survival (17). Based on the expression of 19 m6A regulators, Zheng et al. constructed three molecular subtypes and established a seven-gene signature for ccRCC patients (18). Using two-way hierarchical clustering for methylation array data of ccRCC, three candidate genes with hypermethylation were identified and were significantly associated with metastatic free survival (19). However, limited studies comprehensively analyzed the epigenetic-dysregulated genes in kidney cancer, and less findings on the effect of epigenetic dysregulation on tumorigenesis and tumor pathology from different aspects such as tumor microenvironment and immune response were available.

Therefore, in this study, we focused on differential expressed genes and epigenetic-dysregulated genes concerning H3K27ac,

H3K4me1, and H3K4me3, and identified 51 epigenetic protein-coding genes (epi-PCGs) associated with RCC prognosis. We constructed three molecular subtypes based on 51 epi-PCGs, and found significant differences on tumor microenvironment among the three subtypes. Finally, with the epi-PCGs, we constructed an 8-gene prognostic risk model that demonstrated a stable prediction performance in both the training set and the verification set. Our research results help better understand the abnormal epigenetic regulation of PCG expression in KIRC.

Materials and methods

Data download and preprocessing

The work flow of this study was shown in Figure 1. We downloaded the gene expression profile of kidney renal clear cell carcinoma (KIRC) and expression profile data such as fragments per kilobase million (FPKM), count number of normal samples, and clinical information of corresponding healthy control samples from the TCGA database (The Cancer Genome Atlas, https://www.cancer.gov/about-nci/organization/ccg/research/structural-genomics/tcga),and converted FPKM to TPM (transcript per million). Based on the gene annotation file of GENCODE, the expression profile was divided into long-non coding RNAs (lncRNAs) and positive correlation genes (PCGs), and we converted the Ensembl ID of these genes into Gene Symbol. At the same time, the RECA-EU data set with survival time was downloaded from the International Cancer Genome Consortium (ICGC) (https://dcc.icgc.org/) database. A total of 526 and 91 KIRC samples were included finally in TCGA and ICGC data sets respectively. See Table 1 for the clinical information of the processed samples.

The 450K methylation chip data and preprocessing

In this study, the KIRC chip data (HumanMethylation450 microarray) (20) was downloaded from TCGA database. According to the provided chip data, CpG with cross-reactive probes were removed. We further excluded the unstable methylation sites including CpG sites and single nucleotide sites locating in X/Y chromosome. Based on the sample number of KIRC, the chip data was split into 319 KIRC samples and 160 normal samples. The K-nearest neighbor (KNN) method (21), which uses distance measurement to identify neighboring points and can estimate missing values with the complete data of neighboring observations, was employed here to input missing values in the KIRC sample data.

Histone data and preprocessing

We downloaded the hg19 version of the GSE86091 dataset with paracancerous samples and tumor samples from the Gene Expression Omibus (GEO) database (22). The dataset contained three histone information, namely, H3K4me1, H3K4me3, and H3K27ac.

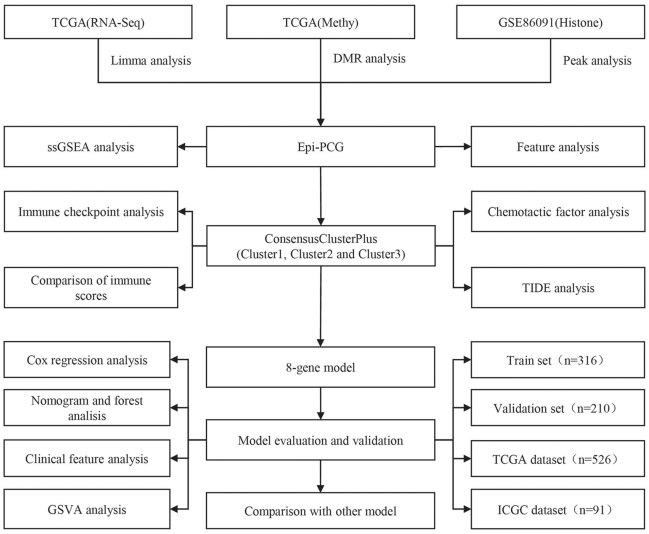

FIGURE 1
The work flow of this study.

10.3389/fimmu.2022.901662

TABLE 1 Clinical information of the sample in TCGA and ICGC datasets.

Clinical Features	TCGA	ICGC
OS		
Alive	356	61
Dead	170	30
Gender		
Male	343	52
Female	183	39
T Stage		
T1	267	
T2	69	
T3	179	
T4	11	
N Stage		
N0	238	
N1	16	
NX	272	
M Stage		
M0	436	
M1	80	
MX	10	
Stage		
I	261	
II	57	
III	123	
IV	82	
X	3	
Grade		
G1	13	
G2	226	
G3	205	
G4	74	
GX	8	
Age		
>60	262	45
<=60	264	46

Identification of PCGs with epigenetic dysregulation

The R package limma (23) was used to identify differentially expressed PCGs in KIRC. The P value was determined by the Benjami-Hochberg method, and PCGs with false discovery rate (FDR)< 0.05 and |log2 fold change (FC)|> 1 were considered significant. Secondly, we screened peaks specific to KIRC based on the physical location of histones-modified peaks, and only the peaks with p< 0.05 were retained as differential peaks. Then GTF file from GENCODE was combined to obtain histone-modified differentially genes. Human enhancer database was downloaded from FANTOM5 to screen gene enhancers. A gene promoter was defined as 2 kb upstream and 0.5 kb downstream of the transcription start site (TSS). The R package ChIPseeker (24) was employed to identify gene promoter. DMR was detected using The Bumphunter method in the R package CHAMP, and the area with BumphunterDMR.p.value< 0.001 was considered as a significant DMR. Finally, PCGs abnormally regulated by epigenetics were defined by the following criteria (1): PCGs were differentially expressed in KIRC and normal samples; (2) promoters or enhancers overlapped at least one differential histone modification region or differentially methylated regions (named epi-PCG, non-epi-PCG).

Genomic characterization of epigenetically dysregulated PCG

To compare the genomic characteristics of PCGs with or without epigenetic dysregulation, we analyzed the exons, transcripts, and number and length of the four types of genes epi-PCG and non-epi-PCG.

PCG genomic map of epigenetic dysregulation characterized by different histone modifications

To explore the epigenetic characteristics of PCG caused by histone modification, the distribution characteristics of the promoters and enhancers of different histone modification epi-PCG on the genome were analyzed.

Functional enrichment analysis on candidate PCGs with epigenetic dysregulation specific in KIRC

To understand the function of epigenetically dysregulated PCG, we used clusterProfiler in the R software package (v3.14.0) (25) to perform KEGG pathway analysis and GO function enrichment analysis on epi-PCGs related genes.

Molecular subtyping of PCGs based on epigenetic dysregulation

From the TCGA and ICGC data sets, univariate analysis on epi-PCGs was performed to screen prognosis-related genes (p< 0.05), followed by molecular subtyping. Genes related to survival in the two data sets were selected as cluster genes, and the samples from the TCGA and ICGC data set were clustered by ConsensusClusterPlus (26) to determine the optimal cluster

number according to the cumulative distribution function (CDF) number. Next, we compared the distribution of pathways in different subtypes, and analyzed the immune microenvironment and chances of KIRC patients benefiting from receiving immunotherapy.

Random grouping of training set samples and single-factor analysis

A total of 526 samples in the TCGA data set were divided into a training set and a validation set. To avoid random distribution error from affecting the stability of subsequent modeling, all the samples were randomly grouped for 100 times without replacement. Here, the group sampling was performed based on the ratio of training set: verification set = 3:2. The most suitable training set and validation set was selected according to the following conditions: 1) The two groups were similar in age distribution and gender ratio; 2) The two randomly grouped data sets had similar numbers of samples after clustering the gene expression profiles. Finally, the training set and test set samples were assessed by chi-square test to validate the grouping. In the training set data, for each epi-PCG, the R package survival coxph function was used to perform univariate Cox analysis. $P< 0.05$ was the threshold to screen genes with prognostic significance.

Least absolute shrinkage and selection operator (Lasso) cox regression for multi-factor risk analysis

To facilitate clinical testing, it is necessary to further reduce the number of prognostic genes in the model while maintaining a high accuracy. The Lasso method shapes a more refined model by constructing a penalty function, and it compresses certain coefficients and sets some coefficients to zero at the same time (27). This method has the advantages of subset shrinkage, and as a biased estimation for processing data with multicollinearity, it can realize the selection of variables while estimating the parameters in solving the problem of multicollinearity in regression analysis. We used glmnet in the R software package to perform lasso cox regression analysis, observed the change trajectory of each independent variable, and used 10-fold cross-validation to build the model, and analyzed the confidence interval under each lambda. Stepwise Akaike information criterion (stepAIC) (28) was employed in ensuring the statistical fit of the model and number of parameters used to fit the model. The stepAIC method in the MASS package starts with the most complex model and deletes a variable in turn to reduce the AIC, with a lower value indicating a better model. This algorithm was used here to reduce the number of genes. The RiskScore calculation formula was:

$$RiskScore = \sum_n \ k = 1 Exp_k * Coef_k$$

(Coef: regression coefficient of genes in multivariate Cox regression analysis, n: total number of genes related to prognosis). The RiskScore of each patient was calculated by the formula. Survminer R package (http://www.sthda.com/english/rpkgs/survminer/) was used to determine the optimal cut-off values. We performed z-score transformation on RiskScore, and z-score = 0 was set as a cut-off for dividing samples into high-risk groups (z-score > 0) and low-risk groups (z-score< 0). The Kaplan-Meier method was used to estimate the survival rate and survival time of different groups.

Functional analysis on the model pathways

The R software package GSVA (29) was used to perform single-sample GSEA analysis on the gene expression profile of the samples. The score of each sample on different functions was calculated to obtain the ssGSEA score of each function in each sample, and we further determined the correlation of these functions with RiskScore.

Cell culture

The HK2 cell line (normal human renal tubular epithelial cell line) and all the four human RCC cell lines (786-O, A498, Caki-1 and ACHN) were obtained from the Cell Bank of Type Culture Collection of the Chinese Academy of Sciences (CBTCCCAS, Shanghai, China). The cells were cultured in RPMI 1640 medium (Gibco, United States) or DMEM medium (Gibco, United States) containing 10% fetal bovine serum (Gibco, United States), 100 U/ml penicillin, and 100 mg/ml streptomycin at 37°C in a humidified incubator with 5% CO_2.

Quantitative real-time PCR

Total RNA extract was prepared from HK2 cells and RCC cells using TRIzol Reagent (Beijing Solarbio Technology Co., Ltd., Beijing, China) according to the manufacturer's instructions. The reverse transcription was performed using the TaKaRa PrimeScriptTM RT-PCR kit (TaKaRa, Mountain View, CA). The qRT-PCR was conducted using the SYBR Premix Ex TaqTM (TaKaRa). Eight epi-PCGs mRNA expression levels were evaluated by the 2-ΔΔCT method. The expression of GAPDH served as an internal control. The primer sequences utilized in the present study are listed in Supplementary Table 1.

Western blot

To measure the protein concentrations, RIPA lysis buffer (R0010, Solarbio, China) supplemented with protease inhibitors (Roche) was used to lyse the HK2 cell line and all four human RCC cell lines. The BCA kit (Pierce, Rockford, IL) was used to measure the protein concentrations. After adding the total protein to loading buffer, it was separated using 10% sodium dodecyl sulfate polyacrylamide gel electrophoresis (SDS-PAGE) and then transferred onto polyvinylidene fluoride (PVDF) membrane (Merck Millipore, Billerica, MA). The membrane was blocked with 5% skimmed milk for one hour and subsequently blocked with primary antibodies against ETV4 (Santa Cruz), SH2B3 (Thermo Fisher Scientific), FATE1 (Santa Cruz), GRK5 (Abcam), MALL (Santa Cruz), HRH2 (ABclonal), SEMA3G (Abcam) and SLC10A6 (Santa Cruz) overnight at 4°C. After the PVDF membrane was washed with TBST, it was incubated with the corresponding secondary antibody for two hours. Identification of the proteins was conducted using Pierce SuperSignal West Pico Chemiluminescent Substrate (Termo Fisher, Waltham, MA), following the instruction of the manufacturer. GAPDH antibody was used as an internal reference.

Statistical analysis

R software (v4.1.0) was used to perform all statistical analysis. Student's t test was conducted between two groups. ANOVA test was performed among three groups. Log-rank test was performed in Kaplan-Meier survival analysis, univariate and multivariate Cox regression analysis. In the relation between RiskScore and clinical features, Wilcoxon test was conducted between two groups, and Kruskal-Wallis test was conducted among four groups. Benjamini & Hochberg correction was used to adjust P values. All parameters without special indication in the methods were set as default. $P< 0.05$ or FDR< 0.05 was considered as significant. *P< 0.05, **P< 0.01, ***P< 0.001, ****P< 0.0001. ns, no significant.

Results

Identification of PCGs with epigenetic dysregulation

To analyze the relationship between PCGs expression and epigenetic changes in KIRC, limma was used to identify significantly differentially expressed genes (a total of 2755 PCGs). Combining histone modification data and methylation data, we finally found 872 epi-PCGs and 18629 non-epi-PCGs. Epi-PCGs accounted for only 4.47% of all the PCGs (872/19501).

The number and length of gene exons and transcripts of epi-PCGs and non-epi-PCGs was compared to show the genomic characteristics of epigenetically dysregulated PCGs. The number of epi-PCG transcripts was more than that of non-epi-PCGs, while the length of epi-PCGs transcripts was shorter than that of non-epi-PCGs (Figures 2A, B). Meanwhile, epi-PCGs had more exons and longer length of exons than those of non-epi-PCGs (Figures 2C, D). Furthermore, we systematically analyzed the epi-PCGs in KIRC, and revealed the epi-PCG landscape characterized by different histone modifications and differentially methylated regions (Figure 1E). The data demonstrated that most of the epigenetically dysregulated PCGs were accompanied by a variety of histone modification abnormalities, and that these abnormal histone modifications were mainly concentrated in the promoter region (Figure 2F).

SsGSEA analysis of dysregulated epi-PCGs

To characterize the potential functions of PCG dysregulation caused by abnormal histone modifications, we systematically analyzed the relationship between the expression of epi-PCGs and the pathways in KIRC. Specifically, we extracted the expression profiles of PCGs caused by different histone modifications, and calculated the enrichment scores of each sample in these PCGs using ssGSEA. It was found that the GSEA scores of 6 kinds of dysregulated histones were significantly higher in tumor samples than normal samples, indicating that these dysregulated histones had cancer-promoting effect (Figure 3A).

In addition, we also evaluated the KEGG Pathway score of each sample and analyzed the relationship between the enrichment score of each type of epi-PCG and KEGG Pathway to obtain relevant KEGG Pathway for each type of epi-PCG. A total of 24 pathways, which were the most relevant KEGG Pathways related to the 6 types of epi-PCG, were shown in Figure 3B. The results indicated that different types of epi-PCG-related pathways had certain consistency. Among these 24 pathways, there were tumor-related pathways such as BLADDER_CANCER, hematopoietic cell lineage, JAK-STAT signaling pathway, immune-related pathways such as Toll like receptor signaling pathway, T cell receptor signaling pathway, natural killer cell mediated cytotoxicity. These data suggested that epi-PCGs were closely related to tumor occurrence, development and immunity.

Epigenetic dysregulation of PCGs was closely related to RNA modification

RNA modification is an important epigenetic feature related to a variety of important biological processes. Here, we analyzed the relationship between 6 types of epi-PCGs and m6A and m5C RNA modifications. Specifically, we extracted the expression profile of m6A, m5C, and m1A in KIRC from TCGA, and the correlation between the enrichment scores of 6 types of epi-PCGs and m6A, m5C, and m1A was analyzed (Figure 4A). We found that these

10.3389/fimmu.2022.901662

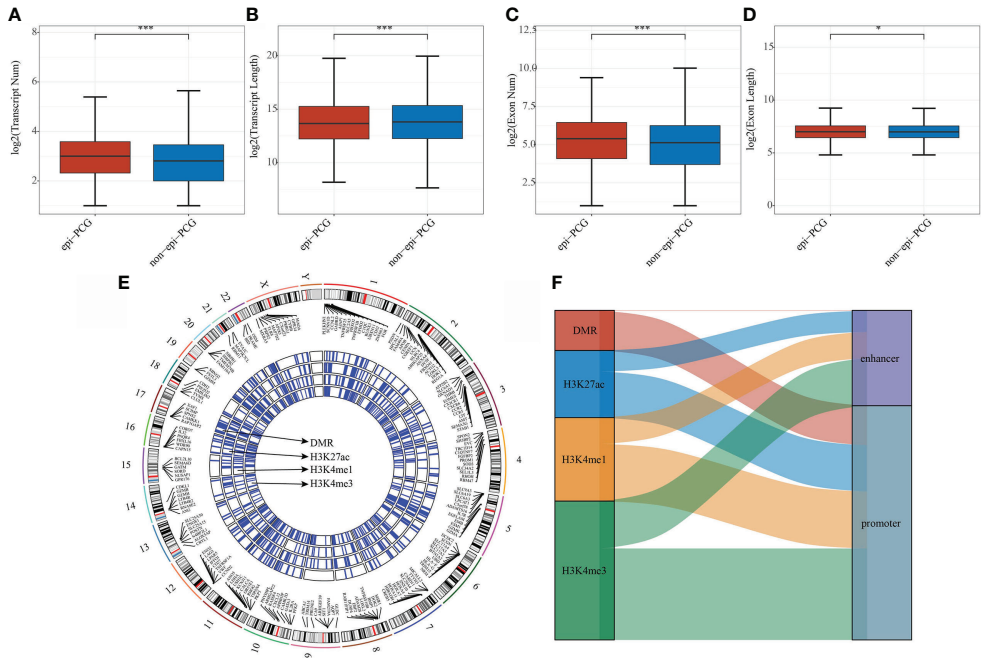

FIGURE 2
Comparison of genomic characteristics of epigenetically dysregulated lncRNA/PCGs (n = 872) and non-epigenetically dysregulated lncRNA/PCGs (n = 18629). **(A)** Comparison of the number of transcripts; **(B)** Comparison of the length of transcripts; **(C)** Comparison of the number of exons; **(D)** Comparison of the lengths of exons; **(E)** Genomic landscape of epi-PCGs characterized by histone modification; **(F)** Location distribution of histone modifications of epi-PCGs. *P < 0.05, ***P < 0.001.

enrichment scores were significantly correlated with m6A, m5C, and m1A. The R software package clusterProfiler (v3.14.0) was further used to perform KEGG pathway analysis and GO function enrichment analysis on the epi-PCGs. For the GO function annotation of genes, 519 BPs with significant differences (FDR<0.05) were annotated; 79 CCs with significant differences (FDR<0.05) were annotated; 48 MFs with significant differences were annotated (FDR<0.05); KEGG pathway enrichment analysis were annotated to 38 significant pathways (FDR<0.05). The top 10 enriched terms were visualized (Figures 4B–E).

Identification of 3 molecular subtypes with prognostic differences based on epi-PCGs

In the TCGA and ICGC data sets, single-factor survival analysis was performed on epi-PCGs, and survival-related genes in both data sets were selected as cluster genes for molecular subtyping. Finally, 51 intersection genes were included (Figure 5A). Analysis of expression differences of the 51 genes between normal and tumor samples showed that these genes had significant differences in expression (Supplementary Figure 1A). In addition, a modification map of some genes on histones was drawn (Supplementary Figures 1B, C). Based on 51 Epi-PCGs, the two data sets were clustered by ConsensusClusterPlus, and the optimal number of clusters was determined according to the cumulative distribution function (CDF). Combining CDF Delta area curve and survival Curve, k = 3 was used to obtain three Epi-PCGs-related subtypes (Figures 5B, C). KM analysis indicated that C2 had a poor prognosis in the TCGA data set, while C1 had a better prognosis (Figure 5D). Similar results were observed in the ICGC data set (Figure 5E).

Studies found that chemokines play a key role in the occurrence and development of tumors. They can mediate a variety of immune cells into the tumor microenvironment, help T cells enter tumor and affect tumor immunity and therapeutic effects. Therefore, we analyzed whether there were expression differences in chemokines among the three molecular subtypes. In the TCGA data set, 26 of 41 chemokines (63.41%) showed significant expression differences in different subtypes (Figure 6A), which suggested that the degree of immune cell infiltration of different subtypes may be different, and that these differences could lead to differences in tumor progression and immunotherapy effects. In addition, 17 of the 18 chemokine receptor genes (94.44%) had significant differences in the expression of the three molecular subtypes (Figure 6B).

10.3389/fimmu.2022.901662

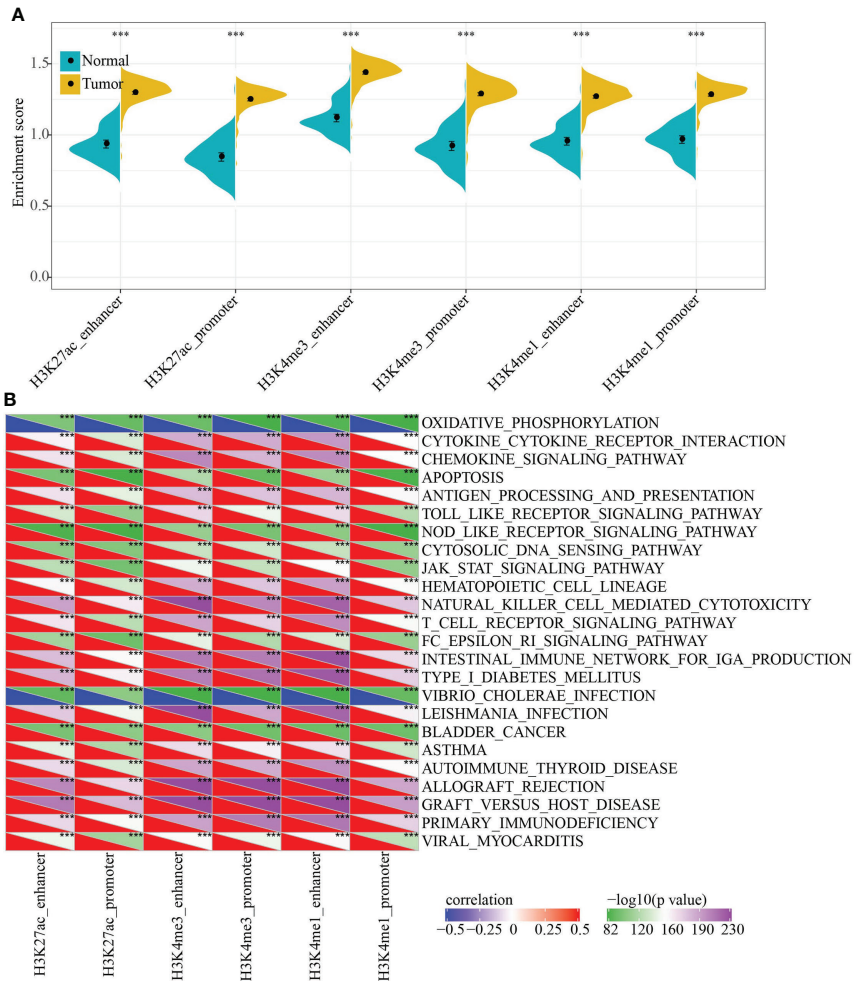

FIGURE 3
Functional enrichment analysis of epi-PCGs. **(A)** Differential expression of 6 kinds of epigenetically dysregulated PCGs in cancer (n = 319) and adjacent cancer (n = 160) tissues; **(B)** The most relevant KEGG Pathway enriched by the 6 kinds of dysregulated PCGs. ***P < 0.001.

CD8 + T cells in the tumor microenvironment can produce interferon-γ (IFNγ) to stimulate the up-regulation of PD-1/PD-L1 and IDO1 gene expression (30, 31). Studies have shown that the up-regulation of IDO1 expression is positively correlated with poor prognosis and tumor progression and metastasis (32, 33). We extracted Th1/IFNγ gene signatures and 47 immune checkpoint-related genes from a previous study (34). In addition, according to Rooney Michael S (35), the average value of GZMA and PRF1 expression levels was used to evaluate the immune cytolysis (CYT) of immune t cell of each patient, then the angiogenesis-related gene set was obtained to evaluate each patient's angiogenesis score (36). The IFNγ score, CYT score and angiogenesis score of each patient were calculated using ssGSEA. It can be observed that there were significant differences in IFNγ scores in each subgroup (Figure 6C). Among them, C1 and C3 had the highest immune T cell cytolysis activity, while that of C2 was the lowest (Figure 6D). C2 had the lowest angiogenesis score (Figure 6E). In the correlation analysis of 47 immune checkpoint-related genes, 43 genes had significant differences in the three subgroups (Figure 6F). These results indicated that different subgroups may respond to immunotherapy differently.

The immune characteristics and pathway characteristics of different molecular subtypes were significant

In the TCGA data set, the CIBERSORT method was used to evaluate the scores of 22 immune cells in each sample, and the distribution of these immune cell scores in the three subgroups

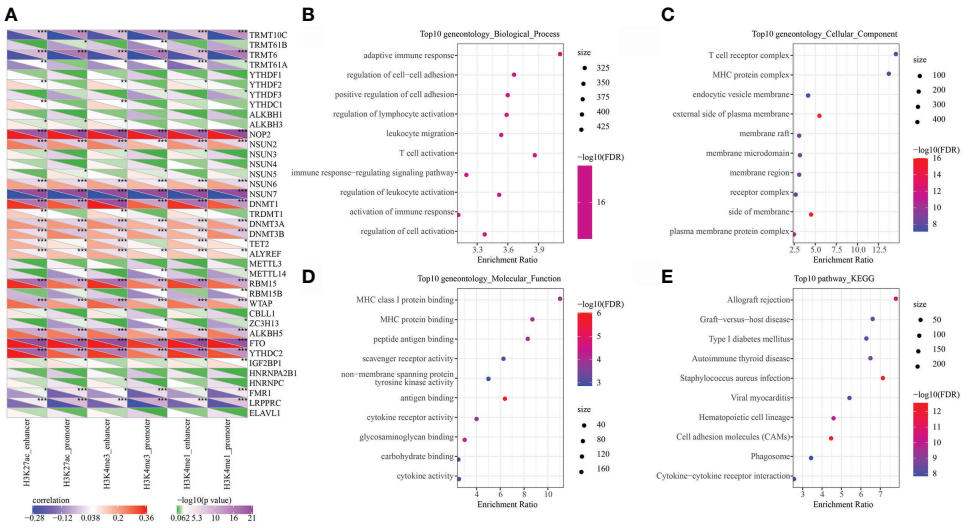

FIGURE 4
Epi-PCGs and RNA modification correlation and functional enrichment analysis. **(A)** Correlation between the enrichment scores of 6 kinds of epigenetic modification; **(B)** Epi-PCGs-enriched BP annotation map; **(C)** Epi-PCGs-enriched CC annotation map; **(D)** Epi-PCGs-enriched MF annotation map; **(E)** Epi-PCGs-enriched KEGG annotation map. The abscissa represents the enrichment score, and the ordinate represents the enriched functions or pathways. The size represents the number of gene enrichment, and the color represents P-value. *P < 0.05, **P < 0.01, ***P < 0.001.

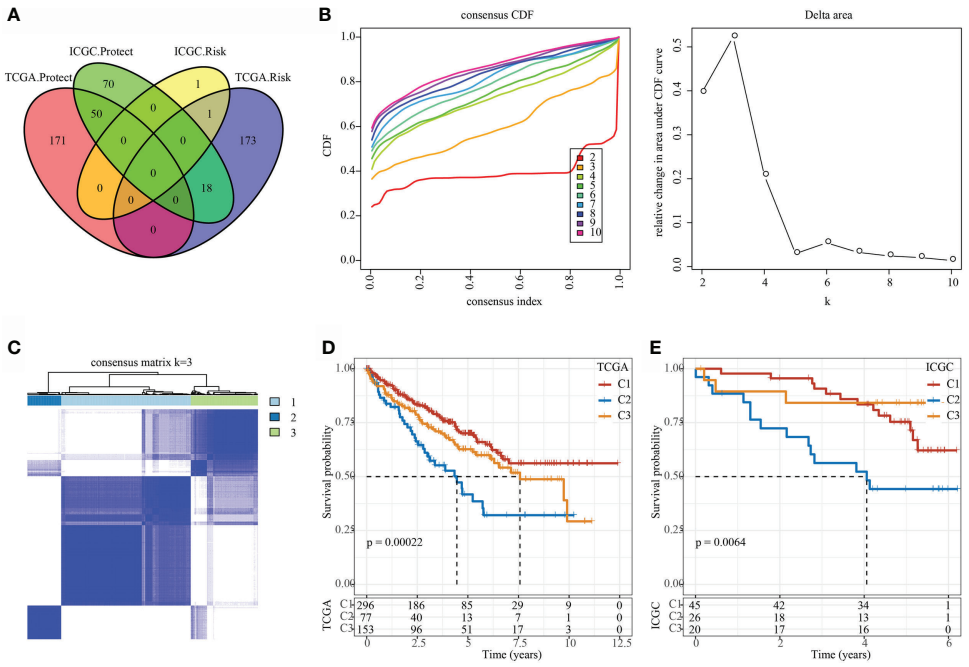

FIGURE 5
Identification of epi-PCGs-related molecular subtypes. **(A)** Venn diagram of prognostic significant genes in TCGA and ICGC data set obtained by univariate Cox regression analysis; **(B)** CDF curve and CDF Delta area curve of TCGA cohort samples (n = 526). Delta area curve of consensus clustering, which indicates the relative change in area under the cumulative distribution function (CDF) curve for each category number k compared with k − 1. The horizontal axis represents the category number k and the vertical axis represents the relative change in area under CDF curve; **(C)** Cluster heat map of TCGA data set samples (n = 526) when k = 3; **(D)** KM curve of the prognosis of the three molecular subtypes in the TCGA data set (n-C1 = 296, n-C2 = 77, and n-C3 = 153); **(E)** KM curve of the prognosis of the three molecular subtypes in the ICGC data set (n-C1 = 45, n-C2 = 26, and n-C3 = 20).

10.3389/fimmu.2022.901662

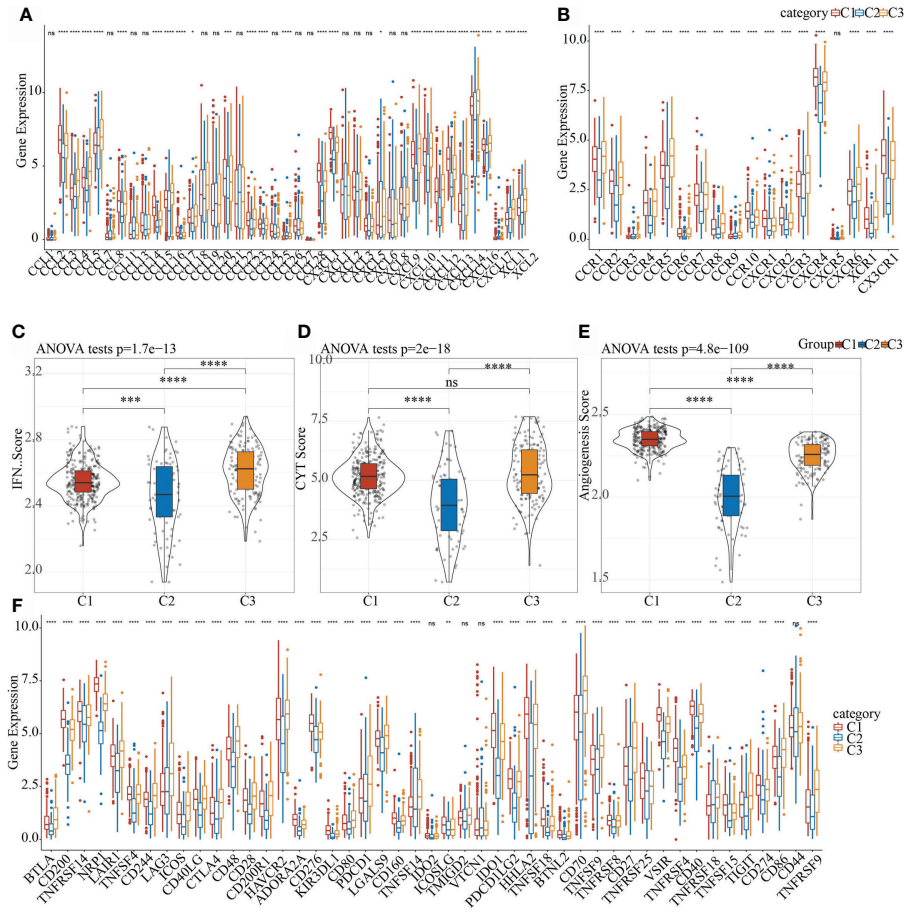

FIGURE 6
Differences in the distribution of chemokines, IFNγ scores, immune T cell cytolysis activity, angiogenesis scores, and immune checkpoint genes in different subgroups. **(A)** Difference in the expression and distribution of chemokines in the TCGA cohort; **(B)** Difference in the expression and distribution of chemokine receptors in the TCGA cohort; **(C)** Difference in the distribution of IFNγ scores in different subgroups in the TCGA cohort; **(D)** Differences in immune T cell cytolysis activity in different subgroups; **(E)** Differences in angiogenesis scores in different subgroups; **(F)** Differences in the expression and distribution of immune checkpoint genes in the TCGA cohort; the significance was tested by analysis of variance, * means p< 0.05; ** means p< 0.01, *** means p< 0.001, **** means p< 0.0001, ns, not significant.

was observed, as shown in Figure 7A. 16 immune cells showed significant differences in different subtypes (Figure 7B). We used the method of ssGSEA to calculate the scores of 28 immune cells (37), then compared their differences in the subtypes, and 28 immune infiltration scores were found to have significant differences in the subtypes (Figure 7C).

C2 molecular subtype had a lower TIDE score

We analyzed the differences of different molecular subtypes in response to immunotherapy and chemotherapy. TIDE (http://tide.dfci.harvard.edu/) software was used to evaluate the potential clinical effects of immunotherapy on our defined molecular subtypes. A higher TIDE prediction score indicated a higher possibility of immune escape, which suggests that the patient is less likely to benefit from immunotherapy. As shown in Supplementary Figure 2, in the TCGA data set, C2 had the lowest TIDE score (Supplementary Figure 2A). At the same time, we also compared the predicted T cell dysfunction scores (Supplementary Figure 2B) and T cell exclusion scores (Supplementary Figure 2C) in different molecular subtypes, and there were also significant differences between different groups.

Establishing a prognostic risk model based on epi-PCG-related genes

The final training set data had a total of 316 samples, and the test set data had a total of 210 samples. See Table 2 for

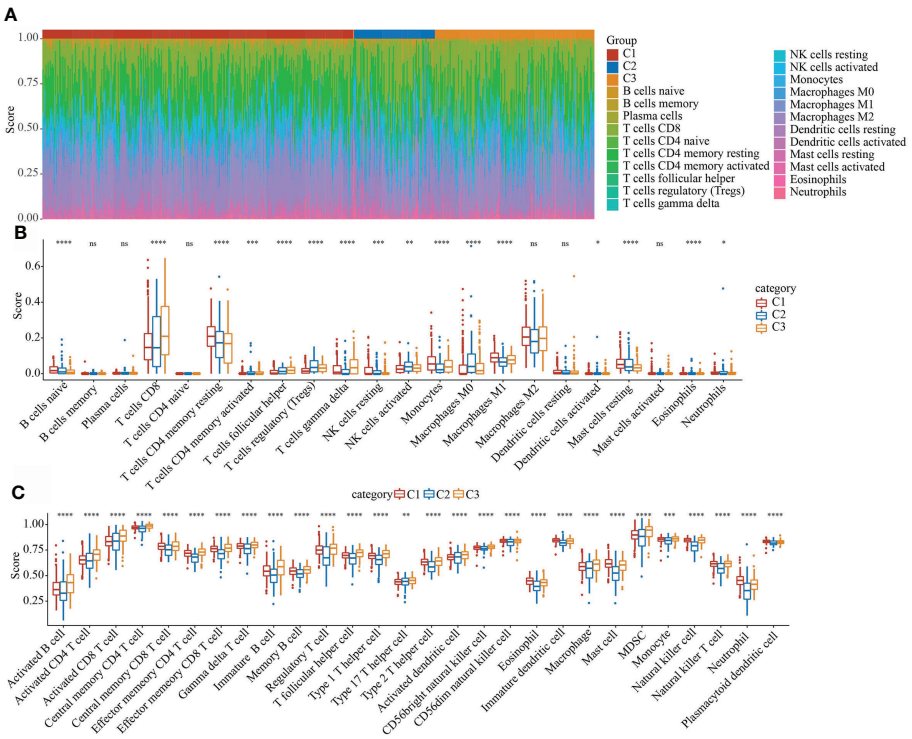

FIGURE 7
Evaluation of immune and pathway characteristics of different molecular subtypes. **(A)** The proportion of the 22 immune cell components of samples in different subgroups. **(B)** Differences in 22 immune cell components of samples in different subgroups; **(C)** Differences in 28 immune infiltration scores in different subgroups. *P < 0.05, **P < 0.01, ***P < 0.001. ns, not significant.

sample information of training set and validation set. Chi-square test was applied to assess the training set and test set samples. The results showed that our grouping was reasonable and there was no significant difference between groups (P > 0.05).

Construction and evaluation of an 8-gene risk model

Using the training set data, univariate Cox analysis was performed for each epi-PCG, and p< 0.05 was the threshold for filtering. Finally, 46 prognostic genes were included. In this study, 46 genes with differences have been identified. We used the R software package glmnet to perform lasso cox regression analysis. Firstly, the change trajectory of each independent variable was analyzed, as shown in Figure 8A. It can be seen that as the lambda gradually increased, the number of independent variable coefficients close to 0 also gradually increased. 10-fold cross-validation was employed to build a model, and the confidence interval under each lambda was determined, as shown in Figure 8B. It can be seen that the model was optimal when lambda = 0.0316. Thus, 10 genes when lambda = 0.0316 were considered as the target genes for further analysis. To reduce the number of genes, the stepAIC method in the MASS package was used, we finally reduced 10 genes to 8 genes. The final RiskScore formula was as follows:

RiskScore=0.28*ETV4+0.631*SH2B3-0.338*FATE1+0.363*GRK5-0.42*MALL-0.196*HRH2-0.354*SEMA3G-0.431*SLC10A6

The RiskScore of each sample was calculated according to the expression level of the samples, and the RiskScore of the sample was shown in Figure 8C. Furthermore, we used the R software package timeROC to analyze the ROC of RiskScore for prognostic classification, and determined the classification efficiency of 1-, 3-, and 5- year prognosis, respectively. As shown in Figure 8D, the model had a high AUC area. Finally, z-score was performed on Riskscore. Samples with Riskscore greater than zero were divided into high-risk groups, while those with Riskscore lower than zero were in low-risk groups, and the KM curve was drawn, as shown in Figure 8E. A significant difference of p< 0.0001 can be found, and here 143 samples were classified into high-risk groups and 173 samples were classified into low-risk groups.

10.3389/fimmu.2022.901662

TABLE 2 Clinical information of TCGA training set and validation set samples.

Clinical Features	TCGA-Train	TCGA-test	P-Value
Gender			
Male	206	137	1
Female	110	73	
T Stage			
T1	158	109	0.6742
T2	46	23	
T3	106	73	
T4	6	5	
N Stage			
N0	141	97	0.3379
N1	7	9	
NX	168	104	
M Stage			
M0	275	161	0.0786
M1	37	43	
MX	4	6	
Stage			
I	157	104	0.1018
II	39	18	
III	81	42	
IV	39	43	
X	0	3	
Grade			
G1	11	2	0.0911
G2	132	94	
G3	127	78	
G4	39	35	
GX	7	1	
Age			
>60	163	99	0.3637
<=60	153	111	

The 8-gene signature had a strong robustness in different cohorts

To evaluate the robustness of the model, the RiskScore of each sample in the TCGA validation set, TCGA entire data set and ICGC data sets were calculating using the same model and the same coefficients as the training set, according to the expression level of the sample. The R software package timeROC was applied to analyze the prognostic classification of the RiskScore of the TCGA validation set. The ROC efficiencies of 1, 3, and 5 years were 0.73, 0.69, and 0.63, respectively (Supplementary Figure 3A). Finally zscore was performed on the Riskscore. Samples with Riskscore greater than zero were divided into high-risk group, whereas those lower than zero were in low-risk group, and the KM curve was drawn. The results showed that the prognosis of patients in the high-risk group was significantly worse than that of the low-risk group ($p< 0.05$, Supplementary Figure 3B). Specifically, 99 samples were classified as high-risk, and 111 samples were classified as low-risk.

In all TCGA data sets, the ROC efficiencies of 1, 3, and 5 years were 0.77, 0.73, and 0.70, respectively (Supplementary Figure 3C). The prognosis of patients in the high-risk group was significantly worse than that of the low-risk group ($p< 0.001$, Supplement Figure 3D). Here, 242 samples were classified as high-risk group, and 284 samples were classified as low-risk group.

Furthermore, we used the independent verification set ICGC to verify the applicability of the model. TimeROC was employed to assess the prognostic classification of the RiskScore on ICGC. The ROC efficiencies of 1, 3, and 5 years were 0.77, 0.73, and 0.70, respectively (Supplementary Figure 3E). Z-score on Riskscore was then performed, and samples with a Riskscore greater than zero were divided into the high-risk group, while those lower than zero were in the low-risk group, and the KM curve was drawn. The results demonstrated that the prognosis of patients in the high-risk group was significantly worse than that of the low-risk group ($p< 0.001$, Supplementary Figure 3F). Of these, 49 samples were classified as high-risk group, and 42 samples were classified as low-risk group.

Riskscore can distinguish different clinical subgroup characteristics

The clinical subgroup characteristics were divided by the Riskscore into high- and low-risk groups. The results demonstrated that Riskscore can significantly distinguish Age, Gender, TMN stage and Grade into two groups with prognostic differences (Figures 9A–M). Furthermore, comparison on the correlation between RiskScore and clinical subgroup characteristics also showed significant differences of Riskscore in T Stage, N Stage, M Stage, Stage, Grade, and Gender (Figures 9N–S, $p< 0.05$).

The relationship between RiskScore and the pathways

We calculated the ssGSEA score of each sample on different functions, and further analyzed the correlation between these functions and RiskScore. The functions with a correlation greater than 0.4 were selected and shown in Supplementary Figure 4A, from which it could be found that one function was positively correlated with the RiskScore, whereas the remaining 22 were negatively correlated with the RiskScore. The most relevant 23 KEGG Pathways were selected and subjected to cluster analysis based on their enrichment scores, as shown in Supplementary Figure 4B. Among the 23 pathways, for example, P53 signaling pathway, increased with the increase of RiskScore, while metabolic

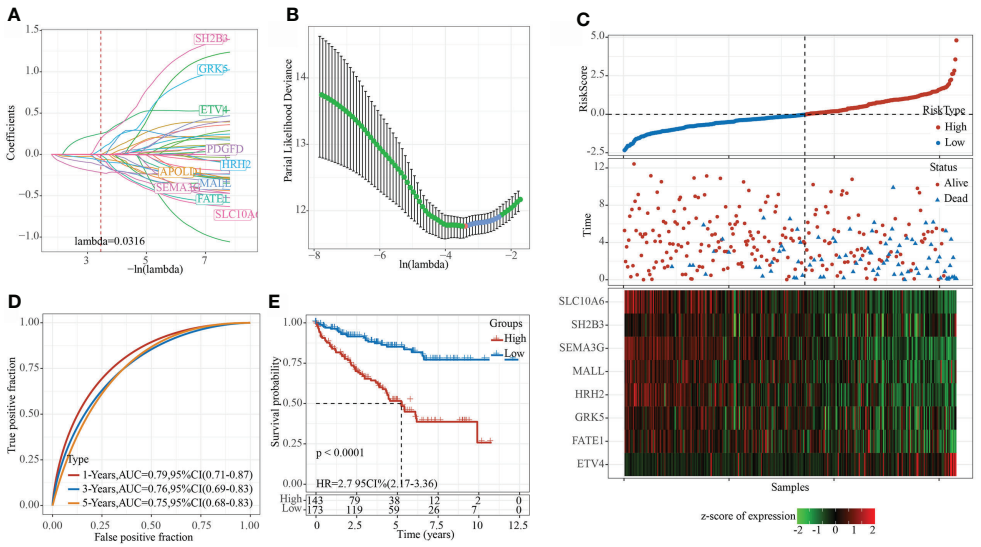

FIGURE 8
Constructing a prognostic model in TCGA data set. **(A)** The change trajectory of each independent variable, the horizontal axis represents the log value of the independent variable lambda, and the vertical axis represents the coefficient of the independent variable; **(B)** The confidence interval under each lambda. **(C)** RiskScore, survival time and survival status and expression of the 8 genes in the TCGA training set; **(D)** ROC curve and AUC of 8-gene signature classification; **(E)** KM survival curve distribution of the 8-gene signature in the training set.

pathways such as fatty acid metabolism, glycolysis gluconeogenesis gluconeogenesis, galactose metabolism decreased with the increase of RiskScore. Moreover, we characterized the protein-protein interaction (PPI) among these eight prognostic genes using the STRING online tool (https://www.networkanalyst.ca/). The result showed that SEMA3G, ETV4, and SH2B3 had a close interaction, and that GRK5 and HRH2 had a close interaction (Supplementary Figure 5), suggesting that they may have a synergetic effect on affecting KIRC prognosis.

The expression of the eight prognostic genes was correlated with immune infiltration and was differential in the three molecular subtypes

Furthermore, we evaluated whether there was a correlation between the expression of prognostic genes and immune cell infiltration. Pearson correlation analysis revealed that the enrichment of M0, M1, and M2 macrophages, and regulatory T cells was obviously correlated with the prognostic genes (Supplementary Figure 6). Especially, a relatively strong correlation was observed between ETV4 and activated CD4 memory T cells (R = 0.30). SEMA3G, SLC10A6, and SH2B3 expression were significantly correlated with regulatory T cells (R = -0.32, -0.38, and -0.35, respectively). In addition, we found the distribution of the expression of eight prognostic genes in three molecular subtypes. C2 subtype with the worst overall survival had the lowest expression of all eight genes in both TCGA and ICGC datasets (Supplementary Figure 7), which was consistent with the previous result that high-risk group had relatively lower expression of these genes (Figure 8C).

The 8-gene signature was an independent prognostic risk factor for KIRC

To validate the independence of the 8-gene signature model in clinical applications, single-factor and multi-factor cox analysis were performed on the TCGA data set. Univariate COX regression analysis demonstrated that RiskType was significantly related to patients' survival. Corresponding multivariate COX regression analysis showed that RiskType (HR = 1.77, 95%CI = 1.39–2.24, p< 1e-5) was still closely related to survival. The above results indicated that the 8-gene signature was an independent prognostic risk factor for KIRC (Supplementary Figures 8A, B).

A nomogram is more effective to display the results of the risk model, and it is more convenient to be applied for predicting the outcome. The nomogram uses the length of the straight line to indicate the degree of influence of different variables on the outcome and the influence of different values of the variables on the outcome. We combined the significant clinical features of Age, M Stage, and RiskScore in multi-factor cox analysis to construct a nomogram model (Supplementary Figure 8C). The

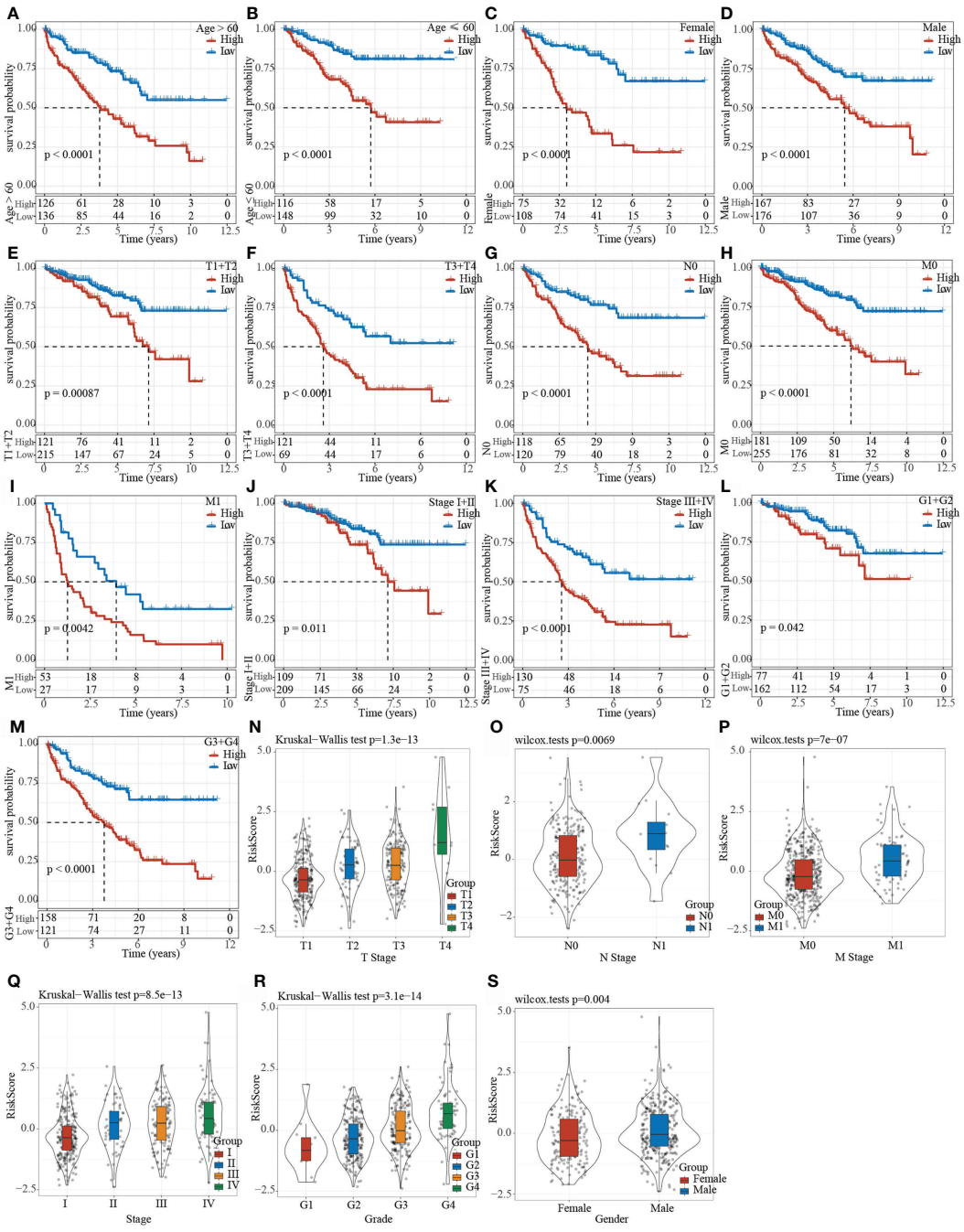

FIGURE 9
Clinical subgroup survival analysis and correlation analysis based on Riskscore. **(A–M)** Prognostic survival curve of clinical characteristics based on Riskscore; **(N–S)** RiskScore comparison in clinical characteristics of TCGA data set.

results demonstrated that RiskScore feature had the greatest impact on the survival rate prediction, indicating that the risk model established based on 5 genes can better predict the prognosis. In addition, we corrected the nomogram data for 1-, 3-, and 5-year survival to visualize the performance of the nomogram (Supplementary Figure 8D), proving that the method had a strong prediction performance. Furthermore, we plotted the DCA diagrams of Age, M Stage, RiskScore and nomogram, and the results showed that our nomogram had a high net benefit (Supplementary Figure 8E).

Comparison of risk models with other models

After referring to the literature, we finally selected 4 prognostic-related risk models, namely, 9-gene signature (Zhong) (38), 7-gene signature (Jiang) (39), 7-gene signature (Chen) (40), and 6-gene signature (Ren) (41), for comparing the prediction performance with our 8-gene model. To make the model comparable, we calculated the riskscore of each KIRC sample in the TCGA using the same method based on the corresponding genes in the 4 models. Z-score was performed on RiskScore, and samples with RiskScore greater than zero were classified into the high-risk group, while those with RiskScore lower than zero were in the low-risk group. The prognostic difference of KIRC samples between the two groups was calculated. The ROC and KIRC-KM curves of the four models were shown in Figure 10. It can be seen that the 1, 3, and 5-year AUC values of the 9-gene signature (Zhong) model were all lower than our model (Figure 10A); the 1- and 3-year AUC values of the 7-gene signature (Jiang) (Figure 10C) and 6-gene signature (Ren) (Figure 10G) models were lower than our model, but the 5-year AUC value was higher than our model; the 1-year AUC value of the 7-gene signature (Chen) model was higher than our model, but the 3- and 5-year AUC values were lower than our model (Figure 10E). The KIRC prognosis of the high- and low group samples predicted by these five models were also different (log rank p< 0.05) (Figures 10B, D, F, H).

Verification of the expression level of 8 epi-PCGs *in vitro*

Furthermore, we detected the mRNA and protein expression levels of 8 epi-PCGs (ETV4, SH2B3, FATE1, GRK5, MALL, HRH2, SEMA3G and SLC10A6) in 4 human kidney cancer cell lines (786-O, A498, Caki-1 and ACHN) and the normal human renal tubular epithelial cell line HK2. As shown in Figure 11A, we observed that the mRNA expression level of ETV4 was significantly increased and the expression levels of SH2B3, FATE1, GRK5, MALL, HRH2, SEMA3G and SLC10A6 were decreased prominently in kidney cancer cells when compared with HK2 cell line. The protein expression level of 8 epi-PCGs was similar to the mRNA expression level (Figure 11B). These findings were consistent with the bioinformatics results, indicating that the differentially expressed epi-PCGs identified in multi-omics data analysis exhibited significant changes in cancer cells.

Discussion

Surgery is currently the main treatment for KIRC, but about 20% of KIRC patients are already at advanced stage by the time of diagnosis and have missed the optimal opportunity for taking surgery (42). Moreover, even with surgical resection, about 30% of patients with localized KIRC tend to develop recurrence and

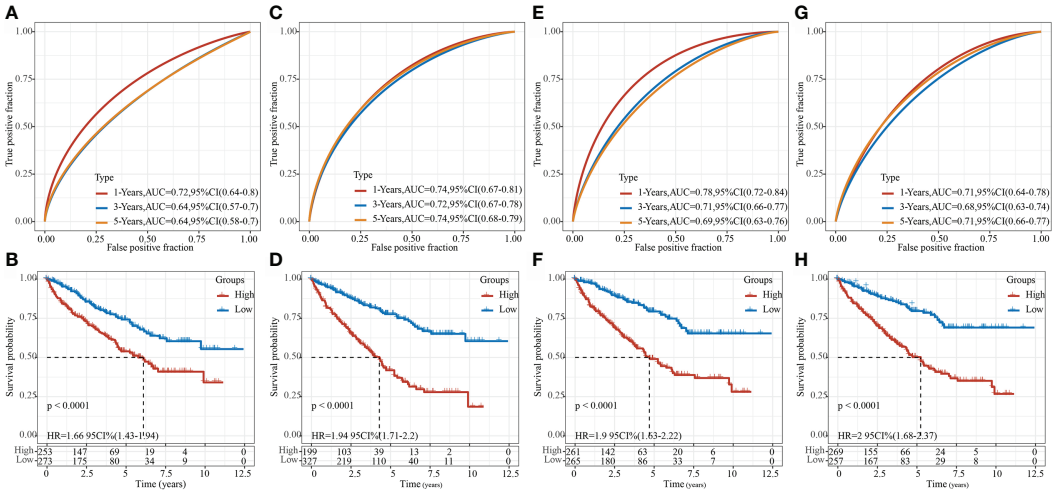

FIGURE 10
Comparison of our risk model with other models. **(A)** ROC of 9-gene signature (Zhong) risk model. **(B)** KM curve of 9-gene signature (Zhong) risk model on high- (n = 253) and low-group (n = 273) samples; **(C)** ROC of 7-gene signature (Jiang) risk model. **(D)** KM curve of 7-gene signature (Jiang) risk model on high- (n = 199) and low-group (n = 327) samples; **(E)** ROC of 7-gene signature (Chen) risk model. **(F)** KM Curve of 7-gene signature (Chen) risk model on high- (n = 261) and low-group (n = 265) samples; **(G)** ROC of the 6-gene signature (Ren) risk model. **(H)** KM curve of 6-gene signature (Ren) risk model on high- (n = 269) and low-group (n = 257) samples.

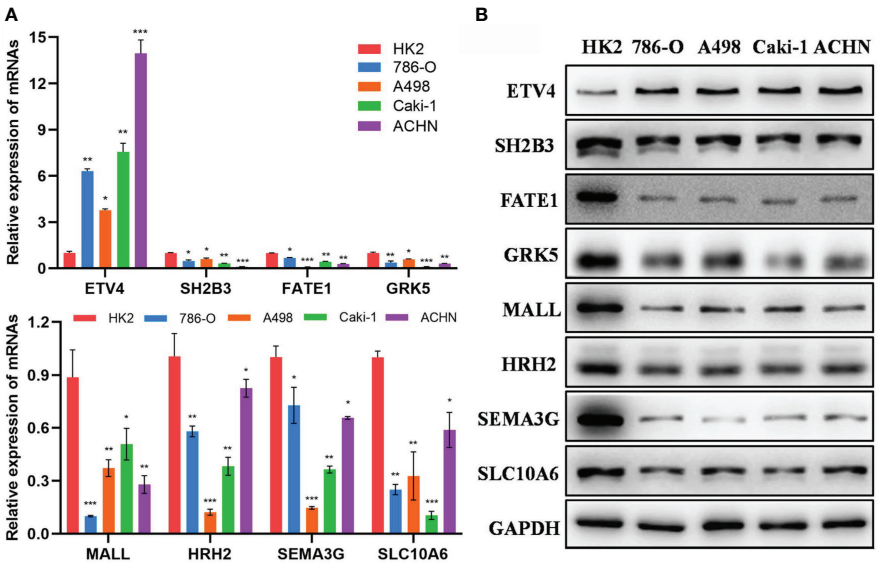

FIGURE 11
Verification of the expression level of 8 epi-PCGs *in vitro*. **(A)** The mRNA expression level of 8 epi-PCGs (ETV4, SH2B3, FATE1, GRK5, MALL, HRH2, SEMA3G and SLC10A6) in 4 kidney cancer cell lines and HK2 cell line. **(B)** The protein expression level of 8 epi-PCGs. *P < 0.05, **P < 0.01, ***P < 0.001.

metastasis, and the 5-year survival rate of patients with distant metastasis is about 8-10% (43, 44). Therefore, there is an urgent need to further understand the molecular mechanism of KIRC occurrence and development to provide more accurate and effective clinical treatment strategies.

Dysregulation of expression of functional proteins in the cell plays a critical role in tumorigenesis, which mostly stems from the dysregulation of expression of its protein-coding genes (PCG). Based on this, we first screened differentially expressed PCGs in KIRC, and then combined with histone modification data and methylation data, we found 872 epi-PCGs and 18629 non-epi-PCGs. Epi-PCGs accounted for only 4.47% of all the PCGs. Although the proportion of epi-PCG was not high, it still pointed to the important role of epigenetic modification in tumors. Previous studies have shown that epigenetic dysfunction, including DNA methylation and histone modification, may have an important impact on the proliferation, apoptosis, migration and invasion of cancer cells. Abnormal epigenetic modifications are detected in a variety of tumor cells (45–48). Further research results showed that epi-PCGs had more transcripts and exons than non-epi-PCGs, but the transcript length was relatively short, indicating that although epi-PCGs accounted for a relatively small proportion, it is possible that the level of transcription protein was decreased. These epi-PCG-related pathways include “bladder cancer”, “hematopoietic cell lineage” (49–51), and “JAK-STAT signaling pathway” (52–54), which are related to tumor progression, indicating that these epi-PCGs play a pivotal role in the occurrence and development of tumors.

To realize clinical application of these epi-PCGs, we established a prognostic gene signature related to epi-PCGs. Lasso regression analysis demonstrated the combination with the largest frequency of occurrence that included 8 genes, namely ETS variant 4 (ETV4), SH2B adapter protein 3 (SH2B3), Fetal and adult testis-expressed transcript protein (FATE1), G protein-coupled receptor kinase 5 (GRK5), MAL-like protein (MALL), Histamine H2 receptor (HRH2), Class-3 semaphorins (SEMA3G) and Solute carrier family 10 member 6 (SLC10A6). The role of these genes in tumors has been reported, but the current research results showed that their contradictory roles in tumors. ETV4, also known as polyomavirus enhancer activator 3 protein (Pea3), is an important member of the ETS transcription factor family. Studies have shown that ETV4 is abnormally expressed in a variety of tumors, and promotes tumor progression through stimulating tumor cell proliferation and metastasis (55–57). SH2B3 is a member of the SH2B family of adaptor proteins, playing a role in negative feedback loop that controls cell growth, development and survival signals. Activated target kinase also induces SH2B3 expression and activation through phosphorylation (58). In tumors, SH2B3 usually changes its role in tumors due to mutations. In leukemias, the enrichment of SH2B3 aberrations may indicate that the loss of SH2B3 contributes to the disease progression and increases the sensitivity of leukemias to Tyrosine kinase inhibitors (59,

60). FATE1 is a gene expressed in fetal and adult testis. In normal tissues, the expression of FATE1 is mainly restricted to the testis and adrenal glands (61), and its expression is up-regulated in a variety of cancers. GRK5 affects the migration of non-small cell lung cancer cells through vinculin (62), moreover, it shows a high expression in breast cancer cells, promotes breast cancer cell metastasis, and is therefore a target for breast cancer treatment (63). MAL-like protein has a transport function, but its molecular role is largely unclear. MALL is normally expressed in laryngeal epithelial cells, and its expression changes in the early stage of carcinogenesis. The expression of MAL is significantly down-regulated (64), and it plays an important role as a binding gene of MUC1 in breast cancer (65). HRH2 is a member of the G protein-coupled receptor family widely expressed in the gastrointestinal tract, and its activity is mediated by cAMP. It has been found that the HRH2 blocker nizatidine can be used for treating advanced liver disease and liver cancer, and is a potential clinical target for liver cancer treatment (66). SEMA3 is the only group of secreted proteins in vertebrate semaphores. They are further subdivided into seven members (SEMA3A to SEMA3G). The members of the SEMA3 family have both tumor-promoting and anti-tumor functions, which are related to cell type and environment (67). SEMA3G has anti-migration and anti-invasion effects on gliomas (68), and is a prognostic gene of KIRC (69). SLC10A6 has been limitedly researched in tumors. Studies have shown that it is widely expressed in breast cancer and promotes breast cancer cell proliferation (70). These results indicated that these genes play an important role in the occurrence and development of tumors in different forms, and may also function critically in the prognosis of KIRC, but this requires further verification.

We also analyzed the RiskScore in different clinical characteristics, and found that for tumors with poor differentiation and higher malignancy (T3-4, N+, M1, and 3), the score was higher, and the prognosis of patients in the high-scoring group with different clinical characteristics was poor. Univariate and multivariate COX regression analysis results showed that RiskScore was an independent prognostic factor for KIRC. The nomogram results confirmed that RiskScore had the strongest ability in accurately predicting the prognosis of KIRC, exceeding the existing TNM and staging. For some clinical stages, the clinical application significance of the risk scoring system constructed in this study was greater. In addition, the RiskScore model was compared with the previous five assessment models. The prognosis of KIRC in the high- and low-risk samples of these five models were different, but our model had a higher AUC value in one of or some of 1-, 3- or 5-year survival predictions. This indicated that the model we developed based on differentially expressed genes combined with epigenetics can better indicate the occurrence and development of KIRC, and was a more effective model, further illustrating the clinical feasibility of our model. On the other hand, as the RiskScore changed, the pathways involved in tumor occurrence and progression were different. For example, we found that among the higher-scored pathways, the enrichment score of pathways such as P53 signaling pathway (71) increased with the increase of RiskScore, while the enrichment score of metabolic pathways such as fatty acid metabolism (72), glycolysis gluconeogenesis (73), galactose metabolism (74) decreased with the increase of RiskScore. Previous literature reports have shown that these pathways are all involved in tumor progression, but they may play different roles in different tumors, and this also requires follow-up research for verification.

Although previous research developed a series of gene signatures for kidney cancer based on epigenetic dysregulation, they focused on m6A regulators or only included limited cancer samples (17–19). Compared to the previous research, the advantage of our study was that we performed a comprehensive analysis on epigenetic dysregulation using multiple data sets. Importantly, we uncovered the relation between epigenetic dysregulation and tumor microenvironment from different aspects such as immune checkpoints, cytokines, immune cells and immune signatures. The different performance of three molecular subtypes to immune checkpoint blockade also demonstrated the important role of epigenetic dysregulation or identified epi-PCGs in tumor microenvironment modulation. The observations highlighted the potential of epi-PCGs serving as prognostic biomarkers for renal cell carcinoma. Compared with the gene signatures of KIRC in the previous studies, our 8-gene prognostic model manifested a higher AUC, which further indicated the critical role of epi-PCGs in the KIRC development and progression. Notably, we verified the expression level of the eight epi-PCGs in kidney cancer cell lines, and the results showed a consistency with the bioinformatics analysis, which further demonstrated the reliability of our analysis and the importance of the eight epi-PCGs in kidney cancer development.

However, in this study, we only analyzed the effect of differential expression of PCGs on KIRC, but did not include the abnormal expression of other non-transcriptional genes. Also, such expression difference lacked verification *in vivo* and *in vitro*. Similarly, the 8-gene signature was only preliminary screened as part of the prognostic RiskScore, but there was a lack of specific research on the role of these genes in KIRC and the detailed relationship among these genes. We will further supplement verification study *in vivo*. In addition, there are some contradictions between some research results in this study and previous research results, and have not yet been fully explained only according to our existing research results.

In conclusion, in this study, we systematically analyzed the abnormal expression of PCGs in KIRC, and combined with histone modifications, we screened 872 epi-PCGs and 18629 non-epi-PCGs. Based on the differentially expressed epi-PCGs-related

genes, KIRC samples were divided into three subtypes, and these subtypes showed significant differences in prognosis. Based on the epi-PCGs, we constructed an 8-gene prognostic risk models that had a strong stability and predictive performance in both the training set and the validation set, and different RiskScores can fully reflect the clinical characteristics of patients. Compared with other existing models, our model had a higher predicting performance. The current findings help better understand the abnormal epigenetic regulation of PCG expression in KIRC. This model is expected to guide clinicians in the prognosis prediction and clinical diagnosis and treatment of KIRC patients with different phenotypes.

Data availability statement

The datasets presented in this study can be found in online repositories. The names of the repository/repositories and accession number(s) can be found in the article/Supplementary Material.

Author contributions

ZW and XL designed the study. LX, SW, RH and SL collected and analyzed data. LX and SW drafted the manuscript. ZW and XL reviewed and revised the manuscript. The manuscript has been approved by all authors for publication.

Conflict of interest

The authors declare that the research was conducted in the absence of any commercial or financial relationships that could be construed as a potential conflict of interest.

Publisher's note

Supplementary material

The Supplementary Material for this article can be found online at: https://www.frontiersin.org/articles/10.3389/fimmu.2022.901662/full#supplementary-material

SUPPLEMENTARY FIGURE 1
Prognosis-related epi-PCGs expression and RNA modification. **(A)** Analysis of the differential expression of prognostic-related epi-PCGs in normal samples and tumor samples. **(B–C)** Histone modification profile of epi-PCGs

SUPPLEMENTARY FIGURE 2
Comparison of TIDE score, T cell dysfunction score and T cell rejection score of molecular subtypes. **(A)** In the TCGA data set, TIDE scores are different in the three molecular subtypes. **(B)** In the TCGA data set, T cell dysfunction scores are different in the three molecular subtypes. **(C)** In the TCGA data set, T cell exclusion scores are different in the three molecular subtypes.

SUPPLEMENTARY FIGURE 3
(A) ROC curve and AUC of the 8-gene signature in TCGA test set; **(B)** KM survival curve of 8-gene signature in TCGA test set. **(C)** ROC curve and AUC of 8-gene signature in TCGA entire data set; **(D)** KM survival curve of 8-gene signature in TCGA entire data set. **(E)** ROC curve and AUC of 8-gene signature in the ICGC cohort; **(F)** KM survival curve of 8-gene signature in the ICGC cohort.

SUPPLEMENTARY FIGURE 4
The relationship between RiskScore and the pathways. **(A)** The correlation coefficient clustering of KEGG pathways greater than 0.4 and the RiskScore; **(B)** ssGSEA scores of KEGG pathways with a correlation greater than 0.4 in each sample as the RiskScore increases, the horizontal axis represents the sample, and the Riskscore increases from left to right.

SUPPLEMENTARY FIGURE 5
The PPI analysis for the eight prognostic genes.

SUPPLEMENTARY FIGURE 6
Pearson correlation analysis between the eight prognostic genes and the ssGSEA score of immune cells. Red and blue indicates positive and negative correlations respectively.

SUPPLEMENTARY FIGURE 7
The expression of eight prognostic genes in three molecular subtypes in TCGA **(A)** and ICGC **(B)** datasets. Kruskal-Wallis test was performed. ns, no significance. ****P < 0.0001.

SUPPLEMENTARY FIGURE 8
Single-factor and multi-factor cox analyses on the 8-gene signature**(A)** Single-factor analysis of TCGA entire data set; **(B)** Multi-factor analysis of TCGA entire data set. **(C)** Nomogram constructed with clinical characteristics and RiskScore; **(D)** Correction chart of survival rate of nomogram; **(E)** DCA chart.

References

1. Bray F, Ferlay J, Soerjomataram I, Siegel RL, Torre LA, Jemal A. Global cancer statistics 2018: GLOBOCAN estimates of incidence and mortality worldwide for 36 cancers in 185 countries. *CA: Cancer J Clin* (2018) 68(6):394–424. doi: 10.3322/caac.21492

2. Anker J, Miller J, Taylor N, Kyprianou N, Tsao CK. From bench to bedside: How the tumor microenvironment is impacting the future of immunotherapy for renal cell carcinoma. *Cells* (2021) 10(11):3231. doi: 10.3390/cells10113231

3. Attalla K, Weng S, Voss MH, Hakimi AA. Epidemiology, risk assessment, and biomarkers for patients with advanced renal cell carcinoma. *Urol Clinics North America* (2020) 47(3):293–303. doi: 10.1016/j.ucl.2020.04.002

4. Kunath F, Schmidt S, Krabbe LM, Miernik A, Dahm P, Cleves A, et al. Partial nephrectomy versus radical nephrectomy for clinical localised renal masses. *Cochrane Database syst Rev* (2017) 5(5):CD012045. doi: 10.1002/14651858.CD012045.pub2

5. Wiechno P, Kucharz J, Sadowska M, Michalski W, Sikora-Kupis B, Jonska-Gmyrek J, et al. Contemporary treatment of metastatic renal cell carcinoma. *Med Oncol (Northwood London England)* (2018) 35(12):156. doi: 10.1007/s12032-018-1217-1

6. Bedke J, Stühler V, Stenzl A, Brehmer B. Immunotherapy for kidney cancer: status quo and the future. *Curr Opin Urol* (2018) 28(1):8–14. doi: 10.1097/mou.0000000000000466

7. Xu W, Atkins MB, McDermott DF. Checkpoint inhibitor immunotherapy in kidney cancer. *Nat Rev Urol* (2020) 17(3):137–50. doi: 10.1038/s41585-020-0282-3

8. Di Cerbo V, Schneider R. Cancers with wrong HATs: the impact of acetylation. *Briefings Funct Genomics* (2013) 12(3):231–43. doi: 10.1093/bfgp/els065

9. Fraga MF, Ballestar E, Villar-Garea A, Boix-Chornet M, Espada J, Schotta G, et al. Loss of acetylation at Lys16 and trimethylation at Lys20 of histone H4 is a common hallmark of human cancer. *Nat Genet* (2005) 37(4):391–400. doi: 10.1038/ng1531

10. Sapienza C, Issa JP. Diet, nutrition, and cancer epigenetics. *Annu Rev Nutr* (2016) 36:665–81. doi: 10.1146/annurev-nutr-121415-112634

11. Busslinger M, Tarakhovsky A. Epigenetic control of immunity. *Cold Spring Harbor Perspect Biol* (2014) 6(6):a019307. doi: 10.1101/cshperspect.a019307

12. Cheng X. Structural and functional coordination of DNA and histone methylation. *Cold Spring Harbor Perspect Biol* (2014) 6(8):a018747. doi: 10.1101/cshperspect.a018747

13. Schenk T, Chen WC, Göllner S, Howell L, Jin L, Hebestreit K, et al. Inhibition of the LSD1 (KDM1A) demethylase reactivates the all-trans-retinoic acid differentiation pathway in acute myeloid leukemia. *Nat Med* (2012) 18(4):605–11. doi: 10.1038/nm.2661

14. van Vlodrop IJH, Joosten SC, De Meyer T, Smits KM, Van Neste L, Melotte V, et al. A four-gene promoter methylation marker panel consisting of GREM1, NEURL, LAD1, and NEFH predicts survival of clear cell renal cell cancer patients. *Clin Cancer Res* (2017) 23(8):2006–18. doi: 10.1158/1078-0432.Ccr-16-1236

15. Evelönn EA, Landfors M, Haider Z, Köhn L, Ljungberg B, Roos G, et al. DNA Methylation associates with survival in non-metastatic clear cell renal cell carcinoma. *BMC Cancer* (2019) 19(1):65. doi: 10.1186/s12885-019-5291-3

16. Angulo JC, Manini C, López JI, Pueyo A, Colás B, Ropero S. The role of epigenetics in the progression of clear cell renal cell carcinoma and the basis for future epigenetic treatments. *Cancers* (2021) 13(9):2071. doi: 10.3390/cancers13092071

17. Zhou J, Wang J, Hong B, Ma K, Xie H, Li L, et al. Gene signatures and prognostic values of m6A regulators in clear cell renal cell carcinoma - a retrospective study using TCGA database. *Aging* (2019) 11(6):1633–47. doi: 10.18632/aging.101856

18. Zheng Z, Mao S, Guo Y, Zhang W, Liu J, Li C, et al. N6–methyladenosine RNA methylation regulators participate in malignant progression and have prognostic value in clear cell renal cell carcinoma. *Oncol Rep* (2020) 43(5):1591–605. doi: 10.3892/or.2020.7524

19. Kang HW, Park H, Seo SP, Byun YJ, Piao XM, Kim SM, et al. Methylation signature for prediction of progression free survival in surgically treated clear cell renal cell carcinoma. *J Korean Med Sci* (2019) 34(19):e144. doi: 10.3346/jkms.2019.34.e144

20. Chen YA, Lemire M, Choufani S, Butcher DT, Grafodatskaya D, Zanke BW, et al. Discovery of cross-reactive probes and polymorphic CpGs in the illumina infinium HumanMethylation450 microarray. *Epigenetics* (2013) 8(2):203–9. doi: 10.4161/epi.23470

21. Zhang Z. Introduction to machine learning: k-nearest neighbors. *Ann Trans Med* (2016) 4(11):218. doi: 10.21037/atm.2016.03.37

22. Yao X, Tan J, Lim KJ, Koh J, Ooi WF, Li Z, et al. VHL deficiency drives enhancer activation of oncogenes in clear cell renal cell carcinoma. *Cancer Discovery* (2017) 7(11):1284–305. doi: 10.1158/2159-8290.Cd-17-0375

23. Ritchie ME, Phipson B, Wu D, Hu Y, Law CW, Shi W, et al. Limma powers differential expression analyses for RNA-sequencing and microarray studies. *Nucleic Acids Res* (2015) 43(7):e47. doi: 10.1093/nar/gkv007

24. Yu G, Wang LG, He QY. ChIPseeker: an R/Bioconductor package for ChIP peak annotation, comparison and visualization. *Bioinf (Oxford England)* (2015) 31(14):2382–3. doi: 10.1093/bioinformatics/btv145

25. Yu G, Wang LG, Han Y, He QY. clusterProfiler: an r package for comparing biological themes among gene clusters. *Omics* (2012) 16(5):284–7. doi: 10.1089/omi.2011.0118

26. Wilkerson MD, Hayes DN. ConsensusClusterPlus: a class discovery tool with confidence assessments and item tracking. *Bioinf (Oxford England)* (2010) 26(12):1572–3. doi: 10.1093/bioinformatics/btq170

27. McEligot AJ, Poynor V, Sharma R, Panangadan A. Logistic LASSO regression for dietary intakes and breast cancer. *Nutrients* (2020) 12(9):2652. doi: 10.3390/nu12092652

28. Zhang Z. Variable selection with stepwise and best subset approaches. *Ann Trans Med* (2016) 4(7):136. doi: 10.21037/atm.2016.03.35

29. Hänzelmann S, Castelo R, Guinney J. GSVA: gene set variation analysis for microarray and RNA-seq data. *BMC Bioinf* (2013) 14:7. doi: 10.1186/1471-2105-14-7

30. Takikawa O, Tagawa Y, Iwakura Y, Yoshida R, Truscott RJ. Interferon-gamma-dependent/independent expression of indoleamine 2,3-dioxygenase. studies with interferon-gamma-knockout mice. *Adv Exp Med Biol* (1999) 467:553–7. doi: 10.1007/978-1-4615-4709-9_68

31. Garcia-Diaz A, Shin DS, Moreno BH, Saco J, Escuin-Ordinas H, Rodriguez GA, et al. Interferon receptor signaling pathways regulating PD-L1 and PD-L2 expression. *Cell Rep* (2017) 19(6):1189–201. doi: 10.1016/j.celrep.2017.04.031

32. Zhang R, Liu H, Li F, Li H, Yu J, Ren X. The correlation between the subsets of tumor infiltrating memory T cells and the expression of indoleamine 2,3-dioxygenase in gastric cancer. *Digestive Dis Sci* (2013) 58(12):3494–502. doi: 10.1007/s10620-013-2837-0

33. Chen JY, Li CF, Kuo CC, Tsai KK, Hou MF, Hung WC. Cancer/stroma interplay *via* cyclooxygenase-2 and indoleamine 2,3-dioxygenase promotes breast cancer progression. *Breast Cancer Res BCR* (2014) 16(4):410. doi: 10.1186/s13058-014-0410-1

34. Danilova L, Ho WJ, Zhu Q, Vithayathil T, De Jesus-Acosta A, Azad NS, et al. Programmed cell death ligand-1 (PD-L1) and CD8 expression profiling identify an immunologic subtype of pancreatic ductal adenocarcinomas with favorable survival. *Cancer Immunol Res* (2019) 7(6):886–95. doi: 10.1158/2326-6066.Cir-18-0822

35. Rooney MS, Shukla SA, Wu CJ, Getz G, Hacohen N. Molecular and genetic properties of tumors associated with local immune cytolytic activity. *Cell* (2015) 160(1-2):48–61. doi: 10.1016/j.cell.2014.12.033

36. Masiero M, Simões FC, Han HD, Snell C, Peterkin T, Bridges E, et al. A core human primary tumor angiogenesis signature identifies the endothelial orphan receptor ELTD1 as a key regulator of angiogenesis. *Cancer Cell* (2013) 24(2):229–41. doi: 10.1016/j.ccr.2013.06.004

37. Şenbabaoğlu Y, Gejman RS, Winer AG, Liu M, Van Allen EM, de Velasco G, et al. Tumor immune microenvironment characterization in clear cell renal cell carcinoma identifies prognostic and immunotherapeutically relevant messenger RNA signatures. *Genome Biol* (2016) 17(1):231. doi: 10.1186/s13059-016-1092-z

38. Zhong W, Huang C, Lin J, Zhu M, Zhong H, Chiang MH, et al. Development and validation of nine-RNA binding protein signature predicting overall survival for kidney renal clear cell carcinoma. *Front Genet* (2020) 11:568192. doi: 10.3389/fgene.2020.568192

39. Jiang H, Chen H, Chen N. Construction and validation of a seven-gene signature for predicting overall survival in patients with kidney renal clear cell carcinoma *via* an integrated bioinformatics analysis. *Anim Cells Syst* (2020) 24(3):160–70. doi: 10.1080/19768354.2020.1760932

40. Chen L, Xiang Z, Chen X, Zhu X, Peng X. A seven-gene signature model predicts overall survival in kidney renal clear cell carcinoma. *Hereditas* (2020) 157(1):38. doi: 10.1186/s41065-020-00152-y

41. Ren X, Ma L, Wang N, Zhou R, Wu J, Xie X, et al. Antioxidant gene signature impacts the immune infiltration and predicts the prognosis of kidney renal clear cell carcinoma. *Front Genet* (2021) 12:721252. doi: 10.3389/fgene.2021.721252

42. Mitchell TJ, Turajlic S, Rowan A, Nicol D, Farmery JHR, O'Brien T, et al. Timing the landmark events in the evolution of clear cell renal cell cancer: TRACERx renal. *Cell* (2018) 173(3):611–23.e17. doi: 10.1016/j.cell.2018.02.020

43. Choueiri TK, Motzer RJ. Systemic therapy for metastatic renal-cell carcinoma. *New Engl J Med* (2017) 376(4):354–66. doi: 10.1056/NEJMra1601333

44. Miao D, Margolis CA, Gao W, Voss MH, Li W, Martini DJ, et al. Genomic correlates of response to immune checkpoint therapies in clear cell renal cell carcinoma. *Sci (New York NY)* (2018) 359(6377):801–6. doi: 10.1126/science.aan5951

45. McDaniel SL, Hepperla AJ, Huang J, Dronamraju R, Adams AT, Kulkarni VG, et al. H3K36 methylation regulates nutrient stress response in saccharomyces cerevisiae by enforcing transcriptional fidelity. *Cell Rep* (2017) 19(11):2371–82. doi: 10.1016/j.celrep.2017.05.057

46. Pfeifer GP. Defining driver DNA methylation changes in human cancer. *Int J Mol Sci* (2018) 19(4):1166. doi: 10.3390/ijms19041166

47. Gujar H, Weisenberger DJ, Liang G. The roles of human DNA methyltransferases and their isoforms in shaping the epigenome. *Genes* (2019) 10(2):172. doi: 10.3390/genes10020172

48. Bauer TL, Collmar K, Kaltofen T, Loeffler AK, Decker L, Mueller J, et al. Functional analysis of non-genetic resistance to platinum in epithelial ovarian cancer reveals a role for the MBD3-NuRD complex in resistance development. *Cancers* (2021) 13(15):3801. doi: 10.3390/cancers13153801

49. Yip RKH, Rimes JS, Capaldo BD, Vaillant F, Mouchemore KA, Pal B, et al. Mammary tumour cells remodel the bone marrow vascular microenvironment to

support metastasis. *Nat Commun* (2021) 12(1):6920. doi: 10.1038/s41467-021-26556-6

50. Siddiqui JA, Pothuraju R, Khan P, Sharma G, Muniyan S, Seshacharyulu P, et al. Pathophysiological role of growth differentiation factor 15 (GDF15) in obesity, cancer, and cachexia. *Cytokine Growth factor Rev* (2022) 64:71–83. doi: 10.1016/j.cytogfr.2021.11.002

51. Siegal T, Benouaich-Amiel A, Bairey O. Neurologic complications of acute myeloid leukemia. diagnostic approach and therapeutic modalities. *Blood Rev* (2022) 53:100910. doi: 10.1016/j.blre.2021.100910

52. Hu X, Li J, Fu M, Zhao X, Wang W. The JAK/STAT signaling pathway: from bench to clinic. *Signal transduction targeted Ther* (2021) 6(1):402. doi: 10.1038/s41392-021-00791-1

53. Zhao M, Dai R. HIST3H2A is a potential biomarker for pancreatic cancer: A study based on TCGA data. *Medicine* (2021) 100(46):e27598. doi: 10.1097/md.0000000000027598

54. Adachi Y, Kamiyama H, Ichikawa K, Fukushima S, Ozawa Y, Yamaguchi S, et al. Inhibition of FGFR reactivates IFNγ signaling in tumor cells to enhance the combined antitumor activity of lenvatinib with anti-PD-1 antibodies. *Cancer Res* (2022) 82(2):292–306. doi: 10.1158/0008-5472.Can-20-2426

55. Gao X, Jiang M, Chu Y, Han Y, Jin Y, Zhang W, et al. ETV4 promotes pancreatic ductal adenocarcinoma metastasis through activation of the CXCL13/CXCR5 signaling axis. *Cancer Lett* (2022) 524:42–56. doi: 10.1016/j.canlet.2021.09.026

56. Dumortier M, Ladam F, Damour I, Vacher S, Bièche I, Marchand N, et al. ETV4 transcription factor and MMP13 metalloprotease are interplaying actors of breast tumorigenesis. *Breast Cancer Res BCR* (2018) 20(1):73. doi: 10.1186/s13058-018-0992-0

57. Zhou Y, Wang M, Shuang T, Liu Y, Zhang Y, Shi C. MiR-1307 influences the chemotherapeutic sensitivity in ovarian cancer cells through the regulation of the CIC transcriptional repressor. *Pathol Res Pract* (2019) 215(10):152606. doi: 10.1016/j.prp.2019.152606

58. Sinclair PB, Ryan S, Bashton M, Hollern S, Hanna R, Case M, et al. SH2B3 inactivation through CN-LOH 12q is uniquely associated with b-cell precursor ALL with iAMP21 or other chromosome 21 gain. *Leukemia* (2019) 33(8):1881–94. doi: 10.1038/s41375-019-0412-1

59. Baughn LB, Meredith MM, Oseth L, Smolarek TA, Hirsch B. SH2B3 aberrations enriched in iAMP21 b lymphoblastic leukemia. *Cancer Genet* (2018) 226-227:30–5. doi: 10.1016/j.cancergen.2018.05.004

60. Maslah N, Cassinat B, Verger E, Kiladjian JJ, Velazquez L. The role of LNK/SH2B3 genetic alterations in myeloproliferative neoplasms and other hematological disorders. *Leukemia* (2017) 31(8):1661–70. doi: 10.1038/leu.2017.139

61. Doghman-Bouguerra M, Granatiero V, Sbiera S, Sbiera I, Lacas-Gervais S, Brau F, et al. FATE1 antagonizes calcium- and drug-induced apoptosis by uncoupling ER and mitochondria. *EMBO Rep* (2016) 17(9):1264–80. doi: 10.15252/embr.201541504

62. Jiang LP, Fan SQ, Xiong QX, Zhou YC, Yang ZZ, Li GF, et al. GRK5 functions as an oncogenic factor in non-small-cell lung cancer. *Cell Death Dis* (2018) 9(3):295. doi: 10.1038/s41419-018-0299-1

63. Sommer AK, Falcenberg M, Ljepoja B, Fröhlich T, Arnold GJ, Wagner E, et al. Downregulation of GRK5 hampers the migration of breast cancer cells. *Sci Rep* (2019) 9(1):15548. doi: 10.1038/s41598-019-51923-1

64. Jiang Y, Chen Y, Gao L, Ye Q, Alonso MA. [Expression pattern of MAL in normal epithelial cells, benign tumor, and squamous cell carcinoma of larynx]. *Lin chuang er bi yan hou tou jing wai ke za zhi = J Clin otorhinolaryngol head Neck Surg* (2009) 23(10):451–3.

65. Fanayan S, Shehata M, Agterof AP, McGuckin MA, Alonso MA, Byrne JA. Mucin 1 (MUC1) is a novel partner for MAL2 in breast carcinoma cells. *BMC Cell Biol* (2009) 10:7. doi: 10.1186/1471-2121-10-7

66. Crouchet E, Bandiera S, Fujiwara N, Li S, El Saghire H, Fernández-Vaquero M, et al. A human liver cell-based system modeling a clinical prognostic liver signature for therapeutic discovery. *Nat Commun* (2021) 12(1):5525. doi: 10.1038/s41467-021-25468-9

67. Toledano S, Nir-Zvi I, Engelman R, Kessler O, Neufeld G. Class-3 semaphorins and their receptors: Potent multifunctional modulators of tumor progression. *Int J Mol Sci* (2019) 20(3):556. doi: 10.3390/ijms20030556

68. Zhang X, Klamer B, Li J, Fernandez S, Li L. A pan-cancer study of class-3 semaphorins as therapeutic targets in cancer. *BMC Med Genomics* (2020) 13(Suppl 5):45. doi: 10.1186/s12920-020-0682-5

69. Gao X, Yang J, Chen Y. Identification of a four immune-related genes signature based on an immunogenomic landscape analysis of clear cell renal cell carcinoma. *J Cell Physiol* (2020) 235(12):9834–50. doi: 10.1002/jcp.29796

70. Karakus E, Zahner D, Grosser G, Leidolf R, Gundogdu C, Sánchez-Guijo A, et al. Estrone-3-Sulfate stimulates the proliferation of T47D breast cancer cells stably transfected with the sodium-dependent organic anion transporter SOAT (SLC10A6). *Front Pharmacol* (2018) 9:941. doi: 10.3389/fphar.2018.00941

71. Rahman N, Khan H, Zia A, Khan A, Fakhri S, Aschner M, et al. Bcl-2 modulation in p53 signaling pathway by flavonoids: A potential strategy towards the treatment of cancer. *Int J Mol Sci* (2021) 22(21):11315. doi: 10.3390/ijms222111315

72. Xu H, Chen Y, Gu M, Liu C, Chen Q, Zhan M, et al. Fatty acid metabolism reprogramming in advanced prostate cancer. *Metabolites* (2021) 11(11):765. doi: 10.3390/metabo11110765

73. Hua Y, Gao L, Li X. Comprehensive analysis of metabolic genes in breast cancer based on multi-omics data. *Pathol Oncol Res POR* (2021) 27:1609789. doi: 10.3389/pore.2021.1609789

74. Ruan S, Zhang Z, Tian X, Huang D, Liu W, Yang B, et al. Compound fuling granule suppresses ovarian cancer development and progression by disrupting mitochondrial function, galactose and fatty acid metabolism. *J Cancer* (2018) 9(18):3382–93. doi: 10.7150/jca.25136

frontiers | Frontiers in Immunology

TYPE Review
PUBLISHED 11 April 2023
DOI 10.3389/fimmu.2023.1175503

OPEN ACCESS

EDITED BY
Mohit Kumar Jolly,
Indian Institute of Science (IISc), India

REVIEWED BY
Vera Svobodova Donnenberg,
University of Pittsburgh, United States
Valeria Lucarini,
Bambino Gesù Children's Hospital (IRCCS), Italy

*CORRESPONDENCE
Martina Musella
martina.musella@unicatt.it;
martinamusella90@gmail.com
Antonella Sistigu
antonella.sistigu@unicatt.it;
antonella.sistigu@gmail.com

†These authors share first authorship

SPECIALTY SECTION
This article was submitted to Cancer Immunity and Immunotherapy, a section of the journal Frontiers in Immunology

RECEIVED 27 February 2023
ACCEPTED 23 March 2023
PUBLISHED 11 April 2023

CITATION
Manduca N, Maccafeo E, De Maria R, Sistigu A and Musella M (2023) 3D cancer models: One step closer to *in vitro* human studies.
Front. Immunol. 14:1175503.
doi: 10.3389/fimmu.2023.1175503

3D cancer models: One step closer to *in vitro* human studies

Nicoletta Manduca[1†], Ester Maccafeo[1†], Ruggero De Maria[1,2], Antonella Sistigu[1*] and Martina Musella[1*]

[1]Dipartimento di Medicina e Chirurgia Traslazionale, Università Cattolica del Sacro Cuore, Rome, Italy, [2]Fondazione Policlinico Universitario 'A. Gemelli' - Istituti di Ricovero e Cura a Carattere Scientifico (IRCCS), Rome, Italy

Cancer immunotherapy is the great breakthrough in cancer treatment as it displayed prolonged progression-free survival over conventional therapies, yet, to date, in only a minority of patients. In order to broad cancer immunotherapy clinical applicability some roadblocks need to be overcome, first among all the lack of preclinical models that faithfully depict the local tumor microenvironment (TME), which is known to dramatically affect disease onset, progression and response to therapy. In this review, we provide the reader with a detailed overview of current 3D models developed to mimick the complexity and the dynamics of the TME, with a focus on understanding why the TME is a major target in anticancer therapy. We highlight the advantages and translational potentials of tumor spheroids, organoids and immune Tumor-on-a-Chip models in disease modeling and therapeutic response, while outlining pending challenges and limitations. Thinking forward, we focus on the possibility to integrate the know-hows of micro-engineers, cancer immunologists, pharmaceutical researchers and bioinformaticians to meet the needs of cancer researchers and clinicians interested in using these platforms with high fidelity for patient-tailored disease modeling and drug discovery.

KEYWORDS

tumor microenvironment, cancer model, spheroids, organoids, microfluidic devices, organ-on-a-chip, drug screening

Abbreviations: ACT, adoptive cell therapy; ADCC, antibody-dependent cellular cytotoxicity; ALI, air-liquid interface; CAF, cancer-associated fibroblast; CAR, chimeric antigen receptor; CEA, carcinoembryonic antigen; CSC, cancer stem cell; CTL, cytotoxic T lymphocyte; DC, dendritic cell; ECM, extracellular matrix; GEMM, genetically engineered mouse model; ICB, immune checkpoint blocker; iToC, immunocompetent Tumor-on-a-Chip; MCTS, multicellular tumor spheroid; NK, natural killer; NSCLS, non-small-cell lung cancer; OoC, Organ-on-a-Chip; PBL, peripheral blood lymphocyte; PBMC, peripheral blood mononuclear cell; PDAC, pancreatic ductal adenocarcinoma; PDO, patient-derived organoid; PDX, patient-derived xenograft; TAM, tumor-associate macrophage; TCR, T cell receptor; TIL, tumor-infiltrating T lymphocyte; TME, tumor microenvironment; TNBC, triple-negative breast cancer; ToC, Tumor-on-a-Chip; 2D, two-dimensional; 3D, three-dimensional.

1 Introduction

Despite the impressive progress in early detection and development of increasingly efficient and tumor-targeted treatments over the past decade, cancer remains a major burden of disease worldwide and one of the leading causes of death (1). Currently, the greatest challenge in oncology is to move away from old "one-size-fits-all" treatments, which, in the majority of cases, work well only for a few patients, toward novel personalized "one dose-one patient" therapeutic approaches (2).

Tumor heterogeneity, within and across cancers, often represents the most significant roadblock in the implementation of effective patient-specific therapies (3–5). Of note, clinical diagnoses are mainly based on tumor biopsies which do not really capture the extensive intratumoral heterogeneity but may hide newly emerging, highly aggressive, tumor clones. Moreover, patients with the same cancer subtypes often present different tumor phenotypes that dynamically evolve during disease progression and clinical treatment, and lead to the most disparate therapeutic responses, including natural and acquired therapeutic resistance (6, 7). It is now well established that tumors are not simple masses of neoplastic cells, but rather heterogeneous collections of infiltrating or resident host non-neoplastic cells [mainly T and B lymphocytes, natural killer (NK) cells, dendritic cells (DCs), monocytes, endothelial cells, perycites, cancer-associated fibroblasts (CAFs), mesenchymal stromal cells and adipocytes], niche-relevant soluble factors (*i.e.*, cytokines, growth factors, metabolites, enzymes, miRNAs) and altered extracellular matrix (ECM) that actively interact with one other and constitute the tumor microenvironment (TME) (8). Increasing evidence highlights that this evolving and reciprocal interplay between cancer cells and TME players is a disease-defining factor as it governs cancer initiation, metastasis and drug resistance and thus represents a promising therapeutic target (9, 10).

In light of this, the chance to achieve the designing of successful personalized anticancer strategies, characterized by more durable and side effect-limited (or even better free) responses, will depend on the ability to accurately model cancer heterogeneity and TME interactions (11). If on the one hand two dimensional (2D) cultures, xenografts and syngeneic mouse models have made the history in cancer research, on the other hand, to date scientists are addressing their focus more and more on three dimensional (3D) *in vitro* systems which can preserve tumor proper genetic, proteomic, morphological and pharmacotypic features while offering the unprecedented possibility to deeply dissect tumor-stroma dynamics.

In this review we present an overview of cancer model (r)evolution over the years (Figure 1) for studying the biological implications of the TME on cancer progression and response to therapy. We critically discuss the opportunities of state-of-the-art *in vitro* 3D cell culture strategies, with an emphasis on cancer spheroids, organoids and Tumor-on-a-Chip (ToC) models, for the development of microphysiological platforms recreating human cancers growing within living organs. In addition, we point out the current limitations and challenges that such novel culture systems should overcome to fully establish, validate and exploit the fidelity of 3D models for cancer research and clinic.

2 Chronicles of conventional cancer models in preclinical research

For many years, *in vitro* 2D cell cultures and *in vivo* xenografts or genetically engineered animal models have been the gold standards in cancer research. Nevertheless, these "conventional" models lack the ability to sustain the complex genetic and phenotypic heterogeneity of the respective human patient-derived tumor samples as well as to model the disease pathogenesis while simultaneously facilitating comprehensive cellular and environmental manipulation (11). Given their wide availability, reproducibility, high-throughput and the overall low cost, 2D monolayer cultures of immortalized cell lines have been widely employed as initial screening models to elucidate the mechanisms of cancer biology and to identify the efficacy and safety of several drug candidates (12, 13). However, a large body of evidence indicates that these systems still present several drawbacks.

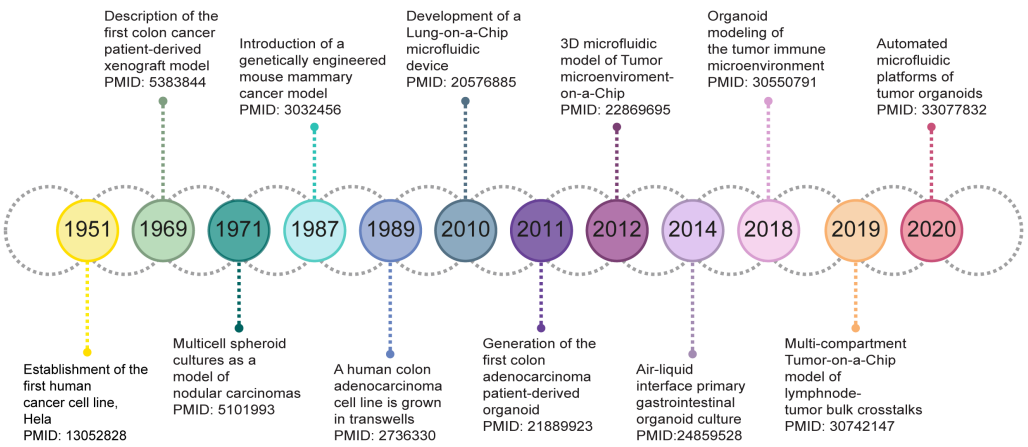

FIGURE 1
Timeline of milestones in the development of 3D cancer models.

First, isolation and culture maintenance of cancer cell lines from patient biopsies may be tricky and unproductive. Second, once cultured, these cells adhere, spread, and grow on a flat synthetic surface, do not conserve the original morphology and polarization, and therefore can potentially lose crucial cellular signaling pathways or change their responses to external *stimuli* (14–16). Third, cells in 2D cultures commonly undergo to extensive clonal selection thus resulting in the establishment of derived cell lines which no longer recapitulate the genetic heterogeneity of parental tumors. Finally, *in vitro* cancer cell lines are rarely flanked by a patient-matched 2D normal tissue counterpart and, most importantly, they do not provide significant information about the intricate network of dynamic interactions within the 3D TME of living patient's tumors, which instead can dramatically affect the efficacy of cancer therapies (17–19). In an attempt to partially simulate the complex *in vivo* cell-cell communications occurring in the TME, 2D co-cultures of cancer cell lines and different types of exogenous and heterogeneous cells [such as peripheral blood mononuclear cells (PBMCs) or CAFs] have been set up (20). In this regard, transwell cell cultures have been exploited to assess the capability of cells to migrate toward a particular chemo-attractant and additionally to test the ability of cancer cells to invade and bypass the ECM and to extravasate by pre-coating the top of the membrane insert with thin layers of ECM gels (such as collagen or Matrigel^{TM}) and endothelial cells (21). Anyway, despite somewhat more complex, such 2D reconstituted systems failed to faithfully model primitive intrinsic tumor stroma and its 3D architecture (22, 23).

Otherwise, preclinical *in vivo* animal models, such as patient-derived xenografts (PDXs) and genetically engineered mouse models (GEMMs), enable unique studies that intrinsically contemplate 3D tumor tissue organization and therefore offer system-level analysis of tumor onset, progression and treatment response (24, 25).

Due to their ability to retain morphologies, architectures and molecular signatures very close to those of the original tumors, PDX mouse models provide promising platforms for personalized cancer medicine (26). Hence, they have been increasingly utilized in both basic and preclinical cancer research as potential tools for biomarker detection, drug screening, drug-resistance mechanism investigation and novel therapy development (27–30). PDXs are generated by transplanting subcutaneously or orthotopically freshly derived patient material into immunodeficient mice. Even though subcutaneous transplantation models allow for easier cell transfer and precise monitoring of tumor formation and growth, orthotopic PDX mouse models better mimic the biological characteristics of the donor tumor in terms of phenotype - cancer heterogeneity and behavior - metastatic potential (31–34). Nevertheless, some important and unavoidable limitations have restricted PDX application in precision cancer therapy. Since they rely on immunocompromised/immunodeficient mice that lack the adaptive immune system, PDX mouse models do not fully recapitulate the surrounding tumor stroma and thus constitute inappropriate tools for the screening and the functional analysis of new immunotherapeutic agents (35). Furthermore, the progressive replacement of human stromal cells with recipient mouse cells may affect drug response predictions (36). In the last years, new humanized PDX mouse models have been generated by engrafting patient-derived tumors into immunodeficient mice bearing CD34+ human hematopoietic stem cells or PBMCs, but cost, time, throughput, and complete immune compatibility, remain unmet challenges (37, 38). Undoubtedly, the main weakness of PDX models is the inability to graft all tumor subtypes. For instance, hormone-sensitive breast cancer has a lower rate of engraftment than triple-negative tumors (39) and, more generally, non-metastatic tumors fail to stably engraft and grow in mice (32, 40). Finally, PDX models suffer from clonal selection pressure upon human tumor tissue engraftment and propagation leading to genetic and phenotypic divergence from the parental tumor (41, 42).

By contrast, GEMMs develop *de novo* tumors in an immunoproficient microenvironment thus enabling the investigation of the native interactions between cancer cells and the surrounding TME and representing valuable tools for testing the potential of cancer immunotherapies (43). Additionally, tumors arising in next-generation GEMMs closely mimic the histopathological and molecular features of their human counterparts, display genetic heterogeneity, and are able to spontaneously progress toward metastatic disease (44, 45). Although GEMMs have been successfully used in preclinical research (as reviewed in (46)) to validate candidate cancer genes and drug targets, assess therapy efficacy, dissect the impact of the TME, and evaluate mechanisms of drug resistance, there are still some aspects that need to be improved. In particular, their overall genetic manipulation is relatively limited and the introduction of novel (non)-germline mutations is a laborious and slow process (24).

On the whole, the development and validation of PDX and GEMM models is expensive, time- and resource-consuming, relatively low-throughput and subject to increasing ethical pressure for replacement solutions according to the 3Rs' principle in animal experimentation (47). As a result of these limitations, even preclinical *in vivo* models generally have a dramatic poor performance (~3%) in terms of predicting the clinical success of next-generation anticancer therapies (48).

3 3D models: Bridging the gap between cell cultures and live tissues

The need to reduce drug failure in clinical trials has encouraged researchers to deploy more sophisticated *in vitro* surrogate systems which can recreate human organs and diseases in the laboratory bench. In recent years, 3D cell models have gained even more attention in cancer research for their ability to closely replicate several hallmarks of *in vivo* tumors. Indeed, unlike 2D cell cultures, such systems provide a more realistic insight of tumor-tissue architecture, multicellular complexity and dynamic interplay between cancer cells and TME thus holding the great promise for many applications in tissue engineering, drug development, and precision medicine (49, 50). In the following sections, we will explore, in order of biological and technological complexity, the characteristics and potential applications of the most cutting edge 3D systems (Figure 2).

3.1 Tumor spheroids

Spheroids are one of the best established 3D culture methods for the study of tumor biology (51, 52). As extensively reviewed in (53), spheroids are microsized aggregates of closely-packed cells which accurately recapitulate some important features of solid tumors including internal structure, cellular heterogeneity, cell signaling pathways, ECM deposition, cell-to-cell and cell-to-ECM interactions, growth kinetics, gene expression and drug resistance. These unique characteristics highlight the potential of spheroids to be used as suitable *in vitro* tools for high-throughput screening of anticancer therapeutics (54–56).

Depending on cellular source and preparation protocols, spheroids can be distinguished into four major types, namely: (*i*) multicellular tumor spheroids (MCTSs) assembled using primary cell or cell line suspensions, (*ii*) tumorospheres obtained from solid tumor dissociation, (*iii*) tissue-derived tumorospheres generated from tissue remodeling after partial enzymatic or mechanical dissociation and (*iv*) organotypic multicellular spheroids consisting of cut and minced tumor fragment cultures obtained without dissociation (57). Of these, MCTSs are the best characterized spheroid models and have been widely used to reproduce different solid tumors, such as breast (58), cervical (59), colon (60), lung (61), pancreas (62), and prostate cancer (63), among the others. Currently, multiple techniques, requiring or not the incorporation of an exogenous scaffold, are available for MCTS production (64). In the most commonly employed scaffold-free methods, cells are cultured in conditions that force to strong cell-to-cell interactions and ultimately support cancer cell aggregation and ECM deposition. Several anchorage-independent methodologies have been developed, including the noteworthy hanging drop and liquid overlay protocols, followed by agitation-based, microencapsulation, and magnetic levitation systems (reviewed in detail in (65–67)). By contrast, scaffold-based approaches enable cells to grow dispersed on hydrogels that mimic ECM architecture or anchored to acellular matrices, which may be comprised by natural (*e.g.*, alginate, chitosan, dextran, hyaluronic acid), synthetic *(e.g.*, poly lactic-co-glycolic acid, polycaprolactone, polyvinyl alcohol and polyethylene glycol) biomaterials or decellularized natural ECM (*e.g.*, Matrigel™, collagen, fibrin, gelatin) (50, 68–70). More recently, advances in bioengineering techniques have emphasized the role of microfluidics and 3D bio-printing for the development of more

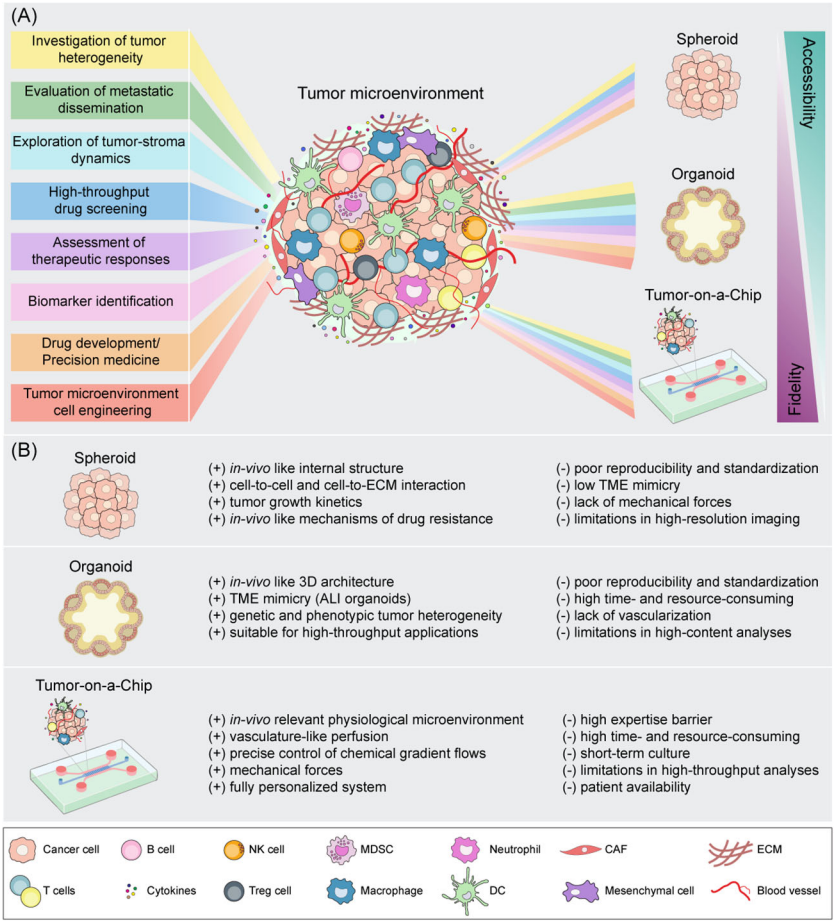

FIGURE 2
Schematic representation of spheroid, organoid and Tumor-on-a-Chip cell culture strategies for tumor microenvironment mimicking. **(A)** Downstream applications of state-of-the-art 3D models according to their accessibility and biological fidelity. **(B)** Benefits (+) and drawbacks (-) of 3D *in vitro* models. CAF, cancer-associated fibroblast; DC, dendritic cell; ECM, extracellular matrix; NK, natural killer; MDSC, myeloid-derived suppressor cell; Treg, regulatory T cell.

complex tumor spheroids with well-defined architecture, composition and high reproducibility which can model various cancer types and stages (71–74). Intriguingly, such Spheroid-on-a-Chip technologies have been proposed as preclinical platforms to investigate tumor angiogenesis, metastatic potential and chemotherapy response in glioblastoma, breast adenocarcinoma and ovarian cancer (73, 75, 76), as detailed below.

MCTCs have the ability to mimic to a great extent the TME thus offering a good representation of oxygen, nutrient, and other soluble factor diffusion and exchange (77). Indeed, if cells grown in monolayer cultures are uniformly exposed to nutrients and oxygen, cancer cells cultured as spheroids instead experience physiochemical gradients similar to those observed in micrometastases and avascular tumors (77). Moving toward the center of the spheroid, oxygen nutrient and pH levels decrease, whereas the amounts of carbon dioxide, lactate and waste products increase. Owing to the limited diffusion of nutrients and oxygen, larger spheroids (>500 μM in diameter) display an internal structure consisting of different cell layers: an inner anoxic and acidic core containing necrotic cells, a middle hypoxic zone of quiescent/senescent cells and an outer layer of highly proliferating cells (55, 78–80). Such heterogeneous multilayered organization is reported to be the key factor behind the use of spheroids as preclinical models to evaluate the therapeutic efficacy of anticancer treatments, including chemotherapy, radiation therapy, and immunotherapy (81–84).

The hypoxic environment found in the core of the spheroids is detrimental for all those drugs known to induce DNA and membrane damage *via* production of reactive oxygen species (*e.g.*, 5-fluorouracil, cisplatin, doxorubicin, and irinotecan) (77, 85, 86). Accordingly, Doublier and co-workers observed that in estrogen receptor-positive MCF7 breast cancer spheroids activation of hypoxia-inducible factor 1 together with an increase of P-glycoprotein expression were responsible for doxorubicin resistance (87). Similarly, Kim and colleagues showed that U251 glioma and U87 astrocytoma cells, grown as spheroids under hypoxia conditions, exhibited increased apoptosis resistance upon exposure to doxorubicin and the caspase-3 activating molecule resveratrol, as compared to monolayer cell cultures (88). Additionally, senescent and necrotic cells that reside in MCTS' inner zones were shown to be more resistant to antiproliferative compounds (*e.g.*, carboplatin, cisplatin, doxorubicin, oxaliplatin, methotrexate, and paclitaxel) than rapidly dividing cells (89, 90). In this regard, different breast cancer cell lines (*i.e.*, BT-549, BT-474, and T-47D) exhibited greater resistance to doxorubicin and paclitaxel associated with higher levels of hypoxia, increased percentages of G0-dormant cell subpopulation and lower expression of cleaved-PARP and caspase-3, when cultivated as 3D MCTSs. Moreover, the peculiar acidic pH of the spheroid core can induce changes in the net charge of some chemotherapeutics (*e.g.*, melphalan, methotrexate, mitoxantrone and vinca alkaloids) thus negatively affecting their intracellular uptake (91–93).

Importantly, the deposition of ECM proteins and the close ECM-cells and cell-cell physical interactions are known to increase spheroid density, leading to a higher interstitial fluid pressure which is responsible for the impaired penetration of anticancer drugs (94, 95). Therefore, compact and larger MCTCs are often more resistant to both chemotherapy and radiotherapy than loosely aggregated cells (96, 97). Of note, due to their structural similarities with *in vivo* solid tumors, MCTCs may also be used to improve the predictive value of nanomedicine screening and their physicochemical properties, by modeling the selective penetration, accumulation, retention, and distribution of drug-loaded nanocarriers within the tumor mass (98, 99).

MCTCs can be constituted exclusively of cancer cells (homotypic spheroids) or of cancer cells co-cultured with other cell types (heterotypic spheroids) such as fibroblasts, endothelial cells or immune cells (53, 58). Such heterotypic MCTCs are shown to be extremely helpful for studying tumor-immune system interactions and testing immunotherapeutic agents. Intriguingly, Coureau et al. recently exploited *in vitro* heterotypic co-cultures of human colorectal cancer MCTSs with immune cells to assess the infiltration, activation and function of T and NK cells. They showed that allogeneic T and NK cells infiltrated cell line-derived spheroids, inducing immune-mediated cancer cell killing and 3D structure destruction *via* the engagement of the activating receptor NKG2D (100) while cancer cells tried to evade immune recognition by upregulating HLA-E, ligand of the inhibitory receptor NKG2A expressed by CD8 T and NK cells. The simultaneous antibody targeting of both NKG2D ligands on cancer cells, in order to elicit an antitumor antibody-dependent cellular cytotoxicity (ADCC), and of the inhibitory receptor NKG2A on immune cells, highlighted an increased immune cell infiltration as well as a greater antitumor response (100). Ultimately, the authors confirmed these results in autologous co-cultures of colorectal cancer patient-derived spheroids and tumor-infiltrating lymphocytes (TILs) to generate a clinically relevant functional assay to the study of immunotherapies (100). A heterotypic colon carcinoma spheroid model was also used to evaluate the anticancer immune response of allogeneic Vδ2 γδ T lymphocytes triggered by zoledronate or cetuximab (101). Furthermore, gastric and ovarian MTCS models have been exploited to test the therapeutic efficacy of chimeric antigen receptor (CAR) T cells targeting the mesothelin antigen (102), whose preclinical and clinical testing in combination with immune checkpoint blockade (ICB)-based therapy has been extensively discussed in (103–105). Of interest, Dordick's group have recently developed a high throughput 3D tumor spheroid microarray consisting of a 330 micropillar-microwell sandwich platform where NK cells are co-cultured with pancreatic (MiaPaCa-2) or breast cancer cell lines (MCF-7 and MDA-MB-231) to faithfully recapitulate the hypoxic TME and investigate NK-cell mediated cell cytotoxicity in combination with the two monoclonal antibodies Trastuzumab and Atezolizumab (106).

Overall, these models are limited by the absence of stromal cells, which are usually present in the TME and are critical to the establishment of a chemoresistant cancer cell niche (107). Driven by the enticing possibility of improving cellular heterogeneity in MCTS cultures, Jeong et al. established a more clinically relevant colorectal cancer model by combining 3D co-culture with microfluidic technology. Specifically, tumor spheroids were grown within a collagen matrix-incorporated microfluidic chip and co-cultivated with CAFs in a microscale distance away, allowing

mutual microenvironmental interactions culminating in CAF activation, as demonstrated by the increase of α-smooth muscle actin (α-SMA) expression and migratory activity, as well as the induction of resistance to the chemotherapeutic paclitaxel (108).

To further complicate the system, a scaffold-free MCTS consisting of a triple co-culture of pancreatic cancer cells (PANC-1), fibroblasts (MRC-5) and endothelial cells (HUVEC) was assembled to closely mimic the *in vivo* influence of the surrounding TME on cancer cell therapeutic resistance (109). Remarkably, a heterotypic spheroid model composed of tumor cells, fibroblasts, and immune cells was developed to assess the efficacy of novel cancer immunotherapy agents [*i.e.*, IL-2 variant and tumor- or fibroblast-targeted T cell bispecific antibody] both as monotherapy and in combination (110). To better understand the role of macrophages in the TME using spheroids, Rebelo et al., developed a 3D culture model based on alginate microencapsulation and stirred culture strategies which enclosed tumor cell spheroids of non-small cell lung carcinoma (NSCLC), CAFs and monocytes. In such a way, they successfully recreated an immunosuppressive TME enriched in cytokines/chemokines (IL-4, IL-10, IL-13, CCL24, CXCL1), ECM elements (collagen type I, IV and fibronectin) and metalloproteases (MMP1/9), supporting cell migration and monocyte polarization toward an M2-like macrophage phenotype (109, 111). Similarly, Kuen et al., established pancreatic cancer spheroids consisting of different cancer cell lines (PaTu-8902, BxPc3, HPAC, and MiaCaPa-2) and MRC-5 fibroblasts, which then incubated with peripheral blood-derived monocytes. Such monocytes were able to penetrate into the spheroids, reflecting the *in vivo* tumor infiltration, and differentiated into M2-like macrophages (112).

Despite their huge potential, several issues still exist which hinder the application of MCTSs as high-fidelity preclinical cancer models. The main challenges concern the lack of standard protocols and methods to establish spheroids of uniform size and shape. In addition, some techniques are associated with low-throughput and difficulty in retrieving cells for readout analysis. Indeed, if on the one hand homotypic MCTS models provide a too simplistic tissue representation, on the other hand they are more suitable for high-throughput screenings. Conversely, heterotypic MCTSs strengthen the *in vitro* representation of TME but requires a mindful optimization of the cellular composition in terms of cell ratios and cell media components, consequently affecting the throughput (113). Furthermore, spheroids do not reproduce the complexity observed in the 3D tissue architecture of living organs nor incorporate mechanical forces (such as fluid shear stress, hydrostatic pressure and tissue deformation) that can significantly influence cancer cell behavior (114). Although nowadays a plethora of techniques are commonly employed to perform phenotypic and genetic analysis of tumor spheroids, such experimental procedures conceal several drawbacks. For instance, standard biochemical assays to evaluate viability and cytotoxicity (such as the acid phosphatase activity, the MTT, the Trypan Blue exclusion, and the lactate dehydrogenase assay) were found to be inefficient in 3D spheroids, usually due to the incomplete probe penetration and limited sensitivity (115–118). Optical, phase contrast, confocal, fluorescence and electron microscopic techniques are reported to be particularly valuable for characterizing spheroid size, morphology and internal organization (119–121). However, 3D model imaging is generally affected by poor light penetration, light scattering by cells, and high background (117, 118, 122). Flow cytometry and western blotting application on 3D structures can also be challenging. Indeed, both the techniques require spheroid enzymatic dissociation into single cell suspensions which inevitably leads to the loss of important information on marker spatial distribution (123–125).

To date, considerable efforts are being made to improve large-scale production of spheroids under highly reproducible conditions and to further adapt quantitative analysis and imaging techniques to such 3D models, in order to extract significant biological data and allow for high-throughput screening of anticancer drugs.

3.2 Tumor organoids

Organoids originally arise as 3D *in vitro* stem cell derived cultures that recapitulate the cellular variety, architectural organization and function of their *in vivo* normal tissue counterparts and have the ability to self-organize and self-renew (126–128). Since their discovery, organoids represented an ideal model for studying organ development (129) and host-pathogen interactions (130) by bridging the gap between *in vivo* animal models and *in vitro* 2D cell culture systems. The first attempts of generating organ-specific models *in vitro* date back to the early 2000's, when Sasai and colleagues demonstrated that embryonic stem cells could differentiate and self-assemble into 3D apico-basally polarized cerebral cortical tissues (131). Shortly after, Sato et al. established gut organoids from single mouse adult intestinal stem cells in specific culture conditions mimicking the *in vivo* stem cell niche and favoring the dynamic proliferation and differentiation of the intestinal crypt epithelium (132). This seminal work paved the way to grow other organotypic cultures of multiple mouse and human epithelial tissues, including colon (133), pancreas (134), liver (135), prostate (136–138), stomach (139), lung (140), endometrium (141), fallopian tubes (142), taste buds (143), salivary and mammary glands (144, 145), retina (131) and brain (131, 146).

Over the years, organoid technology promptly adapted to tumor biology providing a novel low-cost approach for cancer modeling and therapy development. Since they usually derive from one or few cells, and follow the different stages of cancer development, tumor organoids preserve key histopathological, genetic and phenotypic features of the parent tumor and retain cancer cell heterogeneity to a greater extent (126, 127, 147). Therefore organoids emerge as promising research tools to improve translational research and may have a potential relevance in clinical decision making (148).

To date, cancer organoids may be generated by multiple strategies. On the one hand genetic engineering of organoids from wild-type tissues or induced pluripotent stem cells provides a unique opportunity for determining the mechanisms of cancer initiation and progression in specific organs, the tumor niche factor requirements and the mutation pattern-related cellular response to anticancer therapies (149–151). Starting from available healthy human tissue-derived organoids, different reports exploited CRISPR-Cas9 genome

editing to introduce combinations of common driver mutations and model the multi-hit oncogenic transformation in colorectal (151–153), brain (154), gastric (155), pancreatic (156) and breast (157) cancer. Of note, numerous studies have focused on genetically engineered colorectal cancer organoids carrying oncogenic mutations in Wnt, EGFR, TP53 and TGFβ/BMP signaling pathways to gain deeper insights into the metastatic dissemination program. Surprisingly, although such organoids efficiently grew *in vivo* as invasive tumors, only when transplanted into their orthotopic environment, they were able to develop primary tumors that spontaneously formed distant liver and lung metastases as result of progressive loss of stem cell-niche dependency (158, 159). Organoids were also used to investigate the contribution of cancer stem cells (CSCs) to colorectal cancer clinical progression. Intriguingly, two seminal works from de Sauvage and from Sato teams, demonstrated how the selective CSC depletion restricted primary tumor growth but did not result in tumor regression, owing to the extensive cellular plasticity of human colorectal cancer cells. Indeed, proliferative differentiated cancer cells constantly attempt to replenish the CSC state leading to rapid tumor recurrence upon treatment cessation (160, 161). Remarkably, tumor organoids have also been derived from transgenic mouse strains to study the effects of a particular oncogenic mutation in the context of a specific genetic background. In this regard, Kuo and colleagues demonstrated that TGFβ receptor 2 was implicated in metastatic gastric cancer (162), whereas Fearon's group showed that the transcription factor CDX2 and BRAFV600E mutations cooperated to promote serrated colorectal cancer development (163).

Given the ability of genome-editing technologies to repair disease-causing genes, as previously demonstrated for the mutated dysfunctional CFTR allele in intestinal stem cell organoids of cystic fibrosis patients (164), genetic engineered cancer organoids are now revolutionarily investigated to test the possibility of reverting particular oncogenic mutations and the so leaded tumorigenic phenotype. Although cancer is genetically much more complex, with tumors typically harboring hundreds of mutations, it was shown that restoration of APC expression recovers crypt homeostasis in a colorectal cancer mouse model and derived organoids (165).

On the other hand, a large body of evidence has provided a proof-of-concept for generating patient-derived organoids (PDOs) which have shown relevant phenotypic and genetic resemblances with their original tumor specimens (166–168) and a tremendous potential in personalized cancer therapy (169). Unlike conventional cancer models, PDOs can be robustly propagated from a small sample size derived from solid/liquid biopsies or surgical resections of primary tumors (167), circulating cancer cells (170) and metastatic lesions (168, 171).

Since the establishment of the first colon adenocarcinoma PDO by Sato et al. (133), long-term tumor organoid cultures were successfully generated from a wide range of other primary colon (167, 172), oesophagus (173), pancreas (174), lung (175), stomach (176), liver (177), ovarian (178), breast (145), brain (179) and prostate (170, 180) cancer tissues, as well as from urothelial (181) and renal carcinoma (182). Importantly, the success rate of organoid generation from these selected cancer subtypes was almost always reported to be >70% and notably higher than that for traditional cancer cell lines (~20–30%) (183). Moreover, follow-up analyses of such 3D models suggest that organoids have the ability to preserve long-term parent tumor's biology including (epi)genetic, proteomic, morphological and pharmacotypic features. In addition, as PDOs are relatively easy to establish and cheap to maintain, they are suitable for high-throughput applications in the context of precision cancer treatments and help predict treatment responses and stratify individual patients to specific therapeutic regimens.

Therefore several "living biobanks" of PDOs capturing the histological and mutational heterogeneity of human cancers (like colon, pancreas, breast, prostate, liver, lung, stomach, ovary, kidney, bladder, and brain, among the others) have been created in recent years providing a representative collection of well-characterized models for preclinical drug screening and for predicting patient outcomes, as extensively discussed by others (147, 184). In 2015 van de Wetering et al. created the first organoid biobank from colorectal cancer patients consisting of 20 primary tumors matched with adjacent normal-tissue derived organoid cultures. By developing a robotized high-throughput drug screening, they tested 83 compounds (including standard-of-care chemotherapeutics and new targeted inhibitors) across the organoid panel and correlated drug sensitivity with cancer genomic features to identify molecular signatures and clinically relevant biomarkers associated with drug responses (167). In line with this previous report, Sato and colleagues generated a larger biobank of 55 colorectal cancer organoids derived from different histological subtypes and clinical stages, including the poorly differentiated adenocarcinoma, mucinous adenocarcinoma, and neuroendocrine carcinoma and observed a progressive decrease in niche factor requirements during adenoma-carcinoma transition, reflecting accumulation of multiple mutations (172). Interestingly, the authors underscored cancer organoids' ability to model distinct histopathological features and genetic signatures of their parental tumor counterparts also following xenotransplantation under the kidney capsule of immunodeficient mice, suggesting that such 3D culture systems can be effectively employed to validate *in vitro* drug responses in a more complex *in vivo* environment (172). Similarly, Ooft et al. derived a collection of PDOs from metastatic colorectal cancer patients to predict responsiveness to standard-of-care chemotherapy (185). These organoids were able to predict responses of the biopsied lesion in more than 80% of patients treated with irinotecan-based therapies without misclassifying patients who would have benefited from treatment. Conversely, such predictive value was not identified for 5-fluorouracil or oxaliplatin combined treatment, probably because of the lack of the surrounding TME, which might influence the efficacy of one treatment more than the other. Additionally, to test the potential of organoids to evaluate drug responses in preclinical settings, Verissimo et al. utilized a colorectal cancer organoid panel to evaluate the effect of different RAS pathway inhibitors that are currently used in the clinic, either as single agents or in combinations. Using this strategy, the authors confirmed that the presence of mutant RAS strongly correlated with resistance to these targeted therapies. Moreover, they highlighted that combinatorial targeting of the EGFR-MEK-ERK pathway in RAS mutant

organoids effectively suppressed tumor growth by inducing a transient cell-cycle arrest rather than cell death (186). Moreover, Ganesh et al., established a biorepository of 65 patient-derived rectal cancer organoid cultures from patients with primary, metastatic or recurrent disease to study individual responses following chemoradiation (187).

As pancreatic cancer is one of the most lethal malignancies with high recurrence rate and a minor survival benefit following systemic therapy, different libraries of primary pancreatic ductal adenocarcinoma PDOs were generated to determine prognosis-predictive gene expression signatures (156, 174). Notably, Tiriac et al., attempted to fully recapitulate the mutational spectrum and transcriptional subtypes of primary pancreatic cancer and hence established pancreatic cancer organoids from a comprehensive cohort of 138 patients. Detailed pharmacotyping of these organoid lines revealed genetic and transcriptomic signatures associated with anticancer drug response that could potentially correlate with patient clinical outcomes. Interestingly, by focusing their attention on 9 patients with advanced pancreatic adenocarcinoma, they obtained a retrospective clinical follow-up which perfectly matched with PDO chemosensitivity profile (174). Recently, a living biobank of more than 100 breast cancer organoids was generated from a wide variety of primary and metastatic tumors broadly recapitulating the diversity of the disease. Besides preserving the typical breast cancer morphology and histopathology, most of these organoids also retained the hormone receptor and the HER2 status of the original tumors allowing *in vitro* drug screens that were consistent with patient response (145).

Alongside these large biobanks, smaller PDO collections from advanced prostate and primary liver cancer were generated that helped validate that tumor organoids recapitulate molecular and genomic diversity of cancer subtypes and enable physiologically relevant drug screens (170, 177).

Kim et al. reported a method for successfully creating a living biobank of 80 lung cancer organoids that were assessed for drug sensitivity to both cytotoxic (*i.e.*, docetaxel) and targeted agents (*i.e.*, olaparib, erlotinib and crizotonib). According to what observed in patients, organoids exhibited a mutation-based drug sensitivity profile. Therefore, as expected, responses to olaparib (PARP inhibitor), erlotinib (EGFR tyrosine kinase inhibitor) and crizotonib (c-Met inhibitor) correlated with BRCA2, EGFR and MET mutational status, respectively (175). Moreover, Vlachogiannis et al., applied PDOs to predict the clinical outcomes of gastrointestinal cancer patients undergoing a compound library of drugs (encompassing chemotherapeutics, immunotherapeutics and targeted therapy agents) either already approved in the clinic or currently in clinical trials. By comparative analysis of the drug sensitivity of patients with metastatic gastrointestinal cancers and that of corresponding PDO models, they showed that the PDO model can accurately recapitulate patient responses in the clinic and could be implemented in personalized medicine programs to define cancer vulnerabilities while improving treatment responses (171). Two organoid platforms that capture intra- and interpatient heterogeneity were also successfully developed from multiple stages and subtypes of ovarian cancer. PDO drug screening of both chemotherapeutics (platinum/taxanes) and targeted agents (PIK3K/AKT/mTOR inhibitors or PARP inhibitors) revealed relevant differences in drug sensitivity which significantly correlated with clinical responses (188, 189).

In 2020, Calandrini et al. described the first pediatric cancer organoid biobank consisting of tumor and matching normal organoid cultures from over 50 children with different subtypes of kidney cancer, including Wilms tumors, malignant rhabdoid tumors, renal cell carcinomas, and congenital mesoblastic nephromas. By using this approach, they identified treatments with the best therapeutic ratio, considering both tumor efficacy and normal tissue toxicity (190). Yao et al. established a living organoid biobank of locally advanced rectal cancer and showed that PDOs could predict chemoradiation responses in patients (191). Yet, Lee et al., screened 50 drugs in organoid models of bladder cancer, expressing the FGF receptor, mitogen-activated protein kinase, and the mechanistic target of rapamycin inhibitors (192). More recently, Song and colleagues reported methods for generating and biobanking high-fidelity patient-derived glioblastoma organoids to test personalized therapies and model CAR T cell-based immunotherapy (179).

A less described application of organoids lies in a better understanding and prediction of treatment-related side effects, which is often observed with targeted therapy. As organoids can be generated from both healthy and tumor tissues of the same patient, they offer the possibility to screen for drugs that specifically target tumor cells while leaving normal cells unharmed thus potentially reducing toxicities in clinical trials (193).

Despite the multiple downstream therapeutic applications of tumor organoids, the lack of stromal components and of an immune-competent microenvironment may hamper the implementation of this approach in a clinical setting. Therefore significant efforts have already being made in order to incorporate aspects of the TME into the cancer organoid system and thus to decipher complex tumor immune cell crosstalks, to identify immune evasion mechanisms and to determine the effectiveness of various immunotherapeutic approaches (194).

Three main strategies have been developed to date to capture TME cell heterogeneity and heterotypic cell interactions, specifically: (*i*) reconstituted submerged cultures (195), (*ii*) holistic microfluidic 3D cultures (196), and (*iii*) air-liquid interface (ALI) cultures (197).

In reconstituted TME models, organoids containing exclusively cancer cells, derived from mechanically and enzymatically dissociated tissues, are cultured in ECM domes (*e.g.*, Matrigel™ or Cultrex® Basement Membrane Extract) and submerged beneath tissue culture medium. Exact culture conditions are customized for specific tumor histologies, but often include various growth factors and/or pathway inhibitors which allow stem cells to undergo self-renewal and differentiation (*e.g.*, in intestinal organoids) (20). To model the TME, exogenous immune cells, such as those from autologous peripheral blood or tumor bulk, are isolated and subsequently co-cultured with grown organoids. Such submerged reconstituted PDOs are suitable for modeling cancer disease and for screening drug efficacy by recapitulating not only the genetic and phenotypic diversity of original tumors, but also the functional patient responses to clinical treatment (187, 198). Several reconstitution approaches were developed by supplementing PDO

cultures with CAFs. Interestingly, human ductal adenocarcinoma (PDAC) organoids co-cultured with CAFs revealed that CAF-secreted Wnt drives organoid growth in Wnt-non-producing PDAC subtypes (156). Additionally, co-culture of murine pancreatic stellate cells with PDAC organoids revealed desmoplastic stroma production and heterogeneous CAF differentiation into two distinct subtypes: IL-6-expressing inflammatory CAFs activated by paracrine secreted factors from tumor cells, and high αSMA-expressing myofibroblast-like CAFs that interact with tumor cells (199). Of note, in another study reconstituted PDOs enabled the identification of IL-1 and TGFβ as tumor-secreted ligands responsible of shaping the above-mentioned CAF heterogeneity (200). Similarly, Ebbing, van der Zalm et al. co-cultured oesophageal adenocarcinoma organoids with patient-derived CAFs and found that stromal-derived IL-6 drove epithelial-to-mesenchymal transition and therapeutic resistance (201). Diverse immune cell reconstitution of submerged Matrigel™ organoids has also been performed. By co-culturing patient-matched CAFs and peripheral blood lymphocytes (PBLs) with PDAC organoids, Tsai et al. demonstrated myofibroblast-like CAF activation and tumor organoid lymphocyte infiltration (202). A noteworthy study reported a more complex setup involving a triple co-culture of mouse gastric tumor organoids, DCs and cytotoxic T lymphocytes (CTLs). In the presence of anti- PD-L1 neutralizing antibody, antigen stimulated-CTLs killed gastric tumor organoids, suggesting that the reconstitution of multiple immune cells may allow the study of tumor–immune and immune–immune cell crosstalks (203). Furthermore, reconstitution models of tumor organoids with autologous PBLs hold the potential to predict the functionality of TILs after ICB-based therapy. In a proof-of-principle study, Ramsay and colleagues co-cultured human colorectal cancer organoids with TILs and observed that exposition to anti–PD-1 antibody partially restored antitumor immunity of PD1-expressing T cells (204). Accordingly, Voest's group generated tumor-reactive $CD4^+$ and $CD8^+$ T lymphocytes by co-culturing autologous PBMCs with colorectal cancer or NSCLC PDOs, in medium supplemented with IL-2, anti-CD28, and anti-PD1 (195, 205). In a clinical study with early stage colon cancer patients treated with neoadjuvant immunotherapy, Chalabi et al. used the same autologous organoid and PBMC co-culture system to potentially correlate *ex vivo* induced T cell reactivity to patient response. However, T cell reactivity could only be partly linked to clinical response, due to the absence of anti-CTLA4 in the co-culture system and lack of key TME constituents (206). Organoid-based immune assays have also been explored to provide a rationale for combination treatments of targeted MEK or BRAF inhibitors with multiple ICB agents (207).

Given their adaptability, tumor organoids have been applied for numerous other immunotherapeutic approaches. In this regard, Gonzalez-Exposito et al. used patient-derived colorectal cancer organoids to gain insight into treatment response to cibisatamab, a carcinoembryonic antigen (CEA)-targeting bispecific antibody (208) demonstrating that heterogeneity and plasticity of CEA expression conferred low sensitivity to such an agent. Moreover, tumor organoids may support studies in the field of adoptive cellular therapy (ACT), including the use of tumor TIL, NK, and CAR-T cell treatments. Intriguingly, Schnalzger et al. used available matching normal and tumor organoids to explore tumor antigen-specific cytotoxicity of CAR-NK cells (209).

Otherwise, holistic TME models preserve, as a cohesive unit, the intrinsic immune microenvironment of tumor specimens along with tumor cells. Of interest, spheroid-based organotypic cultures within collagen gels in 3D microfluidic culture devices have been adapted to culture murine- or patient-derived tumors (114). Briefly, tumor spheroids from syngeneic immunocompetent murine models and patient tumor specimens, such as melanoma and Merkel cell carcinoma, were mixed with collagen gels, injected into microfluidic devices and cultured for 1–2 weeks (196, 210, 211). Flow cytometric immune cell profiling showed that such organotypic cultures were able to retain cancer cells as well as autologous lymphoid and myeloid cell populations while recapitulating the *in vivo* therapeutic sensitivity and resistance profile to PD-1 blockade (211). *In vitro* culture systems are further being deployed to explore novel mechanisms, therapeutic combinations, and putative biomarkers relevant to ICB response and resistance. In another study, small-molecule screening identified CDK4/6 inhibitors as compounds enhancing T cell activation in PD-1-overexpressing Jurkat T cells. Combination of CDK4/6 inhibition and PD-1 blockade significantly induced tumor cell death *in vitro* in MC38 murine-derived organoids, as evidenced by tumor live/dead staining as well as by T cell-mediated tumor growth inhibition *in vivo* in syngeneic MC38 and CT26 mouse models (210).

More recently, ALI cultures offer a valuable and more sophisticated alternative to co-culture the original tumor epithelium *en bloc* with its native stromal and immune cells without any reconstitution (212). In this method tumor organoids from minced primary tissue fragments containing both tumor cells and immune components are embedded in a collagen gel within an inner transwell dish. Culture medium in an outer dish diffuses *via* the permeable transwell into the inner dish and the top of collagen layer is exposed to air *via* an ALI, allowing cells access to a sufficient oxygen supply (197). Initially, ALI organoid method was developed to culture different normal tissues, including small intestine, colon, stomach, and pancreas, which were shown to comprise both epithelial and mesenchymal components. Subsequently, this technology was extended to the establishment of PDOs from human biopsies, such as melanoma, renal cell carcinoma, and non-small cell lung cancer, as well as from murine tumors in syngeneic immunocompetent mice (197). ALI PDOs preserve not only the genetic alterations of the original tumor, but also the complex cellular composition and architecture of the TME. Indeed, both tumor parenchyma and stroma are retained, including fibroblasts and a variety of endogenous infiltrating immune cell populations, such as TAMs, T cells [T helper (Th), cytotoxic (Tc), regulatory (Treg), and exhausted (Tex)], NK cells, and B cells (197).

Strikingly, the ALI PDOs could preserve the T cell receptor (TCR) heterogeneity found in the original tumor and model immune checkpoint-dependent mechanisms of immune suppression (197). Indeed, ALI organoids grown from mouse tumors inoculated into syngeneic immunocompetent mice (*i.e.*, B16-SIY, MC38, and A20) and from diverse human cancer

biopsies, (such as NSCLC, melanoma, and renal cell carcinoma) exhibited antigen-specific clonal $CD8^+$ T cell expansion, activation and subsequent tumor killing in response to anti-PD-1/PD-L1 antibodies (213).

As extensively discussed, tumor organoids have undoubtedly emerged as physiological relevant *in vitro* models to study cancer biology. However, to realize their full potential, key challenges need to be addressed. First, the use of non-standardized and ill-defined culture protocols across cancer organoid studies (*i.e.*, cancer tissue source, medium formulations, animal-derived 3D matrices) introduces a huge technical variability that leads to a misrepresentation of cancer's intrinsic biological heterogeneity which may potentially affect drug development and biomarker discovery (214). Second, for several cancer subtypes the efficiency of organoid derivation is extremely low and to date only few studies were able to adapt the organoid approach for non-epithelial cancers (11, 127). Third, established organoid cultures often include only cancer cells and do not support long-term co-culture of other TME cell types (212). In the future, the development of next-generation tumor organoids will require a meticulous patient-specific understanding of the *in vivo* tumor niche in order to identify the necessary medium components to maintain non-neoplastic cells in culture and favor heterotypic interactions. Last, but not the least, organoids are significantly high time- and resource-consuming and in order to become highly relevant model for translational applications they require optimization of high-throughput and high-content functional readout analyses, as already described for spheroids.

3.3 Tumor-on-a-Chip models

Organ-on-a-Chip (OoC)-technology is a rapidly evolving, highly innovative, and promising tool that allows *in vitro* microscale biomimetics of human organs. By flanking and integrating cell biology with microengineering and microfluidics, OoCs model physiological and pathological tissue microenvironments thus breaking conventional *in vitro* and *in vivo* impasses (215). Specifically, OoCs are multichannel microfluidic cell-culture devices hosting multiple cell types organized in a 3D tissue, and even organ, structure in order to model with high fidelity, and to control with high precision, key structural and functional units including, but not limited to, vasculature-like perfusion, heterotypic cellular interactions, flows of chemical gradients and mechanical forces (216–219). These features make OoCs accurate human-relevant models critical to address questions that conventional cell culture and animal models do not (220, 221). Indeed, conventional *in vitro* models are not complex enough to recapitulate tissue/organ pathophysiology, and animal models do not faithfully mimic human disease and natural and therapy-induced response (218). Since their first introduction in basic research in the early 2000s (222–224), OoCs rapidly became a valuable asset to model and dissect a wide range of pathologies across all human organs (225–231) as well as to screen and test various therapeutics (232, 233). For the sake of completeness, as the OoC field is constantly evolving, new devices with improved functionality, integration, and automation are emerging that recapitulate multi-organ-, body-, and even patient-on-chip complexities at once, as exhaustively covered in (234–237). Therefore, the key advantage of OoCs is the unique possibility, they offer, to recreate a patient-tailored disease model taking into consideration the genetic make-up, sex and gender features that affect drug response (238). Of note, OoCs enable high-throughput, high-resolution, live imaging, which allows to track cell trajectories and quantify heterotypic cell interaction times at once. In addition, end point assays could be performed to interrogate recovered cell states at transcriptomic, proteomic and biochemical/metabolic levels and to analyze cell secretome on perfused cell culture media (239). All these aspects render OoC platforms perfect tools for cancer research, which led to the rise of the ToC concept (202, 240–242) (Table 1). Today we dispose of state-of-the-art ToC platforms that allow, in a less than 1-inch chip, to precisely recapitulate and timely control critical hallmarks of the TME and to integrate all tissue components while envisioning in real-time cell-to-cell interactions and co-evolutions (243, 244). In particular, immunocompetent ToC (iToCs) models are emerging as precious tools to analyze and manipulate crucial aspects affecting both cancer onset and progression as well as response to therapy (245, 246). Indeed, 2D cell culture models do not recapitulate the TME and *in vivo* animal models do not effectively resemble its immune contexture and the response to immunogenic and immune-based therapies (247, 248). By *in vitro* mimicking human immunity, advanced iToCs address these unmet challenges and help understand natural and therapy-induced evolutive pressures as well as predict the clinical efficacy and safety outcomes of tested drugs (245). In addition, by integrating TME biomimicry with vasculature-like perfusion, iToCs allow to tightly control and manipulate oxygen and nutrient supply, the release of growth factors and cytokines and the interaction with ECM components (249, 250) and to recapitulate and systematically depict the communication between cells in disease progression and metastatic dissemination in an unprecedented detail (251, 252). First generation iToCs were designed to represent study-tailored TME where cell types and positions reflect experimental needs and specific research questions. In their simplest form, iToCs have been used to study 2D cell migration and immune cell chemotaxis in response to chemokine and immune alarmin gradients (246, 253–257). Immune cell trajectories and interaction with cancer cells were real-time monitored and quantified by time-lapse microscopy and automated tracking analysis (246, 254–257). In a bit more complex system, we and others analyzed competitive immune chemoattractant forces of cancer cells with diverse immunogenicity by culturing in opposite, microchannel connected, chambers three different cell types (246, 254, 257, 258). Similar devices have been used to study cancer cell interactions with stromal and immune cells when cultured in separate chambers (259). In a seminal study, Yu and collaborators described a reconfigurable iToC allowing the spatiotemporal control of paracrine signaling between pancreatic cancer cells and TAMs (260). According to a fit-for-purpose approach, the authors assembled a 'stackable' multi-culture system, in which each cell component was cultured in a distinct layer, and then stacked,

TABLE 1 Summary of Tumor-on-a Chip platforms.

Tumor-on-a-Chip models	Cell types	Applications	Drugs	References (PMID)
Lung Cancer	A549, H1975, H560, LCA-1, NCI-H1650, H2052 spheroids, BE063-T, BE069-T spheroids	drug response and resistance, evaluation of photodynamic therapy, tumor-stroma crosstalks, tumor-bacteria crosstalks, tumor migration and metastasis	Gefitinib, Afatinib, Osimertinib, Erlotinib, Cisplatin	36005014, 29029734, 29020635, 26088102, 29686328, 27606718
Breast Cancer	ductal carcinoma in situ cells, MCF10A, HMT-3522, BC tumor organoids, MDA-MB-231, SUM-159, SK-BR-3 spheroids	tumor invasiveness and metastasis, angiogenesis, cell cytotoxicity, drug sensitivity, metabolic adaptation	Doxorubicin, Tirapazamine, Paclitaxel, Taxol	27549930,30482722, 30723584, 30393802, 27678304, 33094918, 36278146
Prostate Cancer	DU145, LNCaP, C4–2, PC3, BCaP	TME mimicking, immunological studies, drug testing	Docetaxel, Paclitaxel	30810874, 28371753, 33034643, 31427781
Colorectal Cancer	CRC-268, Caco-2, HCT116, SW620, SW480, HT-29, MC38 spheroids, CT26 spheroids, colon organoids	angiogenesis, tumor-stroma crosstalks, immunological studies, drug sensitivity, nanomedicine, pharmacokinetic, pharmacodynamic, tumor metastasis	Bevacizumab, FOLFOX, Oxaliplatin, Pazopanib, Vincristine, CMCht/PAMAM dendrimer nanoparticles loaded with gemcitabine, Doxorubicin, Pembrolizumab, Ipilimumab, 5-fluorouracil	30393802, 27549930, 31131324, 28544639, 27796335, 27391808, 28439087, 20126684, 29101162, 34113836
Pancreatic Cancer	PAC, PANC-1, PDAC162, PDAC175, PD7591, MH6883, PD883, MH6556, S2-028, KPC2, eKIC, mKIC, PDOs	immunological studies, TME mimicking, EMT investigation, drug resistance, tumor-stroma crosstalks, tumor invasiveness	Gemcitabine, All-trans retinoic acid, Clodrosome, Paclitaxel	32930334, 31489365, 31546820, 31997571, 35450328, 29329547
Melanoma	MNT-1, WM-115, LOX-IMVI, A-375, SK-Mel-28 spheroids	angiogenesis, tumor-stroma crosstalks, tumor migration, drug resistance, immunological studies	Vemurafenib	33533390, 26542093, 36671624
Ovarian Cancer	SK-OV-3, OV90, OVCAR-3,A2780	angiogenesis, tumor-stroma crosstalks, TME mimicking, immunological studies, tumor invasiveness, tumor-platelet crosstalks, tumor metastasis	Cisplatin, Revacept	28544639, 34290095, 32851999, 33524968, 35995621
Brain Cancer	U-251 MG, primary GBM cell culture, U87 spheroids, GS5, SKNBE, PC9-BrM3	TME mimicking, drug screening, tumor cell heterogeneity, tumor metastasis	Temozolomide, Tirapazime, Cisplatin, Irinotecan, Isotretinoid	31148598, 27151082, 27796335, 31016107, 29158813, 31034948

TME, tumor microenvironment; EMT, epithelial-to-mesenchymal transition; PDO, patient-derived organoid; GBM, glioblastoma.

unstacked, and dynamically reconfigured over the course of the study in order to control the spatial and temporal interaction of these subsets. By manoeuvering the system, the authors recapitulated the *in vivo* observation that paracrine signaling from more aggressive prostate cancer cell variants tips the balance of TAM polarization toward an anti-inflammatory, M2-like phenotype which, in turn, promotes the formation of new blood vessels by signaling with endothelial cells (260). Similar findings were described by Guo et al. and Kim et al. in a NSCLC and triple-negative breast cancer (TNBC) model, respectively (260–262). As ECM meshwork is known to deeply condition cancer immunosurveillance and therapeutic response (263–265), more complex iToC systems including ECM scaffolds were developed that allowed researchers to create a 3D TME where testing with high fidelity the therapeutic effects of immune-based drugs (266–269). More recently, *ex vivo* cultures of human tumor tissues were introduced in iToCs as a representative platform to profile ICB-based therapies (211). Notably, within this setting, elaborated iToCs have been designed that are characterized by a tightly planned spatial compartmentalization allowing immune cell migration from lymphnodes to blood circulation up to the TME, with the intent to faithfully reproduce the human cancer-immunity cycle (245, 270, 271). In particular, Shim et al. established a first model of multi-compartment iToC that recapitulates lymphnode-tumor bulk crosstalks through a continuous perfusion of culture medium (272). In the effort to integrate measurements of additional chemical and physical cues (*e.g.*, oxygen levels, cytokine and chemokine flows, ECM stiffness and remodeling, lymphatic shear stress and blood perfusion, among the others) working in the TME, *in vitro* iToCs have been combined with multiscale *in silico* modeling (273, 274). This systematic analysis offers a panoply of combined factors and dynamics molding overall tumor behavior in terms of progression and therapeutic response (273, 274). Specifically, oxygen levels in ToC models have been tuned either

by the introduction of physical barriers (266), or by placing the device into an hypoxic, adjustable culture chamber (266), or by naturally generating hypoxic cores within cancer spheroids (275). Cytokine-, chemokine- and alarmin-based flow gradients can be either pre-established in dedicated device sinks (276), or naturally triggered by the addition of soluble factors (277), or cancer cell death inducers (246, 257). As ECM composition and stiffness were shown to play a role in immune cell infiltration and therapeutic response (278), cancer matrices with diverse composition, porosity and density have been used and the ability to either impede immune cell migration, or promote immune-cancer cell crosstalk have been tested (266, 279). Lymphatic and blood perfusion are crucial players within the TME as they affect immune cell homing and cancer cell diffusion to distant sites (280–282). However, conventional *in vitro* cancer models almost always lack vascular perfusion. In this sense, iToCs represent a significant step forward, as they inherently include vessel-like microchannels that researchers took advantage of for studying neo-angiogenesis (283), cancer cell spreading through intravasation (284) and extravasation (285), and off-target effects of anticancer treatments (286). Moving forward in complexity and fidelity, through careful study design and co-culture selection, researchers have integrated cancer spheroids and organoids in iToC models (219, 287, 288). Chemical and biological drug testing are the most promising applications of cancer organoids-on-a-Chip as this merger greatly improves the fidelity of TME *in vitro* reconstruction. Hence, on the one hand cancer organoids, as described above, are miniaturized tumors that follow intrinsic developmental programs, developing from self-organizing stem cells, and resembling their *in vivo* counterparts better than any other *in vitro* modeling, on the other hand microfluidic platforms are man-made constructs in which heterotypic cell components and their microenvironment are precisely controlled (288). Moving forwards, the design of multi-organoids in iToCs could open the possibility to test drugs on patients routinely excluded from clinical trials, such as children and pregnant women. However, despite the impressive advances in iToC field and the enormous potential these models offer, issues remain that need to be addressed to reach the ambitious goal to broadly apply iToCs in biomedical research (289, 290). Indeed, it is still not possible to assess some systemic drug toxicities and side effects currently studied using animal models (*e.g.*, vomiting, diarrhea and alopecia). Integration of *in silico* modeling and artificial intelligence-based data analysis could maybe help in this sense and circumvent this limitation to some degree. Moreover, iToCs need to be improved in terms of throughput, adaptability and manufacturing. Indeed, (*i*) the high *in vivo* relevance of these models comes at the price of low throughput, as only a few replicates can be performed at once; (*ii*) the culture microenvironment needs to be adapted to the according patient-derived tumor, in a fit-for-purpose approach; and (*iii*) the high cost and the availability of equipment and materials to realize iToCs are a challenge to scale-up the manufacture (289–291).

In sum, while ToC models are still unable to fully replace animal studies, the ever growing flow of innovation in the design and development of microfluidic iToC technologies will continue to provide ripe rewards for the cancer research and will help to solve unmet challenges in both basic biology and clinical patient management, particularly in the field of immune-oncology and cancer immunotherapy, as comprehensively reviewed in (245).

Concluding remarks

The improvement and integration of cancer spheroids, organoids and iToCs into cancer research, drug development pipelines and patient care hold great potential as these models offer biologic fidelity along with experimental control as never before. Hence, 3D cancer models help recreate, in a stepwise manner, the complexity of the TME by making possible to decipher, monitor and timely maneuver the roles of individual cell players and of their reciprocal interactions on tumor progression and (immune)therapy response. Joining forces, know-hows and skills from micro-engineers, cancer immunologists, pharmaceutical researchers and bioinformaticians is anticipated to achieve the ambitious goal of overcoming the near-term challenges of these platforms in order to expand their implementation in disease modeling and drug discovery. Our vision is that, the selection of the right 3D cancer model for each experimental purpose, and the proper reconstitution and handling of the immune system, allow the development of integrated high fidelity TME representations and help to explore fundamental biology, and to tackle key issues of drug testing with critical impact on clinical management. This ultimately will help refine, reduce and replace animal studies, while helping human patients.

Author contributions

MM conceived the review. MM, AS and RD wrote the manuscript with constructive input from all authors. NM and EM prepared display items under the supervision of MM. All authors contributed to the article and approved the submitted version.

Funding

MM is supported by the AIRC-FIRC fellowship n. 25558.

Conflict of interest

The authors declare that the research was conducted in the absence of any commercial or financial relationships that could be construed as a potential conflict of interest.

Publisher's note

References

1. Siegel RL, Miller KD, Fuchs HE, Jemal A. Cancer statistics, 2022. *CA: Cancer J Clin* (2022) 72:7–33. doi: 10.3322/caac.21708

2. Aboulkheyr Es H, Montazeri L, Aref AR, Vosough M, Baharvand H. Personalized cancer medicine: An organoid approach. *Trends Biotechnol* (2018) 36:358–71. doi: 10.1016/j.tibtech.2017.12.005

3. Dagogo-Jack I, Shaw AT. Tumour heterogeneity and resistance to cancer therapies. *Nat Rev Clin Oncol* (2018) 15:81–94. doi: 10.1038/nrclinonc.2017.166

4. Ramon YCS, Sese M, Capdevila C, Aasen T, De Mattos-Arruda L, Diaz-Cano SJ, et al. Clinical implications of intratumor heterogeneity: Challenges and opportunities. *J Mol Med* (2020) 98:161–77. doi: 10.1007/s00109-020-01874-2

5. Vitale I, Shema E, Loi S, Galluzzi L. Intratumoral heterogeneity in cancer progression and response to immunotherapy. *Nat Med* (2021) 27:212–24. doi: 10.1038/s41591-021-01233-9

6. Aldea M, Andre F, Marabelle A, Dogan S, Barlesi F, Soria JC. Overcoming resistance to tumor-targeted and immune-targeted therapies. *Cancer Discovery* (2021) 11:874–99. doi: 10.1158/2159-8290.CD-20-1638

7. Gatenby RA, Brown JS. Integrating evolutionary dynamics into cancer therapy. *Nat Rev Clin Oncol* (2020) 17:675–86. doi: 10.1038/s41571-020-0411-1

8. Anderson NM, Simon MC. The tumor microenvironment. *Curr Biol CB* (2020) 30:R921–5. doi: 10.1016/j.cub.2020.06.081

9. Valkenburg KC, de Groot AE, Pienta KJ. Targeting the tumour stroma to improve cancer therapy. *Nat Rev Clin Oncol* (2018) 15:366–81. doi: 10.1038/s41571-018-0007-1

10. Roma-Rodrigues C, Mendes R, Baptista PV, Fernandes AR. Targeting tumor microenvironment for cancer therapy. *Int J Mol Sci 20* (2019) 20(4):840. doi: 10.3390/ijms20040840

11. LeSavage BL, Suhar RA, Broguiere N, Lutolf MP, Heilshorn SC. Next-generation cancer organoids. *Nat Mater* (2022) 21:143–59. doi: 10.1038/s41563-021-01057-5

12. Jensen C, Teng Y. Is it time to start transitioning from 2D to 3D cell culture? *Front Mol Biosci* (2020) 7:33. doi: 10.3389/fmolb.2020.00033

13. Wilding JL, Bodmer WF. Cancer cell lines for drug discovery and development. *Cancer Res* (2014) 74:2377–84. doi: 10.1158/0008-5472.CAN-13-2971

14. Duval K, Grover H, Han LH, Mou Y, Pegoraro AF, Fredberg J, et al. Modeling physiological events in 2D vs. 3D cell culture. *Physiology* (2017) 32:266–77. doi: 10.1152/physiol.00036.2016

15. Gillet JP, Varma S, Gottesman MM. The clinical relevance of cancer cell lines. *J Natl Cancer Inst* (2013) 105:452–8. doi: 10.1093/jnci/djt007

16. Katt ME, Placone AL, Wong AD, Xu ZS, Searson PC. *In vitro* tumor models: Advantages, disadvantages, variables, and selecting the right platform. *Front Bioeng Biotechnol* (2016) 4:12. doi: 10.3389/fbioe.2016.00012

17. McMillin DW, Negri JM, Mitsiades CS. The role of tumour-stromal interactions in modifying drug response: challenges and opportunities. *Nat Rev Drug Discovery* (2013) 12:217–28. doi: 10.1038/nrd3870

18. Melissaridou S, Wiechec E, Magan M, Jain MV, Chung MK, Farnebo L, et al. The effect of 2D and 3D cell cultures on treatment response, EMT profile and stem cell features in head and neck cancer. *Cancer Cell Int* (2019) 19:16. doi: 10.1186/s12935-019-0733-1

19. Stock K, Estrada MF, Vidic S, Gjerde K, Rudisch A, Santo VE, et al. Capturing tumor complexity *in vitro*: Comparative analysis of 2D and 3D tumor models for drug discovery. *Sci Rep* (2016) 6:28951. doi: 10.1038/srep28951

20. Yuki K, Cheng N, Nakano M, Kuo CJ. Organoid models of tumor immunology. *Trends Immunol* (2020) 41:652–64. doi: 10.1016/j.it.2020.06.010

21. Justus CR, Leffler N, Ruiz-Echevarria M, Yang LV. *In vitro* cell migration and invasion assays. *J Visual Experiments JoVE* (2014) (88):51046. doi: 10.3791/51046

22. Riedl A, Schlederer M, Pudelko K, Stadler M, Walter S, Unterleuthner D, et al. Comparison of cancer cells in 2D vs 3D culture reveals differences in AKT-mTOR-S6K signaling and drug responses. *J Cell Sci* (2017) 130:203–18. doi: 10.1242/jcs.188102

23. Turetta M, Ben FD, Brisotto G, Biscontin E, Bulfoni M, Cesselli D, et al. Emerging technologies for cancer research: Towards personalized medicine with microfluidic platforms and 3D tumor models. *Curr Med Chem* (2018) 25:4616–37. doi: 10.2174/0929867325666180605122633

24. Kersten K, de Visser KE, van Miltenburg MH, Jonkers J. Genetically engineered mouse models in oncology research and cancer medicine. *EMBO Mol Med* (2017) 9:137–53. doi: 10.15252/emmm.201606857

25. Lai Y, Wei X, Lin S, Qin L, Cheng L, Li P. Current status and perspectives of patient-derived xenograft models in cancer research. *J Hematol Oncol* (2017) 10:106. doi: 10.1186/s13045-017-0470-7

26. Bhimani J, Ball K, Stebbing J. Patient-derived xenograft models-the future of personalised cancer treatment. *Br J Cancer* (2020) 122:601–2. doi: 10.1038/s41416-019-0678-0

27. Bertotti A, Migliardi G, Galimi F, Sassi F, Torti D, Isella C, et al. A molecularly annotated platform of patient-derived xenografts ("xenopatients") identifies HER2 as an effective therapeutic target in cetuximab-resistant colorectal cancer. *Cancer Discovery* (2011) 1:508–23. doi: 10.1158/2159-8290.CD-11-0109

28. Cho SY, Kang W, Han JY, Min S, Kang J, Lee A, et al. An integrative approach to precision cancer medicine using patient-derived xenografts. *Mol Cells* (2016) 39:77–86. doi: 10.14348/molcells.2016.2350

29. Hidalgo M, Amant F, Biankin AV, Budinska E, Byrne AT, Caldas C, et al. Patient-derived xenograft models: An emerging platform for translational cancer research. *Cancer Discovery* (2014) 4:998–1013. doi: 10.1158/2159-8290.CD-14-0001

30. Hidalgo M, Bruckheimer E, Rajeshkumar NV, Garrido-Laguna I, De Oliveira E, Rubio-Viqueira B, et al. A pilot clinical study of treatment guided by personalized tumorgrafts in patients with advanced cancer. *Mol Cancer Ther* (2011) 10:1311–6. doi: 10.1158/1535-7163.MCT-11-0233

31. De Angelis ML, Francescangeli F, Nicolazzo C, Xhelili E, La Torre F, Colace L, et al. An orthotopic patient-derived xenograft (PDX) model allows the analysis of metastasis-associated features in colorectal cancer. *Front Oncol* (2022) 12:869485. doi: 10.3389/fonc.2022.869485

32. DeRose YS, Wang G, Lin YC, Bernard PS, Buys SS, Ebbert MT, et al. Tumor grafts derived from women with breast cancer authentically reflect tumor pathology, growth, metastasis and disease outcomes. *Nat Med* (2011) 17:1514–20. doi: 10.1038/nm.2454

33. Gao H, Korn JM, Ferretti S, Monahan JE, Wang Y, Singh M, et al. High-throughput screening using patient-derived tumor xenografts to predict clinical trial drug response. *Nat Med* (2015) 21:1318–25. doi: 10.1038/nm.3954

34. Hoffman RM. Patient-derived orthotopic xenografts: better mimic of metastasis than subcutaneous xenografts. *Nat Rev Cancer* (2015) 15:451–2. doi: 10.1038/nrc3972

35. Choi Y, Lee S, Kim K, Kim SH, Chung YJ, Lee C. Studying cancer immunotherapy using patient-derived xenografts (PDXs) in humanized mice. *Exp Mol Med* (2018) 50:1–9. doi: 10.1038/s12276-018-0167-1

36. Yada E, Wada S, Yoshida S, Sasada T. Use of patient-derived xenograft mouse models in cancer research and treatment. *Future Sci OA* (2018) 4:FSO271. doi: 10.4155/fsoa-2017-0136

37. Jespersen H, Lindberg MF, Donia M, Soderberg EMV, Andersen R, Keller U, et al. Clinical responses to adoptive T-cell transfer can be modeled in an autologous immune-humanized mouse model. *Nat Commun* (2017) 8:707. doi: 10.1038/s41467-017-00786-z

38. Zhao Y, Shuen TWH, Toh TB, Chan XY, Liu M, Tan SY, et al. Development of a new patient-derived xenograft humanised mouse model to study human-specific tumour microenvironment and immunotherapy. *Gut* (2018) 67:1845–54. doi: 10.1136/gutjnl-2017-315201

39. Zhang X, Claerhout S, Prat A, Dobrolecki LE, Petrovic I, Lai Q, et al. A renewable tissue resource of phenotypically stable, biologically and ethnically diverse, patient-derived human breast cancer xenograft models. *Cancer Res* (2013) 73:4885–97. doi: 10.1158/0008-5472.CAN-12-4081

40. Tetteh PW, Kretzschmar K, Begthel H, Born Mvd, Korving J, Morsink F, et al. Generation of an inducible colon-specific cre enzyme mouse line for colon cancer research. *Proc Natl Acad Sci United States America* (2016) 113:11859–64. doi: 10.1073/pnas.1614057113

41. Ben-David U, Ha G, Tseng YY, Greenwald NF, Oh C, Shih J, et al. Patient-derived xenografts undergo mouse-specific tumor evolution. *Nat Genet* (2017) 49:1567–75. doi: 10.1038/ng.3967

42. Day CP, Merlino G, Van Dyke T. Preclinical mouse cancer models: a maze of opportunities and challenges. *Cell* (2015) 163:39–53. doi: 10.1016/j.cell.2015.08.068

43. Olson B, Li Y, Lin Y, Liu ET, Patnaik A. Mouse models for cancer immunotherapy research. *Cancer Discovery* (2018) 8:1358–65. doi: 10.1158/2159-8290.CD-18-0044

44. Hill W, Caswell DR, Swanton C. Capturing cancer evolution using genetically engineered mouse models (GEMMs). *Trends Cell Biol* (2021) 31:1007–18. doi: 10.1016/j.tcb.2021.07.003

45. McFadden DG, Politi K, Bhutkar A, Chen FK, Song X, Pirun M, et al. Mutational landscape of EGFR-, MYC-, and kras-driven genetically engineered mouse models of lung adenocarcinoma. *Proc Natl Acad Sci United States America* (2016) 113:E6409–17. doi: 10.1073/pnas.1613601113

46. Singh M, Murriel CL, Johnson L. Genetically engineered mouse models: closing the gap between preclinical data and trial outcomes. *Cancer Res* (2012) 72:2695–700. doi: 10.1158/0008-5472.CAN-11-2786

47. Byrne AT, Alferez DG, Amant F, Annibali D, Arribas J, Biankin AV, et al. Interrogating open issues in cancer precision medicine with patient-derived xenografts. *Nat Rev Cancer* (2017) 17:254–68. doi: 10.1038/nrc.2016.140

48. Wong CH, Siah KW, Lo AW. Estimation of clinical trial success rates and related parameters. *Biostatistics* (2019) 20:273–86. doi: 10.1093/biostatistics/kxx069

49. Bissell MJ. Goodbye flat biology - time for the 3rd and the 4th dimensions. *J Cell Sci* (2017) 130:3–5. doi: 10.1242/jcs.200550

50. Rodrigues J, Heinrich MA, Teixeira LM, Prakash J. 3D *In vitro* model (R) evolution: Unveiling tumor-stroma interactions. *Trends Cancer* (2021) 7:249–64. doi: 10.1016/j.trecan.2020.10.009

51. Hirschhaeuser F, Menne H, Dittfeld C, West J, Mueller-Klieser W, Kunz-Schughart LA. Multicellular tumor spheroids: An underestimated tool is catching up again. *J Biotechnol* (2010) 148:3–15. doi: 10.1016/j.jbiotec.2010.01.012

52. Sant S, Johnston PA. The production of 3D tumor spheroids for cancer drug discovery. *Drug Discovery Today Technol* (2017) 23:27–36. doi: 10.1016/j.ddtec.2017.03.002

53. Costa EC, Moreira AF, de Melo-Diogo D, Gaspar VM, Carvalho MP, Correia IJ. 3D tumor spheroids: An overview on the tools and techniques used for their analysis. *Biotechnol Adv* (2016) 34:1427–41. doi: 10.1016/j.biotechadv.2016.11.002

54. LaBarbera DV, Reid BG, Yoo BH. The multicellular tumor spheroid model for high-throughput cancer drug discovery. *Expert Opin Drug Discovery* (2012) 7:819–30. doi: 10.1517/17460441.2012.708334

55. Mehta G, Hsiao AY, Ingram M, Luker GD, Takayama S. Opportunities and challenges for use of tumor spheroids as models to test drug delivery and efficacy. *J Controlled Release* (2012) 164:192–204. doi: 10.1016/j.jconrel.2012.04.045

56. Zanoni M, Piccinini F, Arienti C, Zamagni A, Santi S, Polico R, et al. 3D tumor spheroid models for *in vitro* therapeutic screening: A systematic approach to enhance the biological relevance of data obtained. *Sci Rep* (2016) 6:19103. doi: 10.1038/srep19103

57. Weiswald LB, Bellet D, Dangles-Marie V. Spherical cancer models in tumor biology. *Neoplasia* (2015) 17:1–15. doi: 10.1016/j.neo.2014.12.004

58. Costa EC, Gaspar VM, Coutinho P, Correia IJ. Optimization of liquid overlay technique to formulate heterogenic 3D co-cultures models. *Biotechnol Bioeng* (2014) 111:1672–85. doi: 10.1002/bit.25210

59. Daum AK, Dittmann J, Jansen L, Peters S, Dahmen U, Heger JI, et al. ITIH5 shows tumor suppressive properties in cervical cancer cells grown as multicellular tumor spheroids. *Am J Trans Res* (2021) 13:10298–314.

60. Ludwig K, Tse ES, Wang JY. Colon cancer cells adopt an invasive phenotype without mesenchymal transition in 3-d but not 2-d culture upon combined stimulation with EGF and crypt growth factors. *BMC Cancer* (2013) 13:221. doi: 10.1186/1471-2407-13-221

61. Amann A, Zwierzina M, Gamerith G, Bitsche M, Huber JM, Vogel GF, et al. Development of an innovative 3D cell culture system to study tumour–stroma interactions in non-small cell lung cancer cells. *PloS One* (2014) 9:e92511. doi: 10.1371/journal.pone.0092511

62. Dufau I, Frongia C, Sicard F, Dedieu L, Cordelier P, Ausseil F, et al. Multicellular tumor spheroid model to evaluate spatio-temporal dynamics effect of chemotherapeutics: Application to the gemcitabine/CHK1 inhibitor combination in pancreatic cancer. *BMC Cancer* (2012) 12:15. doi: 10.1186/1471-2407-12-15

63. Takagi A, Watanabe M, Ishii Y, Morita J, Hirokawa Y, Matsuzaki T, et al. Three-dimensional cellular spheroid formation provides human prostate tumor cells with tissue-like features. *Anticancer Res* (2007) 27:45–53.

64. Han SJ, Kwon S, Kim KS. Challenges of applying multicellular tumor spheroids in preclinical phase. *Cancer Cell Int* (2021) 21:152. doi: 10.1186/s12935-021-01853-8

65. Breslin S, O'Driscoll L. Three-dimensional cell culture: The missing link in drug discovery. *Drug Discovery Today* (2013) 18:240–9. doi: 10.1016/j.drudis.2012.10.003

66. Fennema E, Rivron N, Rouwkema J, van Blitterswijk C, de Boer J. Spheroid culture as a tool for creating 3D complex tissues. *Trends Biotechnol* (2013) 31:108–15. doi: 10.1016/j.tibtech.2012.12.003

67. Nath S, Devi GR. Three-dimensional culture systems in cancer research: Focus on tumor spheroid model. *Pharmacol Ther* (2016) 163:94–108. doi: 10.1016/j.pharmthera.2016.03.013

68. Andersen T, Auk-Emblem P, Dornish M. 3D cell culture in alginate hydrogels. *Microarrays* (2015) 4:133–61. doi: 10.3390/microarrays4020133

69. Ferreira LP, Gaspar VM, Mano JF. Design of spherically structured 3D *in vitro* tumor models -advances and prospects. *Acta Biomater* (2018) 75:11–34. doi: 10.1016/j.actbio.2018.05.034

70. Lee JM, Park DY, Yang L, Kim EJ, Ahrberg CD, Lee KB, et al. Generation of uniform-sized multicellular tumor spheroids using hydrogel microwells for advanced drug screening. *Sci Rep* (2018) 8:17145. doi: 10.1038/s41598-018-35216-7

71. Heinrich MA, Liu W, Jimenez A, Yang J, Akpek A, Liu X, et al. 3D bioprinting: From benches to translational applications. *Small* (2019) 15:e1805510. doi: 10.1002/smll.201805510

72. Kingsley DM, Roberge CL, Rudkouskaya A, Faulkner DE, Barroso M, Intes X, et al. Laser-based 3D bioprinting for spatial and size control of tumor spheroids and embryoid bodies. *Acta Biomater* (2019) 95:357–70. doi: 10.1016/j.actbio.2019.02.014

73. Ko J, Ahn J, Kim S, Lee Y, Lee J, Park D, et al. Tumor spheroid-on-a-chip: A standardized microfluidic culture platform for investigating tumor angiogenesis. *Lab Chip* (2019) 19:2822–33. doi: 10.1039/C9LC00140A

74. Lee SW, Hong S, Jung B, Jeong SY, Byeon JH, Jeong GS, et al. *In vitro* lung cancer multicellular tumor spheroid formation using a microfluidic device. *Biotechnol Bioeng* (2019) 116:3041–52. doi: 10.1002/bit.27114

75. Collins T, Pyne E, Christensen M, Iles A, Pamme N, Pires IM. Spheroid-on-chip microfluidic technology for the evaluation of the impact of continuous flow on metastatic potential in cancer models in vitro. *Biomicrofluidics* (2021) 15:044103. doi: 10.1063/5.0061373

76. Dadgar N, Gonzalez-Suarez AM, Fattahi P, Hou X, Weroha JS, Gaspar-Maia A, et al. A microfluidic platform for cultivating ovarian cancer spheroids and testing their responses to chemotherapies. *Microsyst Nanoeng* (2020) 6:93. doi: 10.1038/s41378-020-00201-6

77. Daster S, Amatruda N, Calabrese D, Ivanek R, Turrini E, Droeser RA, et al. Induction of hypoxia and necrosis in multicellular tumor spheroids is associated with resistance to chemotherapy treatment. *Oncotarget* (2017) 8:1725–36. doi: 10.18632/oncotarget.13857

78. Huang BW, Gao JQ. Application of 3D cultured multicellular spheroid tumor models in tumor-targeted drug delivery system research. *J Controlled Release* (2018) 270:246–59. doi: 10.1016/j.jconrel.2017.12.005

79. Rodrigues T, Kundu B, Silva-Correia J, Kundu SC, Oliveira JM, Reis RL, et al. Emerging tumor spheroids technologies for 3D *in vitro* cancer modeling. *Pharmacol Ther* (2018) 184:201–11. doi: 10.1016/j.pharmthera.2017.10.018

80. Rolver MG, Elingaard-Larsen LO, Pedersen SF. Assessing cell viability and death in 3D spheroid cultures of cancer cells. *J Visual Experiments JoVE* (2019) 148. doi: 10.3791/59714-v

81. Al-Ramadan A, Mortensen AC, Carlsson J, Nestor MV. Analysis of radiation effects in two irradiated tumor spheroid models. *Oncol Lett* (2018) 15:3008–16. doi: 10.3892/ol.2017.7716

82. Boucherit N, Gorvel L, Olive D. 3D tumor models and their use for the testing of immunotherapies. *Front Immunol* (2020) 11:603640. doi: 10.3389/fimmu.2020.603640

83. Lovitt CJ, Shelper TB, Avery VM. Evaluation of chemotherapeutics in a three-dimensional breast cancer model. *J Cancer Res Clin Oncol* (2015) 141:951–9. doi: 10.1007/s00432-015-1950-1

84. Nunes AS, Barros AS, Costa EC, Moreira AF, Correia IJ. 3D tumor spheroids as *in vitro* models to mimic *in vivo* human solid tumors resistance to therapeutic drugs. *Biotechnol Bioeng* (2019) 116:206–26. doi: 10.1002/bit.26845

85. Al-Akra L, Bae DH, Leck LYW, Richardson DR, Jansson PJ. The biochemical and molecular mechanisms involved in the role of tumor micro-environment stress in development of drug resistance. *Biochim Biophys Acta Gen Subj* (2019) 1863:1390–7. doi: 10.1016/j.bbagen.2019.06.007

86. Liang J, Liu B. ROS-responsive drug delivery systems. *Bioeng Trans Med* (2016) 1:239–51. doi: 10.1002/btm2.10014

87. Doublier S, Belisario DC, Polimeni M, Annaratone L, Riganti C, Allia E, et al. HIF-1 activation induces doxorubicin resistance in MCF7 3-d spheroids *via* p-glycoprotein expression: a potential model of the chemo-resistance of invasive micropapillary carcinoma of the breast. *BMC Cancer* (2012) 12:4. doi: 10.1186/1471-2407-12-4

88. Kim JW, Ho WJ, Wu BM. The role of the 3D environment in hypoxia-induced drug and apoptosis resistance. *Anticancer Res* (2011) 31:3237–45.

89. Imamura Y, Mukohara T, Shimono Y, Funakoshi Y, Chayahara N, Toyoda M, et al. Comparison of 2D- and 3D-culture models as drug-testing platforms in breast cancer. *Oncol Rep* (2015) 33:1837–43. doi: 10.3892/or.2015.3767

90. Reynolds DS, Tevis KM, Blessing WA, Colson YL, Zaman MH, Grinstaff MW. Breast cancer spheroids reveal a differential cancer stem cell response to chemotherapeutic treatment. *Sci Rep* (2017) 7:10382. doi: 10.1038/s41598-017-10863-4

91. Cowan DS, Tannock IF. Factors that influence the penetration of methotrexate through solid tissue. *Int J Cancer* (2001) 91:120–5. doi: 10.1002/1097-0215(20010101)91:1<120::AID-IJC1021>3.0.CO;2-Y

92. Raghunand N, Mahoney B, van Sluis R, Baggett B, Gillies RJ. Acute metabolic alkalosis enhances response of C3H mouse mammary tumors to the weak base mitoxantrone. *Neoplasia* (2001) 3:227–35. doi: 10.1038/sj.neo.7900151

93. Wojtkowiak JW, Verduzco D, Schramm KJ, Gillies RJ. Drug resistance and cellular adaptation to tumor acidic pH microenvironment. *Mol Pharmaceutics* (2011) 8:2032–8. doi: 10.1021/mp200292c

94. Heldin CH, Rubin K, Pietras K, Ostman A. High interstitial fluid pressure - an obstacle in cancer therapy. *Nat Rev Cancer* (2004) 4:806–13. doi: 10.1038/nrc1456

95. Minchinton AI, Tannock IF. Drug penetration in solid tumours. *Nat Rev Cancer* (2006) 6:583–92. doi: 10.1038/nrc1893

96. Buffa FM, West C, Byrne K, Moore JV, Nahum AE. Radiation response and cure rate of human colon adenocarcinoma spheroids of different size: The significance of hypoxia on tumor control modelling. *Int J Radiat Oncol Biol Phys* (2001) 49:1109–18. doi: 10.1016/S0360-3016(00)01533-9

97. Thakuri PS, Gupta M, Plaster M, Tavana H. Quantitative size-based analysis of tumor spheroids and responses to therapeutics. *Assay Drug Dev Technol* (2019) 17:140–9. doi: 10.1089/adt.2018.895

98. Millard M, Yakavets I, Zorin V, Kulmukhamedova A, Marchal S, Bezdetnaya L. Drug delivery to solid tumors: The predictive value of the multicellular tumor spheroid model for nanomedicine screening. *Int J Nanomed* (2017) 12:7993–8007. doi: 10.2147/IJN.S146927

99. Mo I, Sabino IJ, Melo-Diogo D, Lima-Sousa R, Alves CG, Correia IJ. The importance of spheroids in analyzing nanomedicine efficacy. *Nanomedicine* (2020) 15:1513–25. doi: 10.2217/nnm-2020-0054

100. Courau T, Bonnereau J, Chicoteau J, Bottois H, Remark R, Assante Miranda L, et al. Cocultures of human colorectal tumor spheroids with immune cells reveal the therapeutic potential of MICA/B and NKG2A targeting for cancer treatment. *J Immunother Cancer* (2019) 7:74. doi: 10.1186/s40425-019-0553-9

101. Varesano S, Zocchi MR, Poggi A. Zoledronate triggers Vdelta2 T cells to destroy and kill spheroids of colon carcinoma: Quantitative image analysis of three-dimensional cultures. *Front Immunol* (2018) 9:998. doi: 10.3389/fimmu.2018.00998

102. Zhang Z, Jiang D, Yang H, He Z, Liu X, Qin W, et al. Modified CAR T cells targeting membrane-proximal epitope of mesothelin enhances the antitumor function against large solid tumor. *Cell Death Dis* (2019) 10:476. doi: 10.1038/s41419-019-1711-1

103. Adusumilli PS, Zauderer MG, Riviere I, Solomon SB, Rusch VW, O'Cearbhaill RE, et al. A phase I trial of regional mesothelin-targeted CAR T-cell therapy in patients with malignant pleural disease, in combination with the anti-PD-1 agent pembrolizumab. *Cancer Discovery* (2021) 11:2748–63. doi: 10.1158/2159-8290.CD-21-0407

104. Cherkassky L, Morello A, Villena-Vargas J, Feng Y, Dimitrov DS, Jones DR, et al. Human CAR T cells with cell-intrinsic PD-1 checkpoint blockade resist tumor-mediated inhibition. *J Clin Invest* (2016) 126:3130–44. doi: 10.1172/JCI83092

105. Grosser R, Cherkassky L, Chintala N, Adusumilli PS. Combination immunotherapy with CAR T cells and checkpoint blockade for the treatment of solid tumors. *Cancer Cell* (2019) 36:471–82. doi: 10.1016/j.ccell.2019.09.006

106. Gopal S, Kwon SJ, Ku B, Lee DW, Kim J, Dordick JS. 3D tumor spheroid microarray for high-throughput, high-content natural killer cell-mediated cytotoxicity. *Commun Biol* (2021) 4:893. doi: 10.1038/s42003-021-02417-2

107. Jin MZ, Jin WL. The updated landscape of tumor microenvironment and drug repurposing. *Signal Transduct Targeted Ther* (2020) 5:166. doi: 10.1038/s41392-020-00280-x

108. Jeong SY, Lee JH, Shin Y, Chung S, Kuh HJ. Co-Culture of tumor spheroids and fibroblasts in a collagen matrix-incorporated microfluidic chip mimics reciprocal activation in solid tumor microenvironment. *PloS One* (2016) 11:e0159013. doi: 10.1371/journal.pone.0159013

109. Lazzari G, Nicolas V, Matsusaki M, Akashi M, Couvreur P, Mura S. Multicellular spheroid based on a triple co-culture: A novel 3D model to mimic pancreatic tumor complexity. *Acta Biomater* (2018) 78:296–307. doi: 10.1016/j.actbio.2018.08.008

110. Herter S, Morra L, Schlenker R, Sulcova J, Fahrni L, Waldhauer I, et al. A novel three-dimensional heterotypic spheroid model for the assessment of the activity of cancer immunotherapy agents. *Cancer Immunol Immunother CII* (2017) 66:129–40. doi: 10.1007/s00262-016-1927-1

111. Rebelo SP, Pinto C, Martins TR, Harrer N, Estrada MF, Loza-Alvarez P, et al. 3D-3-culture: A tool to unveil macrophage plasticity in the tumour microenvironment. *Biomaterials* (2018) 163:185–97. doi: 10.1016/j.biomaterials.2018.02.030

112. Kuen J, Darowski D, Kluge T, Majety M. Pancreatic cancer cell/fibroblast co-culture induces M2 like macrophages that influence therapeutic response in a 3D model. *PloS One* (2017) 12:e0182039. doi: 10.1371/journal.pone.0182039

113. Abbott RD, Kaplan DL. Strategies for improving the physiological relevance of human engineered tissues. *Trends Biotechnol* (2015) 33:401–7. doi: 10.1016/j.tibtech.2015.04.003

114. Sontheimer-Phelps A, Hassell BA, Ingber DE. Modelling cancer in microfluidic human organs-on-chips. *Nat Rev Cancer* (2019) 19:65–81. doi: 10.1038/s41568-018-0104-6

115. Friedrich J, Eder W, Castaneda J, Doss M, Huber E, Ebner R, et al. A reliable tool to determine cell viability in complex 3-d culture: the acid phosphatase assay. *J Biomol Screening* (2007) 12:925–37. doi: 10.1177/1087057107306839

116. Ho WY, Yeap SK, Ho CL, Rahim RA, Alitheen NB. Development of multicellular tumor spheroid (MCTS) culture from breast cancer cell and a high throughput screening method using the MTT assay. *PloS One* (2012) 7:e44640. doi: 10.1371/journal.pone.0044640

117. Mittler F, Obeid P, Rulina AV, Haguet V, Gidrol X, Balakirev MY. High-content monitoring of drug effects in a 3D spheroid model. *Front Oncol* (2017) 7:293. doi: 10.3389/fonc.2017.00293

118. Sirenko O, Mitlo T, Hesley J, Luke S, Owens W, Cromwell EF. High-content assays for characterizing the viability and morphology of 3D cancer spheroid cultures. *Assay Drug Dev Technol* (2015) 13:402–14. doi: 10.1089/adt.2015.655

119. Gomez-Cortes JC, Diaz-Carmona JJ, Padilla-Medina JA, Calderon AE, Gutierrez AIB, Gutierrez-Lopez M, et al. Electrical impedance tomography technical contributions for detection and 3D geometric localization of breast tumors: A systematic review. *Micromachines* (2022) 13:496. doi: 10.3390/mi13040496

120. Ma HL, Jiang Q, Han S, Wu Y, Cui Tomshine J, Wang D, et al. Multicellular tumor spheroids as an *in vivo*-like tumor model for three-dimensional imaging of chemotherapeutic and nano material cellular penetration. *Mol Imaging* (2012) 11:487–98. doi: 10.2310/7290.2012.00012

121. Murali VS, Chang BJ, Fiolka R, Danuser G, Cobanoglu MC, Welf ES. An image-based assay to quantify changes in proliferation and viability upon drug treatment in 3D microenvironments. *BMC Cancer* (2019) 19:502. doi: 10.1186/s12885-019-5694-1

122. Robertson FM, Ogasawara MA, Ye Z, Chu K, Pickei R, Debeb BG, et al. Imaging and analysis of 3D tumor spheroids enriched for a cancer stem cell phenotype. *J Biomol Screening* (2010) 15:820–9. doi: 10.1177/1087057110376541

123. Beaumont KA, Anfosso A, Ahmed F, Weninger W, Haass NK. Imaging- and flow cytometry-based analysis of cell position and the cell cycle in 3D melanoma spheroids. *J Visual Experiments JoVE* (2015) 106:e53486. doi: 10.3791/53486

124. Mischiati C, Ura B, Roncoroni L, Elli L, Cervellati C, Squerzanti M, et al. Changes in protein expression in two cholangiocarcinoma cell lines undergoing formation of multicellular tumor spheroids in vitro. *PloS One* (2015) 10:e0118906. doi: 10.1371/journal.pone.0118906

125. Donnenberg VS, Zhang JJ, Moravcikova E, Meyer EM, Lu H, Carson CT, et al. Antibody-based cell-surface proteome profiling of metastatic breast cancer primary explants and cell lines. *Cytomet Part A J Int Soc Anal Cytol* (2018) 93:448–57. doi: 10.1002/cyto.a.23300

126. Clevers H. Modeling development and disease with organoids. *Cell* (2016) 165:1586–97. doi: 10.1016/j.cell.2016.05.082

127. Drost J, Clevers H. Organoids in cancer research. *Nat Rev Cancer* (2018) 18:407–18. doi: 10.1038/s41568-018-0007-6

128. Lancaster MA, Knoblich JA. Organogenesis in a dish: modeling development and disease using organoid technologies. *Science* (2014) 345:1247125. doi: 10.1126/science.1247125

129. Lancaster MA, Renner M, Martin CA, Wenzel D, Bicknell LS, Hurles ME, et al. Cerebral organoids model human brain development and microcephaly. *Nature* (2013) 501:373–9. doi: 10.1038/nature12517

130. Dang J, Tiwari SK, Lichinchi G, Qin Y, Patil VS, Eroshkin AM, et al. Zika virus depletes neural progenitors in human cerebral organoids through activation of the innate immune receptor TLR3. *Cell Stem Cell* (2016) 19:258–65. doi: 10.1016/j.stem.2016.04.014

131. Eiraku M, Watanabe K, Matsuo-Takasaki M, Kawada M, Yonemura S, Matsumura M, et al. Self-organized formation of polarized cortical tissues from ESCs and its active manipulation by extrinsic signals. *Cell Stem Cell* (2008) 3:519–32. doi: 10.1016/j.stem.2008.09.002

132. Sato T, Vries RG, Snippert HJ, de Wetering Mv, Barker N, Stange DE, et al. Single Lgr5 stem cells build crypt-villus structures *in vitro* without a mesenchymal niche. *Nature* (2009) 459:262–5. doi: 10.1038/nature07935

133. Sato T, Stange DE, Ferrante M, Vries RG, Van Es JH, Van den Brink S, et al. Long-term expansion of epithelial organoids from human colon, adenoma, adenocarcinoma, and barrett's epithelium. *Gastroenterology* (2011) 141:1762–72. doi: 10.1053/j.gastro.2011.07.050

134. Boj SF, Hwang CI, Baker LA, Chio II, D.D. Engle V, Jager M, et al. Organoid models of human and mouse ductal pancreatic cancer. *Cell* (2015) 160:324–38. doi: 10.1016/j.cell.2014.12.021

135. Huch M, Gehart H, van Boxtel R, Hamer K, Blokzijl F, Verstegen MM, et al. Long-term culture of genome-stable bipotent stem cells from adult human liver. *Cell* (2015) 160:299–312. doi: 10.1016/j.cell.2014.11.050

136. Chua CW, Shibata M, Lei M, Toivanen R, Barlow LJ, Bergren SK, et al. Single luminal epithelial progenitors can generate prostate organoids in culture. *Nat Cell Biol* (2014) 16:951–61, 1-4. doi: 10.1038/ncb3047

137. Drost J, Karthaus WR, Gao D, Driehuis E, Sawyers CL, Chen Y, et al. Organoid culture systems for prostate epithelial and cancer tissue. *Nat Protoc* (2016) 11:347–58. doi: 10.1038/nprot.2016.006

138. Karthaus WR, Iaquinta PJ, Drost J, Gracanin A, van Boxtel R, Wongvipat J, et al. Identification of multipotent luminal progenitor cells in human prostate organoid cultures. *Cell* (2014) 159:163–75. doi: 10.1016/j.cell.2014.08.017

139. Bartfeld S, Bayram T, van de Wetering M, Huch M, Begthel H, Kujala P, et al. *In vitro* expansion of human gastric epithelial stem cells and their responses to bacterial infection. *Gastroenterology* (2015) 148:126–136 e6. doi: 10.1053/j.gastro.2014.09.042

140. Rock JR, Onaitis MW, Rawlins EL, Lu Y, Clark CP, Xue Y, et al. Basal cells as stem cells of the mouse trachea and human airway epithelium. *Proc Natl Acad Sci United States America* (2009) 106:12771–5. doi: 10.1073/pnas.0906850106

141. Turco MY, Gardner L, Hughes J, Cindrova-Davies T, Gomez MJ, Farrell L, et al. Long-term, hormone-responsive organoid cultures of human endometrium in a chemically defined medium. *Nat Cell Biol* (2017) 19:568–77. doi: 10.1038/ncb3516

142. Kessler M, Hoffmann K, Brinkmann V, Thieck O, Jackisch S, Toelle B, et al. The notch and wnt pathways regulate stemness and differentiation in human fallopian tube organoids. *Nat Commun* (2015) 6:8989. doi: 10.1038/ncomms9989

143. Ren W, Lewandowski BC, Watson J, Aihara E, Iwatsuki K, Bachmanov AA, et al. Single Lgr5- or Lgr6-expressing taste stem/progenitor cells generate taste bud cells ex vivo. *Proc Natl Acad Sci United States America* (2014) 111:16401–6. doi: 10.1073/pnas.1409064111

144. Maimets M, Rocchi C, Bron R, Pringle S, Kuipers J, Giepmans BN, et al. Long-term *In vitro* expansion of salivary gland stem cells driven by wnt signals. *Stem Cell Rep* (2016) 6:150–62. doi: 10.1016/j.stemcr.2015.11.009

145. Sachs N, de Ligt J, Kopper O, Gogola E, Bounova G, Weeber F, et al. A living biobank of breast cancer organoids captures disease heterogeneity. *Cell* (2018) 172:373–386 e10. doi: 10.1016/j.cell.2017.11.010

146. Mariani J, Simonini MV, Palejev D, Tomasini L, Coppola G, Szekely AM, et al. Modeling human cortical development *in vitro* using induced pluripotent stem cells. *Proc Natl Acad Sci United States America* (2012) 109:12770–5. doi: 10.1073/pnas.1202944109

147. Sachs N, Clevers H. Organoid cultures for the analysis of cancer phenotypes. *Curr Opin Genet Dev* (2014) 24:68–73. doi: 10.1016/j.gde.2013.11.012

148. Veninga V, Voest EE. Tumor organoids: Opportunities and challenges to guide precision medicine. *Cancer Cell* (2021) 39:1190–201. doi: 10.1016/j.ccell.2021.07.020

149. Crespo M, Vilar E, Tsai SY, Chang K, Amin S, Srinivasan T, et al. Colonic organoids derived from human induced pluripotent stem cells for modeling colorectal cancer and drug testing. *Nat Med* (2017) 23:878–84. doi: 10.1038/nm.4355

150. Drost J, van Boxtel R, Blokzijl F, Mizutani T, Sasaki N, Sasselli V, et al. Use of CRISPR-modified human stem cell organoids to study the origin of mutational signatures in cancer. *Science* (2017) 358:234–8. doi: 10.1126/science.aao3130

151. Drost J, van Jaarsveld RH, Ponsioen B, Zimberlin C, van Boxtel R, Buijs A, et al. Sequential cancer mutations in cultured human intestinal stem cells. *Nature* (2015) 521:43–7. doi: 10.1038/nature14415

152. Matano M, Date S, Shimokawa M, Takano A, Fujii M, Ohta Y, et al. Modeling colorectal cancer using CRISPR-Cas9-mediated engineering of human intestinal organoids. *Nat Med* (2015) 21:256–62. doi: 10.1038/nm.3802

153. Takeda H, Kataoka S, Nakayama M, Ali MAE, Oshima H, Yamamoto D, et al. CRISPR-Cas9-mediated gene knockout in intestinal tumor organoids provides functional validation for colorectal cancer driver genes. *Proc Natl Acad Sci United States America* (2019) 116:15635–44. doi: 10.1073/pnas.1904714116

154. Bian S, Repic M, Guo Z, Kavirayani A, Burkard T, Bagley JA, et al. Genetically engineered cerebral organoids model brain tumor formation. *Nat Methods* (2018) 15:631–9. doi: 10.1038/s41592-018-0070-7

155. Nanki K, Toshimitsu K, Takano A, Fujii M, Shimokawa M, Ohta Y, et al. Divergent routes toward wnt and r-spondin niche independency during human gastric carcinogenesis. *Cell* (2018) 174:856–869 e17. doi: 10.1016/j.cell.2018.07.027

156. Seino T, Kawasaki S, Shimokawa M, Tamagawa H, Toshimitsu K, Fujii M, et al. Human pancreatic tumor organoids reveal loss of stem cell niche factor dependence during disease progression. *Cell Stem Cell* (2018) 22:454–467 e6. doi: 10.1016/j.stem.2017.12.009

157. Dekkers JF, Whittle JR, Vaillant F, Chen HR, Dawson C, Liu K, et al. Modeling breast cancer using CRISPR-Cas9-Mediated engineering of human breast organoids. *J Natl Cancer Inst* (2020) 112:540–4. doi: 10.1093/jnci/djz196

158. Fumagalli A, Drost J, Suijkerbuijk SJ, van Boxtel R, de Ligt J, Offerhaus GJ, et al. Genetic dissection of colorectal cancer progression by orthotopic transplantation of engineered cancer organoids. *Proc Natl Acad Sci United States America* (2017) 114:E2357–64. doi: 10.1073/pnas.1701219114

159. Fumagalli A, Suijkerbuijk SJE, Begthel H, Beerling E, Oost KC, Snippert HJ, et al. A surgical orthotopic organoid transplantation approach in mice to visualize and study colorectal cancer progression. *Nat Protoc* (2018) 13:235–47. doi: 10.1038/nprot.2017.137

160. de Sousa e Melo F, Kurtova AV, Harnoss JM, Kljavin N, Hoeck JD, Hung J, et al. A distinct role for Lgr5(+) stem cells in primary and metastatic colon cancer. *Nature* (2017) 543:676–80. doi: 10.1038/nature21713

161. Shimokawa M, Ohta Y, Nishikori S, Matano M, Takano A, Fujii M, et al. Visualization and targeting of LGR5(+) human colon cancer stem cells. *Nature* (2017) 545:187–92. doi: 10.1038/nature22081

162. Nadauld LD, Garcia S, Natsoulis G, Bell JM, Miotke L, Hopmans ES, et al. Metastatic tumor evolution and organoid modeling implicate TGFBR2 as a cancer driver in diffuse gastric cancer. *Genome Biol* (2014) 15:428. doi: 10.1186/s13059-014-0428-9

163. Sakamoto N, Feng Y, Stolfi C, Kurosu Y, Green M, Lin J, et al. BRAF(V600E) cooperates with CDX2 inactivation to promote serrated colorectal tumorigenesis. *eLife* (2017) 6:e20331. doi: 10.7554/eLife.20331

164. Schwank G, Koo BK, Sasselli V, Dekkers JF, Heo I, Demircan T, et al. Functional repair of CFTR by CRISPR/Cas9 in intestinal stem cell organoids of cystic fibrosis patients. *Cell Stem Cell* (2013) 13:653–8. doi: 10.1016/j.stem.2013.11.002

165. Dow LE, O'Rourke KP, Simon J, Tschaharganeh DF, van Es JH, Clevers H, et al. Apc restoration promotes cellular differentiation and reestablishes crypt homeostasis in colorectal cancer. *Cell* (2015) 161:1539–52. doi: 10.1016/j.cell.2015.05.033

166. Gao D, Chen Y. Organoid development in cancer genome discovery. *Curr Opin Genet Dev* (2015) 30:42–8. doi: 10.1016/j.gde.2015.02.007

167. van de Wetering M, Francies HE, Francis JM, Bounova G, Iorio F, Pronk A, et al. Prospective derivation of a living organoid biobank of colorectal cancer patients. *Cell* (2015) 161:933–45. doi: 10.1016/j.cell.2015.03.053

168. Weeber F, van de Wetering M, Hoogstraat M, Dijkstra KK, Krijgsman O, Kuilman T, et al. Preserved genetic diversity in organoids cultured from biopsies of human colorectal cancer metastases. *Proc Natl Acad Sci United States America* (2015) 112:13308–11. doi: 10.1073/pnas.1516689112

169. Pauli C, Hopkins BD, Prandi D, Shaw R, Fedrizzi T, Sboner A, et al. Personalized *In vitro* and *In vivo* cancer models to guide precision medicine. *Cancer Discovery* (2017) 7:462–77. doi: 10.1158/2159-8290.CD-16-1154

170. Gao D, Vela I, Sboner A, Iaquinta PJ, Karthaus WR, Gopalan A, et al. Organoid cultures derived from patients with advanced prostate cancer. *Cell* (2014) 159:176–87. doi: 10.1016/j.cell.2014.08.016

171. Vlachogiannis G, Hedayat S, Vatsiou A, Jamin Y, Fernandez-Mateos J, Khan K, et al. Patient-derived organoids model treatment response of metastatic gastrointestinal cancers. *Science* (2018) 359:920–6. doi: 10.1126/science.aao2774

172. Fujii M, Shimokawa M, Date S, Takano A, Matano M, Nanki K, et al. A colorectal tumor organoid library demonstrates progressive loss of niche factor requirements during tumorigenesis. *Cell Stem Cell* (2016) 18:827–38. doi: 10.1016/j.stem.2016.04.003

173. Li X, Francies HE, Secrier M, Perner J, Miremadi A, Galeano-Dalmau N, et al. Organoid cultures recapitulate esophageal adenocarcinoma heterogeneity providing a model for clonality studies and precision therapeutics. *Nat Commun* (2018) 9:2983. doi: 10.1038/s41467-018-05190-9

174. Huang L, Holtzinger A, Jagan I, BeGora M, Lohse I, Ngai N, et al. Ductal pancreatic cancer modeling and drug screening using human pluripotent stem cell- and patient-derived tumor organoids. *Nat Med* (2015) 21:1364–71. doi: 10.1038/nm.3973

175. Kim M, Mun H, Sung CO, Cho EJ, Jeon HJ, Chun SM, et al. Patient-derived lung cancer organoids as *in vitro* cancer models for therapeutic screening. *Nat Commun* (2019) 10:3991. doi: 10.1038/s41467-019-11867-6

176. Seidlitz T, Merker SR, Rothe A, Zakrzewski F, von Neubeck C, Grutzmann K, et al. Human gastric cancer modelling using organoids. *Gut* (2019) 68:207–17. doi: 10.1136/gutjnl-2017-314549

177. Broutier L, Mastrogiovanni G, Verstegen MM, Francies HE, Gavarro LM, Bradshaw CR, et al. Human primary liver cancer-derived organoid cultures for disease modeling and drug screening. *Nat Med* (2017) 23:1424–35. doi: 10.1038/nm.4438

178. Hill SJ, Decker B, Roberts EA, Horowitz NS, Muto MG, Worley MJJr., et al. Prediction of DNA repair inhibitor response in short-term patient-derived ovarian cancer organoids. *Cancer Discovery* (2018) 8:1404–21. doi: 10.1158/2159-8290.CD-18-0474

179. Jacob F, Salinas RD, Zhang DY, Nguyen PTT, Schnoll JG, Wong SZH, et al. And biobank recapitulates inter- and intra-tumoral heterogeneity. *Cell* (2020) 180:188–204 e22. doi: 10.1016/j.cell.2019.11.036

180. Beshiri ML, Tice CM, Tran C, Nguyen HM, Sowalsky AG, Agarwal S, et al. A PDX/Organoid biobank of advanced prostate cancers captures genomic and phenotypic heterogeneity for disease modeling and therapeutic screening. *Clin Cancer Res* (2018) 24:4332–45. doi: 10.1158/1078-0432.CCR-18-0409

181. Mullenders J, de Jongh E, Brousali A, Roosen M, Blom JPA, Begthel H, et al. Mouse and human urothelial cancer organoids: A tool for bladder cancer research. *Proc Natl Acad Sci United States America* (2019) 116:4567–74. doi: 10.1073/pnas.1803595116

182. Batchelder CA, Martinez ML, Duru N, Meyers FJ, Tarantal AF. Three dimensional culture of human renal cell carcinoma organoids. *PloS One* (2015) 10:e0136758. doi: 10.1371/journal.pone.0136758

183. Kodack DP, Farago AF, Dastur A, Held MA, Dardaei L, Friboulet L, et al. Primary patient-derived cancer cells and their potential for personalized cancer patient care. *Cell Rep* (2017) 21:3298–309. doi: 10.1016/j.celrep.2017.11.051

184. Kretzschmar K. Cancer research using organoid technology. *J Mol Med* (2021) 99:501–15. doi: 10.1007/s00109-020-01990-z

185. Ooft SN, Weeber F, Dijkstra KK, McLean CM, Kaing S, van Werkhoven E, et al. Patient-derived organoids can predict response to chemotherapy in metastatic colorectal cancer patients. *Sci Trans Med* (2019) 11:eaay2574. doi: 10.1126/scitranslmed.aay2574

186. Verissimo CS, Overmeer RM, Ponsioen B, Drost J, Mertens S, Verlaan-Klink I, et al. Targeting mutant RAS in patient-derived colorectal cancer organoids by combinatorial drug screening. *eLife 5* (2016) 5:e18489. doi: 10.7554/eLife.18489

187. Ganesh K, Wu C, O'Rourke KP, Szeglin BC, Zheng Y, Sauve CG, et al. A rectal cancer organoid platform to study individual responses to chemoradiation. *Nat Med* (2019) 25:1607–14. doi: 10.1038/s41591-019-0584-2

188. de Witte CJ, Espejo Valle-Inclan J, Hami N, Lohmussaar K, Kopper O, Vreuls CPH, et al. Patient-derived ovarian cancer organoids mimic clinical response and exhibit heterogeneous inter- and intrapatient drug responses. *Cell Rep* (2020) 31:107762. doi: 10.1016/j.celrep.2020.107762

189. Kopper O, de Witte CJ, Lohmussaar K, Valle-Inclan JE, Hami N, Kester L, et al. An organoid platform for ovarian cancer captures intra- and interpatient heterogeneity. *Nat Med* (2019) 25:838–49. doi: 10.1038/s41591-019-0422-6

190. Calandrini C, Schutgens F, Oka R, Margaritis T, Candelli T, Mathijsen L, et al. An organoid biobank for childhood kidney cancers that captures disease and tissue heterogeneity. *Nat Commun* (2020) 11:1310. doi: 10.1038/s41467-020-15155-6

191. Yao Y, Xu X, Yang L, Zhu J, Wan J, Shen L, et al. Patient-derived organoids predict chemoradiation responses of locally advanced rectal cancer. *Cell Stem Cell* (2020) 26:17–26 e6. doi: 10.1016/j.stem.2019.10.010

192. Lee SH, Hu W, Matulay JT, Silva MV, Owczarek TB, Kim K, et al. Tumor evolution and drug response in patient-derived organoid models of bladder cancer. *Cell* (2018) 173:515–528 e17. doi: 10.1016/j.cell.2018.03.017

193. Meng Q. Three-dimensional culture of hepatocytes for prediction of drug-induced hepatotoxicity. *Expert Opin Drug Metab Toxicol* (2010) 6:733–46. doi: 10.1517/17425251003674356

194. Bar-Ephraim YE, Kretzschmar K, Clevers H. Organoids in immunological research. *Nat Rev Immunol* (2020) 20:279–93. doi: 10.1038/s41577-019-0248-y

195. Dijkstra KK, Cattaneo CM, Weeber F, Chalabi M, de Haar Jv, Fanchi LF, et al. Generation of tumor-reactive T cells by Co-culture of peripheral blood lymphocytes and tumor organoids. *Cell* (2018) 174:1586–1598 e12. doi: 10.1016/j.cell.2018.07.009

196. Aref AR, Campisi M, Ivanova E, Portell A, Larios D, Piel BP, et al. 3D microfluidic ex vivo culture of organotypic tumor spheroids to model immune checkpoint blockade. *Lab Chip* (2018) 18:3129–43. doi: 10.1039/C8LC00322J

197. Li X, Ootani A, Kuo C. An air-liquid interface culture system for 3D organoid culture of diverse primary gastrointestinal tissues. *Methods Mol Biol* (2016) 1422:33–40. doi: 10.1007/978-1-4939-3603-8_4

198. Pasch CA, Favreau PF, Yueh AE, Babiarz CP, Gillette AA, Sharick JT, et al. Patient-derived cancer organoid cultures to predict sensitivity to chemotherapy and radiation. *Clin Cancer Res* (2019) 25:5376–87. doi: 10.1158/1078-0432.CCR-18-3590

199. Ohlund D, Handly-Santana A, Biffi G, Elyada E, Almeida AS, Ponz-Sarvise M, et al. Distinct populations of inflammatory fibroblasts and myofibroblasts in pancreatic cancer. *J Exp Med* (2017) 214:579–96. doi: 10.1084/jem.20162024

200. Biffi G, Oni TE, Spielman B, Hao Y, Elyada E, Park Y, et al. IL1-induced JAK/STAT signaling is antagonized by TGFbeta to shape CAF heterogeneity in pancreatic

ductal adenocarcinoma. *Cancer Discovery* (2019) 9:282–301. doi: 10.1158/2159-8290.CD-18-0710

201. Ebbing EA, van der Zalm AP, Steins A, Creemers A, Hermsen S, Rentenaar R, et al. Stromal-derived interleukin 6 drives epithelial-to-mesenchymal transition and therapy resistance in esophageal adenocarcinoma. *Proc Natl Acad Sci United States America* (2019) 116:2237–42. doi: 10.1073/pnas.1820459116

202. Tsai HF, Trubelja A, Shen AQ, Bao G. Tumour-on-a-chip: Microfluidic models of tumour morphology, growth and microenvironment. *J R Soc Interface* (2017) 14:20170137. doi: 10.1098/rsif.2017.0137

203. Chakrabarti J, Holokai L, Syu L, Steele NG, Chang J, Wang J, et al. Hedgehog signaling induces PD-L1 expression and tumor cell proliferation in gastric cancer. *Oncotarget* (2018) 9:37439–57. doi: 10.18632/oncotarget.26473

204. Kong JCH, Guerra GR, Millen RM, Roth S, Xu H, Neeson PJ, et al. Tumor-infiltrating lymphocyte function predicts response to neoadjuvant chemoradiotherapy in locally advanced rectal cancer. *JCO Precis Oncol* (2018) 2:1–15. doi: 10.1200/PO.18.00075

205. Cattaneo CM, Dijkstra KK, Fanchi LF, Kelderman S, Kaing S, van Rooij N, et al. Tumor organoid-t-cell coculture systems. *Nat Protoc* (2020) 15:15–39. doi: 10.1038/s41596-019-0232-9

206. Chalabi M, Fanchi LF, Dijkstra KK, Van den Berg JG, Aalbers AG, Sikorska K, et al. Neoadjuvant immunotherapy leads to pathological responses in MMR-proficient and MMR-deficient early-stage colon cancers. *Nat Med* (2020) 26:566–76. doi: 10.1038/s41591-020-0805-8

207. Ribas A, Lawrence D, Atkinson V, Agarwal S, Miller WHJr., Carlino MS, et al. And MEK inhibition with PD-1 blockade immunotherapy in BRAF-mutant melanoma. *Nat Med* (2019) 25:936–40. doi: 10.1038/s41591-019-0476-5

208. Gonzalez-Exposito R, Semiannikova M, Griffiths B, Khan K, Barber LJ, Woolston A, et al. CEA expression heterogeneity and plasticity confer resistance to the CEA-targeting bispecific immunotherapy antibody cibisatamab (CEA-TCB) in patient-derived colorectal cancer organoids. *J Immunother Cancer* (2019) 7:101. doi: 10.1186/s40425-019-0575-3

209. Schnalzger TE, de Groot MH, Zhang C, Mosa MH, Michels BE, Roder J, et al. 3D model for CAR-mediated cytotoxicity using patient-derived colorectal cancer organoids. *EMBO J* (2019) 38:e100928. doi: 10.15252/embj.2018100928

210. Deng J, Wang ES, Jenkins RW, Li S, Dries R, Yates K, et al. CDK4/6 inhibition augments antitumor immunity by enhancing T-cell activation. *Cancer Discovery* (2018) 8:216–33. doi: 10.1158/2159-8290.CD-17-0915

211. Jenkins RW, Aref AR, Lizotte PH, Ivanova E, Stinson S, Zhou CW, et al. Ex vivo profiling of PD-1 blockade using organotypic tumor spheroids. *Cancer Discovery* (2018) 8:196–215. doi: 10.1158/2159-8290.CD-17-0833

212. Neal JT, Li X, Zhu J, Giangarra V, Grzeskowiak CL, Ju J, et al. Organoid modeling of the tumor immune microenvironment. *Cell* (2018) 175:1972–1988 e16. doi: 10.1016/j.cell.2018.11.021

213. Neal JT, Kuo CJ. Organoids as models for neoplastic transformation. *Annu Rev Pathol* (2016) 11:199–220. doi: 10.1146/annurev-pathol-012615-044249

214. Bock C, Boutros M, Camp JG, Clarke L, Clevers H, Knoblich JA, et al. The organoid cell atlas. *Nat Biotechnol* (2021) 39:13–7. doi: 10.1038/s41587-020-00762-x

215. Wu Q, Liu J, Wang X, Feng L, Wu J, Zhu X, et al. Organ-on-a-chip: recent breakthroughs and future prospects. *Biomed Eng Online* (2020) 19:9. doi: 10.1186/s12938-020-0752-0

216. Ahadian S, Civitarese R, Bannerman D, Mohammadi MH, Lu R, Wang E, et al. Organ-On-A-Chip platforms: A convergence of advanced materials, cells, and microscale technologies. *Adv Healthcare Mater* (2018) 7. doi: 10.1002/adhm.2018007347

217. Bhatia SN, Ingber DE. Microfluidic organs-on-chips. *Nat Biotechnol* (2014) 32:760–72. doi: 10.1038/nbt.2989

218. Ma C, Peng Y, Li H, Chen W. Organ-on-a-Chip: A new paradigm for drug development. *Trends Pharmacol Sci* (2021) 42:119–33. doi: 10.1016/j.tips.2020.11.009

219. Park SE, Georgescu A, Huh D. Organoids-on-a-chip. *Science* (2019) 364:960–5. doi: 10.1126/science.aaw7894

220. Ingber DE. Reverse engineering human pathophysiology with organs-on-Chips. *Cell* (2016) 164:1105–9. doi: 10.1016/j.cell.2016.02.049

221. Peck RW, Hinojosa CD, Hamilton GA. Organs-on-Chips in clinical pharmacology: Putting the patient into the center of treatment selection and drug development. *Clin Pharmacol Ther* (2020) 107:181–5. doi: 10.1002/cpt.1688

222. Sin A, Chin KC, Jamil MF, Kostov Y, Rao G, Shuler ML. The design and fabrication of three-chamber microscale cell culture analog devices with integrated dissolved oxygen sensors. *Biotechnol Prog* (2004) 20:338–45. doi: 10.1021/bp034077d

223. Sung JH, Kam C, Shuler ML. A microfluidic device for a pharmacokinetic-pharmacodynamic (PK-PD) model on a chip. *Lab Chip* (2010) 10:446–55. doi: 10.1039/b917763a

224. Sung JH, Shuler ML. A micro cell culture analog (microCCA) with 3-d hydrogel culture of multiple cell lines to assess metabolism-dependent cytotoxicity of anti-cancer drugs. *Lab Chip* (2009) 9:1385–94. doi: 10.1039/b901377f

225. Chou DB, Frismantas V, Milton Y, David R, Pop-Damkov P, Ferguson D, et al. Author correction: On-chip recapitulation of clinical bone marrow toxicities and patient-specific pathophysiology. *Nat Biomed Eng* (2020) 4:477. doi: 10.1038/s41551-020-0529-6

226. Huh D, Matthews BD, Mammoto A, Montoya-Zavala M, Hsin HY, Ingber DE. Reconstituting organ-level lung functions on a chip. *Science* (2010) 328:1662–8. doi: 10.1126/science.1188302

227. Jang KJ, Otieno MA, Ronxhi J, Lim HK, Ewart L, Kodella KR, et al. Reproducing human and cross-species drug toxicities using a liver-chip. *Sci Trans Med* (2019) 11:eaax5516. doi: 10.1126/scitranslmed.aax5516

228. Kasendra M, Tovaglieri A, Sontheimer-Phelps A, Jalili-Firoozinezhad S, Bein A, Chalkiadaki A, et al. Development of a primary human small intestine-on-a-Chip using biopsy-derived organoids. *Sci Rep* (2018) 8:2871. doi: 10.1038/s41598-018-21201-7

229. Occhetta P, Mainardi A, Votta E, Vallmajo-Martin Q, Ehrbar M, Martin I, et al. Hyperphysiological compression of articular cartilage induces an osteoarthritic phenotype in a cartilage-on-a-chip model. *Nat Biomed Eng* (2019) 3:545–57. doi: 10.1038/s41551-019-0406-3

230. Park TE, Mustafaoglu N, Herland A, Hasselkus R, Mannix R, FitzGerald EA, et al. Hypoxia-enhanced blood-brain barrier chip recapitulates human barrier function and shuttling of drugs and antibodies. *Nat Commun* (2019) 10:2621. doi: 10.1038/s41467-019-10588-0

231. Seo J, Byun WY, Alisafaei F, Georgescu A, Yi YS, Massaro-Giordano M, et al. Multiscale reverse engineering of the human ocular surface. *Nat Med* (2019) 25:1310–8. doi: 10.1038/s41591-019-0531-2

232. Jalili-Firoozinezhad S, Prantil-Baun R, Jiang A, Potla R, Mammoto T, Weaver JC, et al. Modeling radiation injury-induced cell death and countermeasure drug responses in a human gut-on-a-Chip. *Cell Death Dis* (2018) 9:223. doi: 10.1038/s41419-018-0304-8

233. Osaki T, Uzel SGM, Kamm RD. On-chip 3D neuromuscular model for drug screening and precision medicine in neuromuscular disease. *Nat Protoc* (2020) 15:421–49. doi: 10.1038/s41596-019-0248-1

234. Caballero D, Reis RL, Kundu SC. Boosting the clinical translation of organ-on-a-Chip technology. *Bioengineering* (2022) 9:549. doi: 10.3390/bioengineering9100549

235. Ingber DE. Human organs-on-chips for disease modelling, drug development and personalized medicine. *Nat Rev Genet* (2022) 23:467–91. doi: 10.1038/s41576-022-00466-9

236. Ko J, Park D, Lee S, Gumuscu B, Jeon NL. Engineering organ-on-a-Chip to accelerate translational research. *Micromachines* (2022) 13:1200. doi: 10.3390/mi13081200

237. Zhao Y, Kankala RK, Wang SB, Chen AZ. Multi-Organs-on-Chips: Towards long-term biomedical investigations. *Molecules* (2019) 24:675. doi: 10.3390/molecules24040675

238. Engineering tissues and organs: The road to the clinic. *Cell* (2020) 181:22–3. doi: 10.1016/j.cell.2020.03.026

239. Danku AE, Dulf EH, Braicu C, Jurj A, Berindan-Neagoe I. Organ-On-A-Chip: A survey of technical results and problems. *Front Bioeng Biotechnol* (2022) 10:840674. doi: 10.3389/fbioe.2022.840674

240. Caballero D, Kaushik S, Correlo VM, Oliveira JM, Reis RL, Kundu SC. Organ-on-chip models of cancer metastasis for future personalized medicine: From chip to the patient. *Biomaterials* (2017) 149:98–115. doi: 10.1016/j.biomaterials.2017.10.005

241. Shang M, Soon RH, Lim CT, Khoo BL, Han J. Microfluidic modelling of the tumor microenvironment for anti-cancer drug development. *Lab Chip* (2019) 19:369–86. doi: 10.1039/C8LC00970H

242. Sun W, Luo Z, Lee J, Kim HJ, Lee K, Tebon P, et al. Organ-on-a-Chip for cancer and immune organs modeling. *Adv Healthcare Mater* (2019) 8:e1801363. doi: 10.1002/adhm.201801363

243. Albanese A, Lam AK, Sykes EA, Rocheleau JV, Chan WC. Tumour-on-a-chip provides an optical window into nanoparticle tissue transport. *Nat Commun* (2013) 4:2718. doi: 10.1038/ncomms3718

244. Hakanson M, Cukierman E, Charnley M. Miniaturized pre-clinical cancer models as research and diagnostic tools. *Adv Drug Delivery Rev* (2014) 69-70:52–66. doi: 10.1016/j.addr.2013.11.010

245. Maulana TI, Kromidas E, Wallstabe L, Cipriano M, Alb M, Zaupa C, et al. Immunocompetent cancer-on-chip models to assess immuno-oncology therapy. *Adv Drug Delivery Rev* (2021) 173:281–305. doi: 10.1016/j.addr.2021.03.015

246. Musella M, Guarracino A, Manduca N, Galassi C, Ruggiero E, Potenza A, et al. Type I IFNs promote cancer cell stemness by triggering the epigenetic regulator KDM1B. *Nat Immunol* (2022) 23:1379–92. doi: 10.1038/s41590-022-01290-3

247. Bjornson-Hooper ZB, Fragiadakis GK, Spitzer MH, Chen H, Madhireddy D, Hu K, et al. A comprehensive atlas of immunological differences between humans, mice, and non-human primates. *Front Immunol* (2022) 13:867015. doi: 10.3389/fimmu.2022.867015

248. Mestas J, Hughes CC. Of mice and not men: differences between mouse and human immunology. *J Immunol* (2004) 172:2731–8. doi: 10.4049/jimmunol.172.5.2731

249. Sackmann EK, Fulton AL, Beebe DJ. The present and future role of microfluidics in biomedical research. *Nature* (2014) 507:181–9. doi: 10.1038/nature13118

250. van der Meer AD, van den Berg A. Organs-on-chips: Breaking the *in vitro* impasse. *Integr Biol Quantitative Biosci Nano to Macro* (2012) 4:461–70. doi: 10.1039/c2ib00176d

251. Imparato G, Urciuolo F, Netti PA. Organ on chip technology to model cancer growth and metastasis. *Bioengineering* (2022) 9:28. doi: 10.3390/bioengineering9010028

252. Zhang X, Karim M, Hasan MM, Hooper J, Wahab R, Roy S, et al. Cancer-on-a-Chip: Models for studying metastasis. *Cancers* (2022) 14:648. doi: 10.3390/cancers14030648

253. Aung A, Kumar V, Theprungsirikul J, Davey SK, Varghese S. An engineered tumor-on-a-Chip device with breast cancer-immune cell interactions for assessing T-cell recruitment. *Cancer Res* (2020) 80:263–75. doi: 10.1158/0008-5472.CAN-19-0342

254. De Ninno A, Bertani FR, Gerardino A, Schiavoni G, Musella M, Galassi C, et al. Microfluidic Co-culture models for dissecting the immune response in *in vitro* tumor microenvironments. *J Visual Experiments JoVE* (2021) 170. doi: 10.3791/61895

255. Ren X, Alamri A, Hipolito J, Lin F, Kung SKP. Applications of microfluidic devices in advancing NK-cell migration studies. *Methods Enzymol* (2020) 631:357–70. doi: 10.1016/bs.mie.2019.05.052

256. Um E, Oh JM, Park J, Song T, Kim TE, Choi Y, et al. Correction: Immature dendritic cells navigate microscopic mazes to find tumor cells. *Lab Chip* (2019) 19:3140. doi: 10.1039/C9LC90097G

257. Vacchelli E, Ma Y, Baracco EE, Sistigu A, Enot DP, Pietrocola F, et al. Chemotherapy-induced antitumor immunity requires formyl peptide receptor 1. *Science* (2015) 350:972–8. doi: 10.1126/science.aad0779

258. Businaro L, De Ninno A, Schiavoni G, Lucarini V, Ciasca G, Gerardino A, et al. Cross talk between cancer and immune cells: exploring complex dynamics in a microfluidic environment. *Lab Chip* (2013) 13:229–39. doi: 10.1039/C2LC40887B

259. Hsu TH, Kao YL, Lin WL, Xiao JL, Kuo PL, Wu CW, et al. The migration speed of cancer cells influenced by macrophages and myofibroblasts co-cultured in a microfluidic chip. *Integr Biol Quantitative Biosci Nano to Macro* (2012) 4:177–82. doi: 10.1039/C2IB00112H

260. Yu J, Berthier E, Craig A, de Groot TE, Sparks S, Ingram PN, et al. Reconfigurable open microfluidics for studying the spatiotemporal dynamics of paracrine signalling. *Nat Biomed Eng* (2019) 3:830–41. doi: 10.1038/s41551-019-0421-4

261. Guo Z, Song J, Hao J, Zhao H, Du X, Li E, et al. M2 macrophages promote NSCLC metastasis by upregulating CRYAB. *Cell Death Dis* (2019) 10:377. doi: 10.1038/s41419-019-1618-x

262. Kim H, Chung H, Kim J, Choi DH, Shin Y, Kang YG, et al. Macrophages-triggered sequential remodeling of endothelium-interstitial matrix to form pre-metastatic niche in microfluidic tumor microenvironment. *Adv Sci* (2019) 6:1900195. doi: 10.1002/advs.201900195

263. Junttila MR, de Sauvage FJ. Influence of tumour micro-environment heterogeneity on therapeutic response. *Nature* (2013) 501:346–54. doi: 10.1038/nature12626

264. Klemm F, Joyce JA. Microenvironmental regulation of therapeutic response in cancer. *Trends Cell Biol* (2015) 25:198–213. doi: 10.1016/j.tcb.2014.11.006

265. Trono P, Tocci A, Musella M, Sistigu A, Nistico P. Actin cytoskeleton dynamics and type I IFN-mediated immune response: A dangerous liaison in cancer? *Biology* (2021) 10:913. doi: 10.3390/biology10090913

266. Ando Y, Siegler EL, Ta HP, Cinay GE, Zhou H, Gorrell KA, et al. Evaluating CAR-T cell therapy in a hypoxic 3D tumor model. *Adv Healthcare Mater* (2019) 8:e1900001. doi: 10.1002/adhm.201900001

267. Aref AR, Huang RY, Yu W, Chua KN, Sun W, Tu TY, et al. Screening therapeutic EMT blocking agents in a three-dimensional microenvironment. *Integr Biol Quantitative Biosci Nano to Macro* (2013) 5:381–9. doi: 10.1039/C2IB20209C

268. Fischbach C, Chen R, Matsumoto T, Schmelzle T, Brugge JS, Polverini PJ, et al. Engineering tumors with 3D scaffolds. *Nat Methods* (2007) 4:855–60. doi: 10.1038/nmeth1085

269. Pavesi A, Tan AT, Koh S, Chia A, Colombo M, Antonecchia E, et al. A 3D microfluidic model for preclinical evaluation of TCR-engineered T cells against solid tumors. *JCI Insight* (2017) 2:e89762. doi: 10.1172/jci.insight.89762

270. Binnewies M, Roberts EW, Kersten K, Chan V, Fearon DF, Merad M, et al. Understanding the tumor immune microenvironment (TIME) for effective therapy. *Nat Med* (2018) 24:541–50. doi: 10.1038/s41591-018-0014-x

271. Chen DS, Mellman I. Oncology meets immunology: The cancer-immunity cycle. *Immunity* (2013) 39:1–10. doi: 10.1016/j.immuni.2013.07.012

272. Shim S, Belanger MC, Harris AR, Munson JM, Pompano RR. Two-way communication between ex vivo tissues on a microfluidic chip: Application to tumor-lymph node interaction. *Lab Chip* (2019) 19:1013–26. doi: 10.1039/C8LC00957K

273. Kam Y, Rejniak KA, Anderson AR. Cellular modeling of cancer invasion: integration of in silico and *in vitro* approaches. *J Cell Physiol* (2012) 227:431–8. doi: 10.1002/jcp.22766

274. Lee SWL, Seager RJ, Litvak F, Spill F, Sieow JL, Leong PH, et al. Integrated in silico and 3D *in vitro* model of macrophage migration in response to physical and chemical factors in the tumor microenvironment. *Integr Biol Quantitative Biosci Nano to Macro* (2020) 12:90–108. doi: 10.1093/intbio/zyaa007

275. Refet-Mollof E, Najyb O, Chermat R, Glory A, Lafontaine J, Wong P, et al. Hypoxic jumbo spheroids on-A-Chip (HOnAChip): Insights into treatment efficacy. *Cancers* (2021) 13:4046. doi: 10.3390/cancers13164046

276. Haessler U, Kalinin Y, Swartz MA, Wu M. An agarose-based microfluidic platform with a gradient buffer for 3D chemotaxis studies. *Biomed Microdevices* (2009) 11:827–35. doi: 10.1007/s10544-009-9299-3

277. Sai J, Rogers M, Hockemeyer K, Wikswo JP, Richmond A. Study of chemotaxis and cell-cell interactions in cancer with microfluidic devices. *Methods Enzymol* (2016) 570:19–45. doi: 10.1016/bs.mie.2015.09.023

278. Bonnans C, Chou J, Werb Z. Remodelling the extracellular matrix in development and disease. *Nat Rev Mol Cell Biol* (2014) 15:786–801. doi: 10.1038/nrm3904

279. Park D, Son K, Hwang Y, Ko J, Lee Y, Doh J, et al. High-throughput microfluidic 3D cytotoxicity assay for cancer immunotherapy (CACI-IMPACT platform). *Front Immunol* (2019) 10:1133. doi: 10.3389/fimmu.2019.01133

280. Boussommier-Calleja A, Li R, Chen MB, Wong SC, Kamm RD. Microfluidics: A new tool for modeling cancer-immune interactions. *Trends Cancer* (2016) 2:6–19. doi: 10.1016/j.trecan.2015.12.003

281. Moore N, Doty D, Zielstorff M, Kariv I, Moy LY, Gimbel A, et al. A multiplexed microfluidic system for evaluation of dynamics of immune-tumor interactions. *Lab Chip* (2018) 18:1844–58. doi: 10.1039/C8LC00256H

282. Schaaf MB, Garg AD, Agostinis P. Defining the role of the tumor vasculature in antitumor immunity and immunotherapy. *Cell Death Dis* (2018) 9:115. doi: 10.1038/s41419-017-0061-0

283. Cui X, Morales RT, Qian W, Wang H, Gagner JP, Dolgalev I, et al. Hacking macrophage-associated immunosuppression for regulating glioblastoma angiogenesis. *Biomaterials* (2018) 161:164–78. doi: 10.1016/j.biomaterials.2018.01.053

284. Zervantonakis IK, Hughes-Alford SK, Charest JL, Condeelis JS, Gertler FB, Kamm RD. Three-dimensional microfluidic model for tumor cell intravasation and endothelial barrier function. *Proc Natl Acad Sci United States America* (2012) 109:13515–20. doi: 10.1073/pnas.1210182109

285. Boussommier-Calleja A, Atiyas Y, Haase K, Headley M, Lewis C, Kamm RD. The effects of monocytes on tumor cell extravasation in a 3D vascularized microfluidic model. *Biomaterials* (2019) 198:180–93. doi: 10.1016/j.biomaterials.2018.03.005

286. Luque-Gonzalez MA, Reis RL, Kundu SC, Caballero D. Human microcirculation-on-Chip models in cancer research: Key integration of lymphatic and blood vasculatures. *Adv Biosyst* (2020) 4:e2000045. doi: 10.1002/adbi.202000045

287. Takebe T, Zhang B, Radisic M. Synergistic engineering: Organoids meet organs-on-a-Chip. *Cell Stem Cell* (2017) 21:297–300. doi: 10.1016/j.stem.2017.08.016

288. Tuveson D, Clevers H. Cancer modeling meets human organoid technology. *Science* (2019) 364:952–5. doi: 10.1126/science.aaw6985

289. Low LA, Mummery C, Berridge BR, Austin CP, Tagle DA. Organs-on-chips: Into the next decade. *Nat Rev Drug Discovery* (2021) 20:345–61. doi: 10.1038/s41573-020-0079-3

290. Cox MC, Reese LM, Bickford LR, Verbridge SS. Toward the broad adoption of 3D tumor models in the cancer drug pipeline. *ACS Biomater Sci Eng* (2015) 1:877–94. doi: 10.1021/acsbiomaterials.5b00172

291. Jalili-Firoozinezhad S, Miranda CC, Cabral JMS. Modeling the human body on microfluidic chips. *Trends Biotechnol* (2021) 39:838–52. doi: 10.1016/j.tibtech.2021.01.004

frontiers | Frontiers in Immunology

TYPE Review
PUBLISHED 28 April 2023
DOI 10.3389/fimmu.2023.1172262

OPEN ACCESS

EDITED BY
Fabrizio Mattei,
National Institute of Health (ISS), Italy

REVIEWED BY
Pengxiang Yang,
Nantong University, China
Jianbo Liu,
Hunan University, China
Jiacan Su,
Shanghai University, China

*CORRESPONDENCE
Heng Zou
zhcsuxy@csu.edu.cn
Zhong-tao Liu
158202088@csu.edu.cn

†These authors have contributed equally to this work

RECEIVED 23 February 2023
ACCEPTED 17 April 2023
PUBLISHED 28 April 2023

CITATION
Shen C, Zhang Z-j, Li X-x, Huang Y-p, Wang Y-x, Zhou H, Xiong L, Wen Y, Zou H and Liu Z-t (2023) Intersection of nanomaterials and organoids technology in biomedicine.
Front. Immunol. 14:1172262.
doi: 10.3389/fimmu.2023.1172262

Intersection of nanomaterials and organoids technology in biomedicine

Chen Shen[1†], Zi-jian Zhang[1†], Xiao-xue Li[2], Yun-peng Huang[1], Yong-xiang Wang[1], Hui Zhou[1], Li Xiong[1], Yu Wen[1], Heng Zou[1*] and Zhong-tao Liu[1*]

[1]Department of General Surgery, Second Xiangya Hospital, Central South University, Changsha, Hunan, China, [2]Department of Obstetrics and Gynecology, Second Xiangya Hospital, Central South University, Changsha, Hunan, China

Organoids are stem cell-derived, self-organizing, 3D structures. Compared to the conventional 2D cell culture method, 3D cultured organoids contain a variety of cell types that can form functional "micro-organs" and can be used to simulate the occurrence process and physiological pathological state of organ tissues more effectively. Nanomaterials (NMs) are becoming indispensable in the development of novel organoids. Understanding the application of nanomaterials in organoid construction can, therefore, provide researchers with ideas for the development of novel organoids. Here, we discuss the application status of NMs in various organoid culture systems and the research direction of NMs combined with organoids in the biomedical field.

KEYWORDS

nanomaterials, organoids, 3D culture, nanoparticles, biomedicine

1 Introduction

Organoids are 3D structures grown from stem cells that consist of self-organizing organ-specific cell types shaped by cell classification and spatially constrained cell lines (1). These stem cells may be embryonic stem cells (iPSc) derived or adult stem cells (aSCs). During development, organoid formation recapitulates two primary processes of self-organization: cell classification and spatially restricted cell line typing. Human organoids reproduce developmental patterns, thereby replicating the structure and physiology of specific tissue types, making it possible to accurately study human disease and supplant animal experiments.

James Rheinwald and Howard Green first described the long-term culture of normal human epidermal cells in 1975 by combining freshly isolated keratinocytes with multi-mouse 3T3 fibroblasts and isolating keratinocytes without viable fibroblasts (2). However, this method of cell culture resembles two-dimensional plane culture. In 2009, Hans Clevers et al., successfully inoculated adult Lgr5(+) intestinal stem cells from mouse intestines in matrigel and added Wnt pathway agonist R-spondin, TGF-β inhibitor Noggin, epidermal

growth factor, and other stem cell growth factors to cultivate a three-dimensional structure with crypt-like and villiform-like epithelial regions (small-intestinal organoids) (3). Accordingly, it comprised the first organoid to meet the modern definition, ushering in a "new era" in the development of organoid technology. Since then, numerous organoids have emerged, including those of the brain (4), stomach (5), colon (3), liver (6), kidney (7), heart (8), pancreas (9), prostate (10), and numerous other tissues and organs, as well as organoids of various cancerous tissues (11–13). Increased interest in tissue engineering, disease modeling, precision medicine, drug screening, and immunotherapy has resulted from the development of organoid culture (14). The rapid development of organoid technology has introduced novel concepts to the study of a variety of diseases. Using the intraductal transplant organoid (IGO) model, Tuveson et al., developed classical subtypes of pancreatic ductal adenocarcinoma (PDAC) in order to study subtype-dependent therapies that provide a deeper understanding of the genetic and epigenetic dynamics of PDAC (15). Park et al., utilized human colon organoids to evaluate the toxicity induced by SiO2 and TiO2 nanoparticles and to increase the expression of the apoptosis marker Bax/Bcl-2. This study demonstrated a difference in toxicity between 2D models and 3D organoid cultures, highlighting the significance of organoids in drug screening (16). In addition, the organ-on-a-chip, which combines microfluidics and organoid technology, enables precise regulation of the organoid microenvironment as well as precise simulation of multi tissue crosstalk with low heterogeneity (17).

As an emerging 3D physiological model, organoids possess the potential to change the methodology of research in the medical field. However, due to technical limitations, at present, various organoids still have quite a few defects (18). For example, we still cannot very precisely control organoid size, shape, proportion of cellular composition (6). More importantly, researchers cannot control the growth and function of organoids matching (19), which produce internal tissue necrosis after growing to a certain scale. The key to addressing these issues is the development of culture systems. The application of nanomaterials brings new ideas to solve these problems. Nanomaterials are a kind of materials ranging from 1-100 nm (20). Nanomaterials are materials between 1–100 nm in size (20). The use of nanomaterials has altered numerous fields, such as medicine, agriculture, manufacturing, electronic technology (21–23), and their unique optical, magnetic, and electrical properties render them irreplaceable in terms of their application potential. Accordingly, nanomaterials play an increasingly vital role in the field of biomedicine, and also significantly enhance and expand the research value of organoids (24). Mo et al. developed electro spun nanofibers prepared based on P (LLA-CL) copolymer and cultured smooth muscle cell (SMCs) and endothelial cells (ECS) as scaffolds and showed that these cells proliferated well on the nanofibrous scaffolds (25). This study suggests that the nanoscale culture environment will have an impact on the behavior and function of cells. In addition, nanomaterials may promote angiogenic effects in culture systems (26), which is helpful for addressing the problem of imbalance in organoid growth and function. Therefore, we have sufficient reasons to conclude that the application of nanomaterials constructed culture system has a positive effect on 3D culture of organoids.

The relationship between nanomaterials and organoids has been discussed in many excellent reviews (27–31). However, no review has yet been published that focuses on how nanomaterials are extensively involved in organoid construction. Consequently, this review will focus on the application status and future prospects of nanomaterials in the field of organoids, as well as the state of the frontier research for the combined application of organoids and nanomaterials in biomedicine (Figure 1).

2 Use nanomaterials to assist in the construction of organoid 3D culture systems

The advancement of nanomaterial technology has inspired the creation of new organoids, and nanomaterials can aid in the construction of organoids in numerous ways. Organoids are created using two types of stem cells: (1) pluripotent embryonic

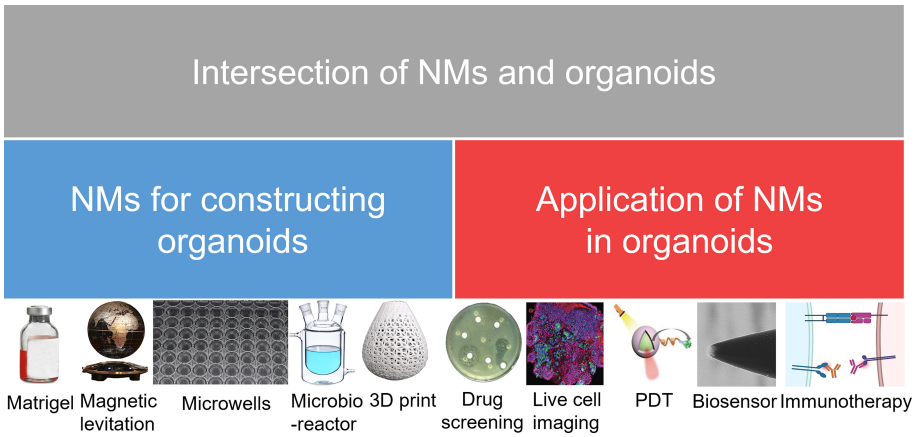

FIGURE 1
Research directions in the development of NMs and organoids. NMs, nanomaterials; PDT, photodynamic therapy.

stem cells (ES), and their synthetic induced pluripotent stem cell (iPS) counterparts, and (2) adult organ-restricted stem cells (aSCs) (32). Conventional organoid culture systems also necessitate 3D solid extracellular matrices containing laminin, collagen, and other growth factors. To encourage organoid differentiation, it is also necessary to add growth-stimulating factors. Different organoids require distinct construction steps and the addition of a growth stimulant. In addition to conventional organoids based on a 3D solid external matrix, various novel organoid-building techniques have been developed in recent years (33). For example, Wiedenmann et al., designed a microwell chip to generate defined 3D aggregates of pancreatic progenitor cells derived from human induced pluripotent stem cells (hiPSCs) and then induced their differentiation into pancreatic duct-like organoids (34). Additionally, Ferreira et al., developed saliva-secreting organoids/microglands using a novel scaffold/substrate-free culture system known as magnetic 3D suspension (M3DL), which assembles and levitates magnetized primary SG-derived cells (SGDCs) so that they can generate their own extracellular matrix (35). Thus, nanomaterials have not only been utilized in conventional methods based on a 3D solid outer matrix, but they also play a significant role in a few novel organoid culture strategies. Accordingly, this review summarizes the key role of nanomaterials in organoid construction with respect to the aforementioned factors.

2.1 The use of nanomaterials to alter the properties of the extracellular matrix

Most existing organoid 3D culture systems were developed primarily on the basis of Matrigel (33). Matrigel, a substance secreted by Engelbreth-Holm-Swarm mouse sarcoma cells (36) contains laminin, type IV collagen, and heparin sulfate proteoglycan 6,7, which promotes cell adhesion, survival, andorganoid formation (37). As a traditional organoid culture system, Matrigel seem to gradually fail to meet the needs of researchers to develop better organoids. Many kinds of hydrogel replacement materials are being used for the development of organoids (38).

Using the properties of nanomaterials, it is possible to modify certain properties of matrix gum in order to create the desired organoid model. For instance, in the study by Bao et al., carbon nanotubes (CNTs) were used to regulate extracellular matrix (ECM) viscosity and intracellular energy metabolism. In addition, CNTs reduced the hardness of the extracellular matrix by reducing elasticity and increasing viscosity. Moreover, carbon nanotubes modified the metabolic profile of intestinal organoids and increased mitochondrial activity, respiration, and nutrient absorption. These synergistic mechanisms promote the proliferation and differentiation of intestinal organoids. This hints at the possibility of CNTs as biomaterials for intestinal tissue engineering (39). Purwada et al., introduced a B-cell follicular organoid composed of nanocomposite biomaterials, on which researchers continuously provided an extracellular matrix (ECM) and intercellular signals to naïve B cells, thereby accelerating the induction of germinal center (GC) response. The silicate nanoparticles complexed with gelatin utilized in this study comprised ultrathin nanomaterials with a high level of anisotropy and functionality. These nanoparticles have great potential in regenerative medicine and drug delivery (40). Luo et al., synthesized bone-forming peptide-1 (BFP-1)-loaded mesoporous silica nanoparticles (pep@MSNs) incorporating adhesion peptides that contained arginine-glycine-aspartate (RGD) domains, which modified alginate hydrogel (RA) system (pep@MSNs-RA) to promote the activity and sequential stimulation of bone differentiation in human mesenchymal stem cells (hMSCs). This ensured enhanced hMSC survival and proliferation in adhesion peptide-modified hydrogels. After the phase of proliferation, BFP-1 then induced bone differentiation of hMSCs derived from pep@MSNs. Additionally, BFP-1was self-captured by an additional cellular peptide cross-linking network formed by receptor-bound ligands (RGDs) on the cell surface, resulting in long-term sustained bone stimulation of hMSCs. The results demonstrated that independent and sequential stimulation of the proliferation and bone differentiation stages synergistically increased hMSC survival, amplification, and osteogenesis compared to stimulation alone or simultaneously (41). Thus, nanomaterials can create new matrigel culture systems and novel organoid models.

2.2 Develop novel microwells with nanomaterials to culture organoids

Low throughput (approximately 4 organoids per square millimeter) and poor repeatability are disadvantages of conventional matrigel-based organoids. Microwells are widely used to capture single cells and are simple to fabricate, convenient to operate, and high-throughput (42).

Thus, additional optimization is required in terms of scale, morphogenetic stability, and compatibility with high-throughput phenotypic analysis. Accordingly, organoid technology based on micropores was developed (43). Shin et al., utilized a microporous array-based 3D culture system with a polycaprolactone (PCL) nanofiber bottom and a polyethylene glycol (PEG) hydrogel wall for efficient bioengineering of human salivary gland organoids that can readily generate uniformly sized 3D organoids. In comparison to Matrigel and nanofiber scaffold cultures, the results demonstrated greater efficacy. The novel aspects of this study were the engineering of nanofibers into a microporous structure and the use of human cells under non-animal and serum-free culture conditions, neither of which have been previously reported (44).

Kim et al., proposed an elliptical microporous array of nanofibers, dubbed the NOVA micropore array, with high AR and high pore density, which was not only capable of collecting cells in microwells with high cell seeding efficiency but also of producing multiple living and functional spheroids in a uniform and stable manner. Not only were human hepatocellular carcinoma (HepG2) cell spheroids cultured on the NOVA microwell array uniform in size and shape, but their viability was also enhanced. This facilitated the scalable production of a variety of living and functional

spheroids and even organoids (45). Park et al., developed a process for fabricating nanofiber concave microvias (NCMs) with tunable size and shape. The use of a series of hemispherical convex electrolyte solution droplets as grounding collectors for electrospinning significantly improved the NCM's degree of freedom in terms of size, shape, and curvature. Accordingly, researchers demonstrated the formation of spheroids from the human hepatoma cell line (HepG2) in NCM. Additionally, HepG2 cells were able to form spheroids that were homogeneous and of controlled size as a result of NCM (46). Thus, nanomaterials can be used to create novel micropores and thus generate novel organoid models, introducing a novel concept for organoid development.

2.3 Nanomaterials participate in the magnetic levitation culture of organoids

In 2010, Souza et al., reported a three-dimensional tissue culture based on cell magnetic levitation. In this study researchers injected magnetic iron oxide and gold nanoparticles into cancer cells and then magnetically suspended the cells in a liquid, thus performing cell culture (47). This is the first time that magnetic levitation technology has been utilized in the field of cell culture. In comparison to conventional culture methods, magnetic levitation culture allows for the manipulation of the geometry of cell masses and the clustering of multiple cell types in co-culture. Accordingly, Haisler et al., developed a comprehensive magnetic levitation method for 3D cell culture (48). Magnetic nanoparticle components consisting of gold nanoparticles, iron oxides, and cell adhesion peptide sequences were delivered to 2D cultured cells to make these cells magnetic, and then magnetism was used to control the cells, suspend the cells at the gas-liquid plane and generate extracellular matrix, and finally construct a 3D model. In general, magnetic levitation 3D tissue culture conforms to this culture method. Moreover, using magnetic levitation, Tseng et al., created 3D models, which were successfully used to construct adipose tissue organoids (fat globules) that preserve the heterogeneity of their constituent cell types *in vitro*. Correspondingly, researchers demonstrated the ability to assemble fat globules from diverse cell types, including adult stem cells (ASCs), endothelial cells, and white blood cells, which regenerate tissue. These fat globules mimicked the organogenesis of white adipose tissue (WAT) and were capable of forming vascular-like endothelial structures with lumens and monocular adipocyte differentiation. This established the foundation for high-throughput WAT culture and analysis (49).

In addition, Tseng et al., used a similar technique to create an organized three-dimensional (3D) bronchiolechial co-culture by layering cells sequentially to mimic natural tissue structures. The 3D co-culture model was assembled from four human cell types in bronchioles: endothelial cells, smooth muscle cells (SMCs), fibroblasts, and epithelial cells (EpiCs). Accordingly, this comprised the first attempt to combine these specialized cell types into an organized bronchiolechial co-culture. Magnetic levitation has been validated as a method for rapidly organizing 3D co-cultures, maintaining phenotype, and inducing extracellular matrix formation (50). Under magnetic levitation, Gaitán-Salvatella et al., were able to create 3D spheres of human fetal osteoblasts (hFOB) in their research. After 14 days of culture, the cell viability of 3D hFOB spheroids indicates that they are still viable. ALP assay, qPCR expression of Col1, ALP, and Itg-β1 molecules, and calcium deposition of alizarin red all demonstrated high levels of biological activity in 3D hFOB spheroids. In the presence of matrix deposition, SEM images allowed the morphological analysis of spheroids resembling 3D microtissues. These findings demonstrate that magnetic levitation culture can produce three-dimensionally stable osteoblast spheroids, and that the engineering application of bone tissue surgical regeneration in three-dimensional construction has a vast potential (Figure 2) (51). Bumpers et al., created for the first time nanomagnetic suspension 3D cultures of breast cancer (BC) and cancer (CRC) cells using carbon-coated cobalt magnetic nanoparticles, in which the suspended BC and CRC cells form microprotrusions. Suspension cultures have a high level of viability and persist for an extended period. In suspended 3D tumor spheres and xenografts of CRC and BC cells, the authors found that N-cadherin and epidermal growth factor receptor activity were highly expressed. Consequently, nanomagnetic levitation 3D cultures tend to form stable BC and CRC microtissues, which may be more applicable to a variety of applications in drug testing or regenerative medicine (52). Thus, in the current strategy for organoid magnetic levitation culture, nanomaterials are typically used to impart magnetic properties to cells, which are then suspended in the culture system by magnetic force, thereby enhancing the culture activity and maneuverability of cells.

2.4 Make bioreactors from nanomaterials and use them for organoid culture

Conventional techniques for organoid preparation are frequently reproducible and require expensive equipment. The bioreactor is a technical method that improves organoid reproducibility and homogeneity, and it can also promote organoid maturation (53). In recent years, there have also been reports of the use of nanomaterials in the construction of bioreactors for the production of novel organoids. Aalders et al., for instance, described a test method that permits the generation of functional cardiac micro-organs comprised of co-cultured cardiomyocytes and cardiac fibroblasts. Nanoparticles of hydrophobic fumed silica powder are used to encapsulate cells suspended in a drop of the medium. Nanoparticles treated with the hydrophobic chemical hexamethyldisilane (nHMDS) resulted in the formation of microbial reactors. These microenvironments were referred to as "liquid marbles" because they promoted cell coalescence and 3D aggregation. In addition, the nHMDS housing then facilitated optimal gas exchange between the liquid contained within and the surrounding environment. This microbial reactor was smaller and, therefore, suitable for higher throughput applications, making it an ideal co-culturing technique. Thus, the researchers demonstrated that the co-culture of cardiac fibroblasts and cardiomyocytes could be a valuable tool for simulating heart

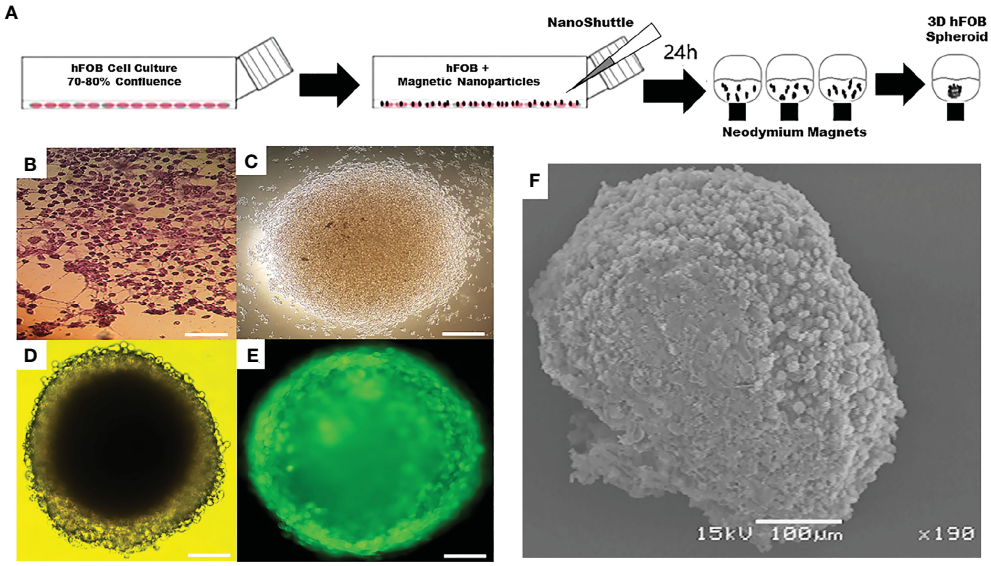

FIGURE 2
Application of magnetic levitation system in organoids. **(A)** Schematic of magnetic levitation technique. A confluent flask of hFOB cells was incubated with NanoShuttle overnight to allow for cell membrane-binding of the magnetic nanoparticles. The next day, the cells were seeded onto 96-well plate placed atop a magnetic drive of 96 neodymium magnets, the magnetic field influencing the hFOB cells to form an air-liquid interface and guide them to aggregate within hours of levitation to form the 3D Spheroid. **(B)** Optical micrograph of 2D tissue culture plate. **(C)** 3D hFOB spheroid after 3 h of magnetic levitation culture. **(D)** 3D hFOB spheroid after 24 h of magnetic levitation culture. **(E)** Fluorescence micrograph of 3D hFOB spheroid after 24 h of magnetic levitation culture. **(F)** Morphology of the 3D hFOB spheroid obtained by SEM with the presence of osteogenic factors incubated for 14 days under magnetic levitation system. FOB: fetal osteoblasts. Adapted with permission from (51), copyright 2021, Frontiers Media S.A.

disease *in vitro* and evaluating cellular interactions to decipher disease mechanisms (54).

Brevini et al., described a protocol that permits the extraction of functional, pancreatic small organs from skin biopsies. The cells were suspended in a drop of medium and encased in hydrophobic polytetrafluoroethylene (PTFE) powder granules to create a "liquid marbles" microbial reactor that promoted cell coalescence and three-dimensional aggregation. In addition, the PTFE housing allowed for optimal gas exchange between the liquid inside and the surrounding environment. Additionally, it can reduce the size of experiments to work in smaller volumes, making it suitable for high-throughput applications (55). In these bioreactors, nanomaterials serve as encapsulation vessels, isolating the reaction system from the surrounding environment. Accordingly, new organoid culture techniques have great potential if other nanomaterial applications can be developed in bioreactors.

2.5 Nanoparticles involved in 3D bioprinting of organoids

Bioprinting is the use of computer-aided technology to pattern the printing of biological and non-living materials through designated 2D or 3D tissues in order to create bioengineered structures (56). The technology of 3D bioprinting is an extension of the technology of organoid culture. Inkjet bioprinting, extrusion bioprinting, and light-assisted bioprinting are common printing techniques (57). For instance, Urkasemsin et al., reported the use of magnetic 3D bioprinting (M3DB) to generate salivary adenoid epithelial organoids from stem cells. The neuronal network of these organoids responded to salivary nerve stimulants. This biological structure was created using a NanoShuttle-PL™ solution containing gold, iron oxide, and polyl-lysine (58). Bowser et al., utilized magnetic nanoparticles to create spinal cord spheroids in a three-dimensional hydrogel construct using magnetic bioprinting. The resulting structure exhibited local cell-cell interactions and long-distance projections that mimicked *in vivo* structures. Magnetic nanoparticles for spheroid formation provide batch-to-batch consistency in size and shape and reduce the need for skilled experimenters to place cultures precisely. This combined approach is a first step toward developing simple methods for integrating spheroids, hydrogel culture, and bioprinting as an alternative to more complex and costly procedures (59). In the study by Li et al., the researchers first 3D-printed a tubular composite scaffold capable of reconstructing bile duct function with real-time MRI imaging properties. Subsequently, then used ultra-small ultraparamagnetic iron oxide (USPIO) nanoparticles dispersed in gelatin methacryloyl (GelMA) as contrast agents to monitor the repair of lesion sites and degeneration of bile ducts in real-time MRI (60). In addition, bioinks combining the excellent shear-thinning properties of nanofiber cellulose (NFC) and the rapid crosslinking ability of sodium alginate were used for 3D bioprinting of human cartilage tissue and cells in the study by Markstedt et al (61).

2.6 Nanomaterials can give organoids more functions

To date, no organoids have accurately represented their corresponding human organs. The development of new

nanomaterials enables the creation of organoid culture systems that resemble human organs more closely. Adding nanomaterials to organoids or developing organoids using the properties of nanomaterials can increase the functionality of organoids, paving the way for future research. Zhang et al., for instance, incorporated $Ti_3C_2T_x$MXene nanomaterials into Matrix in order to regulate Matrigel's properties and demonstrated adequate biocompatibility. $Ti_3C_2T_x$MXene Matrix (MXene Matrigel) controlled the development of cochlear organoids (cochlear tissue) by promoting the formation and maturation of organoid hair cells. In addition, the regenerated hair cells in MXene Matrix exhibited superior electrophysiological properties to those of Matrigel-regenerated hair cells. MXene Matrigel promotes hair cell differentiation by enhancing the mycin (mTOR) signaling pathway, whereas mTOR signaling inhibits hair cell differentiation. MXene Matrix also promotes synaptic formation efficiency and the establishment of innervation between regenerative hair cells grown from cochlear modiolus and helical ganglion neurons (SGNs) in co-culture systems. Accordingly, this method overcomes several limitations of the Matrigel-dependent culture system and significantly accelerates the application of nanomaterials in organoid development and hearing loss research (Figure 3) (62). Additionally, electrospinning was used by Beldjilali-Labro et al., to obtain poly(ϵ-caprolactone) nanofiber sheets, which were coated or uncoated with gold nanoparticles as a potential substrate for electrical stimulation. The differentiation of C2C12 cells was then measured over a seven-day period by the expression of specific genes and the confocal microscopy analysis of the arrangement and length of myotubes. It was demonstrated that multi-scale biological constructs possessed variable mechanical properties, supported skeletal muscle at different developmental stages, and improved the parallel orientation of the muscle tube with a variation of less than 15°. These scaffolds exhibited sustained myogenic differentiation by promoting the regeneration of skeletal muscle tissue (63). Moreover, Bao et al., investigated the beneficial effect of carbon nanotubes (CNTs) with different graphene layers and surface modifications on 3D models of intestinal organoids and demonstrated that CNTs promote the growth of intestinal organoids. Carbon nanotubes modify the metabolic profile of intestinal organoids and increase mitochondrial activity, respiration, and absorption of nutrients. These mechanisms promote the proliferation and differentiation of intestinal organoids through a synergistic effect. Thus, these results indicate that CNT has the potential to be used in intestinal tissue

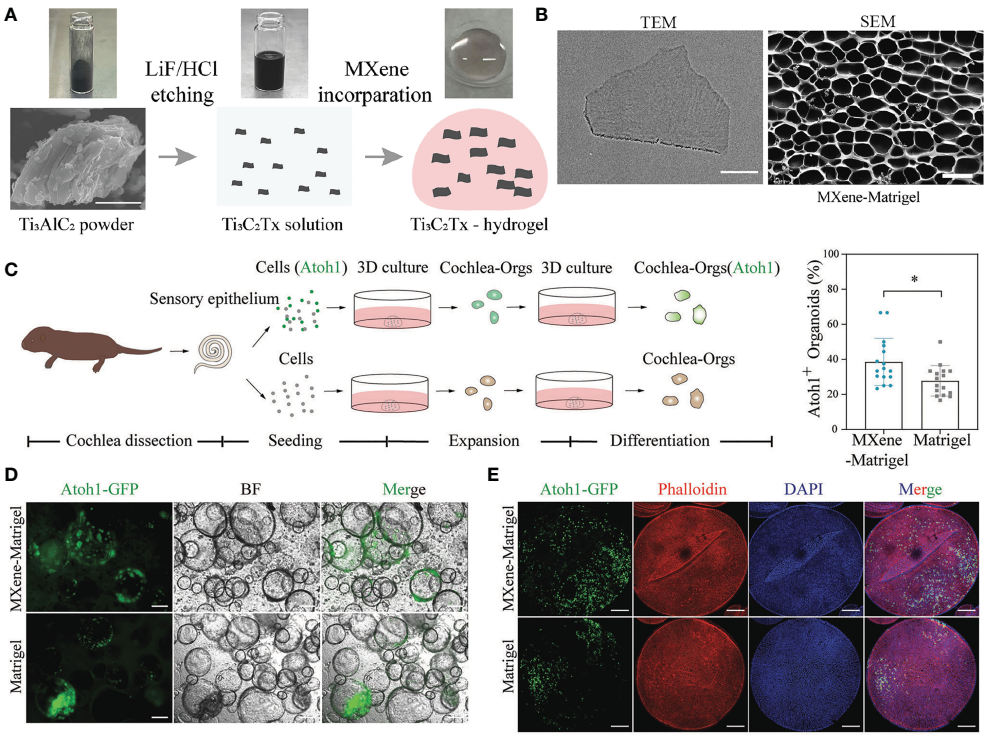

FIGURE 3
$Ti_3C_2T_x$MXene-Matrigel hydrogel potentiated hair cells formation of Cochlea organoids. **(A)** Schematic diagram of the preparation of $Ti_3C_2T_x$MXene-Matrigel. Appropriate amount of $Ti_3C_2T_x$MXene solution was mixed with Matrigel, and the incorporating hydrogel was solidified at 37°C. **(B)** Representative TEM (bar: 200 nm) or SEM (50 μm) image of the $Ti_3C_2T_x$MXene nanosheets. **(C)** Overview of the generation of cochlea hair cells through the differentiation of Cochlea organoids. **(D)** BF and green fluorescent (Atoh1-GFP) images of Cochlea-Orgs after 20 days of differentiation in the differentiationmedium. **(E)** Confocal images of DAPI (blue), early hair cell marker Atoh1-GFP, and phalloidin (red) (bar:100 μm). TEM, transmission electron microscope; SEM, scanning electron microscope; BF, bright field; GFP, green fluorescent protein; DAPI: 4′,6-diamidino-2-phenylindole. Adapted with permission from (62), copyright 2022, Wiley-VCH GmbH.

engineering (38). The main applications mentioned in this section are summarized in Table 1.

3 The combined application of organoids and nanomaterials provides new strategies for disease research

As an emerging physiological model, organoids are applied increasingly in more and more research. Compared with traditional 2D models, organoids based on 3D culture technology and self-organization have characteristics that are closer to the original physiological morphology of organs. Organs are more suitable for research in organ development, drug research and development, and tumor treatment. In addition, organoids developed by patients' own cells are expected to undergo autologous transplantation (64), avoiding the limitations of medical ethics. Using the patient's own tumor cell culture organoids can provide personalized drug screening for patients, achieving precise medical treatment. Nanomaterial technology, as a rapidly changing research field, has been widely applied in various aspects of biomedicine. The chemical and physical properties of substances under nanostructures will undergo significant changes, and many therapeutic strategies have been developed. For example, the excellent optical properties of some nanomaterials have shown great application prospects in photothermal therapy (PTT) for cancer (65). The joint application between nanomaterials and organoids has also attracted the attention of researchers. Organoids can serve as

TABLE 1 Nanomaterials applied to assist in the construction of organoid 3D culture systems.

Methods	Nanomaterials	Organoid type	Functions	References
3D hydrogels	CNTs	Mice intestinal organoid	1. CNTs reduce the hardness of the extracellular matrix; 2. CNTs induce an increase in mitochondrial activity, accelerated cellular respiration and nutrient absorption.	(38)
	SiNP with 25–30 nm in diameter and 1 nm in thickness;obtained from Southern Clay Products Inc., USA	Mice B cell follicle organoid	SiNP increase the stability of the hydrogel system Making it closer to the stiffness of lymphatic tissue.	(39)
	BFP-1 laden MSNs (pep@MSNs)	Human bone organoid	pep@MSNs release BFP-1 to induce osteo-differentiation after cell spreading and expansion.	(40)
microwell array	Nanofibrous concave microwells (NCMs)	NA	Modify the properties of cell spheroids by controlling the shape of nanofibrous concave microwells.	(45)
	Nanofibrous scaffolds	Human parotid epithelial organoid	Increas efficiency of acinar-like organoid formation.	(43)
	Nanofibrous	Human hepatocellular carcinoma organoid	Enable microwell to possess both a high aspect ratio and a high well density	(44)
Magnetic levitation culture	Nanoshuttles (NS), consisting of gold, iron oxide, and poly-l-lysine; NanoShuttle (NS, Nano3D Biosciences, Houston, TX).	Murine adipose tissue organoids	By electrostatic attachment to the cell membrane, the cells are magnetized. When cells are resuspended in medium, they can be suspended from any stiff substrate by clumping them to the air liquid interface with a magnet placed above the culture vessel.	(48)
	NanoShuttle solution of magnetic nanoparticles (NanoShuttleTM-PL)	Human fetal osteoblast organoids	Electrostatically attach to the cell membranes and endowed the cells with magnetic properties	(50)
	A nanoparticle assembly consisting of poly-L-lysine (PLL),* magnetic iron oxide (MIO; Fe3O4, magnetite), and gold nanoparticles	Human bronchiole organoid	Biocompatible nanoparticles are taken up by cells and render them magnetic, allowing them to be magnetically manipulated	(49)
	C-Co nanoparticles	Breast cancer organoid	This nanomaterial can be used for internalization by cancer cells to achieve nanomagnetic suspension, and form three-dimensional cancer microtissues.	(51)
	Nanoshuttle (Greiner Bio-One, Monroe, NC)	Rat spinal cord organoid	Imparting magnetic properties to cells	(58)
	Hydrophobic fumed silica powder nanoparticles	Human cardiac organoid	The nanoparticles assit forming "liquid marbles" structures reducing the scale of the experiment. Thus, this technic enables higherthroughput applications	(53)

(Continued)

TABLE 1 Continued

Methods	Nanomaterials	Organoid type	Functions	References
Bioreactor	NanoShuttle™-PL solution (Nano3D Biosciences, cat. no. 005-NS).	Human salivary gland organoid	Support cell proliferation and metabolism	(57)
	Hydrophobic polytetrafluoroethylene (PTFE) powder particles	Human pancreatic Mini-organoids	Support cell proliferation and metabolism	(54)
3D bioprinting	Nanofibrillated cellulose (NFC)	Human cartilage organoid	This nanomaterial composes a novel bioink with alginate. The novel bioink provids stability for 3D bioprinting of living cells at room temperature and atmospheric pressure.	(60)
	NanoShuttle™-PL	Human secretory epithelial organoid	support cell proliferation and metabolism	(57)
	Ultrasmall superparamagnetic iron oxide (USPIO) nanoparticles	Human bile duct organoid	Serve as the contrast agent to monitor the repair of the lesion site and the degradation of the bile duct in real time by magnetic resonance imaging (MRI)	(59)

models to verify the efficacy of targeted drugs based on nanomaterials and conduct drug screening; In addition, some nanoparticles can be used for live cell imaging and phenotypic analysis in organ like models; In photodynamic and photothermal therapy, researchers have developed many photosensitizers based on nanomaterials and tested them in organoids; The excellent properties of nanomaterials can also be used to develop electrochemical biosensors, which have been tested in organoid models in some studies. This article will discuss the joint application of organoids and nanomaterials in these aspects.

3.1 Drug screening

The 2D monolayer culture technique lacks a substance-signal connection within the organ; consequently, diseased cell types may lack disease-related input signals. In particular, the biological structure of organs, endogenous signaling, and cell-cell interactions may have a direct impact on the pathogenesis of disease. Therefore, 3D-cultured organoids that more closely resemble the physiological state of the human body have emerged as a model for drug testing. The majority of organoid-screenable drugs are chemotherapy drugs, small molecule-targeted drugs, and antibody drugs, among others. For instance, Zhang et al., conducted high-throughput drug screening on organoids derived from 40 patients with hepatocellular carcinoma (HCC) and determined that bortezomib (BTZ) was a highly cytotoxic small molecule against HCC. Using the flash nanocomposite/nanoprecipitation method, the researchers designed and manufactured sustained-release BTZ nanoparticles (BTZ-NP). BTZ-NP formulations demonstrated sustained BTZ release for 30 days. This BTZ-NP formulation was found to be highly effective at reducing tumor size and enhancing *in vivo* survival in three HCC animal models, including when administered via hepatic arteries (66). Kim et al., incorporated gold nanoparticles modified with hyaluronic acid (HA-AuNP) into a muscle bundle-based biohybrid robot that advances in response to electrical stimulation. HA-AuNP was incorporated into the fasciculus in order to increase its propulsion. Due to enhanced differentiation of HA-AuNPs and enhanced fascicular conductivity, the movement of the manufactured biohybrid robot was, therefore, enhanced. Moreover, the addition of positive and negative inotropic drugs produced dramatic motor changes in the manufactured biohybrid robot. Combining neural tissues such as motor neuron organoids and brain organoids, the proposed biohybrid robot demonstrated the potential to screen drugs for neuromuscular diseases (67). Le Joncour et al., described a protocol to obtain a hemo-cerebrospinal fluid barrier (BBTB) mimic by cultivating endothelial cells in contact with astrocytes on inserts at specific cell densities. In addition to evaluating tumor cell targeting in the same assay, this BBTB mimic can be used for quantitative and confocal imaging of nanoparticles crossing the endothelial and astrocyte barriers. In addition, the researchers demonstrated that the obtained data can be used to predict the behavior of nanoparticles in animal models used for preclinical research. This *in vitro* model can be adapted to other neurodegenerative diseases for determining the efficacy of new therapeutic molecules by BBBs and/or supplementation of brain organoids to assess drug efficacy directly (68).

3.2 Live cell imaging

Live-cell imaging refers to live-cell research utilizing time-lapse imaging technology; using live-cell imaging technology, the dynamic life processes involved in the target can be studied, and dynamic processes such as enzyme activity, signal transduction, protein and receptor transport, and membrane recycling process (endocytosis and exocytosis) can be detected. With the aid of live-cell imaging technology, scientists can observe the internal structure and physiological processes of cells in real-time or over time,

thereby enhancing their understanding of cell operation processes. Liu et al., for instance, described *in vitro* luminescence methods for the detection of albumin, a marker of hepatocyte fate, and live-cell labeling with antibody (Ab) and rosean caproic acid (RBHA)-conjugated upconverted nanoparticles (UCNP). They used a "disconnect" strategy: In the presence of albumin, the transfer of energy to the quencher still inhibited the luminescence of the nanoparticles. Correspondingly, luminescence was restored following the albumin-antibody interaction under near-infrared light. UCNPs-Ab-RBHA (UCAR) nanoprobes have a broad detection range for albumin in a variety of biological samples. When applied to hepatic ductal organoid media, UCAR monitors hepatocyte differentiation in real-time by detecting secreted albumin. In addition, UCAR can image cytoalbumin in cells, organoids, and tissues in real-time. Accordingly, UCAR detected a decrease in albumin in liver tissue and serum in a CCl_4-induced model of liver damage. Consequently, biocompatible nanoprobes with excellent stability and sensitivity are available for quantifying and imaging proteins in complex biological environments (Figures 4 A–C) (69). Balyasnikova et al., showed that fluorescent indocyanine lipids (ICL: DiD, DiI) formulated in polyethylene glycolated lipid nanoparticles (PLN) penetrate and accumulate efficiently in basement membrane (GBM). *In vitro* studies have demonstrated that PLN-formulated ICLs penetrate GBM spheroids and organoids more efficiently than liposomal ICLs. In the intracranial GBM model, more than 82% of the extravascular regions of tumors in the PLN group were fluorescence positive for ICL fluorescence 1 h after systemic injection, compared to 13% in the liposome group. In addition, PLN-formulated ICL accumulated in 95% of tumor myeloid suppressors and macrophages, 70% of tumor regulatory T cells, 50% of tumor-associated microglia, and 65% of non-immune cells 48 h after injection. Thus, the PLN-formulated ICLs were superior to pegylated liposomal doxorubicin and fluorescent dextran extravasation, and they accumulate in aggressive tumor margins and brain invaders more effectively. In contrast to liposomes, which are stable *in vitro* and *in vivo* in serum, PLN degraded prior to entering tumors, which may explain the disparity in their extravasation efficiency. These findings suggest an excellent opportunity to enhance therapeutic cargo delivery for invasive GBM (71).

Xie et al., developed a fluorescent probe for COX-2 imaging using a single-step procedure from rofecoxib. Using this novel strategy, six rofecoxib analogs were designed in total. Several analogs retained the relative COX-2-targeting activity of rofecoxib and also exhibited attractive fluorescent properties, which are

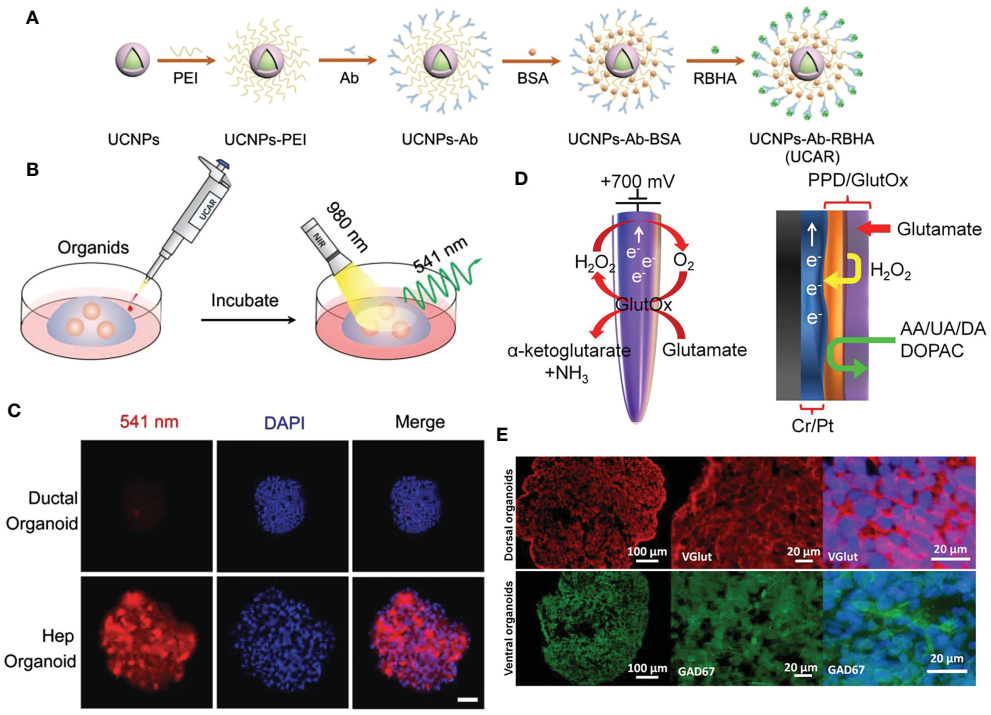

FIGURE 4
NMs for cell imaging and biosensor in organoids. **(A)** The schematic diagram of UCAR synthesis process from NaYF4:Yb3+/Er3+@NaYF4 (UCNPs). **(B)** The schematic illustration of albumin imaging in organoids using UCAR. **(C)** Ductal organoids and hepatocyte organoids were incubated with UCAR (red) for 3 h, followed by fixation and DAPI (blue) staining, and imaged by two-photon microscope under 980 nm excitation (bar: 50 µm). **(D)** Schematic representation of enzymatic reaction that allows detection of glutamate at the microelectrode, and graphical view showing PPD layer acting as a diffusion barrier to biomolecule species. H_2O_2 can reach the electrode while larger molecules are rejected. **(E)** Immunostaining images of hESC-derived cortical dorsal forebrain organoids with strong expression of the glutamatergic marker, vGlut (red) and ventral forebrain organoids with expression of GABAergic neuronal marker, GAD67 (green). UCAR: upconversion nanoparticles, antibody, and rose bengal hexanoic acid; PPD, polypropylene diene monomer; hESC, human embryonic stem cell; GAD67, glutamate decarboxylase 67 kDa isoform. Adapted with permission from (69), copyright 2022, Wiley-VCH GmbH and (70), copyright 2018, Multidisciplinary Digital Publishing Institute.

studied experimentally and theoretically. Compared to Raw 264.7 cells expressing low levels of COX-2 and celecoxib-treated HeLa cells, the most potent analog 2a1, demonstrated strong COX-2 fluorescence imaging in HeLa cells overexpressing COX-2. Using brighter fluorescence in tissue sections or 3D organoids, 2a1 was able to differentiate between human cancer tissue and adjacent tissue. These findings demonstrate the potential of 2a1 as a near-infrared fluorescent COX-2 probe for clinical cancer imaging in humans (72). McCarthy et al., evaluated the ablation potential of CD44-targeted polymer nanoparticles utilizing hyaluronic acid (HA) as a targeting agent and coating it onto hybrid donor-acceptor polymer particles (HDAPPs) to form HA-HDAPPs using tumor organoid technology. In addition, only the photothermal polymer poly[4,4-bis(2-ethylhexyl)-cyclopente[2,1-b; Nanoparticles composed of 3,4-b'] was capable of producing nanoparticles composed of dithiophene-2,6-diyl-alt-2, 1,3-benzoselenodiazole-4,7-diyl] (PCPDTBSe) coated with HA to form HA-BSe NP. Monitoring nanoparticle transport in 3D organoids revealed a uniform diffusion of untargeted HDAPP compared to nanoparticle-matrix interaction-induced attenuated diffusion of HA-HDAPP. Calculating the diffusion curve suggests that HA-HDAPPs transport may be explained by diffusion alone, suggesting nanoparticle/cell-matrix interactions. In addition, photothermal activation revealed that only HA-BSe-NPs significantly reduced the viability of tumor cells in organoids. Although CD44-targeted therapy has limited transport of diagnostic nanoparticles, their targeted retention provides increased heat for enhanced photothermal ablation in 3D, thereby facilitating the evaluation of nanoparticle therapies prior to *in vivo* testing (73). Fang et al. designed the near-infrared small molecule fluorescent probe HD-Br with low toxicity and photostability for super-resolution imaging of lysosomes. Thus, while labeling lysosomes using the properties of the probe, lysosomal and mitochondrial interactions could be dynamically tracked. Due to the optimal near-infrared excitation and emission wavelengths of the probe, 3D imaging of liver organoids and imaging of Caenorhabditis elegans have been performed (74).

3.3 Photodynamic therapy

Photodynamic therapy (PDT) is a promising cancer treatment technology that employs a photosensitizer to irradiate a specific wavelength of light with targeted oxidative killing effects on diseased tissues to treat cancer while minimizing damage to normal tissues (75, 76). Nanomaterials have been commonly used to construct photosensitizer delivery systems and target transport to lesions; accordingly, certain nanomaterials can be used for PDT due to their exceptional fluorescence properties (77). On the contrary, organoids comprise an excellent PDT test bed. Therefore, the combined application of the two can provide researchers with the opportunity to develop new PDTs. By electroporating black phosphorus quantum dots (BPQD) into exosome carriers (EXO), Liu et al., were able to develop a photothermal agent that was highly effective. The resulting BPQDs@EXO nanospheres (BE) exhibited good biocompatibility, long cycle times, and excellent tumor targeting ability, thereby demonstrating remarkable photothermal therapy (PTT) efficiency via efficient tumor ablation *in vivo* (78). Li et al., described a nanoassembled structure based on black phosphorus (BP) nanosheets and composed of cisplatin, BP, polydopamine (PDA), and hyaluronic acid (HA) for controlling cisplatin delivery, referred to as CBPH. In order to create CBPH, the surface of BP was double-modified by PDA and HA, which increased the stability, tumor-targeting ability, and photothermal efficiency of BP. Cisplatin is released in response to internal and external stimuli within the tumor microenvironment. *In vitro* experiments demonstrated that CBPH-treated 4 T1 cells exhibited an increased intracellular content of Pt and Pt-DNA adducts, which improved upon exposure to NIR light, resulting in potent antitumor effects via a synergistic mechanism (79). According to 2D monolayer and 3D organoid studies, the combination of CBPH and NIR phototreatment significantly inhibited the migration, invasion, and regenerative capacity of 4 T1 cells. This novel BP-based nanoassembly with controlled cisplatin tumor delivery and breast cancer metastasis inhibition broadened the application of BP in biomedical fields, thus holding great potential for future advancement (79).

Iqbal et al. used titanium dioxide-adsorbed Fe(iii) to create magnetic Fe-TiO(2) nanocomposites (NC), which played a role in achieving T(1)-weighted MRI contrast enhancement and enhancing the well-known photodynamic therapeutic efficacy of TiO(2) nanoparticles. Interestingly, the proposed NC demonstrated T(1) MRI contrast agent properties comparable to those of commercially available contrast agents. Moreover, the cytotoxicity induced by NCs in conventional methods is negligible and demonstrates significant support for the proliferation of intestinal organoids. It is anticipated that this research will serve as a guide for the development of additional biocompatible magnetic titanium dioxide-based nanosystems with multifaceted properties for biomedical applications (80). Obaid et al., described a (Cet, anti-EGFR mAb) photoimmune nanoconjugate (PIN) as well as *in vitro* and *in vivo* models of stroma-rich dyspancreatic ductal adenocarcinoma (PDAC) utilizing patient-derived pancreatic cancer-associated fibroblasts (PCAFs). In dystopic connective tissue proliferative tumors, Cet-PINs effectively penetrated blood vessels up to 470 μm, and photodynamic activation resulted in parenchymal tumor necrosis, which was not observed in T47D tumors (low EGFR) or when non-targeted constructs were utilized in both tumor types. Photodynamic activation of the Cet needle in dysproliferative tumors resulted in collagen photoregulation and a 1.5-fold decrease in collagen density, indicating that PDP may also be able to inhibit connective tissue formation. In addition, the *in vivo* safety of photodynamically activated Cet-PINs is significantly enhanced in comparison to non-targeted constructs. This is the first study to demonstrate the actual value of NIR-activated PIN-molecule targeting. This combined PIN platform and heterologous cell model paves the way for a wider range of multiplex combination therapies to synergistically control fibroproliferative tumor progression and extend PDAC patient survival (81).

3.4 New electrochemical biosensors

In electrochemical biosensors, the sensitivity of electroanalytical methods and the inherent bioselectivity of the biological component are combined. The biological component in the sensor recognizes its analyte, leading to a catalytic or binding event that ultimately generates an electrical signal monitored by the transducer that is proportional to the analyte concentration. Nanomaterials have exceptional chemical, physical, electrocatalytic, and other properties, in addition to their unique quantum size effects and surface effects, which are anticipated to further improve the performance of electrochemical sensing. Due to their stability, speed, accuracy, and low cost, nano-electrochemical biosensors have attracted a great deal of interest in the field of biomedicine and have made significant progress (82). In recent years, there has been an abundance of nanomaterial-based electrochemical sensors designed to detect specific physiological indicators of organoids for future research. For instance, Nasr et al., have developed a method to functionalize borosilicate glass capillaries with nanostructured textures as electrochemical biosensors to detect the release of glutamate by brain organoids produced by human embryonic stem cells (hESCs) that mimic different brain regions. For the oxidation of glutamate, biosensors exhibit obvious catalytic activity. Enzyme-modified microelectrodes can detect glutamate from 5 μM to 0.5 mM over a broad linear range. At various time points, measurements were performed on organoids, and results were obtained that were consistent. These findings demonstrate the biosensor's dependability and utility for measuring glutamate concentrations over time in a single culture system (Figures 4D, E) (70).

Li et al., describe a procedure for the creation of cardiac cyborg organoids: First, the stretchable grid nanoelectronics are laminated onto continuous stromal sheets containing human induced pluripotent stem cells (hiPSCs) or progenitor cells derived from hiPSCs; subsequently, the cell pieces are aggregated into cell-dense plates by cell-cell attraction-induced cell proliferation and migration; and finally, the stretchable grid nanoelectronics are embedded in the cell plates and folded into tightly packed structures. The subsequent folding of the 2D cell plate/nanoelectron mixture into a 3D structure with a bowl-like geometry results in organ self-organization. Organogenesis unfolds densely packed nanoelectronics and distributes their structures throughout 3D organoids. Embedded three-dimensional nanoelectronics continuously monitor the electrophysiological behavior of stem cells and progenitor cells as they continue to develop and differentiate into various types of cells (83). A cyborg human brain organoid platform with "tissue-like" stretchable mesh nanoelectronics is described by Le Floch et al. By matching the mechanical properties of brain organoids and folding through the organogenesis process of stem cells or progenitor cells, stretchable electrode arrays can be distributed on 3D organoids. The tissue-integrated, stretchable electrode array does not impede brain organoid development, adapts to changes in volume and morphology during brain organoids, and maintains stable electrical contact with neurons within brain organoids throughout development. During early brain organoids development, electrodes coupled seamlessly and non-invasively to neurons allow long-term stable, continuous recording (84).

3.5 Immunotherapeutic studies combining nanomaterials with organoids

Last but not the least, organoids offer new opportunities for tumor immunotherapy. For example, Dijkstra et al. developed tumor organoids by resecting tumor specimens from patients with colorectal cancer (CRC) or doing core needle biopsies. Subsequently, the authors co-cultured tumor organoids and the patient's peripheral blood to construct a 'tumor organoid peripheral blood lymphocyte' co-cultured model and obtained a population of tumor reactive T cells. These T cell populations kill tumor organoids and do not damage healthy tissue organoids, demonstrating that the generation of tumor specific T cells can be effectively induced by co-culture tumor organoids with immune cells, providing a new strategy for tumor immunotherapy (85). However, subject to the limitations of existing organoid structures and functions, organoid based tumor immunotherapy studies often require the participation of other regulators to mimic the complex tumor immune environment. Many studies have shown that nanomaterials exhibit excellent immunomodulatory effects (86). Therefore, combining nanomaterials and organoid technology might be a feasible strategy in the field of tumor immunotherapy. Q. Yin et al. reported a nanoparticle-based approach for immune environment modulation of tumor organoids. researchers formulated nanoparticles containing immunostimulatory substances that activated endogenous T cells in patient derived tumor organoids, and finally such endogenous T cells could exert inhibitory effects on tumor organoids (87). Zhang et al., using human brain organoids and glioblastoma co-cultured model to study the modulation of glial cells by dendritic polyglycerol sulfate (dPGS), demonstrated that dPGS has the effect of reducing inflammatory markers and glioblastoma invasiveness (88). Tumor immunotherapy research strategies of nanomaterials combined with organoids have not received much attention, and as a promising research direction, future investigators may gain more discoveries from them.

4 Outlook and conclusions

This article reviews the application status of NMs in various organoid culture systems and the application direction of NMs in combination with organoids in the biomedical field. Organoids and nanomaterials are two promising technologies that could revolutionize biomedical research. They can be combined to create personalized treatments, diagnostic and therapeutic devices, and various other medical instruments. However, researchers must also consider the magnitude of nanomaterials' toxicity to human tissues; in this regard, organoids serve as a useful model (89). The organoid model can help verify the toxicity of nanomaterials without creating any ethical issues. Numerous studies have demonstrated that not all nanomaterials are non-toxic; Yu et al., for instance, investigated the intestinal toxic effects of

graphene quantum dots (GQDs). Higher doses of OH-GQD caused significant intestinal damage, as evidenced by increased intestinal permeability, villi shortening, and crypt loss. Additionally, the authors used isolated crypts to establish three-dimensional organoid cultures, and the GQD treatment significantly reduced the size of surviving intestinal organoids (90). Hou et al. provided evidence of the toxic effects of plastic nanoparticles on the human intestinal system and explored the mechanisms involved (91). Likewise, the toxicity of some nanomaterials can affect the physiological properties of organoid models. In a study of brain organoids by Huang et al., it was demonstrated that silver nanoparticles inhibited brain organoid development and promoted apoptosis (92), showing neurodevelopme ntal toxicity. Therefore, the toxicity factors of nanomaterials should be taken into account in the development of organoids utilizing nanomaterials.

The application of nanomaterials in the field of organoids is not yet sufficiently advanced. In the studies mentioned in this article, the roles played by nanomaterials have assisted in the construction of cell scaffolds, the delivery of substances, the culture scaffold of cells and so on. Currently, no researchers have been able to use nanomaterials to overcome the limitations of organoid development, yielding landmark breakthrough results. Two reasons may have hindered the development of nanomaterials in the field of organoids: (1) existing nanomaterials technologies have not yet allowed the development of good enough biomaterials to be adapted to the organoid culture system; (2) the physiological and developmental landscape of the organ itself is poorly studied, leading researchers to fail to uncover critical culture factors and culture environments. But either factor, researchers will need more work into nanomaterials or organoids.

In conclusion, the use of nanomaterials can assist researchers in developing organoids that serve as suitable physiological models for disease research. In addition to reducing the duration and cost of drug development, the combination of the two can promote the creation of innovative medical technologies. Accordingly, the biomedical research applications of these two technologies appear to be limitless with further research and development.

Author contributions

CS wrote the main text. Z-jZ designed, wrote the main text, and built the figures. Y-pH, Y-xW, and HZh collected the references. YW and LX reviewed the manuscript, and Z-tH and HZo revised the manuscript. All authors agree to be accountable for the content of the work. All authors contributed to the article and approved the submitted version.

Funding

This research was supported by Fundamental Research Funds for the National Natural Science Foundation of China, No. 81970569, Fundamental Research Funds for the Central Universities of Central South University, No. 2021zzts0367 and Hunan Provincial Innovation Foundation for Postgraduate, No. CX20210369.

Conflict of interest

The authors declare that the research was conducted in the absence of any commercial or financial relationships that could be construed as a potential conflict of interest.

Publisher's note

References

1. Lancaster MA, Knoblich JA. Organogenesis in a dish: modeling development and disease using organoid technologies. *SCIENCE* (2014) 345:1247125. doi: 10.1126/science.1247125

2. Rheinwald JG, Green H. Serial cultivation of strains of human epidermal keratinocytes: the formation of keratinizing colonies from single cells. *CELL* (1975) 6:331–43. doi: 10.1016/s0092-8674(75)80001-8

3. Sato T, Vries RG, Snippert HJ, van de Wetering M, Barker N, Stange DE, et al. Single Lgr5 stem cells build crypt-villus structures *in vitro* without a mesenchymal niche. *NATURE* (2009) 459:262–5. doi: 10.1038/nature07935

4. Qian X, Song H, Ming GL. Brain organoids: advances, applications and challenges. *DEVELOPMENT* (2019) 146:dev166074. doi: 10.1242/dev.166074

5. Pang MJ, Burclaff JR, Jin R, Adkins-Threats M, Osaki LH, Han Y, et al. Gastric organoids: progress and remaining challenges. *Cell Mol Gastroenterol Hepatol* (2022) 13:19–33. doi: 10.1016/j.jcmgh.2021.09.005

6. Prior N, Inacio P, Huch M. Liver organoids: from basic research to therapeutic applications. *GUT* (2019) 68:2228–37. doi: 10.1136/gutjnl-2019-319256

7. Little MH, Combes AN. Kidney organoids: accurate models or fortunate accidents. *Genes Dev* (2019) 33:1319–45. doi: 10.1101/gad.329573.119

8. Nugraha B, Buono MF, von Boehmer L, Hoerstrup SP, Emmert MY. Human cardiac organoids for disease modeling. *Clin Pharmacol Ther* (2019) 105:79–85. doi: 10.1002/cpt.1286

9. Broutier L, Andersson-Rolf A, Hindley CJ, Boj SF, Clevers H, Koo BK, et al. Culture and establishment of self-renewing human and mouse adult liver and pancreas 3D organoids and their genetic manipulation. *Nat Protoc* (2016) 11:1724–43. doi: 10.1038/nprot.2016.097

10. Karkampouna S, La Manna F, Benjak A, Kiener M, De Menna M, Zoni E, et al. Patient-derived xenografts and organoids model therapy response in prostate cancer. *Nat Commun* (2021) 12:1117. doi: 10.1038/s41467-021-21300-6

11. Fitzgerald HC, Dhakal P, Behura SK, Schust DJ, Spencer TE. Self-renewing endometrial epithelial organoids of the human uterus. *Proc Natl Acad Sci U.S.A.* (2019) 116:23132–42. doi: 10.1073/pnas.1915389116

12. Cowan CS, Renner M, De Gennaro M, Gross-Scherf B, Goldblum D, Hou Y, et al. Cell types of the human retina and its organoids at single-cell resolution. *CELL* (2020) 182:1623–40. doi: 10.1016/j.cell.2020.08.013

13. LeSavage BL, Suhar RA, Broguiere N, Lutolf MP, Heilshorn SC. Next-generation cancer organoids. *Nat MATER* (2022) 21:143–59. doi: 10.1038/s41563-021-01057-5

14. Rossi G, Manfrin A, Lutolf MP. Progress and potential in organoid research. *Nat Rev Genet* (2018) 19:671–87. doi: 10.1038/s41576-018-0051-9

15. Miyabayashi K, Baker LA, Deschênes A, Traub B, Caligiuri G, Plenker D, et al. Intraductal transplantation models of human pancreatic ductal adenocarcinoma reveal progressive transition of molecular subtypes. *Cancer Discovery* (2020) 10:1566–89. doi: 10.1158/2159-8290.CD-20-0133

16. Park SB, Jung WH, Kim KY, Koh B. Toxicity assessment of SiO(2) and TiO(2) in normal colon cells, *In Vivo* and in human colon organoids. *MOLECULES* (2020) 25:3594. doi: 10.3390/molecules25163594

17. Zhang H, Chen W, Hu Y, Geng Z, Su J. Bone/cartilage targeted hydrogel: strategies and applications. *Bioactive Materials* (2023) 23:156–69. doi: 10.1016/j.bioactmat.2022.10.028

18. Chen S, Chen X, Geng Z, Su J. The horizon of bone organoid: a perspective on construction and application. *Bioact Mater* (2022) 18:15–25. doi: 10.1016/j.bioactmat.2022.01.048

19. Tang XY, Wu S, Wang D, Chu C, Hong Y, Tao M, et al. Human organoids in basic research and clinical applications. *Signal Transduct Target Ther* (2022) 7:168. doi: 10.1038/s41392-022-01024-9

20. Cheng Z, Li M, Dey R, Chen Y. Nanomaterials for cancer therapy: current progress and perspectives. *J Hematol Oncol* (2021) 14:85. doi: 10.1186/s13045-021-01096-0

21. Valic MS, Zheng G. Research tools for extrapolating the disposition and pharmacokinetics of nanomaterials from preclinical animals to humans. *THERANOSTICS* (2019) 9:3365–87. doi: 10.7150/thno.34509

22. Pomerantseva E, Bonaccorso F, Feng X, Cui Y, Gogotsi Y. Energy storage: the future enabled by nanomaterials. *SCIENCE* (2019) 366:969. doi: 10.1126/science.aan8285

23. Chimene D, Alge DL, Gaharwar AK. Two-dimensional nanomaterials for biomedical applications: emerging trends and future prospects. *Adv MATER* (2015) 27:7261–84. doi: 10.1002/adma.201502422

24. Sood A, Kumar A, Gupta VK, Kim CM, Han SS. Translational nanomedicines across human reproductive organs modeling on microfluidic chips: state-of-the-Art and future prospects. *ACS BIOMATER Sci Eng* (2023) 9:62–84. doi: 10.1021/acsbiomaterials.2c01080

25. Mo XM, Xu CY, Kotaki M, Ramakrishna S. Electrospun P(LLA-CL) nanofiber: a biomimetic extracellular matrix for smooth muscle cell and endothelial cell proliferation. *BIOMATERIALS* (2004) 25:1883–90. doi: 10.1016/j.biomaterials.2003.08.042

26. Chen Y, Gao A, Bai L, Wang Y, Wang X, Zhang X, et al. Antibacterial, osteogenic, and angiogenic activities of SrTiO(3) nanotubes embedded with Ag(2)O nanoparticles. *Mater Sci Eng C Mater Biol Appl* (2017) 75:1049–58. doi: 10.1016/j.msec.2017.03.014

27. Zhang P, Shao N, Qin L. Recent advances in microfluidic platforms for programming cell-based living materials. *Adv MATER* (2021) 33:e2005944. doi: 10.1002/adma.202005944

28. Shapiro RL, DeLong K, Zulfiqar F, Carter D, Better M, Ensign LM. *In vitro* And ex vivo models for evaluating vaginal drug delivery systems. *Adv Drug Delivery Rev* (2022) 191:114543. doi: 10.1016/j.addr.2022.114543

29. Mahapatra C, Lee R, Paul MK. Emerging role and promise of nanomaterials in organoid research. *Drug Discovery Today* (2022) 27:890–9. doi: 10.1016/j.drudis.2021.11.007

30. Cho YH, Park YG, Kim S, Park JU. 3D electrodes for bioelectronics. *Adv MATER* (2021) 33:e2005805. doi: 10.1002/adma.202005805

31. Boix-Montesinos P, Soriano-Teruel PM, Armiñán A, Orzáez M, Vicent MJ. The past, present, and future of breast cancer models for nanomedicine development. *Adv Drug Delivery Rev* (2021) 173:306–30. doi: 10.1016/j.addr.2021.03.018

32. Clevers H. Modeling development and disease with organoids. *CELL* (2016) 165:1586–97. doi: 10.1016/j.cell.2016.05.082

33. Kozlowski MT, Crook CJ, Ku HT. Towards organoid culture without matrigel. *Commun Biol* (2021) 4:1387. doi: 10.1038/s42003-021-02910-8

34. Wiedenmann S, Breunig M, Merkle J, von Toerne C, Georgiev T, Moussus M, et al. Single-cell-resolved differentiation of human induced pluripotent stem cells into pancreatic duct-like organoids on a microwell chip. *Nat BioMed Eng* (2021) 5:897–913. doi: 10.1038/s41551-021-00757-2

35. Ferreira JN, Hasan R, Urkasemsin G, Ng KK, Adine C, Muthumariappan S, et al. A magnetic three-dimensional levitated primary cell culture system for the development of secretory salivary gland-like organoids. *J Tissue Eng Regener Med* (2019) 13:495–508. doi: 10.1002/term.2809

36. Kleinman HK, Martin GR. Matrigel: basement membrane matrix with biological activity. *Semin Cancer Biol* (2005) 15:378–86. doi: 10.1016/j.semcancer.2005.05.004

37. Xu C, Inokuma MS, Denham J, Golds K, Kundu P, Gold JD, et al. Feeder-free growth of undifferentiated human embryonic stem cells. *Nat Biotechnol* (2001) 19:971–4. doi: 10.1038/nbt1001-971

38. Wu X, Wang X, Su J. Hydrogels for bone organoid construction: from a materiobiological perspective. *J MATER Sci Technol* (2022) 136:21–31. doi: 10.1016/j.jmst.2022.07.008

39. Bao L, Cui X, Wang X, Wu J, Guo M, Yan N, et al. Carbon nanotubes promote the development of intestinal organoids through regulating extracellular matrix viscoelasticity and intracellular energy metabolism. *ACS NANO* (2021) 15:15858–73. doi: 10.1021/acsnano.1c03707

40. Purwada A, Jaiswal MK, Ahn H, Nojima T, Kitamura D, Gaharwar AK, et al. Ex vivo engineered immune organoids for controlled germinal center reactions. *BIOMATERIALS* (2015) 63:24–34. doi: 10.1016/j.biomaterials.2015.06.002

41. Luo Z, Zhang S, Pan J, Shi R, Liu H, Lyu Y, et al. Time-responsive osteogenic niche of stem cells: a sequentially triggered, dual-peptide loaded, alginate hybrid system for promoting cell activity and osteo-differentiation. *BIOMATERIALS* (2018) 163:25–42. doi: 10.1016/j.biomaterials.2018.02.025

42. Liu W, He H, Zheng SY. Microfluidics in single-cell virology: technologies and applications. *Trends Biotechnol* (2020) 38:1360–72. doi: 10.1016/j.tibtech.2020.04.010

43. Brandenberg N, Hoehnel S, Kuttler F, Homicsko K, Ceroni C, Ringel T, et al. High-throughput automated organoid culture via stem-cell aggregation in microcavity arrays. *Nat BioMed Eng* (2020) 4:863–74. doi: 10.1038/s41551-020-0565-2

44. Shin HS, Kook YM, Hong HJ, Kim YM, Koh WG, Lim JY. Functional spheroid organization of human salivary gland cells cultured on hydrogel-micropatterned nanofibrous microwells. *Acta BIOMATER* (2016) 45:121–32. doi: 10.1016/j.actbio.2016.08.058

45. Kim D, Lee SJ, Youn J, Hong H, Eom S, Kim DS, et al. And permeable nanofibrous oval-shaped microwell array for the stable formation of viable and functional spheroids. *BIOFABRICATION* (2021) 13:035050. doi: 10.1088/1758-5090/ac044c

46. Park SM, Lee SJ, Lim J, Kim BC, Han SJ, Kim DS. Versatile fabrication of size- and shape-controllable nanofibrous concave microwells for cell spheroid formation. *ACS Appl Mater Interfaces* (2018) 10:37878–85. doi: 10.1021/acsami.8b15821

47. Marques IA, Fernandes C, Tavares NT, Pires AS, Abrantes AM, Botelho MF. Magnetic-based human tissue 3D cell culture: a systematic review. *Int J Mol Sci* (2022) 23:12681. doi: 10.3390/ijms232012681

48. Haisler WL, Timm DM, Gage JA, Tseng H, Killian TC, Souza GR. Three-dimensional cell culturing by magnetic levitation. *Nat Protoc* (2013) 8:1940–9. doi: 10.1038/nprot.2013.125

49. Tseng H, Daquinag AC, Souza GR, Kolonin MG. Three-dimensional magnetic levitation culture system simulating white adipose tissue. *Methods Mol Biol* (2018) 1773:147–54. doi: 10.1007/978-1-4939-7799-4_12

50. Tseng H, Gage JA, Raphael RM, Moore RH, Killian TC, Grande-Allen KJ, et al. Assembly of a three-dimensional multitype bronchiole coculture model using magnetic levitation. *Tissue Eng Part C Methods* (2013) 19:665–75. doi: 10.1089/ten.TEC.2012.0157

51. Gaitán-Salvatella I, López-Villegas EO, González-Alva P, Susate-Olmos F, Álvarez-Pérez MA. Case report: formation of 3D osteoblast spheroid under magnetic levitation for bone tissue engineering. *Front Mol Biosci* (2021) 8:672518. doi: 10.3389/fmolb.2021.672518

52. Bumpers HL, Janagama DG, Manne U, Basson MD, Katkoori V. Nanomagnetic levitation three-dimensional cultures of breast and colorectal cancers. *J Surg Res* (2015) 194:319–26. doi: 10.1016/j.jss.2014.12.036

53. Yin X, Mead BE, Safaee H, Langer R, Karp JM, Levy O. Engineering stem cell organoids. *Cell Stem Cell* (2016) 18:25–38. doi: 10.1016/j.stem.2015.12.005

54. Aalders J, Léger L, Piras D, van Hengel J, Ledda S. Use of transparent liquid marble: microbioreactor to culture cardiospheres. *Methods Mol Biol* (2021) 2273:85–102. doi: 10.1007/978-1-0716-1246-0_5

55. Brevini T, Manzoni E, Ledda S, Gandolfi F. Use of a super-hydrophobic microbioreactor to generate and boost pancreatic mini-organoids. *Methods Mol Biol* (2019) 1576:291–9. doi: 10.1007/7651_2017_47

56. Daly AC, Prendergast ME, Hughes AJ, Burdick JA. Bioprinting for the biologist. *CELL* (2021) 184:18–32. doi: 10.1016/j.cell.2020.12.002

57. Zhu W, Ma X, Gou M, Mei D, Zhang K, Chen S. 3D printing of functional biomaterials for tissue engineering. *Curr Opin Biotechnol* (2016) 40:103–12. doi: 10.1016/j.copbio.2016.03.014

58. Urkasemsin G, Rungarunlert S, Ferreira JN. Bioprinting strategies for secretory epithelial organoids. *Methods Mol Biol* (2020) 2140:243–9. doi: 10.1007/978-1-0716-0520-2_16

59. Bowser DA, Moore MJ. Biofabrication of neural microphysiological systems using magnetic spheroid bioprinting. *BIOFABRICATION* (2019) 12:15002. doi: 10.1088/1758-5090/ab41b4

60. Li H, Yin Y, Xiang Y, Liu H, Guo R. A novel 3D printing PCL/GelMA scaffold containing USPIO for MRI-guided bile duct repair. *BioMed MATER* (2020) 15:45004. doi: 10.1088/1748-605X/ab797a

61. Markstedt K, Mantas A, Tournier I, Martínez ÁH, Hägg D, Gatenholm P. 3D bioprinting human chondrocytes with nanocellulose-alginate bioink for cartilage tissue engineering applications. *BIOMACROMOLECULES* (2015) 16:1489–96. doi: 10.1021/acs.biomac.5b00188

62. Zhang Z, Gao S, Hu YN, Chen X, Cheng C, Fu XL, et al. Ti(3) C(2) t(x) MXene composite 3D hydrogel potentiates mTOR signaling to promote the generation of functional hair cells in cochlea organoids. *Adv Sci (Weinh)* (2022) 9:e2203557. doi: 10.1002/advs.202203557

63. Beldjilali-Labro M, Jellali R, Brown AD, Garcia GA, Lerebours A, Guenin E, et al. Multiscale-engineered muscle constructs: PEG hydrogel micro-patterning on an electrospun PCL mat functionalized with gold nanoparticles. *Int J Mol Sci* (2021) 23:260. doi: 10.3390/ijms23010260

64. Watanabe S, Kobayashi S, Ogasawara N, Okamoto R, Nakamura T, Watanabe M, et al. Transplantation of intestinal organoids into a mouse model of colitis. *Nat Protoc* (2022) 17:649–71. doi: 10.1038/s41596-021-00658-3

65. Chen Y, Gao Y, Chen Y, Liu L, Mo A, Peng Q. Nanomaterials-based photothermal therapy and its potentials in antibacterial treatment. *J CONTROL RELEASE* (2020) 328:251–62. doi: 10.1016/j.jconrel.2020.08.055

66. Li L, Zhang Y, Zhou Y, Hu H, Hu Y, Georgiades C, et al. Quaternary nanoparticles enable sustained release of bortezomib for hepatocellular carcinoma. *HEPATOLOGY* (2022) 76:1660–72. doi: 10.1002/hep.32584

67. Kim D, Shin M, Choi JH, Choi JW. Actuation-augmented biohybrid robot by hyaluronic acid-modified au nanoparticles in muscle bundles to evaluate drug effects. *ACS Sens* (2022) 7:740–7. doi: 10.1021/acssensors.1c02125

68. Le Joncour V, Karaman S, Laakkonen PM. Predicting *In Vivo* payloads delivery using a blood-brain tumor-barrier in a dish. *J Vis Exp* (2019) 146:e59384. doi: 10.3791/59384

69. Liu G, Wei J, Li X, Tian M, Wang Z, Shen C, et al. Near-Infrared-Responded high sensitivity nanoprobe for steady and visualized detection of albumin in hepatic organoids and mouse liver. *Adv Sci (Weinh)* (2022) 9:e2202505. doi: 10.1002/advs.202202505

70. Nasr B, Chatterton R, Yong J, Jamshidi P, D'Abaco GM, Bjorksten AR, et al. Self-organized nanostructure modified microelectrode for sensitive electrochemical glutamate detection in stem cells-derived brain organoids. *Biosensors* (2018) 8:14. doi: 10.3390/bios8010014

71. Balyasnikova IV, Zannikou M, Wang G, Li Y, Duffy JT, Levine RN, et al. Indocarbocyanine nanoparticles extravasate and distribute better than liposomes in brain tumors. *J CONTROL RELEASE* (2022) 349:413–24. doi: 10.1016/j.jconrel.2022.07.008

72. Xie L, Li R, Zheng B, Xie Z, Fang X, Dai T, et al. One-step transformation from rofecoxib to a COX-2 NIR probe for human cancer Tissue/Organoid targeted bioimaging. *ACS Appl Bio Mater* (2021) 4:2723–31. doi: 10.1021/acsabm.0c01634

73. McCarthy B, Cudykier A, Singh R, Levi-Polyachenko N, Soker S. Semiconducting polymer nanoparticles for photothermal ablation of colorectal cancer organoids. *Sci Rep* (2021) 11:1532. doi: 10.1038/s41598-021-81122-w

74. Fang H, Yao S, Chen Q, Liu C, Cai Y, Geng S, et al. *De Novo*-designed near-infrared nanoaggregates for super-resolution monitoring of lysosomes in cells, in whole organoids, and in vivo. *ACS NANO* (2019) 13:14426–36. doi: 10.1021/acsnano.9b08011

75. Zheng YW, Miao XY, Xiong L, Chen B, Kong FH, Zhou JJ, et al. Sulfasalazine sensitizes polyhematoporphyrin-mediated photodynamic therapy in cholangiocarcinoma by targeting xCT. *Front Pharmacol* (2021) 12:723488. doi: 10.3389/fphar.2021.723488

76. Zhang ZJ, Wang KP, Huang YP, Jin C, Jiang H, Xiong L, et al. Comprehensive analysis of the potential immune-related biomarker ATG101 that regulates apoptosis of cholangiocarcinoma cells after photodynamic therapy. *Front Pharmacol* (2022) 13:857774. doi: 10.3389/fphar.2022.857774

77. Zhou H, Liu Z, Zhang Z, Pandey NK, Amador E, Nguyen W, et al. Copper-cysteamine nanoparticle-mediated microwave dynamic therapy improves cancer treatment with induction of ferroptosis. *Bioact Mater* (2023) 24:322–30. doi: 10.1016/j.bioactmat.2022.12.023

78. Liu J, Yi K, Zhang Q, Xu H, Zhang X, He D, et al. Strong penetration-induced effective photothermal therapy by exosome-mediated black phosphorus quantum dots. *SMALL* (2021) 17:e2104585. doi: 10.1002/smll.202104585

79. Li Y, Xiong J, Guo W, Jin Y, Miao W, Wang C, et al. Decomposable black phosphorus nano-assembly for controlled delivery of cisplatin and inhibition of breast cancer metastasis. *J CONTROL RELEASE* (2021) 335:59–74. doi: 10.1016/j.jconrel.2021.05.013

80. Iqbal MZ, Luo D, Akakuru OU, Mushtaq A, Hou Y, Ali I, et al. Facile synthesis of biocompatible magnetic titania nanorods for T(1)-magnetic resonance imaging and enhanced phototherapy of cancers. *J MATER Chem B* (2021) 9:6623–33. doi: 10.1039/d1tb01097b

81. Obaid G, Bano S, Mallidi S, Broekgaarden M, Kuriakose J, Silber Z, et al. Impacting pancreatic cancer therapy in heterotypic in vitro organoids and in vivo tumors with specificity-tuned, NIR-activable photoimmunonanoconjugates: towards conquering desmoplasia? *NANO Lett* (2019) 19:7573–87. doi: 10.1021/acs.nanolett.9b00859

82. Xu J, Hu Y, Wang S, Ma X, Guo J. Nanomaterials in electrochemical cytosensors. *ANALYST* (2020) 145:2058–69. doi: 10.1039/c9an01895f

83. Li Q, Nan K, Le Floch P, Lin Z, Sheng H, Blum TS, et al. Cyborg organoids: implantation of nanoelectronics via organogenesis for tissue-wide electrophysiology. *NANO Lett* (2019) 19:5781–9. doi: 10.1021/acs.nanolett.9b02512

84. Le Floch P, Li Q, Lin Z, Zhao S, Liu R, Tasnim K, et al. Stretchable mesh nanoelectronics for 3D single-cell chronic electrophysiology from developing brain organoids. *Adv MATER* (2022) 34:e2106829. doi: 10.1002/adma.202106829

85. Dijkstra KK, Cattaneo CM, Weeber F, Chalabi M, van de Haar J, Fanchi LF, et al. Generation of tumor-reactive T cells by Co-culture of peripheral blood lymphocytes and tumor organoids. *CELL* (2018) 174:1586–98. doi: 10.1016/j.cell.2018.07.009

86. Aljabali AA, Obeid MA, Bashatwah RM, Serrano-Aroca Á, Mishra V, Mishra Y, et al. Nanomaterials and their impact on the immune system. *Int J Mol Sci* (2023) 24:2008. doi: 10.3390/ijms24032008

87. Yin Q, Yu W, Grzeskowiak CL, Li J, Huang H, Guo J, et al. Nanoparticle-enabled innate immune stimulation activates endogenous tumor-infiltrating T cells with broad antigen specificities. *Proc Natl Acad Sci U.S.A.* (2021) 118:e2016168118. doi: 10.1073/pnas.2016168118

88. Zhang I, Lépine P, Han C, Lacalle-Aurioles M, Chen CX, Haag R, et al. Nanotherapeutic modulation of human neural cells and glioblastoma in organoids and monocultures. *CELLS-BASEL* (2020) 9:2434. doi: 10.3390/cells9112434

89. Zink D, Chuah J, Ying JY. Assessing toxicity with human cell-based *In Vitro* methods. *Trends Mol Med* (2020) 26:570–82. doi: 10.1016/j.molmed.2020.01.008

90. Yu L, Tian X, Gao D, Lang Y, Zhang XX, Yang C, et al. Oral administration of hydroxylated-graphene quantum dots induces intestinal injury accompanying the loss of intestinal stem cells and proliferative progenitor cells. *NANOTOXICOLOGY* (2019) 13:1409–21. doi: 10.1080/17435390.2019.1668068

91. Hou Z, Meng R, Chen G, Lai T, Qing R, Hao S, et al. Distinct accumulation of nanoplastics in human intestinal organoids. *Sci TOTAL Environ* (2022) 838:155811. doi: 10.1016/j.scitotenv.2022.155811

92. Huang Y, Guo L, Cao C, Ma R, Huang Y, Zhong K, et al. Silver nanoparticles exposure induces developmental neurotoxicity in hiPSC-derived cerebral organoids. *Sci TOTAL Environ* (2022) 845:157047. doi: 10.1016/j.scitotenv.2022.157047

frontiers | Frontiers in Immunology

TYPE Original Research
PUBLISHED 02 May 2023
DOI 10.3389/fimmu.2023.1155085

OPEN ACCESS

EDITED BY
Fabrizio Mattei,
National Institute of Health (ISS), Italy

REVIEWED BY
Maarten Fokke Bijlsma,
Academic Medical Center, Netherlands
Sen Yang,
Peking Union Medical College Hospital (CAMS), China

*CORRESPONDENCE
Karla Queiroz
k.queiroz@mimetas.com

RECEIVED 31 January 2023
ACCEPTED 30 March 2023
PUBLISHED 02 May 2023

CITATION
Geyer M, Gaul L-M, D`Agosto SL, Corbo V and Queiroz K (2023) The tumor stroma influences immune cell distribution and recruitment in a PDAC-on-a-chip model. *Front. Immunol.* 14:1155085. doi: 10.3389/fimmu.2023.1155085

The tumor stroma influences immune cell distribution and recruitment in a PDAC-on-a-chip model

Marlene Geyer[1], Lisa-Marie Gaul[1], Sabrina Luigia D`Agosto[2], Vincenzo Corbo[2] and Karla Queiroz[1]*

[1]Mimetas B.V., Oegstgeest, Netherlands, [2]Department of Diagnostic and Public Health, University of Verona, Verona, Italy

The dense tumor stroma of pancreatic ductal adenocarcinoma (PDAC) and its secreted immune active molecules provide a barrier for chemotherapy treatment as well as for immune cell infiltration to the tumor core, providing a challenge for immunotherapeutic strategies. Consequently, the investigation of processes underlying the interaction between the tumor stroma, particularly activated pancreatic stellate cells (PSCs), and immune cells may offer new therapeutic approaches for PDAC treatment. In this study, we established a 3D PDAC model cultured under flow, consisting of an endothelial tube, PSCs and PDAC organoids. This was applied to study the role of the tumor microenvironment (TME) on immune cell recruitment and its effect on partly preventing their interaction with pancreatic cancer cells. We observed that stromal cells form a physical barrier, partly shielding the cancer cells from migrating immune cells, as well as a biochemical microenvironment, that seems to attract and influence immune cell distribution. In addition, stromal targeting by Halofuginone led to an increase in immune cell infiltration. We propose that the here developed model setups will support the understanding of the cellular interplay influencing the recruitment and distribution of immune cells, and contribute to the identification of key players in the PDAC immunosuppressive TME as well as support the discovery of new strategies to treat this immune unresponsive tumor.

KEYWORDS

PDAC, microfluidics, immune cell infiltration, organ-on-a-chip, immuno-oncology

Introduction

Immunotherapy has increasingly become a treatment option for various cancer types. However, PDAC is characterized by an immunosuppressive tumor microenvironment resulting in a challenging tumor to treat with currently approved immunotherapeutic strategies (1). Unsuccessful application of immunotherapies is likely related to the stroma

secreted factors, hypoxia, desmoplasia and abnormal vasculature that favor the formation of an immunosuppressive infiltrate and prevent their interaction with cancer cells (2). Pancreatic stellate cells (PSCs) are predominant in the tumor stroma and exert a relevant role in secreting chemokines, cytokines, growth factors as well as extracellular matrix (ECM) components contributing to a denser tumor tissue (3). Activated PSCs, characterized by α-SMA expression, increase immune dysfunction, these also promote EMT and cancer cell invasion (4). Stroma-derived immunosuppressive molecules include IL-10, IL-6, IL-11, CXCL12, vascular endothelial growth factor (VEGF), transforming growth factor beta (TGF-β) and matrix metalloproteinases (5).

For immune cells to reach the tumor tissue, these first need to exit a blood vessel near the tumor and infiltrate the stroma. Upon receiving signals, these reach the tumor cells, which express tumor antigens to perform their antitumor responses. Stromal cells interact with immune cells through mechanical cues, shielding immune cells from reaching the tumor site and either physically trapping the immune cells upon direct cell-cell contact or chemically upon secretion of immune mediators (6). In addition, immune cells are mainly inactivated or rarely present, suggesting that the immune system is suppressed in PDAC (5, 7). Consequently, the cells are either in paucity and do not function well or are trapped in the tumor stroma unable to reach the tumor cells (8). Activated PSCs, therefore, seem to orchestrate several processes that together promote tumor growth as well as immunosuppression in PDAC.

Murine models have often supported developments in the field of tumor immunity and responses to its targeting. However, advances in cellular and microfluidic technologies are supporting the development of *in vitro* systems that potentially recapitulate key aspects of *in vivo* biology. These systems can be applied for dissecting the contribution of specific cell types as well as their interaction that support specific shaping of the immune microenvironment in diseased tissues (9, 10). In addition, immune migration studies have previously been done in transwells, where migration is gravity driven and likely not a response of immune cells to the formation of chemoattractant gradients (11, 12). Organ-on-chip systems are an alternative that allow 3D cultivation of multiple cell types, enabling cell-cell interactions, cell-matrix interactions, and flow (13, 14).

Considering that the PDAC stroma plays a key role in shaping the immune cell infiltrate, consequently limiting immune responses, we hereby developed and characterized a PDAC-on-a-Chip model to study the role of the endothelium and the stroma in immune cell migration. We envision that this model could provide a valuable understanding on immune cell infiltration in this tumor type as well as enable the development of new therapeutic approaches.

Materials and methods

Cell culture

PDAC organoids were acquired from a tumor resection performed with curative intent at the University and Hospital Trust of Verona. Written informed consent from the donors for research use of the tissue was obtained prior to acquisition of the specimens. Tissues for the generation of models were collected under protocol number 55859, approved by the local Ethics Committee (Comitato Etico Azienda Ospedaliera Universitaria Integrata) to V.C. (Prog. 3456CESC, 27/09/21). The organoids were cultured in a 6-well plate in 10 µl Matrigel (Corning®, 356231, 8.3-10.5 mg/ml) droplets. After seeding, the plate was placed in the incubator with bottom-side up for 15 min. For culturing, hCPLT medium was used, which consists of Advanced Dulbecco's Modified Eagles Medium with Nutrient Mixture F-12 Hams – 500ml (Gibco, #12634-028), GlutaMax – 200mM (Gibco, # 35050-061), Hepes – 1M (Gibco, # 15630-080), Primocin – 50mg/ml (Invivogen # ant-pm-2), B-27 supplement (Gibco, # 17504-044), N-Acetylcysteine (NAC) (Sigma-Aldrich, # A9165-5G), Nicotinamide (Sigma-Aldrich, # N0636), hEGF (Gibco, # PMG8043), TGFβ Receptor inhibitor A83-01 (Tocris, # 2939), FGF10 (Peprotech, # 100-26), mNoggin (Peprotech, # 250-38), R-spondin-1 conditioned medium, Wnt3a conditioned medium, Gastrin (Tocris, # 3006) and Y-27632 Dihydrochloride (Sigma, # Y0503). The cells were harvested using Cell Recovery Solution (Corning®, 354253) and placed on ice for 30 min. The organoids were spun down at 300 g for 5 min, media was removed and incubated with TrypLE Express for 3 min (Gibco, # 12605-028) in the waterbath for enzymatic disruption. The organoids solution was spun down, resuspended in ice-cold media, counted and used.

PSCs (Klon 2.2) were obtained from Marburg University (15) and cultured in DMEM medium (Gibco, 10829-018) with 1% Penicillin/Streptomycin and 10% Fetal Bovine Serum (FBS). Cells were passaged at 80% confluency using Trypsin 2.5% (ThermoFisher, 15090046).

Human Umbilical Vein Endothelial Cells (HUVEC) (Lonza, C2519AS) were cultured in Endothelial Growth Medium (EGM-2) (Lonza, CC-3156) with 1% Penicillin/Streptomycin and 2% FBS (Gibco, 16140-071). The cells were seeded immediately after thawing.

PBMCs were derived from whole blood-derived buffy coats of healthy donors provided by Sanquin. Ficoll-Paque PLUS (15 ml) was added to a 50 ml Leucosep tube and centrifuged at room temperature (RT) for 30 min at 1000 x g. The blood-derived buffy coat was diluted 1:2 with sterile PBS and 25 ml of the diluted buffy coat was added to the Leucosep tube. The tube was centrifuged at RT for 30 min at 800 x g and plasma was carefully removed by aspiration. The PBMC layer was transferred to a 50 ml conical tube and cells were subsequently washed twice with PBS and centrifuged at RT for 10 min at 300 x g. Cell density was assessed with a cell counter.

After isolation, PBMCs were frozen and thawed upon use. For isolation of immune cell types, PBMCs were thawed and different immune cells isolated with their respective kits according to manufacturer's protocol: EasySep Human B Cell Isolation Kit (StemCell Technologies, #17954), EasySep Direct Human T Cell Isolation Kit (StemCell Technologies, #19661), EasySep Human CD4+ T Cell Isolation Kit (StemCell Technologies, #17952), EasySep Human CD8+ T Cell Isolation Kit (StemCell Technologies, #17953), EasySep Direct Human Monocyte Isolation Kit (StemCell Technologies, #19669).

All cells were cultured in a humidified incubator at 5% CO_2 and 37°C, and regularly tested for mycoplasma.

OrganoPlate 3-lane

PDAC models were established in the OrganoPlate 3-lane (Mimetas, the Netherlands), a microfluidic platform, based on a 384-well plate format with 40 microfluidic chips. The OrganoPlate 3- lane consists of two perfusion lanes, and a middle lane used for ECM gel filling. Culture medium is added to the chips through the perfusion inlets and outlets. Cultures are monitored through the observation window.

In the OrganoPlate 3-lane, both Matrigel and Collagen type I (5 mg/ml, AMSbio, #3447-020-01) were used as ECMs. Collagen type I was neutralized in an 8:1:1 ratio with 1 M Hepes buffer (Gibco, #15630-056) and 37 g/L NaHCO3 (sigma, S5761) reaching a final concentration of 4mg/ml. The collagen mix was kept on ice and seeded within 10 min. PSCs were counted and the appropriate number of cells was resuspended in Collagen type I. ECM (2 µl) was loaded into the gel channel and incubated for 15 min at 37°C and 5% CO2 to allow for polymerization of the gel. After incubation, 50 µl of DMEM medium was added to the gel-inlet to prevent the gel from drying out. Next, HUVECs were seeded (10 000 cells per chip) in 2 µl of EGM-2 medium in the top perfusion channel, 50 µl of the same medium was added to the top medium inlet. The plate was incubated vertically in an angle of 75°, with the gel channels facing downwards to allow the cells to attach to the ECM gel for 2 hours. After 2 hours, 50 µl of medium was added to the outlets of the gel and top perfusion channel. Subsequently, PDAC organoids were resuspended in 2 µl Matrigel and seeded in the bottom perfusion channel. The plate was incubated for 15 min until hCPLT medium was added to the bottom lane onto the PDAC organoids compartment. After that, plates were placed in the incubator on a rocking platform (OrganoFlow, Mimetas, the Netherlands) at an inclination of 7° and an interval of 8 min.

Barrier integrity assay

All media was removed from the plate and 80 µl/chip dye was prepared (FITC Dextran 150 kDa (Sigma, Cat#: 46946)). 20 µl of medium was pipetted into the gel and medium in- and outlets and 40 µl of the dye solution was added to the lane containing the endothelial tube in the inlet and 30 µl to the outlet. Leakage of the fluorescent dye from the lumen of the endothelial vessel into the rest of the chip was imaged using the ImageXpress XLS Micro (Molecular Devices). Images were taken for 14 minutes with a 2-minute interval. The images were analysed by extracting the average fluorescence values of the top perfusion channel divided by the average fluorescence value of the bottom perfusion channel for each chip and timepoint, determined in Fiji. The apparent permeability (P_{app}) value (cm/s) was determined:

$$Papp = \frac{\Delta C(receiver) * V(receiver)}{\Delta t * A(barrier) * C(donor)}$$

$\Delta C_{receiver}$ is the difference between the fluorescence intensity measured in the bottom perfusion channel between t=0 and t=14 min, $V_{receiver}$ is the volume of the measured region in the ECM channel, Δt is the time between start of the assay and endpoint (14 min), $A_{barrier}$ is the surface of the ECM barrier with the upper perfusion channel (0.0057 cm^2), and C_{donor} describes the fluorescence intensity measured in the top perfusion channel.

TEER

The electrode board was prepared and the OrganoPlate was equilibrated at RT for 30min. The electrode board of the TEER device (Mimetas, the Netherlands) was placed on top of the plate and TEER measurement was performed.

Transendothelial migration quantification

5 µM MitoTracker Deep Red was added to the PBMCs in AIM-V medium. The cells were incubated in the dark at 37°C for 30 min. After the incubation, PBMCS were washed with medium, resuspended in the appropriate volume of medium and seeded in the top lane of the OrganoPlate upon exchanging EGM-2 medium of HUVECs with a 50:50 mixture of AIM-V and EGM-2 containing the PBMCs.

Imaging of the migration was done with the ImageXpress® Micro XLS confocal microscope (Molecular Devices). Montages were created using Fiji. A migration quantification tool made in Fiji, specifically developed for the OrganoPlate 3-lane was used.

Immunostaining

The content of the OrganoPlates was fixed with 3.7% Formaldehyde (Sigma, # 252549-1L) in HBSS (+Ca/Mg) (Sigma, # 55037C-1000ML) for 15 min. The plates were washed twice with PBS (Gibco, t# 70013065) for 5 min each. PBS was added to all chips, the plate was sealed and stored until used for immunostaining. For staining, the plates were kept on a rocking device during all incubation steps. The cells were first washed for 5 min with washing solution containing 4% FCS (Gibco/ATCC, cat# A13450) in PBS, permeabilized for 10 min with permeabilization buffer containing 0.3% Triton X-100 (Sigma, #T8787) in PBS and washed again for 5 min. The cells were then blocked with 2% FBS, 2% BSA (Sigma, # A2153) and 0.1% Tween20 (Sigma, # P9616) in PBS for 45 min. The primary antibody was prepared in blocking solution and added to the plate for 24h at RT. CD31 (Dako, #M0823) and ICAM-1 (Biotechne, #BBA3) were used in a 1:100 dilution. Alexa Fluor Plus 488 (Invitrogen, #A32723) was used as a secondary antibody in a 1:250 dilution. The secondary antibody was prepared in blocking solution and added to the plate after washing the plate twice for 3 min and incubated for 24 h. The plate was washed again twice for 3 min after incubation. The cells were washed with PBS once for 1 minute, incubated with NucBlue™ Live ReadyProbes™ Reagent (Hoechst 33342) (Invitrogen, R37605) and ActinGreen™ 488 ReadyProbes™ Reagent (Invitrogen, R37110) and the plate was filled with PBS, sealed and kept in the fridge until imaging.

Live and dead assay

Calcein-AM (Lifetechnologies, #C3099), NucBlue Live ReadyProbes Reagent (Life technologies, #R37610) and DraQ7 (BioStatus, #DR71000) were used for staining live and dead cells and the nucleus. The reagents were added to the medium and distributed to the perfusion inlets and outlets. The mix was incubated for 45 min on the rocker and fluorescent imaging was performed.

Luminex

Medium was sampled from the OrganoPlate and added to the pre-ordered plate containing the analyte-specific capture antibodies, which bind to the analytes of interest according to the kit protocol. The Human Magnetic Luminex® Assay was used (bio-techne, #LXSAHM-11). Samples were analyzed on the MAGPIX xPONENT® software. The samples were normalized and compared to standards.

Stromal targeting

For targeting the stroma, several compounds were added as 2 µM solutions to the OrganoPlate after medium was removed on day 4. The following compounds were used: Halofuginone (MedChem Express, #HY-N1584) as a PSC/CAF and SMAD 2/3 inhibitor; Galunisertib (Selleck Chemicals, #S2230) as TGF-β receptor inhibitor; Vismodegib (MedChem Express, #HY-10440) as a SHH pathway inhibitor, Pirfenidone (MedChem Express, #HY-B0673) as a cell cycle inhibitor of CAFs; and Losartan (MedChem Express, #HY-17512) as a TGF-β ligand inhibitor (16).

Statistical analysis

All statistical analyses were conducted in GraphPad Prism version 9 (GraphPad Software, San Diego, CA, USA) and data was presented as mean ± standard deviation (SD). Differences in survival were assessed using one-way or two-way ANOVA in combination with respective Tukey's multiple comparison test or Sidak`s multiple comparison. Luminex data was analysed using Kruskal-Wallis test, correction for multiple comparisons by Dunn's test. A statistical significance of $p \leq 0.05$ was maintained. The significances are shown as asterisks in the figures (* = p< 0,05; ** = p< 0,01; *** = p< 0,001; **** = p< 0,0001). Independent experiments are denoted by N, while replicates per experiment are denoted by n. Sample size was chosen based on the variation and standard deviation between samples to ensure significance of the data. F-tests, descriptive statistics and row analysis were performed to ensure similar variance between the groups.

Results

Development of a PDAC tumor microenvironment on-a-Chip

The stroma is considered the major player in shaping the PDAC immune microenvironment. In order, to recapitulate cellular interactions observed in PDAC tumors, we developed a microfluidic-based PDAC model and subsequently applied it in immune migration studies. PDAC organoids and PSCs were characterized and model setups were established in the OrganoPlate 3-lane (Figures S1, 1A, B). These consist of PDAC organoids, PSCs, endothelial and immune cells. First, the middle lane was seeded with Collagen I type ECM containing PSCs. Subsequently, the top lane was seeded with endothelial HUVEC cells, which self-assembled into a tubule under flow conditions. PDAC organoids were cultured in Matrigel in the bottom lane (Figure 1C). All cell types were seeded on the same day. After cell seeding, cultures were then placed onto an OrganoFlow for perfusion, which enabled nutrient distribution and waste removal (Figures 1D, E). Cultures were allowed to develop for 4 days. For migration studies, the HUVEC tubule was loaded with CMRA labeled PBMCs and the migration towards the PDAC organoids was followed for 72h, cultures were imaged every 24h. Migration of PBMCs was analyzed using an in-house cell counting tool developed in FIJI.

This model setup and variations of it were further used to investigate the role of the tumor microenvironment, particularly the endothelium and PSCs, on immune cell recruitment in PDAC.

Influence of the endothelial inflammatory status in PBMC migration

Inflammation occurs in response to tissue damage and cancer, which usually results in vascular activation and increased recruitment of immune cells towards the site of inflammation (17). Vascular responses such as changes in barrier function were studied in inflamed HUVEC (exposed to 2.25 ng/ml TNFα) as well as in presence of a PDAC tumor compartment.

HUVEC control tubules showed expected morphology as shown by CD31 immunostaining (18). In Figure 2, TNFα treated HUVEC tubules show clear increased ICAM expression (Figure 2A) and permeability (Figures 2B–D), consequently, leading to a better attachment of PBMCs and subsequent migration (Figures 2E, F).

However, HUVEC tubules presented a very poor morphology and a very high leakiness in response to TNFα, for this reason migration experiments were further conducted in absence of TNFα. Although, untreated HUVEC tubules in co-culture with PDAC organoids are more organized, these also present a poor barrier function in presence of PDAC organoids, therefore, recapitulating the leaky blood vessels observed in PDAC tumors (Figures 2D, 3B).

Effect of PDAC stromal barrier on immune cell distribution and migration

After confirming that the endothelium did not retain PBMCs or formed a good barrier in presence of PDAC organoids, the role of the PSCs was further evaluated. To bring more complexity into the model the HUVEC-PDAC model was expanded to include PSCs in the middle lane and create a HUVEC-PSC-PDAC model.

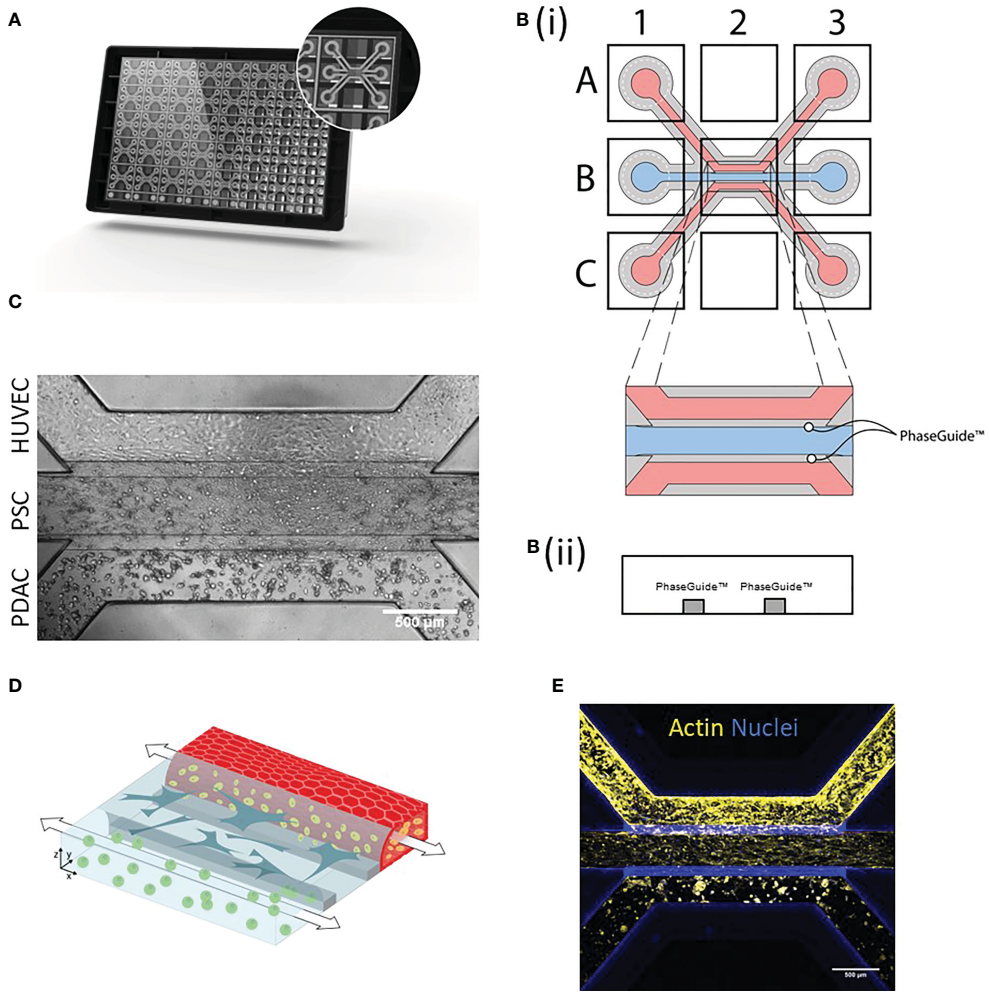

FIGURE 1
PDAC tumor microenvironment-on-a-Chip: **(A)** The OrganoPlate 3-lane comprises 40 chips with 3 microfluidic channels each. **(B)**(i). Endothelial cells were seeded into the top lane (A1) and due to capillary forces, the cells were distributed throughout the lane (A3) and allowed to form a tube. PSCs were loaded into the middle lane (B1) and PDAC organoids into the bottom lane (C1 distribution to C3). **(B)**(ii) Side view of a chip comprising the three lanes with PhaseGuides, that allowed for the compartmentalization of different cell types. Microscopic images were acquired from the observation window, which comprises all three lanes (B2) and which can be seen in **(C)** Phase contrast image shows culture organization in an OrganoPlate 3-lane chip. 4x acquisition, Scale bar=500 µm. Images acquired on the ImageXPress Micro XLS Widefield High-Content Analysis System® (Molecular Devices). **(D)** Schematic representation of the 3D culture, where PBMCs (yellow) migrated from the HUVEC tube (red) through the stroma (blue) to PDAC organoids (green). **(E)** Immunostaining with Actin (yellow) and NucBlue (blue). The cells were imaged on the confocal microscope. Shown are 4x maximum intensity projections, imaged on the ImageXpress Micro Confocal (Molecular Devices). Scale bar= 500 µm.

PSCs grew along the HUVEC tubule, building an additional barrier (Figures 3A–C). Cultures were characterized by actin and nuclei staining and respective 3D reconstruction images (Figure 3A) showed a stromal compartment formed alongside a fully developed HUVEC tubule. TEER and BI measurements in different model set ups indicated, that mainly PSCs were responsible for barrier formation (Figures 3B, C). Next, PBMCs were allowed to migrate in different culture setups. In presence of both PSCs and PDAC, 20-30% of PBMCs were retained in the stromal compartment (Figures 3D, E).

PBMC migration was not observed in HUVEC only controls (Figure 3F). PBMCs migrated within 24-72h in the different model setups tested. The highest numbers of PBMCs to reach the PDAC organoids compartment was observed in the model setup containing PDAC and PSCs in the bottom lane (Figure 3G).

Soluble factors secretion changes in response to PDAC organoids and PSCs crosstalk

To further explore the relevance of the stroma in attracting and influencing the distribution of immune cells in our model, chemokine, cytokine and FGF2 levels were determined in culture supernatants, collected from specific chip compartments, using a Luminex panel containing CCL2, CXCL1, CCL4, CXCL10, CXCL13, IL-6, Il-8, IL-10, TNFα, FGF2 and IFN-γ (Figure 4).

Data are shown as fold change of PDAC organoids compartment in absence of PSCs. Almost all secreted factors were present in the supernatant of the different culture setups, except for INFy and IL10. These cytokines were present in very low concentrations and no significant differences were observed (data

10.3389/fimmu.2023.1155085

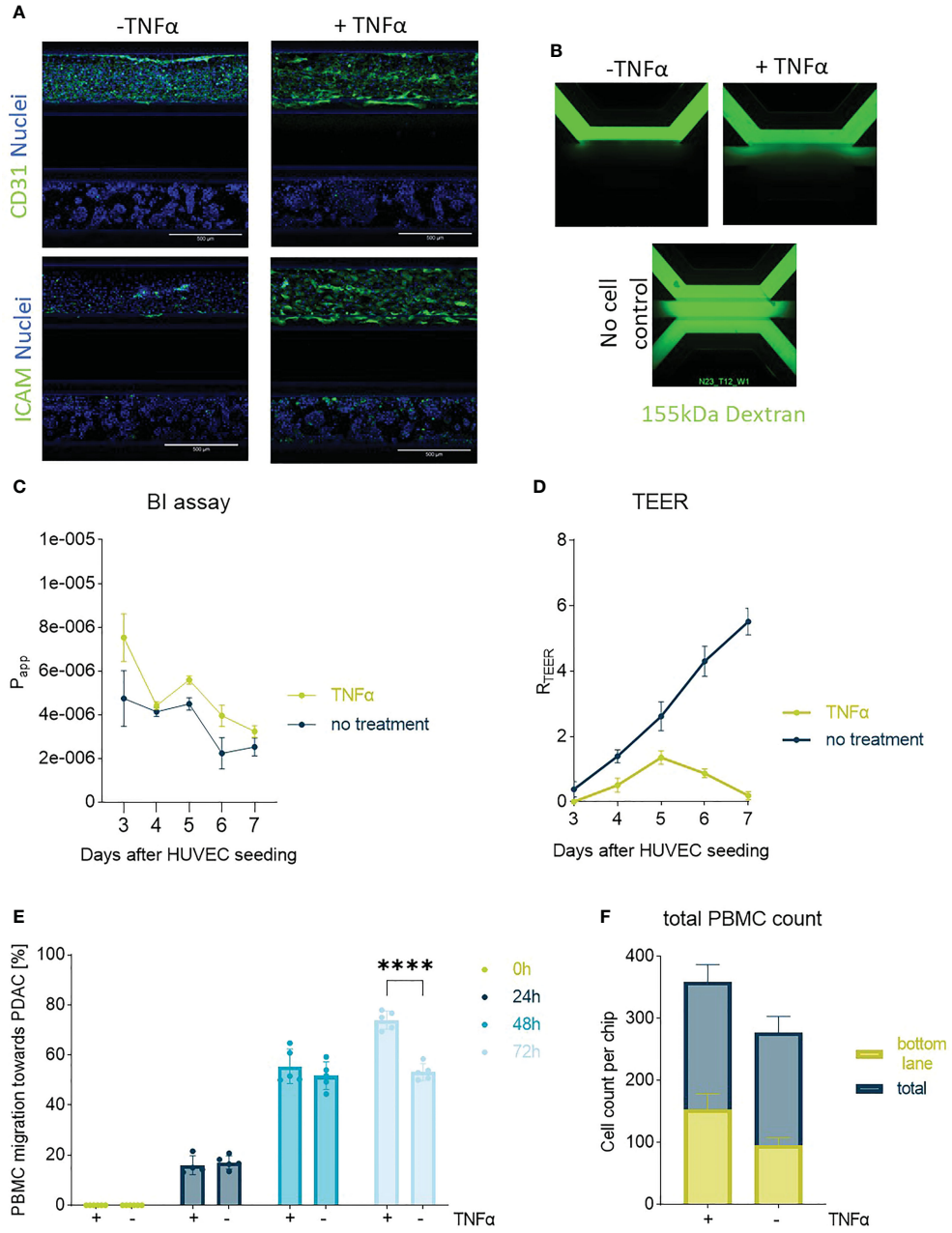

FIGURE 2
Endothelial barrier function and PBMC migration: In **(A)** one of the PDAC-on-Chip model setups is shown, and consists of a HUVEC tubule and PDAC organoids. Confocal imaging revealed the morphology of the HUVEC tube upon treatment with TNFα on day 3. The cells were stained on day 7 with CD31 (green), ICAM (green) and NucBlue (blue). Shown are 10x maximum intensity projections, imaged on the the ImageXpress Micro Confocal (Molecular Devices). Scale bar= 500 µm. **(B)** BI assay determined upon perfusion of a 155 kDa FITC-dextran. The dye diffused through the chip when no cells were present. 4x images acquired on the ImageXPress Micro XLS Widefield High-Content Analysis System® (Molecular Devices). **(C)** Barrier function was assessed with BI assays from day 4-7 after seeding upon perfusion of the chips with medium containing the 155 kDa FITC-dextran and corresponding apparent permeability (Papp) values were calculated. Shown are mean +- SD (N=3, n=3). **(D)** TEER measurements highlighted the role of TNFα in decreasing the barrier function of HUVEC tubes. (N=3, n=3) **(E)** Migration quantification of PBMCs towards PDAC organoids within 72h showed a slight influence of TNFα on PBMC migration behavior. Shown are mean+- SD (N=3, n=3) **(F)** Total cell count of PBMCs located in the chip compared to the number of cells that migrated to the bottom lane within 72h. Shown are mean+- SD (N=3, n=3).

not shown). CCL2 and CXCL13 (Figures 4A, E) were increased in the PSC compartment in presence of PDAC organoids (adjacent channel) compared to PDAC organoids growing in absence of PSCs. TNFα was only increased in the PDAC organoids compartment of the co-culture (Figure 4H). CXCL1, CCL4, IL8 and IL6 were significantly increased in the PSC and PDAC compartments of the co-culture (Figures 4B–D, G). CXCL10 and FGF2 data showed a trend towards increased levels in the co-cultures (Figures 4F, I). FGF2 level was significantly increased in the PSC compartment of the co-culture in comparison to PSCs growing in absence of PDAC organoids (Figure 4I). Heatmap in Figure 4J summarizes the Luminex data and indicate that compartments of

10.3389/fimmu.2023.1155085

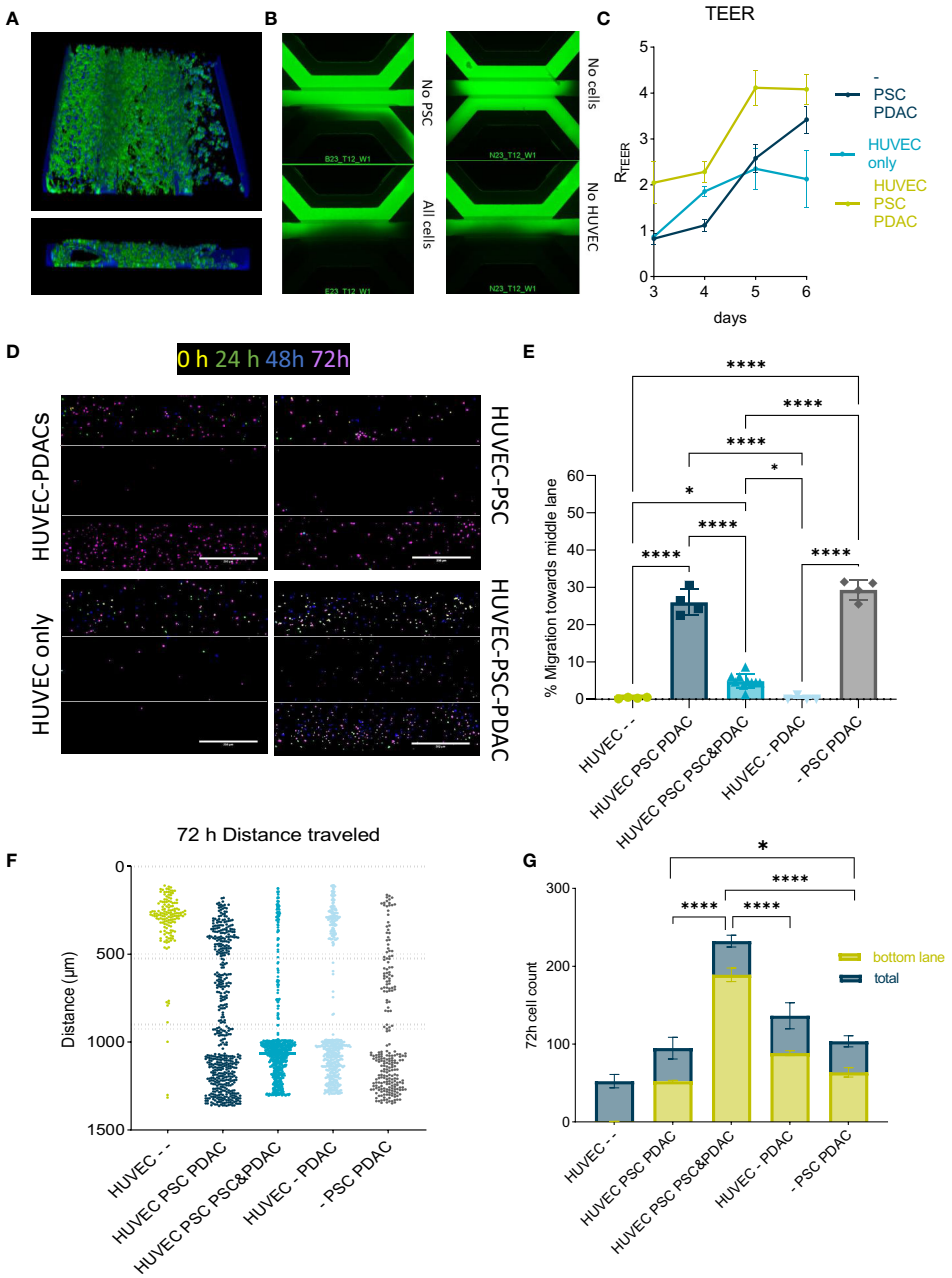

FIGURE 3
Migration of PBMCs in the PDAC TME model: **(A)** Top and side view of the 3D reconstruction of the complete model comprising a HUVEC tubule, PSCs and PDAC organoids. The cells were stained with Actin and NucBlue and imaged on the ImageXpress Micro Confocal (Molecular Devices) **(B)** BI-assay images of the tri-culture system. Perfusion of a 155k Da FIT-C labeled dextran, 4x magnification. Images acquired on the ImageXPress Micro XLS Widefield High-Content Analysis System® (Molecular Devices). **(C)** TEER measurements highlighted the role of PSCs in increasing the barrier function of HUVEC tubules (N=3, n=3). Statistical analysis revealed *p<0,05 for the - PSC PDAC sample and *** p<0,001 for the HUVEC PSCs PDAC sample compared to the HUVEC only control on day 6. **(D)** CMRA staining of migrating PBMCs imaged on the ImageXpress Micro Confocal (Molecular Devices) at 0h, 24h, 48h and 72h after PBMC seeding. 10x acquisition, Scale bar=500 µm. **(E)** Quantification of PBMC numbers in the middle lane. Migration was analyzed with a cell counting tool in FIJI based in confocal images. Shown are mean± SD (N=3, n=3). Data show % of cells that migrated compared to the total amount of cells counted in the chip. **(F)** Migration chart showing the position of single PBMCs and distance they traveled in the OrganoPlate after 72h in different setups. Migration was analyzed with a cell counting tool in FIJI based on confocal imaging. Shown are mean+- SD (N=3, n=3). **(G)** Total cell number of immune cells migrated towards PDACs within 72h versus total number of cells within a chip. Shown are mean+- SD (N=3, n=3).

the co-culture setup show an increase in the secretion of most soluble factors measured. These results indicate that the biochemical microenvironment in our model is complex, and that the PDAC organoids-PSCs crosstalk lead to the increase of immune mediators and being those changes sometimes compartment dependent. In addition, these support the notion that PSCs in addition to a physical barrier, seem to shape a biochemical immune microenvironment as well.

10.3389/fimmu.2023.1155085

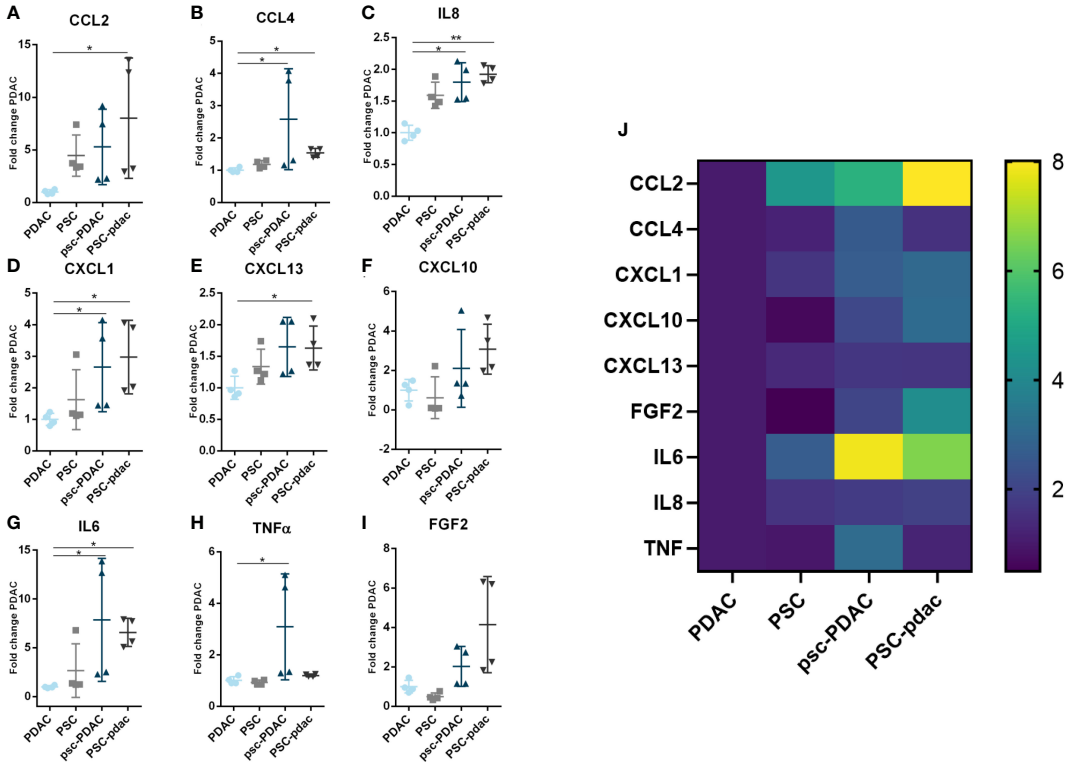

FIGURE 4
Soluble factors secretion: **(A–I)** Fold change of concentration of chemokines from the medium that was harvested from several culture setups. Samples were obtained from the following conditions: PDAC organoids grown in the bottom lane (in absence of PSCs), PSC grown in the bottom lane (in absence of PDAC, organoids), psc-PDAC samples were collected from the PDAC organoids grown in the bottom lane (in presence of a PSC compartment in the middle lane), PSC-pdac were collected from PSC grown in the middle lane (in presence of PDAC organoids growing in the bottom lane). **(J)** Heatmap of Luminex data for concentration fold changes. Luminex data was analyzed using Magpix. Samples were taken from the lane, that is depicted in capital letters. CCL2, CXCL1, CCL4, CXCL10, IL-6, IL-8, TNFα, CXCL13, FGF2, IFNy and IL-10 concentrations were measured in the supernatant (N=1,n=4).

PBMC subtype preferential migration in a PDAC model

PSCs seem to function as a physical barrier as well as contribute with secreted factors that influence PBMCs migration and distribution *in vitro* preventing them in part from reaching the tumor cells. We next characterized the migratory behavior of isolated PBMC subtypes. T-cells were least likely to migrate towards PDAC organoids, whereas monocytes and B-cells were most likely to migrate to this compartment (Figure 5A). Total cell numbers showed, that around 40% of the total B-cell and monocyte population seeded, migrated towards to the organoids, whereas this percentage was much lower for T-cells (Figure 5B).

Influence of stromal targeting on barrier function and immune cell infiltration

To increase the amount of migrating PBMCs and consequent immune infiltrate into the tumor compartment, several stromal targeting compounds were tested. Halofuginone (PSC/CAF and SMAD2/3 inhibitor), Galunisertib (TGF-β receptor inhibitor), Pirfenidon (cell cycle inhibitor of CAFs), Losartan (TGF-β ligand inhibitor) and Vismodegib (SHH pathway inhibitor) were selected to target the PSCs compartment (Figure 6).

Exposure of the stromal compartment to these compounds decreased TEER, confirming that all compounds influenced PSCs barrier. Halofuginone created the biggest drop in TEER (Figure 6A). This effect was accompanied by a significant increase in immune cell infiltration in response to Halofuginone, Losartan and Pirfenidone (24-72h). Migration of PBMCs was slightly increased to the PDAC organoids in the bottom lane and the effect reduced over time (Figure 6B). Halofuginone produced the most consistent increase in immune cell infiltration. This seemed to be associated to the induction of pancreatic stellate cell death as determined with a live and dead assay (Figures 6C, D).

Discussion

We here describe the development and the application of a PDAC microenvironment on-a-Chip model in immune cell migration and infiltration studies. Several model setups were established, these consisted of an endothelial tubule perfused with PBMCs, PSCs (stromal compartment), and PDAC organoids (Figure 1).

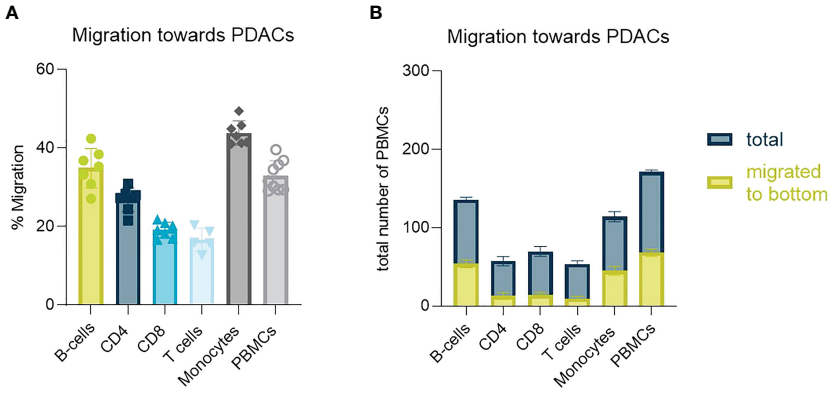

FIGURE 5
Identification of PBMC subtype migration **(A)** Migration percentage of total migrating T-cells, CD4+ T-cells, CD8+ T-cells, B-cells and monocytes towards PDAC organoids in a HUVEC-PDAC setup. Shown are mean+- SD (N=3, n=3). **(B)** Total cell number of diverse immune cell types migrated towards PDAC within 72h versus total number of cells within a chip. Shown are mean+- SD (N=3, n=3).

To study the influence of vascular permeability on PBMC migration, we simulated inflammation upon TNFα exposure to the HUVEC tubule. Endothelial tubules showed a clear morphological change (CD31) and increased ICAM expression in response to TNFα (Figure 2A). As a result, tubules showed a higher Papp (BI assay) and lower TEER measurements, suggesting that TNFα induced a weaker barrier function compared to untreated tubules (Figures 2C, D). TNFα improved PBMC attachment and subsequent transmigration (Figure 2F). Similar behavior was observed in presence of PSCs and PDAC organoids, and for this reason TNFα priming was not needed.

In the model setups composed by HUVEC-PSC-PDAC organoids, stromal cells formed a functional barrier on the interface with the endothelial tubule. 3D reconstruction images (Figure 3A) confirmed that PSCs align along the endothelial tubule and supported the formation of a physical barrier between the vascular and stromal compartments (Figure 3B). HUVECs tubules were leaky and seemed to give a minor contribution to the formation of this barrier, also demonstrated by similar TEER values measured at day 6 in triculture (HUVEC-PSCs-PDAC) and co-culture (PSCs-PDAC) (8) (Figures 3B, C). In presence of PSCs, 30% of migrating PBMCs were partly retained in the PSC compartment, suggesting that the stroma functioned like a barrier and influenced the distribution of part of the PBMC population and prevented its interaction with PDAC organoids (19).

However, two-three times as many cells reached the PDAC organoids compartment when PSCs were co-seeded with organoids in the bottom lane. PSCs seem to change when co-cultivated with PDAC organoids and formed a heterogenous stromal population. This stromal population likely included CAFs which in turn activate PDAC cells, promoting an increase in immunomodulatory chemokine secretion. PBMCs migration in our culture system seemed to depend on the formation of a chemokine gradient since no random migration was observed in absence of PSCs and/or PDAC over 72h (Figure 3). This was in line with previously published data by de Haan et al., 2021 where migration was only observed in presence of a chemokine gradient or a tumor compartment (14). Total numbers of migrating cells indicated the importance of both PDAC organoids and PSCs in immune cell infiltration and distribution. Factors secreted in our on-chip model are normally associated to a negative effect on immune cell trafficking and infiltration into the tumor tissue (20–24). However, when the two cell types were put together, these seem to interact, secreting a higher concentration of several soluble factors (Figure 4). PDAC cells released CCL2, CXCL13 and IL-8, but in lower concentrations than secreted by the PSCs (Figure 4). High concentrations of CXCL1 were released, which is a chemoattractant for neutrophils and non-hematopoietic cells and is associated to immune escape programs (25). CCL4, a chemoattractant for NK-cells and monocytes associated to an immunosuppressive TME was increased (26). CXCL13 plays a role in B cell recruitment, which we also confirmed with the migration data of B-cells, which show the highest migration potential (27) (Figure 5). Overall, PBMCs preferably migrated towards the PDAC organoids. However, direct immune cell-PDAC organoid interactions seemed to be partly prevented by the PSCs by the formation of a physical barrier as well as biochemical microenvironment that influenced immune cell distribution and did not support T cell migration (28). Due to the significant increase in chemokines, we hypothesize, that these serve as factors in immunosuppression, and thus explain the immune cell retention from the PDAC organoids (28).

To overcome the stromal barrier and to increase immune cell infiltration, stromal targeting compounds with different mechanisms of action were tested. All the tested compounds showed a decrease in TEER and barrier function. Halofuginone seemed to be the most promising candidate and Vismodegib the least (Figure 6A). Halofuginone increased immune cell infiltration after 24h and 48h towards PDAC organoids (bottom lane), indicating that this compound weakened stromal barrier function (Figure 6B). The effect was reduced after 48h, suggesting some sort of barrier regeneration and PSC proliferation.

Although this model provides a good insight into stromal functioning in PDAC, it poses limitations regarding complexity

10.3389/fimmu.2023.1155085

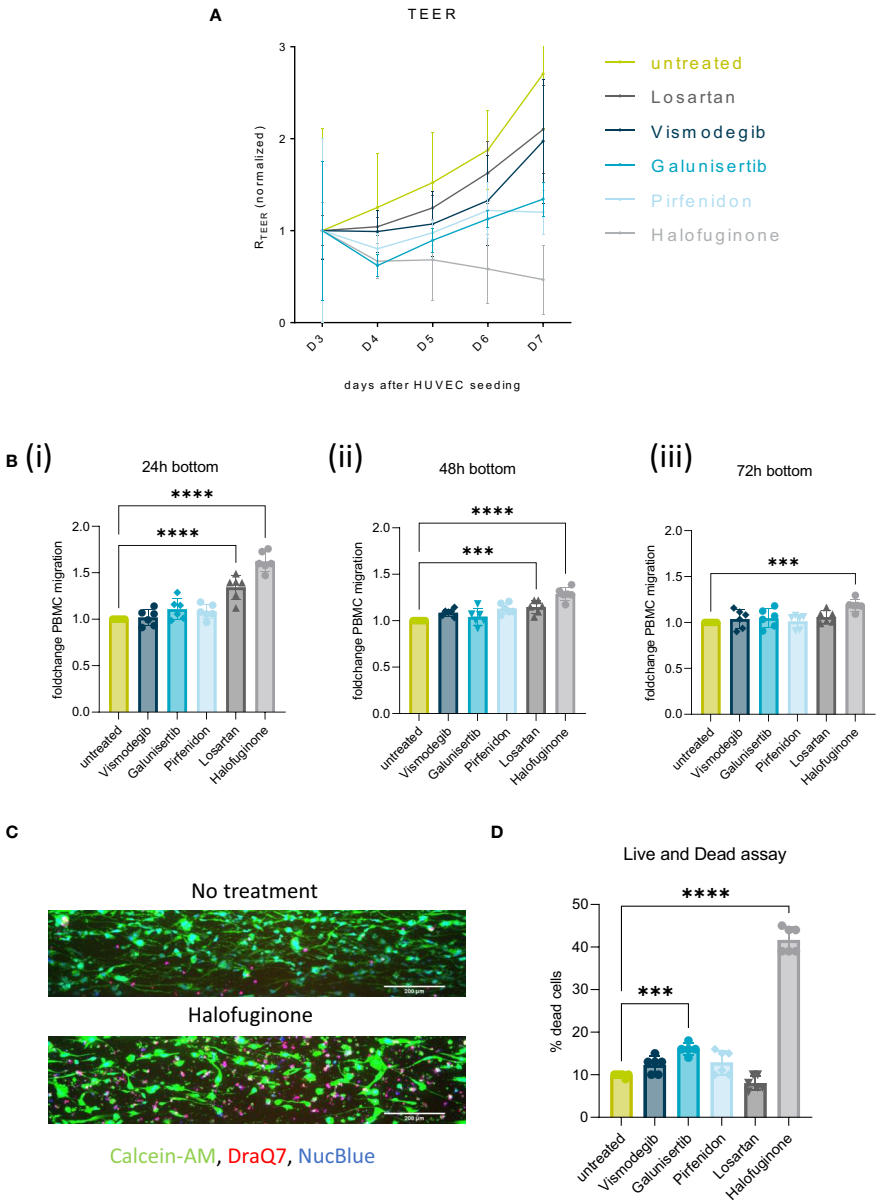

FIGURE 6
Stromal targeting in PDAC: **(A)** Barrier assessment of the culture setups when treated with 2 µM of either Vismodegib, Galunisertib, Pirfenidon, Losartan or Halofuginone with TEER. **(B)** Migration quantification of PBMCs migrated to the PDAC (bottom lane) at 24h(i), 48h(ii) and 72h(iii), when the stroma was treated with 2 µM of either Vismodegib, Galunisertib, Pirfenidon, Losartan or Halofuginone. The data, depicted as fold change, was normalized to the untreated control. Shown are mean +- SD (N=3, n=3). **(C)** Live and Dead assay with DraQ7 (red), Calcein-AM (green) and NucBLue (blue) showing the influence of the compounds on cell death when treated with Halofuginone in the PSC lane. The cells were stained with Calcein-AM, DraQ7 and NucBlue (N=3, n=3), imaged on the ImageXpress Micro Confocal (Molecular Devices). 10x acquisition, Scale bar=200 µm **(D)** Live and Dead assay quantification showing the percentage of dead cells compared to the total number of cells. ***p< 0,001; ****p< 0,0001.

and full *in vivo* translatability. The employed system should evolve to incorporate matched donor materials. In addition, other components of the PDAC stroma should also be included such as CAFs, and its role characterized. Considering given limitations, this model could still be instrumental in the understanding of the formation of PDAC tumor immune infiltrate as well as how to potentially influence cellular therapies (e.g., CAR T cells, TCR engineered T Cells, TILs, NK cells) delivery and effectiveness (29).

Conclusion

Recruitment of immune cells into the tumor tissue is an essential step that shapes the immune microenvironment and defines the ability of a tumor to respond or not to immune targeting strategies. In this study, a significant immunomodulatory role of the PDAC stromal compartment was characterized. This contributes to the formation of a physical barrier as well as the formation of PDAC biochemical

microenvironment. As a result, interaction of immune and tumor cells was partly prevented. Stromal retention of immune cells was in part reversed by Halofuginone. In addition, the study showed the suitability of microfluidic platforms for generating complex models and recapitulating complex cellular interplay involved in the lack of an effective anti-tumor immune response in PDAC.

Data availability statement

The original contributions presented in the study are included in the article/Supplementary Material. Further inquiries can be directed to the corresponding author.

Ethics statement

Written informed consent from the donors for research use of the tissue was obtained prior to acquisition of the specimens. Tissues for the generation of models were collected under protocol number 55859, approved by the local Ethics Committee (Comitato Etico Azienda Ospedaliera Universitaria Integrata) to V.C. (Prog. 3456CESC, 27/09/21)".

Author contributions

Conceptualization: MG. Methodology: MG, L-MG. Investigation and analysis: MG., L-MG. Writing-draft preparation: MG. Writing- review and editing: MG, KQ, VC. Supervision: KQ. Organoid generation: VC, SA. All authors contributed to the article and approved the submitted version.

Funding

This project was supported by an innovation credit (IK17088) from the Ministry of Economic Affairs and Climate of the Netherlands. MG is supported by an European Union's Horizon 2020 research and innovation programme under the Marie Sklodowska-Curie action, Innovative Training Network: PRECODE; grant N: 861196. We thank our colleagues at Mimetas and the PRECODE consortium for the many fruitful discussions.

Conflict of interest

MG, L-MG. and KQ are employees of MIMETAS BV, the Netherlands, which is marketing the OrganoPlate®.

The remaining authors declare that the research was conducted in the absence of any commercial or financial relationships that could be construed as a potential conflict of interest.

The reviewer MFB declared a shared consortium with the authors VC and KQ to the handling Editor.

Publisher's note

Supplementary material

The Supplementary Material for this article can be found online at: https://www.frontiersin.org/articles/10.3389/fimmu.2023.1155085/full#supplementary-material

SUPPLEMENTARY FIGURE 1
Characterization of cells. **(A)**PDAC Pat. 39 organoids grown in Matrigel on a 6-well plate, 4x magnification. **(B)** PSC Klon 2.2 grown in Matrigel on a 6-well plate, 4x magnification. **(C)** Immunostaining of PDAC organoids with CK19 (red) and NucBlue (blue), 10x, imaged on the ImageXpress Micro Confocal (Molecular Devices). **(D)** Immunostaining of PSCs with Vimentin (red) and NucBlue (blue), 10x, imaged on the ImageXpress Micro Confocal (Molecular Devices).

References

1. Fan Jq, Wang MF, Chen HL, Shang D, Das JK, Song J. Current advances and outlooks in immunotherapy for pancreatic ductal adenocarcinoma. *Mol Cancer* (2020) 19(1):32. doi: 10.1186/s12943-020-01151-3

2. Rosenberg A, Mahalingam D. Immunotherapy in pancreatic adenocarcinoma–overcoming barriers to response. *J Gastrointest Oncol* (2018) 9(1):143–59. doi: 10.21037/jgo.2018.01.13

3. Hrabák P, Kalousová M, Krechler T, Zima T. Pancreatic stellate cells - rising stars in pancreatic pathologies. *Physiol Res* (2021), 70:S597–616. doi: 10.33549/physiolres.934783

4. Erkan M, Kurtoglu M, Kleeff J. The role of hypoxia in pancreatic cancer: a potential therapeutic target? *Expert Rev Gastroenterol Hepatol* (2016) 10(3):301–16. doi: 10.1586/17474124.2016.1117386

5. Ajina R, Weiner LM. T-Cell immunity in pancreatic cancer. *Pancreas* (2020) 49:1014–23. doi: 10.1097/MPA.0000000000001621

6. Huber M, Brehm CU, Gress TM, Buchholz M, Alhamwe BA, von Strandmann EP, et al. The immune microenvironment in pancreatic cancer. *Int J Mol Sci* (2020), 10 (3):1–33. doi: 10.3390/ijms21197307

7. Clark CE, Hingorani SR, Mick R, Combs C, Tuveson DA, Vonderheide RH. Dynamics of the immune reaction to pancreatic cancer from inception to invasion. *Cancer Res* (2007) 67(19):9518–27. doi: 10.1158/0008-5472.CAN-07-0175

8. von Bernstorff W, Voss M, Freichel S, Schmid A, Vogel I, J6hnk C, et al. *Clinical cancer research 925s [Internet]* (2001). Available at: http://aacrjournals.org/clincancerres/article-pdf/7/3/925s/2079800/925s.pdf.

9. Krzastek SC, Goliadze E, Zhou S, Petrossian A, Youniss F, Sundaresan G, et al. Dendritic cell trafficking in tumor-bearing mice. *Cancer Immunol Immunother* (2018) 67:1939–47. doi: 10.1007/s00262-018-2187-z

10. Mestas J, Hughes CCW. Of mice and not men: Differences between mouse and human immunology. *J Immunol* (2004) 172(5):2731–8. doi: 10.4049/jimmunol.172.5.2731

11. Ledgerwood LG, Lal G, Zhang N, Garin A, Esses SJ, Ginhoux F, et al. The sphingosine 1-phosphate receptor 1 causes tissue retention by inhibiting the entry of peripheral tissue T lymphocytes into afferent lymphatics. *Nat Immunol* (2008) 9(1):42–53. doi: 10.1038/ni1534

12. Deng Y, Herbert JA, Smith CM, Smyth RL. An in vitro transepithelial migration assay to evaluate the role of neutrophils in respiratory syncytial virus (RSV) induced epithelial damage. *Sci Rep* (2018) 8(1):6777. doi: 10.1038/s41598-018-25167-4

13. Geyer M, Queiroz K. Microfluidic platforms for high-throughput pancreatic ductal adenocarcinoma organoid culture and drug screening. *Front. Cell Dev. Biol., Sec. Molecular and Cellular Pathology* (2021) 9. doi: 10.3389/fcell.2021.761807

14. de Haan L, Suijker J, van Roey R, Berges N, Petrova E, Queiroz K, et al. A microfluidic 3D endothelium-on-a-chip model to study transendothelial migration of T cells in health and disease. *Int J Mol Sci* (2021) 22(15):8234. doi: 10.3390/ijms22158234

15. Jesnowski R, Fürst D, Ringel J, Chen Y, Schrödel A, Kleeff J, et al. Immortalization of pancreatic stellate cells as an *in vitro* model of pancreatic fibrosis: deactivation is induced by matrigel and n-acetylcysteine. *Lab Invest* (2005) 85 (10):1276–91. doi: 10.1038/labinvest.3700329

16. Polani F, Grierson PM, Lim KH. Stroma-targeting strategies in pancreatic cancer: Past lessons, challenges and prospects. *World J Gastroenterol* (2021) 27 (18):2105–21. doi: 10.3748/wjg.v27.i18.2105

17. Jang D, Lee AH, Shin HY, Song HR, Park JH, Kang TB, et al. The role of tumor necrosis factor alpha (TNF-α) in autoimmune disease and current TNF-α inhibitors in therapeutics. *Int J Mol Sci* (2021) 22(5):2719. doi: 10.3390/ijms22052719

18. Hosein AN, Brekken RA, Maitra A. Pancreatic cancer stroma: an update on therapeutic targeting strategies. *Nat Rev Gastroenterol Hepatol* (2020) 17(8):487–505. doi: 10.1038/s41575-020-0300-1

19. Watt J, Kocher HM. The desmoplastic stroma of pancreatic cancer is a barrier to immune cell infiltration. *Oncoimmunology* (2013) 2(12):e26788. doi: 10.4161/onci.26788

20. Taniguchi K, Karin M. IL-6 and related cytokines as the critical lynchpins between inflammation and cancer. *Semin Immunol* (2014) 26(1):54–74. doi: 10.1016/j.smim.2014.01.001

21. Callaway CS, Delitto AE, D'Lugos AC, Patel R, Nosacka RL, Delitto D, et al. IL-8 released from human pancreatic cancer and tumor-associated stromal cells signals through a CXCR2-ERK1/2 axis to induce muscle atrophy. *Cancers (Basel)* (2019) 11 (12):1863. doi: 10.3390/cancers11121863

22. Mannino MH, Zhu Z, Xiao H, Bai Q, Wakefield MR, Fang Y. The paradoxical role of IL-10 in immunity and cancer. *Cancer Lett* (2015) 367(2):103–7. doi: 10.1016/j.canlet.2015.07.009

23. Zaidi MR, Merlino G. The two faces of interferon-γ in cancer. *Clin Cancer Res* (2011) 17(19):6118–24. doi: 10.1158/1078-0432.CCR-11-0482

24. Huang H, Zhou W, Chen R, Xiang B, Zhou S, Lan L. CXCL10 is a tumor microenvironment and immune infiltration related prognostic biomarker in pancreatic adenocarcinoma. *Front Mol Biosci* (2021) 8. doi: 10.3389/fmolb.2021.611508

25. Ciummo SL, D'Antonio L, Sorrentino C, Fieni C, Lanuti P, Stassi G, et al. The c-X-C motif chemokine ligand 1 sustains breast cancer stem cell self-renewal and promotes tumor progression and immune escape programs. *Front Cell Dev Biol* (2021) 9. doi: 10.3389/fcell.2021.689286

26. Romero JM, Grünwald B, Jang GH, Bavi PP, Jhaveri A, Masoomian M, et al. A four-chemokine signature is associated with a t-cell–inflamed phenotype in primary and metastatic pancreatic cancer. *Clin Cancer Res* (2020) 26(8):1997–2010. doi: 10.1158/1078-0432.CCR-19-2803

27. Gao SH, Liu SZ, Wang GZ, Zhou GB. CXCL13 in cancer and other diseases: Biological functions, clinical significance, and therapeutic opportunities. *Life* (2021) 11 (12):1282. doi: 10.3390/life11121282

28. Garg B, Giri B, Modi S, Sethi V, Castro I, Umland O, et al. NFκB in pancreatic stellate cells reduces infiltration of tumors by cytotoxic T cells and killing of cancer cells, *via* up-regulation of CXCL12. *Gastroenterology* (2018) 155(3):880–91. doi: 10.1053/j.gastro.2018.05.051

29. Du W, Pasca di Magliano M, Zhang Y. Therapeutic potential of targeting stromal crosstalk-mediated immune suppression in pancreatic cancer. *Front Oncol* (2021) 11. doi: 10.3389/fonc.2021.682217

frontiers | Frontiers in Immunology

TYPE Original Research
PUBLISHED 15 May 2023
DOI 10.3389/fimmu.2023.1115536

OPEN ACCESS

EDITED BY
Jason T. George,
Texas A&M University, United States

REVIEWED BY
Gabriele Nasello,
Leuven Brain Institute, KU Leuven, Belgium
Ayesha Sohail,
COMSATS University, Islamabad Campus, Pakistan
Luis Nestor Coria De Los Rios,
Instituto Tecnológico de Tijuana, Mexico

*CORRESPONDENCE
Alexander B. Brummer
brummerab@cofc.edu
Christine E. Brown
cbrown@coh.org
Russell C. Rockne
rrockne@coh.org

RECEIVED 04 December 2022
ACCEPTED 27 March 2023
PUBLISHED 15 May 2023

CITATION
Brummer AB, Xella A, Woodall R, Adhikarla V, Cho H, Gutova M, Brown CE and Rockne RC (2023) Data driven model discovery and interpretation for CAR T-cell killing using sparse identification and latent variables. *Front. Immunol.* 14:1115536. doi: 10.3389/fimmu.2023.1115536

Data driven model discovery and interpretation for CAR T-cell killing using sparse identification and latent variables

Alexander B. Brummer[1,2*], Agata Xella[3], Ryan Woodall[1], Vikram Adhikarla[1], Heyrim Cho[4], Margarita Gutova[5], Christine E. Brown[3*] and Russell C. Rockne[1*]

[1]Division of Mathematical Oncology, Department of Computational and Quantitative Medicine, Beckman Research Institute, City of Hope National Medical Center, Duarte, CA, United States, [2]Department of Physics and Astronomy, College of Charleston, Charleston, SC, United States, [3]Department of Hemtaology and Hematopoietic Cell Translation and Immuno-Oncology, Beckman Research Institute, City of Hope National Medical Center, Duarte, CA, United States, [4]Department of Mathematics, University of California, Riverside, Riverside, CA, United States, [5]Department of Stem Cell Biology and Regenerative Medicine, Beckman Research Institute, City of Hope National Medical Center, Duarte, CA, United States

In the development of cell-based cancer therapies, quantitative mathematical models of cellular interactions are instrumental in understanding treatment efficacy. Efforts to validate and interpret mathematical models of cancer cell growth and death hinge first on proposing a precise mathematical model, then analyzing experimental data in the context of the chosen model. In this work, we present the first application of the sparse identification of non-linear dynamics (SINDy) algorithm to a real biological system in order discover cell-cell interaction dynamics in *in vitro* experimental data, using chimeric antigen receptor (CAR) T-cells and patient-derived glioblastoma cells. By combining the techniques of latent variable analysis and SINDy, we infer key aspects of the interaction dynamics of CAR T-cell populations and cancer. Importantly, we show how the model terms can be interpreted biologically in relation to different CAR T-cell functional responses, single or double CAR T-cell-cancer cell binding models, and density-dependent growth dynamics in either of the CAR T-cell or cancer cell populations. We show how this data-driven model-discovery based approach provides unique insight into CAR T-cell dynamics when compared to an established model-first approach. These results demonstrate the potential for SINDy to improve the implementation and efficacy of CAR T-cell therapy in the clinic through an improved understanding of CAR T-cell dynamics.

KEYWORDS

dynamical systems, latent variables, CAR T-cells, antigen binding, allee effect, SINDy, glioblastoma, cell therapy

1 Introduction

Dynamical systems modeling is one of the most successfully implemented methodologies throughout mathematical oncology (1). Applications of these *model first* approaches have led to important insights in fundamental cancer biology as well as the planning and tracking of treatment response for patient cohorts (2–9). Simultaneously, the last twenty years have seen explosive growth in the study and application of data-driven methods. These *data first* approaches, initially implemented as machine learning methods for imaging and genomics analyses, have seen much success (10, 11). However, such approaches are often limited to classification problems and fall short when the intention is to identify and validate mathematical models of the underlying dynamics. Recent efforts by us and others have aimed to develop methodologies that bridge these *model first* and *data first* approaches (12–14).

In this work, we combine the methods of latent variable discovery and sparse identification of nonlinear dynamics (SINDy) (15–17) to analyze experimental *in vitro* cell killing assay data for chimeric antigen receptor (CAR) T-cells and glioblastoma cancer cells (18). This experimental data, featuring high temporal resolution, offers a unique opportunity to conduct an *in situ* test of the SINDy model discovery method. Interpretation of the discovered SINDy model is conducted under the expectation of a predator-prey interaction in which the cancer cells function as the prey and the CAR T-cells the predator (19).

Predator-prey systems are a broad class of ordinary differential equations (ODEs) that aim to characterize changes in populations between two or more groups of organisms in which at least one survives *via* predation on another. Originally applied to the study of plant herbivory (20) and fishery monitoring (21) in the early 20th century, predator-prey models have since become a workhorse of ecology, evolutionary biology, and most recently mathematical oncology (19, 22). Importantly, predator-prey models underpin much of the computational modeling of CAR T-cell killing, particularly in the context of *in vitro* cell killing assays (7, 23). An important example of these is the CAR T-cell Response in GliOma (CARRGO) model, a model that characterizes the *in vitro* interactions between CAR T-cells and glioma cells (18). The CARRGO model has shed light on the underlying biological mechanisms of action (18, 23), has informed effective dosing strategies for combination CAR T-cell and targeted radionuclide therapy (24), and CAR T-cell therapy in combination with the anti-inflammatory steroid Dexamethasone (25).

Despite the success of the CARRGO model, it is limited in the scope of potential phenomena that it can capture in regards to the precise interactions between the CAR T-cells and glioma cells. In this work, we use the SINDy modeling framework to incorporate important extensions to the CARRGO model. These extensions are: predator growth that is dependent on the density of prey, also known as a functional response (26, 27); individual predator and prey growth that saturates at some maximum value (logistic growth) (18), or has a population threshold below which collapse occurs (the Allee effect) (28, 29); and predator-prey interactions in which one or two CAR T-cells are bound to a single cancer cell at once, referred to as single or double binding, respectively (23, 30). Other efforts of extending CAR T-cell modeling have looked at fractional order derivatives (31) and stochastic dynamics (32) in the context of CAR T-cell treatment for viral infections, specifically coronaviruses. Our treatment focuses on integer order derivatives and deterministic dynamics.

An ever-present challenge to quantitative biologists is fitting a proposed model to experimental data, also known as parameter estimation or model inference. On one hand, quantitative biologists seek models that capture as much biological realism and complexity as possible. On the other hand, increasing model complexity increases the computational challenge to accurately, confidently, and expediently determine model parameter values. This approach is further complicated if a researcher chooses to compare competing or complementary models (33, 34). An alternative approach, examined in this paper, is to leverage newly developed methods rooted in data science and machine learning which identify the strength of individual mathematical terms as candidates for an explanatory model. These methods are often referred to as dynamic mode decomposition, symbolic regression, or sparse identification.

Dynamic mode decomposition (DMD) is a data driven technique that interrogates time-series data by performing a singular value decomposition (SVD) on carefully structured matrices of the given data (13, 35). In this formalism, the orthonormal basis vectors generated by singular value decomposition serve as linear generators of the system dynamics such that forward prediction can be performed absent a known underlying mathematical model. Alternatively, SINDy identifies the specific mathematical terms that give rise to the observed dynamics governed by ordinary and partial differential equation models (15). SINDy achieves this by regressing experimental data onto a high-dimensional library of candidate model terms, and it has proven successful in climate modeling (36), fluid mechanics (37), and control theory (38). Since the initial publication of SINDy, several extensions have been studied, including: discovery of rational ordinary differential equations (39, 40); robust implementation with under-sampled data (41) or excessive noise (42); or incorporation of physics informed neural networks when particular symmetries are known to exist (43).

In its original and subsequent implementations, the CARRGO model demonstrated valuable utility in quantifying CAR T-cell killing dynamics when treating glioblastoma. Inferences of the underlying biological dynamics were made by examining how model parameter values changed along gradients of effector:target (E:T) ratios or as a function of other combination therapy concentrations. This is in direct contrast to the SINDy methodology, where the discovery of different model terms provides insight into the underlying biological dynamics as a result of variation along the E:T gradient. Here we compare these two modelling frameworks on the same data set to provide further insight into the trade-offs of *data first* versus *model first* approaches.

In this paper we utilize our experimental data to test these and other aspects of the DMD and SINDy frameworks. In Section 2.2 we introduce the families of models that are anticipated to be

simultaneously biologically relevant and identifiable by SINDy, and we introduce a new approach to performing SINDy-based model inference. In Section 2.3.1 we present the latent variable analysis based on DMD that is used to generate the time-series CAR T-cell trajectories based on those of the cancer cells and the known boundary values for the CAR T-cells. In Section 2.3.2 we introduce the SINDy methodology in the particular context of our application. Results of our approach are presented in Section 3 where we (1) highlight how the discovered models vary as a result of different initial conditions in the cancer cell and CAR T-cell populations and (2) examine how well the discovered models found in this *data first* approach compare to a typical *model first* in characterizing the experimental data. In Section 4 we demonstrate how our results can guide experimental design to validate the predictions made by the discovered models, and we elaborate on some of the challenges encountered in this study.

2 Materials and methods

2.1 Experimental setup

The data analyzed in this study come from previously conducted experiments whose procedures are described in Sahoo et al. (18) and Brummer et al. (25), and summarized in Figure 1. The primary brain tumor cell line studied (PBT128) was selected for its endogenous high and relatively uniform expression of IL13Rα2 antigen (89.11% IL13Rα2+) (25). This cell line was derived from glioblastoma tumor resection tissue as described in (44, 45). To generate IL13Rα2-targeted CAR T-cell lines, healthy donor CD62L+ naive and memory T-cells were lentivirally transduced to express second-generation 4-1BB-containing CAR that utilizes the IL13 cytokine with an E12Y engineered mutation as the IL13Rα2 targeting domain (46).

Cell killing experiments were conducted and monitored with an xCELLigence cell analyzer system. Measurements of cancer cell populations are reported every 15 minutes through changes in electrical impedance as cancer cells adhere to microelectrode plates, and are reported in units of Cell Index (CI), where 1 CI ≈ 10K cells (47–49). Flow cytometry was used to count the non-adherent CAR T-cells upon termination of the experiment. Measurements of CAR T-cell populations are reported in units of CI for the purposes of working in a common scale. We used the conversion factor of 1 CI ≈ 10K cells. Cancer cells were seeded at 10K – 20K cells and left either untreated or treated with only CAR T-cells, with treatments occurring 24 hours after seeding and monitored for 6-8 days (Figure 1). CAR T-cell treatments were performed with effector-to-target ratios (E:T) of 1:4, 1:8, and 1:20. All experimental conditions were conducted in duplicate.

2.2 Effective interaction models

Challenges to the *model first* approach to systems biology are (1) deciding on a sufficiently comprehensive model that captures all pertinent phenomena and (2) fitting the selected model to available data. Researchers are tasked with justifying their decisions in selecting candidate models. Yet, a common feature of dynamical systems models are the presence of ratios of polynomials. Such terms in ODEs can be difficult for the convergence of optimization algorithms to global solutions due to the possible existence of multiple local solutions within the model parameter space (50). In such instances researchers must either rely on high performance computational methods, have collected a vast amount of

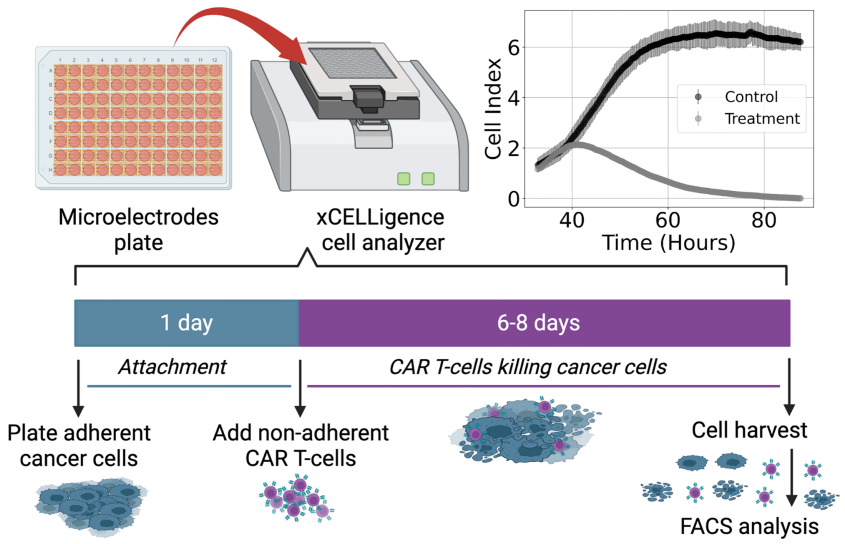

FIGURE 1
Diagram of experimental procedure highlighting use of microelectrode plates in an xCELLigence cell analyzer system and sample Cell Index (CI) measurements for control and treatment groups (E:T = 1:4). This system utilizes real-time voltage measurements to determine CI values representative of the adherent cancer cell population as a function of time. CAR T-cells are added following 24 hours of cancer cell expansion and attachment. After 6-8 days of monitoring the cancer cell growth and death dynamics, cells are harvested and enumerated using flow cytometry.

experimental data, or both. To address this problem, we utilize binomial expansions of candidate model terms under the assumptions of CAR T-cell treatment success and fast, irreversible reaction kinetics. In the following sections we present the space of possible models anticipated to characterize our experimental system, and the steps necessary to reduce the complexity of these candidate models.

The dynamical model that our experimental system is anticipated to follow is defined generically as,

$$\frac{dx}{dt} = \mathcal{G}_x(x) - x\mathcal{B}_x(y) \tag{1}$$

$$\frac{dy}{dt} = \mathcal{G}_y(y) + y\mathcal{R}(x) - x\mathcal{B}_y(y) \tag{2}$$

where $\mathcal{G}_x$ and $\mathcal{G}_y$ represent a growth-death model for the cancer cells, x, and the CAR T-cells, y. $\mathcal{B}_x$ and $\mathcal{B}_y$ represent a binding model for whether single or pairs of CAR T-cells attack individual cancer cells, and $\mathcal{R}$ represents a model for the CAR T-cell functional response. In the subsections below, we explore different families of models representing the terms in the above equations. Explicitly, we examine different types of (a) growth and death models, (b) functional response models, and (c) CAR T-cell-cancer cell binding models.

2.2.1 Growth and death

We consider three different growth-death models for both the cancer cells and CAR T-cells. These are logistic growth, and the weak and strong Allee effect models, presented as,

$$\mathcal{G}_x(x) = \begin{cases} \rho_x x\left(1 - \frac{x}{K_x}\right) & \textit{Logistic growth} \quad (3) \\ \rho_x x\left(1 - \frac{x}{K_x}\right)\left(1 + \frac{x}{A_x}\right) & \textit{Weak Allee effect} \quad (4) \\ \rho_x x\left(1 - \frac{x}{K_x}\right)\left(\frac{x}{B_x} - 1\right) & \textit{Strong Allee effect} \quad (5) \end{cases}$$

for $\mathcal{G}_x(x)$, and similarly for $\mathcal{G}_y(y)$. Here, ρ_x is the net growth rate, K_x is the population carrying capacity, A_x is a weak parameterization of deviations from logistic growth, and B_x is the threshold for population survival or death absent predation. All model parameters are assumed positive, with the added constraint that $K_x > B_x > 0$. We anticipate similar growth models for the CAR T-cells, $\mathcal{G}_y(y)$, with allowance of different models for the different cell types and model constants. Logistic growth is commonly favored for its simplicity in experimental systems (18, 24, 25), while there is growing evidence that Allee effects are required for accurate characterization of low density cancer cell populations (28, 29, 51, 52) or as the result of directed movement (53), the latter of which being an observable feature of CAR T-cell behavior using bright field imaging (18, 25).

In Figure 2, graphs of population growth rates versus population size and population size versus time are presented for each growth model and for a variety of initial conditions. Parameter values used were $\rho = 0.75$ hrs^{-1}, $K = 10$ CI, $A = 5$ CI, and $B = 5$ CI. Examination of the logistic growth model in Figure 2A and the weak Allee effect in Figure 2B demonstrates similar population saturation at the carrying capacity $K = 10$ CI, but a slight deviation between how the models reach saturation. Specifically, the weak Allee effect exhibits a reduced per capita growth rate at low population densities compared to logistic growth. Examination of Figure 2C demonstrates the crucial difference between the strong Allee effect and either of the logistic growth or weak Allee effect through the existence of a minimum population threshold, B, above which the population will persist, and below which the population will die off.

Due to the fact that SINDy produces discovered models in their polynomial form without factoring, or grouping of terms together, we must consider the un-factored polynomial form of each model. To determine appropriate constraints on the model coefficients, we will expand the growth models and factor by common monomials. Doing so for $\mathcal{G}_x(x)$ and dropping the subscript gives the following,

$$\mathcal{G}_x(x) = \begin{cases} \rho_x x - \frac{\rho_x}{K_x}x^2 & \textit{Logistic growth} \quad (6) \\ \rho_x x + \left(\frac{\rho_x}{A_x} - \frac{\rho_x}{K_x}\right)x^2 - \frac{\rho_x}{K_x A_x}x^3 & \textit{Weak Allee effect} \quad (7) \\ -\rho_x x + \left(\frac{\rho_x}{K_x} + \frac{\rho_x}{B_x}\right)x^2 - \frac{\rho_x}{K_x B_x}x^3 & \textit{Strong Allee effect} \quad (8) \end{cases}$$

and similarly for $\mathcal{G}_y(y)$. Here we can see that the coefficients for x and x^2 can be positive or negative, but the coefficients for x^3 must be

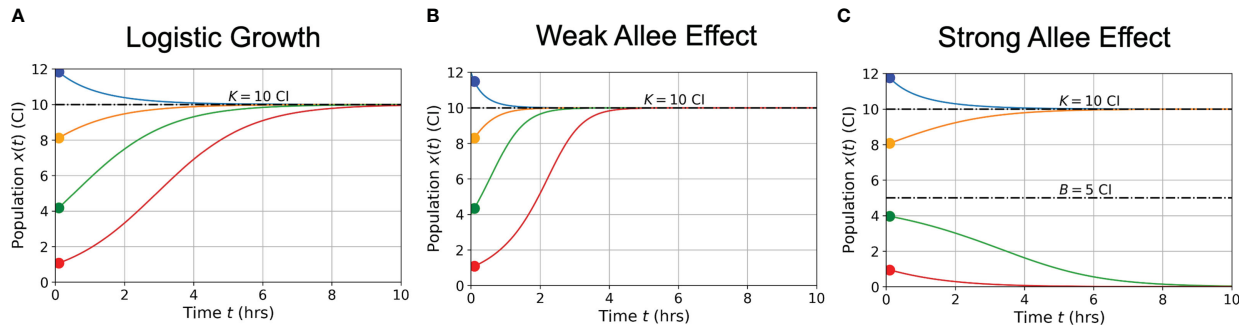

FIGURE 2
Conceptual graphs of population size (in cell index - CI) versus time (in hours - hrs) for the three growth models presented in Eqs. (3)-(5): logistic growth **(A)** weak Allee effect **(B)** strong Allee effect **(C)**. Model parameter values are: $\rho = 0.75$ hrs^{-1}, $K = 10$ CI, $A = 5$ CI, and $B = 5$ CI. Colors correspond to different initial cell populations, which are the same for each model presented (blue = 12 CI, orange = 8 CI, green = 4 CI, red = 1 CI).

fixed as negative values, where we have absorbed the minus signs in Eqs. (7)-(8) into ρ_x/K_xA_x.

2.2.2 CAR T-cell-cancer cell binding

Cell binding models characterize the rates of formation and disassociation of conjugate pairs of species, also referred to as interaction molecules (Figure 3A). These models historically are known as Hill-Langmuir functions for their originating studies in hemoglobin formation (54) and gas adsorption on material surfaces (55), yet perhaps are better known for their use in modeling enzyme reaction kinetics, or Michaelis-Menten kinetics (56). The same modeling principles have been extended to examine cell binding in T-cell and cancer cell interactions (2, 23, 30). An important challenge to the field of cancer immunotherapy modeling is characterizing higher-order cell binding dynamics. That is, the formation of conjugates that consist of multiple CAR T-cells attacking single cancer cells (Figure 3A). These cancer cell-CAR T-cell conjugates are hypothesized to form as either a consequence of increased effector to target ratios or as a result of increased antigen density on target cells. As our experiment uses one single cell line with a high and uniform antigen expression level of IL13Rα2, we assume on average all cancer cells have approximately the same antigen density. We thus focus our attention to experimental variation in the effector to target ratios.

Following the work of Li et al. (30), we incorporate *fast irreversible* single and double cell binding into our generic model landscape. Here, fast binding implies that conjugate formation and dissociation occur quickly enough to maintain equilibrium in the conjugate populations, I_1 and I_2, such that $dI_1/dt = 0$ and $dI_2/dt = 0$. While irreversible means that all conjugate formation leads to death, or $k_{-1}^{(1)} = 0$ and $k_{-1}^{(2)} = 0$. These assumptions are consistent with the conditions of relatively higher effector to target ratios, or high antigen densities on target cells. They also imply that a mixture of conjugates and dissociates may exist, but that the dynamics

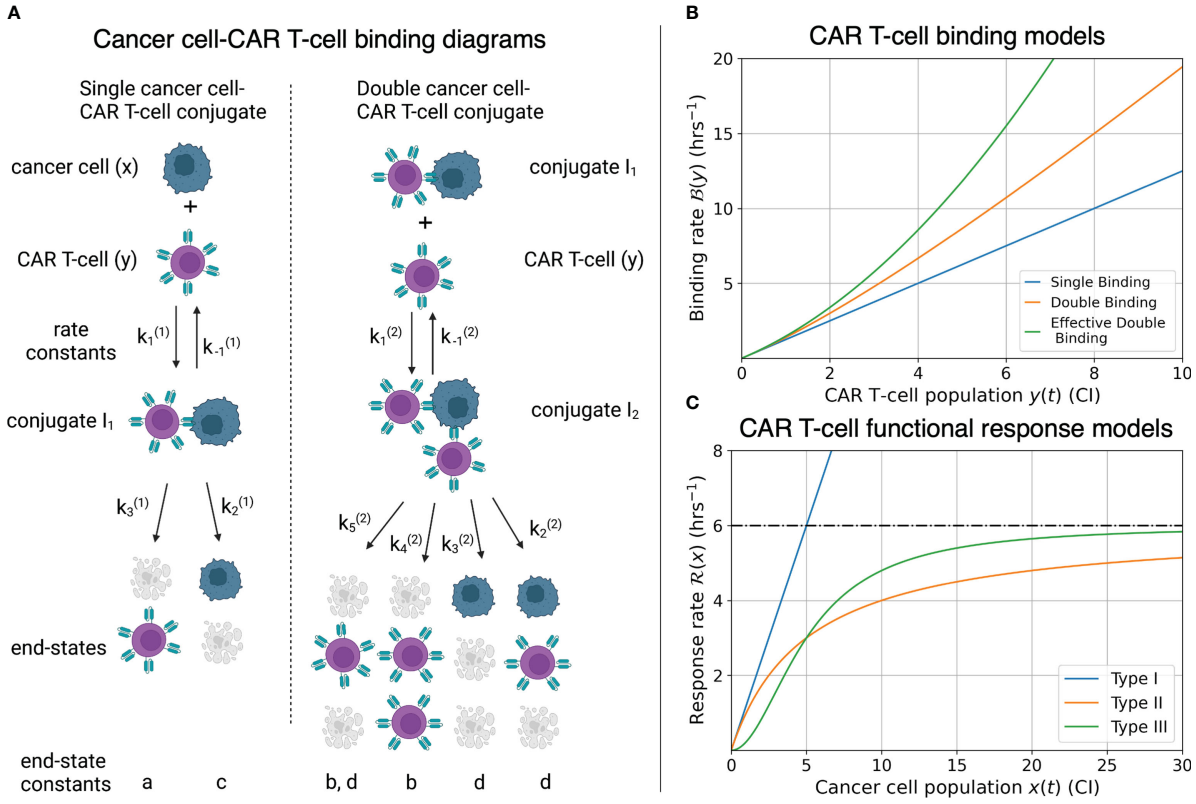

FIGURE 3

(A) Compartmental model for single and double CAR T-cell-cancer cell binding. Expressions for how rate constants ($k_i^{(j)}$) contribute to the growth or death of the cancer cell and CAR T-cell populations are presented in Eqs. (9)-(14). See (30) for further development and analysis of the cell binding model. **(B)** Graphs of binding rate versus CAR T-cell population for the single binding, double binding, and effective double binding models in Eqs. (9)-(12), (16), and (18). Model parameters for antigen bindings are: a = 20 CI^{-2} hrs^{-2} and h = 16 CI^{-1} hrs^{-1} for single binding; a = 20 CI^{-2} hrs^{-2}, b = 5 CI^{-3} hrs^{-2}, h = 16 CI^{-1} hrs^{-1}, and k = 2 CI^{-2} hrs^{-1} for double binding; and a = 20 CI^{-2} hrs^{-2}, b = 2.75 CI^{-3} hrs^{-2}, h = 16 CI^{-1} hrs^{-1}, and k = 2 CI^{-2} hrs^{-1} for effective double binding. These parameter values were chosen to highlight how well the effective double binding model can approximate both the single and double binding models at low CAR T-cell population values, y < 1 CI. Note that since the original double binding model in this scenario is concave-up, the effective double binding model parameters should be chosen to match concavity. This requirement sets a positivity constraint on the quadratic term in Eqs. (16) and (18). **(C)** Graphs of CAR T-cell response rates versus cancer cell population for different functional response models. Model parameters for functional responses are: p = 6/5 CI^{-1} hrs^{-1} for Type I; p =CI^{-1} and g = 5 CI for Types II and III. Note overlap of Types I and II functional responses for x < 1 CI, and distinct differences in concavity between Types II (negative) and III (positive) for x < 2 CI. These characteristics correspond to Type I and Type II functional responses being indistinguishable at low cancer cell populations, and Type II and Type III being differentiated by fast-then-slow response rates (Type II) versus slow-then-fast response rates (Type III).

happen such that the conjugate populations are fixed and do not change with time. Furthermore, we only consider the higher-order binding scenario of two CAR T-cells to one cancer cell. Solving for the contributions to the cancer and CAR T-cell populations due to binding dynamics results in,

$$\mathcal{B}_x(y) = \begin{cases} \frac{ay}{h} & \textit{Single Binding} \quad (9) \\ \frac{ay+by^2}{h+ky} & \textit{Double Binding} \quad (10) \end{cases}$$

$$\mathcal{B}_y(y) = \begin{cases} \frac{cy}{h} & \textit{Single Binding} \quad (11) \\ \frac{cy+dy^2}{h+ky} & \textit{Double Binding} \quad (12) \end{cases}$$

where the constants a, b, c, and d are defined in terms of the association rate constants, $k_1^{(1)}$ and $k_1^{(2)}$, and the death rate constants $k_2^{(1)}, k_3^{(1)}, k_2^{(2)}, k_3^{(2)}, k_4^{(2)}$, and $k_5^{(2)}$ from Figure 3A as follows,

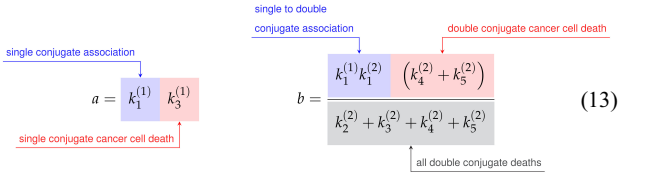

$$a = k_1^{(1)} k_3^{(1)} \qquad b = \frac{k_1^{(1)} k_1^{(2)} \left(k_4^{(2)} + k_5^{(2)}\right)}{k_2^{(2)} + k_3^{(2)} + k_4^{(2)} + k_5^{(2)}} \quad (13)$$

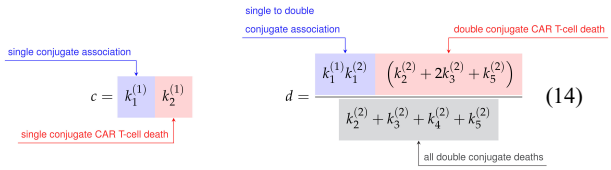

$$c = k_1^{(1)} k_2^{(1)} \qquad d = \frac{k_1^{(1)} k_1^{(2)} \left(k_2^{(2)} + 2k_3^{(2)} + k_5^{(2)}\right)}{k_2^{(2)} + k_3^{(2)} + k_4^{(2)} + k_5^{(2)}} \quad (14)$$

Finally, the constant h is the sum of the single conjugate death rates, $h = k_2^{(1)} + k_3^{(1)}$, and the constant k is simply a renaming of the double conjugate association rate, $k_1^{(2)}$. As the variable renaming is admittedly complicated, the constants a, b, c, and d are defined to quickly identify end states of conjugate formation and have been located next to their corresponding interaction products in Figure 3A.

The per-cancer cell binding models are graphed in Figure 3B. Model parameter values used for the single and double cell binding models in Eqs. (9)-(18) are: a = 20 CI^{-2} hrs^{-2}, and h = 16 CI^{-1} hrs^{-1} for single binding; and a = 20 CI^{-2} hrs^{-2}, b = 5 CI^{-3} hrs^{-2}, h = 16 CI^{-1} hrs^{-1}, and k = 2 CI^{-2} hrs^{-1} for double binding. We highlight that we are restricting ourselves to scenarios where increases in the CAR T-cell population during a given trial leads to increases in the likelihood of double binding, which results in super-linear increase of per-cancer cell binding. This restriction enforces concavity of the effective double cell binding model which we explore next. It is possible for the double binding model to exhibit a sub-linear increase in per-cancer cell antigen binding as the CAR T-cell population increases, and an overall decrease in cancer cell killing. However, this scenario does not agree with our experimental data of increased killing with increased effector-to-target ratios.

Importantly, the rational forms of the binding rates typically complicate determination of parameter values in conventional dynamical modeling. To reduce model complexity, we take advantage of potential differences between the rates of conjugate association and conjugate death that can give rise to simplifications. If the product of the CAR T-cell population and the rate of forming double conjugates, ky, is small compared to the sum of the rates of single conjugate deaths, h, then $ky/h < 1$, and we can again perform a binomial expansion in the cell binding denominators. A second way of interpreting this condition is to require the number of CAR T-cells to remain small compared to the ratio of the rate of double conjugate formation to the sum of the rates of single conjugate deaths, $y < h/k$. Performing the binomial expansion and truncating again at $\mathcal{O}(y^2)$ results in the following effective models of cell binding,

$$\mathcal{B}_x(y) = \begin{cases} \frac{ay}{h} & \textit{Effective Single Binding} \quad (15) \\ \frac{ay}{h} + \frac{(bh-ak)y^2}{h^2} & \textit{Effective Double Binding} \quad (16) \end{cases}$$

$$\mathcal{B}_x(y) = \begin{cases} \frac{cy}{h} & \textit{Effective Single Binding} \quad (17) \\ \frac{cy}{h} + \frac{(dh-ck)y^2}{h^2} & \textit{Effective Double Binding} \quad (18) \end{cases}$$

Here the effective double conjugate antigen binding model takes the form of the exact single conjugate binding model plus a correction due to double conjugate formation. Eqs. (16) and (18) are graphed in Figure 3B, using the parameter values of a = 20 CI^{-2} hrs^{-2}, b = 2.75 CI^{-3} hrs^{-2}, h = 16 CI^{-1} hrs^{-1}, and k = 2 CI^{-2} hrs^{-1}. These values are chosen to demonstrate that the effective double binding model can accurately approximate both the exact single and double binding models for small CAR T-cell populations, y < 1CI. Importantly, we note that if the parameter values b or d are sufficiently small, corresponding to low double conjugate CAR T-cell or cancer cell death rates, then the quadratic terms in Eqs. (16) and (18) will be negative, and the concavity of the effective double binding model deviate significantly from the exact model. This phenomenological consideration of the effective models sets an important constraint on the positivity of the coefficients for the quadratic terms in Eqs. (16) and (18), which we will revisit in Section 2.3.

2.2.3 Functional response

We next consider the first three types of functional response models that characterize how the CAR T-cells respond, or expand, in the presence of cancer cells. These models are defined as,

$$\mathcal{R}(x) = \begin{cases} px & \textit{Type I} \quad (19) \\ \frac{px}{g+x} & \textit{Type II} \quad (20) \\ \frac{px^2}{g^2+x^2} & \textit{Type III} \quad (21) \end{cases}$$

where p is the predator response, or CAR T-cell response rate, and g is the prey population density threshold at which predator behavior changes (e.g. fast-to-slow or slow-to-fast rates of killing). Functional responses model changes in predator hunting due to the prey density, generally defined with respect to some prey population threshold, here denoted as g. The population dependence on predator hunting behavior can also be interpreted as a handling time for distinguishing between time spent seeking prey, or recognizing cancer cells, and time spent consuming and attacking prey (19, 26, 27).

The three types of functional responses are graphed in Figure 3C. In a Type I functional response, the predator response is constant for all prey population sizes. The interpretation of this response is that there are no differences in time or cost between all predator functions (searching and capture). In a Type II functional response the predator response is linear at low prey density (mirroring a Type I behavior) yet saturates at high prey density. Finally, in a Type III functional response the predator response is low at low prey densities, reflecting the potential for cancer cells to escape immune surveillance, yet again saturates at high prey densities, with a linear response at intermediate prey densities.

As with the binding rate models, the rational forms of Types II and III functional responses present challenges to model discovery methods. Thus, we assume a significant level of effectiveness in CAR T-cell treatment such that the cancer cell population remains relatively low with respect to the functional response threshold, that is $x < g$, or $x/g < 1$. CAR T-cell effectiveness is demonstrated in Figure 1, where the control cancer cell population is shown to achieve a maximum population of approximately 6.5 CI, while the treatment population of $E{:}T$ = 1:4 reaches a maximum population of approximately 2 CI. The approximation condition permits the use of a binomial expansion about $x = 0$ on the denominators for the Types II and III functional responses, resulting in,

$$\mathcal{R}(x) = \begin{cases} px & Type\ \ I \quad (22) \\ \frac{px}{g}\left(1 - \frac{x}{g} + \frac{x^2}{g^2} + \sum_{j=3}^{\infty}(-1)^j\left(\frac{x}{g}\right)^j\right) & Type\ \ II \quad (23) \\ \frac{px^2}{g^2}\left(1 - \frac{x^2}{g^2} + \frac{x^4}{g^4} + \sum_{j=3}^{\infty}(-1)^j\left(\frac{x^2}{g^2}\right)^j\right) & Type\ \ III \quad (24) \end{cases}$$

Further assuming that contributions to the functional response models of $\mathcal{O}(x^3/g^3)$ or greater are negligible, we terminate the expansions at $\mathcal{O}(x^2/g^2)$ to arrive at the following effective functional response models,

$$\mathcal{R}(x) = \begin{cases} px & Type\ \ I \quad (25) \\ \frac{px}{g} - \frac{px^2}{g^2} & Type\ \ II \quad (26) \\ \frac{px^2}{g^2} & Type\ \ III \quad (27) \end{cases}$$

It is important to highlight that the leading order term for the expansion for a Type II functional response is indistinguishable from a Type I functional response. This feature is reflected by the overlap in the graphs of the Type I and Type II responses presented in Figure 3, where the cancer cell population is small, $x \in [0, 1]$CI, compared to the value of g = 5 CI. As the cancer cell population increases, the density dependence of the CAR T-cells starts to take effect as demonstrated by the parabolic contribution of the Type II response. In contrast to this, the expansions for functional responses of Types II and III are significantly unique from one another. Specifically, only expansions for Type II can lead to odd-powered terms in x, and although both expansions can express similar even-powered terms, they come with different concavities. That is, at small cancer populations the Type II functional response is characterized as a concave down parabola, while the Type III functional response is characterized as a concave up parabola. This difference regarding the positivity of the terms that are of second-order dependence in x corresponds to the different density dependent behaviors of the CAR T-cells at small cancer cell populations, specifically that Type II is a fast-to-slow response rate while Type III is a slow-to-fast response rate.

By performing the approximations used to derive Eqs. (26)-(27), and using truncated terms, we have reduced the complexity of the functional response terms. This step will simplify the process of model discovery. However, since this step assumes that the prey population remains small compared to the functional response threshold, the number of terms needed in Eqs. (23)-(24) for accurate characterization of the system dynamics may vary as a result of experimental variation in the effector to target ratio of the CAR T-cells and the cancer cells. This variation in the effector to target ratio may also influence the structure of other interaction terms, specifically those pertaining to the single or paired binding dynamics.

2.2.4 Landscape of effective models

To gain a broader perspective of the overall form of our ODE models, we substitute the effective models for functional responses and antigen binding into Eqs. (1)-(2), arriving at,

$$\frac{dx}{dt} = \mathcal{G}_x(x) - \tilde{a}xy - \tilde{b}xy^2 \quad (28)$$

$$\frac{dy}{dt} = \mathcal{G}_y(y) \pm \alpha xy \pm \beta x^2 y - \tilde{c}xy^2 \quad (29)$$

where $\mathcal{G}$ again represents any of the potential growth-death models under consideration, $\tilde{a} = a/h$ and $\tilde{b} = (bh - ak)/h^2$ are redefined constants (both assumed to be positive) for the coefficients of the effective single and double binding models for the cancer cells, $\alpha xy = (p/g - c/h)xy$ and represents the combination of first order terms for CAR T-cell response and single binding, $\beta x^2 y = (p/g^2)xy$ and represents the potential second order term from the CAR T-cell response, and $\tilde{c}xy^2 = ((dh - ck)/h^2)xy^2$ represents the effective double binding model for the CAR T-cells. We have explicitly used ± notation to indicate that we do not know *a priori* the signs for the xy and x^2y terms in Eq. (29), as these are determined by the relative contributions of Type I and first order Type II-like CAR T-cell responses and single antigen binding for the xy term, and whether or not second order Type II or first order Type III CAR T-cell response is occurring for the x^2y term. The benefit of the approach demonstrates the presence and/or sign conventions of the various model coefficients that we determine using the SINDy model discovery

algorithm can be directly interpreted in terms of different underlying biological phenomena.

2.3 Model discovery

Our implementation of the model discovery techniques of dynamic mode decomposition and sparse identification of nonlinear dynamics (SINDy) is performed in two stages. First is latent variable analysis, the extraction of the latent variable representing the CAR T-cell population from the time-varying cancer cell population. The second step is implementation of SINDy, whereupon the functional terms of the underlying models describing the dynamical system are determined.

2.3.1 Latent variable analysis

Despite having only measured the initial and final CAR T-cell populations, we can utilize latent variable analysis to infer the hidden CAR T-cell dynamics from the cancer cell dynamics. We do this using the delay coordinate embedding of Taken's Theorem to reconstruct the attractor of the system that is known to exist in more dimensions than those measured (13, 15, 57). The first step in this approach is to assemble a Hankel matrix, H, by stacking delayed time-series of the cancer cell measurements $x(t)$ as follows,

$$H = \begin{bmatrix} x(t_1) & x(t_2) & x(t_3) & \cdots & x(t_{N-(m-1)\tau}) \\ x(t_{1+\tau}) & x(t_{2+\tau}) & x(t_{3+\tau}) & \cdots & x(t_{N-(m-2)\tau}) \\ x(t_{1+2\tau}) & x(t_{2+3\tau}) & x(t_{3+4\tau}) & \cdots & x(t_{N-(m-3)\tau}) \\ \vdots & \vdots & \vdots & \ddots & \vdots \\ x(t_{1+(m-1)\tau}) & x(t_{2+(m-2)\tau}) & x(t_{3+(m-3)\tau}) & \cdots & x(t_N) \end{bmatrix} \quad (30)$$

where τ, known as the embedding delay, represents the size of the time-delay we use, and m, known as the embedding dimension, represents both the number of rows that we assemble in the Hankel matrix and, importantly, the number of anticipated latent variables we expect to find.

To minimize the effects of experimental noise on the results of Taken's Theorem, we splined our cancer cell trajectories and re-sampled at the same experimental sampling rate of one measurement per 15 minutes. The function *smooth.spline* from the programming language **R** was used to perform the splining. This function uses cubic splines to approximate trajectories, with a penalty term to control for trajectory curvature. The number of knots used to spline each trajectory were determined by inspection, and are recorded in the analysis code available at https://github.com/alexbbrummer/CART_SINDy. Further details on the splining methods used are available in (57).

To determine optimal values for τ and m, we can use two separate formulae to inform the decisions (58). The optimal time delay is determined by the value of τ which minimizes the mutual information between measurements. This is done by dividing the interval $[x_{min}, x_{max}]$ into j equally sized partitions, and calculating the probability P_k that a measurement of the time series is in the k^{th} partition, and the probability $P_{h,k}$ that a measurement x_i is in the h^{th} partition while the neighboring measurement $x_{i+\tau}$ is in the k^{th} partition. Mutual information is given by

$$I(\tau) = \sum_{h=1}^{j}\sum_{k=1}^{j} - P_{h,k}(\tau) \log \frac{P_{h,k}(\tau)}{P_h P_k}. \quad (31)$$

The optimal time-delay to use for a given time series is selected by finding the value of τ which results in the first minimum value in mutual information, or $\arg \min|_\tau \{I(\tau)\}$. A graph of mutual information versus time delay is presented in Supplemental Figure S1A. For our cancer cell time series data, this optimal time delay value was found to be $\tau = 1$.

To determine the embedding dimension, m, we calculate the number of false nearest neighbors to a given measurement as the time series is embedded in successively greater dimensional spaces. This calculation is done to ensure that the attractor constructed from the latent variables remains smooth upon embedding. We perform the calculation iteratively by starting with a point $p(i)$ in an m -dimensional embedding, and identifying a neighboring point $p(j)$ such that the distance between and $p(j)$ is less than a constant value typically chosen as the standard deviation of the data. Next, the normalized distance between the points $p(i)$ and $p(j)$ in the $m+1$ -dimensional embedding is calculated using the following expression,

$$R_i = \frac{|x(t_{i+m\tau}) - x(t_{j+m\tau})|}{||p(i) - p(j)||} \quad (32)$$

R_i is calculated across the entire time series and iteratively for greater embeddings, $m = 1, 2, 3, \ldots$. False nearest neighbors are identified when $R_i > R_{threshold}$, where $R_{threshhold} = 10$ has been identified as satisfactory for most datasets (58). The ideal embedding dimension m is finally determined as that which results in a negligible fraction of false nearest neighbors. In Supplementary Figure S1B we present the calculated fraction of false nearest neighbors versus embedding the dimension. For our dataset, we identified $m = 2$ as the ideal embedding dimension, indicating the existence of one latent variable that we interpret as representing the CAR T-cell population.

Using values of $\tau = 1$ for the time delay and $m = 2$ for the embedding dimension results in the following form of the Hankel matrix,

$$H = \begin{bmatrix} x(t_1) & x(t_2) & x(t_3) & \cdots & x(t_{N-1}) \\ x(t_2) & x(t_3) & x(t_4) & \cdots & x(t_N) \end{bmatrix} \quad (33)$$

To extract the latent variable that represents the CAR T-cell time series, we perform a singular value decomposition of the Hankel matrix, $H = U\Sigma V^*$ (13, 15). Here, the columns of V represent scaled and standardized versions of both the original data in the first column, and approximations of the latent data in the subsequent columns. As our experimental procedure measured the initial and final CAR T-cell populations, our final step was to re-scale and offset the latent CAR T-cell variable extracted from the second column of V. We note that latent variable analysis is conducted on each trial for each experimental condition separately. In Figure 4 we present the measured cancer cells and CAR T-cells in addition to the discovered latent CAR T-cell time series for each effector to target ratio considered for the first of the two duplicate trials. In the

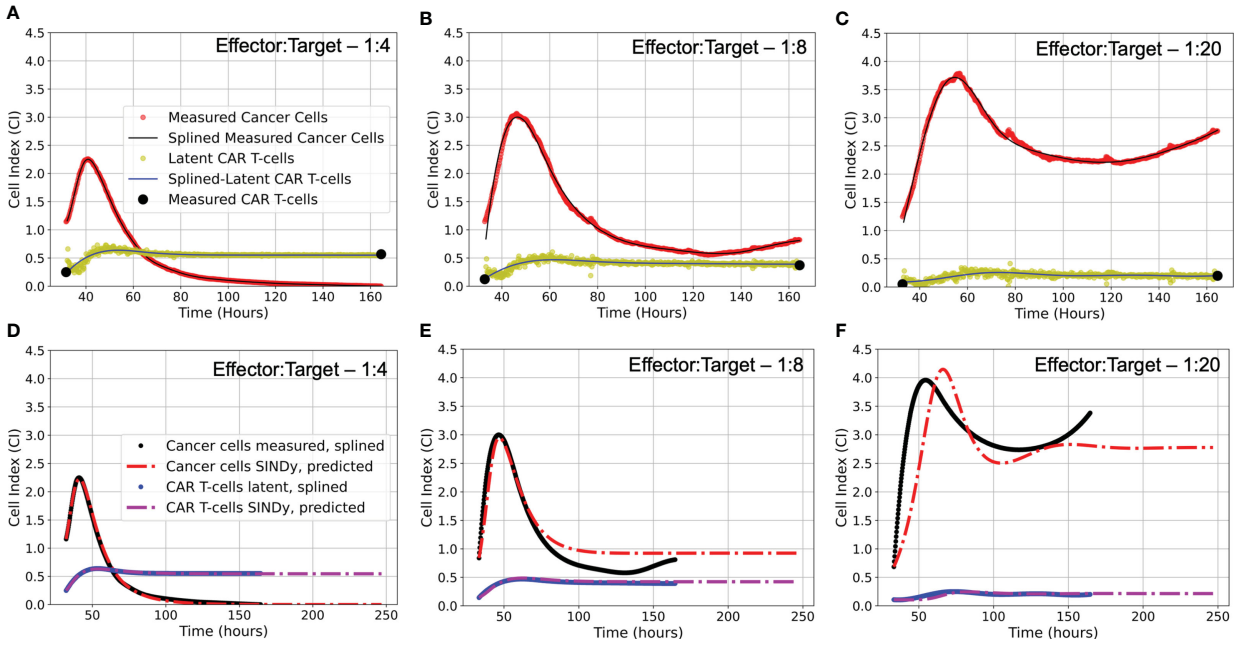

FIGURE 4
(A-C) Latent variable analysis results for first of two experimental replicates each E:T ratio examined. Presented are the cancer cell index measurements from the xCELLigence machine in red, overlaid with the splined measurements for the cancer cells in black; the two endpoint measurements for the CAR T-cell levels enumerated by flow cytometry in black, with the CAR T-cell population trajectory as determined by latent variable analysis in yellow, overlaid with the splined CAR T-cell trajectory in blue. Note that despite the CAR T-cell populations being measured with flow cytometry, we have converted levels to units of Cell Index for ease of comparison with the cancer cells, using a conversion factor of 1 CI ≈ 10,000 cells. **(D-F)** Predicted trajectories of discovered models compared to splined measurements of cancer cells and CAR T-cells for same data presented in **(A-C)**. Splined cancer cell and CAR T-cell measurements are in black and blue, respectively. Predicted trajectories for cancer cells are the red dot-dashed lines, while the CAR T-cells are the purple dot-dashed lines. To examine stability of SINDy-discovered models, both simulations and forward predictions are presented to show steady-state behavior. Note that the best fits between predictions and measurements occur in the high E:T scenario, where assumptions made regarding treatment success and low cancer cell populations in determining model candidate terms are best adhered. As the E:T ratios get smaller, increasing deviation between discovered model predictions and splined measurements can be qualitatively observed. This is likely due to weakening of assumptions of treatment success and low cancer cell populations associated with the low E:T conditions. See Supplemental Material Figure S2 for equivalent latent variable analysis results and SINDy-predicted trajectories for the second set of experimental replicates.

Supplemental Material Figure S2 we present the results of the latent variable analysis for the second of the two duplicate trials.

2.3.2 Sparse identification of non-linear dynamics

SINDy is a data-driven methodology that discovers dynamical systems models through symbolic regression (13, 15). From a conceptual perspective, SINDy allows for the transformation of an analytical, first-order, non-linear dynamical systems model, expressed as

$$\frac{d}{dt}x(t) = f(x(t)) \tag{34}$$

to a linearized matrix-model, expressed as

$$\dot{X} = \Theta(X)\Xi \tag{35}$$

where $\dot{X}$ are numerical time-derivatives of our measured data, $\Theta(X)$ is a library of candidate functions that may describe the data and is evaluated on the measured data, and Ξ consists of the coefficients for the model terms from $\Theta(X)$ that describe the time-varying data $\dot{X}$. The objective of SINDy is to identify the sparsest version of Ξ, where sparsity is defined as the compromise between fewest number of non-zero terms with the greatest level of accuracy. In the context of our measurements for populations of cancer cells, $x(t)$, and CAR T-cells, $y(t)$, and the anticipated models for cell growth and interactions, $\dot{X}$ takes the following form,

$$\dot{X} = \begin{bmatrix} \dot{x}^T(t_1) \\ \dot{x}^T(t_2) \\ \vdots \\ \dot{x}^T(t_N) \end{bmatrix} = \begin{bmatrix} \dot{x}(t_1) & \dot{y}(t_1) \\ \dot{x}(t_2) & \dot{y}(t_2) \\ \vdots & \vdots \\ \dot{x}(t_N) & \dot{y}(t_N) \end{bmatrix} \tag{36}$$

And $\Theta(X)$ is expressed as,

$$\Theta(X) = \begin{bmatrix} | & | & | \\ X & X^2 & X^3 \\ | & | & | \end{bmatrix} \tag{37}$$

$$\Theta(X) = \begin{bmatrix} x(t_1) & y(t_1) & x(t_1)^2 & x(t_1)y(t_1) & y(t_1)^2 & x(t_1)^3 & x(t_1)^2y(t_1) & x(t_1)y(t_1)^2 & y(t_1)^3 \\ x(t_2) & y(t_2) & x(t_2)^2 & x(t_2)y(t_2) & y(t_2)^2 & x(t_2)^3 & x(t_2)^2y(t_2) & x(t_2)y(t_2)^2 & y(t_1)^3 \\ \vdots & \vdots & \vdots & \vdots & \vdots & \vdots & \vdots & \vdots & \vdots \\ x(t_N) & y(t_N) & x(t_N)^2 & x(t_N)y(t_N) & y(t_N)^2 & x(t_N)^3 & x(t_N)^2y(t_N) & x(t_N)y(t_N)^2 & y(t_1)^3 \end{bmatrix} \tag{38}$$

By solving the matrix-inverse problem in Eq. (35), we can find the column vectors Ξ that determine the coefficients for the model terms ξ that form the non-linear dynamical system best describing

the measured data. To construct $\dot{X}$ and $\Theta(X)$ from our duplicate trial experiments, the data from the repeated trials is stacked row-wise. Thus, only a single model will be discovered to explain all data for a given set of experimental conditions (e.g. effector-to-target ratios). Having repeat measurements is an important aspect for SINDy to converge on an accurate model, thus performing SINDy on averages of experimental trials undermines performance. For experimental conditions that have an abundance of experimental replicates, an AI-inspired division of data into training and testing sets can be conducted (59).

Once $\dot{X}$ and $\Theta(X)$ have been constructed, a simple least-squares algorithm for solving Eq. (35) will result in a dense coefficient vector Ξ, thus we enforce sparsity of the coefficient vector Ξ through the method of sparse relaxed regularized regression (SR3) (60), where we seek optimization of the expression,

$$\min_{\Xi,W} \frac{1}{2}||\dot{X} - \Theta(\Xi)||^2 + \lambda R(W) + \frac{1}{2\nu}||\Xi - W||^2 \tag{39}$$

where W is the relaxed coefficient matrix that approximates Ξ, $R(W)$ is the regularization of W, and ν and λ are hyper parameters that control how precisely W approximates Ξ and the strength of the regularization, respectively. For our problem, we chose to regularize under the ℓ 1-norm with $\nu = 1 \times 10^{-5}$. To determine the value of λ, we followed the approach taken in (39) in which we repeat the analysis for a range of λ values from $\lambda \in [10^{-8}, 10^{1}]$ to calculate Pareto fronts between the root-mean-squared error between the measured and subsequently predicted values of X and the number of active terms from our library. In Supplementary Figure S3 we present Pareto fronts for each of the experimental conditions for the varying effector to target ratios.

As discussed in Section 2.2, there are a variety of constraints we can expect for possible coefficients based on expected signs, or the absence of particular terms. An extension to SINDy allows for the incorporation of these constraints to ensure spurious terms are not discovered (61).

To make clear the constraints that were imposed, we can re-write Eq. (35) symbolically and in terms of the coefficients $\xi_{i,j}$ as,

$$\dot{x} = \xi_{1,1}x + \xi_{1,2}y + \xi_{1,3}x^2 + \xi_{1,4}xy + \xi_{1,5}y^2 + \xi_{1,6}x^3 + \xi_{1,7}x^2y + \xi_{1,8}xy^2 + \xi_{1,9}y^3 \tag{40}$$

$$\dot{y} = \xi_{2,1}x + \xi_{2,2}y + \xi_{2,3}x^2 + \xi_{2,4}xy + \xi_{2,5}y^2 + \xi_{2,6}x^3 + \xi_{2,7}x^2y + \xi_{2,8}xy^2 + \xi_{2,9}y^3 \tag{41}$$

Then, the constraints that are imposed as per the anticipated effective models from Section 2.2 are,

$$\xi_{1,2} = 0 \quad \xi_{1,4} < 0 \quad \xi_{1,5} = 0 \quad \xi_{1,6} < 0 \tag{42}$$

$$\xi_{1,7} = 0 \quad \xi_{1,8} < 0 \quad \xi_{1,9} = 0 \quad \xi_{2,1} = 0 \tag{43}$$

$$\xi_{2,3} = 0 \quad \xi_{2,6} = 0 \quad \xi_{2,8} < 0 \quad \xi_{2,9} < 0 \tag{44}$$

while the other 6 coefficients in $\xi_{i,j}$ are left to freely vary.

Implementation of SINDy SR3 with constraints was performed using PySindy, a package designed for a wide array of implementations of the SINDy algorithm for spatio-temporal model discovery written in the programming language Python (16, 17). Included in the Supplemental Material are the associated datasets and Jupyter notebooks used for this study.

Finally, we highlight that the implementation of SINDy which we are relying on is designed specifically for explicit ordinary differential equations. An extension of SINDy exists for discovering ODEs with ratios of polynomials (39, 40), however this variation requires a significantly greater volume of data than that which we could collect. This is the underlying motivation behind our efforts to derive the effective models, thereby converting them into explicit ODEs and making effective usage of the volume of experimental data available by the study methods most usable for model discovery.

3 Results

3.1 Discovered models and simulated comparison

Upon implementing SINDy on the CAR T-cell cancer cell killing data and performing the Pareto front analysis described in Section 2.3, we identified three distinct models describing the experimental data. Model selection is presented in Supplementary Figure S3, where we present the tradeoffs between model complexity, represented by the number of activated library terms, and either the threshold λ or the root-mean-squared-error between the measured data and simulated data for each identified model. Our examination of the Pareto fronts found models with eight terms for E:T of 1:4, and 1:8, and a six term model for an E:T of 1:20. Below we summarize each of these models and in relation to how well they predict the measured data in Figure 4. We synthesize the coefficients and associated model categories for growth in Table 1 and for the CAR T-cell functional response and cell binding in Table 2.

3.1.1 High E:T discovered model

For the E:T = 1:4 data, the SINDy-discovered model takes the following form,

$$\frac{dx}{dt} = 0.121x + 0.061x^2 - 0.018x^3 - 0.593xy^2 \tag{45}$$

$$\frac{dy}{dt} = 0.191y - 0.351y^2 + 0.035xy - 0.009x^2y \tag{46}$$

Factoring the terms related to single-species growth, we arrive at,

$$\frac{dx}{dt} = \underbrace{0.121x\left(1 - \frac{x}{4.792}\right)\left(\frac{x}{1.421} + 1\right)}_{\text{Weak Allee}} \underbrace{- 0.593xy^2}_{\text{Double Binding}} \tag{47}$$

$$\frac{dy}{dt} = \underbrace{0.191y\left(1 - \frac{y}{0.544}\right)}_{\text{Logistic}} \underbrace{+ 0.035xy - 0.009x^2y}_{\text{Type II Response}} \tag{48}$$

TABLE 1 Coefficients for discovered growth model terms across all effector to target ratios.

E:T	Growth of cancer cells (x)	Growth rate ρ_x (hrs^{-1})	Carrying capacity K_x (CI)	Allee constants A_x,B_x (CI)	Growth of CAR T-cells (y)	Growth rate ρ_y (hrs^{-1})	Carrying capacity K_y (CI)	Allee constants A_y,B_y (CI)
1:4	Weak Allee	0.121	4.792	1.421	Logistic	0.191	0.544	–[1]
1:8	Weak Allee	0.237	6.413	3.08	Logistic	0.112	0.313	–
1:20	Logistic	0.15	12.5	–	–	–	–	–

[1] – indicates term not discovered.

From Eqs. (47)-(48) we can interpret the discovered types of growth models and interactions. For cancer cell growth in Eq. (47), the observable structure indicates a weak Allee effect, with a growth rate of $\rho = 0.121$ hrs^{-1}, a carrying capacity of $K = 4.792$ CI, and an Allee constant of $A = 1.421$ CI. For the CAR T-cells we find a logistic growth model with growth rate $\rho = 0.191$ hrs^{-1} and carrying capacity $K = 0.544$ CI. From the coefficients of $\alpha = 0.051$ CI^{-1} hrs^{-1} on xy and $\beta = -0.009$ CI^{-2} hrs^{-1} on x^2y for the CAR T-cells, we can infer a Type II functional response as the signs are positive and negative, respectively. Finally, the presence of an xy^2 term in the cancer cells with a coefficient of $\tilde{b} = 0.063CI^{-2}$ hrs^{-1} indicates the occurrence of double binding, notably in the absence of both the xy term in the cancer cells and the xy^2 term in the CAR T-cells.

3.1.2 Medium E:T discovered model

The SINDy-discovered model for the E:T = 1:8 data takes the following form,

$$\frac{dx}{dt} = 0.237x + 0.04x^2 - 0.012x^3 - 0.626xy \tag{49}$$

$$\frac{dy}{dt} = 0.112y - 0.358y^2 + 0.051xy - 0.009x^2y \tag{50}$$

Factoring the terms related to single-species growth, we arrive at,

$$\frac{dx}{dt} = \underbrace{0.237x\left(1-\frac{x}{6.413}\right)\left(\frac{x}{3.08}+1\right)}_{\text{Weak Allee}} \underbrace{-0.626xy}_{\text{Single Binding}} \tag{51}$$

$$\frac{dy}{dt} = \underbrace{0.112y\left(1-\frac{y}{0.313}\right)}_{\text{Logistic}} \underbrace{+0.051xy - 0.009x^2y}_{\text{Type II Response}} \tag{52}$$

The model discovered for medium E:T is largely similar to that at high E:T. A weak Allee effect in growth is observed for the cancer cells, with growth rate $\rho = 0.237$ hrs^{-1}, carrying capacity $K = 6.413$ CI, and Allee constant $A = 3.08$ CI, while a logistic growth is observed for the CAR T-cells with growth rate $\rho = 0.112$ hrs^{-1} and carrying capacity $K = 0.313$ CI. We also observe a Type II CAR T-cell functional response, again indicated from the sign of the coefficients of $\alpha = 0.051$ CI^{-1} hrs^{-1} and $\beta = -0.01$ CI^{-2} hrs^{-1} on the xy and xy^2 terms being positive and negative, respectively. Unlike the high E:T scenario however, here we find evidence only of single binding from the sole presence of an xy term in the cancer cells with a coefficient of $\tilde{a} = -0.626$ CI^{-1} hrs^{-1}.

3.1.3 Low E:T discovered model

Finally, for the E:T = 1:20 data the discovered model is,

$$\frac{dx}{dt} = 0.150x - 0.012x^2 - 0.545xy \tag{53}$$

$$\frac{dy}{dt} = -0.002xy + 0.005x^2y - 0.063xy^2 \tag{54}$$

Factoring the terms related to single-species growth, we arrive at,

$$\frac{dx}{dt} = \underbrace{0.15x\left(1-\frac{x}{12.5}\right)}_{\text{Logistic}} \underbrace{-0.545xy}_{\text{Single Binding}} \tag{55}$$

$$\frac{dy}{dt} = \underbrace{-0.002xy + 0.005x^2y}_{\text{Type III Response}} \underbrace{-0.063xy^2}_{\text{Double Binding}} \tag{56}$$

In this scenario we find significantly different growth and interaction models. The cancer cells show logistic growth, with growth rate $\rho = 0.15$ hrs^{-1} and carrying capacity $K = 12.5$ CI, while the CAR T-cells have no growth model. This time, as the signs for the coefficients of $\alpha = -0.002$ CI^{-1} hrs^{-1} and $\beta = 0.005$ CI^{-2} hrs^{-1} on the xy and x^2y terms for the CAR T-cells are now negative and positive, respectively, we infer a Type III functional response. Interestingly, we find a mixture of indicators for both single binding and double binding. This comes from the presence of only the xy term in the cancer cell model with a coefficient of $\tilde{a} = -0.545$ CI^{-1} hrs^{-1}, and of an xy^2 term in the CAR T-cell model with a coefficient of $\tilde{c} = -0.063$ CI^{-2} hrs^{-1}.

All three E:T ratios of 1:4, 1:8, and 1:20 resulted in discovered models that accurately characterized the data, with root-mean-squared-errors of 0.02, 0.195, and 0.359, respectively. We highlight the discovery of consistent growth models of a weak Allee effect for the cancer cells and logistic growth for the CAR T-cells for the E:T ratios of 1:4 and 1:8. Importantly, the growth rates and carrying capacity for these scenarios were found to be comparable across E:T ratios. Interestingly, we observe a Type II

TABLE 2 Coefficients for discovered interaction model terms across all effector to target ratios.

E:T	Response of CAR T-cells	Type I & II response α (Cl^{-1} hrs^{-1})	Type II & III response β (Cl^{-2} hrs^{-1})	Cancer cell-CAR T-cell binding	Single binding $\tilde{a}$ (Cl^{-1} hrs^{-1})	Double binding $\tilde{b}$ (Cl^{-2} hrs^{-1})	Double binding $\tilde{c}$ (Cl^{-2} hrs^{-1})
1:4	Type II	0.035	−0.009	Double	–[1]	0.593	–
1:8	Type II	0.051	−0.009	Single	0.626	–	–
1:20	Type III	−0.002	0.005	Mixed	0.545	–	0.063

[1] – indicates term not discovered.

functional response in the CAR T-cells functional response for both E:T = 1:4 and 1:8, and a transition to Type III for E:T = 1:20. Similarly, our discovered models indicate a transition from double to single binding as the E:T ratio changed from 1:4 to 1:8, and a model with mixed single and double binding terms was discovered for the E:T = 1:20.

3.2 Comparison with CARRGO model

We compared the *data first* model discovery methodology of SINDy against the CARRGO model, a traditional *model first* approach originally used to analyze and interpret the CAR T-cell killing dynamics (18, 25). The CARRGO model is defined as,

$$\frac{dx}{dt} = \underbrace{\rho_x x\left(1-\frac{x}{K_x}\right)}_{\text{Logistic}} \underbrace{-\tilde{a}xy}_{\text{Single Binding}} \tag{57}$$

$$\frac{dy}{dt} = \underbrace{-\theta y}_{\text{Exponential Death}} \underbrace{+\alpha xy}_{\text{Type I Response}} \tag{58}$$

where we have expressed the parameter variables of the CARRGO model in terms of those used in the SINDy model for ease of comparison. From here we can see that the CARRGO model assumes logistic growth in the cancer cells, single binding between the cancer cells and CAR T-cells, a Type I functional response in the CAR T-cells, and exponential CAR T-cell death.

In Figure 5 are graphs of the best-fit versions of both the CARRGO model and SINDy discovered models for each E:T ratio. These fits were performed using the Levenberg-Marquadt optimization (LMO) algorithm, which requires initial guesses and bounds for each model parameter value. For the CARRGO model published parameter values were used for the starting guesses, while for the SINDy discovered models the discovered parameter values served as the guesses. Upper and lower bounds on the LMO search space were set at 80% and 120% of the originally identified parameter values, respectively, and are listed in the Supplemental Tables. In Table 3 we present the model-fitting statistics for the reduced chi-squared, $\tilde{\chi}^2$, Akaike information criteria (AIC), and Bayesian information criteria (BIC) methods, as well as the parameters determined by LMO. Importantly, we note that fits were performed on data points representing averages and ranges for the two experimental trials at each E:T ratio from only the measured data.

We find that across the three statistical tests considered, the CARRGO model performs slightly better than the SINDy discovered models at E:T = 1:4 and E:T = 1:20, whereas the SINDy discovered model for E:T = 1:8 performed better than the CARRGO model (Table 3). Interestingly, the CARRGO model predictions for the CAR T-cell trajectories fail to intercept the final CAR T-cell values, whereas the SINDy discovered models do. This result highlights a key difference between these two approaches, particularly that the SINDy approach required generating a time-series trajectory for the CAR T-cells that enforced interception with the final CAR T-cell measurement. Alternatively, traditional optimization methods like LMO weight each data point by the range of measurement uncertainty, allowing for the possibility of significant deviation from the final CAR T-cell measurements as long as such deviations can be compensated with better fitting elsewhere amongst the data.

Another essential difference between the CARRGO and SINDy predictions regarding the CAR T-cell trajectories is the CAR T-cell response at the high E:T ratio of E:T = 1:4. Specifically, the CARRGO model predicts that the CAR T-cells reach a maximum population exceeding the maximum population of cancer cells. This result has significant translational implications for CAR T-cell therapy related to patient immune response that we address in the discussion section.

Despite the noted differences, the overall similarities between the CARRGO and SINDy models is demonstrated by the order of magnitude agreement in most shared parameter values, specifically the cancer cell growth rate ρ_x, the cancer cell carrying capacity K_x, and the CAR T-cell functional response coefficient α for the specific scenarios of E:T = 1:4 and E:T = 1:8 (Table 3). Taken together, these results demonstrate significant value in the SINDy methodology when compared to established procedures for parameter estimation.

3.3 Model stability

An important question in performing model discovery for dynamical systems is in relation to the overall stability. Automating the task of examining stability for every discovered

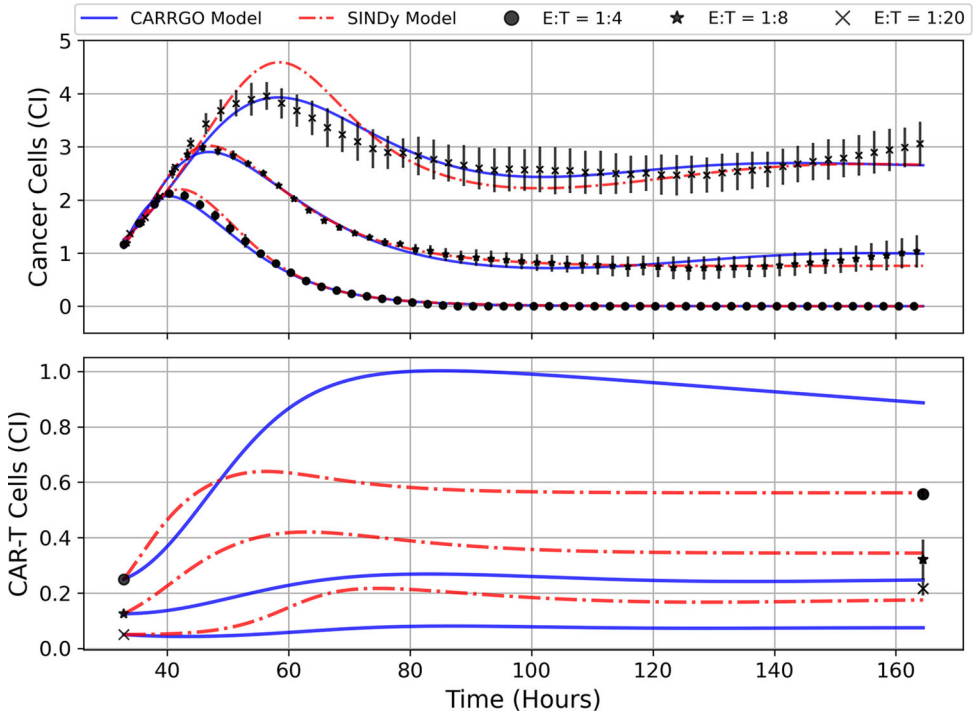

FIGURE 5
Predictions of cell trajectories for E:T ratios of 1:4, 1:8, and 1:20 from CARRGO model (blue) and SINDy model (red). Model fits for both CARRGO and SINDy were performed using Levenberg-Marquadt Optimization (LMO) on data aggregated across experimental replicates. Initial LMO parameter value guesses were determined by parameter values from SINDy or from published CARRGO model values. Data points represent the mean of all experimental replicates, while error bars represent the ranges across replicates. Of note are the differences in CARRGO and SINDy model predictions for the final CAR T-cell values compared to measurements, and the notable difference in when the maximum CAR T-cell population is reached between CARRGO and SINDy models. Note that experimental measurements have been down-sampled to 25% to allow for visualization.

model is challenging given the combination of symbolic computation with floating point coefficients. However, by predicting forward in time for each of the models and experimental replicates we can qualitatively characterize the stability (see Figure 4).

For the E:T = 1:4 scenario, both the data and model indicate complete cancer cell death, with the model accurately maintaining a cancer cell population of zero. We note that in several of the alternate discovered models produced by SINDy, the cancer cell population would become negative in the forward predicted regime. This unrealistic result can be used as an aide in ruling out alternative models.

For the E:T = 1:8 and 1:20 scenarios, both the data and models indicate cancer cell-CAR T-cell coexistence, with the forward predictions reaching non-oscillatory steady states. Despite the discovered models being the ones with the best accuracy, they all struggle to match the observed oscillatory frequency, particularly in the E:T = 1:20 scenario. These results demonstrate the capability of SINDy to discover models with variability in solution stability, a core feature of nonlinear dynamical systems.

TABLE 3 Fitting statistics for CARRGO and SINDy models and comparison of shared parameters.

Model –E:T	$\tilde{\chi}^2$	AIC	BIC	Cancer growth rate ρ (hrs^{-1})	Cancer carrying capacity K_x (Cl)	Cancer killing $\bar{a}$ (Cl^{-1} hrs^{-1})	CAR T response α (Cl^{-1} hrs^{-1})
CARRGO –1:4	13.6	1380	1400	0.471	3.70	0.555	0.0318
SINDy –1:4	23.0	1660	1700	0.116	4.78	–[1]	0.0327
CARRGO –1:8	0.919	-39.6	-18.3	0.361	6.82	1.26	0.015
SINDy –1:8	0.401	-474	-440	0.190	7.06	0.588	0.0436
CARRGO –1:20	3.14	609	631	0.206	7.69	1.81	0.0195
SINDy –1:20	3.55	674	700	0.123	11.1	0.540	-0.0024

Fitting statistics considered are the reduced chi-squared, $\tilde{\chi}^2$, the Akaike information criteria (AIC) and Bayesian information criteria (BIC). Of note are the scores indicating a better fit for the CARRGO model at E:T = 1:4 and 1:20, despite differences in the endpoint CAR T-cell population predictions in Figure 5. Furthermore, we observe generally favorable agreement between parameter estimates, suggesting the data first approach of SINDy as a viable alternative to traditional model first parameter inference methods.
[1] – indicates term not discovered.

3.4 Parameter identifiability

To better understand the rarity of the discovered models and their respective coefficients, we examined histograms for the coefficients of each of the model terms along the Pareto fronts for each E:T ratio, presented in Supplementary Figure S4. This approach allows us to qualitatively assess parameter identifiability by seeing the extent to which variability in coefficient values exists, and at the expense of prediction accuracy. For most active terms encountered, the coefficients corresponding to the selected models based on the Pareto front analysis were the most commonly occurring values until deactivation (elimination from discovered models). However, in a few situations we see that the coefficient values corresponding to the greatest model accuracy were relatively rare, and varied significantly as increasingly more terms were removed. This occurs in the coefficients for the x and xy^2 terms in the cancer cells for the E:T = 1:4 scenario in Supplementary Figure S4A, and the x and xy terms in the cancer cells for both the E:T = 1:8 and 1:20 scenarios in Supplementary Figures S4B, C. These terms were shown to be the final remaining active terms in discovered model, suggesting that they are capable of capturing the greatest extent of variation in our cancer cell-CAR T-cell killing data. Of note once again is that amongst these dominant interaction terms we see a transition from those indicative of double binding at high E:T ratios to single binding at medium and low E:T ratios.

4 Discussion

We examined *in vitro* experimental CAR T-cell killing assay data for a human-derived glioblastoma cell line (Figure 1). From our results we infer transitions in the phenomenological killing behavior of the CAR T-cells as a consequence of varying their initial concentration compared to the cancer cells. Our discovered models predict that at high effector to target ratios (E:T = 1:4) the CAR T-cell levels respond according to a Type II functional response in which they survive and/or expand faster at low density, and slower at high density, and they predominantly form double binding conjugates with cancer cells prior to cell killing. At medium E:T ratios of E:T = 1:8 our discovered model again predicts the CAR T-cells undergoing a Type II functional response, but now forming only singly bound conjugates prior to cell killing. At low E:T ratios of E:T = 1:20 our discovered model predicts the CAR T-cells shift to a Type III functional response, in which they survive and/or expand slower at low density, and faster at high density. In this final scenario we find a mixture of single and double conjugate formation occurring. Finally, our discovered models predict the growth strategies of the cancer cells as being a weak Allee effect at high and medium E:T ratios, and logistic at low E:T ratios, while the cancer cells are predicted to follow logistic growth for high and medium E:T ratios. Model coefficients used to deduce these results are found in Tables 1 and 2, and model simulations and forward predictions are shown in Figure 4.

A crucial result of this work is the comparison between the *data first* approach of SINDy to the traditional *model first* approach of CARRGO. Despite the discovered SINDy models having more degrees of freedom (i.e. mathematical terms) than the CARRGO model, both models were found to perform comparably as indicated in Figure 5 and Table 3. Yet, there are key differences regarding the interpretation of these two approaches. Traditional *model first* approaches like the CARRGO model assume a strict individual model that may exhibit variation in its coefficients or model parameters to reflect variation in the underlying biology or experimental conditions. On the other hand, one of the strengths of the *data first* approach of SINDy is that these coefficient variations can be shifted onto discovery of altogether different model terms. As we show, these different terms can have direct interpretations related to the underlying biology and dynamics. For example in (18), variation in the CAR T-cell response due to changes in the experimental E:T ratio could only be indicated through variation in the coefficients of the Type I functional response term, or the value of α in Eq. (58). Specifically, increases in α were interpreted as a high CAR T-cell response rate, or CAR T-cell expansion, and decreases in α were interpreted as a low response rate, or as CAR T-cell exhaustion. Whereas the SINDy model predicts entirely different CAR T-cell functional response terms, providing greater interpretation of these transitions in the CAR T dynamics and biology. Specifically, a Type II functional response at high and medium E:T, or a fast-to-slow CAR T-cell response rate, and a Type III functional response at low E:T, or a slow-to-fast CAR T-cell response that is again suggestive of exhaustion.

4.1 Interpreting discovered coefficients

We demonstrate the value of the effective model parameters for inferring underlying biology by considering the high E:T model presented in Eqs. (47)-(48). In this scenario, a Type II functional response in the CAR T-cells is deduced from the negative sign on β, corresponding to the concave down parabolic nature of the CAR T-cell functional response with fast proliferation at low cancer cell density and slow proliferation at high cancer cell density (Figure 3). The implication that cancer cell killing is induced by double binding of CAR T-cells to cancer cells comes from multiple terms. The most direct indicator is $\tilde{b} \neq 0$, where $\tilde{b} = (bh - ak)/k^2$ with bh/k representing the rate of cancer cell death from double conjugates, and a/k the rate of cancer cell death from single conjugates. Supporting indicators come from the positive sign on $\alpha = p/g - c/h$, suggesting that the CAR T-cell death rate from single conjugate formation, c/h is small compared to the leading order CAR T-cell response rate, p/g. Further evidence is in the inactivation of the xy term in the $\dot{x}(t)$ equation with coefficient $\tilde{a}$. Here, $\tilde{a} = a/h$ is the rate of cancer cell death from single conjugate formation, whose absence suggests that double binding formation is predominantly responsible for cancer cell death.

A similar analysis of model coefficients for the low and medium E:T ratio scenarios predicts a transition in the interactions between the CAR T-cells and cancer cells. Specifically, our approach predicts that the CAR T-cells form double conjugate pairs with high E:T

ratios, then switch to single conjugate pairs at medium and low E:T ratios. Similarly, our results predict a transition in the functional response, indicating Type II functional responses in the CAR T-cells for high E:T ratios and Type III responses in the low E:T ratios. These transitions in detected model terms are phenomenologically consistent with the interactions being dependent on CAR T-cell density, and highlight the hypothesis generating strength of *data first* model discovery techniques. Namely, the prediction of CAR T-cell killing dynamics being dependent on the relative abundance of CAR T-cells compared to cancer cells. We next present several opportunities for experimental testing of these model predictions.

4.2 Challenges and limitations

A challenge to the implementation of SINDy is data sparsity. Despite having high temporal resolution of the cancer cell trajectories (1 measurement per 15 minutes), the CAR T-cell populations consisted of only the initial and final measurements. To resolve sparsity in the CAR T-cell levels, we used latent variable analysis to extract the CAR T-cell trajectory from an approximation to the attractor of the dynamical system as determined by the cancer cell trajectory. We note that in determining the dimensionality of the latent variable subspace, we selected an embedding dimension of $m = 2$ despite the appearance of further benefit in using an embedding dimension of $m = 3$, as indicated in Supplementary Figure 2B. This choice was made due to our experimental limitations in only having flow cytometry data for the CAR T-cells at the initial and final time points, and no further data with which to constrain any additional latent variables. The existence of a second latent variable, as suggested by the third embedding dimension, could be due to single or double binding conjugates if the reaction rates are sufficiently slow, or, alternatively, a biochemical secretion that is modulating the cancer cell and CAR T-cell interactions. Future experimental and modeling efforts may further illuminate the nature of this third state variable, which we discuss in the Future directions section.

One potential limitation with latent variable analysis is that the trajectories retrieved through Taken's Theorem are not guaranteed to be unique, but rather will be diffeomorphic to the true latent variable. That is, subject to topological stretching or skewing, which translates to variation in discovered model coefficients. This effect can be seen in Bakarji et al. (62), where the coefficients of the latent variables discovered for the two-state, predator-prey model are not in precise agreement to those used in the original simulation. However, it is important to note that the model terms discovered by SINDy with this methodology are biologically insightful, even though the coefficients multiplying the discovered model terms on latent variables may be subject to variation. Importantly, we provide further experimental information for the latent CAR-T cell variable through bounding of the initial and final CAR-T cell trajectory with direct measurements. Likewise, we only discover terms which are structurally identifiable through model inversion, minimizing the potential for diffeomorphic skewing of CAR-T cell trajectories to be discovered from Taken's Theorem.

A second challenge is that our data in total consists of two trials for each effector-to-target ratio. While there exist SINDy implementations designed to discover models with ratios of polynomials, the approaches require prohibitively many experimental trials to ensure accuracy (39, 40). To resolve sparsity in the number of experimental trials, we derived effective interaction models of cancer cell and CAR T-cell dynamics from model ODE terms with ratios of the polynomials using binomial approximations. These effective interaction models allowed for the identification of multiple constraints on the library function space used in SINDy, and guided our inferential analysis of the discovered models.

4.3 Future directions and clinical applications

To validate the hypothesized binding and functional response dynamics, we propose two potential experiments. Both experiments rely on similar initial conditions as those conducted for this study, but in one we propose the use of bright field microscopy and live cell imaging to visually inspect CAR T-cell dynamics at different points in time and for the different E:T ratios. By tracking in real-time the growth, motility, and interactions of the different cells present, this approach ought to aide in distinguishing different cell phenotypes by identifying occurrences of single and double binding types as well as the different functional responses (63). The second experiment would be to conduct endpoint analyses using flow cytometry to determine the population of CAR T-cells throughout the trajectory. This experiment would test the different CAR T-cell predictions from the CARRGO model and the SINDy models, most notably the predicted time to reach maximum CAR T-cell populations (Figure 5). Furthermore, targeted staining can provide information on the number of CAR T-cell generations and the ratio of helper T-cells (CD4+) to cytotoxic, killer T-cells (CD8+). These metrics may better inform the number of true effector cells responsible for killing cancer cells, allowing for more accurate characterization of the CAR T-cell response. These experiments additionally serve to test the validity of our latent variable analysis, which uses the cancer cell trajectory to predict the CAR T-cell trajectory as presented in Figure 4. Future experiments will also extend this analysis to include other CAR designs, including evaluating the impact of costimulatory signaling, CAR affinity and target density on modeling of CAR T-cell killing dynamics.

These and other experiments are essential for introducing additional elements and agents present in the tumor microenvironment and for extending this work to *in vivo* applications. Currently, our implementation of SINDy is on a highly controlled experimental system in order to isolate the interaction dynamics between the CAR T-cells and the glioma cells and to validate the SINDy methodology. An important challenge to overcome is extending the SINDy framework to incorporate additional aspects of *in vivo* systems. To achieve this, intermediate experiments to conduct are killing assays in two- and

three-dimensional *in vitro* tissue model systems that mimic the tumor microenvironment (64). The proposed experiments are crucial for adapting use of the SINDy framework for clinical applications.

The clinical relevance of the *data first* framework is in the domain of precision medicine. The approach naturally caters to *in situ* monitoring of patient response to therapy and forecasting future trajectories. An open question in this field is determining the sufficient number of early measurements necessary for accurate forecasting, and quantifying the extent of reliable forward prediction. This type of application falls under the field of control theory, in which real-time measurements for systems such as navigation, fluid dynamics and disease monitoring can inform model-based interventions (15). Control theory has been identified as a key tool in achieving optimized individual treatment outcomes, yet challenges are ever-present in parsimonious model selection. The SINDy methodology may help streamline and simplify the model selection process, while simultaneously incorporating control theory methods for treatment optimization. As an example related to the experiments considered here, one could envision a therapeutic intervention to administer more CAR T-cells in the low E:T ratio of 1:20 as soon as the Type III functional response and single binding dynamics are predicted in a patient. This intervention would serve to push the dynamics of the patients immune response into the double biding and Type II response regime, thereby improving therapeutic efficacy.

5 Conclusions

In this work we present the first, to our knowledge, application of the sparse identification of non-linear dynamics (SINDy) methodology to a real biological system. We used SINDy with highly time-resolved experimental data to discover biological mechanisms underlying CAR T-cell-cancer cell killing dynamics. Our implementation highlights the hypothesis generating potential of data-driven model discovery and illuminates challenges for future extensions and applications. To overcome challenges related to data limitation, we utilized latent variable analysis to construct the trajectory of the CAR T-cells, and we implemented binomial expansions to simplify specific model terms. Our results predict key mechanisms and transitions in the interaction dynamics between the CAR T-cells and cancer cells under different experimental conditions that may be encountered in the application of these therapies in human patients. Specifically, we identified transitions from double CAR T-cell binding to single CAR T-cell binding, and from fast-to-slow CAR T-cell responses (Type II) to slow-to-fast responses (Type III). Both transitions occur as a result of decreasing the relative abundances of CAR T-cells to cancer cells (initial E:T ratios). Importantly, these results demonstrate the potential for *data first* model discovery methods to provide deeper insight into the underlying dynamics and biology than *model first* approaches, and offer a new avenue for integrating predictive modeling into precision medicine and cancer therapy by an improved mechanistic understanding of cancer progression and efficacy of CAR T-cell therapy.

Data availability statement

The datasets presented in this study can be found in online repositories. The names of the repository/repositories and accession number(s) can be found below: https://github.com/alexbbrummer/CART_SINDy.

Author contributions

Conceptualization, AB and RR; methodology, AB, RW, VA, HC, and RR; validation, AB, RR; formal analysis, AB; investigation, AB; resources, MG, CB, and RR; data curation, AB; writing—original draft preparation, AB; writing—review and editing, AB, AX, RW, VA, HC, MG, CB, and RR; visualization, AB, AX, RW, VA, and RR; supervision, CB and RR; project administration, AB and RR; funding acquisition, CB and RR. All authors contributed to the article and approved the submitted version.

Funding

Research reported in this work was supported by the National Cancer Institute of the National Institutes of Health under grant numbers R01CA254271 (CB), R01NS115971 (CB, RR), and P30CA033572, the Marcus Foundation, and the California Institute of Regenerative Medicine (CIRM) under CLIN2-10248 (CB).

Conflict of interest

The authors declare that the research was conducted in the absence of any commercial or financial relationships that could be construed as a potential conflict of interest.

Publisher's note

Supplementary material

The Supplementary Material for this article can be found online at: https://www.frontiersin.org/articles/10.3389/fimmu.2023.1115536/full#supplementary-material

References

1. Rockne RC, Hawkins-Daarud A, Swanson KR, Sluka JP, Glazier JA, Macklin P, et al. The 2019 mathematical oncology roadmap. *Phys Biol* (2019) 16:041005. doi: 10.1088/1478-3975/ab1a09

2. Kuznetsov VA, Makalkin IA, Taylor MA, Perelson AS. Nonlinear dynamics of immunogenic tumors: parameter estimation and global bifurcation analysis. *Bull Math Biol* (1994) 56:295–321. doi: 10.1016/S0092-8240(05)80260-5

3. de Pillis LG, Radunskaya AE, Wiseman CL. A validated mathematical model of cell-mediated immune response to tumor growth. *Cancer Res* (2005) 65:7950–8. doi: 10.1158/0008-5472.CAN-05-0564

4. Roy M, Finley SD. Computational model predicts the effects of targeting cellular metabolism in pancreatic cancer. *Front Physiol* (2017) 8:217. doi: 10.3389/fphys.2017.00217

5. Stein AM, Grupp SA, Levine JE, Laetsch TW, Pulsipher MA, Boyer MW, et al. Tisagenlecleucel model-based cellular kinetic analysis of chimeric antigen receptor–t cells. *CPT: Pharmacometrics Syst Pharmacol* (2019) 8:285–95. doi: 10.1002/psp4.12388

6. West J, You L, Zhang J, Gatenby RA, Brown JS, Newton PK, et al. Towards multidrug adaptive therapy. *Cancer Res* (2020) 80:1578–89. doi: 10.1158/0008-5472.CAN-19-2669

7. Kimmel GJ, Locke FL, Altrock PM. The roles of t cell competition and stochastic extinction events in chimeric antigen receptor t cell therapy. *Proc R Soc B* (2021) 288:20210229. doi: 10.1098/rspb.2021.0229

8. Owens K, Bozic I. Modeling car t-cell therapy with patient preconditioning. *Bull Math Biol* (2021) 83:1–36. doi: 10.1007/s11538-021-00869-5

9. Mascheroni P, Savvopoulos S, Alfonso JCL, Meyer-Hermann M, Hatzikirou H. Improving personalized tumor growth predictions using a bayesian combination of mechanistic modeling and machine learning. *Commun Med* (2021) 1:1–14. doi: 10.1038/s43856-021-00020-4

10. Lambin P, Leijenaar RT, Deist TM, Peerlings J, De Jong EE, Van Timmeren J, et al. Radiomics: the bridge between medical imaging and personalized medicine. *Nat Rev Clin Oncol* (2017) 14:749. doi: 10.1038/nrclinonc.2017.141

11. Zhou M, Leung A, Echegaray S, Gentles A, Shrager JB, Jensen KC, et al. Non-small cell lung cancer radiogenomics map identifies relationships between molecular and imaging phenotypes with prognostic implications. *Radiology* (2018) 286:307–15. doi: 10.1148/radiol.2017161845

12. Kamb M, Kaiser E, Brunton SL, Kutz JN. Time-delay observables for koopman: theory and applications. *SIAM J Appl Dynamical Syst* (2020) 19:886–917. doi: 10.1137/18M1216572

13. Brunton SL, Budišić M, Kaiser E, Kutz JN. Modern koopman theory for dynamical systems. *SIAM Rev* (2022) 64:229–340. doi: 10.1137/21M1401243

14. Frankhouser DE, O'Meally D, Branciamore S, Uechi L, Zhang L, Chen YC, et al. Dynamic patterns of microrna expression during acute myeloid leukemia state-transition. *Sci Adv* (2022) 8:eabj1664. doi: 10.1126/sciadv.abj1664

15. Brunton SL, Proctor JL, Kutz JN. Discovering governing equations from data by sparse identification of nonlinear dynamical systems. *Proc Natl Acad Sci* (2016) 113:3932–7. doi: 10.1073/pnas.1517384113

16. de Silva BM, Champion K, Quade M, Loiseau JC, Kutz JN, Brunton SL. Pysindy: a python package for the sparse identification of nonlinear dynamical systems from data. *J Open Source Software* (2020) 5:2104. doi: 10.21105/joss.02104

17. Kaptanoglu AA, de Silva BM, Fasel U, Kaheman K, Goldschmidt AJ, Callaham J, et al. Pysindy: a comprehensive python package for robust sparse system identification. *J Open Source Software* (2022) 7:3994. doi: 10.21105/joss.03994

18. Sahoo P, Yang X, Abler D, Maestrini D, Adhikarla V, Frankhouser D, et al. Mathematical deconvolution of car t-cell proliferation and exhaustion from real-time killing assay data. *J R Soc Interface* (2020) 17:20190734. doi: 10.1098/rsif.2019.0734

19. Hamilton PT, Anholt BR, Nelson BH. Tumour immunotherapy: lessons from predator–prey theory. *Nat Rev Immunol* (2022) 22:1–11. doi: 10.1038/s41577-022-00719-y

20. Lotka AJ. *Elements of physical biology*. Baltimore, Md., U.S.A.: Williams & Wilkins (1925), 20.

21. Volterra V. Variazioni e fluttazioni del numero d'individui in specie animali conviventi. *Memoria della Reale Accademia Nazionale dei Lincei* (1926) 22:31–113.

22. Kareva I, Luddy KA, O'Farrelly C, Gatenby RA, Brown JS. Predator-prey in tumor-immune interactions: a wrong model or just an incomplete one? *Front Immunol* (2021) 21:3391. doi: 10.3389/fimmu.2021.668221

23. Chaudhury A, Zhu X, Chu L, Goliaei A, June CH, Kearns JD, et al. Chimeric antigen receptor t cell therapies: a review of cellular kinetic-pharmacodynamic modeling approaches. *J Clin Pharmacol* (2020) 60:S147–59. doi: 10.1002/jcph.1691

24. Adhikarla V, Awuah D, Brummer AB, Caserta E, Krishnan A, Pichiorri F, et al. A mathematical modeling approach for targeted radionuclide and chimeric antigen receptor t cell combination therapy. *Cancers* (2021), 13. doi: 10.3390/cancers13205171

25. Brummer AB, Yang X, Ma E, Gutova M, Brown CE, Rockne RC. Dose-dependent thresholds of dexamethasone destabilize car t-cell treatment efficacy. *PloS Comput Biol* (2022) 18:e1009504. doi: 10.1371/journal.pcbi.1009504

26. Holling CS. The components of predation as revealed by a study of small-mammal predation of the european pine sawfly1. *Can Entomologist* (1959) 91:293–320. doi: 10.4039/Ent91293-5

27. Gatenby RA. Population ecology issues in tumor growth. *Cancer Res* (1991) 51:2542–7.

28. Böttger K, Hatzikirou H, Voss-Böhme A, Cavalcanti-Adam EA, Herrero MA, Deutsch A. An emerging allee effect is critical for tumor initiation and persistence. *PloS Comput Biol* (2015) 11:1–14. doi: 10.1371/journal.pcbi.1004366

29. Johnson KE, Howard G, Mo W, Strasser MK, Lima EABF, Huang S, et al. Cancer cell population growth kinetics at low densities deviate from the exponential growth model and suggest an allee effect. *PloS Biol* (2019) 17:1–29. doi: 10.1371/journal.pbio.3000399

30. Li R, Sahoo P, Wang D, Wang Q, Brown CE, Rockne RC, et al. Modeling interaction of glioma cells and car t-cells considering multiple car t-cells bindings. *ImmunoInformatics* (2023) 9:100022. doi: 10.1016/j.immuno.2023.100022

31. Sohail A, Yu Z, Arif R, Nutini A, Nofal TA. Piecewise differentiation of the fractional order car-t cells-sars-2 virus model. *Results Phys* (2022) 33:105046. doi: 10.1016/j.rinp.2021.105046

32. Al-Utaibi KA, Nutini A, Sohail A, Arif R, Tunc S, Sait SM. Forecasting the action of car-t cells against sars-corona virus-ii infection with branching process. *Modeling Earth Syst Environ* (2021) 8:1–9. doi: 10.1007/s40808-021-01312-3

33. Gábor A, Banga JR. Robust and efficient parameter estimation in dynamic models of biological systems. *BMC Syst Biol* (2015) 9:1–25.

34. Mitra ED, Hlavacek WS. Parameter estimation and uncertainty quantification for systems biology models. *Curr Opin Syst Biol* (2019) 9:9–18. doi: 10.1016/j.coisb.2019.10.006

35. Schmid PJ. Dynamic mode decomposition of numerical and experimental data. *J Fluid Mechanics* (2010) 656:5–28. doi: 10.1017/S0022112010001217

36. Yadav N, Ravela S, Ganguly AR. Machine learning for robust identification of complex nonlinear dynamical systems: applications to earth systems modeling. (2020). doi: 10.48550/ARXIV.2008.05590

37. Alves EP, Fiuza F. Data-driven discovery of reduced plasma physics models from fully kinetic simulations. *Phys Rev Res* (2022) 4:033192. doi: 10.1103/PhysRevResearch.4.033192

38. Ren Y, Adams C, Melz T. Uncertainty analysis and experimental validation of identifying the governing equation of an oscillator using sparse regression. *Appl Sci* (2022). doi: 10.3390/app12020747

39. Mangan NM, Brunton SL, Proctor JL, Kutz JN. Inferring biological networks by sparse identification of nonlinear dynamics. *IEEE Trans Molecular Biol Multi-Scale Commun* (2016) 12:52–63. doi: 10.1109/TMBMC.2016.2633265

40. Kaheman K, Kutz JN, Brunton SL. Sindy-pi: a robust algorithm for parallel implicit sparse identification of nonlinear dynamics. *Proc R Soc A* (2020) 476:20200279. doi: 10.1098/rspa.2020.0279

41. Kaiser E, Kutz JN, Brunton SL. Sparse identification of nonlinear dynamics for model predictive control in the low-data limit. *Proc R Soc A* (2018) 474:20180335. doi: 10.1098/rspa.2018.0335

42. Messenger DA, Bortz DM. Weak sindy: galerkin-based data-driven model selection. *Multiscale Modeling Simulation* (2021) 19:1474–97. doi: 10.1137/20M1343166

43. Chen Z, Liu Y, Sun H. Physics-informed learning of governing equations from scarce data. *Nat Commun* (2021) 12:1–13. doi: 10.1038/s41467-021-26434-1

44. Brown CE, Starr R, Aguilar B, Shami AF, Martinez C, D'Apuzzo M, et al. Stem-like tumor-initiating cells isolated from il13rα2 expressing gliomas are targeted and killed by il13-zetakine–redirected t cells. *Clin Cancer Res* (2012) 18:2199–209. doi: 10.1158/1078-0432.CCR-11-1669

45. Brown CE, Alizadeh D, Starr R, Weng L, Wagner JR, Naranjo A, et al. Regression of glioblastoma after chimeric antigen receptor t-cell therapy. *New Engl J Med* (2016) 375:2561–9. doi: 10.1056/NEJMoa1610497

46. Brown CE, Aguilar B, Starr R, Yang X, Chang WC, Weng L, et al. Optimization of il13rα2-targeted chimeric antigen receptor t cells for improved anti-tumor efficacy against glioblastoma. *Mol Ther* (2018) 46:31–44. doi: 10.1016/j.ymthe.2017.10.002

47. Moniri MR, Young A, Reinheimer K, Rayat J, Dai LJ, Warnock GL. Dynamic assessment of cell viability, proliferation and migration using real time cell analyzer system (rtca). *Cytotechnology* (2015) 67:379–86. doi: 10.1007/s10616-014-9692-5

48. Xing JZ, Zhu L, Gabos S, Xie L. Microelectronic cell sensor assay for detection of cytotoxicity and prediction of acute toxicity. *Toxicol Vitro* (2006) 20:995–1004. doi: 10.1016/j.tiv.2005.12.008

49. Chiu CH, Lei KF, Yeh WL, Chen P, Chan YS, Hsu KY, et al. Comparison between xcelligence biosensor technology and conventional cell culture system for real-time monitoring human tenocytes proliferation and drugs cytotoxicity screening. *J Orthopaedic Surg Res* (2017) 12:1–13. doi: 10.1186/s13018-017-0652-6

50. Hanke M. *Conjugate gradient type methods for ill-posed problems*. New York: Longman Scientific and Technical (1995).

51. Fadai NT, Simpson MJ. Population dynamics with threshold effects give rise to a diverse family of allee effects. *Bull Math Biol* (2020) 82:1–22. doi: 10.1007/s11538-020-00756-5

52. Fadai NT, Johnston ST, Simpson MJ. Unpacking the allee effect: determining individual-level mechanisms that drive global population dynamics. *Proc R Soc A* (2020) 476:20200350. doi: 10.1098/rspa.2020.0350

53. Cosner C, Rodriguez N. The effect of directed movement on the strong allee effect. *SIAM J Appl Mathematics* (2021) 81:407–33. doi: 10.1137/20M1330178

54. Hill AV. The possible effects of the aggregation of the molecules of haemoglobin on its dissociation curves. *Proc Physiol Soc* (1910) 40:i–vii. doi: 10.1113/jphysiol.1910.sp001386

55. Langmuir I. The adsorption of gases on plane surfaces on glass, mica and platinum. *J Am Chem Soc* (1918) 40:1361–403. doi: 10.1021/ja02242a004

56. Michaelis L, Menten ML. Die kinetik der invertinwirkung. *Biochemische Z* (1913) 49:352.

57. Brummer AB, Hunt D, Savage V. Improving blood vessel tortuosity measurements via highly sampled numerical integration of the frenet-serret equations. *IEEE Trans Med Imaging* (2021) 26:297–309. doi: 10.1109/TMI.2020.3025467

58. Kodba S, Perc M, Marhl M. Detecting chaos from a time series. *Eur J Phys* (2004) 40:205. doi: 10.1088/0143-0807/26/1/021

59. Rudy SH, Brunton SL, Proctor JL, Kutz JN. Data-driven discovery of partial differential equations. *Sci Adv* (2017) 3:e1602614. doi: 10.1126/sciadv.1602614

60. Zheng P, Askham T, Brunton SL, Kutz JN, Aravkin AY. A unified framework for sparse relaxed regularized regression: Sr3. *IEEE Access* (2018) 7:1404–23.

61. Champion K, Zheng P, Aravkin AY, Brunton SL, Kutz JN. A unified sparse optimization framework to learn parsimonious physics-informed models from data. *IEEE Access* (2020) 8:169259–71. doi: 10.1109/ACCESS.2020.3023625

62. Bakarji J, Champion K, Kutz JN, Brunton SL. Discovering governing equations from partial measurements with deep delay autoencoders. (2022). doi: 10.48550/ARXIV.2201.05136

63. Barney LE, Hall CL, Schwartz AD, Parks AN, Sparages C, Galarza S, et al. Tumor cell–organized fibronectin maintenance of a dormant breast cancer population. *Sci Adv* (2020) 6:eaaz4157. doi: 10.1126/sciadv.aaz4157

64. Galarza S, Kim H, Atay N, Peyton SR, Munson JM. 2d or 3d? how cell motility measurements are conserved across dimensions in vitro and translate in vivo. *Bioeng Trans Med* (2020) 5:e10148. doi: 10.1002/btm2.10148

frontiers | Frontiers in Immunology

TYPE Perspective
PUBLISHED 07 June 2023
DOI 10.3389/fimmu.2023.1173546

OPEN ACCESS

EDITED BY
Mohit Kumar Jolly,
Indian Institute of Science (IISc), India

REVIEWED BY
Jyothi S. Prabhu,
St. John's Research Institute, India
Theinmozhi Arulraj,
Johns Hopkins University, United States
Sara Sadat Aghamiri,
University of Nebraska-Lincoln,
United States

*CORRESPONDENCE
Rukmini Kumar
rukmini@vantage-research.net

RECEIVED 24 February 2023
ACCEPTED 23 May 2023
PUBLISHED 07 June 2023

CITATION
Kumar R, Qi T, Cao Y
and Topp B (2023) Incorporating
lesion-to-lesion heterogeneity into
early oncology decision making.
Front. Immunol. 14:1173546.
doi: 10.3389/fimmu.2023.1173546

Incorporating lesion-to-lesion heterogeneity into early oncology decision making

Rukmini Kumar[1]*, Timothy Qi[2], Yanguang Cao[2,3] and Brian Topp[4]

[1]Vantage Research Inc., Lewes, DE, United States, [2]Division of Pharmacotherapy and Experimental Therapeutics, Eshelman School of Pharmacy, The University of North Carolina at Chapel Hill, Chapel Hill, NC, United States, [3]Lineberger Comprehensive Cancer Center, The University of North Carolina at Chapel Hill, Chapel Hill, NC, United States, [4]Quantitative Pharmacology & Pharmacometrics, Immuno-oncology, Merck & Co., Inc., Rahway, NJ, United States

RECISTv1.1 (Response Evaluation Criteria In Solid Tumors) is the most commonly used response grading criteria in early oncology trials. In this perspective, we argue that RECISTv1.1 is ambiguous regarding lesion-to-lesion variation that can introduce bias in decision making. We show theoretical examples of how lesion-to-lesion variability causes bias in RECISTv1.1, leading to misclassification of patient response. Next, we review immune checkpoint inhibitor (ICI) clinical trial data and find that lesion-to-lesion heterogeneity is widespread in ICI-treated patients. We illustrate the implications of ignoring lesion-to-lesion heterogeneity in interpreting biomarker data, selecting treatments for patients with progressive disease, and go/no-go decisions in drug development. Further, we propose that Quantitative Systems Pharmacology (QSP) models can aid in developing better metrics of patient response and treatment efficacy by capturing patient responses robustly by considering lesion-to-lesion heterogeneity. Overall, we believe patient response evaluation with an appreciation of lesion-to-lesion heterogeneity can potentially improve decision-making at the early stage of oncology drug development and benefit patient care.

KEYWORDS

QSP model, lesion-to-lesion heterogeneity, RECIST v1.1, dissociated response, oncology clinical trials

Introduction

Patients with stage IV cancer generally have primary lesions as well as metastatic lesions spread across multiple organs. Mounting evidence shows that each lesion differs in genetic mutations, clonal composition, pathophysiology, and this complexity results in differential response to therapy (1–4). The present method for scoring response to therapy, RECISTv1.1, yields a patient-level response based largely on an aggregate change in the sum of target lesion diameters without an appropriate appreciation of lesion-to-lesion

heterogeneity. Here, we argue that tracking aggregate change leads to bias in decision making. Therefore, we advocate for lesion-level analysis in drug development decision-making (Go/No-Go decisions, biomarker analysis, identifying combination strategies) and to potentially inform clinical drug adjustment decisions. Further we also show Quantitative Systems Pharmacology (QSP) modeling approaches that explicitly include multiple lesions can be used for decision support.

Overview of RECIST v1.1

The Response Evaluation Criteria in Solid Tumors (RECIST) criteria are a set of guidelines for evaluating patient response to oncology treatment (5). There are several versions of RECIST, with version 1.1 being the standard method applied to virtually all oncology trials for solid tumors. Patient responses are classified into one of four strata: Complete Response (CR), Partial Response (PR), Stable Disease (SD), or Progressive Disease (PD). This classification occurs each time a patient receives a CT or MRI scan (usually every 6-8 weeks) and repeats until the end of the trial, patient death, or loss of follow-up.

The definition of each RECISTv1.1 response classification is shown in Table 1. When patients have multiple lesions, a subset of lesions is designated "target" lesions and measured at each scan (RECIST guidelines recommend target lesions should be representative lesions amenable to repeated measurement, up to 5 and no more than 2 per organ (5). The sum of their diameters is tracked and evaluated to determine patient response. The remaining lesions are designated "non-target" lesions and simply reported as present, absent, or progressing. If the number of lesions increases during the trial, these lesions are defined as new metastatic lesions. Complete Response requires the elimination of all target and non-target lesions and the absence of any new metastatic lesions. Partial Response requires a >30% reduction in the sum of target lesion diameters and the absence of non-target growth or appearance of new lesions. Disease progression is more complex. A patient is assigned a RECISTv1.1 classification of Progressive Disease if they show >20% growth in target lesions and/or unequivocal progression of non-target lesions and/or the appearance of new metastatic lesions.

Biases in RECISTv1.1

Patient level outcomes tracked by RECIST hide important individual lesion level dynamics. Trial outcomes are commonly visualized by so-called "spaghetti plots" that display the change in the sum of lesion diameters for each patient over time (Figure 1A). End users may read these graphs as if they were derived from

TABLE 1 RECIST v1.1 criteria for patient classification.

	Δ Change in the Sum of diameters of Target Lesions	Non-Target Lesions	New Lesions
Complete Response[#]	-100%	Absent	Absent
Partial Response[#]	<-30%	Not Progressing	Absent
Stable Disease[#]	-30% to + 20%	No Progressing	Absent
Progression*	>+20%	Progressing	Present

[#]All three conditions are required.
*PD is declared if any one of these three conditions are met.

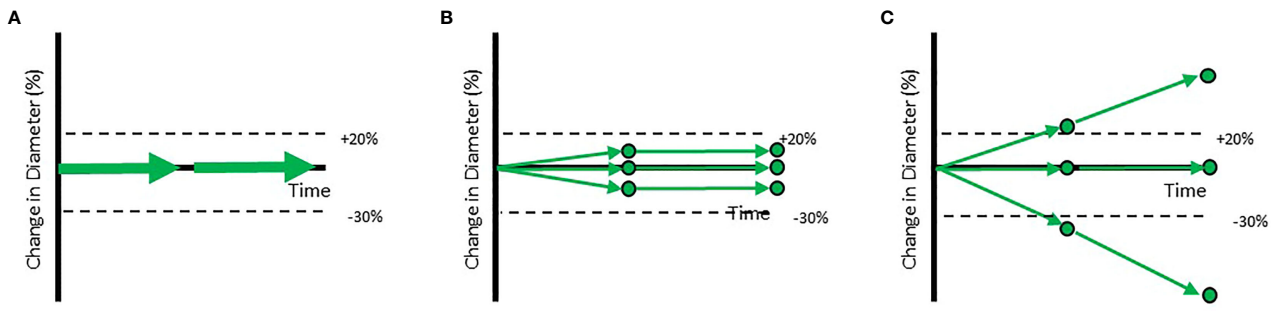

FIGURE 1
Example trajectories of patients with a RECISTv1.1 classification of Stable Disease. Each of the circles represents individual lesions in the patients. The aggregate response is represented by arrows. **(A)** Shows the standard visualization of aggregate response to therapy based on the Sum of Longest Diameters. **(B)** Shows a patient with a homogeneous response while **(C)** shows a patient with a heterogeneous response at the lesion level. When aggregate diameter changes by >20% (shown in labelled dotted line), the patient is classified as Progressive Disease. When aggregate diameter changes by < -30% (shown in labelled dotted line), the patient is classified as a Partial Responder. When all lesions have disappeared, the patient is classified as a Completer Responder.

homogeneous responses across all lesions in the patient (Figure 1B). However, the reality is generally more complex (Figure 1C). While the patients in Figures 1B, C receive the same RECISTv1.1 classification (Stable Disease), these patients are different in clinically meaningful ways; inferences of drug efficacy and treatment approach should differ for each of them.

A RECISTv1.1 classification of Progressive Disease (PD) is generally considered drug failure (a lack or loss of efficacy). Three examples of PD are provided in Figure 2. The first patient is a prototypical example of drug failure. Every target lesion grows, every non-target lesion grows, and new metastatic lesions appear. Clearly, the investigational drug displays minimal or no efficacy in this patient. In the second patient, half of the target lesions grow while the other half shrink. This results in a classification of PD via non-target progression and/or the appearance of new metastatic lesions. Despite a RECISTv1.1 classification of PD, this patient gained meaningful benefit in half of their lesions. Assuming the goal is to minimize or eliminate *all* lesions, this investigational drug may be effective as part of a combination therapy. The third patient gains meaningful benefit in all pre-existing tumors but is classified as PD due to the appearance of a new metastatic lesion. New metastatic lesions can appear transiently before stabilizing or shrinking shortly after appearance (6). Although the drug displays clear and continuing efficacy in most lesions, it is considered to have failed the patient by RECISTv1.1.

Criteria such as iRECIST have been developed to account for some variability seen in response to immunotherapy. The bias with new transient lesion can be avoided by using iRECIST criteria due to the need for PD classification to be confirmed on a follow-up scan (7). However, variability among the target lesion response will still not be captured by current scoring frameworks. Additional regulatory guidance may lead to broader adoption of iRECIST & other novel scores by drug development companies, thereby leading to better decision-making.

A recent study analyzing continuing effect of ICI (anti PD1) therapy in patients classified as PD from multiple trial data

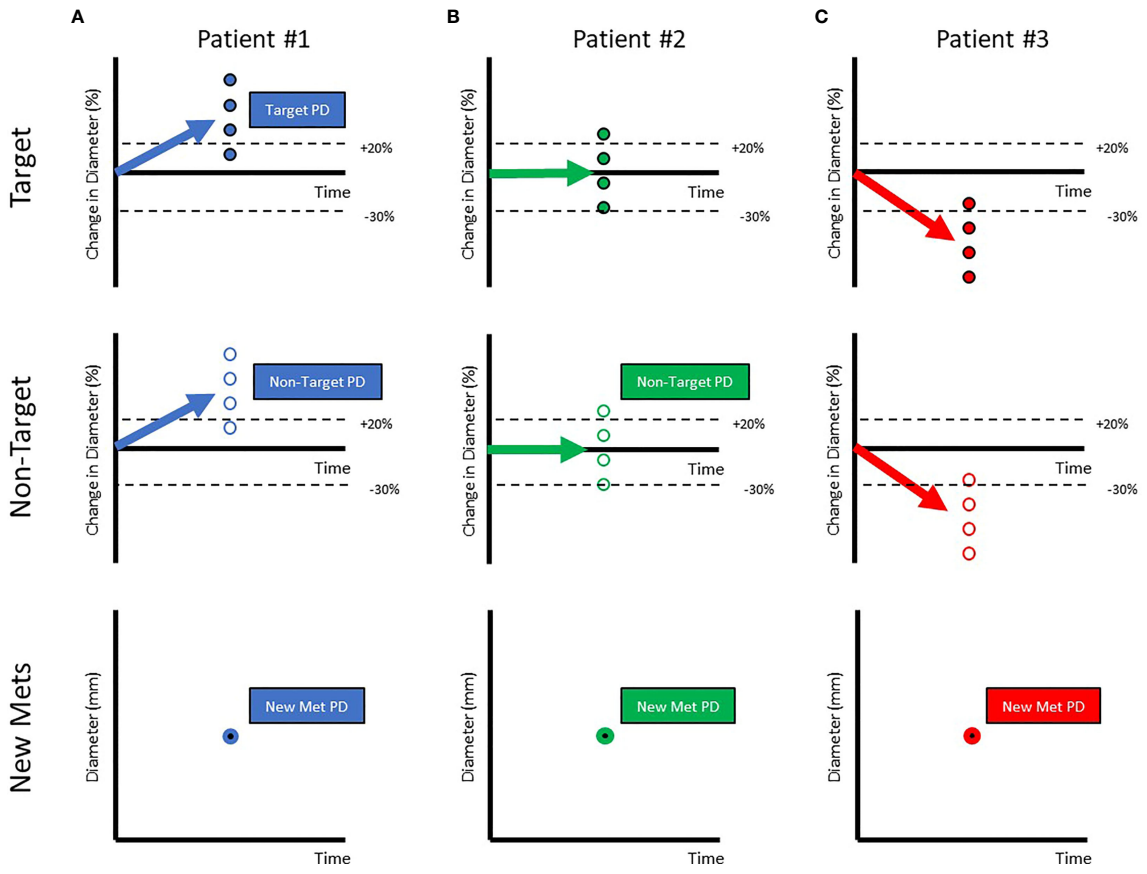

FIGURE 2
Patients classified as Progressive Disease can be very variable in the response of their target, non-target & appearance of metastatic lesions. Each of the circles represents individual lesions in the patients (Target Lesions: Filled Circles, Non-target Lesions: Open Circles, New Metastatic Lesions:Filled with bold border). The aggregate response is represented by arrows. When aggregate diameter changes by >20% **(A)** (shown in labelled dotted line), the patient is classified as Progressive Disease. When aggregate diameter changes by < -30% **(B)** (shown in labelled dotted line), the patient is classified as a Partial Responder. When all lesions have disappeared, the patient is classified as a Completer Responder **(C)**.

concluded that treatment beyond progression with ICI might be appropriate for selected patients (8). Adding a combination therapy to address progression while maintaining the original therapy to control responding lesions is being attempted as a strategy in several recent trials (9, 10). Results from such trials will inform future directions for clinical care.

In addition to vastly different patients being classified as PD, RECISTalso describes vastly different patients as Objective Responders (Complete or Partial Response). Figure 3A shows a prototypical Objective Responder. This patient is expected to gain a survival benefit from the investigational drug. However, Figure 3B shows an Objective Responder whose disease rebounds early in the trial and is unlikely to experience meaningful benefit. Since RECIST captures the "best overall response", this patient can be classified as a responder. Figure 3C shows another Objective Responder that drops out of the trial early due to an adverse event. Again, this patient does not display an ideal response to therapy but is classified as Objective Responder. Figure 3D shows a patient that gains a stable 29% reduction in tumor burden but is *not* classified as an Objective Responder since the criterion is a 30% reduction. A continuous metric may provide a more meaningful interpretation of this data. Figure 3E shows a patient with prolonged stable disease. This patient likely benefits from therapy but is *not* considered a responder. Figure 3F shows a patient with transient progression that also appears to benefit from therapy but is also *not* considered an Objective Responder.

Clinical data shows lesion-to-lesion heterogeneity

In a recent paper (11), we quantified lesion-to-lesion heterogeneity observed in patients with melanoma, NSCLC, and gastric cancer who were treated with pembrolizumab. Most patients displayed a mixture of growing, stable, and shrinking target lesions at the time of being classified as Progressive Disease (PD) (Figure 4). Figure shows a standard waterfall plot, with the bars representing the change in the sum of longest diameters for patients with melanoma that displayed primary progression (PD at first scan) on pembrolizumab therapy. Surprisingly, only 50% of these patients show a clinically meaningful increase in aggregate tumor burden (ΔSLD > +20%). More surprisingly, the change in size of individual lesions in these patients (dots) spanned a range of 120%. In other words, a patient with no net change in their sum of lesion diameters generally showed individual lesion responses ranging from -60% to +60%.

Other groups have also pointed out the limitations of RECIST for classifying heterogeneous responses to immunotherapy (sometimes calling it 'dissociated response') and called for better ways to evaluate patient response (12–16). Although new guidelines (like iRECIST) have been developed to improve and complement RECISTv1.1 in cancer immunotherapy trials, the lesion-to-lesion heterogeneity remains largely underappreciated.

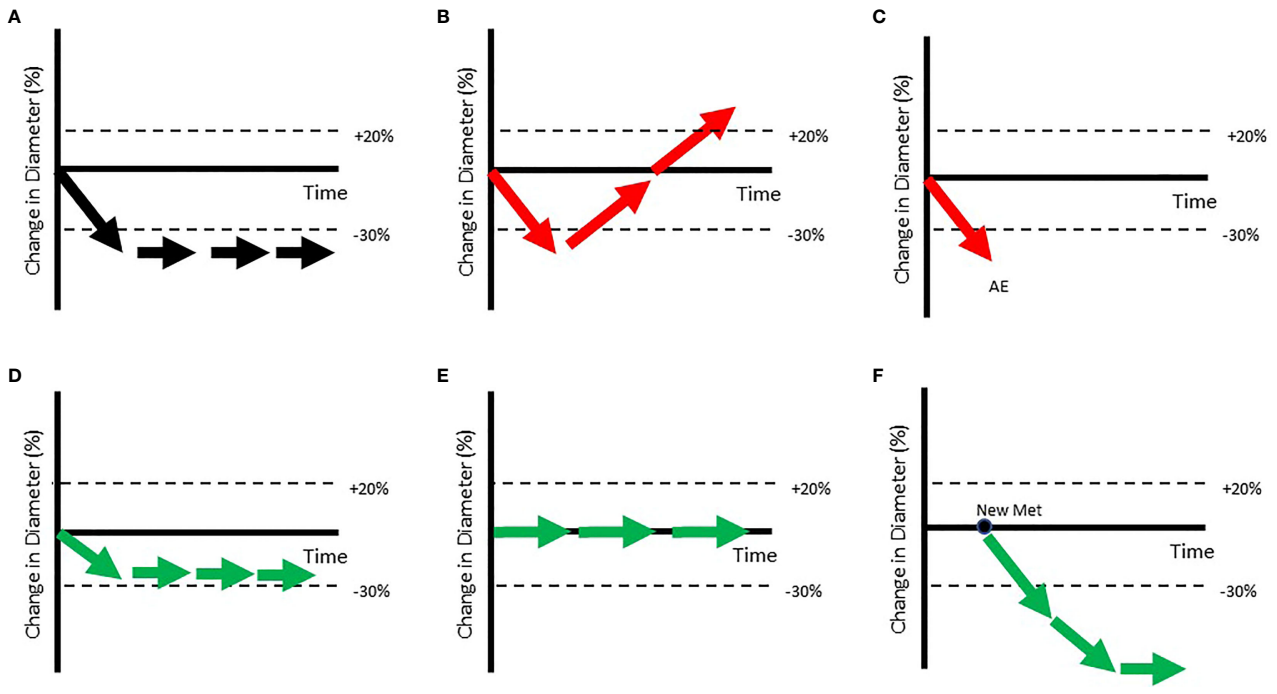

FIGURE 3
Patients with very different trajectories can be classified as Objective Responders. **(A)** Shows a prototypical Objective Responder. However, **(B, C)** show patients classified as Objective Responders who may not show such ideal trajectories (shown in red arrow). In **(B)** a patient who briefly shows reduction is classified as an Objective Responder as duration of response is not accounted for when RECIST response is assigned. In **(C)** the patient is classified as an Objective Responder, even though they dropped out at the first point due to an Adverse Event (AE). Others who arguably benefit may still not be classified as Objective Responders (shown in green arrows in bottom row). **(D)** Shows a patient whose tumor has stabilized just above the dSLD < -30% threshold. **(E)** Shows a patient who shows clear benefit from the therapy as tumor growth is inhibited but will be considered a non-responder as the lesion has not shrunk. **(F)** Shows a patient with a new metastatic lesion who will be classified as Progressive Disease even though that lesion may shrink on further treatment.

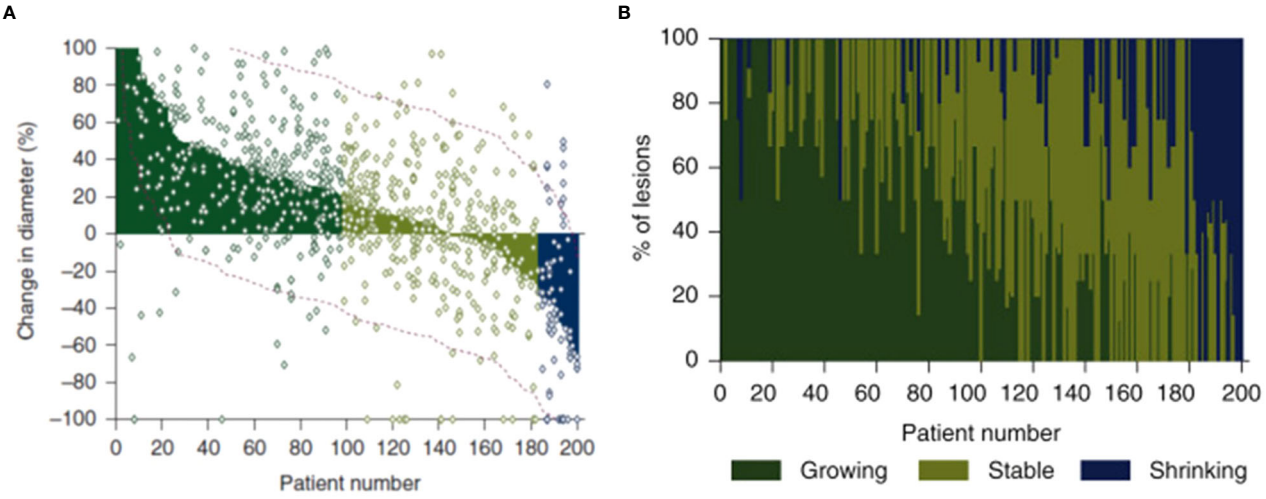

FIGURE 4
In these figures, patients are ordered from worst aggregate response (greatest dSLD, Patient#1) to the best aggregate response (least dSLD, Patient #200). In **(A)** we show the dSLD in solid coloring & the variability in individual lesion change in diameters is also show as dots. The red dotted lines represent standard deviation of the lesions change in per patient. In **(B)** we show the fraction of growing (change in diameter >20%), stable & shrinking (change in diameter < -20%) lesions in each of the patients. Reproduced (11) from with permission.

Implications of ignoring lesion-to-lesion heterogeneity in decision-making

Misleading interpretations of biomarkers sampling

Biomarkers are used to identify responder populations and generate insight into the mechanisms driving success or failure. In IO trials, however, biomarkers are usually analyzed from an archived tumor sample or a non-target lesion sample (17–19). While biomarkers are occasionally evaluated in target lesions, they are generally analyzed at the patient level, rather than at the lesion level. For patients with lesion-to-lesion heterogeneity, it can be unclear whether the biomarker result was derived from a growing or shrinking lesion. In Figure 2A, every lesion is growing; the tumor sample is from a growing lesion. However, in Figure 2B, only half of the lesions are growing. It is unclear whether the tumor sample was derived from a growing or shrinking lesion. In Figure 2C, all lesions were shrinking; the tumor sample was derived from a shrinking lesion, despite the patient-level characterization of Progressive Disease (PD). Our analysis of lesion-to-lesion heterogeneity in melanoma shows that only ~50% of target lesions progressed in PD patients (11). This suggests that approximately 50% of biomarker results in RECIST PD patients may be from lesions that shrink on treatment.

Potential solutions to this problem include collecting biomarker samples from target lesions (so we know whether the sampled

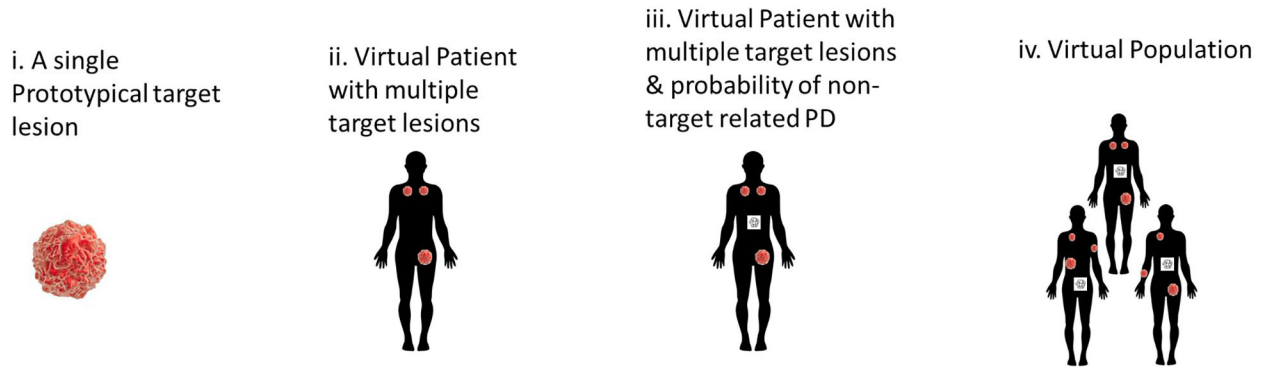

FIGURE 5
Hierarchical development of QSP model that provides a framework to incorporate lesion-to-lesion heterogeneity i. A single well-mixed lesion with interactions between tumor & immune system ii. Multiple target lesions within a single Virtual Patient tracked. The multiple target lesions have different growth rates, sizes etc. When ΔSLD>+20%, the patient is classified as PD iii. A stochastic model periodically predicts the probability of non-target driven PD (any one of non-target lesion growth or metastases or drop-out for other reasons). At this stage, the patient can be classified as PD when such an event occurs iv. A Virtual Population with such VPs that is calibrated to be consistent with reported clinical data – such as waterfall charts, RECIST scores, PFS curves.

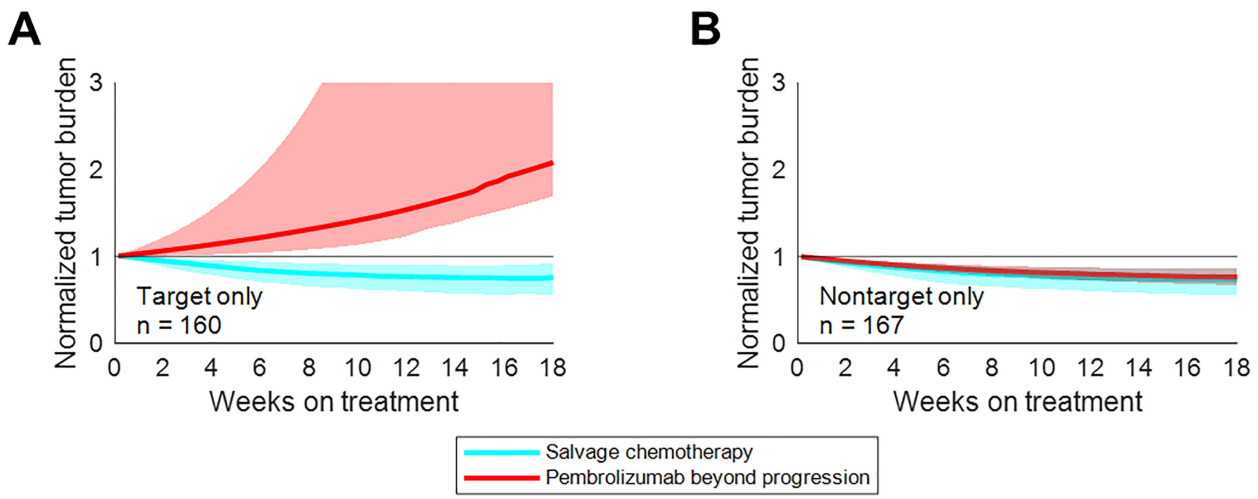

FIGURE 6
Treatment beyond progression may control tumor burden after nontarget progression on pembrolizumab. Median tumor burden in patients from an N=1000 simulated trial receiving pembrolizumab beyond progression (red) or salvage chemotherapy (cyan). **(A)** Patients with target progression without non-target progression or new metastases. **(B)** Patients with non-target progression or new metastases without target progression. Solid lines represent medians, while shaded regions indicate interquartile ranges. Reproduced from with permission.

lesions grew or shrank and samples at the time of progression). However, given the challenges of lesion biopsies, measuring circulating biomarkers like ctDNA (20) at baseline and at the time of progression to identify changes in biomarker prevalence may be more practical. More work needs to be done to understand the relationship between these biomarkers and lesion heterogeneity.

Does progressive disease justify drug discontinuation?

In early immune-oncology studies, RECISTv1.1 PD was listed as a cause for investigational treatment discontinuation that necessitated switching to a subsequent therapy. Several oncologists continued dosing despite the recommendation given that their patients were doing well, despite having Progressive Disease per RECISTv1.1 (21, 22). As a result, immunotherapy discontinuation decisions now rely upon alternative metrics, such as irRECIST, iRECIST, and WHO criteria (7, 23, 24).

Here, we propose a lesion-level treatment strategy. If all lesions are growing, the patient should switch to a new therapy. If all lesions are shrinking, the patient should remain on the existing therapy. Patients with a mixture of growing and shrinking lesions should do both (remain on existing while adding on a new therapy). and other such strategies for dealing with complexity and heterogeneity need to be tested in clinical trials as well as evaluated using in QSP models that account for lesion-to-lesion variability.

Personalized medicine focused on addressing every lesion

We have argued (25), based on simulation analysis of lesion-to-lesion heterogeneity, that checkpoint combinations may be ineffective for patients whose immunologically 'hot' lesions are already shrinking due to pembrolizumab; non-responding 'cold' lesions may be unaffected by other immunotherapies that depend on T-cell activation. In contrast, immunotherapy combinations may be most impactful for patients with 'intermediate' T-cell infiltration ('warm' lesions) that are inadequately controlled by a single checkpoint. For other patients, therapies effective against cold tumors (e.g., chemotherapy, oncolytic viruses, targeted therapy) may be more effective combination agents to eliminate non-responding lesions. Understanding individual paths to progression is critical for determining the right combination therapy to offer to a patient. This may be facilitated by on-therapy biomarker samples from progressing lesions or ctDNA samples at the time of progression. Of note, decisions about continuing or switching treatment in the context of heterogeneous response across metastatic lesions should be made on a case-by-case basis, taking into consideration multiple factors such as the patient's disease history, molecular profile, and treatment goals.

Go/No-go decisions in drug development

Go/No-go decisions in early oncology drug development are driven by RECISTv1.1-based scores such as Objective Response Rate (ORR, % of patients who are classified CR+PR) and Progression-Free Survival (PFS) curves. Here we argue that patient-level (vs. lesion-level) definitions of efficacy can introduce bias into Go/No-Go decisions. First, RECISTv1.1 underestimates efficacy by classifying patients with mixed responses to therapy as having failed therapy. These patients benefit (in a subset of lesions), suggesting that the investigational agent may be effective as part of a combination therapy. Second, RECISTv1.1 underestimates efficacy in patients that are treated beyond progression. Approximately 50%

of patients are treated beyond progression, many for prolonged periods of time (8). This suggests that many practitioners do not consider RECISTv1.1 PD as drug failure (lack or loss of efficacy). Third, ORR overestimates efficacy in patients who gain only transient benefit (due to rebound or intolerability). Chemotherapy, for example, tend to elicit better ORR but worse survival than ICI drugs. Finally, heterogeneity in biomarker samples can make it harder to identify responder populations.

We propose that the goal of cancer therapy is to shrink as many lesions as possible, as deeply as possible, for as long as possible. Thus, the first index in any improved scoring framework should include the percentage of lesions that are responding. It is important to know whether the investigational drug or combination controls a larger number of lesions per patient than standard of care regimens. The second and third indices are depth and duration of tumor response. This comprises an area under the curve calculation from the lesion-size-over-time spaghetti plot. However, instead of stopping the plot at the time of RECISTv1.1 progression, the curve would continue until the investigational drug is discontinued and a new therapy is initiated. This would provide high scores for patients who remain on therapy for prolonged periods of time, even RECISTv1.1 non-responders who display stable disease or transient progression.

Framework to incorporate lesion-to-lesion heterogeneity in QSP models to support drug development

QSP models in Immune-Oncology have been used in various stages of drug development to support decision-making (26–29) They play a unique role in enabling integration of knowledge and data from multiple trials among the quantitative approaches available to drug developers. QSP model developers should consider incorporating the complex nature of clinical responses including lesion-to-lesion variability. This allows for simulated trajectories to capture the various paths to Progressive Disease (PD) seen in the clinical data and a more nuanced understanding of how a novel therapy has performed in a clinical trial.

We recently published two mathematical models of immune-mediated tumor killing that incorporate lesion-to-lesion heterogeneity. The first paper (25) investigated the limited utility of combination immune therapy in melanoma patients with a mixture of "hot" and "cold" lesions. The second paper evaluated the propensity for patients to benefit from treatment with pembrolizumab beyond progression based on the nature of their original progressive disease (30).

The first paper developed a multi-scale model of tumor and immune cells interactions. In brief, the model included three levels: lesions, patients, and populations (Figure 5). This contrasts with models which have a single average lesion per patient. In each lesion, tumor cells were assumed to grow exponentially and can be killed by activated CD8 T cells. The multiple lesions within each patient were variable in many parameters, including initial number of cancer cells, growth rate, and immune infiltration (number of T Cells) (31). In addition, non-target lesion related factors leading to Progressive Disease were modeled as a probabilistic model dependent on tumor burden.

When QSP models are calibrated to capture population RECIST scores and progression over time, not explicitly accounting for individual causes of progression, it may hinder mechanistic understanding. For instance, a model of aggregate tumor burden may predict high efficacy for checkpoint combinations in most patients. However, when accounting for lesion-to-lesion variability, the model (25) predicted that adding ipilimumab to pembrolizumab had minimal effect on "hot" lesions (that responded well to pembrolizumab monotherapy) and cold lesions (that did not respond to either immune therapy). Instead, the combination was most effective in "warm" tumors and thus most impactful in patients with exclusively "hot" and "warm" tumors. These predictions need to be verified clinically but provide a framework to account for this complexity. In ongoing work, we connect such lesion level response to Progression Free Survival (PFS) and Overall Survival (OS) to gain additional mechanistic understanding and predictive capability (32).

The second paper evaluated salvage chemotherapy versus pembrolizumab beyond progression in a virtual clinical trial of patients with non-small cell lung cancer (NSCLC) who progressed on pembrolizumab (30). We applied empirical tumor growth models coupled with statistical sampling strategies to inform the probability of a given tumor lesion to respond to treatment beyond progression. Lesion level responses were simulated with organ-specific probabilities and magnitudes of response, as previously reported (14). Furthermore, a tumor-burden dependent probability of progression from non-target lesion growth or the appearance of new metastases was applied to facilitate the stratification of patients by the nature of their original progression.

While uniformly switching to salvage chemotherapy yielded better population-level outcomes than uniformly maintaining pembrolizumab beyond progression, there was a subset of patients for whom pembrolizumab beyond progression yielded longer progression-free survival. These patients tended to be those whose initial progression was due to non-target lesion growth or the appearance of new metastases – not those with target lesion growth (Figure 6). Prospective trials evaluating pembrolizumab beyond progression in this setting may be warranted.

Achieving systemic tumor control across all metastatic lesions is critical for long-term patient survival but remains a distant goal. High lesion-level response heterogeneity persists, conferring many dissociated responses across metastatic lesions. We developed a statistical metric - "Gower distance" to quantify response heterogeneity across metastatic lesion, which was found closely associated with drug efficacy and long-term patient survival (33). In addition, we developed mathematical models to investigate lesion-specific heterogeneity in terms of their dynamics in growth, response, and progression during treatment. We found that organ-level progression sequence is closely associated with long-term survival; in

addition, patients with metastatic colorectal cancer whose first lesion-level progression occurs in the liver often have worse survival (15, 34).

Several groups have developed effective QSP models of immune-mediated tumor killing (35–38). Most QSP models develop Virtual Populations of patients with cancer and predict clinical outcomes assuming each patient has only a single average tumor (26, 27). This simplification may be appropriate in some cases (for example, in pre-clinical setting with a single lesion per animal or to explore tumor-immune interactions in a single lesion) but could result in misleading estimates of clinical efficacy when calibrated to RECISTv1.1 scores.

In the clinical setting, most patients display a mixed response due to inherent pathophysiological heterogeneity. Virtual patients in QSP models need to be more realistic to identify the combination therapies capable of generating broad and sustained responses in the clinic. It is encouraging to see more efforts in this direction (39).

Summary and next steps

- Lesion-to-lesion heterogeneity remains underappreciated in oncology trials. Mounting evidence shows that RECISTv1.1 criteria are too broad to adequately characterize patient benefit from therapy, especially cancer immunotherapy. We should include individual lesion responses to improve the assessment of drug efficacy and patient benefit.
- Ignoring lesion-to-lesion heterogeneity could bias our decision-making process in oncology trials. We should interpret individual lesion-derived biomarkers with caution, as they may not reflect the characteristics of other lesions. More attention should be paid to patients categorized as progressors per RECISTv1.1, as many of their lesions may still be responding or have already stabilized. For these patients, combination therapy should be considered over discontinuation of current treatment.
- We should work together within our cancer research community to develop and validate more data-driven approaches to evaluate drug efficacy. Lesion-to-lesion heterogeneity should be considered during the QSP model development, clinical trial simulations, and statistical modeling to support better decision-making.

Author contributions

All authors listed have made a substantial, direct, and intellectual contribution to the work, and approved it for publication.

Conflict of interest

Author BT reports employment at the company Merck Sharp & Dohme Corp., a subsidiary of Merck & Co., Inc., Kenilworth, NJ, United States, and is a shareholder in Merck & Co., Inc., Kenilworth, NJ, United States. Author RK was employed by the company Vantage Research Inc. Vantage Research was engaged by MSD as a Contract Research Organization.

The remaining authors declare that the research was conducted in the absence of any commercial or financial relationships that could be construed as a potential conflict of interest.

Publisher's note

References

1. Reuben A, Spencer C, Prieto P, Gopalakrishnan V, Reddy S, Miller J, et al. Genomic and immune heterogeneity are associated with differential responses to therapy in melanoma. *NPJ Genom Med* (2017) 2(10). doi: 10.1038/s41525-017-0013-8

2. Sanborn J, Chung J, Purdom E, Wang N, Kakavand H, Wilmott J, et al. Phylogenetic analyses of melanoma reveal complex patterns of metastatic dissemination. *Proc Natl Acad Sci U S A.* (2015) 112(35):10995. doi: 10.1073/pnas.1508074112

3. Hugo W, Zaretsky J, Sun L, Song C, Moreno BH, Hu-Lieskovan S, et al. Genomic and transcriptomic features of response to anti-PD-1 therapy in metastatic melanoma. *Cell* (2016) 165:35–44. doi: 10.1016/j.cell.2016.02.065

4. Al Bakir M, Huebner A, Martínez-Ruiz C, Grigoriadis K, Watkins TBK, Pich O, et al. The evolution of non-small cell lung cancer metastases in TRACERx. *Nature* (2023) 616(7957):534–42. doi: 10.1038/s41586-023-05729-x

5. Eisenhauer E, Therasse P, Bogaerts J, Schwartz L, Sargent D, Ford R, et al. New response evaluation criteria in solid tumours: revised RECIST guideline (version 1.1). *Eur J Cancer* (2009) 45(2):228–47. doi: 10.1016/j.ejca.2008.10.026

6. Simard J, Smith M, Chandra S. Pseudoprogression of melanoma brain metastases. *Curr Oncol Rep* (2018) 20(11):91. doi: 10.1007/s11912-018-0722-x

7. Wolchok J, Hoos A, O'Day S, Weber J, Hamid O, Lebbé C, et al. Guidelines for the evaluation of immune therapy activity in solid tumors: immune-related response criteria. *Clin Cancer Res* (2009) 15(23):7412–20. doi: 10.1158/1078-0432.CCR-09-1624

8. Beaver JA, Hazarika M, Mulkey F, Mushti S, Chen HHK, Sridhara R, et al. Patients with melanoma treated with an anti-PD-1 antibody beyond RECIST progression: a US food and drug administration pooled analysis. *Lancet Oncol* (2018) 19(2):229–39. doi: 10.1016/S1470-2045(17)30846-X

9. Shoushtari AN, Olszanski AJ, Nyakas M, Hornyak TJ, Wolchok JD, Levitsky V, et al. Pilot study of ONCOS-102 and pembrolizumab: remodeling of the tumor microenvironment and clinical outcomes in advanced melanoma. *Clin Cancer Res* (2023) 29(1):100–9. doi: 10.1158/1078-0432.CCR-22-2046

10. Arance A, de la Cruz-Merino L, Petrella TM, Jamal R, Ny L, Carneiro A, et al. Phase II LEAP-004 study of lenvatinib plus pembrolizumab for melanoma with confirmed progression on a programmed cell death protein-1 or programmed death ligand 1 inhibitor given as monotherapy or in combination. *J Clin Oncol* (2023) 41 (1):75–85. doi: 10.1200/JCO.22.00221

11. Topp B, Thiagarajan K, De Alwis D, Snyder A, Hellmann M. Lesion-level heterogeneity of radiologic progression in patients treated with pembrolizumab. *Ann Oncol* (2021) 32(12):1618–25. doi: 10.1016/j.annonc.2021.09.006

12. Ippolito D, Maino C, Ragusi M, Porta M, Gandola D, Franzesi C, et al. Immune response evaluation criteria in solid tumors for assessment of atypical responses after immunotherapy. *World J Clin Oncol* (2021) 12(5):323–34. doi: 10.5306/wjco.v12.i5.323

13. Guan Y, Feng D, Yin B, Li K, Wang J. Immune-related dissociated response as a specific atypical response pattern in solid tumors with immune checkpoint blockade. *Ther Adv Med Oncol* (2022) 14. doi: 10.1177/17588359221096877

14. Osorio J, Arbour K, Le D, Durham J, Plodkowski A, Halpenny D, et al. Lesion-level response dynamics to programmed cell death protein (PD-1) blockade. *J Clin Oncol* (2019) 37(36):3546–55. doi: 10.1200/JCO.19.00709

15. Zhou J, Cipriani A, Liu Y, Fang G, Li Q, Cao Y. Mapping lesion-specific response and progression dynamics and inter-organ variability in metastatic colorectal cancer. *Nat Commun* (2023) 14(1). doi: 10.1038/s41467-023-36121-y

16. Topp B, Snyder A, Wolchok J. RECISTv1.1 progression in oncology: shades of gray. *Cancer Cell* (2023) 23)00138-1:S1535–6108. doi: 10.1016/j.ccell.2023.04.012

17. Hessey S, Fessas P, Zaccaria S, Jamal-Hanjani M, Swanton C. Insights into the metastatic cascade through research autopsies. *Trends Cancer* (2023). doi: 10.1016/j.trecan.2023.03.002

18. Loi S, Salgado R, Schmid P, Cortes J, Cescon DW, Winer EP, et al. Association between biomarkers and clinical outcomes of pembrolizumab monotherapy in patients with metastatic triple-negative breast cancer: KEYNOTE-086 exploratory analysis. *JCO Precis Oncol* (2023), 7:e2200317. doi: 10.1200/PO.22.00317

19. Tomlins SA, Khazanov NA, Bulen BJ, Hovelson DH, Shreve MJ, Lamb LE, et al. Development and validation of an integrative pan-solid tumor predictor of PD-1/PD-L1 blockade benefit. *Commun Med* (2023) 3(1):14. doi: 10.1038/s43856-023-00243-7

20. Vellanki PJ, Ghosh S, Pathak A, Fusco MJ, Bloomquist EW, Tang S, et al. Regulatory implications of ctDNA in immuno-oncology for solid tumors. *J immunother Cancer* (2022) 11(2). doi: 10.1136/jitc-2022-005344

21. Zhou H, Sun Y, Xiu W, Han J, Zhong L, Suo J, et al. Overall survival benefit of continuing immune checkpoint inhibitors treatment post dissociated response in patients with advanced lung cancer. *J Cancer Res Clin Oncol* (2020) 146(11):2979–88. doi: 10.1007/s00432-020-03282-y

22. Fukuokaya W, Kimura T, Yanagisawa T, Kimura S, Tsuzuki S, Koike Y, et al. Clinical benefit of continuing pembrolizumab treatment beyond progression in patients with metastatic urothelial carcinoma. *Cancer Immunol Immunother* (2022) 71(1):229–36. doi: 10.1007/s00262-021-02980-x

23. Emens L, Adams S, Cimino-Mathews A, Disis M, Gatti-Mays M, Ho A, et al. Society for immunotherapy of cancer (SITC) clinical practice guiddeline on immunotherapy for the treatment of breast cancer. *J Immunother Cancer.* (2021) 9 (8):e002597. doi: 10.1136/jitc-2021-002597

24. Somarouthu B, Lee S, Urban T, Sadow C, Harris G, Kambadakone A. Immune-related tumour response assessment criteria: a comprehensive review. *Br J Radiol* (2018) 91(1084):20170457. doi: 10.1259/bjr.20170457

25. Kumar R, Thiagarajan K, Jagannathan L, Liu L, Mayawala K, de Alwis D, et al. Beyond the single average tumor: understanding IO combinations using a clinical QSP model that incorporates heterogeneity in patient response. *CPT Pharmacom Syst Pharmacol* (2021) 10(7):684–95. doi: 10.1002/psp4.12637

26. Chelliah V, Lazarou G, Bhatnagar S, Gibbs J, Nijsen M, Ray A, et al. Quantitative systems pharmacology approaches for immuno-oncology: adding virtual patients to the development paradigm. *Clin Pharmacol Ther* (2021) 109(3):605–18. doi: 10.1002/cpt.1987

27. Sancho-Araiz A, Mangas-Sanjuan V, Trocóniz I. The role of mathematical models in immuno-oncology: challenges and future perspectives. *Pharmaceutics* (2021) 13(7):1016. doi: 10.3390/pharmaceutics13071016

28. Valentinuzzi D, Jeraj R. Computational modelling of modern cancer immunotherapy. *Phys Med Biol* (2020) 65(24). doi: 10.1088/1361-6560/abc3fc

29. Butner J, Wang Z. Predicting immune checkpoint inhibitor response with mathematical modeling. *Immunotherapy* (2021) 13(14):1151–5. doi: 10.2217/imt-2021-0209

30. Qi T, Cao Y. Virtual clinical trials: a tool for predicting patients who may benefit from treatment beyond progression with pembrolizumab in non-small cell lung cancer. *CPT Pharmacom Syst Pharmacol* (2023) 12(2):236–49. doi: 10.1002/psp4.12896

31. Erdag G, Schaefer JT, Smolkin ME, Deacon DH, Shea SM, Dengel LT, et al. Immunotype and immunohistologic characteristics of tumor-infiltrating immune cells are associated with clinical outcome in metastatic melanoma. *Cancer Res* (2012) 72 (5):1070–80. doi: 10.1158/0008-5472.CAN-11-3218

32. Channavazzala M, Thiagarajan K, Ray T, et al. Using an IO QSP model to re-define efficacy, discontinuation criteria, and biomarker analysis. *ACoP11* (2020).

33. Zhou J, Li Q, Cao Y. Spatiotemporal heterogeneity across metastases and organ-specific response informs drug efficacy and patient survival in colorectal cancer. *Cancer Res* (2021) 81(9):2522–33. doi: 10.1158/0008-5472.CAN-20-3665

34. Zhou J, Liu Y, Zhang Y, Li Q, Cao Y. Modeling tumor evolutionary dynamics to predict clinical outcomes for patients with metastatic colorectal cancer: a retrospective analysis. *Cancer Res* (2020) 80(3):591–601. doi: 10.1158/0008-5472.CAN-19-1940

35. Milberg O, Gong C, Jafarnejad M, Bartelink IH, Wang B, Vicini P, et al. A QSP model for predicting clinical responses to monotherapy, combination and sequential therapy following CTLA-4, PD-1, and PD-L1 checkpoint blockade. *Sci Rep* (2019) 9 (11286). doi: 10.1038/s41598-019-47802-4

36. Peskov K, Azarov I, Chu et al L. Quantitative mechanistic modeling in support of pharmacological therapeutics development in immuno-oncology. *Front Immunol* (2019) 10:924. doi: 10.3389/fimmu.2019.00924

37. Siewe N, Friedman A. Optimal timing of steroid initiation in response to CTLA-4 antibody in metastatic cancer: a mathematical model. *PloS One* (2022) 17(11): e0277248. doi: 10.1371/journal.pone.0277248

38. Butner J, Wang Z, Elganainy D, Al Feghali K, Plodinec M, Calin G, et al. A mathematical model for the quantification of a patient's sensitivity to checkpoint inhibitors and long-term tumour burden. *Nat BioMed Eng.* (2021) 5(4):297–308. doi: 10.1038/s41551-020-00662-0

39. Leete J, Zager M, Musante C, Shtylla B, Qiao W. Sources of inter-individual variability leading to significant changes in anti-PD-1 and anti-PD-L1 efficacy identified in mouse tumor models using a QSP framework. *Front Pharmacol* (2022) 13:1056365. doi: 10.3389/fphar.2022.1056365

frontiers | Frontiers in Immunology

TYPE Review
PUBLISHED 28 June 2023
DOI 10.3389/fimmu.2023.1135148

OPEN ACCESS

EDITED BY
Fabrizio Mattei,
National Institute of Health (ISS), Italy

REVIEWED BY
Frank Momburg,
German Cancer Research Center (DKFZ), Germany
Cai Zhang,
Shandong University, China

*CORRESPONDENCE
Valentina Carannante
carann@kth.se
Björn Önfelt
onfelt@kth.se

RECEIVED 31 December 2022
ACCEPTED 05 June 2023
PUBLISHED 28 June 2023

CITATION
Carannante V, Wiklund M and Önfelt B (2023) *In vitro* models to study natural killer cell dynamics in the tumor microenvironment. *Front. Immunol.* 14:1135148. doi: 10.3389/fimmu.2023.1135148

In vitro models to study natural killer cell dynamics in the tumor microenvironment

Valentina Carannante[1]*, Martin Wiklund[1] and Björn Önfelt[1,2]*

[1]Department of Applied Physics, Science for Life Laboratory, KTH Royal Institute of Technology, Stockholm, Sweden, [2]Center for Infectious Medicine, Department of Medicine Huddinge, Science for Life Laboratory, Karolinska Institutet, Stockholm, Sweden

Immunotherapy is revolutionizing cancer therapy. The rapid development of new immunotherapeutic strategies to treat solid tumors is posing new challenges for preclinical research, demanding novel *in vitro* methods to test treatments. Such methods should meet specific requirements, such as enabling the evaluation of immune cell responses like cytotoxicity or cytokine release, and infiltration into the tumor microenvironment using cancer models representative of the original disease. They should allow high-throughput and high-content analysis, to evaluate the efficacy of treatments and understand immune-evasion processes to facilitate development of new therapeutic targets. Ideally, they should be suitable for personalized immunotherapy testing, providing information for patient stratification. Consequently, the application of *in vitro* 3-dimensional (3D) cell culture models, such as tumor spheroids and organoids, is rapidly expanding in the immunotherapeutic field, coupled with the development of novel imaging-based techniques and -omic analysis. In this paper, we review the recent advances in the development of *in vitro* 3D platforms applied to natural killer (NK) cell-based cancer immunotherapy studies, highlighting the benefits and limitations of the current methods, and discuss new concepts and future directions of the field.

KEYWORDS

NK cells, tumor microenvironment, tumor spheroids, tumor organoids, microscopy, flow cytometry, tissue sectioning, live cell imaging

Abbreviations: 3D, three-dimensional; NK, natural killer; TME, tumor microenvironment; 2D, two-dimensional; PDMS, polydimethylsiloxane; ECM, extracellular matrix; iPS, induced pluripotent stem cells; PBMC, peripheral blood mononuclear cell; IFN, interferon; TNF, tumor necrosis factor; IL, interleukin; ADCC, antibody-depended cellular cytotoxicity; dNK, decidual NK; IP, interferon-inducible protein; HSC, hepatic stellate cells; DC, dentric cell; CAR, chimeric antigen receptor; TGF, transforming growth factor; LAK, lymphokine-activated killer cells; poly-HEMA, poly-2-hydroxyethyl methylacrylate; ULA, ultra-low attachment; PEG, polyethylene glycol; UCB, umbilical cord blood; USW, ultrasonic standing waves; ^{51}Cr, chromium-51; LDH, lactate dehydrogenase (LDH); PLGA-MnO_2 NPs, poly(lactic-co-glycolic) manganese dioxide nanoparticles; HSPC, hematopoietic stem and progenitor cells; CSR, chimeric switch receptors.

1 Introduction

Immunotherapy comprises a large set of therapeutical strategies aimed at using or improving immune cell activity against tumors. Natural killer (NK) cells are NKp46^{+} innate lymphocytes that participate in cancer immune surveillance, by eliminating tumor cells by cell-mediated cytotoxicity and pro-inflammatory cytokine release (1). Our ability to design efficient NK-based therapies requires broad knowledge of NK cell behavior in the tumor environment (TME) and screening platforms that reproduce such environments *in vitro*. NK cell activity has mostly been studied using two-dimensional (2D) cultures *in vitro*, and mouse models *in vivo*. These models have provided invaluable information in terms of phenotypic and functional characterization of NK cells. However, they present multiple limitations in terms of translational potential.

2D cell cultures are frequently used in research since they are easy to handle and well compatible with wide range of assays, especially if they involve cells growing in suspension, such as lymphocytes. However, a vast proportion of cells constituting human tissue are adherent. Generally, oxygen plasma-treated polystyrene surfaces in combination with serum-supplemented cell culture media are used to support cell adhesion and maintenance. Other materials that have been used in the microfluidic field and also demonstrated to be suitable for adherent cell growth include polydimethylsiloxane (PDMS) (2), cyclo-olefin polymer (3), polymethyl-methacrylate (4) and polycarbonate (5). Independently of the material used, adherent cells that interact with flat surfaces tend to distribute as monolayers. But cell monolayers are far from being representative of the three-dimensional (3D) architecture of the original tissue. The third dimension matters as the function of a cell in a tissue is dependent on its position in relation to the extracellular matrix (ECM) and the surrounding cells (6, 7). The composition of the ECM, cell-to-cell adhesion and mechanical stress contribute to cell proliferation, differentiation, and migration (8–11). The gradients of gas and nutrients in a tissue determine cell fate, shaping their metabolic and apoptotic programs (12–14). Chemotactic gradients modulate the direction and dynamics of cell migration (15). This combination of biomechanical and biochemical cues present in the tissues might have significant implications for NK cell-mediated tumor surveillance and response to treatment (16, 17). Since 2D cell cultures show multiple limitations in reproducing the original features of human tissues (18), their use for research is usually complemented with mouse models, such as genetically engineered mouse models, patient-derived tumor xenografts and humanized mice. Mouse models can provide valuable information on the aetiology and the progression of diseases, as well as safety of therapies, but they are not optimal models for immunotherapy screening and precision medicine. Mouse models are also very expensive, not suitable for high-throughput testing, and they do not fully recapitulate the stromal composition of human tissue.

To overcome these limitations, a wide variety of techniques have been developed and optimized for routine use of 3D cultures in biological research (18–21). 3D cultures are commonly categorized into scaffold-based and scaffold-free cultures. In scaffold-based 3D cultures, a substrate is provided to simulate the properties of ECM and promote cell adhesion (Figure 1A) (22–28), and they are commonly applied in bone and myocardial tissue regeneration (29). Scaffold-free 3D cultures rely on the formation of multicellular aggregates by promoting the adhesion of cells to each other rather than to a substrate (Figure 1B). Scaffold-free 3D cultures are low-cost and they guarantee high levels of reproducibility (18). Their main applications include studies of solid tumor models, immune cell-solid tumor interaction, drug screening and formation of organotypic models. The term "spheroids" generically refers to tight cellular aggregates with spherical shape (Figure 1B). They can be composed of multiple cell types (heterotypic spheroids) or a single cell type (homotypic spheroids). The term "organoids" usually refers to 3D cultures composed of multiple cell types with specific localization and roles within the aggregates, resembling the composition, organization and function of the original tissue (30). Such specialization within the organoids is usually obtained driving the differentiation of stem cells (induced-pluripotent stem cells (iPS), primary stem cells, adult stem cells) *in vitro*. In this regard, organoids are effectively small reproductions of organs *in vitro* (Figure 1C).

The boundaries between "spheroids" and "organoids" become less clear in the context of tumors, i.e. tissue that by definition lose structural and functional organization (31). For simplicity, we will collectively refer to 3D models used to recapitulate tumor tissue as "tumor spheroids". In the following sections, we describe the currently available methods to characterize NK cell phenotype, cytotoxicity and infiltration in tumor spheroids, as well as their application in immunotherapy testing. The application of tumor spheroids in the NK cell field goes back to the late 70´, their use remained sporadic until very recently. Nowadays, the development of new tools for culture and data analysis is boosting the application of tumor spheroids in NK cell research.

2 Natural killer cells

NK cells are innate lymphocytes that promote immune surveillance and tissue homeostasis (32). Fast activation is one of the key features of NK cells, which contributed to their discovery: in 1975, R. Kiessling, E. Klein and H. Wigzell reported their identification of "naturally occurring lymphocytes" able to "spontaneously kill" mouse Moloney leukemia cells (33, 34). The term "spontaneously" referred to their ability to be cytotoxic *in vitro* within an hour, without requiring prior exposure to the same tumor cells (33, 34). Rapid effector functions and lack of prior sensitization markedly distinguishes NK cells from T cells, that require 6 hours (with co-stimulation) up to 30 hours (in the absence of co-stimulation) to be fully activated (35). Cell-mediated cytotoxicity and pro-inflammatory cytokine release are the most prominent NK cell effector functions (36). However, multiple NK cell subsets with varying functions have been reported since their discovery.

NK cells express the cell surface marker NKp46, and they can be found in the body as circulating or tissue-resident cells (37). Circulating NK cells, also called "conventional" NK cells,

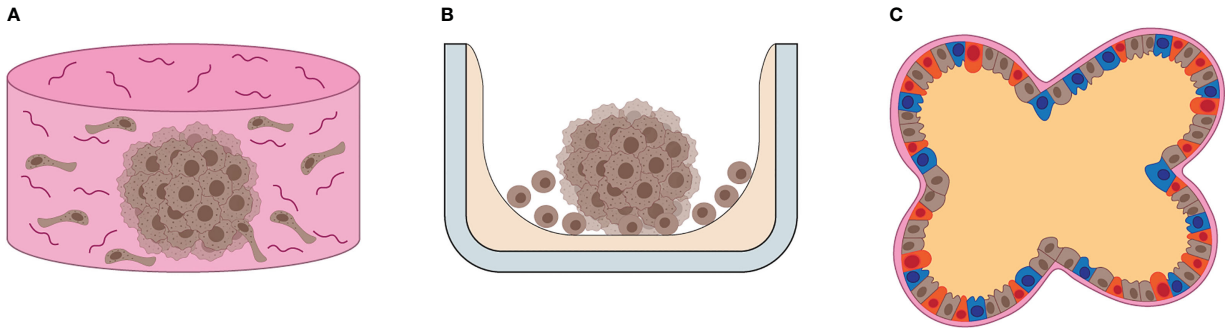

FIGURE 1
Overview of 3D cultures. **(A)** Illustration of scaffold-based 3D cell culture. Scaffolds resemble the ECM composition and 3D architecture of human tissues, providing support for cells to grow and differentiate *in vitro*. **(B)** Illustration of scaffold-free 3D cell culture. Often the substrate (gray) is coated by a non-adhesive, inert chemical (beige), which promotes cell-to-cell interaction, ECM and growth factor release, leading to the formation of self-sustained 3D cell cultures *in vitro*. **(C)** The illustration depicts the general features of organoids, such as multicellular composition, defined cellular distribution, cell differentiation and basolateral specialization of functions, such as EMC production in the basal area and fluid release in the apical area of cells.

represent 5-15% of peripheral blood mononuclear cells (PBMCs). They constantly travel between spleen, lymph nodes and inflamed tissues using blood and lymphatic vessels (38). Tissue-resident NK cells can be found in the liver, lung, adipose tissue, and uterus during pregnancy (39).

Two main NK cell subsets have been characterized in humans: $CD56^{Bright}$ $CD16^{-}$ and $CD56^{Dim}$ $CD16^{+}$ (40). $CD56^{Bright}$ $CD16^{-}$ NK cells are preferentially distributed in lymph nodes, tonsils, and uterus, and they show strong cytokine production (1, 41). $CD56^{Dim}$ $CD16^{+}$ cells represent approximately 90% of circulating NK cells in blood and spleen, and their main features are cytotoxic activity and cytokine production (42). $CD56^{Bright}$ $CD16^{-}$ NK cells express high levels of CCR7 and L-selectin, while both receptors are absent on $CD56^{Dim}$ NK cells (43, 44). On the other hand, $CD56^{Dim}$ $CD16^{+}$ NK cells present high levels of CXCR1, CX3CR1 and Chem23, chemokine receptors that drive their recruitment into inflamed tissues (45–47). Migration into peripheral tissues is assisted by additional adhesion proteins, such as low-affinity ligands for E-selectin and P-selectin, that promote leukocyte rolling on the vascular bed, and high-affinity integrins that mediate firm adhesion to endothelial cells and subsequent trans-endothelial migration (1).

NK cytolytic activity is mediated by both release of perforin/granzyme granules and death receptor activation (Figure 2) (48). Cytokines produced by NK cells comprise pro-inflammatory mediators, such as interferon γ (IFN-γ) and tumor necrosis factor-α (TNF-α), and immunosuppressive mediators, such as interleukin (IL)-10. NK cells also secrete growth factors, such as granulocyte macrophage colony-stimulating factor and granulocyte colony-stimulating factor (45), and several chemokines, including CCL2, CCL3, CCL4 and CCL5 (49). In addition, NK cells can perform antibody-depended cellular cytotoxicity (ADCC). ADCC is a potent type of cell-mediated cytotoxicity that relies on antibody crosslinking on the target cell (1). At early phases of immune responses, NK cells produce IFN-γ, promoting the immunoglobulin isotype switch towards IgG in B cells. At late phases of the immune responses and during antigen re-challenge, NK cells use the CD16a receptor, also called FcγRIIIa, to recognize target cells covered with IgG immunoglobulins. Such recognition induces a strong release of granzyme and perforin, that ultimately kills the target cell. ADCC also represents an example of cross-talk between NK cells and adaptive immunity.

NK cell activation is regulated by a dynamic system of inhibitory and activating signals. This system mainly relies on cell surface receptors that discriminate between healthy and unhealthy cells (36). Thus, tumor cells become susceptible to NK cells due to increased expression of activating ligands and/or decreased expression of inhibitory ligands (50). The main NK cell activating receptors are CD16, NKG2D, DNAM-1 and the natural cytotoxicity receptors (NCRs) NKp30, NKp44 and NKp46 (51), while CD94/NKG2A (C-type Lectin superfamily glycoproteins) (51), TIGIT (52, 53), LAG-3 and TIM-3 are inhibitory receptors. In addition, NK cells express KIR receptors, which are encoded by the KIR polygenic and polymorphic locus that includes both activating and inhibitory variants. Two KIRs haplotypes have been characterized in humans, A and B, differing in the amount of inhibitory and activating KIRs, respectively (54). KIR receptors recognize the ubiquitously expressed HLA class I molecules (HLA-A, HLA-B, HLA-C). NK cells constantly undergo a process of education that finely tunes their responsiveness, optimizing their ability to mount an immune response against cells with reduced HLA class I expression (typically virus-infected and tumor cells), while maintaining tolerance to self (healthy tissues expressing HLA class I) (55–57). NK response is potentiated by co-stimulatory receptors, such as CD2 and 2B4, and cytokines, such as IL-2, IL-15, IL-12, IL-18 and IL-21 (58). Cytokine exposure, as well as receptor activation, can trigger the differentiation of memory NK subsets, defined as long-lived, self-renewing NK cells showing enhanced effector function and proliferative capacity during secondary exposure to pathogens (59).

The NK cell activities described so far are mainly pro-inflammatory. However, NK cells also play a major role in tissue homeostasis (Figure 2) (39). Such a role is well-exemplified by decidual NK cells (dNK). dNK cells are poorly cytotoxic tissue-

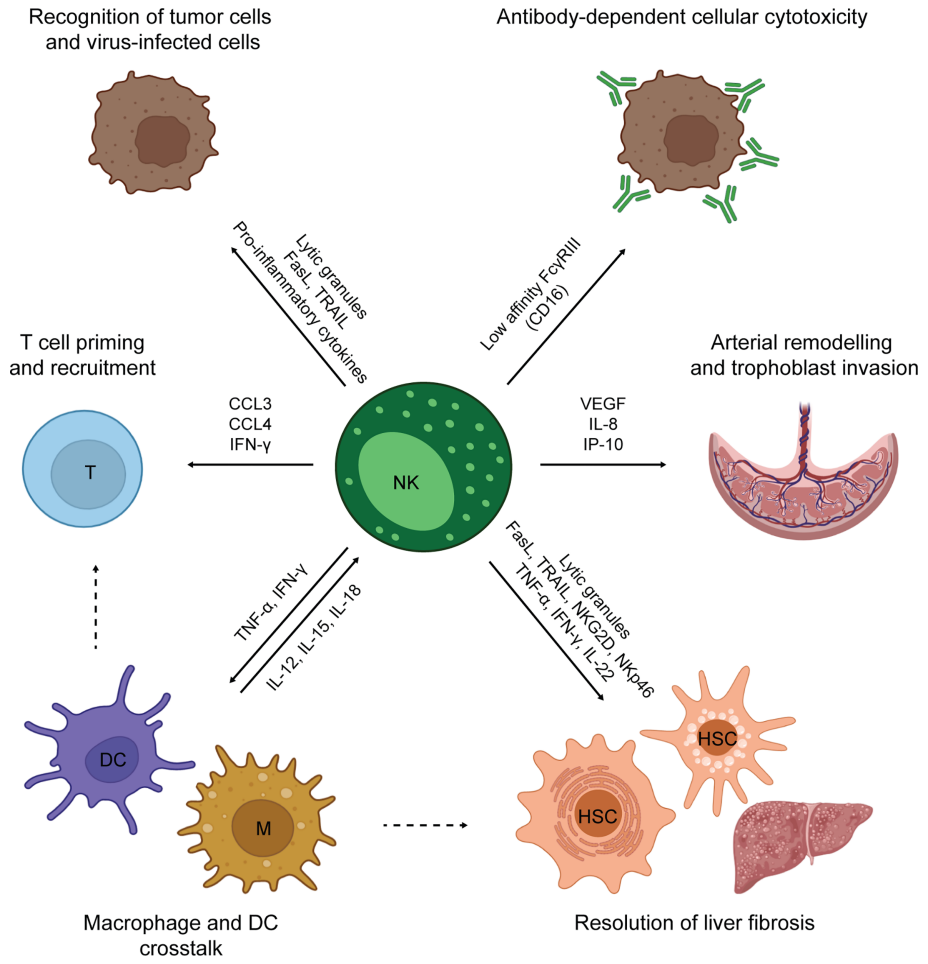

FIGURE 2
Overview of NK cell functions.

resident NK cells found in pregnant endometrial tissue to orchestrate placenta development. First, dNK cells produce angiogenic factors to re-model the uterine arterial system (60, 61). Secondly, they control extra-villous trophoblast cell invasion of spiral arteries, releasing IL-8 and interferon-inducible protein-10 (IP-10) (62). Both steps are crucial for ensuring a positive outcome of pregnancy (63). NK cells exist also in the adult liver and adipose tissues. After liver damage, NK cells collaborate with macrophages and hepatic stellate cells (HSC) in the resolution of fibrosis. In addition, cytotoxic NK cells kill hepatic stellate cells, specifically discerning between quiescent and activated cells (64). In adipose tissue, NK can sustain a local Th1 response and contribute to obesity-associated metabolic disease (65). NK cells are also involved in the prevention of autoimmunity, being able to kill immature dendritic cells (DCs) (66) and activated T cells (67, 68). In this review, we have primarily focused on the use of spheroids cultures to study the role of NK cells in cancer immune surveillance. However, multiple 3D models have been developed to study dNK cells and their role in pregnancy (69–74).

NK cells are key players in cancer immune surveillance and a variety of NK cell-based therapies are currently being developed and tested in Phase I/II clinical trials. Their ability to perform ADCC is taken into consideration while designing antibody-based immunotherapeutic strategies, and a plethora of activating receptors and co-receptors are used to produce new chimeric antigen receptor (CAR)-NK products for cellular immunotherapy. Compared to T cells, NK cell-based therapies show a better safety profile, rarely inducing severe adverse effects such as cytokine release syndrome and neurotoxicity. In addition, NK cells are not involved in graft-versus-host disease reactions, allowing the development of cell products from multiple sources, such as allogenic donors, cell lines and iPS cells, without safety concerns. Despite being effective in the treatment of hematopoietic cancers, the efficacy of NK cells in solid tumors is dramatically suppressed by the TME. For instance, presence of hypoxia (75) and acidic pH (76) affect NK cell survival and activity in the solid tumors (76–81). Tumor cells and fibroblasts cooperate in producing soluble factors that directly suppress NK cells, such as TGF-β (82), indoleamine 2,3-dioxygenase (83), adenosine and prostaglandin E2 (84). Expression of NK receptors and/or their corresponding ligands is often affected by the tumor microenvironment leading to decreased tumor recognition by NK cells (85–87).

To better understand, predict and possibly target NK cell inhibition in the tumor microenvironment, tumor spheroid

cultures that mimic solid cancers have been developed and adopted to NK cell research. In the next paragraphs, we will describe the currently available methods for spheroid formation applied to NK cell studies.

3 Methods of spheroid formation applied to NK cell studies

3.1 Spinner cultures

The application of spheroid cultures in the immunology field began in the late 70′ as models to study tumor allografts. Few methods of spheroid formation were available at that time, and the "spinner cultures" were among those. The method is based on culturing tumor cells in spinner flasks at constant stirring rates, promoting cell-to-cell interaction while preventing cell adhesion to the bottom of the flask (Figure 3A) (96). Sutherland et al. established mouse mammary sarcoma spheroids incubating cells in spinner flasks for 3-4 weeks (88). The spheroids were then exposed to allogenic mixed lymphocyte cultures (88) or implanted in the peritoneal cavity of allogenic mice (89–91) to study the effect of alloreactivity and immunization in solid tumors (88, 90). The spheroid implants could then be recovered to characterize the composition and the rate of immune cell infiltration (89, 91, 97). Similarly, Iwasaki et al. used the method to study the infiltration and cytolytic capacity of lymphokine activated killer (LAK) cells in human malignant glioma spheroids (98).

The spinner culture method allows great flexibility in terms of number of spheroids obtained, since different quantities can be produced simply scaling up or down the number of cells seeded and the volume of culture medium. The method is also easy-to-use and cost-effective. Areas of intense cell proliferation and necrosis, as well as cell migration and cell-to-cell interaction were detected within the spinner culture spheroids by image analysis (96, 98–100), making the method suitable to study tumor progression *in vitro*. In addition, proteomic profiling of glioma spinner cultures revealed substantial differences compared to monolayer cultures in terms of metabolism, antigen presentation and HLA-E expression, allowing He et al. to study the role of NKG2A in tumor resistance to NK cell therapy (101).

Nowadays, the application of spinner cultures to NK cell studies is quite rare, due to the limitations of the method. Cell aggregation is simply driven by cell-to-cell collision, limiting the use of the spinner cultures to cell types that adhere to each other without additional support. The incubation time is cell type-dependent, and a large variation of spheroid size can be observed within the same experiment, while many applications require homogeneously shaped and sized spheroid. In addition, the optimal stirring rate to prevent cell adhesion to the flask bottom might differ across cell types, requiring optimization steps for each experimental setup. Lastly, the process of spheroid formation cannot be monitored directly due to the constant agitation, and the spheroids need to be transferred to a different plate or substrate to be visualized by microscopy.

3.2 Liquid-overlay method

A spheroid-formation method that addresses some of the limitations of spinner cultures is the liquid-overlay technique (102–104). This technique involves covering cell culture surfaces with a thin layer of non-adhesive coating, preventing cell attachment to the substrate, and therefore favoring cell-to-cell interaction (Figure 3B) (103). Cell suspensions are simply transferred on top of the coated plates, and stable spheroid formation is obtained in a few days (102, 104). The thin and the transparent coating allows direct assessment of spheroid formation with standard transmission and fluorescence microscopes, reducing the sample handling steps. The use of the coating itself reduces the optimization steps required in the spinner cultures to set the proper spinning rate for each cell type.

The mostly used non-adhesive coating is the agarose gel, obtained by dissolving agarose powder in distilled water or buffers (phosphate buffer solution, cell culture medium) at concentrations usually spanning from 0.5% to 1.5% w/v (weight/volume) (104–106). Another commonly used non-adhesive coating is poly-2-hydroxyethyl methylacrylate (poly-HEMA) dissolved in ethanol (107). Apart from the chemical composition, agarose and poly-HEMA gels also differ in preparation time and long-term stability. The preparation of poly-HEMA plates requires three days (107), while agarose coating can be performed in few hours (104). However, poly-HEMA coated plates can be stored long-term at room temperature, while agarose gels are less stable, and degradation might occur over long-term cell cultures (108). In the last decades, multiple coatings have been developed that are commercially available as liquid solutions or through buying pre-coated culture plates. An example is represented by the ultra-low attachment (ULA) plates. ULA-plates are cell culture plates pre-coated with hydrophilic and neutrally charged hydrogel that prevents cell adhesion to the plastic. They are single-use and available in multiple formats.

Similar to spinner cultures, spheroids generated with the liquid-overlay techniques show necrotic (104–106, 109) and hypoxic (110) cores, deposition of ECM rich in collagen (I, III, IV, V) (111), fibronectin and laminin (112–114), and cell-to-cell and cell-to-matrix communication (105). These features make the liquid overlay-derived spheroids biologically relevant *in vitro* models. The method has been used to characterize the cytolytic activity and infiltration of NK cells in human glioma spheroids (115, 116), correlating NK activity with morphological and physical changes of the spheroids, such as loss of surface coherence (115), formation of cytoplasmic blebs (111), chromatin condensation (111, 116) and weight variation (117). It has also been used to identify adhesion molecules (112), receptors (106, 112, 114, 118–120) and metabolic pathways (121) involved in NK cell infiltration and cytotoxicity, as well as to test therapeutic strategies that enhance NK cell activity (105, 110, 120, 122–128). Importantly, the liquid-overlay technique is compatible with the use of primary material (124, 129–131), allowing the maintenance of tumor tissue explants up to a few weeks *in vitro*, retaining connective tissue components, endothelial cells, macrophage-like cells and blood capillaries (116).

10.3389/fimmu.2023.1135148

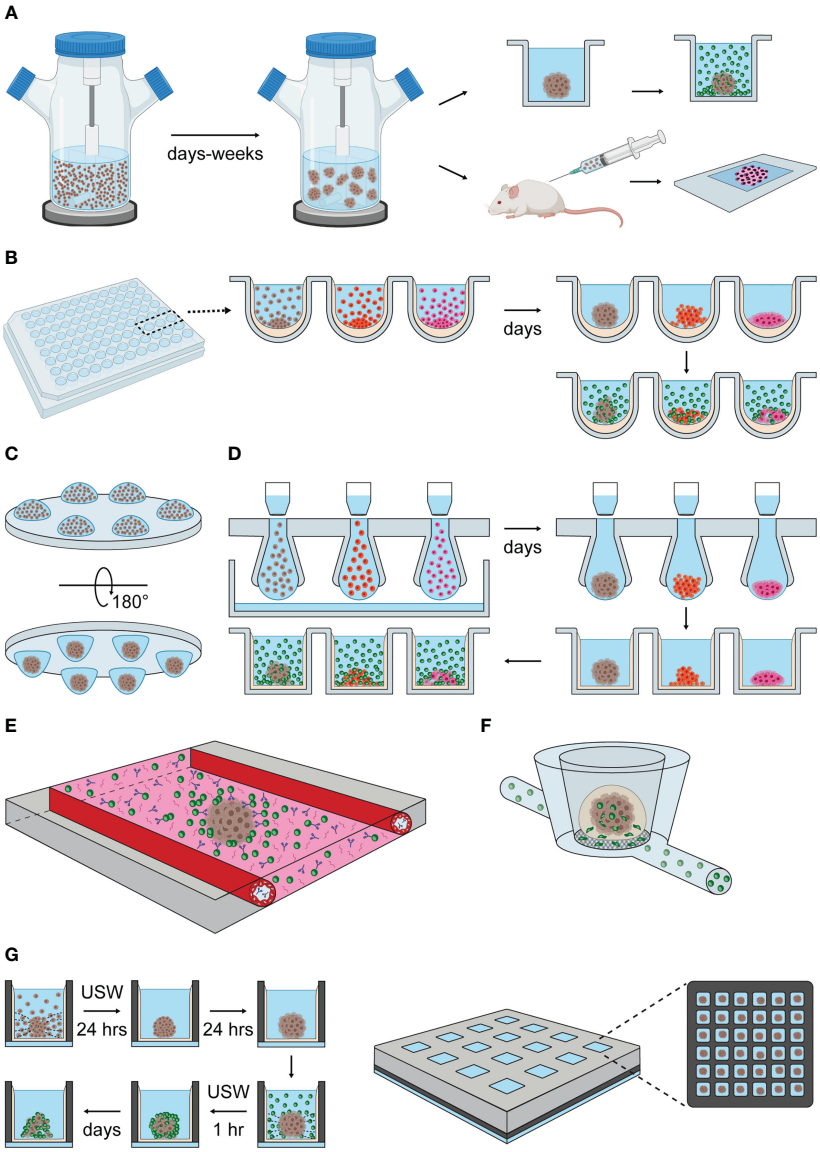

FIGURE 3
Methods of spheroid formation applied to NK cell research. **(A)** Spinner cultures. Tumor cell suspensions are transferred into spinner flasks that provide constant agitation and promote cell aggregation. Spheroid formation is reached within days or a few weeks, depending on the adhesive properties of each cell type. Spheroids generated by spinner cultures have been exposed to allogenic lymphocyte cultures (upper panel to the right) and implanted in allogenic mice (lower panel to the right) to study NK cell infiltration and clearance of tumors (88–91). **(B)** Liquid-overlay method. Cell suspensions are seeded into standard culture plates pre-treated with non-adhesive coatings, such as agarose or poly-HEMA, that indirectly promote spheroid formation by preventing cell adhesion to the plate. Gravity and cell confinement in wells facilitate cell aggregation (spheroids are obtained within a few days). NK cells can be co-cultured with tumor spheroids to study their infiltration and cytotoxic capacity *in vitro*. **(C)** Hanging-drop cultures. Drops of cell suspension is dispensed onto a standard culture plate, that is turned upside-down. Surface tension and gravity enforce the formation of a single spheroid per drop within a few days. **(D)** Illustrations of hanging-drop platforms compatible with long-term and high-throughput spheroid cultures, based on the general features of 3D Biomatrix and InSphero plates. Multiple drops are formed by transferring cell suspension into the inlets of an array plate. Liquid reservoirs prevent drop evaporation. After spheroid formation, each drop is displaced into a single well of an ULA plate by pipetting additional medium on top of the inlets or by centrifugation. From this point, the hanging drop-derived spheroids can be used as described in the liquid-overlay section. **(E)** Schematic representation of the microfluidic platform developed by Ayuso et al. (92). The microfluidic device consists of a central chamber filled with collagen type I hydrogel, hanging drop-derived spheroids and NK cells. Antibody solutions are perfused through two lateral channels covered with endothelial cells. **(F)** Schematic representation of the MIVO device developed by Marrella et al. (93, 94). Alginate-derived spheroids are transferred into the top chamber of the MIVO device, which resembles a trans-well insert. NK cell suspensions are perfused through capillaries running under the chambers containing spheroids, allowing NK cells to migrate through the trans-well membrane and infiltrate the tumor spheroid (95). **(G)** USW-induced spheroid formation in microwell chip. Left panel: cells are seeded into a glass-bottom microwell array chip coated with non-adhesive coating. USW exposure induce the formation of single spheroids in the center of each well. This step is followed by a period of spheroid stabilization in the absence of USW. Once spheroids are formed, NK cells are seeded into the wells under USW exposure to promote NK cell-spheroid interaction. The characterization of NK cell infiltration and killing in tumor spheroids can be performed directly in the chip by imaging, or off-chip by retrieving the samples from the chambers. Right panel: illustration of the multichambered microwell chip with 16 chambers, each containing 36 microwells, giving a total of 576 microwells per chip.

The simplicity and scalability of the liquid-overlay technique contributed to the vast application of this method to multiple areas of biology research, especially immunology. However, the method still presents some flaws. Compared to spinner flasks, tumor cells are subjected to even less forces inducing cell-to-cell interaction, as the method solely relies on cell self-aggregation in the absence of substrate anchorage. Accordingly, a substantial number of solid tumor-derived cell lines fail to form anything but loose cell aggregates rather than compact spheroids in the liquid-overlay platform (102, 104, 107). Interestingly, very low success rate of spheroid formation is observed using healthy, non-cancerogenic cells (102, 104).

The ECM is essential player in cell-to-cell adhesion (132), and the quantity and the quality of ECM production by various cell types might influence their ability to form spheroids. Accordingly, the addition of ECM components to the liquid-overlay cultures has been shown to increase the spheroid tightness in some tumor models (107). Another strategy to improve the success rate of spheroid formation is to use U-bottom multi-well plates: gravity forces combined with the U-shaped well geometry promote cell sedimentation in the middle of the well, increasing the probability of cell-to-cell interactions. This strategy addresses the issue of multiple and heterogeneous spheroid formation, as single and homogeneous spheroids per well are more frequently obtained compared to other plate formats. In addition, spheroid confinement in a single well facilitates the detection of qualitative and quantitative spheroid changes over time by live-imaging. However, the U-shape and the optical properties of the commonly used plastic surfaces are not compatible with high-quality and high-resolution imaging, and sample transferring is still required for detailed analysis of biological processes, possibly affecting the integrity of the sample.

3.3 Hanging-drop method

The hanging-drop method is another popular technique for spheroid formation (133). Hanging drop cultures can be obtained by simply dispensing small aliquots of cell suspension (15-25 µl) in a plate, which is subsequently placed upside-down (Figure 3C). Gravity enforces cell assembly at the liquid-air interface at the bottom of the hanging drops, and one-spheroid per drop is usually obtained within a few days (133–135). The liquid drops are preserved due to surface tension but evaporation needs to be limited in long-term cultures to maintain appropriate osmolality levels (136).

Tung et al. developed a hanging drop platform for long-term culture and high-throughput analysis (136). Cell suspensions is pipetted into the 384 holes of an array plate, where the hydrophilic surface and gravity favor the formation of the hanging drops. Liquid reservoirs at the edge of the plate and a tray filled with water provides humidity while a plate lid limits evaporation (136). This implementation overcomes some drawbacks of the original hanging-drop method, such as rapid dehydration and laborious sample handling. This platform is commercially available in multiple formats from 3D Biomatrix.

InSphero developed a user-friendly hanging-drop platform compatible with long-term cultures and high-quality imaging. The InSphero culture system follows the 3D Biomatrix design, with a hanging-drop array made of multiple inlets inserted between a lid and a liquid reservoir (137). A distinct feature of the InSphero method is that the formed spheroids are transferred into a ULA-plate (Gravity-Trap ULA plate or Akura plates) by adding liquid on top of the inlets or by centrifugation. The spheroids can be maintained in the ULA plates for long-term culture, where liquid evaporation occurs at slow rate, and media exchange can easily be performed (138). The spheroids are confined in a small area (1 mm-diameter) at the bottom of the well, which is flat and made of thin clear plastic, facilitating live, automated and high-quality imaging (138–140). A similar implementation is also available nowadays from 3D Biomatrix (Figure 3D). The 3D Biomatrix and InSphero platforms are compatible with both manual and fully automated handling.

The hanging drop method generates spheroids from a variety of cell types, such as tumor cell lines or cells derived primary tumors or healthy tissue (102, 125, 133). Cell differentiation and extensive secretion of extracellular matrix (133), as well as inner regions of necrosis and hypoxia (141) have been described. Herter et al. obtained heterotypic spheroids of adenocarcinoma cells and fibroblasts (142). The heterotypic spheroid model has been used to evaluate the combinatorial effect of IL-2 variant and tumor- or fibroblast-targeted T cell bispecific antibodies on T, NK and NKT cell activation, cytokine and chemokine secretion, spheroid killing and infiltration (142). Interestingly, the fibroblasts spontaneously arranged in the spheroid core, as also reported by others using different cell types and spheroid culture methods (122, 139, 142). The hanging drop technique has also been applied to immune therapy screening, for instance to test the effect of rituximab on NK cell ADCC in primary follicular lymphoma spheroids (125), and to evaluate different protocols of NK cell activation in colorectal carcinoma models (135). In summary, the hanging drop method is an easy-to-use technique to generate biologically relevant tumor models *in vitro*, it is compatible with multiple end-point assays, live and high-quality imaging, and high-throughput screening. However, the hanging-drop method does not fully address the problem of heterogeneous structural integrity between cell lines, as multiple cases of loose aggregates can be found literature (133).

3.4 Scaffold-based spheroid cultures

In vivo, NK cells migrate through the supportive tissue, and the stroma composition influences their infiltrative capacity, as well as tumor aggressiveness and therapeutic responses. Similarly, the spheroid stiffness, together with the amount and the composition of the ECM, shapes NK cell activity *in vitro* (112, 115, 143, 144). Therefore, the properties of the ECM should be considered when evaluating NK cell-spheroid interactions.

A strategy to include ECM-like conditions and chemokine gradients in the assays is to introduce scaffolds in the cultures. Examples of such scaffolds are hydrogels or porous inserts that can

be obtained from animals (e.g., fibrous gelatin, collagen, Matrigel, chitosan, hyaluronic acid, silk fibroin), plants (e.g., alginate) or by synthetic production (e.g., polyethylene glycol, polylactic acid, poly-ϵ-caprolactone, polyurethans) (24, 25, 28, 145). Scaffolds used in NK cell 3D research are mostly hydrogel-based, and they include Matrigel (95, 144, 146), collagen type I hydrogels (92, 143, 147–149), alginate hydrogel (95, 150) and functionalized hydrogel based on polyethylene glycol (PEG) (151).

Schnalzger el al. established heterotypic cultures of normal and tumor colon organoids together with primary fibroblasts in Matrigel to evaluate the efficacy and the specificity of EpCAM-CAR-NK92 cells (144). Similarly, Gopal et al. tested NK92-CD16 cytotoxicity in combination with chemotherapy and antibody-based immunotherapy against pancreatic and breast cancer cells embedded in Matrigel, using a newly designed high-throughput micropillar-microwell sandwich platform (146).

Ayuso et al. combined the use of hanging drop spheroid formation (scaffold-free method), rat-derived collagen type I hydrogel (scaffold-based method) and microfluidics to study antibody penetration, ADCC, and NK cell chemotactic migration and infiltration in breast cancer spheroids (Figure 3E) (92). This microfluidic device consisted of a central chamber filled with collagen type I hydrogel, flanked by two lateral lumens covered with endothelial cells to mimic blood vessels. Hanging drop-derived spheroids were transferred into the central chamber and embedded together with NK cells in collagen, while a solution containing IL-2-conjugated CD16-EpCAM bispecific antibody was perfused through the later lumens. Using this method, the authors could follow the dynamic of antibody penetration, NK cell chemotactic migration and ADCC by imaging (92).

Marrella et al. developed alginate spheres to study the effect of IFN-γ exposure on NK cell ligand expression in neuroblastoma spheroids (150). The same group combined the use of alginate spheres with the MIVO fluidic platform (93, 94) to study the mechanisms of NK cell extravasation and tumor infiltration (Figure 3F) (95). The MIVO platform consists of a trans-well system connected to a closed-loop fluidic circuit (93, 94). The top chamber of the trans-well (donor chamber) contained alginate-derived neuroblastoma spheroids. NK cells were constantly perfused through the bottom chamber (receiver chambers) and the capillaries of the fluidic circuit, which mimics the blood circulation. The porous membrane physically separating the donor and the receiver chambers prevented alginate spheres to fall into the receiver chamber (95). The spheroids and the cell suspension could be recovered and used for a variety of end-point analysis. For instance, the authors used flow cytometry to compare the proportion of $CD16^+$ $CD45^+$ cells in circulating, extravasated and spheroid-infiltrated NK cells (95).

Animal- and plant-derived hydrogels, such as collagen and Matrigel, present some limitations, such as batch-to-batch variability, long-term instability, cell degradation and immunogenicity, therefore synthetic hydrogels might be preferred for some applications (28). For instance, Temple et al. developed arginine-glycine-aspartic acid functionalized PEG hydrogels to study the effect of matrix metalloproteinases and integrins on NK cells migration (151). The authors also showed decreased NK cell infiltration in non-small lung cancer 3D cultures releasing soluble MICA and TGF-β (151).

The scaffold-based spheroid cultures are biologically relevant systems to study leukocyte transmigration and tissue infiltration, however they are often not compatible with high-throughput screening and live cell imaging. This, combined with the fact that the procedures to recover cells from the hydrogels are quite laborious, limits their large-scale application, and it is one of the reasons why scaffold-free technologies are still usually preferred.

3.5 Miniaturized platforms for spheroid studies

Another strategy to enhance the interplay of spheroid and NK cells is the use miniaturized cell culture platforms. In miniaturized platforms, the well dimensions are tailored to the spheroid dimension, ensuring physical confinement, facilitating cell detection and cell-to-cell interaction. The miniaturization scales down the volumes and cell number required to set up and maintain cultures, enabling spheroid formation when the material is scarce (as with many patient samples). We already described a few examples of scaffold-based microfluidic and miniaturized platforms in the previous paragraph (146, 148). Here, we will focus on scaffold-free miniaturized spheroid cultures for NK cell research.

Nguyen et al. designed a miniaturized microfluidic platform to enhance NK interaction with tumor and cardiac spheroids and study the specificity of NK cell killing and the secondary effects on healthy tissue (152). Their microchip, adapted from the Akura Flow MPS discovery platform (153), features two individual perfusion channels with 10 communicating compartments and medium reservoirs at both ends (152, 153). Spheroids were formed in ULA plates and then transferred into the compartments, and NK cells were introduced to the cultures through the medium reservoirs. Perfusion across the medium reservoirs and the spheroid compartments, and therefore NK-spheroid interaction, was driven by gravity simply tilting the microchip along its long axis. The process is automated using a tilting stage (152, 153). The authors showed the relevance of the method by perfusing umbilical cord blood (UCB)-derived NK cells into colorectal tumor spheroids and cardiac microtissues placed in distinct communing compartments. The experiment demonstrated the specificity of UCB-NK cell cytotoxicity towards colorectal tumor spheroids, but it also showed the presence of infiltrating UCB-NK cells in the cardiac spheroids along with signs of arrhythmia, possibly induced by pro-inflammatory cytokines detected in the supernatant (152). Cells and culture medium can easily be recovered by pipetting for cellular and proteomic analysis, while end-point imaging can be performed directly on the chip. However, dynamic of NK cell adhesion and infiltration cannot be entirely followed by live imaging, due to the tilting procedure, and the spheroid culture cannot be performed directly on the microchip.

Our group has developed a scaffold-free microwell chip platform to study the dynamics of NK cells in tumor spheroids (154–156). One of the main advantages of this platform is that all

the experimental phases (spheroid formation, treatment and NK cell incubation, analysis) can be performed on the chip, which is compatible with high-resolution and live cell imaging. Spheroids and NK cells can also be retrieved by standard pipetting for off-chip analysis (155). The spheroid formation is obtained by seeding cell suspensions in a silicon microwell array chip covered with a non-adhesive coating and inducing cell aggregation by ultrasonic standing waves (USW) (Figure 3G) (155, 156). In microfluidics and other miniaturized systems, ultrasound has found use in various applications where either suspended cells or the fluid is manipulated by acoustic radiation pressure. This technology field is often called microscale acoustofluidics (157). We specifically use this technology to induce cell aggregation and formation of single, homogeneous and compact spheroids in each well (154, 158–161). When the USW is turned off, cellular production of ECM proteins and formation of tight intercellular connections continue, enabling long-term spheroid cultures. Importantly, acoustic trapping is also performed while setting up the co-cultures, to induce NK cell-spheroid interaction (156, 161). Importantly, the physical force field of the USW is gentle to cells even at long continuous exposures (several days) (157).

Different microwell chip designs have been developed during the years (155, 156, 159, 161). The most recent is a multichambered microwell chip, with 16 compartments each containing 36 microwells, allowing the simultaneous production and analysis of 576 spheroids (36 spheroid replicates for each experimental condition) (156). The microwell array is made in silicon, which is bonded to a glass bottom layer that is compatible with high-quality imaging. A thin and transparent non-adhesive coating is applied at the bottom of the wells to prevent cell adhesion (162). A PDMS frame separates the wells into compartments serving as liquid reservoirs (typically 50 µl are used for each compartment). Contamination and evaporation are prevented by placing a coverslip on top of the PDMS frame (156).

Fast image acquisition combined with high-resolution imaging enables high-throughput screening at chamber levels with detailed analysis of biological processes at the single microwell level. The method allowed studies of how combinatorial treatments affect NK cell infiltration and activity in tumor spheroids, quantifying the amount and the timing of killing (155). The method is also compatible with the formation of a wide range of homotypic spheroids (kidney, thyroid, ovarian, hepatic, non-small lung cancer cell carcinomas) (155, 156, 161), heterotypic and patient-derived spheroids (unpublished results), the latter particularly facilitated by the low material requirement.

The main limitations of the miniaturized platforms described here are related to the number of conditions that can be tested in parallel and the number of cells that can be retrieved from the chips for further analysis.

In this section, we have described the methods used for spheroid formation in the field of NK cell research. Each technique presents advantages and limitations, which should be carefully evaluated when choosing experimental strategy. The choice of method to use should be driven by two main questions: Which method provides the most relevant 3D features to study the mechanisms of interest? Which method is compatible with the analysis/assays we want to perform? In the next section, we will describe the available assays to characterize NK cell behavior and phenotype in cancer spheroids.

4 Methods to study NK cell activity in tumor spheroids

The discovery of novel cell types and their characterization is closely related to our ability to detect their function. As a matter of fact, various immune cell types have been identified through observation of their activity, which historically preceded their phenotypic characterization. This is also the case for NK cells, initially identified for their ability to "spontaneously kill" tumor cells *in vitro* (40, 163, 164), and later characterized for their serial killing capacity in single cell screening assays (165–167). A variety of well-established assays and cutting-edge technologies are routinely used to screen NK cell activity on tumor cell monolayers (165, 167–174). However, a limited number of them is suitable for studying NK cell cytotoxicity in tumor spheroids.

Compared to 2D systems, developing functional assays for 3D cultures is more demanding. The challenges are intrinsically related to the physical properties of the spheroids. Accurate imaging of 3D objects beyond ≈50 µm is challenging. High cellular density and ECM deposition generate light scattering, limiting the detection of NK cytotoxicity in the inner areas of the spheroids. Therefore, enzymatic dissociation or tissue sectioning are performed to isolate and characterize infiltrating NK cells, but these processes cause loss of spatial information and dynamics. In addition, introducing sample processing steps slows down the analysis and might cause experimental artifacts. Consequently, very few technologies that combine high-throughput cytotoxicity screening and high-resolution analysis of killing mechanisms are available, and multiple methodologies might be required to fully dissect NK cytotoxicity in tumor spheroids.

A lot of research is currently undergoing to overcome these limitations. In this section, we describe the methodologies described in literature.

4.1 Bulk assays or methods based on radioisotope-cell labeling and luminescence

Traditionally, Chromium-51 (^{51}Cr) release assay has been the gold-standard method to quantify NK cell cytotoxicity against tumor cell suspension or monolayers (175). The procedure involves culturing NK cells with tumor cells pre-labeled with sodium chromate. NK cell cytolytic activity causes loss of tumor cell membrane integrity, and consequent release of ^{51}Cr radioisotope in the supernatant, which can be detected by either γ or β counters. Thus, quantification of the released ^{51}Cr is a measurement of NK cell cytotoxicity. Being quantitative, ^{51}Cr release assay is particularly adapted to compare the susceptibility of different cell types to various immunotherapeutic treatments (175).

^{51}Cr release assay has also been used to study NK cell cytotoxicity against tumor spheroids (115, 129, 130, 176),

coupling the conventional quantification of killing with the identification of dead areas by autoradiography (115). While ensuring high sensitivity, the use of radioactive material also represents the main limitation of the method. Multiple precautions should be taken while using ^{51}Cr to ensure the staff safety and proper waste disposal, and license to work with radioactivity must be granted. This limitation motivated the development of colorimetric and luminescence assays to measure the release of non-radioactive intracellular contents, such as lactate dehydrogenase (LDH) and adenosine 5′-triphosphate.

LHD is a cytosolic enzyme that catalyses the conversion of lactate to pyruvate via NAD^+ reduction to NADH. NADH is a used by the reductase as co-factor to catalyze reduction reactions. A typical strategy to measure the LHD released in the supernatants of NK and spheroid co-cultures is to use a mix containing the reductase, its substrate, together with lactate and NAD. For instance, the LHD assay has been used by Murphy et al. to show the importance of addressing hypoxia to improve the efficacy of cell therapy (110). To increase the oxygen supply in the spheroid core, they developed biocompatible poly(lactic-co-glycolic) manganese dioxide nanoparticles (PLGA-MnO_2 NPs) that catalyse oxygen production from tumor-derived hydrogen peroxide. By treating hypoxic breast cancer spheroids with PLGA-MnO_2 NPs, they demonstrated a decreased presence of HIF-1α^+ tumor cells in the core associated with a significant reduction of immunosuppressive factors such as adenosine and lactate production. This phenotype was accompanied by an increased NK cell-mediated cytotoxicity and IFN-γ production in the treated spheroids (110).

Bulk methods are high-throughput, therefore good for screening NK activity against multiple targets and combinatorial treatments. However, they provide no information about cell phenotype, neither the kinetics and the localization of NK cell killing and infiltration. Therefore, they are mainly used as end-point assays for screening multiple conditions, sometimes used as a guide for finding the best experimental conditions and performing more detailed analysis by flow cytometry or imaging.

4.2 Flow cytometry of tumor spheroids

Flow cytometry provides a rapid, quantitative and multi-parametric analysis of single cells. Applications of standard flow cytometry include identification of cell types based on lineage markers, quantitative expression of membrane-bound and intracellular molecules, and analysis of cell status and function. The multi-parametric power of flow cytometry mostly derives from the ability to collect and differentiate multiple fluorophores. Depending on the number of lasers, detectors and filter combinations, the most recent configurations of commercially available flow cytometers can discriminate more than 30 different emitting fluorophores (177–179). Flow cytometers can detect cells and particles within 0.2-150 μm in diameter, although the use specialized systems can allow the detection outside this range.

Flow cytometry is frequently applied to spheroid research as end-point assay to quantify NK cell infiltration, characterize the viability, proliferation and phenotype of NK cells and tumor cells isolated from spheroid cultures, and to analyze functional parameters, such as degranulation and cytokine production of spheroid-infiltrating NK cells. A strategy to separate spheroid-infiltrating NK cells from extra-tumoral NK cells is to collect the culture supernatant (extra-tumoral NK cell fraction) and the spheroid mass (spheroid-infiltrating NK cell fraction) in different tubes prior to tissue processing and immunostaining (106, 112, 119, 180). Flow cytometry analysis of the two fractions showed enrichment of NK cells and $CD8^+$ T cells in the spheroid core (112, 119), demonstrating a better infiltrative ability of these two populations compared to $CD4^+$ T cells, further enhanced by IL-15 activation (119).

Similar to what has been observed in tumor patients (118), spheroid-infiltrating NK cells tend to lose the expression of NKG2D and DNAM-1 (119, 124). NK2GD expression could be partially restored by blocking MICA/B, contributing to better NK cell cytotoxicity and infiltration (119). The levels of soluble NKG2D ligands are high in the plasma obtained from tumor patients, and their levels tend to decrease after surgery, further proving their implication in cancer progression. In line with that, Giannattasio et al. showed abundant shedding of NKG2D ligands in cervical carcinoma spheroids, associated with decreased expression of the membrane-bound form (106). Increased HLA class I expression has also been observed in tumor spheroids compared to monolayer cultures (181).

NK cell cytotoxicity can be analyzed by flow cytometry calculating the percentage of dead tumor cells, identified with apoptotic markers and/or cell impermeant dyes. Combinatorial staining with Annexin V and 7-AAD or propidium iodine staining is frequently used to quantify early and late apoptosis of spheroid-derived tumor cells and NK cells (119, 125, 180, 182, 183). Veneziani et al. performed flow cytometry analysis of patient-derived neuroblastoma spheroids co-cultured with NK cells and Nutlin-3, characterizing the phenotype of NK cells together with the apoptotic state of tumor cells. They demonstrated up-regulation of ULBPs, PVR and Nectin-2 on Nutlin-3-treated tumor cells, associated with increased NK cell cytotoxicity (183). NK cell functionality can also be inferred by qualitative and quantitative assessment of cytokine production and granule content (IFN-γ, TNF-α, MIP-1α, perforin, granzyme B) and granule release (CD107a).

The main advantage of flow cytometry is the multi-parametric analysis of single cells at high-throughput. Despite the considerable amount of information that can be retrieved, flow cytometry lacks spatial and temporal resolution. Additionally, it can introduce technical artifacts. Such risk can be reduced by using mild dissociation agents and decreasing the time between the dissociation and the flow cytometry acquisition. NK cell killing over time can only assessed by preparing multiple NK-tumor co-cultures and analyzing them at different timepoints, with technical variability affecting the robustness of the assay. Therefore, it would be preferable to use flow cytometry for a single-timepoint experiment and move to other techniques when spatial information and dynamics are part of the biological question.

4.3 Measuring NK cell cytotoxicity by detecting spheroid physical changes

NK cell activity can cause variations of the spheroid physical properties, such as diameter, volume, and weight, which can be detected and quantified to estimate NK cell-mediated spheroid killing (117, 119, 127, 142, 183). Rademacher et al. monitored the diameter of sarcoma spheroids over time by widefield microscopy to study the effect of IL-12 on NK92 cytotoxicity and infiltration. They detected a reduction of spheroid diameter incubating NK92 cells with IL-12-engireed osteosarcoma cells, suggesting a positive effect of IL-12 on NK cell activity in 3D (127). Similarly, the reduction of spheroid volume was used to evaluate the benefits of cytokine activation on PBMC cytotoxicity against heterotypic and homotypic colorectal cancer spheroids (119, 142). Sargenti et al. developed a fluidic platform to estimate NK cell cytotoxicity and infiltration measuring spheroid weight and diameter (117). The method is based on tracking the motion of spheroids falling into a vertical flow channel using a brightfield imaging system (117, 184). Analyzing spheroids obtained from four different colorectal tumor cell lines, the authors were able to correlate the mass density with the degree of spheroid compactness (117). Co-incubation with NK cells led to a significant reduction of spheroid weight and diameter, while a temporary increase of spheroid mass density was associated to NK cell infiltration (117). There are reports saying that spheroid volume does not affect NK cytotoxicity (97, 115), while spheroid cellular density and compactness do (115, 117). The analysis of spheroid physical properties represents a fast, non-invasive and easily accessible method to measure NK cell cytotoxicity. However, its application is arguably limited, due to lack of sensitivity and information. During early phases of NK killing, spheroids often get partly disintegrated and less compact, leading to increased volume which may seem contradictory. In addition, NK cell infiltration itself might induce volume and mass changes, which are difficult to isolate and subtract from the quantification. The method itself does not provide information regarding the mechanisms of NK cell killing and spheroid death. To overcome these limitations, the study of spheroid physical properties is usually combined with histological characterization and other cell labeling-based quantitative analysis.

4.4 Measuring NK cell cytotoxicity and infiltration by detecting spheroid histological changes

A method to characterize NK cell cytotoxicity and infiltration in the spheroids is by performing histochemical staining of sections. Various histological changes have been associated with NK cell activity in tumor spheroids, such as loss of surface integrity (98, 115), formation of cytoplasmic blebs, chromatin condensation (111, 116) and mitochondrial swelling (98). Simply using immunostaining and haematoxylin/eosin counterstaining, Kaaijk et al. described two modalities of LAK killing in glioma spheroids: a) apoptosis, characterized by loss of cell volume, chromatin condensation and formation and apoptotic bodies; b) necrosis, identified by loss of fibrillary structure and acquisition of smooth appearance in the cytoplasm, loss of membrane integrity and swollen nuclei (116). Studying the relative position of LAK and dead glioma cells in spheroid tissue sections, Jääskeläinen et al. localized tumor cell death in areas devoid of LAK infiltration, speculating that contact-independent killing modalities mediated by soluble factors could play a role (111). Contact-mediated killing has been demonstrated by Iwasaki et al. imaging ultrathin spheroid sections by transmission electron microscopy (98). Using this technique, the authors captured the formation of tight cytoplasmic interdigitations between effector and target cells in the spheroid core, and the development of intracytoplasmatic dense granules that usually precedes degranulation (98).

To introduce the temporal factor, it is possible to collect and stain spheroids at different times, to follow the progressive infiltration and cytotoxicity of NK cells toward the core (98, 112, 115). To quantify this behavior, there have been multiple attempts to classify NK cell infiltration or/and spheroid death (98, 105). For instance, Jääskeläinen et al. calculated the density of LAK cells in three different spheroid areas, corresponding to the periphery (100 µm depth from the spheroid surface), the intermediate layer (100 µm to 200 µm depth) and the core (200 µm to 300 µm depth) to quantify the involvement of adhesion molecules on LAK infiltration. According to their findings, the expression of adhesion molecules varied in the different areas and it was strongly influenced by the secretory activity of LAK cells. For instance, the levels of CD54 were weak in periphery of glioma spheroids and intense in the intermediate rim in the absence of LAK cells, while the expression intensified along the frontier of migrating cells possibly due to IFN-γ release. Blocking CD54 completely prevented LAK migration into the spheroids, showing the relevance of this pathway for NK infiltration (112).

Iwasaki et al. classified the activity of LAK cells into four categories based on both infiltration and cell damage: grade I) effectors in contact with the spheroid surface and little target death; grade II) effector infiltration into the outer third layer of the spheroid accompanied by target cell death; grade III) target death detected in the middle layer of the spheroid; grade IV) target death detected in the core of the spheroid (98). Garcia de Palazzo et al. developed a similar system to classify the histological changes of colon cancer spheroids and quantify the effect of CA19-9-CD16 bispecific antibody on LAK 3D killing (105). Based on haematoxylin/eosin staining, they classified the histological damage into five grades calculating the percentage of necrosis in relation to the control condition (105).

Histochemistry can be also applied for the analysis of NK cell status in the TME. For instance, Weil et al. detected apoptotic NK cells in the core of head and neck squamous cell carcinoma spheroids following soluble MICA exposure (118), demonstrating the detrimental effect of soluble NKG2D ligands on NK cell-mediated tumor surveillance (118, 185).

Despite these efforts, the use of spheroid morphological changes to quantify NK cytotoxicity remains problematic, suffering from subjective evaluation and lack of universal classification. Lack of three-dimensionality and time resolution represent additional limitations. Tissue reconstruction could retrieve 3D spatial

information, but it is technically difficult and rarely performed. The kinetics of NK cytotoxicity can be studied performing time-course assays on spheroid replicates, however limited time resolution (usually day-scale) and sample availability makes live cell imaging a preferred option, which is also compatible with cell tracking. Despite these limitations, histological analysis is considered a valuable and very informative option as end-point assays and qualitative analysis, especially to confirm data obtained by other techniques (119, 135). The recent development in the field, such as the release of methodology and machines for automated multiplexed staining and analysis (e.g. Hyperion, MACSima, CODEX), will most likely increase the use of this technique to NK cell and spheroid studies.

4.5 Measuring NK cell cytotoxicity and infiltration using fluorescence microscopy

A variety of fluorescent dyes have been developed to characterize cell status, such as viability, apoptosis, necrosis, proliferation, and metabolism. If properly chosen, these markers can provide information on the killing modality. For this reason, coupling cell labeling with fluorescence-based imaging techniques is a particularly suitable strategy to characterize NK cell cytotoxicity in tumor spheroids.

The workflow involves cell labeling before, during, or at the end of the cytotoxicity assay, and detection by the appropriate microscopes, such as widefield, confocal, light sheet or two-photon fluorescence microscopes. The variation of the fluorescence intensity during NK-spheroid co-cultures can be quantified, such as loss of viability and proliferation markers, or acquisition of necrotic/apoptotic markers, providing an unbiased evaluation of NK cell activity. In addition, live cell imaging can be performed to study the kinetic of spheroid death and NK cell infiltration with good temporal resolution.

Giannattasio et al. followed the infiltration of Hoechst-labeled NK cells into CFSE-labeled cervical carcinoma spheroids for 48 hours with 30 minutes time resolution using widefield fluorescence microscopy, showing NK cell proliferation and accumulation at the periphery of the spheroids (106). To characterize the spheroid inner areas, imaging techniques with 3D resolution, such as confocal, light sheet and two-photon microscopy, can be easier than sectioning. These techniques provide spatial information of NK cell infiltration and killing while preserving sample integrity. An additional benefit is low sample consumption, as time courses and 3D characterization can be performed simultaneously on a single sample. Imaging a single focal plane inside the breast cancer spheroids with 30 second resolution, Ayuso et al. tracked NK92 chemotaxis towards the spheroid core (92). Using this strategy, they were able to describe the directionality and the modality of NK cell migration, capturing NK cell bodies squeezing between tumor cell junctions to reach the inner areas of the spheroid (92). They quantified NK cell infiltration and spheroid killing, showing that increasing effector-to-target ratios positively influenced NK cell ability to kill multiple spheroid layers (92, 106, 123, 135).

Hoogstad-van Evert et al. analyzed the activity of hematopoietic stem and progenitor cells (HSPC)-NK cells on ovarian cancer spheroids using a similar approach (123). They performed live cell confocal imaging on a single focal plane to study the dynamics of HSPC-NK cell cytotoxicity over five hours. As an end-point assay, they imaged multiple focal planes to collect data from a 60 µm spheroid section, which allowed them to quantify dead tumor cells in relation to tissue depth (123).

In vitro, NK cell killing of tumor cell suspensions manifests within a few minutes from stimulation, and it persists for few days before NK exhaustion and/or dysfunctionality occurs. The killing mechanisms can shift over time, as well as tumor cells susceptibility. For these reasons, long-term assays are usually considered particularly appropriate for the characterization of NK cell killing modalities. The duration of the assay is particularly important in 3D, where the infiltration of NK cells and the diffusion of soluble factors influence the killing dynamics. Phototoxicity and photostability are two important parameters to take into consideration while performing long-term imaging assays, as both could introduce technical artifacts and reduce the test sensitivity. For these reasons, internal controls should always be run to test the phototoxicity levels, and dyes resistant to photobleaching and cell-mediated degradation are recommended. If phototoxicity and photostability are properly addressed, long-term imaging assays could be very informative.

Our own time-course analysis revealed high inter-donor heterogeneity in terms of killing dynamics, and it predicted donor-specific long-term and short-term response to combinatorial treatment *in vitro* (Figure 4) (156, 186). We tracked NK cell-mediated cytotoxicity of renal and ovarian cancer spheroids for three days combining the use of two fluorescent dyes: a mitochondrial activity reporter (TMRM) as viability marker, and a caspase-3/7 activity reporter as apoptotic marker (Figure 4A). As expected, NK cell activity induced a cumulative loss of spheroid viability over time (Figures 4A, B). However, a detailed characterization of the time-courses showed high variation in killing dynamics and long-term response to combinatorial therapy among NK donors. In the same assay, the analysis of caspase-3/7 intensity curves revealed the time of maximum NK cell-mediated apoptotic death, corresponding to the peak of fluorescent intensity. In addition, the combined used of two dyes allowed us to normalize the amount of apoptotic death for the initial spheroid viability, providing a more sensitive parameter for comparing different spheroid types (Figure 4C). Thanks to the long-term stability of the dyes, we were able to perform 3D confocal microscopy at the end of the live imaging assays to localize tumor cell apoptosis (156). Knowing when NK cell populations reach their maximum activity could be valuable information for designing personalized combinatorial therapy. It could also reveal the presence of different NK populations active at different times.

Courau et al. combined long-term live imaging with flow cytometric end-point analysis to study the contribution of each PBMC population to spheroid cytotoxicity and infiltration (119). They observed infiltration and killing of colorectal cancer spheroids under IL-15 exposure, mainly driven by NK and $CD8^+$ T cells. The presence of activated PBMCs induced HLA-expression on tumor

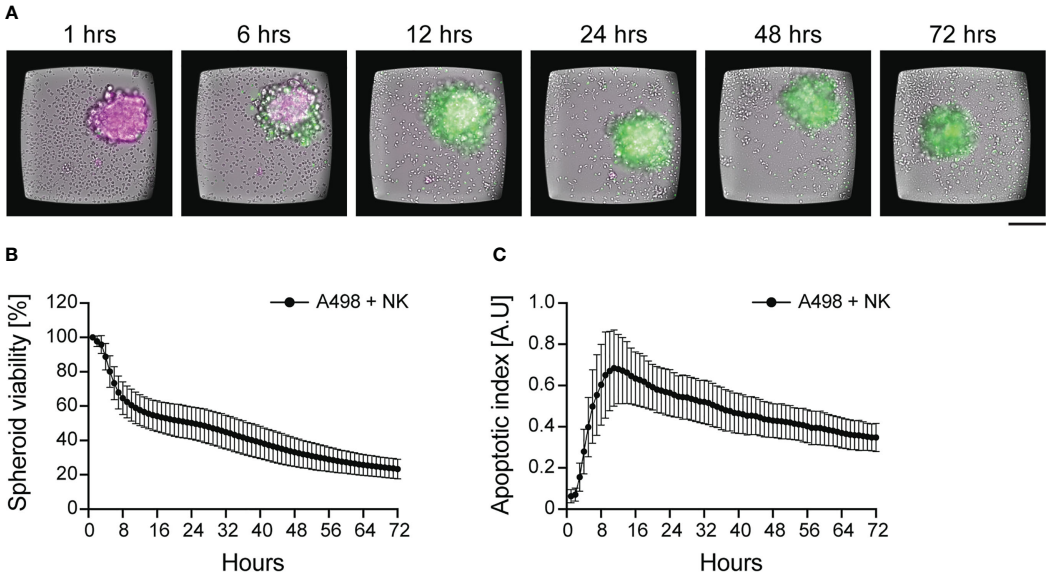

FIGURE 4
Dynamics of NK cell cytotoxicity against tumor spheroids. IL-15 activated NK cells were incubated with pre-formed renal carcinoma spheroids and imaged for 72 hours. **(A)** Time-lapse sequence of NK cell killing of renal carcinoma spheroids analyzed by live imaging. TMRM (in magenta) and a caspase-3/7 activity reporter (in green) were used to detect spheroid viability and apoptosis, respectively. NK cells can be seen in the brightfield channel. Scale bar: 100 µm. **(B, C)** Time-course of spheroid viability **(B)** and apoptotic index **(C)** from a single microwell chip chamber (n=36). The data were presented in Carannante et al. (186).

spheroids, while infiltrated NK cells showed a reduction of NKG2D expression. Coupling anti-MICA/B antibody with anti-NKG2A checkpoint blockade enhanced spheroid apoptosis and PBMC infiltration (119).

If multiple set of assays are planned, it is a common practice to genetically modify tumor cells to stably express fluorescent proteins (120, 123, 125, 135, 144, 180, 187). This strategy allows direct assessment of spheroid viability by measuring the variation of fluorescence intensity, removing the need of additional staining steps. For instance, Susek et al. applied this strategy to study the efficacy of chimeric switch receptors (CSR) for cell-based immunotherapy (120). To revert PD-1-mediated NK cell inhibition, they designed a PD-1-CSR replacing the inhibitory intracellular domains of PD-1 with activating motifs. They quantified the activity of PD-1-CSR NK-92 cells against renal carcinoma spheroids expressing red fluorescent protein by live imaging, demonstrating good specificity and cytotoxic activity of the cell product (120). Lanuza et al. used EGFP-transfected colorectal carcinoma cells to facilitate the detection of the spheroid area, used to quantify the cytotoxic effect of different effector-to-target ratios over time (135).

We used GFP-transfected NK92 to visualize the formation effector-to-target cell contacts in renal carcinoma spheroids using light sheet microscopy (Figure 5A) (188). Särchen et al. combined the use of fluorescently labeled proteins with cell death markers to calculate spheroid killing as the ratio between the two parameters, allowing a fair comparison between spheroids heterogeneous in size. Using this method, they showed the positive effects of BH3 mimetics on NK cell killing of pediatric cancer spheroids (187). Cell transfection with fluorescent proteins presents multiple advantages, such as reducing the optimization steps and facilitating the analysis. However, this approach is not suitable for all types of cells and applications since the transfection efficiency varies among cell types, with some being very resistant to genetic modifications, and cell manipulation is not compatible with the characterization of primary tumor samples, such as patient-derived tumor spheroids, since it might cause loss of the original sample features.

Apart from choosing the right labeling strategy, phototoxicity and photostability could be minimized by choosing microscopy techniques particularly suited for live 3D imaging, such as light sheet microscopy instead of confocal microscopy (189). Confocal microscopes involve a single objective for both illumination and detection, and 3D resolution is achieved generating signal from out-of-focus planes, which is then filtered out to detect the focal plane of interest. This design leads to relatively high photobleaching and phototoxicity, while sacrificing fluorescent signal to achieve optical sectioning. However, smaller spheroids can be imaged live with good results by confocal microscopy for a limited time, for instance to quantify NK cell infiltration (see example in Figure 5B). In light sheet microscopes, two separate objectives are used for illuminating the sample and detecting the signal. The illumination objective focuses a sheet of light to the plane of interest, and the detection objective collects light from the excited focal plane. Using this design, only the focal plane of interest is illuminated, causing little photobleaching and phototoxicity. Since the whole focal plane is imaged, the acquisition is dramatically faster than point-scanning confocal imaging (190, 191). These features make light sheet microscopy particularly suitable for imaging fast biological events

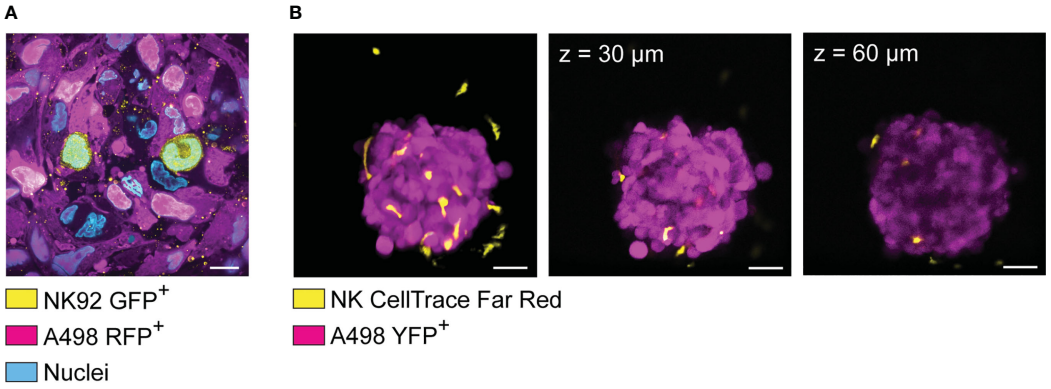

FIGURE 5
Visualization of spheroid-infiltrating NK cells by light sheet microscopy and confocal microscopy. **(A)** Light sheet microscopy image showing NK92 cells (yellow) infiltrating a renal carcinoma spheroid (magenta). RFP$^+$ A498 renal carcinoma spheroids were incubated with GFP$^+$ NK92 cells for 2 hours before undergoing tissue expansion in deionized water and imaged by light sheet microscopy. **(B)** YFP$^+$ A498 renal carcinoma spheroids were incubated with resting NK for 48 hours before being imaged by confocal microscopy. NK cells were detected in both extra-tumoral and intra-tumoral areas. However, the signal was progressively lost at increased depth. Left panel: 3D rendered confocal stack of an A498 renal carcinoma spheroid (magenta) co-cultured with NK cells (yellow). Central panel: optical section of the spheroid showed in the left panel (z = 30 µm). Central panel: optical section of the spheroid showed in the left panel (z = 60 µm).

in thick samples, such as cell division and NK cell infiltration in tumor spheroids (192). Thick samples scattering large amount of light can be imaged using multi-view acquisition, i.e., imaging the sample from multiple angles and combining the information during post-processing (190). This feature has been used by Del Bano et al. to study the effect of anti-mesothelin/CD16 bispecific antibody on NK cell infiltration in triple negative breast cancer spheroids (109). We combined cell transfection with fluorescent proteins, light sheet microscopy and tissue expansion to achieve detailed visualization of spheroid-infiltrating NK cells (Figure 5A) (188). Specifically, RFP$^+$ renal carcinoma spheroids were incubated with GFP$^+$ NK92 cells for 2 hours before undergoing tissue expansion and light sheet microscopy imaging. This technique is suitable for imaging the details of NK cell interactions with tumor cells in thick samples (188), for instance to obtain snapshots of killing mechanisms, metabolic activity, or receptor modulation. Like every technique, also light sheet microscopy presents its own disadvantages. The sample is commonly embedded in hydrogel, and some embedding media are not compatible with all cell types. The embedding procedure can be quite laborious, it can affect sample viability, and it is not compatible with high-throughput analysis. Finally, a typical light sheet microscopy experiment generates large amount of data, which are time consuming to transfer and process, and require high computational and storage capacity.

5 Conclusions

Since immunotherapy became a standard clinical practice, multiple cases of innate and acquired resistance have been reported, pointing out that more research is needed to understand the mechanisms of immunosuppression and to predict individual responses to treatment. To gain more knowledge, we need robust *in vitro* systems suitable for immuno-oncology studies. The characterization of NK cells in the original tumor tissues is challenging due to limited infiltration and tumor-driven changes in their phenotype (193). 3D cultures represent a fantastic tool to overcome these issues. The application spans from identifying the reasons behind poor NK cell performance in solid tumors, to developing and testing new strategies to boost their activity. The 3D platforms currently available allow analysis of cell phenotype, spatial distribution, and function. Phenotype, localization, and function can be analyzed at different levels, from gene expression to cell morphology and dynamics. Despite the broad range of characterization that they allow, their full potential is rarely exploited. In NK cell research, tumor spheroids are still mainly used as "support assays" to confirm data obtained from 2D assays or *in vivo*. The main application remains testing NK cells in combination with other therapies, most of the time without providing a full characterization of neither NK cells nor tumor spheroids. It is not rare to find qualitative data of NK cell infiltration and killing with no quantification provided. The main challenges are to obtain high-throughput, high-quality and quantitative imaging, as well as biologically relevant models of the solid tumor microenvironment. In this regard, rigorous validation of the model should be performed by comparing the 3D architecture and the cellular composition of the original tissue with the *in vitro* 3D culture, following its evolution over time. This is particularly important for NK cell research, considering the impact that tissue architecture, cellular and extracellular composition has on immune cell migration and cytotoxic capability. More developed use of 3D cultures combined with automated analysis pipelines, perhaps artificial intelligence-driven, could expand their application to NK cell mechanistic studies and quantitative analysis. Still, more research is needed to fully understand and exploit the possibilities that 3D cultures can offer.

Author contributions

VC and BÖ drafted the content of the manuscript. VC wrote the first draft of the manuscript that was edited by to its final form by VC, MW, and BÖ. All authors contributed to the article and approved the submitted version.

Funding

We thank The Knut and Alice Wallenberg Foundation (Grant No 2018.0106), The Swedish Research Council (Grant No 2019-04925), The Swedish Foundation for Strategic Research (Grant No SBE13-0092), The Swedish Childhood Cancer Foundation (Grant No MT2019-0022), The Swedish Cancer Foundation (Grant No 19 0540 Pj) for financial support.

Conflict of interest

The authors declare that the research was conducted in the absence of any commercial or financial relationships that could be construed as a potential conflict of interest.

Publisher's note

References

1. Cooper MA, Fehniger TA, Caligiuri MA. The biology of human natural killer-cell subsets. *Trends Immunol* (2001) 22:633–40. doi: 10.1016/S1471-4906(01)02060-9

2. Lee JN, Jiang X, Ryan D, Whitesides GM. Compatibility of mammalian cells on surfaces of poly(dimethylsiloxane). *Langmuir* (2004) 20:11684–91. doi: 10.1021/la048562+

3. Su X, Young EWK, Underkofler HAS, Kamp TJ, January CT, Beebe DJ. Microfluidic cell culture and its application in high-throughput drug screening: cardiotoxicity assay for hERG channels. *J Biomol Screen* (2011) 16:101–11. doi: 10.1177/1087057110386218

4. Wei C-W, Cheng J-Y, Young T-H. Elucidating *in vitro* cell-cell interaction using a microfluidic coculture system. *BioMed Microdevices* (2006) 8:65–71. doi: 10.1007/s10544-006-6384-8

5. Chang C-W, Cheng Y-J, Tu M, Chen Y-H, Peng C-C, Liao W-H, et al. A polydimethylsiloxane–polycarbonate hybrid microfluidic device capable of generating perpendicular chemical and oxygen gradients for cell culture studies. *Lab Chip* (2014) 14:3762–72. doi: 10.1039/C4LC00732H

6. Perez-Moreno M, Jamora C, Fuchs E. Sticky business: orchestrating cellular signals at adherens junctions. *Cell* (2003) 112:535–48. doi: 10.1016/S0092-8674(03)00108-9

7. Kusindarta DL. The role of extracellular matrix. In: Kaoud HWE-HA hay E-S editor. *Tissue Regeneration* Chapter 5. Rijeka: IntechOpen (2018). doi: 10.5772/intechopen.75728

8. Altman GH, Horan RL, Martin I, Farhadi J, Stark PRH, Volloch V, et al. Cell differentiation by mechanical stress. *FASEB J* (2002) 16:270–2. doi: 10.1096/fj.01-0656fje

9. Poltavets V, Kochetkova M, Pitson SM, Samuel MS. The role of the extracellular matrix and its molecular and cellular regulators in cancer cell plasticity. *Front Oncol* (2018) 8:431. doi: 10.3389/fonc.2018.00431

10. Koohestani F, Braundmeier AG, Mahdian A, Seo J, Bi J, Nowak RA. Extracellular matrix collagen alters cell proliferation and cell cycle progression of human uterine leiomyoma smooth muscle cells. *PloS One* (2013) 8:e75844–4. doi: 10.1371/journal.pone.0075844

11. López-Martínez C, Huidobro C, Albaiceta GM, López-Alonso I. Mechanical stretch modulates cell migration in the lungs. *Ann Transl Med* (2018) 6:28. doi: 10.21037/atm.2017.12.08

12. Mason EF, Rathmell JC. Cell metabolism: an essential link between cell growth and apoptosis. *Biochim Biophys Acta (BBA) - Mol Cell Res* (2011) 1813:645–54. doi: 10.1016/j.bbamcr.2010.08.011

13. Clanton TL, Hogan MC, Gladden LB. Regulation of cellular gas exchange, oxygen sensing, and metabolic control. *Compr Physiol* (2013) 13(3):1135–90. doi: 10.1002/cphy.c120030

14. Lin X, Chen Q, Liu W, Zhang J, Wang S, Lin Z, et al. Oxygen-induced cell migration and on-line monitoring biomarkers modulation of cervical cancers on a microfluidic system. *Sci Rep* (2015) 5:9643. doi: 10.1038/srep09643

15. Petrie Aronin CE, Zhao YM, Yoon JS, Morgan NY, Prüstel T, Germain RN, et al. Migrating myeloid cells sense temporal dynamics of chemoattractant concentrations. *Immunity* (2017) 47:862–874.e3. doi: 10.1016/j.immuni.2017.10.020

16. Stojanovic A, Correia MP, Cerwenka A. Shaping of NK cell responses by the tumor microenvironment. *Cancer Microenviron* (2013) 6:135–46. doi: 10.1007/s12307-012-0125-8

17. Balkwill FR, Capasso M, Hagemann T. The tumor microenvironment at a glance. *J Cell Sci* (2012) 125:5591–6. doi: 10.1242/jcs.116392

18. Costa EC, Moreira AF, de Melo-Diogo D, Gaspar VM, Carvalho MP, Correia IJ. 3D tumor spheroids: an overview on the tools and techniques used for their analysis. *Biotechnol Adv* (2016) 34:1427–41. doi: 10.1016/j.biotechadv.2016.11.002

19. Fennema E, Rivron N, Rouwkema J, van Blitterswijk C, de Boer J. Spheroid culture as a tool for creating 3D complex tissues. *Trends Biotechnol* (2013) 31:108–15. doi: 10.1016/j.tibtech.2012.12.003

20. Zimmermann M, Box C, Eccles SA. Two-dimensional vs. three-dimensional in vitro tumor migration and invasion assays. In: *BMC systems biology*. Totowa, NJ: Humana Press (2013). p. 227–52. doi: 10.1007/978-1-62703-311-4_15

21. Breslin S, O'Driscoll L. Three-dimensional cell culture: the missing link in drug discovery. *Drug Discovery Today* (2013) 18:240–9. doi: 10.1016/j.drudis.2012.10.003

22. Bergenheim F, Fregni G, Buchanan CF, Riis LB, Heulot M, Touati J, et al. A fully defined 3D matrix for ex vivo expansion of human colonic organoids from biopsy tissue. *Biomaterials* (2020) 262:120248. doi: 10.1016/j.biomaterials.2020.120248

23. Angres BM, Wurst H. 3-d life biomimetic hydrogels. *Technol Platforms 3D Cell Culture* (2017), 197–221. doi: 10.1002/9781118851647.ch9

24. Kleinman HK, McGarvey ML, Hassell JR, Star VL, Cannon FB, Laurie GW, et al. Basement membrane complexes with biological activity. *Biochemistry* (1986) 25:312–8. doi: 10.1021/bi00350a005

25. Kleinman HK, Martin GR. Matrigel: basement membrane matrix with biological activity. In: *Seminars in cancer biology*. Elsevier (2005) 15(5):378–86.

26. Caicedo-Carvajal CE, Liu Q, Remache Y, Goy A, Suh KS. Cancer tissue engineering: a novel 3D polystyrene scaffold for *In vitro* isolation and amplification of lymphoma cancer cells from heterogeneous cell mixtures. *J Tissue Eng* (2011) 2011:362326. doi: 10.4061/2011/362326

27. Zhao X, Zhang S, Spirio L. PuraMatrix. In: *Scaffolding in tissue engineering*. CRC Press (2005). p. 217–38. doi: 10.1201/9781420027563.ch15

28. Aisenbrey EA, Murphy WL. Synthetic alternatives to matrigel. *Nat Rev Mater* (2020) 5:539–51. doi: 10.1038/s41578-020-0199-8

29. Carletti E, Motta A, Migliaresi C. Scaffolds for tissue engineering and 3D cell culture BT. In: Haycock JW, editor. *3D cell culture: methods and protocols*. Totowa, NJ: Humana Press (2011). p. 17–39. doi: 10.1007/978-1-60761-984-0_2

30. de Souza N. Organoids. *Nat Methods* (2018) 15:23. doi: 10.1038/nmeth.4576

31. Bar-Ephraim YE, Kretzschmar K, Clevers H. Organoids in immunological research. *Nat Rev Immunol* (2020) 20:279–93. doi: 10.1038/s41577-019-0248-y

32. Artis D, Spits H. The biology of innate lymphoid cells. *Nature* (2015) 517, 293–301. doi: 10.1038/nature14189

33. Kiessling R, Klein E, Wigzell H. "Natural" killer cells in the mouse. i. cytotoxic cells with specificity for mouse moloney leukemia cells. specificity and distribution according to genotype. *Eur J Immunol* (1975) 5:112–7. doi: 10.1002/eji.1830050208

34. Kiessling R, Klein E, Pross H, Wigzell H. "Natural" killer cells in the mouse. II. cytotoxic cells with specificity for mouse moloney leukemia cells. Characteristics of the killer. *Cell Eur J Immunol* (1975) 5:117–21. doi: 10.1002/eji.1830050209

35. Mak TW, Saunders ME. 14 - T cell activation. In: Mak TW, Saunders ME, editors. *The immune response*. Burlington: Academic Press (2006). p. 373–401. doi: 10.1016/B978-012088451-3.50016-8

36. Vivier E. Functions of natural killer cells. *Nat Immunol* (2008) 9:503–10. doi: 10.1038/ni1582

37. Seillet C, Belz GT, Huntington ND. Development, homeostasis, and heterogeneity of NK cells and ILC1. *Curr Top Microbiol Immunol* (2016) 395. doi: 10.1007/82_2015_474

38. Robertson MJ, Ritz J. Biology and clinical relevance of human natural killer cells. *Blood* (1990) 76:2421. doi: 10.1182/blood.V76.12.2421.2421

39. Hashemi E, Malarkannan S. Tissue-resident NK cells: development, maturation, and clinical relevance. *Cancers (Basel)* (2020) 12:1553. doi: 10.3390/cancers12061553

40. Santoli D, Trinchieri G, Moretta L, Zmijewski CM, Koprowski H. Spontaneous cell-mediated cytotoxicity in humans. distribution and characterization of the effector cell. *Clin Exp Immunol* (1978) 33:309–18.

41. Carrega P, Ferlazzo G. Natural killer cell distribution and trafficking in human tissues. *Front Immunol* (2012) 3:347. doi: 10.3389/fimmu.2012.00347

42. Robertson MJ, Soiffer RJ, Wolf SF, Manley TJ, Donahue C, Young D, et al. Response of human natural killer (NK) cells to NK cell stimulatory factor (NKSF): cytolytic activity and proliferation of NK cells are differentially regulated by NKSF. *J Exp Med* (1992) 175(3):779–88. doi: 10.1084/jem.175.3.779

43. Campbell JJ, Qin S, Unutmaz D, Soler D, Murphy KE, Hodge MR, et al. Unique subpopulations of CD56+ NK and NK-T peripheral blood lymphocytes identified by chemokine receptor expression repertoire. *J Immunol* (2001) 166:6477–82. doi: 10.4049/jimmunol.166.11.6477

44. Juelke K, Killig M, Luetke-Eversloh M, Parente E, Gruen J, Morandi B, et al. CD62L expression identifies a unique subset of polyfunctional CD56dimNK cells. *Blood* (2010) 116:1299–307. doi: 10.1182/blood-2009-11-253286

45. Cooper MA, Fehniger TA, Turner SC, Chen KS, Ghaheri BA, Ghayur T, et al. Human natural killer cells: a unique innate immunoregulatory role for the CD56 (bright) subset. *Blood* (2001) 97:3146–51. doi: 10.1182/blood.V97.10.3146

46. Parolini S, Santoro A, Marcenaro E, Luini W, Massardi L, Facchetti F, et al. The role of chemerin in the colocalization of NK and dendritic cell subsets into inflamed tissues. *Blood* (2007) 109(9):3625–32. doi: 10.1182/blood-2006-08-038844

47. Gregoire C, Chasson L, Luci C, Tomasello E, Geissmann F, Vivier E, et al. The trafficking of natural killer cells. *Immunol Rev* (2007) 220:169–82. doi: 10.1111/j.1600-065X.2007.00563.x

48. Seillet C, Belz GT. Differentiation and diversity of subsets in group 1 innate lymphoid cells. *Int Immunol* (2016) 28:3–11. doi: 10.1093/intimm/dxv051

49. Robertson MJ. Role of chemokines in the biology of natural killer cells. *J Leukoc Biol* (2002) 71:173–83. doi: 10.1189/JLB.71.2.173

50. Sun H, Sun C, Xiao W. Expression regulation of co-inhibitory molecules on human natural killer cells in response to cytokine stimulations. *Cytokine* (2014) 65:33–41. doi: 10.1016/j.cyto.2013.09.016

51. Moretta A, Bottino C, Mingari MC, Biassoni R, Moretta L. What is a natural killer cell? *Nat Immunol* (2002) 3:6–8. doi: 10.1038/ni0102-6

52. Stanietsky N, Simic H, Arapovic J, Toporik A, Levy O, Novik A, et al. The interaction of TIGIT with PVR and PVRL2 inhibits human NK cell cytotoxicity. *Proc Natl Acad Sci U.S.A.* (2009) 106:17858–63. doi: 10.1073/pnas.0903474106

53. Yu X, Harden K C, Gonzalez L, Francesco M, Chiang E, Irving B, et al. The surface protein TIGIT suppresses T cell activation by promoting the generation of mature immunoregulatory dendritic cells. *Nat Immunol* (2009) 10:48–57. doi: 10.1038/ni.1674

54. Parham P, Norman PJ, Abi-Rached L, Guethlein LA. Human-specific evolution of killer cell immunoglobulin-like receptor recognition of major histocompatibility complex class I molecules. *Philos Trans R Soc B* (2012) 367:800–11. doi: 10.1098/rstb.2011.0266

55. Kadri N, Wagner AK, Ganesan S, Kärre K, Wickström S, Johansson MH, et al. Dynamic regulation of NK cell responsiveness. In: *Current topics in microbiology and immunology* Springer, Cham (2015) 395:95–114. doi: 10.1007/82_2015_485

56. Brodin P, Kärre K, Höglund P. NK cell education: not an on-off switch but a tunable rheostat. *Trends Immunol* (2009) 30:143–9. doi: 10.1016/j.it.2009.01.006

57. Kärre K, Ljunggren HG, Piontek G, Kiessling R. Selective rejection of h–2-deficient lymphoma variants suggests alternative immune defence strategy. *Nature* (1986) 319:675–8. doi: 10.1038/319675a0

58. Smith MA, Maurin M, Cho HI, Becknell B, Freud AG, Yu J, et al. PRDM1/Blimp-1 controls effector cytokine production in human NK cells. *J Immunol* (2010) 185:6058–67. doi: 10.4049/jimmunol.1001682

59. O'Sullivan TE, Sun JC, Lanier LL. Natural killer cell memory. *Immunity* (2015) 43:634–45. doi: 10.1016/j.immuni.2015.09.013

60. Vacca P, Mingari MC, Moretta L. Natural killer cells in human pregnancy. *J Reprod Immunol* (2013) 97(1):14–9. doi: 10.1016/j.jri.2012.10.008

61. Kalkunte SS, Mselle TF, Norris WE, Wira CR, Sentman CL, Sharma S. Vascular endothelial growth factor c facilitates immune tolerance and endovascular activity of human uterine NK cells at the maternal-fetal interface. *J Immunol* (2009) 182:4085–92. doi: 10.4049/jimmunol.0803769

62. Hanna J, Goldman-Wohl D, Hamani Y, Avraham I, Greenfield C, Natanson-Yaron S, et al. Decidual NK cells regulate key developmental processes at the human fetal-maternal interface. *Nat Med* (2006) 12:1065–74. doi: 10.1038/nm1452

63. le Bouteiller P. Human decidual NK cells: unique and tightly regulated effector functions in healthy and pathogen-infected pregnancies. *Front Immunol* (2013) 4:404. doi: 10.3389/fimmu.2013.00404

64. Tosello-Trampont A, Surette FA, Ewald SE, Hahn YS. Immunoregulatory role of NK cells in tissue inflammation and regeneration. *Front Immunol* (2017) 8:301. doi: 10.3389/fimmu.2017.00301

65. O'Sullivan TE, Rapp M, Fan X, Weizman O-E, Bhardwaj P, Adams NM, et al. Adipose-resident group 1 innate lymphoid cells promote obesity-associated insulin resistance. *Immunity* (2016) 45:428–41. doi: 10.1016/j.immuni.2016.06.016

66. Fernandez NC, Flament C, Crépineau F, Angevin É, Vivier É, Zitvogel L. Dendritic cells (DC) promote natural killer (NK) cell functions: dynamics of the human DC/NK cell cross talk. *Eur Cytokine Netw* (2002) 13(1):17–27.

67. Nielsen N, Ødum N, Ursø B, Lanier LL, Spee P. Cytotoxicity of CD56bright NK cells towards autologous activated CD4+ T cells is mediated through NKG2D, LFA-1 and TRAIL and dampened *via* CD94/NKG2A. *PloS One* (2012) 7:e31959. doi: 10.1371/journal.pone.0031959

68. Cerboni C, Zingoni A, Cippitelli M, Piccoli M, Frati L, Santoni A. Antigen-activated human T lymphocytes express cell-surface NKG2D ligands *via* an ATM/ATR-dependent mechanism and become susceptible to autologous NK-cell lysis. *Blood J Am Soc Hematol* (2007) 110:606–15. doi: 10.1182/blood-2006-10-052720

69. Helige C, Hagendorfer G, Smolle J, Dohr G. Uterine natural killer cells in a three-dimensional tissue culture model to study trophoblast invasion. *Lab Invest* (2001) 81:1153–62. doi: 10.1038/labinvest.3780327

70. Helige C, Ahammer H, Hammer A, Huppertz B, Frank H-G, Dohr G. Trophoblastic invasion *in vitro* and *in vivo*: similarities and differences. *Hum Reprod* (2008) 23:2282–91. doi: 10.1093/humrep/den198

71. Abbas Y, Turco MY, Burton GJ, Moffett A. Investigation of human trophoblast invasion. *vitro. Hum Reprod Update* (2020) 26:501–13. doi: 10.1093/humupd/dmaa017

72. Abbas Y, Oefner CM, Polacheck WJ, Gardner L, Farrell L, Sharkey A, et al. A microfluidics assay to study invasion of human placental trophoblast cells. *J R Soc Interface* (2017) 14. doi: 10.1098/rsif.2017.0131

73. Sheridan MA, Fernando RC, Gardner L, Hollinshead MS, Burton GJ, Moffett A, et al. Establishment and differentiation of long-term trophoblast organoid cultures from the human placenta. *Nat Protoc* (2020) 15:3441–63. doi: 10.1038/s41596-020-0381-x

74. Sheridan MA, Zhao X, Fernando RC, Gardner L, Perez-Garcia V, Li Q, et al. Characterization of primary models of human trophoblast. *Development* (2021) 148. doi: 10.1242/dev.199749

75. Petrova V, Annicchiarico-Petruzzelli M, Melino G, Amelio I. The hypoxic tumour microenvironment. *Oncogenesis* (2018) 7. doi: 10.1038/s41389-017-0011-9

76. Wang JX, Choi SYC, Niu X, Kang N, Xue H, Killam J, et al. Lactic acid and an acidic tumor microenvironment suppress anticancer immunity. *Int J Mol Sci* (2020) 21:1–14. doi: 10.3390/ijms21218363

77. Harmon C, Robinson MW, Hand F, Almuaili D, Mentor K, Houlihan DD, et al. Lactate-mediated acidification of tumor microenvironment induces apoptosis of liver-resident NK cells in colorectal liver metastasis. *Cancer Immunol Res* (2019) 7:335–46. doi: 10.1158/2326-6066.CIR-18-0481

78. Brand A, Singer K, Koehl GE, Kolitzus M, Schoenhammer G, Thiel A, et al. LDHA-associated lactic acid production blunts tumor immunosurveillance by T and NK cells. *Cell Metab* (2016) 24:657–71. doi: 10.1016/j.cmet.2016.08.011

79. Ni J, Wang X, Stojanovic A, Zhang Q, Wincher M, Bühler L, et al. Single-cell RNA sequencing of tumor-infiltrating NK cells reveals that inhibition of transcription factor HIF-1α unleashes NK cell activity. *Immunity* (2020) 52:1075–1087.e8. doi: 10.1016/j.immuni.2020.05.001

80. Solocinski K, Padget MR, Fabian KP, Wolfson B, Cecchi F, Hembrough T, et al. Overcoming hypoxia-induced functional suppression of NK cells. *J Immunother Cancer* (2020) 8. doi: 10.1136/jitc-2019-000246

81. Balsamo M, Manzini C, Pietra G, Raggi F, Blengio F, Mingari MC, et al. Hypoxia downregulates the expression of activating receptors involved in NK-cell-mediated target cell killing without affecting ADCC. *Eur J Immunol* (2013) 43:2756–64. doi: 10.1002/eji.201343448

82. Ghiringhelli F, Ménard C, Terme M, Flament C, Taieb J, Chaput N, et al. CD4 + CD25 + regulatory T cells inhibit natural killer cell functions in a transforming growth factor–β–dependent manner. *J Exp Med* (2005) 202:1075–85. doi: 10.1084/jem.20051511

83. Li T, Yang Y, Hua X, Wang G, Liu W, Jia C, et al. Hepatocellular carcinoma-associated fibroblasts trigger NK cell dysfunction *via* PGE2 and IDO. *Cancer Lett* (2012) 318(2):154–61. doi: 10.1016/j.canlet.2011.12.020

84. Balsamo M, Scordamaglia F, Pietra G, Manzini C, Cantoni C, Boitano M, et al. Melanoma-associated fibroblasts modulate NK cell phenotype and antitumor cytotoxicity. *Proc Natl Acad Sci* (2009) 106(49):20847–52. doi: 10.1073/pnas.0906481106

85. Pietra G, Manzini C, Rivara S, Vitale M, Cantoni C, Petretto A, et al. Melanoma cells inhibit natural killer cell function by modulating the expression of activating receptors and cytolytic activity. *Cancer Res* (2012) 72(6):1407–15. doi: 10.1158/0008-5472.CAN-11-2544

86. El-Gazzar A, Groh V, Spies T. Immunobiology and conflicting roles of the human NKG2D lymphocyte receptor and its ligands in cancer. *J Immunol* (2013) 191:1509–15. doi: 10.4049/jimmunol.1301071

87. Tarazona R, Borrego F, Vaage JT, Kohrt HE, Chester C, Fritsch K. Natural killer cell immunomodulation: targeting activating. *inhibitory Co-stimulatory Receptor Signaling Cancer immunotherapy* (2015) 6:601. doi: 10.3389/fimmu.2015.00601

88. Sutherland RM, MacDonald HR, Howell RL. Multicellular spheroids: a new model target for *In vitro* studies of immunity to solid tumor allografts: brief communication. *JNCI: J Natl Cancer Institute* (1977) 58:1849–53. doi: 10.1093/jnci/58.6.1849

89. Sordat B, MacDonald HR, Lees RK. The multicellular spheroid as a model tumor allograft. III. morphological and kinetic analysis of spheroid infiltration and destruction. *Transplantation* (1980) 29:103–12. doi: 10.1097/00007890-198002000-00004

90. MacDonald HR, Howell RL. The multicellular spheroid as a model tumor allograft. i. quantitative assessment of spheroid destruction in alloimmune mice. *Transplantation* (1978) 25:136–40. doi: 10.1097/00007890-197803000-00008

91. MacDonald HR, Howell RL, McFarlane DL. The multicellular spheroid as a model tumor allograft. II. characterization of spheroid-infiltrating cytotoxic cells. *Transplantation* (1978) 25:141–5. doi: 10.1097/00007890-197803000-00009

92. Ayuso JM, Truttschel R, Gong MM, Humayun M, Virumbrales-Munoz M, Vitek R, et al. Evaluating natural killer cell cytotoxicity against solid tumors using a microfluidic model. *Oncoimmunology* (2019) 8:1–11. doi: 10.1080/2162402X.2018.1553477

93. Marrella A, Buratti P, Markus J, Firpo G, Pesenti M, Landry T, et al. *In vitro* demonstration of intestinal absorption mechanisms of different sugars using 3D organotypic tissues in a fluidic device. *ALTEX* (2020) 37:255–64. doi: 10.14573/altex.1908311

94. Marrella A, Varani G, Aiello M, Vaccari I, Vitale C, Mojzisek M, et al. 3D fluid-dynamic ovarian cancer model resembling systemic drug administration for efficacy assay. *ALTEX* (2021) 38:82–94. doi: 10.14573/altex.2003131

95. Marzagalli M, Pelizzoni G, Fedi A, Vitale C, Fontana F, Bruno S, et al. A multi-organ-on-chip to recapitulate the infiltration and the cytotoxic activity of circulating NK cells in 3D matrix-based tumor model. *Front Bioeng Biotechnol* (2022) 10:945149. doi: 10.3389/fbioe.2022.945149

96. Mclimans WF, Davis EV, Glover FL, Rake GW. The submerged culture of mammalian cells; the spinner culture. *J Immunol* (1957) 79:428–33. doi: 10.4049/jimmunol.79.5.428

97. Lord EM, Burkhardt G. Assessment of *in situ* host immunity to syngeneic tumors utilizing the multicellular spheroid model. *Cell Immunol* (1984) 85:340–50. doi: 10.1016/0008-8749(84)90248-x

98. Iwasaki K, Kikuchi H, Miyatake SI, Aoki T, Yamasaki T, Oda Y. Infiltrative and cytolytic activities of lymphokine-activated killer cells against a human glioma spheroid model. *Cancer Res* (1990) 50:2429–36.

99. Sutherland RM, McCredie JA, Inch WR. Growth of multicell spheroids in tissue culture as a model of nodular carcinomas. *J Natl Cancer Inst* (1971) 46:113–20. doi: 10.1093/jnci/46.1.113

100. Sutherland RM, Durand RE. Growth and cellular characteristics of multicell spheroids. *Recent Results Cancer Res* (1984) 95:24–49. doi: 10.1007/978-3-642-82340-4_2

101. He W, Kuang Y, Xing X, Simpson RJ, Huang H, Yang T, et al. Proteomic comparison of 3D and 2D glioma models reveals increased HLA-e expression in 3D models is associated with resistance to NK cell-mediated cytotoxicity. *J Proteome Res* (2014) 13:2272–81. doi: 10.1021/pr500064m

102. Kelm JM, Fussenegger M. Microscale tissue engineering using gravity-enforced cell assembly. *Trends Biotechnol* (2004) 22:195–202. doi: 10.1016/j.tibtech.2004.02.002

103. Carlsson J, Yuhas JM. Liquid-overlay culture of cellular spheroids. *Recent Results Cancer Res* (1984) 95:1–23. doi: 10.1007/978-3-642-82340-4_1

104. Yuhas JM, Li AP, Martinez AO, Ladman AJ. A simplified method for production and growth of multicellular tumor spheroids. *Cancer Res* (1977) 37:3639–43.

105. Garcia de Palazzo I, Holmes M, Gercel-Taylor C, Weiner LM. Antitumor effects of a bispecific antibody targeting CA19-9 antigen and CD16. *Cancer Res* (1992) 52:5713–9.

106. Giannattasio A, Weil S, Kloess S, Ansari N, Stelzer EHK, Cerwenka A, et al. Cytotoxicity and infiltration of human NK cells in *in vivo*-like tumor spheroids. *BMC Cancer* (2015) 15:351. doi: 10.1186/s12885-015-1321-y

107. Ivascu A, Kubbies M. Rapid generation of single-tumor spheroids for high-throughput cell function and toxicity analysis. *J Biomol Screen* (2006) 11:922–32. doi: 10.1177/1087057106292763

108. Lawrenson K, Grun B, Gayther SA. Heterotypic three-dimensional in vitro modeling of stromal-epithelial interactions during ovarian cancer initiation and progression. *J Vis Exp* (2012):e4206. doi: 10.3791/4206

109. del Bano J, Florès-Florès R, Josselin E, Goubard A, Ganier L, Castellano R, et al. A bispecific antibody-based approach for targeting mesothelin in triple negative breast cancer. *Front Immunol* (2019) 10:1593. doi: 10.3389/fimmu.2019.01593

110. Murphy DA, Cheng H, Yang T, Yan X, Adjei IM. Reversing hypoxia with PLGA-encapsulated manganese dioxide nanoparticles improves natural killer cell response to tumor spheroids. *Mol Pharm* (2021) 18:2935–46. doi: 10.1021/acs.molpharmaceut.1c00085

111. Jääskeläinen J, Lehtonen E, Heikkilä P, Kalliomäki P, Timonen T. Damage to multicellular human h-2 glioma spheroids incubated with LAK cells: an ultrastructural study. *J Natl Cancer Inst* (1990) 82:497–501. doi: 10.1093/jnci/82.6.497

112. Jääskeläinen J, Mäenpää A, Patarroyo M, Gahmberg CG, Somersalo K, Tarkkanen J, et al. Migration of recombinant IL-2-activated T and natural killer cells in the intercellular space of human h-2 glioma spheroids *in vitro*. a study on adhesion molecules involved. *J Immunol* (1992) 149:260–8. doi: 10.4049/jimmunol.149.1.260

113. Nederman T, Norling B, Glimelius B, Carlsson J, Brunk U. Demonstration of an extracellular matrix in multicellular tumor spheroids. *Cancer Res* (1984) 44:3090–7.

114. Lee YE, Yuk CM, Lee M, Han K-C, Jun E, Kim TS, et al. Facile discovery of a therapeutic agent for NK-mediated synergistic antitumor effects using a patient-derived 3D platform. *Biomater Sci* (2022) 10:678–91. doi: 10.1039/d1bm01699g

115. Jääskeläinen J, Kalliomäki P, Paetau A, Timonen T. Effect of LAK cells against three-dimensional tumor tissue. *In vitro* study using multi-cellular human glioma spheroids as targets. *J Immunol* (1989) 142:1036–45. doi: 10.4049/jimmunol.142.3.1036

116. Kaaijk P, Troost D, Dast PK, van den Berg F, Leenstra S, Bosch DA. Cytolytic effects of autologous lymphokine-activated killer cells on organotypic multicellular spheroids of gliomas *in vitro*. *Neuropathol Appl Neurobiol* (1995) 21:392–8. doi: 10.1111/j.1365-2990.1995.tb01076.x

117. Sargenti A, Musmeci F, Bacchi F, Delprete C, Cristaldi DA, Cannas F, et al. Physical characterization of colorectal cancer spheroids and evaluation of NK cell infiltration through a flow-based analysis. *Front Immunol* (2020) 11:564887. doi: 10.3389/fimmu.2020.564887

118. Weil S, Memmer S, Lechner A, Huppert V, Giannattasio A, Becker T, et al. Natural killer group 2D ligand depletion reconstitutes natural killer cell immunosurveillance of head and neck squamous cell carcinoma. *Front Immunol* (2017) 8:387. doi: 10.3389/fimmu.2017.00387

119. Courau T, Bonnereau J, Chicoteau J, Bottois H, Remark R, Assante Miranda L, et al. Cocultures of human colorectal tumor spheroids with immune cells reveal the therapeutic potential of MICA/B and NKG2A targeting for cancer treatment. *J Immunother Cancer* (2019) 7:74. doi: 10.1186/s40425-019-0553-9

120. Susek KH, Schwietzer YA, Karvouni M, Gilljam M, Keszei M, Hussain A, et al. Generation of NK cells with chimeric-switch receptors to overcome PD1-mediated inhibition in cancer immunotherapy. *Cancer Immunol Immunother* (2022) 72:1153–67. doi: 10.1007/s00262-022-03317-y

121. González-Llorente L, Santacatterina F, García-Aguilar A, Nuevo-Tapioles C, González-García S, Tirpakova Z, et al. Overexpression of mitochondrial IF1 prevents metastatic disease of colorectal cancer by enhancing anoikis and tumor infiltration of NK cells. *Cancers (Basel)* (2019) 12:22. doi: 10.3390/cancers12010022

122. Hoffmann TK, Schirlau K, Sonkoly E, Brandau S, Lang S, Pivarcsi A, et al. A novel mechanism for anti-EGFR antibody action involves chemokine-mediated leukocyte infiltration. *Int J Cancer* (2009) 124:2589–96. doi: 10.1002/ijc.24269

123. Hoogstad-van Evert JS, Cany J, van den Brand D, Oudenampsen M, Brock R, Torensma R, et al. Umbilical cord blood CD34+ progenitor-derived NK cells efficiently kill ovarian cancer spheroids and intraperitoneal tumors in NOD/SCID/IL2Rgnull mice. *Oncoimmunology* (2017) 6:e1320630. doi: 10.1080/2162402X.2017.1320630

124. Maas RJ, Hoogstad-van Evert JS, van der Meer JM, Mekers V, Rezaeifard S, Korman AJ, et al. TIGIT blockade enhances functionality of peritoneal NK cells with altered expression of DNAM-1/TIGIT/CD96 checkpoint molecules in ovarian cancer. *Oncoimmunology* (2020) 9:1843247. doi: 10.1080/2162402X.2020.1843247

125. Decaup E, Rossi C, Gravelle P, Laurent C, Bordenave J, Tosolini M, et al. A tridimensional model for NK cell-mediated ADCC of follicular lymphoma. *Front Immunol* (2019) 10:1943. doi: 10.3389/fimmu.2019.01943

126. Guti E, Regdon Z, Sturniolo I, Kiss A, Kovács K, Demény M, et al. The multitargeted receptor tyrosine kinase inhibitor sunitinib induces resistance of HER2 positive breast cancer cells to trastuzumab-mediated ADCC. *Cancer Immunol Immunother* (2022) 71:2151–68. doi: 10.1007/s00262-022-03146-z

127. Rademacher MJ, Cruz A, Faber M, Oldham RAA, Wang D, Medin JA, et al. Sarcoma IL-12 overexpression facilitates NK cell immunomodulation. *Sci Rep* (2021) 11:8321. doi: 10.1038/s41598-021-87700-2

128. Aarsund M, Segers FM, Wu Y, Inngjerdingen M. Comparison of characteristics and tumor targeting properties of extracellular vesicles derived from primary NK cells or NK-cell lines stimulated with IL-15 or IL-12/15/18. *Cancer Immunol Immunother* (2022) 71:2227–38. doi: 10.1007/s00262-022-03161-0

129. Ochalek T, von Kleist S. Study of the susceptibility of human colorectal tumor explants to LAK-cell lysis: comparison of various cytotoxicity tests. *J Clin Lab Anal* (1993) 7:155–63. doi: 10.1002/jcla.1860070305

130. Ochalek T, von Kleist S. Study of the resistance of tumor-cell spheroids to penetration and lysis by activated effector cells. *Int J Cancer* (1994) 57:399–405. doi: 10.1002/ijc.2910570318

131. Knelson EH, v. IE, Tarannum M, Campisi M, Lizotte PH, Booker MA, et al. Activation of tumor-cell STING primes NK-cell therapy. *Cancer Immunol Res* (2022) 10:947–61. doi: 10.1158/2326-6066.CIR-22-0017

132. Goodman SR. Cell adhesion and the extracellular matrix. In: *Goodman's medical cell biology*. Elsevier (2021). p. 203–47. doi: 10.1016/B978-0-12-817927-7.00007-7

133. Kelm JM, Timmins NE, Brown CJ, Fussenegger M, Nielsen LK. Method for generation of homogeneous multicellular tumor spheroids applicable to a wide variety of cell types. *Biotechnol Bioeng* (2003) 83:173–80. doi: 10.1002/bit.10655

134. Keller GM. *In vitro* differentiation of embryonic stem cells. *Curr Opin Cell Biol* (1995) 7:862–9. doi: 10.1016/0955-0674(95)80071-9

135. Lanuza PM, Vigueras A, Olivan S, Prats AC, Costas S, Llamazares G, et al. Activated human primary NK cells efficiently kill colorectal cancer cells in 3D spheroid cultures irrespectively of the level of PD-L1 expression. *Oncoimmunology* (2018) 7: e1395123. doi: 10.1080/2162402X.2017.1395123

136. Tung Y, Hsiao AY, Allen SG, Torisawa Y, Ho M, Takayama S. High-throughput 3D spheroid culture and drug testing using a 384 hanging drop array. *Analyst* (2011) 136:473–8. doi: 10.1039/c0an00609b

137. Drewitz M, Helbling M, Fried N, Bieri M, Moritz W, Lichtenberg J, et al. Towards automated production and drug sensitivity testing using scaffold-free spherical tumor microtissues. *Biotechnol J* (2011) 6:1488–96. doi: 10.1002/biot.201100290

138. Messner S, Agarkova I, Moritz W, Kelm JM. Multi-cell type human liver microtissues for hepatotoxicity testing. *Arch Toxicol* (2013) 87:209–13. doi: 10.1007/s00204-012-0968-2

139. Wardwell-Swanson J, Suzuki M, Dowell KG, Bieri M, Thoma EC, Agarkova I, et al. A framework for optimizing high-content imaging of 3D models for drug discovery. *SLAS Discovery* (2020) 25:709–22. doi: 10.1177/2472555220929291

140. Title AC, Karsai M, Mir-Coll J, Grining ÖY, Rufer C, Sonntag S, et al. Evaluation of the effects of harmine on β-cell function and proliferation in standardized human islets using 3D high-content confocal imaging and automated analysis. *Front Endocrinol (Lausanne)* (2022) 13:854094. doi: 10.3389/fendo.2022.854094

141. Badea MA, Balas M, Dinischiotu A. Biological properties and development of hypoxia in a breast cancer 3D model generated by hanging drop technique. *Cell Biochem Biophys* (2022) 80:63–73. doi: 10.1007/s12013-021-00982-1

142. Herter S, Morra L, Schlenker R, Sulcova J, Fahrni L, Waldhauer I, et al. A novel three-dimensional heterotypic spheroid model for the assessment of the activity of cancer immunotherapy agents. *Cancer Immunol Immunother* (2017) 66:129–40. doi: 10.1007/s00262-016-1927-1

143. Park D, Son K, Hwang Y, Ko J, Lee Y, Doh J, et al. High-throughput microfluidic 3D cytotoxicity assay for cancer immunotherapy (CACI-ImpacT platform). *Front Immunol* (2019) 10:1133. doi: 10.3389/fimmu.2019.01133

144. Schnalzger TE, de Groot MH, Zhang C, Mosa MH, Michels BE, Röder J, et al. 3D model for CAR-mediated cytotoxicity using patient-derived colorectal cancer organoids. *EMBO J* (2019) 38. doi: 10.15252/embj.2018100928

145. Tibbitt MW, Anseth KS. Hydrogels as extracellular matrix mimics for 3D cell culture. *Biotechnol Bioeng* (2009) 103:655–63. doi: 10.1002/bit.22361

146. Gopal S, Kwon S-J, Ku B, Lee DW, Kim J, Dordick JS. 3D tumor spheroid microarray for high-throughput, high-content natural killer cell-mediated cytotoxicity. *Commun Biol* (2021) 4:893. doi: 10.1038/s42003-021-02417-2

147. Ishikura H, Takahashi C, Kanagawa K, Togashi M, Koyanagi T, Yoshiki T. Susceptibility of renal tubular cells to lymphokine-activated killer (LAK) cells: application of culture system using a collagen gel matrix. *Virchows Arch B Cell Pathol Incl Mol Pathol* (1993) 63:115–21. doi: 10.1007/BF02899250

148. Ayuso JM, Virumbrales-Muñoz M, Lacueva A, Lanuza PM, Checa-Chavarria E, Botella P, et al. Development and characterization of a microfluidic model of the tumour microenvironment. *Sci Rep* (2016) 6:36086. doi: 10.1038/srep36086

149. Ayuso JM, Rehman S, Virumbrales-Munoz M, McMinn PH, Geiger P, Fitzgerald C, et al. Microfluidic tumor-on-a-chip model to evaluate the role of tumor environmental stress on NK cell exhaustion. *Sci Adv* (2021) 7:1–14. doi: 10.1126/sciadv.abc2331

150. Marrella A, Dondero A, Aiello M, Casu B, Olive D, Regis S, et al. Cell-laden hydrogel as a clinical-relevant 3D model for analyzing neuroblastoma growth, immunophenotype, and susceptibility to therapies. *Front Immunol* (2019) 10:1876. doi: 10.3389/fimmu.2019.01876

151. Temples MN, Adjei IM, Nimocks PM, Djeu J, Sharma B. Engineered three-dimensional tumor models to study natural killer cell suppression. *ACS Biomater Sci Eng* (2020) 6:4179–99. doi: 10.1021/acsbiomaterials.0c00259

152. Nguyen OTP, Misun PM, Lohasz C, Lee J, Wang W, Schroeder T, et al. An immunocompetent microphysiological system to simultaneously investigate effects of anti-tumor natural killer cells on tumor and cardiac microtissues. *Front Immunol* (2021) 12:781337. doi: 10.3389/fimmu.2021.781337

153. Lohasz C, Rousset N, Renggli K, Hierlemann A, Frey O. Scalable microfluidic platform for flexible configuration of and experiments with microtissue multiorgan models. *SLAS Technol* (2019) 24:79–95. doi: 10.1177/2472630318802582

154. Christakou AE, Ohlin M, Onfelt B, Wiklund M. Ultrasonic three-dimensional on-chip cell culture for dynamic studies of tumor immune surveillance by natural killer cells. *Lab Chip* (2015) 15:3222–31. doi: 10.1039/C5LC00436E

155. Olofsson K, Carannante V, Ohlin M, Frisk T, Kushiro K, Takai M, et al. Acoustic formation of multicellular tumor spheroids enabling on-chip functional and structural imaging. *Lab Chip* (2018) 18:2466–76. doi: 10.1039/c8lc00537k

156. Sandström N, Carannante V, Olofsson K, Sandoz PA, Moussaud-Lamodière EL, Seashore-Ludlow B, et al. Miniaturized and multiplexed high-content screening of drug and immune sensitivity in a multichambered microwell chip. *Cell Rep Methods* (2022) 2:100256. doi: 10.1016/j.crmeth.2022.100256

157. Wiklund M. Acoustofluidics 12: biocompatibility and cell viability in microfluidic acoustic resonators. *Lab Chip* (2012) 12:2018. doi: 10.1039/c2lc40201g

158. Wiklund M, Önfelt B. Ultrasonic manipulation of single cells. In: *Single-Cell Analysis. Methods in Molecular Biology* Humana Press (2012). 853 p. 177–96. doi: 10.1007/978-1-61779-567-1_14

159. Wiklund M, Christakou AE, Ohlin M, Iranmanesh I, Frisk T, Vanherberghen B, et al. Ultrasound-induced cell-cell interaction studies in a multi-well microplate. *Micromachines (Basel)* (2014) 5:27–49. doi: 10.3390/mi5010027

160. Vanherberghen B, Manneberg O, Christakou A, Frisk T, Ohlin M, Hertz HM, et al. Ultrasound-controlled cell aggregation in a multi-well chip. *Lab Chip* (2010) 10:2727–32. doi: 10.1039/c004707d

161. Christakou AE, Ohlin M, Vanherberghen B, Khorshidi MA, Kadri N, Frisk T, et al. Live cell imaging in a micro-array of acoustic traps facilitates quantification of natural killer cell heterogeneity. *Integr Biol (Camb)* (2013) 5:712–9. doi: 10.1039/c3ib20253d

162. Nagahashi K, Teramura Y, Takai M. Stable surface coating of silicone elastomer with phosphorylcholine and organosilane copolymer with cross-linking for repelling proteins. *Colloids Surf B Biointerfaces* (2015) 134:384–91. doi: 10.1016/j.colsurfb.2015.07.040

163. Kiessling R, Klein E, Wigzell H. "Natural" killer cells in the mouse. i. cytotoxic cells with specificity for mouse moloney leukemia cells. specificity and distribution according to genotype. *Eur J Immunol* (1975) 5:112–7. doi: 10.1002/eji.1830050208

164. Kiessling R, Klein E, Pross H, Wigzell H. "Natural" killer cells in the mouse. II. cytotoxic cells with specificity for mouse moloney leukemia cells. characteristics of the killer cell. *Eur J Immunol* (1975) 5:117–21. doi: 10.1002/eji.1830050209

165. Guldevall K, Vanherberghen B, Frisk T, Hurtig J, Christakou AE. Imaging immune surveillance of individual natural killer cells confined in microwell arrays. *PloS One* (2010) 5:15453. doi: 10.1371/journal.pone.0015453

166. Vanherberghen B, Olofsson PE, Forslund E, Sternberg-Simon M, Khorshidi MA, Pacouret S, et al. Classification of human natural killer cells based on migration behavior and cytotoxic response. *Blood* (2013) 121:1326–34. doi: 10.1182/blood-2012-06-439851

167. Guldevall K, Brandt L, Forslund E, Olofsson K, Frisk TW, Olofsson PE, et al. Microchip screening platform for single cell assessment of NK cell cytotoxicity. *Front Immunol* (2016) 7:119. doi: 10.3389/fimmu.2016.00119

168. Herberman RB, Aoki T, Nunn M, Lavrin DH, Soares N, Gazdar A, et al. Specificity of 51Cr-release cytotoxicity of lymphocytes immune to murine sarcoma virus. *J Natl Cancer Inst* (1974) 53:1103–11. doi: 10.1093/jnci/53.4.1103

169. Alter G, Malenfant JM, Altfeld M. CD107a as a functional marker for the identification of natural killer cell activity. *J Immunol Methods* (2004) 294:15–22. doi: 10.1016/j.jim.2004.08.008

170. Granger JE, Appledorn DM. Kinetic measurement of apoptosis and immune cell killing using live-cell imaging and analysis. *Methods Mol Biol* (2021) 2255:197–212. doi: 10.1007/978-1-0716-1162-3_17

171. Höppner M, Luhm J, Schlenke P, Koritke P, Frohn C. A flow-cytometry based cytotoxicity assay using stained effector cells in combination with native target cells. *J Immunol Methods* (2002) 267:157–63. doi: 10.1016/s0022-1759(02)00167-9

172. Bryceson YT, Fauriat C, Nunes JM, Wood SM, Björkström NK, Long EO, et al. Functional analysis of human NK cells by flow cytometry. *Methods Mol Biol* (2010) 612:335–52. doi: 10.1007/978-1-60761-362-6_23

173. Godoy-Ramirez K, Franck K, Gaines H. A novel method for the simultaneous assessment of natural killer cell conjugate formation and cytotoxicity at the single-cell level by multi-parameter flow cytometry. *J Immunol Methods* (2000) 239:35–44. doi: 10.1016/s0022-1759(00)00161-7

174. Erbe AK, Wang W, Gallenberger M, Hank JA, Sondel PM. *Natural killer cells*. Somanchi SS, editor. New York, NY: Springer New York (2016) p. 4370–1. doi: 10.1007/978-1-4939-3684-7

175. Brunner KT, Mauel J, Cerottini JC, Chapuis B. Quantitative assay of the lytic action of immune lymphoid cells on 51-cr-labelled allogeneic target cells *in vitro*; inhibition by isoantibody and by drugs. *Immunology* (1968) 14:181–96.

176. Hirte HW, Clark DA. Factors determining the ability of cytokine-activated killer cells to lyse human ovarian carcinoma targets. *Cell Immunol* (1991) 136:122–32. doi: 10.1016/0008-8749(91)90387-Q

177. Schmit T, Klomp M, Khan MN. An overview of flow cytometry: its principles and applications in allergic disease research. *Methods Mol Biol* (2021) 2223:169–82. doi: 10.1007/978-1-0716-1001-5_13

178. van der Velden VHJ, Scid T. Modern flow cytometry. *Erasmus* (2015) 83(1):1–6.

179. Shapiro HM, Telford WG. Lasers for flow cytometry: current and future trends. *Curr Protoc Cytom* (2018) 83. doi: 10.1002/cpcy.30

180. van der Meer JMR, Maas RJA, Guldevall K, Klarenaar K, de Jonge PKJD, Evert JSHH, et al. IL-15 superagonist n-803 improves IFNγ production and killing of leukemia and ovarian cancer cells by CD34+ progenitor-derived NK cells. *Cancer Immunology Immunotherapy* (2021) 70:1305–21. doi: 10.1007/s00262-020-02749-8

181. Holmes TD, El-Sherbiny YM, Davison A, Clough SL, Blair GE, Cook GP. A human NK cell Activation/Inhibition threshold allows small changes in the target cell surface phenotype to dramatically alter susceptibility to NK cells. *J Immunol* (2011) 186:1538–45. doi: 10.4049/jimmunol.1000951

182. Morimoto T, Nakazawa T, Matsuda R, Nishimura F, Nakamura M, Yamada S, et al. Evaluation of comprehensive gene expression and NK cell-mediated killing in glioblastoma cell line-derived spheroids. *Cancers (Basel)* (2021) 13:4896. doi: 10.3390/cancers13194896

183. Veneziani I, Infante P, Ferretti E, Melaiu O, Battistelli C, Lucarini V, et al. Nutlin-3a enhances natural killer cell–mediated killing of neuroblastoma by restoring p53-dependent expression of ligands for NKG2D and DNAM-1 receptors. *Cancer Immunol Res* (2021) 9:170–83. doi: 10.1158/2326-6066.CIR-20-0313

184. Cristaldi DA, Sargenti A, Bonetti S, Musmeci F, Delprete C, Bacchi F, et al. A reliable flow-based method for the accurate measure of mass density, size and weight of live 3D tumor spheroids. *Micromachines (Basel)* (2020) 11:1–13. doi: 10.3390/mi11050465

185. Klöss S, Chambron N, Gardlowski T, Weil S, Koch J, Esser R, et al. Cetuximab reconstitutes pro-inflammatory cytokine secretions and tumor-infiltrating capabilities of sMICA-inhibited NK cells in HNSCC tumor spheroids. *Front Immunol* (2015) 6:543. doi: 10.3389/fimmu.2015.00543

186. Carannante V, Sandström N, Olofsson K, Van Ooijen H, Hell B, Wiklund M, et al. "Generation of tumor spheroids in microwells to study NK cell cytotoxicity, infiltration and phenotype.,". *Methods Cell Biol Acad Press* (2023). doi: 10.1016/bs.mcb.2023.01.001

187. Särchen V, Shanmugalingam S, Kehr S, Reindl LM, Greze V, Wiedemann S, et al. Pediatric multicellular tumor spheroid models illustrate a therapeutic potential by combining BH3 mimetics with natural killer (NK) cell-based immunotherapy. *Cell Death Discovery* (2022) 8:11. doi: 10.1038/s41420-021-00812-6

188. Edwards SJ, Carannante V, Kuhnigk K, Ring H, Tararuk T, Hallböök F, et al. High-resolution imaging of tumor spheroids and organoids enabled by expansion microscopy. *Front Mol Biosci* (2020) 7:208. doi: 10.3389/fmolb.2020.00208

189. Huisken J, Swoger J, del Bene F, Wittbrodt J, Stelzer EHK. Optical sectioning deep inside live embryos by selective plane illumination microscopy. *Science* (2004) 305:1007–9. doi: 10.1126/science.1100035

190. Weber M, Mickoleit M, Huisken J. *Light sheet microscopy. 1st ed*. Elsevier Inc (2014) p. 193–215. doi: 10.1016/B978-0-12-420138-5.00011-2

191. Reynaud EG, Kržič U, Greger K, Stelzer EHK. Light sheet-based fluorescence microscopy: more dimensions, more photons, and less photodamage. *HFSP J* (2008) 2:266–75. doi: 10.2976/1.2974980

192. Lorenzo C, Frongia C, Jorand R, Fehrenbach J, Weiss P, Maandhui A, et al. Live cell division dynamics monitoring in 3D large spheroid tumor models using light sheet microscopy. *Cell Div* (2011) 6:22. doi: 10.1186/1747-1028-6-22

193. Krneta T, Gillgrass A, Chew M, Ashkar AA. The breast tumor microenvironment alters the phenotype and function of natural killer cells. *Cell Mol Immunol* (2016) 13:628–39. doi: 10.1038/cmi.2015.42

Frontiers in Immunology

Explores novel approaches and diagnoses to treat immune disorders.

The official journal of the International Union of Immunological Societies (IUIS) and the most cited in its field, leading the way for research across basic, translational and clinical immunology.

Discover the latest Research Topics

See more →

Frontiers

Avenue du Tribunal-Fédéral 34
1005 Lausanne, Switzerland
frontiersin.org

Contact us

+41 (0)21 510 17 00
frontiersin.org/about/contact